4 May 2007 | S10

Science

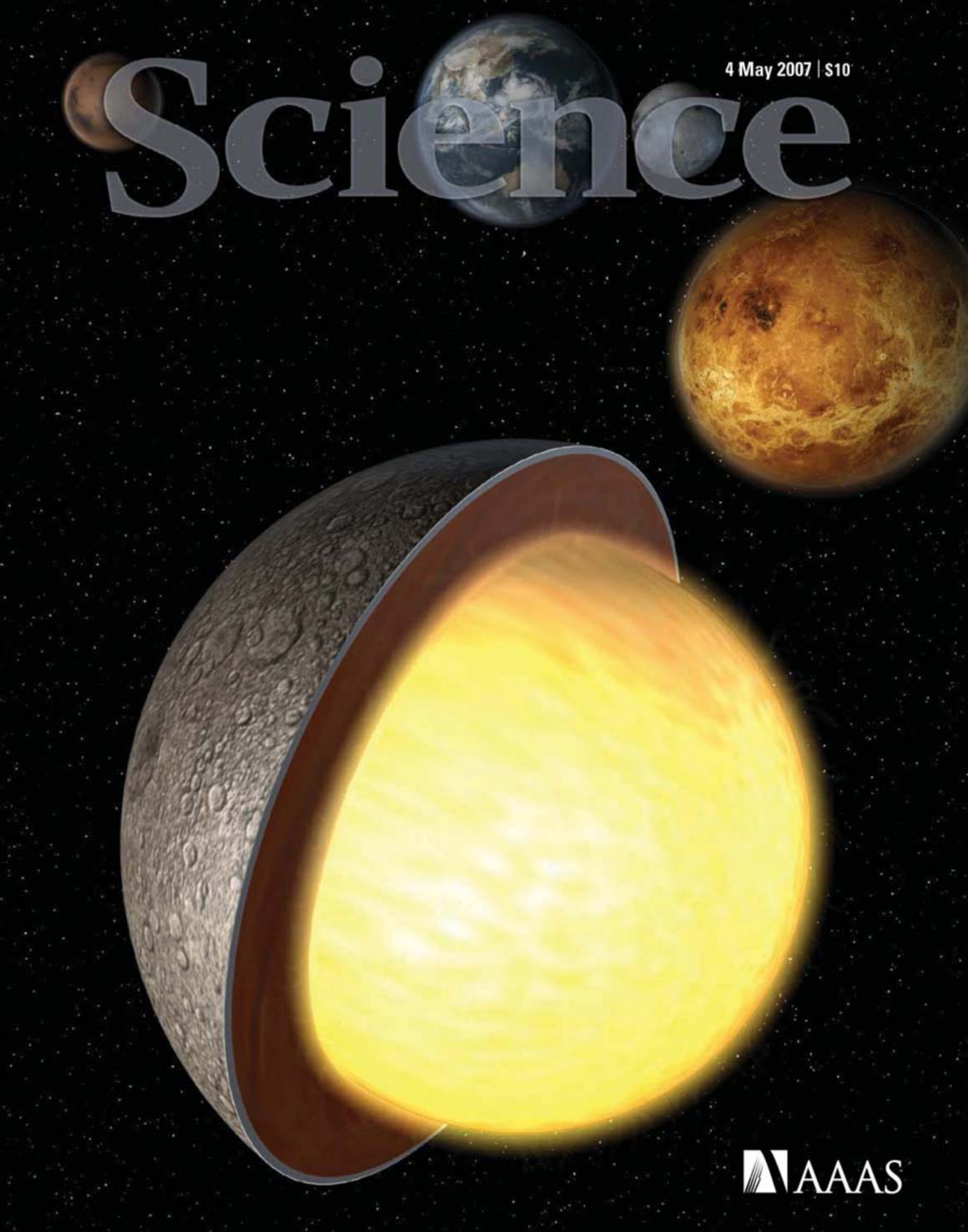

AAAS

Numbers Don't Lie

Greater than 400
IVIS Imaging Systems

Installed in 25 Countries
Around the World

More than 360 Peer
Reviewed Publications

Numbers don't lie – Caliper is the world leader in optical imaging.

Caliper offers the most comprehensive suite of imaging instrumentation and reagents, including the new XenoFluor fluorescence imaging kits – delivering the most complete in vivo imaging solution available.

To find out more visit
ASM General Meeting,
May 21st – 25th,
Toronto, Canada
Booth 238

What's in your lab?
www.xenogen.com/numbers

Caliper LifeSciences

XENOGEN
now part of Caliper Life Sciences

Believe it!

DNA Sequencing for $2.50 per reaction.

- Read length up to 900 bases.
- High quality electropherograms.
- Fast turnaround.
- Plasmid and PCR purification available.

$2.50 per reaction!

POLYMORPHIC
Polymorphic DNA Technologies, Inc.℠

Polymorphic exclusively uses ABI 3730XL sequencers.
Data delivered via secure FTP, email or CD.
No charge for standard sequencing primers.
384 sample minimum order.
96 well plates only—no tubes.

www.polymorphicdna.com
info@polymorphicdna.com

1125 Atlantic Ave., Ste. 102
Alameda, CA 94501

888.362.0888

For more information please visit www.polymorphicdna.com

For research use only. © Polymorphic DNA Technologies, 2005

GE Healthcare

ÄKTA™

100,000 scientists working with proteins believe in ÄKTA, UNICORN and wizards.

To 100,000 scientists worldwide, ÄKTA™ sets the standard in protein purification. All systems in the ÄKTAdesign™ family work with intelligent UNICORN™ software, which makes it easy to control every stage of your purification process. But we're never content to stand still. The result is products like ÄKTAxpress™, which can solve low expression and double-tagged protein purification challenges, and ÄKTApurifier™, a time-saving automated protein purification system that can be configured to suit your personal application and workflow needs.

By continually developing technology that can turn your scientific ideas into reality, we're bringing science to life and helping transform healthcare.

We call it Protein Separations Re-imagined.

Discover the legendary purification power of UNICORN and ÄKTA, visit www.gehealthcare.com/akta

imagination at work

GE Healthcare Bio-Sciences AB, a General Electric Company.
Björkgatan 30, 751 84 Uppsala, Sweden
© 2007 General Electric Company – All rights reserved.
GE09-06. First printed 2006

Volume 316, Issue 5825

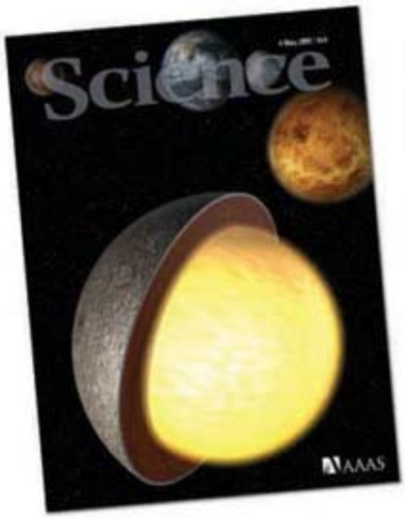

COVER

Artist's conception of Mercury, with a cutaway showing the molten core revealed by high-precision radar data. This finding will help to understand the internal structure, thermal evolution, and magnetic field generation of terrestrial planets. Mercury's surface is from Mariner 10 images. See page 710.

Image: Christopher Bickel/Science

DEPARTMENTS

655 *Science* Online
657 This Week in *Science*
662 Editors' Choice
666 Contact *Science*
669 Random Samples
671 Newsmakers
762 New Products
763 *Science* Careers

EDITORIAL

661 Turning the Tables with Mary Jane
by Donald Kennedy

NEWS OF THE WEEK

Congress Gives Rousing Support to Cluster of Innovation Bills 672
European Research Council Deluged After First Call for Proposals 672
Deep Ringing of the Sun Hints at a Speedy Core 673
>> Science *Express Report by R. A. García* et al.
DOE Cures Pork Project With Peer Review 674
European Union Outlines Vision for Unifying Space Policy 675
SCIENCESCOPE 675
Report Urges More Coordination to Improve Science and Math 676
Long-Awaited Genetic Nondiscrimination Bill Headed for Easy Passage 676
Inquest Flags Little-Known Danger of High-Containment Labs 677

NEWS FOCUS

A World Without Corals? 678
Fractured Paradise
Palau Combats Coral Bleaching
Thymosins: Clinical Promise After a Decades-Long Search 682
Science in Zimbabwe: Researchers Struggle to Adapt to Economic, Political Turmoil 684
Variable Evolution 686

LETTERS

An Intelligent Crow Beats a Lab *A. Straub* 688
Prototype Resilient, Self-Modeling Robots
J. Schmidhuber Response *H. Lipson, V. Zykov, J. Bongard*
Can a Nuclear Weapon Really Be "Safer"? *M. Neuschatz*
Using Radiocarbon Dating in Jerusalem *E. Boaretto*
Oops, That's Not Really a Diamond *A. P. Whipple*
Coal's Future: Clearing the Air *G. H. Rau and K. Caldeira*
CORRECTIONS AND CLARIFICATIONS 691

BOOKS *ET AL.*

The Cigarette Century The Rise, Fall, and Deadly Persistence of the Product That Defined America 692
A. M. Brandt, reviewed by R. N. Proctor
High Tech Trash Digital Devices, Hidden Toxics, and Human Health 693
E. Grossman, reviewed by R. Nagle

POLICY FORUM

Environmental Biology and Human Disease 695
D. Schwartz and F. Collins

PERSPECTIVES

Dance of the Embryo 697
R. R. Behringer
>> *Research Article p. 719*
How Nanowires Grow 698
V. Schmidt and U. Gösele
>> *Report p. 729*
The New Face of Catalysis 699
D. L. Feldheim
>> *Report p. 732*
Signaling to the Nucleus with a Loaded GUN 700
D.-P. Zhang
>> *Research Article p. 715*
Hot News on Mercury's Core 702
S. C. Solomon
>> *Research Article p. 710*
Photosynthesis from the Protein's Perspective 703
S. S. Skourtis and D. N. Beratan
>> *Report p. 747*

693

CONTENTS continued >>

QIAcube — pure efficiency

New

Winner of the New Product Award (NPA) Designation of the Association for Laboratory Automation (ALA) 2007

reddot design award winner 2007

reddot design award product design 2007

- Eliminate manual processing steps
- Continue to use trusted QIAGEN spin-column kits
- Free up your time with affordable, automated sample preparation
- Purify DNA, RNA, or proteins from up to 12 samples per run
- Standardize your results and increase your productivity

Contact QIAGEN today or visit www.qiagen.com/MyQIAcube .

QIAGEN®

Sample & Assay Technologies

AUTOQIAcube04075 1WW

Science

CONTENTS

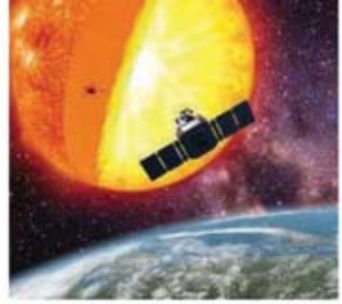

SCIENCE EXPRESS

www.sciencexpress.org

GENETICS

A Common Allele on Chromosome 9 Associated with Coronary Heart Disease
R. McPherson et al.
10.1126/science.1142447

A Common Variant on Chromosome 9p21 Affects the Risk of Myocardial Infarction
A. Helgadottir et al.
10.1126/science.1142842

About one of every four Caucasians carries a sequence variation at a regulatory region of chromosome 9 that confers an elevated risk of heart disease.

ASTROPHYSICS

Tracking Solar Gravity Modes: The Dynamics of the Solar Core
R. A. Garcia et al.
Satellite detection of deep buoyancy-driven oscillations within the Sun implies that the solar core is spinning faster than the surrounding radiative zone.
10.1126/science.1140598

>> *News story p. 673*

CELL BIOLOGY

How Synaptotagmin Promotes Membrane Fusion
S. Martens, M. M. Kozlov, H. T. McMahon
A synaptic vesicle protein completes the final steps of membrane fusion by causing membrane curvature when triggered by a pulse of calcium.
10.1126/science.1142614

REVIEW

PHYSICS

Ultracold Neutral Plasmas 705
T. C. Killian

BREVIA

CLIMATE CHANGE

Recent Climate Observations Compared to Projections 709
S. Rahmstorf et al.
Sea level and global mean air temperatures have risen more since 1990 than climate models used in the IPCC predicted, and IPCC projections may underestimate future sea levels.

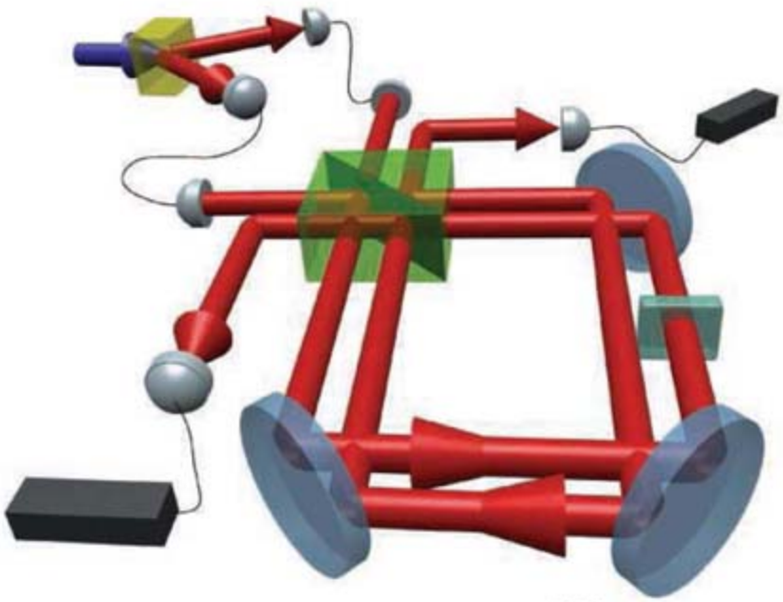

726

RESEARCH ARTICLES

PLANETARY SCIENCE

Large Longitude Libration of Mercury Reveals a Molten Core 710
J. L. Margot, S. J. Peale, R. F. Jurgens, M. A. Slade, I. V. Holin
Radar measurements of Mercury's spin state and the oscillation of its orbit imply that the planet has a partially molten iron core that is decoupled from the mantle.
>> *Perspective p. 702*

PLANT SCIENCE

Signals from Chloroplasts Converge to Regulate Nuclear Gene Expression 715
S. Koussevitzky et al.
In a critical regulatory loop for plants, damaged chloroplasts signal their status to the nucleus via a single signaling pathway and its key component, GUN1.
>> *Perspective p. 700*

DEVELOPMENTAL BIOLOGY

Blastocyst Axis Is Specified Independently of Early Cell Lineage But Aligns with the ZP Shape 719
Y. Kurotaki, K. Hatta, K. Nakao, Y. Nabeshima, T. Fujimori
Time-lapse imaging shows that the axis of the mouse embryo is not specified intrinsically but is influenced by the shape of the overlying zona pellucida.
>> *Perspective p. 697*

REPORTS

PHYSICS

Quantum Coherent Tunable Coupling of Superconducting Qubits 723
A. O. Niskanen et al.
The temporal coupling of two optimally biased qubits can be switched on and off with a third intermediate qubit.

PHYSICS

Beating the Standard Quantum Limit with Four-Entangled Photons 726
T. Nagata, R. Okamoto, J. L. O'Brien, K. Sasaki, S. Takeuchi
Sets of four-entangled photons and their interference patterns can be used to yield precise measurements beyond the assumed limit.

CONTENTS continued >>

HARVARD | BUSINESS | SCHOOL
EXECUTIVE EDUCATION

LEADING SCIENCE-BASED ENTERPRISES

JUNE 26–29, 2007

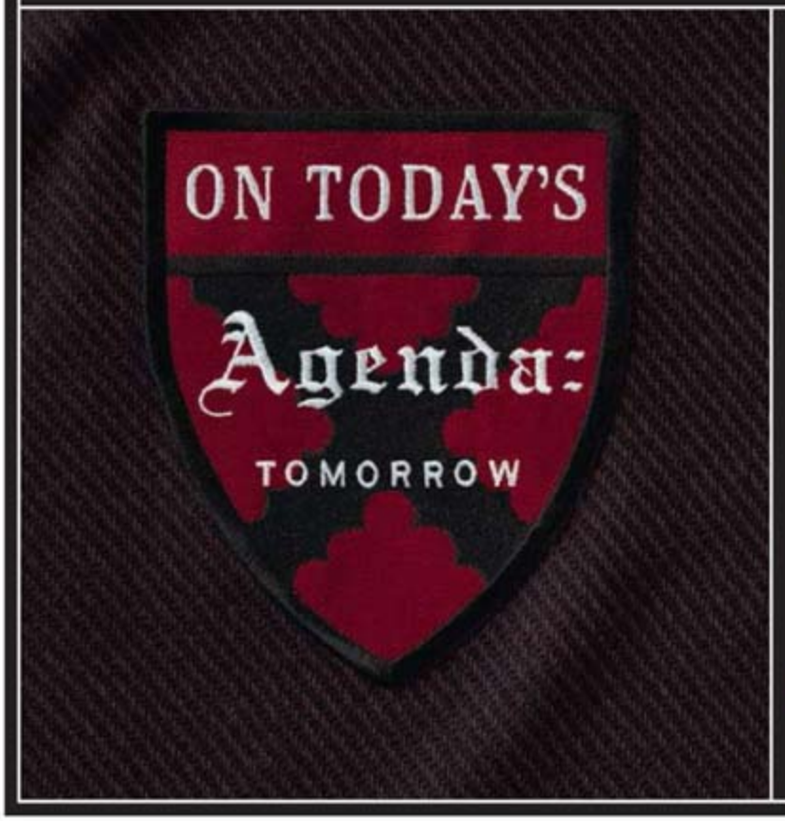

Leadership. Groundbreaking ideas. Bringing products to market. New discoveries in science and technology are not unusual. But only a select number of companies are able to successfully move their research from the lab into the marketplace. Leading Science-Based Enterprises at Harvard Business School is a unique Executive Education program with emphasis on identifying breakthroughs, managing resource-allocation decisions, dealing with financial markets, and retaining top technical and scientific talent.

Learn more at www.exed.hbs.edu/pgm/lsbesm/

4th IAS Conference

ON HIV PATHOGENESIS, TREATMENT AND PREVENTION

www.ias2007.org

International AIDS Society
Stronger Together

in partnership with
ashm

Exhibit at IAS 2007 to reach 5,000 HIV clinicians, researchers and experts
For more information: *exhibitions@ias2007.org*

REPORTS *CONTINUED...*

MATERIALS SCIENCE

Germanium Nanowire Growth Below the Eutectic Temperature 729
S. Kodambaka, J. Tersoff, M. C. Reuter, F. M. Ross
Semiconductor nanowires can be grown using liquid or solid catalysts at temperatures below that of a stable liquid.
>> *Perspective p. 698*

CHEMISTRY

Synthesis of Tetrahexahedral Platinum Nanocrystals with High-Index Facets and High Electro-Oxidation Activity 732
N. Tian, Z.-Y. Zhou, S.-G. Sun, Y. Ding, Z. L. Wang
Electrochemical synthesis converts larger platinum nanospheres on glassy carbon electrodes into nanocrystals with up to 24 faces, providing a higher catalytic activity.
>> *Perspective p. 699*

GEOGRAPHY

Roadless Space of the Conterminous United States 736
R. D. Watts et al.
Converting the average distance to any road within a landscape into a volume metric yields a measure of roadless space for use in ecology and urban planning.

PLANETARY SCIENCE

Pyroclastic Activity at Home Plate in Gusev Crater, Mars 738
S. W. Squyres et al.
The Mars Exploration Rover Spirit has mapped rocks in an exposed impact crater that formed from a volcanic explosion, perhaps when basaltic magma met subsurface water.

ECOLOGY

Local Replenishment of Coral Reef Fish Populations in a Marine Reserve 742
G. R. Almany et al.
A surprisingly large fraction (~60%) of larvae from coral reef fish return to their home reef after dispersal.

MOLECULAR BIOLOGY

Developmentally Regulated piRNA Clusters Implicate MILI in Transposon Control 744
A. A. Aravin et al.
A small class of RNA found only in the germ line helps to suppress transposons—parasitic DNA elements—in mice, as they do in *Drosophila*.

BIOCHEMISTRY

Protein Dynamics Control the Kinetics of Initial Electron Transfer in Photosynthesis 747
H. Wang et al.
The initial charge separation in photosynthesis is limited by protein motion, rather than by a static electron transfer rate.
>> *Perspective p. 703*

BIOMEDICINE

Reducing Endogenous Tau Ameliorates Amyloid β–Induced Deficits in an Alzheimer's Disease Mouse Model 750
E. D. Roberson et al.
Mice with cognitive deficits resembling Alzheimer's disease show improvement when levels of a protein found in neurofibrillary tangles are transgenically reduced.

IMMUNOLOGY

Regulation of NF-κB Activation in T Cells via Association of the Adapter Proteins ADAP and CARMA1 754
R. B. Medeiros et al.
An adapter protein that links antigen activation of immune cells to cell adhesion also acts through a signaling protein complex to induce immune response genes.

NEUROSCIENCE

Specialized Inhibitory Synaptic Actions Between Nearby Neocortical Pyramidal Neurons 758
M. Ren, Y. Yoshimura, N. Takada, S. Horibe, Y. Komatsu
Unexpectedly, the main excitatory neurons in the mouse cortex strongly inhibit each other via axon-to-axon activation of inhibitory interneurons.

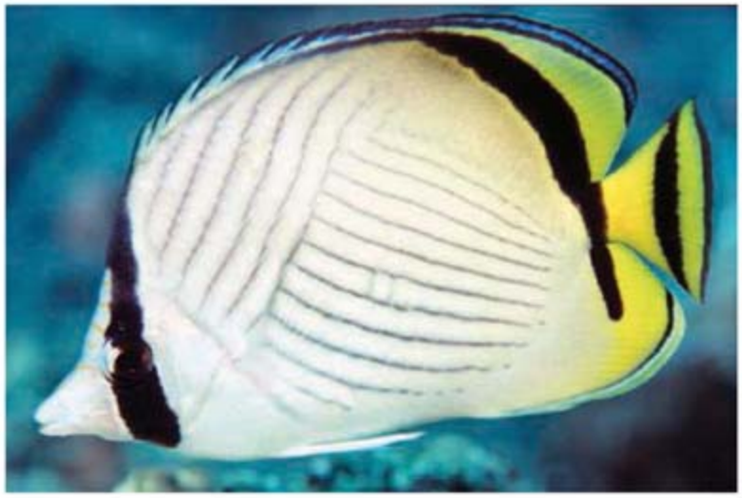

742

AAAS
ADVANCING SCIENCE, SERVING SOCIETY

SCIENCE (ISSN 0036-8075) is published weekly on Friday, except the last week in December, by the American Association for the Advancement of Science, 1200 New York Avenue, NW, Washington, DC 20005. Periodicals Mail postage (publication No. 484460) paid at Washington, DC, and additional mailing offices. Copyright © 2007 by the American Association for the Advancement of Science. The title SCIENCE is a registered trademark of the AAAS. Domestic individual membership and subscription (51 issues): $142 ($74 allocated to subscription). Domestic institutional subscription (51 issues): $710; Foreign postage extra: Mexico, Caribbean (surface mail) $55; other countries (air assist delivery) $85. First class, airmail, student, and emeritus rates on request. Canadian rates with GST available upon request, GST #1254 88122. Publications Mail Agreement Number 1069624. **Printed in the U.S.A.**

Change of address: Allow 4 weeks, giving old and new addresses and 8-digit account number. **Postmaster:** Send change of address to AAAS, P.O. Box 96178, Washington, DC 20090–6178. **Single-copy sales:** $10.00 current issue, $15.00 back issue prepaid includes surface postage; bulk rates on request. **Authorization to photocopy** material for internal or personal use under circumstances not falling within the fair use provisions of the Copyright Act is granted by AAAS to libraries and other users registered with the Copyright Clearance Center (CCC) Transactional Reporting Service, provided that $18.00 per article is paid directly to CCC, 222 Rosewood Drive, Danvers, MA 01923. The identification code for *Science* is 0036-8075. *Science* is indexed in the *Reader's Guide to Periodical Literature* and in several specialized indexes.

CONTENTS continued >>

Institutional Site License Available

Q What can *Science* STKE give me?

A The definitive resource on cellular regulation

STKE – Signal Transduction Knowledge Environment offers:

- A weekly electronic journal
- Information management tools
- A lab manual to help you organize your research
- An interactive database of signaling pathways

STKE gives you essential tools to power your understanding of cell signaling. It is also a vibrant virtual community, where researchers from around the world come together to exchange information and ideas. For more information go to www.stke.org

To sign up today, visit promo.aaas.org/stkeas

Sitewide access is available for institutions.
To find out more e-mail stkelicense@aaas.org

Science stke AAAS

SCIENCENOW

www.sciencenow.org DAILY NEWS COVERAGE

The Handy Way of Speaking
Flexibility of ape hand gestures gives clues to evolution of language.

Life Faces Cosmic Energy Crisis
Physicists foresee a bleak future for living things in the universe.

Small Organism, No Small Feat
Unicellular alga regulates its genes just like plants and animals do.

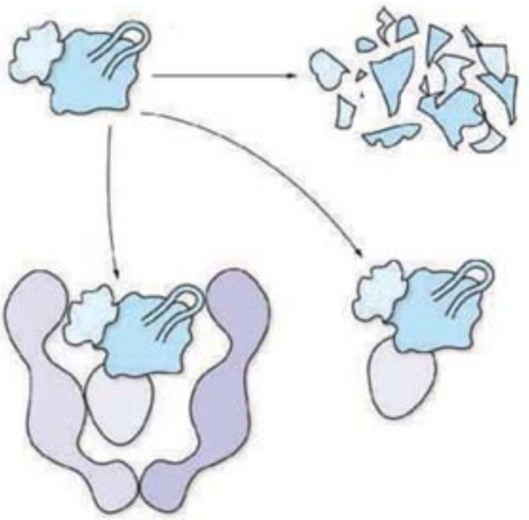

Chaperoning kinases.

SCIENCE'S STKE

www.stke.org SIGNAL TRANSDUCTION KNOWLEDGE ENVIRONMENT

PERSPECTIVE: Cdc37 Regulation of the Kinome—When to Hold 'Em and When to Fold 'Em
L. M. Karnitz and S. J. Felts
The chaperone Cdc37 may play a key role in chaperoning most of the protein kinases in yeast.

GLOSSARY
New terms include STEP (a phosphatase), MAVS (an adapter), and AhR (a receptor).

A physicist airs his music.

SCIENCE CAREERS

www.sciencecareers.org CAREER RESOURCES FOR SCIENTISTS

SPAIN: Dancing with the Mysterious Lady
E. Pain
A passion for music led physicist Sebastián Grinschpun to become a science communicator in Spain.

US: A Tunnel to Atlanta
B. Benderly
Ethnic networks help channel international graduate students and postdocs to American labs.

US: Responding to Violence in Schools
P. Shulman
Aaron Kupchik studies school violence and concludes that the cure is often worse than the disease.

UK: From the Archives—Ask Dr. Bridget
K. Arney
An erstwhile agony aunt offers irreverent advice for women working in science laboratories.

GRANTSNET: May 2007 Funding News
GrantsNet Staff
Learn about the latest research funding, scholarships, fellowships, and internships.

SCIENCEPODCAST

Listen to the 4 May *Science* Podcast to hear about Mercury's molten core, coral reefs in peril, roadless space in the U.S., and more.
www.sciencemag.org/about/podcast.dtl

CREDIT (SCIENCE CAREERS): FERRAN IZQUIERDO

Separate individual or institutional subscriptions to these products may be required for full-text access.

2007/08 NEB catalog & technical reference is now available.

in a word, essential.

www.neb.com

NEW ENGLAND BioLabs® Inc.
the leader in enzyme technology

New England Biolabs Inc.
240 County Road, Ipswich, MA 01938 USA 1-800-NEB-LABS Tel. (978) 927-5054 Fax (978) 921-1350 info@neb.com
Canada Tel. (800) 387-1095 info@ca.neb.com • **China** Tel. 010-82378266 beijing@neb-china.com
Germany Tel. 0800/246 5227 info@de.neb.com • **Japan** Tel. +81 (0)3 5669 6191 info@neb-japan.com
UK Tel. (0800) 318486 info@uk.neb.com
For a complete list of international offices, please visit www.neb.com

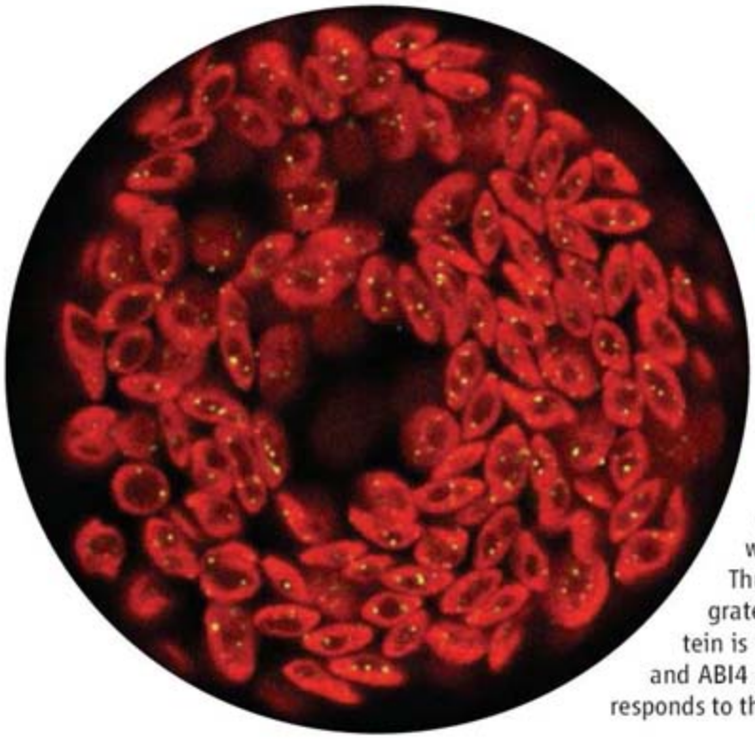

<< Plastid Distress Signal

Plastids, including plant chloroplasts, are built and operated largely under the control of the nuclear genome. Largely, but not exclusively, plastids carry their own residual genome and can talk back when things go awry. **Koussevitzky *et al.*** (p. 715, published online 29 March; see the Perspective by **Zhang**) now show that several signaling pathways that carry news of disaster from the plastid to the nucleus actually converge into one signaling pathway before the news emerges from the chloroplast. Thus, the nucleus receives a coherent report that integrates several aspects of chloroplast function. Gun1 protein is identified as a key integrator within the chloroplast, and ABI4 as a key transcription factor within the nucleus that responds to the news by altering gene transcription.

The Cold Side of Plasmas

Ionized gases, or plasmas, are present throughout the universe over a wide range of densities and temperatures. Some are extremely hot, such as in the Sun's corona; others are very dense plasmas found within white dwarfs. **Killian** (p. 705) reviews recent work on an exotic class of plasmas in which the ions move in a neutralizing background of electrons at low temperatures. The ions undergo a rich variety of collective motions that provide challenges to computational efforts, but may answer some of the current questions about planetary interiors and laser-compressed materials.

Mercury's Molten Core

Mercury is expected to have a metal core and silicate mantle, but thermal models make a wide range of predictions about the physical state of its core. Although the existence of a magnetic field is suggestive of a molten core dynamo, the field could be caused by remnant magnetization. **Margot *et al.*** (p. 710; see the cover and the Perspective by **Solomon**) have used a novel technique of radar speckle interferometry to probe Mercury's rotation dynamics. The planet wobbles in longitude in synchrony with its 88-day orbital period. Couplings between the planet's spin axis, wobble, and orbit suggest that the mantle of Mercury is decoupled from a core that is at least partially molten.

Dynamic Qubit Coupling

Large-scale quantum information processing will require that the interactions between individual qubits be controlled while retaining quantum coherence. Dynamic coupling of the qubits would simplify the circuitry and allow the system to be broken up into smaller units. **Niskanen *et al.*** (p. 723) demonstrate dynamic switching of the coupling of two superconducting flux qubits via a third intermediate qubit, and illustrate the coherence retention by running a quantum algorithm that detects hackers trying to infiltrate the system.

Entangled Quantum Metrology

The use of entangled quantum-mechanical systems is expected to lead to improvements in precision measurements beyond what can be achieved with classical physics techniques. **Nagata *et al.*** (p.726) used sets of four entangled photons to demonstrate how interference measurements can reveal patterns expected of light one-quarter the wavelength of the photon used. Their results open the way for applications to high-precision measurements and the development of quantum metrology with multiple entangled states.

Platinum Nanocrystals with High-Index Facets

For catalytic applications, metals are often used as nanoparticles to increase their surface area and to create a high density of steps and defects that can act as active sites for reactions. Nonetheless, most of a metal nanocrystal's surface is made up of "low index" surfaces such as {111} facets that are flat and relatively free of defects. **Tian *et al.*** (p. 732; see the Perspective by **Feldheim**) report on an electrochemical route that creates tetrahexahedral (THH) platinum nanoparticles (with a diameter of ~100 nanometers) from larger Pt nanospheres that had been deposited on glass carbon electrodes. A series of square-wave redox pulses create these smaller nanocrystals that exhibit 24 high-index facets such as the highly stepped {730} or {530} facets. Relative to the rounded Pt nanospheres, the THH particles exhibit much higher activity for the electro-oxidation of formic acid and ethanol for the same surface area.

Going Off Road

The density and distribution of roads is at the center of major questions in ecology, use of natural resources, and urban and transportation planning. A useful measure for comparison and analysis of change over time needs to be relatively scale independent and sensitive to both the number of roads within an area and their distribution. **Watts *et al.*** (p. 736) developed a metric based on the distance to a road in a defined area, which essentially represents a volume. They have applied this metric, and the per capita equivalent, to all of the counties in the United States.

Continued on page 659

CREDITS (TOP TO BOTTOM): AJT NOTT; USGS

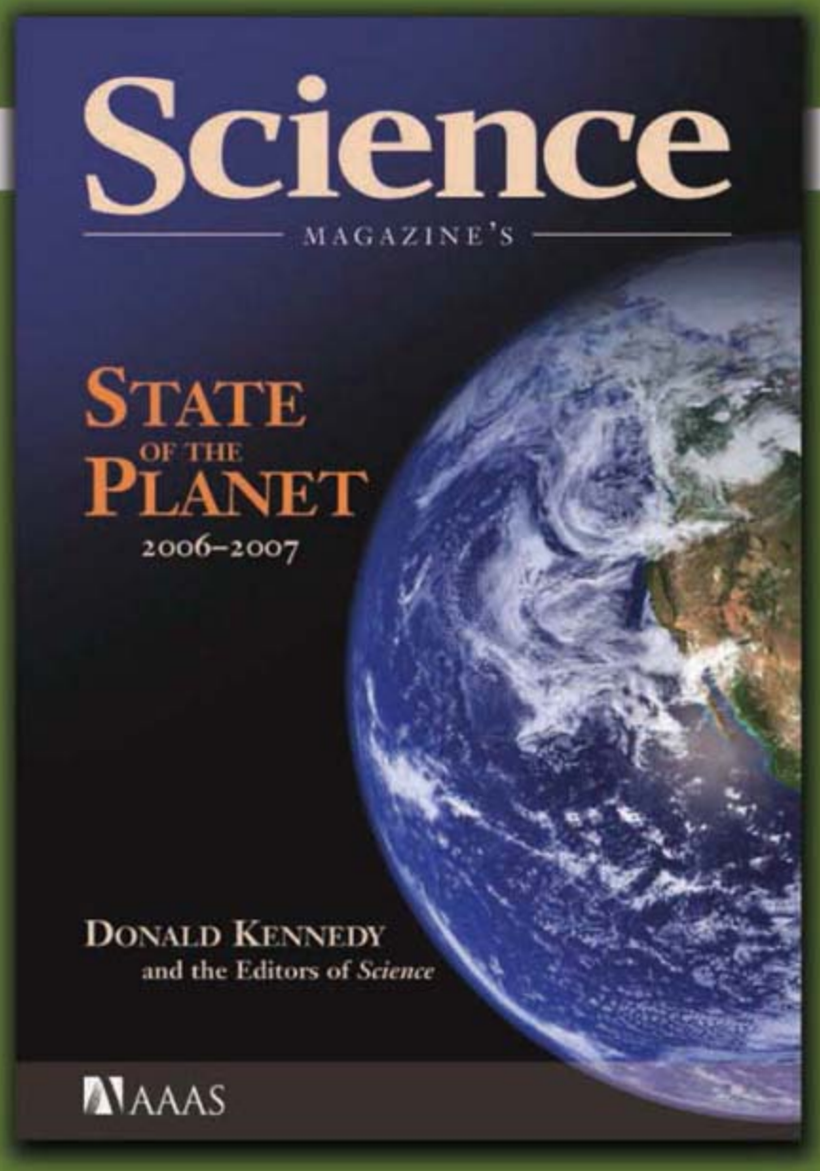

Science Magazine's

State of the Planet 2006-2007

Donald Kennedy, Editor-in-Chief, and the Editors of *Science*

The American Association for the Advancement of Science

The most authoritative voice in science, *Science* magazine, brings you current knowledge on the most pressing environmental challenges, from population growth to biodiversity loss.

COMPREHENSIVE • CLEAR • ACCESSIBLE

ISLANDPRESS

Science
AAAS

islandpress.org

Continued from page 657

Extrinsic Developmental Patterning

Fly, worm, and frog embryos sport maternal factors to specify early asymmetry and axis development, but opinions differ whether asymmetry in the mammalian embryo is prepatterned or if the axis is specified later in development. **Kurotaki *et al.*** (p. 719, published online 19 March; see the Perspective by **Behringer**) used real-time whole-cell tracing and a transgenic mouse line with labeled chromosomes to follow cell lineages in vitro and in vivo. No lineage dependency was observed up to the four-cell stage with regard to the embryo axis; however, cell lineage and the embryonic axis were affected by physical restriction via the zona pellucida. Thus, axis positioning of the early mouse embryo is specified by factors outside the embryo and not by factors within the blastomeres.

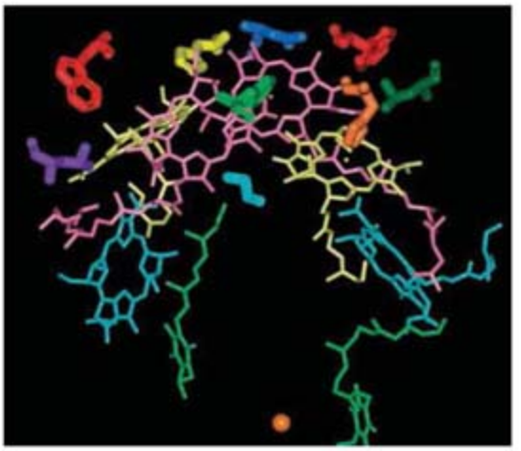

CREDIT: WANG *ET AL.*

Modeling Photosynthetic Energy Conversion

The initial energy conversion step in the photosynthetic reaction center transfers an electron from an excited donor to a neighboring acceptor. The rate of this electron transfer has been difficult to model based on a static barrier between initial and charge-separated states. **Wang *et al.*** (p. 747; see the Perspective by **Skourtis and Beratan**) show that protein dynamics dictates the kinetics. They measured protein relaxation dynamics during electron transfer and could quantitatively fit the electron transfer rates of wild-type and several mutant bacterial reaction centers with a reaction diffusion model for electron transfer that incorporates the dynamics.

Tau Reduction and Cognitive Decline

The brain pathology in Alzheimer's disease involves both neurofibrillary tangles rich in the protein tau and plaques containing amyloid-β peptide (Aβ), but the relative contribution of each to cognitive impairment is unclear. **Roberson *et al.*** (p. 750) find that cognitive and neuronal deficits in two transgenic mouse models of Alzheimer's disease are prevented when endogenous tau production is eliminated or reduced by 50%. The effect of tau reduction was robust, despite the absence of tau mutations, hyperphosphorylation, overexpression, or aggregation into neurofibrillary tangles in these models. Tau reduction did not block plaque-associated neuritic dystrophy, indicating that neuritic dystrophy can be dissociated both from tau and from Aβ-induced cognitive impairments.

Adapting the Adapter

Adapter proteins connect the proteins involved in multiple cell signaling pathways. In T cells, the adapter protein ADAP regulates certain signals from the T cell receptor (TCR) that influence the function of integrin adhesion receptors. **Medeiros *et al.*** (p. 754) found that ADAP also associates directly with another adapter, CARMA1, a membrane-associated protein that couples TCR signaling to the activation of the core transcription factor NF-κB. This association involved the assembly of a multiprotein complex that failed to form in the absence of ADAP and corresponded with impaired NF-κB activity. The study introduces a key new step in regulating the pathway that connects TCR activation with the transcriptional response to infection.

Synaptic Communication

The traditional view of pyramidal neurons, which are excitatory, is that they can only excite their downstream target cells. However, **Ren *et al.*** (p. 758) report that cortical pyramidal neurons can elicit an inhibitory synaptic current in another neighboring pyramidal neuron. These unusual responses were caused by axo-axonic disynaptic connections onto γ-aminobutyric acid (GABA)–releasing terminals located on or near the soma of the postsynaptic pyramidal cell. These so-called interpyramidal inhibitory postsynaptic currents were remarkably large and frequent, which suggests that they play an important role.

PERU
& the Incas
July 29–August 8, 2007

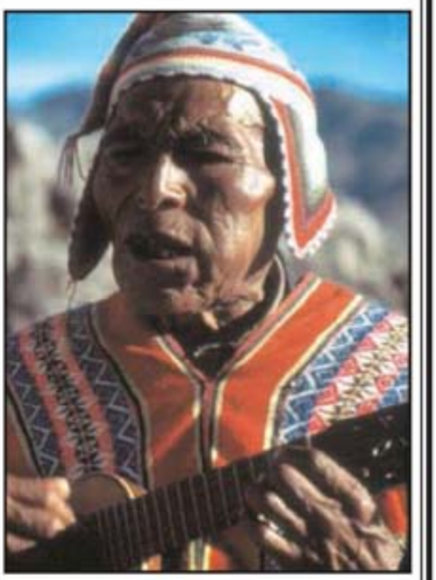

You are invited to join ***Dr. Douglas Sharon****, an expert on Peru, on this 11-day expedition to explore the cultural heritage and scenic wonders of this Andean nation.*

Highlights of the trip include ***Cuzco*** *and* ***Machu Picchu****, heart of the Inca Empire and one of the archaeological wonders of the world. You will also go flightseeing above the 2000-year-old figures of butterflies, hummingbirds, and a condor at the Nazca Lines; see the step pyramids of* ***Pachacamac*** *and the fascinating museums of* ***Lima****.*

Peru has been inhabited by people for at least 12,000 years. Its rich cultural heritage from Chavin to Moche, from Nazca to Inca, is revealed in their jewelry, pottery, weavings, architecture, and agricultural developments. The coastal lowlands have seen numerous cultures flourish, fade, and be assimilated in the next wave of man's quest. $3,695 twin share + air.

For a detailed brochure, please call (800) 252-4910

AAAS *Travels*

17050 Montebello Road
Cupertino, California 95014
Email: AAASInfo@betchartexpeditions.com

Science Alerts in Your Inbox

Get daily and weekly E-alerts on the latest breaking news and research!

This Week in *Science*
Summaries of research content

***Science* Magazine TOC**
Weekly table of contents

***Science* News This Week**
Brief summaries of the journal's news content

***Science* Posting Notification**
Alert when weekly issue is posted

Science*NOW Daily Alert
Daily headline summary

***Science*NOW Weekly Alert**
Weekly headline summary

***Science* Express Notification**
Articles published in advance of print

Editors' Choice
Highlights of the recent literature

STKE TOC
Weekly table of contents

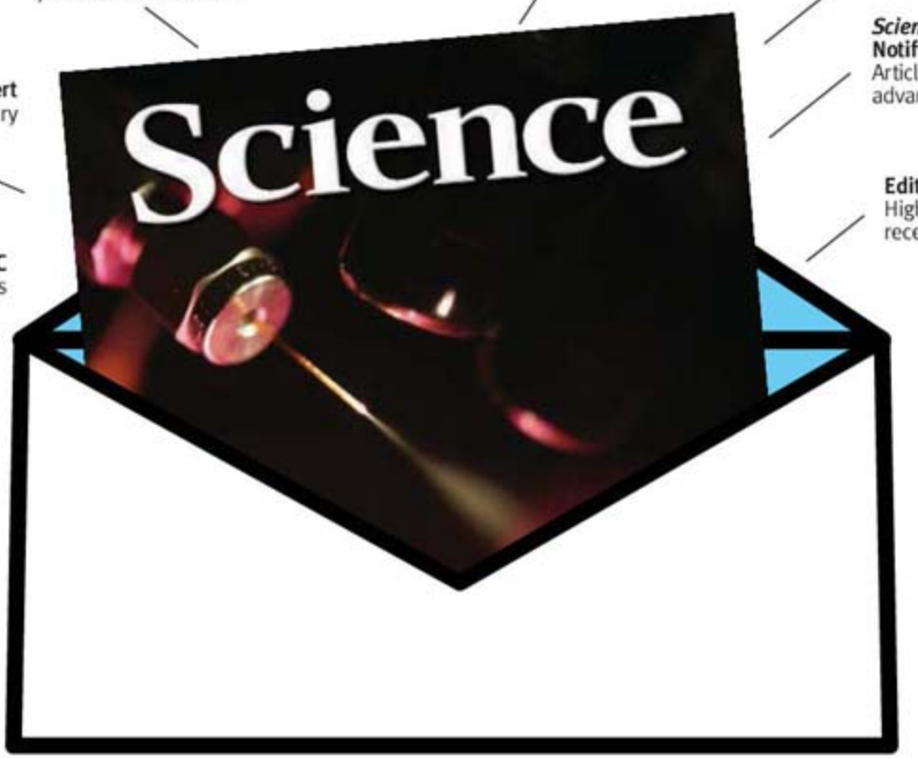

Get the latest news and research from *Science* as soon as it is published. Sign up for our e-alert services and you can know when the latest issue of *Science* or *Science* Express has been posted, peruse the latest table of contents for *Science* or *Science*'s Signal Transduction Knowledge Environment, and read summaries of the journal's research, news content, or Editors' Choice column, all from your e-mail inbox. To start receiving e-mail updates, go to:

http://www.sciencemag.org/ema

Science
AAAS

Donald Kennedy is the Editor-in-Chief of *Science*.

Turning the Tables with Mary Jane

SOME OF THIS IS ABOUT—MARIJUANA. JUST SO YOU'LL KNOW, THERE'S NOTHING IN HERE about what we were all doing back in the day (though of course, we never inhaled). The reason to give marijuana some attention here is a legal case that has wedged open an important chapter in the relationship between law and science. It pits some health activists against a law in the United States called the Data Quality Act (DQA). The turnaround is that DQA has usually helped industry fight off regulation. Not this time; here's the background.

Many basic scientists would be uneasy if their primary data—not what's in their publications, but what's in the lab notebooks—would be available for others to fiddle around with and then publish a different conclusion. But in another scientific culture, that's routine. In the U.S. Food and Drug Administration, where science has regulatory outcomes, inspectors go regularly into labs to look at the books.

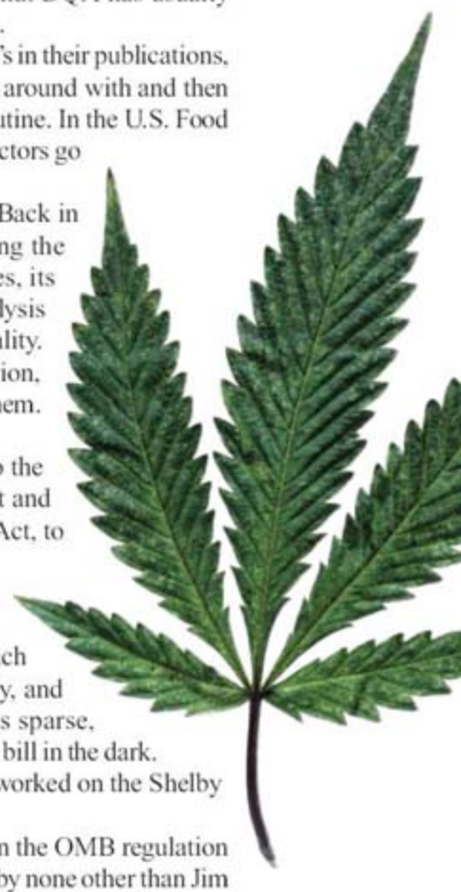

Well, these cultures occasionally merge to generate political action. Back in the '90s when the U.S. Environmental Protection Agency was revising the National Ambient Air Quality Standards for ozone and small particles, its staff used the Six Cities Study, a Harvard School of Public Health analysis demonstrating a correlation between particulate concentrations and mortality. Recognizing that Six Cities could escalate the risk of particulate regulation, industry demanded the primary data tapes so that they could reanalyze them. Harvard said no, but soon Congress took over.

First, Senator Richard Shelby (R-AL) introduced an Amendment to the 1999 Omnibus Appropriation Bill charging the Office of Management and Budget (OMB) to guarantee access, under the Freedom of Information Act, to data produced with the use of federally funded research. After two rounds of rule-making, OMB issued a final order putting the Shelby Amendment in regulatory form. That opened the door to the DQA, an amendment to the Paperwork Reduction Act of 1980. OMB, in response, required each agency to establish guidelines ensuring the "quality, objectivity, utility, and integrity" of information it disseminates. DQA's legislative history is sparse, because like the Shelby Amendment, it was tacked onto an appropriations bill in the dark. Its real author was an industry lobbyist named Jim Tozzi, who had also worked on the Shelby Amendment. Thus, the DQA is often called "Son of Shelby."

It should not surprise us that the DQA has seen heavy use. The ink on the OMB regulation had scarcely dried when the Center for Regulatory Effectiveness, headed by none other than Jim Tozzi, urged its constituents to use DQA to challenge the "junk science" offered to support health and environmental regulation. Naturally, the Center for Progressive Reform exhorted its troops to get active on the other side. Who won? It wasn't even close. By 2004, the Washington Post had counted 39 serious challenges under the DQA, of which 32 had been filed by industry or industry organizations.

Now, back to marijuana. Americans for Safe Access (ASA), a group advocating marijuana availability for severely ill patients needing pain or nausea relief, petitioned the Department of Health and Human Services (HHS) under the DQA in 2004. They alleged that HHS made false statements in its publications and its Web site, in particular that marijuana "has no currently accepted medical use in treatment in the United States." ASA cited an Institute of Medicine study that acknowledged benefits from the use of marijuana and cannabinoid derivatives and referenced double-blind clinical trials demonstrating relief from pain and vomiting. HHS delayed a response for months beyond its own deadline, rejected the petition, and then rejected the appeal.

ASA finally brought its case to federal court, asking it to substitute for the agency's false statement one that says, "Adequate and well-recognized studies show the efficacy of marijuana in the treatment of nausea, loss of appetite, pain and spasticity." Will the judge make HHS change, giving ASA the injunctive relief it seeks? We'll have to wait to see whether this case turns the tables on DQA, but it's already clear that HHS has violated its own DQA guidelines—going, you might say, one toke over the line.

-Don Kennedy

10.1126/science.1143936

CREDIT: GETTY IMAGES

EVOLUTION

Survival Aids

Agarics—fungi that include the common mushroom—are diverse in morphology and in ecological niche: puffballs, gilled mushrooms, decomposers of wood, and mutualistic partners to ants. Alas, tracing their evolutionary radiations has been hampered by the dearth of fossil samples.

Garnica *et al.* have performed a molecular analysis of nuclear genes and a microscopic analysis of agaric spore structures in order to better understand the organization of this group. Using these two features, they rearranged relationships, such that some species were flung apart and others recognized as more closely related than previously thought. It appears that one major evolutionary innovation led to the acquisition of thicker walls and darker pigmentation of the spores. The authors suggest that these sturdier spores were better able to tolerate the relatively harsher conditions on dry land (and, in some cases, in herbivore digestive tracts), where water conservation and resistance to ultraviolet radiation can be a great help. — PJH

Mycol. Res. **111**, 10.1016/j.mycres.2007.03.019 (2007).

CELL BIOLOGY

Outside Inside

In macrophages that have been infected by HIV-1, the newly synthesized virions bud into an intracellular compartment, which has been thought to be derived from endosomes because it contains the endosomal membrane protein CD63. However, there currently is some controversy about the site of viral budding because a variety of viral components are directly targeted to the plasma membrane and because virus assembly has clearly been observed on the surface of infected T cells.

Deneka *et al.* show that, although the budding compartment in macrophages appears at first glance to be intracellular, it is in fact still connected to the cell surface and can be accessed directly from the extracellular milieu. The authors identify several of the membrane proteins—three members of a protein family known as tetraspanins, CD81, CD9, and CD53—that define this unanticipated plasma membrane domain, and confirm that a similar compartment exists in uninfected cells. These membrane-delimited structures were accessible to two membrane-impermeant molecules (horseradish peroxidase and ruthenium red) added to the external medium and also to antibodies (as long as the cells were kept at 4°C to prevent active uptake). These findings are consistent with recent work by Welsch *et al.* and by Jouvenet *et al.* that together support the notion that HIV normally buds from the plasma membrane during productive infection. — SMH

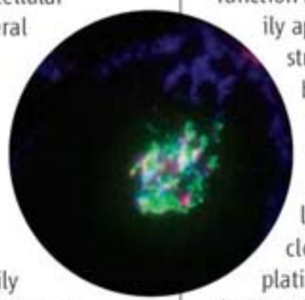

"Intracellular" compartments accessible to horseradish peroxide (blue) and anti-CD81 (red) contain virus (green).

J. Cell Biol. **177**, 329 (2007); *PLoS Pathog.* **3**, e36 (2007); *PLoS Biol.* **4**, e435 (2006).

CHEMISTRY

A Material Difference for DFT

The accuracy of density functional theory (DFT) calculations, which is limited by the approximate treatment of the exchange-correlation (XC) functional, can be tested for small systems by wave-function methods. In systems too large to easily apply such a test, especially those with strong electron correlations, it has often been hoped that the errors in total energies would cancel out when differences were evaluated. An example where this cancellation fails is the low-coverage adsorption of CO on close-packed surfaces of copper and platinum, for which DFT calculations favor the threefold hollow site over the experimentally determined "on top" site (binding to just one metal atom) by at least 0.4 eV. Hu *et al.* performed high-level quantum chemistry calculations on small metal clusters (copper and silver) to evaluate the XC energy error of DFT. The XC correction (the difference between the energy from DFT and that from the higher method) varies for different methods and continues to change as cluster size increases. However, because of the short-range nature of this error, the differences in the XC correction between different types of sites on the cluster converge to a constant at cluster sizes as small as ~20 atoms. By applying this correction to the DFT results, the authors obtained the correct on-top site preference for CO on copper, as well as the correct result for silver. This approach can also be applied to bulk systems and defects. — PDS

Phys. Rev. Lett. **98**, 176103 (2007).

BIOCHEMISTRY

Through the Side Door

The hydrolysis of peptide bonds is a commonplace biochemical reaction and is catalyzed by innumerable proteases and peptidases, most of which have excruciatingly well-documented mechanisms. Because both of the reaction substrates are hydrophilic, it is not surprising that these enzymes are found and do function in aqueous compartments; a handful of proteases are, however, integral membrane proteins. Recent structural descriptions of the bacterial enzyme GlpG have placed the catalytic serine residue at a depth of about 10 Å beneath the surface of the lipid bilayer, which fits with the predicted location of the hydrolyzed peptide bonds in known intramembrane protease substrates.

Baker *et al.* have mutated carefully chosen

CREDITS (TOP TO BOTTOM): GARNICA *ET AL.*, *MYCOL. RES.* **111**, 10.1016/J.MYCRES.2007.03.019 (2007); DENEKA *ET AL.*, *J. CELL BIOL.* **177**, 329 (2007).

residues in GlpG and assessed the ability of the mutants to cleave the *Drosophila* protein Spitz, which is the substrate of the *Drosophila* intramembrane protease Rhomboid. They find that the substrate is likely to gain access, not by lifting the lidlike L1 loop on top of the active site, but by entering from within the lipid bilayer via a displacement of transmembrane helix 5, in a manner that is reminiscent of the translocon-mediated expulsion of newly synthesized membrane proteins. — GJC

Proc. Natl. Acad. Sci. U.S.A. 10.1073/pnas.0700814104 (2007).

CHEMISTRY

Water Lends a Hand

Although the global chirality of molecular aggregates is strongly influenced by the individual chirality of the building blocks, it is not generally a simple matter to predict one from the other. In a series of careful experiments, Johnson *et al.* uncover the subtle environmental factors that determine the helical handedness of rosette nanotubes assembled in solution from small organic heterocycles bearing a chiral side chain. The heterocycles (which are self-complementary toward hydrogen bonding) first form hexameric supermacrocycles, which in turn stack into a helical arrangement. Dissolution of a single enantiomer of this building block in methanol gives rise to one helical isomer, but addition of as little as 1% water to the solvent instead induces opposite helicity in the stacks. The authors show that the water-induced product is thermodynamically favored, but faces a larger kinetic barrier than its counterpart to formation in pure methanol (though aggregation in both senses appears to be accelerated in the absence of water). They further find that chiral inversion of the kinetic isomer in methanol can be catalyzed by the thermodynamic isomer. Inversion is also possible at an early stage by heating, though after 3 days the kinetic isomer becomes stereochemically locked, a result attributed in part to extensive solvation. — MSL

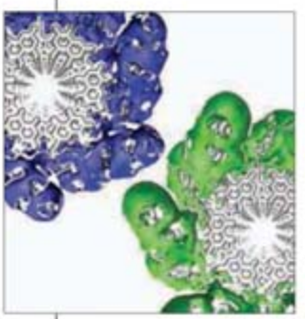

Rosette helical stacks.

J. Am. Chem. Soc. **129**, 5735 (2007).

CREDIT: JOHNSON *ET AL.*, *J. AM. CHEM. SOC.* **129**, 5735 (2007)

Science stke AAAS

www.stke.org

<< miRNAs Have Big Effects in the Heart

MicroRNAs (miRNAs) are important regulators of gene expression during development, through their ability to turn off the translation of targeted mRNAs. Two studies describe how miRNAs contribute to heart development and physiology [see also van Rooij *et al.*, *Science* **316**, 575 (2007)]. Yang *et al.* show that *miR-1* abundance increases in patients with coronary heart disease and in rat models of cardiac infarction (heart attack), specifically in the ischemic area relative to the expression in the nonischemic area. Arrhythmias often occur after a heart attack and, in the rat model, delivery of an antisense oligonucleotide (which decreases the abundance of *miR-1* in the myocardium) decreased postinfarct arrhythmias. Conversely, overexpression of *miR-1* increased the occurrence of postinfarct arrhythmias and promoted arrhythmia in healthy hearts. The pathophysiology appeared to result from slowed conduction and depolarization of the heart, which were reversed by treatment with the *miR-1* antisense oligonucleotide. Sequences complementary to *miR-1* were present in the 3′-untranslated regions of the transcripts for the Kir2.1 subunit of the potassium channel, which is primarily responsible for setting the resting membrane potential, and for the connexin 43 gap junction protein. Indeed, these two proteins were less abundant in rats that had experienced myocardial infarction, and this drop was eliminated if the rats were treated with the antisense oligonucleotide to *miR-1*. To verify that these two proteins were responsible for the arrhythmias, each was knocked down by RNA interference, and this caused arrhythmias in ischemic hearts.

Zhao *et al.* examined the role of *miR-1-2* in heart development and found that homozygous knockout mice showed an increased occurrence of death due to ventricular septal defects, which may have been the result of increased abundance of the transcription factor Hand2 (a key regulator of cardiac morphogenesis). Mice that survived exhibited cardiac hyperplasia due to an increased number of postnatal cells undergoing cell division. These mice also exhibited cardiac arrhythmias, which appeared to be due to altered potassium channel abundance as a consequence of increased abundance of the transcription factor Irx5 (a repressor of the potassium channel gene *Kcnd2*). — NRG

Nat. Med. **13**, 486 (2007); *Cell* **129**, 303 (2007).

Q: How can I organize and protect my back issues of *Science*?

A: Custom-made library file cases!

Designed to hold 12 issues, these handsome storage boxes are covered in a rich burgundy leather-like material. Each slipcase includes an attractive label with the *Science* logo.

Great gift idea!

One $15
Three $40
Six $80

Order Form

TNC Enterprises Dept.SC
P.O. Box 2475
Warminster, PA 18974

Please send me _____ slipcases.

Add $3.50 per slipcase for postage and handling. PA residents add 6% sales tax. Cannot ship outside U.S.

Name *(Please print)*

Address *(No P.O. Box numbers please)*

City, State, Zip

Bill my: ☐ Master Card ☐ VISA ☐ AmEx

Name

Card No. Exp. Date

Signature

Order online:
www.tncenterprises.net/sc

Unconditionally Guaranteed

SPOTLIGHT: SINGAPORE

Dr. Judith Swain Leads the Singapore Institute for Clinical Sciences

Professor Judith L. Swain is the founding Executive Director of the Singapore Institute for Clinical Sciences (a research institute of the Agency for Science, Technology and Research, A*Star). Widely regarded as one of the world's leading molecular cardiologists, she served as Professor of Medicine, Dean for Translational Medicine and the Founding Director of the College of Integrated Life Sciences at University of California San Diego. Prior to her tenure at UCSD, she served as Arthur Bloomfield Professor and Chair of the Department of Medicine at the Stanford University School of Medicine. Professor Swain's research interest has been in cardiovascular system development and now includes human performance in extreme and complex environments.

Q&A

What unique opportunities does Singapore present for biomedical research?

The biomedical research effort in Singapore is unique in several ways. First and foremost, there is a clear and long-term commitment by the government to the biomedical research enterprise. Second, there is an excellent basic research community already in place, and the facilities and resources to support these investigators.

What is Singapore's advantage?

Clinical and translational research requires a coordinated effort between the basic research institutes, medical schools and hospitals and the biotechnology and pharmaceutical industries. Singapore is small and nimble enough to bring these different components together in a way that is difficult, if not impossible, to do in other places.

What else about Singapore attracted you to the country?

There is a "can do" attitude in Singapore that is infectious. Also, the people I work with are wonderful and have been terrific about introducing us to the culture of Singapore. I've spent the last 25 years recruiting physician investigators and building translational and clinical research programs. The move to Singapore allows me to help develop programs in a region of the world that is rapidly growing and where there is a strong commitment to building and supporting the biomedical research enterprise.

Please tell us about the Singapore Institute for Clinical Sciences (SICS)?

The goal of this new A*STAR institute is to become a bridge for research programs between the other more basic research institutes in A*STAR and the medical schools and hospitals in Singapore. For instance, a new program in our institute will focus on metabolic diseases such as diabetes and obesity, and will span from laboratory-based studies to studies in humans.

Translational medicine is one of today's hot buttons. How do you see scientists in Singapore contributing to its development?

I define translational medicine as a two-way process — utilizing knowledge gained from the laboratory to develop new therapies and diagnostic agents, as well as utilizing the knowledge gained from studying patients to better understand disease processes. The strong basic science carried out in Singapore, together with outstanding medical care provided by clinicians and clinician investigators and strong public and private support for research, provide all the ingredients necessary for success in translational research. Additionally, Singapore is uniquely suited to play a leading role in understanding diseases that have a high incidence in Asians and in developing therapies to treat these diseases.

Who are some of the scientists you look forward to working with in Singapore?

As I am fond of saying, clinical and translational research is a team sport. I have already met a number of scientists — basic scientists, clinician investigators, engineers — at A*STAR and the medical schools and very much enjoy working with a wide range of people here.

Are there other areas of research in Singapore that you feel are particularly significant?

I'm impressed with the physical and computer sciences in Singapore. The students as a whole are well versed in math and science and there is real excitement about undertaking quantitative science. Young scholars in Singapore have an advantage over those in other places because of the strength of math and science education in the schools.

What role have opportunities in stem cell research played in your decision to move?

Singapore's approach to stem cell research is an excellent indication of Singapore's approach to science in general: study the issues, provide a strong ethical framework in which to work, and then get going. It is nice to see a country able to articulate the issues, develop a plan and then carry out that plan in a timely fashion.

How will Singapore's Biopolis complex help further your research? What do you like about the Biopolis?

The Biopolis is a wonderful facility in which to do science. The laboratories and equipment are state of the art. But the best thing about the Biopolis is the people — wonderful and inquisitive trainees, excellent staff and strong lead scientists.

Biopolis, Singapore's biomedical sciences hub

See you in Singapore at:

Healthcare Information & Management Systems Society (HIMSS)
May 15-18, 2007
www.himssasiapac.org

27th International Epilepsy Conference
July 8-12, 2007
www.epilepsysingapore2007.org

AIGS World Glaucoma Congress
July 18-21, 2007
www.globalaigs.org

18th WONCA World Conference, Genomics & Family Medicine
July 24-27
www.wonca2007.com

American Association for Cancer Research (AACR) Centennial Conference: Translational Cancer Medicine
November 4-8, 2007
www.aacr.org

World Healthcare Congress Asia 2008
www.worldcongress.com

For more information, contact:

Singapore Exhibition & Convention Bureau

1156 Avenue of the Americas
Suite 702
New York, NY 10036
(212) 302-4861
newyork@stb.gov.sg

5670 Wilshire Blvd.
Suite 1550
Los Angeles, CA 90036
(323) 677-0808
losangeles@stb.gov.sg

www.visitsingapore.com/businessevents

www.sciencemag.org

Science

1200 New York Avenue, NW
Washington, DC 20005
Editorial: 202-326-6550, FAX 202-289-7562
News: 202-326-6581, FAX 202-371-9227

Bateman House, 82-88 Hills Road
Cambridge, UK CB2 1LQ
+44 (0) 1223 326500, FAX +44 (0) 1223 326501

SUBSCRIPTION SERVICES For change of address, missing issues, new orders and renewals, and payment questions: 866-434-AAAS (2227) or 202-326-6417, FAX 202-842-1065. Mailing addresses: AAAS, P.O. Box 96178, Washington, DC 20090-6178 or AAAS Member Services, 1200 New York Avenue, NW, Washington, DC 20005

INSTITUTIONAL SITE LICENSES please call 202-326-6755 for any questions or information

REPRINTS: Author Inquiries 800-635-7181
Commercial Inquiries 803-359-4578

PERMISSIONS 202-326-7074, FAX 202-682-0816

MEMBER BENEFITS Bookstore: AAAS/BarnesandNoble.com bookstore www.aaas.org/bn; Car purchase discount: Subaru VIP Program 202-326-6417; Credit Card: MBNA 800-847-7378; Car Rentals: Hertz 800-654-2200 CDP#343457, Dollar 800-800-4000 #AA1115; AAAS Travels: Betchart Expeditions 800-252-4910; Life Insurance: Seabury & Smith 800-424-9883; Other Benefits: AAAS Member Services 202-326-6417 or www.aaasmember.org.

science_editors@aaas.org	(for general editorial queries)
science_letters@aaas.org	(for queries about letters)
science_reviews@aaas.org	(for returning manuscript reviews)
science_bookrevs@aaas.org	(for book review queries)

Published by the American Association for the Advancement of Science (AAAS), *Science* serves its readers as a forum for the presentation and discussion of important issues related to the advancement of science, including the presentation of minority or conflicting points of view, rather than by publishing only material on which a consensus has been reached. Accordingly, all articles published in *Science*—including editorials, news and comment, and book reviews—are signed and reflect the individual views of the authors and not official points of view adopted by the AAAS or the institutions with which the authors are affiliated.

AAAS was founded in 1848 and incorporated in 1874. Its mission is to advance science and innovation throughout the world for the benefit of all people. The goals of the association are to: foster communication among scientists, engineers and the public; enhance international cooperation in science and its applications; promote the responsible conduct and use of science and technology; foster education in science and technology for everyone; enhance the science and technology workforce and infrastructure; increase public understanding and appreciation of science and technology; and strengthen support for the science and technology enterprise.

INFORMATION FOR AUTHORS

See pages 120 and 121 of the 5 January 2007 issue or access www.sciencemag.org/feature/contribinfo/home.shtml

EDITOR-IN-CHIEF **Donald Kennedy**
EXECUTIVE EDITOR **Monica M. Bradford**
DEPUTY EDITORS **R. Brooks Hanson, Barbara R. Jasny, Katrina L. Kelner**
NEWS EDITOR **Colin Norman**

EDITORIAL SUPERVISORY SENIOR EDITOR Phillip D. Szuromi; SENIOR EDITOR/PERSPECTIVES Lisa D. Chong; SENIOR EDITORS Gilbert J. Chin, Pamela J. Hines, Paula A. Kiberstis (Boston), Marc S. Lavine (Toronto), Beverly A. Purnell, L. Bryan Ray, Guy Riddihough, H. Jesse Smith, Valda Vinson, David Voss; ASSOCIATE EDITORS Jake S. Yeston, Laura M. Zahn; ONLINE EDITOR Stewart Wills; ASSOCIATE ONLINE EDITOR Tara S. Marathe; BOOK REVIEW EDITOR Sherman J. Suter; ASSOCIATE LETTERS EDITOR Etta Kavanagh; EDITORIAL MANAGER Cara Tate; SENIOR COPY EDITORS Jeffrey E. Cook, Cynthia Howe, Harry Jach, Barbara P. Ordway, Jennifer Sills, Trista Wagoner; COPY EDITORS Lauren Kmec, Peter Mooreside; EDITORIAL COORDINATORS Carolyn Kyle, Beverly Shields; PUBLICATIONS ASSISTANTS Ramatoulaye Diop, Chris Filiatreau, Joi S. Granger, Jeffrey Hearn, Lisa Johnson, Scott Miller, Jerry Richardson, Brian White, Anita Wynn; EDITORIAL ASSISTANTS Maris M. Bish, Emily Guise, Patricia M. Moore, Jennifer A. Seibert; EXECUTIVE ASSISTANT Sylvia S. Kihara; ADMINISTRATIVE SUPPORT Maryrose Madrid

NEWS SENIOR CORRESPONDENT Jean Marx; DEPUTY NEWS EDITORS Robert Coontz, Eliot Marshall, Jeffrey Mervis, Leslie Roberts; CONTRIBUTING EDITORS Elizabeth Culotta, Polly Shulman; NEWS WRITERS Yudhijit Bhattacharjee, Adrian Cho, Jennifer Couzin, David Grimm, Constance Holden, Jocelyn Kaiser, Richard A. Kerr, Eli Kintisch, Andrew Lawler (New England), Greg Miller, Elizabeth Pennisi, Robert F. Service (Pacific NW), Erik Stokstad; INTERN John Simpson; CONTRIBUTING CORRESPONDENTS Barry A. Cipra, Jon Cohen (San Diego, CA), Daniel Ferber, Ann Gibbons, Robert Irion, Mitch Leslie, Charles C. Mann, Evelyn Strauss, Gary Taubes; COPY EDITORS Linda B. Felaco, Rachel Curran, Sean Richardson; ADMINISTRATIVE SUPPORT Scherraine Mack, Fannie Groom; BUREAUS Berkeley, CA: 510-652-0302, FAX 510-652-1867, New England: 207-549-7755, San Diego, CA: 760-942-3252, FAX 760-942-4979, Pacific Northwest: 503-963-1940

PRODUCTION DIRECTOR James Landry; SENIOR MANAGER Wendy K. Shank; ASSISTANT MANAGER Rebecca Doshi; SENIOR SPECIALISTS Jay Covert, Chris Redwood; SPECIALIST Steve Forrester; PREFLIGHT DIRECTOR David M. Tompkins; MANAGER Marcus Spiegler; SPECIALIST Jessie Mudjitaba

ART DIRECTOR Kelly Buckheit Krause; ASSOCIATE ART DIRECTOR Aaron Morales; ILLUSTRATORS Chris Bickel, Katharine Sutliff; SENIOR ART ASSOCIATES Holly Bishop, Laura Creveling, Preston Huey, Nayomi Kevitiyagala; ASSOCIATE Jessica Newfield; PHOTO EDITOR Leslie Blizard

SCIENCE INTERNATIONAL

EUROPE (science@science-int.co.uk) EDITORIAL: INTERNATIONAL MANAGING EDITOR Andrew M. Sugden; SENIOR EDITOR/PERSPECTIVES Julia Fahrenkamp-Uppenbrink; SENIOR EDITORS Caroline Ash (Geneva: +41 (0) 222 346 3106), Stella M. Hurtley, Ian S. Osborne, Stephen J. Simpson, Peter Stern; ASSOCIATE EDITOR Joanne Baker EDITORIAL SUPPORT Alice Whaley; Deborah Dennison ADMINISTRATIVE SUPPORT Janet Clements, Jill White; NEWS: EUROPE NEWS EDITOR John Travis; DEPUTY NEWS EDITOR Daniel Clery; CORRESPONDENT Gretchen Vogel (Berlin: +49 (0) 30 2809 3902, FAX +49 (0) 30 2809 8365); CONTRIBUTING CORRESPONDENTS Michael Balter (Paris), Martin Enserink (Amsterdam and Paris), John Bohannon (Vienna); INTERN Krista Zala

ASIA Japan Office: Asca Corporation, Eiko Ishioka, Fusako Tamura, 1-8-13, Hirano-cho, Chuo-ku, Osaka-shi, Osaka, 541-0046 Japan; +81 (0) 6 6202 6272, FAX +81 (0) 6 6202 6271; asca@os.gulf.or.jp; ASIA NEWS EDITOR Richard Stone +66 2 662 5818 (rstone@aaas.org); CONTRIBUTING CORRESPONDENTS Dennis Normile (Japan: +81 (0) 3 3391 0630, FAX 81 (0) 3 5936 3531; dnormile@gol.com); Hao Xin (China: + 86 (0) 10 6307 4439 or 6307 3676, FAX +86 (0) 10 6307 4358; cindyhao@gmail.com); Pallava Bagla (South Asia: +91 (0) 11 2271 2896; pbagla@vsnl.com)

AFRICA Robert Koenig (contributing correspondent, rob.koenig@gmail.com)

EXECUTIVE PUBLISHER **Alan I. Leshner**
PUBLISHER **Beth Rosner**

FULFILLMENT & MEMBERSHIP SERVICES (membership@aaas.org) DIRECTOR Marlene Zendell; MANAGER Waylon Butler; SYSTEMS SPECIALIST Andrew Vargo; CUSTOMER SERVICE SUPERVISOR Pat Butler; SPECIALISTS Laurie Baker, Tamara Alfson, Karena Smith, Vicki Linton, Latoya Casteel; CIRCULATION ASSOCIATE Christopher Refice; DATA ENTRY SUPERVISOR Cynthia Johnson; SPECIALISTS Tomeka Diggs, Tarrika Hill, Erin Layne

BUSINESS OPERATIONS AND ADMINISTRATION DIRECTOR Deborah Rivera-Wienhold; BUSINESS MANAGER Randy Yi; SENIOR BUSINESS ANALYST Lisa Donovan; BUSINESS ANALYST Jessica Tierney; FINANCIAL ANALYSTS Michael LoBue, Farida Yeasmin; RIGHTS AND PERMISSIONS: ADMINISTRATOR Emilie David; ASSOCIATE Elizabeth Sandler; MARKETING DIRECTOR John Meyers; MARKETING MANAGERS Darryl Walter, Allison Pritchard; MARKETING ASSOCIATES Julianne Wielga, Mary Ellen Crowley, Catherine Featherston, Alison Chandler, Lauren Lamoureux; INTERNATIONAL MARKETING MANAGER Wendy Sturley; MARKETING EXECUTIVE Jennifer Reeves; MARKETING/MEMBER SERVICES EXECUTIVE Linda Rusk; JAPAN SALES Jason Hannaford; SITE LICENSE SALES DIRECTOR Tom Ryan; SALES AND CUSTOMER SERVICE Mehan Dossani, Kiki Forsythe, Catherine Holland, Wendy Wise; ELECTRONIC MEDIA: MANAGER Lizabeth Harman; PROJECT MANAGER Trista Snyder; ASSISTANT MANAGER Lisa Stanford PRODUCTION ASSOCIATES Nichele Johnston, Kimberly Oster

ADVERTISING DIRECTOR WORLDWIDE AD SALES Bill Moran

PRODUCT (science_advertising@aaas.org); CONSUMER & SPONSORSHIP SALES MANAGER Tina Morra: 202-326-6542 MIDWEST Rick Bongiovanni: 330-405-7080, FAX 330-405-7081 • WEST COAST/W. CANADA Teola Young: 650-964-2266 EAST COAST/E. CANADA Christopher Breslin: 443-512-0330, FAX 443-512-0331 • UK/EUROPE/ASIA Julie Skeet: +44 (0) 1223- 326-524, FAX +44 (0) 1223-325-532 JAPAN Mashy Yoshikawa: +81 (0) 33235 5961, FAX +81 (0) 33235 5852 SENIOR TRAFFIC ASSOCIATE Deiandra Simms

COMMERCIAL EDITOR Sean Sanders: 202-326-6430

CLASSIFIED (advertise@sciencecareers.org); U.S.: RECRUITMENT SALES MANAGER Ian King: 202-326-6528, FAX 202-289-6742; INSIDE SALES MANAGER: MIDWEST/CANADA Daryl Anderson: 202-326-6543; NORTHEAST: Allison Millar: 202-326-6572; SOUTHEAST: Tina Burks: 202-326-6577; WEST: Nicholas Hintibidze: 202-326-6533; SALES COORDINATORS Erika Bryant, Rohan Edmonson, Leonard Marshall, Shirley Young; INTERNATIONAL: SALES MANAGER Tracy Holmes: +44 (0) 1223 326525, FAX +44 (0) 1223 326532; SALES Christina Harrison; SALES ASSISTANT Louise Moore; JAPAN: Jason Hannaford: +81 (0) 52 757 5360, FAX +81 (0) 52 757 5361; ADVERTISING PRODUCTION OPERATIONS MANAGER Deborah Tompkins; SENIOR PRODUCTION SPECIALISTS Robert Buck, Amy Hardcastle; SENIOR TRAFFIC ASSOCIATE Christine Hall; PUBLICATIONS ASSISTANT Mary Lagnaoui

AAAS BOARD OF DIRECTORS RETIRING PRESIDENT, CHAIR John P. Holdren; PRESIDENT David Baltimore; PRESIDENT-ELECT James J. McCarthy; TREASURER David E. Shaw; CHIEF EXECUTIVE OFFICER Alan I. Leshner; BOARD John E. Dowling, Lynn W. Enquist, Susan M. Fitzpatrick, Alice Gast, Linda P. B. Katehi, Cherry A. Murray, Thomas D. Pollard, Kathryn D. Sullivan

AAAS
ADVANCING SCIENCE, SERVING SOCIETY

SENIOR EDITORIAL BOARD

John I. Brauman, *Chair, Stanford Univ.*
Richard Losick, *Harvard Univ.*
Robert May, *Univ. of Oxford*
Marcia McNutt, *Monterey Bay Aquarium Research Inst.*
Linda Partridge, *Univ. College London*
Vera C. Rubin, *Carnegie Institution of Washington*
Christopher R. Somerville, *Carnegie Institution*
George M. Whitesides, *Harvard University*

BOARD OF REVIEWING EDITORS

Joanna Aizenberg, *Bell Labs/Lucent*
R. McNeill Alexander, *Leeds Univ.*
David Altshuler, *Broad Institute*
Arturo Alvarez-Buylla, *Univ. of California, San Francisco*
Richard Amasino, *Univ. of Wisconsin, Madison*
Meinrat O. Andreae, *Max Planck Inst., Mainz*
Kristi S. Anseth, *Univ. of Colorado*
John A. Bargh, *Yale Univ.*
Cornelia I. Bargmann, *Rockefeller Univ.*
Marisa Bartolomei, *Univ. of Penn. School of Med.*
Brenda Bass, *Univ. of Utah*
Ray H. Baughman, *Univ. of Texas, Dallas*
Stephen J. Benkovic, *Pennsylvania St. Univ.*
Michael J. Bevan, *Univ. of Washington*
Ton Bisseling, *Wageningen Univ.*
Mina Bissell, *Lawrence Berkeley National Lab*
Peer Bork, *EMBL*
Dianna Bowles, *Univ. of York*
Robert W. Boyd, *Univ. of Rochester*
Paul M. Brakefield, *Leiden Univ.*
Dennis Bray, *Univ. of Cambridge*
Stephen Buratowski, *Harvard Medical School*
Jillian M. Buriak, *Univ. of Alberta*
Joseph A. Burns, *Cornell Univ.*
William P. Butz, *Population Reference Bureau*
Peter Carmeliet, *Univ. of Leuven, VIB*
Gerbrand Ceder, *MIT*
Mildred Cho, *Stanford Univ.*
David Clapham, *Children's Hospital, Boston*
David Clary, *Oxford University*
J. M. Claverie, *CNRS, Marseille*
Jonathan D. Cohen, *Princeton Univ.*
Stephen M. Cohen, *EMBL*
Robert H. Crabtree, *Yale Univ.*
F. Fleming Crim, *Univ. of Wisconsin*
William Cumberland, *UCLA*
George Q. Daley, *Children's Hospital, Boston*
Edward DeLong, *MIT*
Emmanouil T. Dermitzakis, *Wellcome Trust Sanger Inst.*
Robert Desimone, *MIT*
Dennis Discher, *Univ. of Pennsylvania*
Scott C. Doney, *Woods Hole Oceanographic Inst.*
W. Ford Doolittle, *Dalhousie Univ.*
Jennifer A. Doudna, *Univ. of California, Berkeley*
Julian Downward, *Cancer Research UK*
Denis Duboule, *Univ. of Geneva*
Christopher Dye, *WHO*
Richard Ellis, *Cal Tech*
Gerhard Ertl, *Fritz-Haber-Institut, Berlin*
Douglas H. Erwin, *Smithsonian Institution*
Barry Everitt, *Univ. of Cambridge*
Paul G. Falkowski, *Rutgers Univ.*
Ernst Fehr, *Univ. of Zurich*
Tom Fenchel, *Univ. of Copenhagen*
Alain Fischer, *INSERM*
Jeffrey S. Flier, *Harvard Medical School*
Chris D. Frith, *Univ. College London*
John Gearhart, *Johns Hopkins Univ.*
Wulfram Gerstner, *Swiss Fed. Inst. of Technology*
Charles Godfray, *Univ. of Oxford*
Jennifer M. Graves, *Australian National Univ.*
Christian Haass, *Ludwig Maximilians Univ.*
Dennis L. Hartmann, *Univ. of Washington*
Chris Hawkesworth, *Univ. of Bristol*
Martin Heimann, *Max Planck Inst., Jena*
James A. Hendler, *Univ. of Maryland*
Ray Hilborn, *Univ. of Washington*
Ove Hoegh-Guldberg, *Univ. of Queensland*
Ary A. Hoffmann, *La Trobe Univ.*
Ronald R. Hoy, *Cornell Univ.*
Evelyn L. Hu, *Univ. of California, Santa Barbara*
Olli Ikkala, *Helsinki Univ. of Technology*
Meyer B. Jackson, *Univ. of Wisconsin Med. School*
Stephen Jackson, *Univ. of Cambridge*
Steven Jacobsen, *Univ. of California, Los Angeles*
Peter Jonas, *Universität Freiburg*
Daniel Kahne, *Harvard Univ.*
Bernhard Keimer, *Max Planck Inst., Stuttgart*
Elizabeth A. Kellog, *Univ. of Missouri, St. Louis*
Alan B. Krueger, *Princeton Univ.*
Lee Kump, *Penn State*
Mitchell A. Lazar, *Univ. of Pennsylvania*
Virginia Lee, *Univ. of Pennsylvania*
Anthony J. Leggett, *Univ. of Illinois, Urbana-Champaign*
Michael J. Lenardo, *NIAID, NIH*
Norman L. Letvin, *Beth Israel Deaconess Medical Center*
Olle Lindvall, *Univ. Hospital, Lund*
Richard Losick, *Harvard Univ.*
Ke Lu, *Chinese Acad. of Sciences*
Andrew P. MacKenzie, *Univ. of St. Andrews*
Raul Madariaga, *École Normale Supérieure, Paris*
Anne Magurran, *Univ. of St. Andrews*
Michael Malim, *King's College, London*
Virginia Miller, *Washington Univ.*
Yasushi Miyashita, *Univ. of Tokyo*
Richard Morris, *Univ. of Edinburgh*
Edvard Moser, *Norwegian Univ. of Science and Technology*
Andrew Murray, *Harvard Univ.*
Naoto Nagaosa, *Univ. of Tokyo*
James Nelson, *Stanford Univ. School of Med.*
Roeland Nolte, *Univ. of Nijmegen*
Helga Nowotny, *European Research Advisory Board*
Eric N. Olson, *Univ. of Texas, SW*
Erin O'Shea, *Harvard Univ.*
Elinor Ostrom, *Indiana Univ.*
Jonathan T. Overpeck, *Univ. of Arizona*
John Pendry, *Imperial College*
Philippe Poulin, *CNRS*
Mary Power, *Univ. of California, Berkeley*
Molly Przeworski, *Univ. of Chicago*
David J. Read, *Univ. of Sheffield*
Les Real, *Emory Univ.*
Colin Renfrew, *Univ. of Cambridge*
Trevor Robbins, *Univ. of Cambridge*
Barbara A. Romanowicz, *Univ. of California, Berkeley*
Nancy Ross, *Virginia Tech*
Edward M. Rubin, *Lawrence Berkeley National Lab*
J. Roy Sambles, *Univ. of Exeter*
Jürgen Sandkühler, *Medical Univ. of Vienna*
David S. Schimel, *National Center for Atmospheric Research*
Georg Schulz, *Albert-Ludwigs-Universität*
Paul Schulze-Lefert, *Max Planck Inst., Cologne*
Terrence J. Sejnowski, *The Salk Institute*
David Sibley, *Washington Univ.*
Montgomery Slatkin, *Univ. of California, Berkeley*
George Somero, *Stanford Univ.*
Joan Steitz, *Yale Univ.*
Elsbeth Stern, *ETH Zürich*
Thomas Stocker, *Univ. of Bern*
Jerome Strauss, *Virginia Commonwealth Univ.*
Marc Tatar, *Brown Univ.*
Glenn Telling, *Univ. of Kentucky*
Marc Tessier-Lavigne, *Genentech*
Michiel van der Klis, *Astronomical Inst. of Amsterdam*
Derek van der Kooy, *Univ. of Toronto*
Bert Vogelstein, *Johns Hopkins*
Christopher A. Walsh, *Harvard Medical School*
Graham Warren, *Yale Univ. School of Med.*
Colin Watts, *Univ. of Dundee*
Julia R. Weertman, *Northwestern Univ.*
Jonathan Weissman, *Univ. of California, San Francisco*
Ellen D. Williams, *Univ. of Maryland*
R. Sanders Williams, *Duke University*
Ian A. Wilson, *The Scripps Res. Inst.*
Jerry Workman, *Stowers Inst. for Medical Research*
John R. Yates III, *The Scripps Res. Inst.*
Martin Zatz, *NIMH, NIH*
Huda Zoghbi, *Baylor College of Medicine*
Maria Zuber, *MIT*

BOOK REVIEW BOARD

John Aldrich, *Duke Univ.*
David Bloom, *Harvard Univ.*
Angela Creager, *Princeton Univ.*
Richard Shweder, *Univ. of Chicago*
Ed Wasserman, *DuPont*
Lewis Wolpert, *Univ. College, London*

25 years of delivering next-generation systems

Accelerate your time to publish

Human disease researchers bridge diverse research areas to advance the medical field, moving forward in small but steady strides. Your road requires perseverance and demands commitment. Over the past 25 years, Applied Biosystems has helped to pave the way with cutting-edge technology for genetic analysis. AB offers reagents, instruments, and software for applications including DNA sequencing, fragment analysis, and genotyping—accelerating scientific research.

To find out more, visit: info.appliedbiosystems.com/hdr

Applied Biosystems

For Research Use Only. Not for use in diagnostic procedures. This instrument is authorized for use in DNA sequencing and fragment analysis under process claims of U.S. Patent Nos. 5,821,058 and 5,332,666 and under all process claims for DNA sequence and fragment analysis of U.S. and foreign counterpart patents owned or licensable by Applied Biosystems. The Applied Biosystems 3130/3130x/Genetic Analyzers include patented technology licensed from Hitachi, Ltd., as part of a strategic partnership between Applied Biosystems and Hitachi, Ltd., as well as patented technology of Applied Biosystems. Applied Biosystems and AB (Design) are registered trademarks and Applera is a trademark of the Applera Corporation or its subsidiaries in the US and/or certain other countries. ©2007 Applied Biosystems. All rights reserved.

Does your next career step need direction?

There's only one place to go for career advice if you value the expertise of *Science* and the long experience of AAAS in supporting career advancement - ScienceCareers.org. The pages of *Science* and our website ScienceCareers.org offer:

- Thousands of job postings
- Funding information
- Career advice articles and tools
- Networking opportunities

www.sciencecareers.org

Malaria-causing plasmodium.

Taking Aim at Little-Studied Diseases

Is the Achilles' heel of the malaria parasite one of the proteins that enable it to proliferate prodigiously in human liver cells? Or maybe one of the genes that activate when it takes up residence in a female mosquito's salivary glands? This new database, launched by an international team of scientists, can help pin down potential drug targets for malaria and other diseases, mainly tropical ones, that have gotten short shrift from pharmaceutical companies.

NET WATCH

For five killer pathogens, including the tuberculosis bacterium and the parasite that causes African sleeping sickness, the TDR Targets Database compiles genomics data from GeneDB, Tuberculist, and other sources. Users hoping to improve their molecular marksmanship can hunt for proteins by structural features, including how many segments penetrate the cell membrane, or by whether they are essential for survival. The entries also rank potential targets on measures such as "druggability," which indicates whether small molecules are likely to stymie them. >>
tdrtargets.org

Wolf Clones in the Clear

Seoul National University announced last week that despite some sloppy editing of their report, researchers have indeed cloned two wolves. Readers questioned some statistics in the report, published in March in the journal *Cloning and Stem Cells*, and the journal took it off its Web site (*Science*, 20 April, p. 347). But after an investigation, the university accepted researcher Byung-Cheon Lee's claim that he had made a simple mistake in calculating the success rate for wolf cloning. Furthermore, it appears that a junior researcher accidentally pasted in the wrong table showing some DNA data. The journal is waiting to receive the official report before putting the revised paper back online.

Shivering With the Sun

The sun vibrates like a ringing bell. Now scientists are finding that the whole Earth and many things on and near it—even cell phones—dance along.

What carries the tune is the thin solar wind blowing through the solar system. When statistician David Thomson of Queen's University in Kingston, Canada, and colleagues reported that the wind vibrates at the same distinctive frequencies as the sun, skepticism ran deep (*Science*, 14 July 1995, p. 160). Turbulence should wipe out such solar vibrations, or modes. But those doubts are lifting, and now the team has extended its search for solar modes.

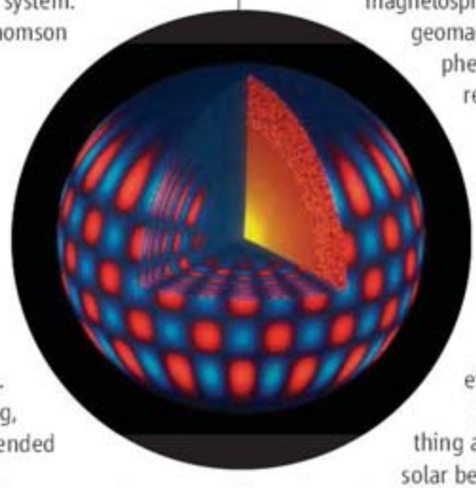

The sun oscillates in and out (reds and blues).

In the May *Proceedings of the IEEE*, the researchers will describe how they used mathematical methods to unearth signals buried in the random noise of geophysical records. They have found solar modes jiggling Earth's plasma-filled magnetosphere, the ionosphere, the geomagnetic field, the atmosphere, and Earth itself as revealed in seismic records of the planet's "hum." While troubleshooting a Midwestern cell-phone system, Thomson stumbled across solar-mode frequencies in upswings in the rate of dropped calls, related perhaps to effects in the ionosphere. Finding Earth and everything around it shimmying to a solar beat "is a little bit hard to swallow," says seismologist John Orcutt of Scripps Institution of Oceanography in San Diego, California. But at least on the seismic side that he's looked at, "I think it's a good, strong story."

A Long-Lost Relative

Lonesome George, a Galápagos giant tortoise locally known as Solitario Jorge, is called the "rarest living creature" by Guinness World Records. After a futile worldwide search in zoos to find others from his home island of Pinta and failed efforts to get him to mate—including flying in a Swiss zoologist to extract some sperm—70-year-old George seemed destined to stay the last of his species.

Until now. A team of geneticists led by Adalgisa Caccone and Jeffrey Powell at Yale University report this week in *Current Biology* that, after analyzing DNA from 27 tortoises on neighboring Isabela Island, they've found a relative. One male turned out to be a cross between the native species (*Geochelone becki*) and George's (*G. abingdoni*). Caccone says she plans to lead a bigger expedition back to the Isabela Island turtle population—which may number up to 8000—to sample 1000 more. "Chances are quite high that there's a pure Pinta individual out there," says Caccone, which means hope yet for finding George a mate or even an extended family.

"It's good to have a positive story in our world of diminishing biodiversity," says Oliver Ryder, a geneticist at the San Diego Zoo in California. But just in case no kin turn up, the zoo hopes to add tissue from George to their Noah's Ark of cell lines, perhaps one day to clone a twin.

CREDITS (TOP TO BOTTOM): NATIONAL SOLAR OBSERVATORY; LESTER V. BERGMAN/CORBIS; ALIZON LLERENA

From primates to proteomics research

For careers in science, turn to *Science*

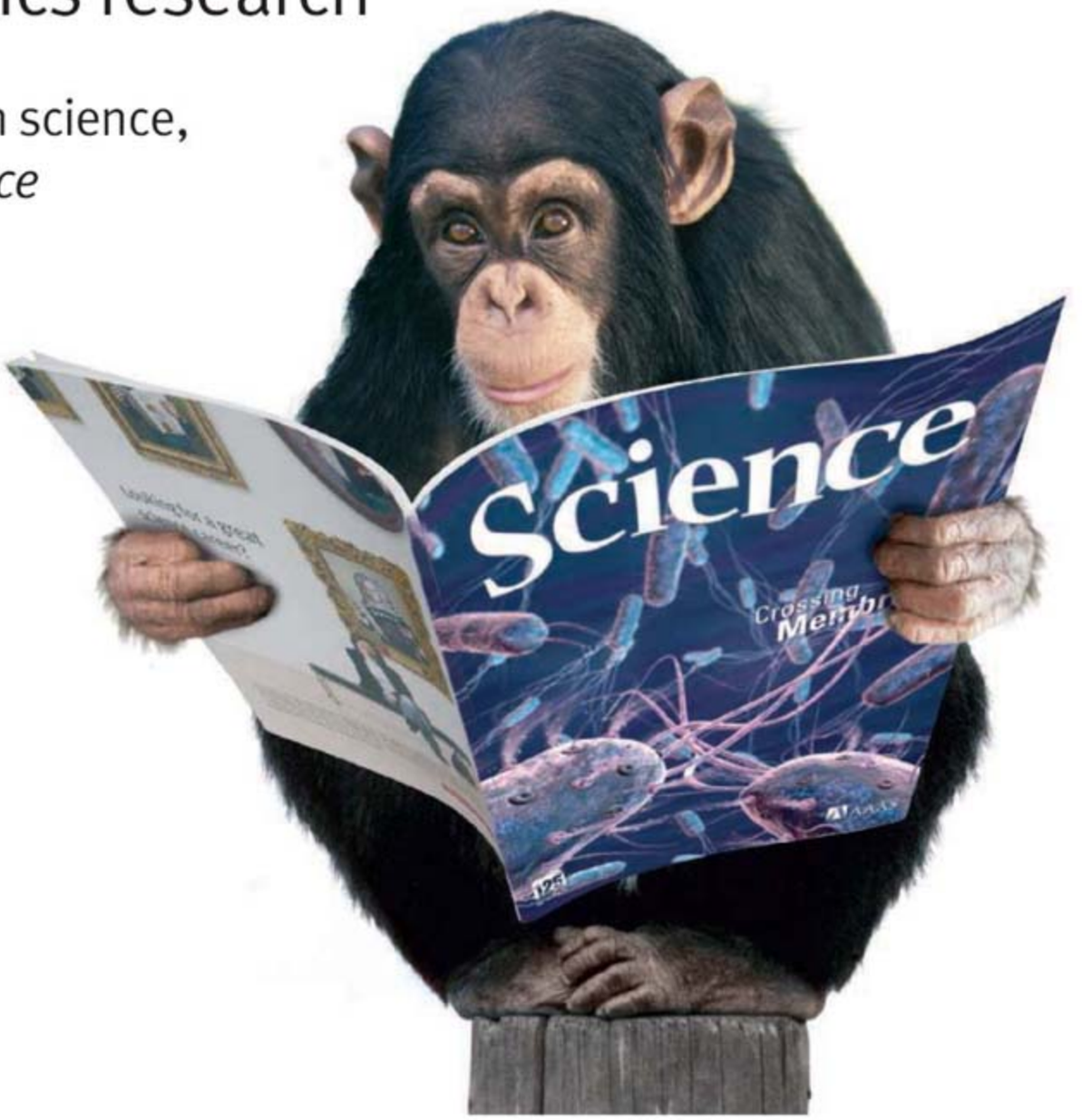

Don't get lost in the career jungle. At ScienceCareers.org we know science. We are committed to helping you find the right job, and to delivering the useful advice you need. Our knowledge is firmly founded on the expertise of *Science*, the premier scientific journal, and the long experience of AAAS in advancing science around the world. ScienceCareers.org is the natural selection.

www.sciencecareers.org

Features include:

- Thousands of job postings
- Career tools from Next Wave
- Grant information
- Resume/CV Database
- Career Forum

ScienceCareers.org

We know science AAAS

EDITED BY YUDHIJIT BHATTACHARJEE

MONEY MATTERS

STAR COMPANY. It sounds like the opening of some nerdy joke: A billionaire and a cosmologist go for a horse-drawn carriage ride. But Texas oil magnate George Mitchell and famed cosmologist Stephen Hawking did just that last month at Mitchell's 2400-hectare spread outside Houston. The unlikely bond is part of Mitchell's effort to elevate his alma mater, Texas A&M University in College Station, into the highest ranks in cosmology and theoretical physics.

Since he met Hawking in 2002, Mitchell has donated slightly more than $50 million to support cosmology research at Texas A&M, helping to create a center for fundamental physics and endowing 10 chaired professorships. He is also chipping in $250,000 per year to support collaborations between Texas A&M researchers and Hawking and colleagues at the University of Cambridge in the U.K.

"I've been interested in cosmology since I was 15 years old, but I had to find something in which I could make a living," says the 87-year-old Mitchell. He became a petroleum engineer and founded Mitchell Energy and Development Corp., which he sold in 2002. "George is a remarkable man," Hawking told the *Houston Chronicle* last month. "He has enabled us … to attack some of the most challenging problems in cosmology."

AWARDS

NSF HONORS. Exciting, informative, possibly even bubbly: These descriptions of a chemistry demonstration also define the personality of Bassam Shakhashiri, who has spent a lifetime popularizing chemistry. On 14 May, the National Science Foundation (NSF) will bestow its Public Service Award on Shakhashiri, a chemistry professor at the University of Wisconsin, Madison, for raising public understanding of science.

As head of NSF's education directorate in the 1980s, Shakhashiri helped revive a budget slashed during the first years of the Reagan Administration. He has worked tirelessly to spread science literacy at every possible venue—from classrooms to retirement homes. He's brought his "Science Is Fun" message to radio and television, where he's known for his annual PBS program "Once Upon a Christmas Cheery in the Lab of Shakhashiri." "I urge fellow scientists to commit themselves to promoting science literacy," he says.

NSF is also recognizing physicist Shirley Jackson, president of Rensselaer Polytechnic Institute in Troy, New York, for her contributions to research, education, and policy. The Vannevar Bush Award is the foundation's tribute to a lifetime of public service.

Got a tip for this page? E-mail people@aaas.org

FUELING DRUG DISCOVERY. Three researchers whose work revolutionized drug development have won one of medicine's most lucrative prizes. The $500,000 Albany Medical Center Prize in Medicine and Biomedical Research, awarded last week, will be shared by Robert Lefkowitz, 64, of Duke University Medical Center in Durham, North Carolina; Solomon Snyder, 68, of Johns Hopkins University School of Medicine in Baltimore, Maryland; and Ronald Evans, 58, of the Salk Institute for Biological Studies in San Diego, California.

The three, friends but rarely collaborators, set out several decades ago to find and characterize receptors, proteins on the inside or outside of a cell that bind to different molecules and help determine how cells behave. In the 1970s, when they began looking for receptors, there was "tremendous skepticism as to whether such things really existed," says Lefkowitz, who trained as a cardiologist before being drawn to the lab.

Inspired partly by President Richard Nixon's war on heroin, Snyder discovered the opioid receptor, the target of this class of drug. Lefkowitz hit on receptors for adrenaline and noradrenaline, and Evans found a key hormone receptor. Since then, other scientists have discovered hundreds more receptors that have helped drug companies craft new therapies for asthma, cancer, schizophrenia, high blood pressure, and other conditions.

Honors >>

HOT STREAK. A medical doctor who turned to research, Japanese immunologist Shizuo Akira chose innate immunity as a topic 10 years ago at a time when most work in the field concentrated on acquired immunity. Today, the Osaka University researcher's name is on everybody's lips, to judge by the scientific literature.

For the second year in a row, Akira has earned the title of Thomson Scientific's "Hottest Researcher," thanks to authoring seven of the most highly cited scientific papers over the last 2-year period. Akira's work focuses on what are called Toll-like receptors (TLRs), which play a crucial role in the early immune response to invading pathogens. Bruce Beutler, an immunologist at Scripps Research Institute in San Diego, California, says Akira not only created knockout mice for all 10 known TLRs but also determined the function of these receptors and showed how the signaling molecules interact. "Shizuo has been adroit in picking an emerging topic and going after it in an enviable way," says Beutler.

Akira laughs when asked whether he can score a third time. His main area—the signaling pathway involving TLRs—has been well explored. And he has "no idea" whether he can continue to best the competition as the field moves on to other topics.

CREDITS (TOP TO BOTTOM): ANNA N. ZYTKOW; MICHAEL FORSTER ROTHBART, UNIVERSITY OF WISCONSIN, MADISON, UNIVERSITY COMMUNICATIONS; SHIZUO AKIRA

Beyond earmarks 674

A space plan for Europe 675

U.S. SCIENCE POLICY

Congress Gives Rousing Support To Cluster of Innovation Bills

The U.S. Senate has a reputation for looking at the big picture, the House for attending to details. Both bodies followed that pattern last week, passing a collection of bills that would significantly boost the government's support for research and training. The White House opposes most of the bills, which draw heavily from a 2005 National Academies' report, but the lopsided margins of victory suggest that they could become law if the Democratic-controlled Congress decides to make them a priority.

A House united. Representative Bart Gordon (D–TN) touts the Democrats' innovation agenda after last week's votes.

The Senate bill, called the America COMPETES Act (S. 761), is the more impressive accomplishment. The acronym sums up its sweeping nature: Creating Opportunities to Meaningfully Promote Excellence in Technology, Education, and Science. Nearly 2 years in the making, it is a bipartisan measure with 63 co-sponsors and the support of the chairs and ranking members of three committees with jurisdiction over most of civilian science and education across several federal agencies. "This legislation represents the best way for our country to keep its brainpower advantage, and our brainpower advantage is the way we keep good-paying jobs from going overseas," said Senator Lamar Alexander (R–TN), after the 25 April vote, immodestly calling it "the biggest piece of legislation in Congress this year."

The bill, which passed by a margin of 88 to 8, would authorize a 5-year doubling of the National Science Foundation's (NSF's) budget and lesser but still substantial hikes for the Office of Science at the Department of Energy (DOE) and the National Institute of Standards and Technology (NIST). It would fund new and expanded education and training programs at NSF, DOE, and the Department of Education at all levels, from elementary through graduate schools. In a statement before the vote opposing passage, the White House budget office called the authorization levels "excessive and inappropriate" and complained about the "unnecessary bureaucracy and education programs." The Administration has proposed a 10-year budget doubling for NSF, DOE science, and NIST's in-house labs in its American Competitiveness Initiative (*Science*, 17 February 2006, p. 929).

Meanwhile, the House is moving several ▶

RESEARCH FUNDING

European Research Council Deluged After First Call for Proposals

When the leaders of the European Research Council (ERC) started planning their first call for proposals last year, they expected an enthusiastic response from scientists seeking a slice of the €290 million in research funds—perhaps as many as 3000 applications for the 200 to 250 grants the ERC planned to give out to young researchers in 2007. Instead, when the deadline for the first round had passed last week, 9167 proposals had flooded in—an "astonishing" number, says Helga Nowotny, vice-chair of the ERC's scientific council.

Although a clear vote of confidence for the new funding agency, Nowotny says, the response by Europe's scientists also poses an acute problem: how to winnow out more than 97.5% of the proposals on a very tight timetable. "It's horrendous," says Frank Gannon, the outgoing head of the European Molecular Biology Organization in Heidelberg, Germany. "Numbers like that are very hard to handle for any funding agency."

The ERC will give out basic research grants to individual scientists, based only on the quality of their grant proposal. That's a novelty for the E.U., which has traditionally funded large networks of labs and companies across the continent to do mostly applied research.

The deluge won't compromise the review process, promises ERC Chair Fotis Kafatos of Imperial College London. The agency is enlisting hundreds of extra reviewers to provide written analyses of grants to the 20 review panels originally planned.

A possible downside of the mammoth number of proposals is that a very low success rate may discourage future applicants. But Nowotny points out that a scientist's investment of time—preparing a four-page proposal—is relatively small for the payoff. The review panels will be asked to pare down the applicants by more than 90% during meetings in June, so that those who make it through have between a 30% and 50% chance during the second stage, which includes writing a more detailed proposal and possibly interviews. Meanwhile, the ERC is preparing to launch a second funding round for advanced researchers later this year.

The huge interest in this first round sends a clear message to European politicians, says Peter Nijkamp, chair of the Dutch funding agency NWO: The ERC was sorely needed, but its budget—€7.5 billion for 2007 to 2013—is "absolutely insufficient."

–MARTIN ENSERINK

CREDIT: HOUSE COMMITTEE ON SCIENCE AND TECHNOLOGY

Threatened reefs
678

Evolutionary mosaics
686

bills that are part of a package the Democrats call their Innovation Agenda; it predates the president's proposal and also relies heavily on the academies' *Rising Above the Gathering Storm* report (*Science*, 21 October 2005, p. 423). Last week, with fewer than two dozen dissenters, the House passed H.R. 362, which would boost NSF programs to train more science and math teachers and encourage more students to pursue research careers, and H.R. 363, which increases support for young investigators. This week, it was expected to pass reauthorization bills for NSF and NIST. Waiting in the wings is a bill to create a nimble energy research entity modeled after the Pentagon's Defense Advanced Research Projects Agency. The piecemeal legislation is consistent with the philosophy of the chair of the House Science and Technology Committee, Representative Bart Gordon (D–TN), who believes that more tightly focused bills stand a better chance of passage in the House.

The Senate is not expected to take up the House bills, meaning that the next steps could be a conference committee appointed by Senate Majority Leader Harry Reid (D–NV) and House Speaker Nancy Pelosi (D–CA). But the final format of such legislation is hazy at this point. "Given the overwhelming support for these bills, if they really want to make it happen, they can do it," says one agency lobbyist. "But how do they craft the right package? That's the question." **–JEFFREY MERVIS**

ASTROPHYSICS

Deep Ringing of the Sun Hints at a Speedy Core

How do you peer through a star's worth of multimillion-degree roiling plasma to grasp the innermost workings of the sun? Very steadily, for a very long time, from very far away, it turns out.

Researchers report online in *Science* this week (www.sciencemag.org/cgi/content/abstract/1140598) their analysis of 10 years of continuous observation from a perch just sunward of Earth. They believe they are the first to reliably detect excruciatingly subtle vibrations in the solar surface coming from the sun's very core. Using the newly identified oscillations as a probe, they have found strong hints that the core is rotating faster than the rest of the sun. Such extra zip may be left over from the sun's formation.

"People have been looking for these [vibrations] for 30 years," says solar physicist John Harvey of the National Solar Observatory in Tucson, Arizona. If confirmed, he says, the discovery is "going to be one of the big milestones of helioseismology"—the field in which researchers study the solar interior using the sun's bell-like ringing set off by internal churnings.

Probing the shallow solar interior has long been routine, but helioseismologists had never before detected "g modes" of vibration. Some of these long-sought waves pass through the tiny solar core where fusion reactions power our star. Little wonder they've eluded searchers. The g (for gravity) mode vibrations probably originate when down-rushing plumes pummel the stable deep interior. Some of the resulting waves continue downward and pass through the core but eventually reach the surface. By then, however, they are feeble, raising or lowering the surface at only a few millimeters per second.

To detect such subtle breathing of the surface, helioseismologists Rafael García of the Astrophysics Service of the French Atomic Energy Commission in Saclay and colleagues went to the Global Oscillation at Low Frequencies (GOLF) instrument onboard the Solar and Heliospheric Observatory. GOLF had been staring at the sun for 10 years, measuring how the entire solar disk rises and falls by examining sunlight for any Doppler shift. According to solar theory, some g modes should be raising and lowering a whole hemisphere every few hours or so amid the far stronger, shallowly propagating p (soundlike) modes and noise of the turbulent sun.

CREDIT: SMM (IAC)

One hot onion. The spaceborne GOLF instrument can peel back the layers of the sun to probe the core (central white zone) using solar vibrations.

Relying on the long observational record and the distinctive spacing of g-mode periods, García and his colleagues report that they have detected the signature of g modes in GOLF data, with a likelihood of 99.5% or better. With less confidence, by comparing the observations with model g modes, they see signs that the core is spinning three to five times faster than the overlying middle layer of the sun. That extra spin could be lingering from the sun's formation, while the outer layers have lost much of their rotational momentum over the eons to the mass of solar wind particles flung into space.

García and his colleagues "are likely to have seen an interesting pattern of g modes," says Juri Toomre of the University of Colorado, Boulder. "The trouble is there are not enough constraints to make very many inferences" about the core. Many poorly known properties of the core affect the character of g modes, he notes. "It's just a very tough game." To score more points in the g-mode game, researchers are looking to replace the aging GOLF instrument with an even keener eye in the sky.

–RICHARD A. KERR

U.S. SCIENCE FUNDING

DOE Cures Pork Project With Peer Review

Long dependent on the patronage of a powerful U.S. senator, a New Mexico neuroimaging center has discovered a new route to government research dollars: the front door at the Department of Energy (DOE). But the way it got there has left some lawmakers with the impression that the center is still benefiting from its congressional patron.

Like other facilities with special ties to Capitol Hill, the Mental Illness and Neuroscience Discovery (MIND) Institute at the University of New Mexico in Albuquerque began this year with a daunting challenge. The final 2007 federal budget was largely devoid of earmarks (see graph): money that lawmakers designate for pet projects, bypassing an agency's competitive funding procedures. The MIND Institute has received roughly $10 million a year from DOE since 1999 courtesy of Senator Pete Domenici (R–NM), a longtime chair or ranking member of the Senate panel that oversees DOE's Office of Science and an outspoken advocate of mental health research.

But this spring, for the first time, the MIND Institute successfully ran the gauntlet of DOE's peer-review system and is about to receive $7 million for neuroimaging studies on schizophrenia, addiction, and criminal behavior. The MIND Institute is one of only a handful of institutions to avail themselves of an unusual opportunity: After Congress stripped earmarks from the 2007 budget, DOE said it would be willing to review proposals from institutions that were in line to receive earmarked funds. Even before DOE officially announced that offer, however, the MIND Institute had already submitted a 700-page proposal. DOE spokesperson Aimee Whitelaw says three others have applied, and one is pending.

Created in 1999, the center has shared a large fraction of each year's earmark with its partners, including Massachusetts General Hospital in Boston. In 2003, the MIND Institute moved into the new Pete and Nancy Domenici Hall, and 2 years later, Domenici said he hoped that the MIND Institute was "moving in a direction of self-sufficiency." Indeed, last year the institute won a $2.2 million competitive grant from the Pentagon's Defense Advanced Research Projects Agency to study accelerated learning; it also hired two researchers who had funding from the National Institutes of Health.

Staffers say the money has been put to good use, and outsiders generally agree. Neuroscientist Kent Kiehl says that distributed computing facilities worthy of "a Fortune-500 company" helped attract him from Yale University. The ability to pool subjects drawn from the MIND Institute's network of partners, he adds, will enhance his research with magnetic resonance imaging to diagnose psychotic disorders. Neuroscientist Don Rojas of the University of Colorado, Denver, unaffiliated with the MIND Institute, sees "a lot of potential" in the institute's solid infrastructure and personnel. "But they don't have a measurable scientific product yet," he says.

Despite the institute's positive steps toward independence, Domenici sought $12 million for it in the 2007 spending bill moving through Congress last year. When the new Democratic majority decided in December to remove all domestic earmarks from the final bill, MIND Institute staffers immediately sought guidance from DOE staffers and Domenici's office. In January, DOE's Michael Viola visited the institute. "He told us what the format should be, what they expected," says institute science director Vincent Clark. On 30 January, says MIND Institute Director John Rasure, his team submitted its proposal.

That rapid response gave the institute a jump on the competition. On 2 February, DOE circulated an internal memo explaining that the agency would fund "meritorious proposals" from earmark recipients and asking staff to look out for such projects. On 14 February, Senator John McCain (R–AZ), a critic of such pork-barrel projects, entered the memo into the Congressional Record as part of a statement trumpeting the lack of earmarks in 2007.

After House members of DOE's spending panel learned of the MIND Institute application, they scolded Raymond Orbach, director of DOE's Office of Science, for not telling them directly about DOE's new policy. "So what we're all getting at here is fairness," said Representative David Hobson (R–OH), ranking member of the House Energy and Water spending panel, at a 14 March hearing. Representative Mike Simpson (R–ID) said the Administration's "unwilling[ness] to have transparency" on DOE's earmarks was "hypocrisy" given the White House's stated aversion to pork. Six days after the hearing, Orbach sent a letter to the roughly 125 institutions that received earmarked DOE funds in 2006 informing them of the memo. "Everyone was treated the same," says Whitelaw of the process.

It's not clear how many earmarks will make it into the 2008 budget wending its way through Congress. A House appropriations aide says that there's been an avalanche of requests, and House Appropriations Chair David Obey (D–WI) is considering omitting them again. But few expect Domenici and Senator Robert Byrd (D–WV), chair of the Senate spending panel and a prodigious earmarker, to give up without a fight. **–ELI KINTISCH**

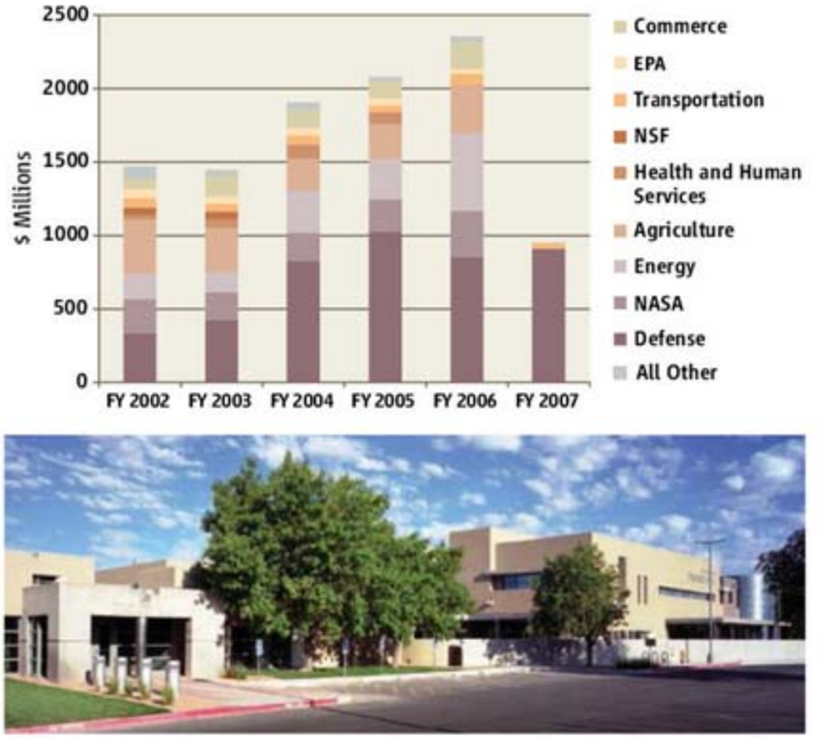

Funding squeeze. Last year's decision to tighten the spigot on the flow of congressional earmarks in annual spending bills forced the MIND Institute (*above*) to seek another way to obtain federal support.

CREDITS (TOP TO BOTTOM): AAAS; JOHN YOST, COURTESY OF THE MIND INSTITUTE

Hitching a ride. The European Union endorses ESA's successful launcher program.

CREDIT: S. CORVAJA/ESA 2003

SPACE SCIENCE

European Union Outlines Vision For Unifying Space Policy

The European Union (E.U.) doesn't have its own astronauts, operate any satellites, or launch any rockets. The E.U. doesn't even have a space research center, but last week, after 2 years of deliberation, it revealed its much-heralded space policy. The aim is to bring more coordination and coherence to Europe's space programs, which are currently spread among national agencies and the European Space Agency (ESA). European space scientists, however, are underwhelmed. "This will change very little for space science in Europe because there is no more money," says Roger Bonnet, director of the International Space Science Institute in Bern, Switzerland, and former head of science at ESA.

The E.U. is a major consumer of earth-observation data and sees space industry as a strategic arena in which European companies can compete worldwide. Yet it has had little direct influence on ESA's programs or the activities of countries such as France, Germany, and Italy that maintain active national space agencies. ESA's modus operandi doesn't necessarily take into account the E.U.'s wider political, social, and economic goals. Moreover, ESA's 17 members include some that are not part of the E.U., whereas the E.U. has 27 member states.

Despite this difference, E.U. officials and ESA Director General Jean-Jacques Dordain agreed in 2005 to develop a Europe-wide space policy. The document revealed last week—which must still be ratified by ESA's Council and E.U. ministers during May—calls for greater coordination to meet shared objectives and avoid duplication. It also encourages synergy between civil and military space efforts and mandates the E.U., ESA, and national agencies to find funding for two key programs: the Galileo navigation satellites, and an earth-observing system called Global Monitoring for Environment and Security (GMES).

GMES aims to provide European policymakers and other civil users with continuous data on, for example, land use, pollution, floods, forest fires, and earthquake damage. Günter Verheugen, E.U. vice-president responsible for enterprise and industry, has said that this system will likely cost €2.4 billion. Galileo will be a commercial rival to the U.S. Global Positioning System (*Science*, 23 December 2005, p. 1893). The E.U. is asking industry to pay for two-thirds of the €2.1 billion cost of building the system and all of the operating costs.

Bonnet calls these two projects test cases for the new E.U. space policy. "Until we see success in these projects, the policy is no more than a piece of paper," he says. Challenges await. The consortium of eight companies that the E.U. chose to build and operate the system has bickered long and hard over the division of work and missed deadlines. Meanwhile, Russia is rejuvenating its Glonass navigation system, and China appears to be building one as well—all unwanted competition for Galileo.

Some space researchers are concerned about the increasingly close relationship between ESA and the E.U. According to ESA rules, science spending is ring-fenced, and all members must contribute to it. That wouldn't necessarily be the case if ESA became an E.U. institution, says Alan Smith, director of the U.K.'s Mullard Space Science Laboratory. "A lot depends on how ESA sees its future," he says.

–DANIEL CLERY

SCIENCESCOPE

Expert Panel Faults Expert Panels

Scientists increasingly set the long-term research agenda for NASA through decadal studies conducted by the National Academies' National Research Council (NRC) in fields from earth sciences to astrophysics. But those studies have come under fire recently from NASA chief Michael Griffin, who argues that the NRC routinely—and dramatically—underestimates the cost of future missions and then complains when the cash-strapped agency must scale back or cancel projects.

This week, an NRC study acknowledged that the surveys, although largely successful, are saddled with "notable problems" such as overly rosy cost estimates and an inability to take into account changing budgets and agency planning cycles. For example, the panel notes, skyrocketing costs for large missions from the Mars Viking to the Hubble Space Telescope ended up penalizing a host of smaller research missions. The study proposes adding cost experts to future panels and obtaining independent cost estimates of NASA missions. It also advises putting international or interagency projects under special scrutiny.

Meanwhile, last week AAAS (which publishes *Science*) joined the growing chorus calling for NASA and the National Oceanic and Atmospheric Administration to restore funding for planned earth science missions—a crisis outlined by the earth sciences decadal survey released earlier this year. **–ANDREW LAWLER**

Paper Cloned

A Korean fertility expert, Sook-Hwan Lee, has been banned from publishing in the U.S. journal *Fertility and Sterility* for 3 years. The ban follows revelations about a 2005 paper that editors learned had previously been published in a Korean journal. Lee, director of the Human Genetics Laboratory at CHA General Hospital in Seoul, was listed as corresponding author on both papers.

The paper, which involved examining mitochondrial DNA in patients with ovarian failure, was first published in 2004 in the *Korean Journal of Obstetrics and Gynecology* by Jeong Hwan Kim, who had worked with Lee as a doctoral student. The English version appeared in the December 2005 issue of *Fertility and Sterility*. Although the paper has been retracted, the retraction "does not reflect on the scientific validity of the paper," said the journal's publisher, the American Society for Reproductive Medicine, which adds that none of Lee's co-authors knew about the duplication.

–CONSTANCE HOLDEN

STEM EDUCATION

Report Urges More Coordination To Improve Science and Math

Many U.S. educators and policy experts believe that the country's decentralized management of education by state and local government bodies is hampering nationwide efforts to improve science, technology, engineering, and math (STEM) education. But a new draft plan, drawn up by the board that oversees the National Science Foundation, suggests a way to get around that problem without abandoning 2 centuries of local control over schools.

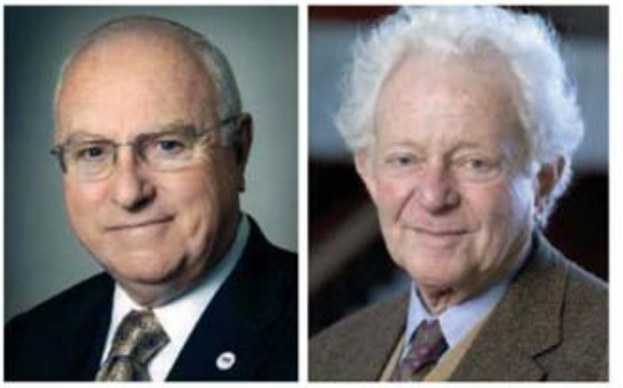

In harmony. Beering (*left*) and Lederman believe that a national coordinating body is needed to reform U.S. STEM education.

The proposal from the National Science Board, requested by the previous Congress, recommends creating a federally chartered body with representatives from the states, the federal government, and the education and business communities. The National Council on STEM Education would coordinate initiatives across federal agencies and work with the states to help them adopt a core set of content standards, link state assessments to those national standards, and create a system of national certification for STEM teachers.

The proposal has come from a blue-ribbon commission, co-chaired by physics Nobelist Leon Lederman, which the board set up last year to tackle the issue (*Science*, 7 April 2006, p. 45). "There is a serious disconnect between the different elements of the school system in this country, with each of 15,000 school boards doing their own thing," says Steve Beering, chair of the board. "The commission felt that there was a clear need for a nationally coordinated effort to bring about some standardization in content and teaching."

The idea has drawn mixed reactions. "Anything at the federal level that would help the states improve science and math education is a good idea," says Jodi Peterson of the National Science Teachers Association ▶

GENETIC DISCRIMINATION

Long-Awaited Genetic Nondiscrimination Bill Headed for Easy Passage

Twelve years after it was first introduced in the U.S. House of Representatives, a genetic nondiscrimination bill finally appears to be on its way to becoming law.

The House passed H.R. 493, the Genetic Information Nondiscrimination Act (GINA), on 25 April by a vote of 420 to 3. Although action on a Senate version of the bill has not yet been scheduled, the Senate unanimously passed versions of GINA in 2003 and 2005, and President George W. Bush has announced his support of the measure. The sticking point had always been in the House, where the Republican leadership, reflecting opposition from some business groups, blocked the bill from coming to a vote. With the Republicans swept out of power in the 2006 elections, the bill moved quickly to the floor and is expected to pass the Senate this month.

GINA bans group health plans and insurance companies from denying coverage or charging higher premiums to healthy individuals based on genetic information. It also applies to employers, preventing the use of genetic information in hiring, firing, or job-placement decisions.

In public opinion polls over the years, a growing majority of respondents have indicated a desire for the legislation. Now, said Representative Louise M. Slaughter (D–NY), chief sponsor of the bill, GINA "will allow us to realize the tremendous potential of genetic research without jeopardizing one of the most fundamental privacies that can be imagined."

Advocates of the bill claim that many people are afraid to undergo genetic tests—for instance, to detect a mutation that increases risk of breast cancer—for fear that insurers or employers will discriminate against them based on that information. And a 2000 survey of genetic counselors indicated that, for the same reason, more than half would not submit charges for genetic tests to insurance companies.

Advocate. Francis Collins of the National Human Genome Research Institute has long supported the bill.

Supporters of the legislation cite instances of discrimination based on confusion about genetic information, such as denial of jobs to healthy African Americans who carried one copy of the sickle cell anemia gene. In a recent case, Slaughter reported, a mother who has α_1 antitrypsin disease was denied health insurance for her two children based on their carrier status, even though they were not affected by the disease.

The threat of genetic discrimination has also hindered research, said Francis Collins, director of the National Human Genome Research Institute in Bethesda, Maryland, at a House hearing in March. "Unless Americans are convinced that the information will not be used against them, the era of personalized medicine will never come to pass," he said.

Until now, the privacy of genetic information has been protected by "a largely untested patchwork" of federal and state regulations, according to the Genetics and Public Policy Center (GPPC) at Johns Hopkins University in Baltimore, Maryland. GPPC head Kathy Hudson says that the main resistance to GINA has come from groups such as the Chamber of Commerce concerned with infringements on employers' decision-making freedom. But in the end, advocates prevailed. As Hudson notes, "it's pretty hard to vote for discrimination."

–CONSTANCE HOLDEN

CREDITS: (TOP, LEFT TO RIGHT) PURDUE NEWS SERVICE; FERMILAB, VISUAL MEDIA SERVICES; (BOTTOM) GENOME.GOV

(NSTA). But others worry that the new organization will simply increase the current welter of agencies and organizations active on the issue. "It will lead to more bureaucracy, more meetings, and more talk," predicts Chester Finn Jr., president of the Fordham Institute, an education nonprofit based in Washington, D.C.

"We're not talking about establishing a new federal agency," responds Jo Anne Vasquez, a University of Arizona, Tucson, education professor and board member who is a former NSTA president. "And we are well aware that the states and local school districts are ultimately responsible for education." The proposed body would be a nerve center for activity at the state level, she says, providing expertise and guidance in the same way that the National Academies provide advice to the federal government.

Selling the idea to state officials will also be tough because of fears that it could undermine their authority. "We are in favor of better coordination between federal agencies and better coordination of educational activities within each state," says Joan Wodiska of the National Governors Association (NGA) in Washington, D.C. But states are wary of anything that smacks of a top-down approach, including a national curriculum. Besides, states are already working together to improve STEM education and economic competitiveness, Wodiska says, pointing to an ongoing NGA initiative known as Innovation America that is aimed at getting states to share best practices.

Proponents admit that it will take time for everyone to get comfortable with the concept. "We expect many to say: 'Oh, it's so difficult' [to reform education nationally]," says Lederman. "We know it's difficult, but it's needed." **–YUDHIJIT BHATTACHARJEE**

RESEARCH SAFETY

Inquest Flags Little-Known Danger of High-Containment Labs

MELBOURNE, AUSTRALIA—A coroner issued a stern rebuke to Australia's national science agency last week, accusing the Commonwealth Scientific and Industrial Research Organisation (CSIRO) of "complacency" in the death of a senior technician in 2001. CSIRO officials say they have tightened laboratory safety since the accident and hope that the researcher's death will serve as a warning to high-security biology labs around the world.

The tragedy unfolded on the afternoon of 10 December 2001, when Set Van Nguyen, 44, entered a containment room at CSIRO's Australian Animal Health Laboratory (AAHL) in Geelong, Victoria. The chamber houses lethal pathogens such as bat-borne lyssavirus and is kept under low pressure to ensure that air flows inward. In the days leading up to Nguyen's death, the containment room had been malfunctioning, according to findings from an inquest released last week by Geelong coroner Audrey Jamieson. For roughly 4 days, sensors registered diminishing levels of oxygen in the room, and a liquid-nitrogen tank inside was leaking, the inquest found. AAHL made two announcements over its PA system about the breakdown and posted warning signs outside the airlock, says AAHL biosafety officer Gordon Abraham. Adds AAHL Director Martyn Jeggo, "We thought we had a truly fail-safe system with bells, flashing alarms, and meters giving oxygen readings."

Nguyen was no novice: A 13-year CSIRO veteran, part of his job was to train other staff members how to use the airlock system, Jeggo says. Around 4:15 p.m., Nguyen entered the chamber, apparently intending to collect a specimen from the cooler and to post more warning signs, says Abraham. A digital readout outside the chamber indicated that oxygen levels inside were 0.03%. After Nguyen's alarmed wife showed up at the lab early the next morning, AAHL staff found his body in the airlock. According to the coroner's report, he was still clutching the empty vial in his right hand with the warning signs on the floor next to him.

Jamieson ruled that Nguyen died of acute oxygen deficiency. He may have passed out instantly, says Jeggo, adding that "most people including myself" may not have been aware of the risk of rapid loss of consciousness. "I remember the adage: You can live without oxygen for 3 minutes, without water for 3 days, and without food for 3 weeks. I'd change that," says Abraham. "Without oxygen, you go unconscious in 3 seconds and die within 3 minutes."

In her report on the inquest, held last year, Jamieson said that Nguyen's death "can only be attributed to a level of complacency" at CSIRO. Although not singling out any individual for blame, she criticized AAHL for, among other things, failing to educate staff about the risks of nitrogen and not keeping better track of staff.

The findings are "probably an accurate reflection of the lab at that time," says CSIRO Chief Executive Geoff Garrett. Since Nguyen's death, he notes, CSIRO has "implemented serious interventions in health and safety" at AAHL and 50 other facilities. "We need to engineer out any risk of human error," says Jeggo. Now at AAHL, containment doors lock down if oxygen levels fall below 19.5%, and electronic cards ensure that every employee can be located while at work.

In an e-mail to all CSIRO staff after the coroner's report, Garrett expressed "deep condolences" to Nguyen's family and sought to draw a line under the affair. "We have learned several important lessons from this tragedy to help us ensure that a similar event should never happen again," he said.

–ELIZABETH FINKEL

CREDIT: FRANK FILIPPI/CSIRO

Lab tragedy. The Australian Animal Health Laboratory has tightened safety since the accidental death of a technician in one of its high-security rooms for dangerous pathogens.

Elizabeth Finkel is a writer in Melbourne, Australia.

A World Without Corals?

Besieged by pathogens, predators, and people, the "rainforests of the sea" may soon face their ultimate foe: rising ocean acidity driven by CO_2 emissions

KHURA BURI, THAILAND—In the shallow waters off Lan Island in the Andaman Sea, Kim Obermeyer kicks his flippers and glides over a silent graveyard. Scattered below are shards of staghorn and other branching corals, shattered in fragments that look like detached finger bones. The conservation biologist swims farther out to sea, darts to the bottom, and peers under an overturned *Porites* coral head the size of a Volkswagen Beetle. Obermeyer points to a brown ribbon underneath: a ragged colony soaking up just enough sun to have survived the tsunami that struck on 26 December 2004.

As a horrific tragedy unfolded on shore that day, ecosystems below the ocean's surface were getting hammered. Across Southeast Asia, the titanic waves ripped apart shallow reefs and buried others in silt. But tsunamis are not the worst threat. The main menaces are largely human-wrought: from divers clumsily breaking off chunks of coral to mass die-offs and bleaching of coral triggered by spikes in ocean temperatures. Last month, the Intergovernmental Panel on Climate Change (IPCC) forecast "more frequent coral bleaching events and widespread mortality" with average global temperature increases of 1° to 3°C.

Surveys suggest that 20% of the reefs on Earth, the largest living structures on the planet, have been destroyed in the past few decades. Another 50% are ailing or verging on collapse. "Reefs are likely to witness a significant ecological crisis in the coming half-century—because of us," says coral specialist Camilo Mora of Dalhousie University in Halifax, Canada.

The decline of coral reefs may have staggering consequences. Globally, reefs generate about $30 billion per year in fishing, tourism, and protection to coasts from storm surges, says Mora. Although reefs cover a minuscule fraction (0.1%) of seabed, they are second only to rainforests in biodiversity, sheltering or nourishing up to 9 million species—a third of all known marine life forms—including 4000 kinds of fish. "To predict that reefs will change dramatically across the globe in the matter of a single generation should keep people up at night," says Ove Hoegh-Guldberg, director of the Centre for Marine Studies at the University of Queensland in St. Lucia, Australia.

There are a few rays of light in this bleak seascape. Attempts to rehabilitate tsunami-damaged reefs are showing promising results. Some reefs blighted by bleaching have mounted spectacular comebacks. And efforts to limit fishing and human activity have paid dividends in healthier reefs and revived local fisheries. Over the past decade, hundreds of marine protected areas have been established to safeguard reefs, including innovative MPAs in Palau designed to help corals bounce back after bleaching (see sidebar, p. 680).

Yet these gains could be erased by what's shaping up as the gravest threat of all. As the oceans soak up more and more of the carbon dioxide that humans pump into the atmosphere, marine chemistry is changing. CO_2 emissions "have the potential to create chemical conditions in the ocean that have not occurred since the dinosaurs became extinct," says ecologist Kenneth Caldeira of the Carnegie Institution of Washington in Palo Alto, California. Dissolved in water, CO_2 becomes carbonic acid. Caldeira coined a term for this process in a paper in 2003: "ocean acidification." By midcentury, ocean pH could dip so low that corals would be unable to form their calcium carbonate skeletons.

"Acidification is the big elephant in the room," says Terence Hughes, director of the Australian Research Council's Centre of Excellence for Coral Reef Studies at James Cook University in Townsville, Australia. Reef building would grind to a halt, with grievous implications. If CO_2 emissions are not curtailed, Hughes predicts, "we'll eventually see reefs dominated by sea anemones and

CREDIT: COURTESY OF NIPHON PHONGSUWAN/PMBC

Artificial limbs. Thai researchers attempt to save tsunami-damaged coral in January 2005; robust growth 2 years later (*below, right*).

algae." Put another way, "soon we'll be having jellyfish and chips," says biologist Michael Kendall of the Plymouth Marine Laboratory in the United Kingdom. In the darkest scenarios, most corals will be toast.

A multiheaded monster

As coral reefs slip toward chronic frailty, a picture of what this means to the world has begun to emerge. Coral scientists, backed by an army of snorkeling and diving volunteers, have put a watch on critical reefs among the nearly 300,000 square kilometers charted to date. Hidden gems continue to come to light, including a giant deep-water reef in turbid waters off northern Australia. "Not much is known about the reef because nobody wants to swim in that area. It's infested with crocodiles," says oceanographer Alan Strong, senior consultant to the U.S. National Oceanic and Atmospheric Administration's (NOAA's) Coral Reef Watch.

A recurring theme of this heightened scrutiny is that reefs are vulnerable on many fronts. A March 2005 earthquake off Indonesia, for example, was as brutal as the 2004 tsunami, lifting some reefs clear out of the water (*Science*, 20 October 2006, p. 406). Corals are susceptible to pathogens and predators, too. The crown-of-thorns starfish, a periodic invader, denudes coral outcroppings with the efficiency of a slash-and-burn farmer. Meanwhile, corals are perpetually besieged by filamentous algae, which are held in check by fish that nibble at them. Overfishing can tilt the balance, as can sewage or agricultural runoff, which infuse seawater with algae-feeding nutrients. These abuses, along with coastal development, "are having fantastically large and negative impacts on reefs around the world," says John Pandolfi, a coral reef expert at the University of Queensland in Brisbane, Australia.

The latest and perhaps biggest present danger for reefs is bleaching. When sea surface temperatures exceed their normal summer high by 1°C or more for a few weeks running, coral polyps, for reasons not entirely understood, expel their zooxanthellae, the symbiotic algae that lend corals color and provide nutrients. The polyps turn pale and starve. "If they don't get their zooxanthellae back in a month or so, they die," says Obermeyer.

The dangers of bleaching came to the fore in 1998, when a potent one-two climate punch—a strong El Niño warming in central tropical Pacific waters, followed by a La Niña that heated western Pacific regions—killed 16% of living corals worldwide (*Science*, 27 October 2000, p. 682). Some reefs have rallied from severe bleaching—recently and dramatically, off Darwin Island in the Galápagos. "We'd given up on the Galápagos" after a 1982–83 bleaching event annihilated most of the archipelago's reefs, says Strong. Now, he says, "it seems to be really coming back." However, many bleached reefs are still sickly. At least half of those destroyed in 1998 have not recovered, according to the authoritative *Status of Coral Reefs of the World: 2004*, compiled by the Global Coral Reef Monitoring Network (GCRMN).

The catastrophic 1998 bleaching, and regional occurrences since then, highlight the vulnerability of reefs to global warming. "That's when we realized that corals could be a kind of canary in a coal mine," says Jeremy Goldberg, co-author of a GCRMN report on tsunami-inflicted reef damage. Delicate staghorn and elkhorn corals, for example, were listed as threatened in the Caribbean in May 2006 under the U.S. Endangered Species Act. "Branching corals that are sensitive to bleaching might disappear," warns reef ecologist Thamasak Yeemin of Ramkhamhaeng University in Bangkok.

Some reefs are more tolerant to bleaching. However, says Hoegh-Guldberg, "the movement toward hardier communities of

FRACTURED PARADISE

PHUKET, THAILAND—Like thousands of tourists who flock to the chic resort island of Phuket in southern Thailand, marine biologist Niphon Phongsuwan recently spent a weekend under the waves, taking in the region's breathtaking coral reefs. Unlike the tourists, Niphon had an extra reason to enjoy the view: His innovative attempt to rehabilitate tsunami-damaged reefs is showing remarkable progress.

Two of the most-savaged reefs lie off Phuket's Paradise Beach and Lolana Bay on nearby Phi Phi Island. During surveys carried out a few days after the tsunami, Niphon and his colleagues at the Phuket Marine Biological Center discovered the shallow seabed at Paradise and Lolana littered with pieces of branching corals, particularly staghorn and other members of the *Acropora* genus. Realizing that the polyps would be abraded to death in the rough-and-tumble waters, Niphon's group gathered up hundreds of *Acropora* fragments in a bid to save them.

Aboard a research vessel, the team glued the coral fragments into holes drilled in concrete cinder blocks. They joined blocks with steel bars to help the structure weather strong currents and placed them in various configurations in either shallow reef flats, less than 2 meters deep at low tide, or on reef slopes about 7 meters deep. Blocks in the reef flats—natural *Acropora* habitat—were battered by waves, and most polyps died. But corals transplanted to reef slopes at Lolana Bay thrived and have grown at a rate equivalent to naturally occurring Phuket corals, Niphon says. The "unexpected" findings, he says, suggest that *Acropora* "can adapt well to a new environmental setting." The hope is that the growing thickets of branching coral will provide a breeding population: seed stock for polyps that mend damaged reefs and pioneer new ones.

The coral growth over 2 years is "impressive," says oceanographer Alan Strong, senior consultant to the U.S. National Oceanic and Atmospheric Administration's Coral Reef Watch. For *Acropora*, he says, the low-tech cinder blocks may offer a cheap alternative to the leading artificial reef product: Reef Balls, molded concrete forms that cost as much as several thousand dollars and range up to 2 meters in girth.

Strong and others caution that although coral reefs can be rehabilitated, they cannot be built from scratch. "No one has ever reconstituted a reef," says Hughes. And some experts wonder whether reef rehab is worth the effort at all, as it addresses a symptom of decline, not the cause. "Inevitably, this kind of work is like treating cancer with a Band-Aid," says John Pandolfi, a coral reef expert at the University of Queensland in Brisbane, Australia. "It makes us feel good, but our money is better spent elsewhere." **–R.S.**

CREDIT: COURTESY OF NIPHON PHONGSUWAN/PMBC

Fragile beauty. Palau's marine protected areas aim to safeguard corals from bleaching.

PALAU COMBATS CORAL BLEACHING

BABELDOAB, PALAU—A giant clam's purplish-green intake valve, big enough to swallow a fist, snaps shut when a diver drifts close. The magnificent meter-wide mollusk in Ebiil Channel is a symbol of survival, whereas a beige, 2-meter-wide table coral nearby is a vivid example of rapid recovery. In the summer of 1998, unusually warm ocean temperatures killed a third of the reefs ringing this tiny archipelago in the western Pacific. But here in the Ebiil Channel Conservation Area off Babeldoab, Palau's main island, underwater denizens have roared back to life with exceptional vigor.

Ebiil's inspiring comeback is the basis for an ambitious experiment. The Nature Conservancy, a U.S. nonprofit, is helping Palau establish the world's first national network of marine protected areas (MPAs) aimed at thwarting bleaching, a phenomenon in which warm ocean waters trigger corals to expel symbiotic algae and starve (see main text). Some corals can resist or recover from bleaching. The Palau network intends to safeguard the hardier varieties—and offer some immunization against future bleaching events as global temperatures rise.

"It's not a new idea, but they are the first to go through with it, and that's great," says Charles Birkeland, a coral specialist at the University of Hawaii, Manoa. "Just limiting fishing isn't going to save our reefs. We need extra protection for the ones that are resisting bleaching, so they can serve as a brood stock for recovery."

Long before the nightmare of '98, Palau had built an impressive record in marine stewardship. The country boasts one of the highest proportions of territory set aside for MPAs in the world, with about a third of its near-shore waters—1300 square kilometers of reefs and lagoons—under varying fishing restrictions. Other Pacific nations are following Palau's lead: In the past decade, the number of MPAs grew from two to 189 in Fiji and from one to 20 in the Solomon Islands. "One village closes fishing in an area, the fish come back after a few years, and soon the next village wants one too," says Michael Guilbeaux

fewer coral species is hardly a 'win.' " Coral abundance is still plummeting, and even resistant corals may succumb in a warmer world, he says. "As climate change accelerates, we will lose an increasing number of coral species, making ecosystems less resilient to other pressures."

A case in point is the widespread bleaching in the Caribbean Sea in 2005–06. At one reef off St. John, part of the U.S. Virgin Islands, "before people knew it, a disease infected the coral that had survived the bleaching. What was left was totally wiped out," Strong says. "You can see how this gets to be a multiheaded monster." NOAA and U.S. National Park Service scientists are now searching for clues to why some corals survived whereas others perished.

In an attempt to boost reef survival, governments have been setting up MPAs, which range from free-for-all recreational parks to no-take zones that bar fishing. Fewer than 3% of the world's reefs lie inside no-take MPAs, says Mora. Many reefs are being fished out. Raising the specter of a pending food crisis, a recent study found that 27 of 49 island countries are exploiting their reef fisheries in an unsustainable way, reports a team led by Nicholas Dulvy of the Centre for Environment, Fisheries, and Aquaculture Science in Lowestoft, U.K., in the 3 April issue of *Current Biology*.

Lax enforcement and lack of local buy-in have undercut many MPAs. "If communities are not involved, they are very unlikely to support an MPA imposed on them," says

Morning commute. Kim Obermeyer (*far right*) leads Earthwatch volunteers on an inspection of a tsunami-damaged reef in the Andaman Sea.

Obermeyer, coordinator for Reef Check Thailand. With volunteers from Reef Check and a second nonprofit, Earthwatch, Obermeyer endeavors to involve villagers—and here near Khura Buri, the Ranong Coastal Resources Research Center of Kasetsart University—in reef monitoring. "This is the only way to succeed," he says.

MPAs and measures such as stanching sewage and runoff cannot prevent bleaching. But resilience—the capacity of a reef to absorb recurrent bleaching and still function—*can* be enhanced, Hughes says. In 2002, more than half of Australia's 40,000-square-kilometer Great Barrier Reef bleached. Two years later, Australia created the world's largest no-take zones, extending fishing bans covering 4.6% of the reef to more than 33%. "This initiative provides real insurance cover against the inevitable impacts of climate change," says Hoegh-Guldberg.

To test this approach, Hughes and colleagues caged some reef sections and left others open to grazing by parrotfish, known by their fused, beaklike teeth. Polyps reestablished on open reef three times faster than on caged sections, they report in the 20 February issue of *Current Biology*. The study shows that reef management after bleaching "has a big effect on the recovery

CREDITS (TOP TO BOTTOM): STEPHEN FRINK/CORBIS; R. STONE/*SCIENCE*

of the Community Conservation Network in Honolulu, Hawaii.

Palau got off to a flying start thanks to a traditional culture that frowns on overfishing and a leader who champions MPAs. "The best way to protect our natural heritage is to use it as a source of income," President Thomas Remengesau Jr. told *Science*. "Tourism is the sustainable thing for us." Palau's prosperity—nearly all adults are employed—comes largely from its 50,000 tourist divers each year. Reefs vibrant with fish are a top priority. Last November, Remengesau sought to export that credo by challenging the rest of Micronesia to set aside 30% of near-shore waters for protection by 2020.

Even for conservation-minded Palau, the massive 1998 bleaching event, which decimated reefs around the world, was a wake-up call. Three-quarters of barrier reef corals at Palau's Rock Islands lagoon, a popular diving site, perished. Ebiil, another barrier reef, was 98% destroyed. Inshore, many reefs fared better because they are accustomed to higher temperatures, whereas others survived because turbid waters and shade limited the sun's damage, says Rod Salm, a marine scientist in the Conservancy's Honolulu office who developed the bleach-resilience project.

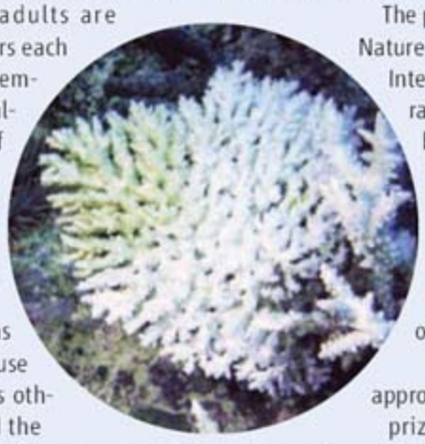

Burnt by the sun. Bleaching signals severe stress.

A critical insight led to a bold plan. Most reefs like Ebiil that have bounced back from bleaching are down current from reefs that suffered little, suggesting that coral larvae and fish from healthy reefs fueled the rapid recovery, Salm says. With that in mind, Noah Idechong (pronounced Idda-ONG), founder of the Palau Conservation Society, and others proposed weaving the nation's hodgepodge of MPAs into an ensemble, linked by currents, called the Protected Areas Network. "The key is to protect all the different reef types that survived bleaching or recovered exceptionally fast, because they will provide the larvae that will help damaged areas recover," says Salm. "These reefs don't necessarily have the fish density that would make fishermen want to protect them."

The proposal resonated with Western donors. In 2005, The Nature Conservancy pledged $2 million, and Conservation International $1 million, to a trust, provided that Palau raises $9 million from other sources—which should not be a problem, says Eric Verheij, acting director of The Nature Conservancy's Palau office. The endowment's interest, along with a diver tax, should yield $2.1 million a year for monitoring and antipoaching patrols. Idechong says he expects that the network, with one-third more area under protection than now, will be operational in 2 years.

Ebiil's rainbow reefs testify to the promise of that approach. Gliding past 2-meter strands of black coral, so prized by jewelers that it has been wiped out in many parts of the Pacific, Verheij zeroes in on what appears to be lifeless coral rubble. On closer inspection, the coral skeleton has been melded together by coralline algae and is studded with young polyps: a nursery of tiny phoenixes rising from the ashes of bleaching. Back on the boat, Verheij explains his philosophy. "Since you can't protect everything," he says, "you try to protect the healthiest." That philosophy seems to be paying off in Palau.

–CHRISTOPHER PALA

Christopher Pala is a writer based in Honolulu, Hawaii.

rate," Hoegh-Guldberg says. But the strategy works only in the short run; nations must move rapidly to stem greenhouse gas emissions, he says. "It is next to useless not to do the two things together."

A mortal blow?

Until bleaching reared its head, many experts viewed rising sea levels as the chief peril of global warming for coral—and a relatively toothless one at that. "We thought reefs would respond by just growing higher," says Strong. "Nobody was talking about changing sea chemistry." Then researchers came to the creeping realization that rising ocean acidity is likely to throw a spanner in coral physiology.

The threat is glaringly simple. Currently, ocean pH hovers around 8.1. Carbon dioxide absorbed into the water column lowers the pH, and as it falls, fewer carbonate ions are available for shell-building critters to grab. Even in present conditions, corals are fighting an uphill battle: Erosion removes 80% of the calcium carbonate laid down. Acidification will accelerate that process as rising carbonic acid levels deplete carbonate. Eventually, corals, plankton, and other organisms will fail to form skeletons. And coral skeletons are to reefs what girders are to skyscrapers. "You have a potential world in which reefs and the limestone frameworks they have built are in net erosion," says Hoegh-Guldberg.

IPCC scenarios of global emissions and ocean circulation indicate that by mid-century, atmospheric CO_2 levels could reach more than 500 parts per million, and near the end of the century they could be above 800 ppm. The latter figure would decrease surface water pH by roughly 0.4 units, slashing carbonate ion concentration by half, paleocoral expert C. Mark Eakin, coordinator of NOAA's Coral Reef Watch, testified last month at a hearing in the U.S. House of Representatives. Ocean pH would be "lower than it has been for more than 20 million years," he said. And that does not factor in possible acidification from carbon-sequestration schemes now being considered.

Some coral species facing their acid test may become shape shifters to avoid extinction. New findings indicate that corals can survive acidic conditions in a sea anemone–like form and resume skeleton-building when returned to normal marine conditions (*Science*, 30 March, p. 1811). However, by pH 7.9, says Caldeira, "there would be a good chance reefs would be gone."

The potential for an acid-induced coral cataclysm has cast a pall on the tight-knit community of reef specialists. "The reality of coral reefs is very dark, and it is very easy for people to judge coral reef scientists as pessimists," says Mora. "We're becoming alarmist," adds Strong—for good reason, he insists. "How are reefs going to handle acidification? It's not like sewage or runoff, where you may be able to just turn off the spigot." Queensland's Pandolfi, however, argues that it's "too early to make really definitive doom-and-gloom statements."

No one disputes that urgent action on greenhouse gas emissions is essential. "We could still have vibrant reefs in 50 years time," Hughes says. But these will not be the reefs we know today. "They will be dominated by a different suite of species," says Hughes, who notes that the shakedown is already under way.

More likely, steps to rein in emissions will be too little, too late—and the world will have to brace for the loss of reefs. In Southeast Asia, says Hoegh-Guldberg, the threat of millions of people losing their livelihoods must be factored into policy planning. Coastal dwellings throughout the tropics will have to be strengthened against higher waves. Then there is the intangible, aesthetic deprivation if coral reefs wither and wink out. "Without their sheer beauty," Hughes says, "the world would be an impoverished place." **–RICHARD STONE**

CREDIT: TEGAN C. HOFFMANN

BIOMEDICINE

Thymosins: Clinical Promise After a Decades-Long Search

From an unorthodox experiment, two proteins have emerged that could prove useful in fighting infections and cancer and healing wounds

Thirty-three years ago, pediatric immunologists Arthur Ammann and Diane Wara of the University of California, San Francisco (UCSF), carried out a dramatic clinical experiment. Hoping to save the life of a 5-year-old girl named Heather whose immune system had failed, they gave her a mix of proteins called thymosin fraction 5 obtained from bovine thymus glands. The series of injections worked. Heather survived into her early 20s before succumbing to lymphoma.

This success at the dawn of the biotech age identified thymosins as a promising source of new therapies. Although other so-called biological response modifiers (BRMs), such as the immune-stimulating interferons, are now widely used in the clinic, for the most part, the thymosins have remained in the background. Now, some individual proteins isolated from thymosin fraction 5 may be poised to fulfill their early promise.

In late March, leading researchers in the thymosin field came together at George Washington University Medical Center in Washington, D.C., for a symposium entitled "Thymosins in Health and Disease." Two came in for the greatest attention: thymosin α_1, which is already approved for treating hepatitis B and C in several countries, although not in the United States, and is a potential cancer therapy; and thymosin β_4, which might be useful for treating hard-to-heal wounds—including diabetic ulcers, bedsores, damaged corneas, and possibly even heart muscle injured by heart attacks. "It's really a wonderful molecule because it does so many things," says ophthalmologist Gabriel Sosne of the Detroit Medical Center in Michigan, who has been studying thymosin β_4's effects on corneal damage.

Immune booster

The thymosins' origins trace back to work done more than 40 years ago by Allan Goldstein, then a postdoc at Albert Einstein College of Medicine in New York City. Goldstein's goal was to isolate the hormones assumed to underlie maturation of the immune system's T (for thymus-derived) cells, whose functions include helping the body defend itself against viral infections. In the course of that work, Goldstein produced thymosin fraction 5, which fostered immune cell function both in culture and in mice lacking thymus glands.

Subsequent work showed that fraction 5 contains at least 40 proteins. Goldstein's lab, now at George Washington University School of Medicine, has isolated several of them, including thymosin α_1 in 1972 and thymosin β_4 in 1981.

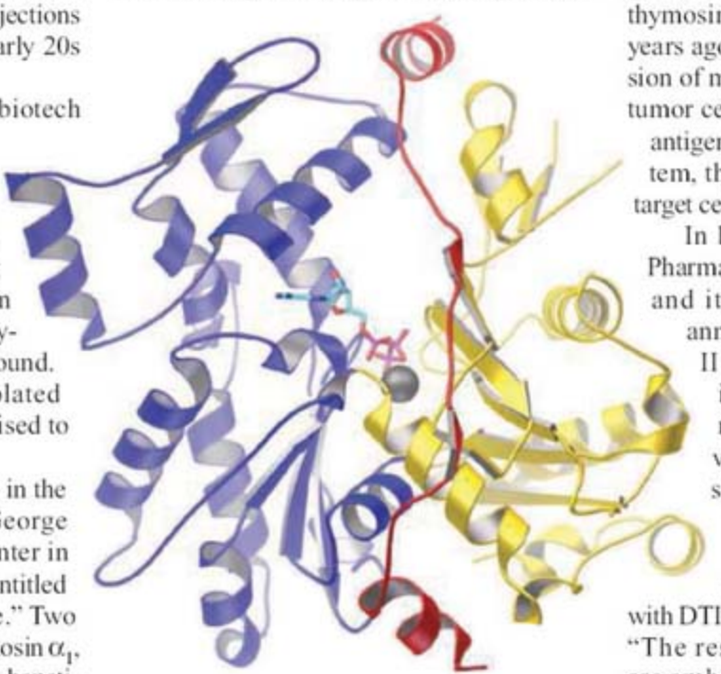

Actin binder. In this structure, thymosin β_4 (red) is attached to the protein actin, an interaction that helps regulate actin filament formation.

Strictly speaking, neither protein is a thymic hormone as originally conceived: Both are made in cells throughout the body as well as in the thymus. They are not related structurally, and both are small: Thymosin α_1 consists of just 28 amino acids, and thymosin β_4 contains 43. But their clinical potential could be big.

An early sign that thymosin α_1 might have clinical value came in work by Enrico Garaci of the Istituto Superiore di Sanità and the University of Rome, "Tor Vegata," and his colleagues. About 20 years ago, they found that thymosin α_1 cooperates with other BRMs, including interferon and interleukins, to bolster the activity of immune cells known as natural killers, which are thought to help the body fight off cancer. Garaci proposed that combining thymosin α_1 with chemotherapy drugs and interferon or interleukin might therefore produce more effective cancer therapies.

Studies in animal models seemed to bear that out. For example, when the researchers treated mice that had Lewis lung carcinoma with thymosin α_1, interferon, and cyclophosphamide, they found that "this combination totally cures the tumors," Garaci says. Before they disappeared, the tumors became packed with immune cells.

This good response may be due, he suggests, to another immune-boosting action of thymosin α_1 that his team discovered a few years ago. The protein increases the expression of major histocompatibility proteins on tumor cell surfaces. These proteins display antigens for recognition by the immune system, thus "increasing the visibility of the target cells," Garaci says.

In December of last year, SciClone Pharmaceuticals in San Mateo, California, and its European partner Sigma-Tau announced the results of a large phase II trial of treatment regimens that included thymosin α_1 in advanced melanoma patients. The average survival time of 94 patients who got the standard melanoma therapy consisting of a dacarbazine drug (DTIC) and interferon α was 6.6 months, whereas that of 98 patients treated with DTIC plus thymosin α_1 was 10.6 months. "The results were so promising that we are embarking on a phase III study," said SciClone's Cynthia Tuthill at the meeting.

Thymosin α_1's ability to bolster immune responses also caught the interest of virologists who treat hepatitis B and C. But even though the protein is widely used abroad, particularly in China, which has a big hepatitis B problem, the results of clinical trials conducted so far have been mixed. SciClone has found, for example, that adding the thymosin to pegylated interferon α in the treatment of hepatitis C patients produces no statistically significant improvement.

Still, small clinical trials have indicated that adding thymosin α_1 to a drug regimen that includes the antiviral drug ribavirin as well as pegylated interferon α does lead to better responses than those produced by ribavirin and the interferon alone. SciClone and Sigma-Tau are now putting that to the test in a phase III trial that will include more than 500 patients. Results are expected in June 2008.

CREDIT: XUE BO, ALDELEKE AGUDA, ROBERT ROBINSON

"I think [thymosin α_1] may have a role as third drug [for hepatitis treatment] but not as a first or second," says Vinod Rustgi, a specialist in liver diseases at Georgetown Medical Center in Washington, D.C. He also notes that the thymosin has been given to numerous people to date, and side effects have been virtually nonexistent.

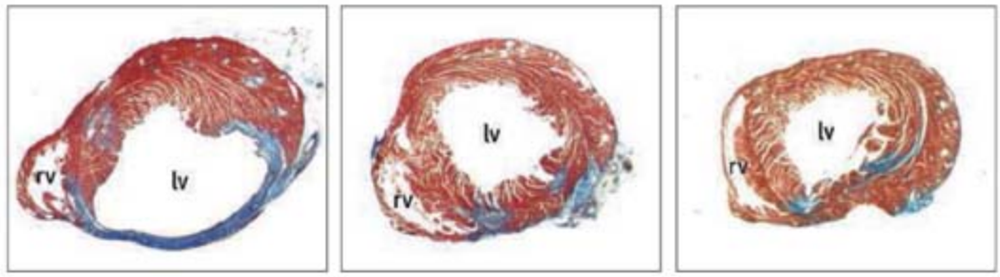

Heart muscle protector? In the mouse heart at left, the wall of the left ventricle (lv) is very thin, the result of damage caused by tying off a coronary artery. But injecting thymosin β_4 into either the peritoneum (*middle*) or the heart itself (*right*) largely prevents that damage.

Mobility controller

Thymosin β_4's mode of action is very different from that of thymosin α_1, as a series of serendipitous discoveries in the early 1990s revealed. One of these came from Daniel Safer, then working with Vivianne Nachmias at the University of Pennsylvania School of Medicine in Philadelphia. While looking at how cells link together monomers of the protein actin to create polymeric filaments, which are important for cell migration, among other things, they found that thymosin β_4 ties up the actin monomers until appropriate cell signals trigger filament formation.

At roughly the same time, Hynda Kleinman's team at the National Institute of Child Health and Human Development (NICHD) in Bethesda, Maryland, was looking for genes involved in new blood vessel formation, or angiogenesis. Among those the researchers found was none other than the gene encoding thymosin β_4. Angiogenesis requires the migration of the endothelial cells that form blood-vessel linings, and when the NICHD group tested thymosin β_4's effects on endothelial-cell migration, they were "astonished," Kleinman says: A very small amount of the protein—1 nanogram—could promote the cell movements.

Symposium co-organizers. Allan Goldstein (*top*) and Enrico Garaci.

Even so, Kleinman recalls, journals weren't interested in publishing the discovery of yet another angiogenesis factor, so she decided to see whether thymosin β_4 works in another model that requires cell movements, namely wound healing. It did, promoting healing by stimulating the migration of epidermal cell migration into experimental skin wounds on rodents and also stimulating collagen and blood-vessel formation. RegeneRx Pharmaceuticals in Bethesda, Maryland, a company founded by Goldstein, has begun clinical trials to test whether thymosin β_4 can help treat chronic skin wounds such as bedsores and diabetic ulcers. (Kleinman, now retired from NICHD, is a member of the RegeneRx scientific and medical advisory board.)

Recent work also suggests that thymosin β_4 therapy may help heal corneal damage, which Sosne, also a member of the RegeneRx advisory board, describes as "a big clinical problem." Current treatments, he notes, can reduce the inflammation that often follows a corneal injury, but "there's nothing an ophthalmologist can do to promote" healing of the wound itself.

In work begun while a postdoc in Kleinman's lab, Sosne has shown that in animals, thymosin β_4 both reduces inflammation and promotes the healing of alkali-induced wounds to the cornea. He has already treated one human patient on a compassionate basis, a diabetic woman who was blind in one eye and in danger of losing her sight in the other one after surgery. Fourteen days of treatment with drops containing thymosin β_4 did bring about healing, although a minor injury caused the wound to reappear. At the end of March, RegeneRx announced that it was beginning a phase II trial to assess the safety and efficacy of thymosin eye drops in diabetic patients who had eye repair surgeries.

RegeneRx also plans a phase I trial aimed at assessing the safety of thymosin β_4 injections as a possible therapy for heart attack victims. In late 2004, Ildiko Bock-Marquette, Deepak Srivastava, and their colleagues at the University of Texas Southwestern Medical Center in Dallas found that the protein is involved both in heart development and the maintenance of the adult heart. "Thymosin β_4 appears to regulate the migration, survival, and perhaps even the beating frequency" of cardiac muscle cells, says Srivastava, who is now at UCSF and also a RegeneRx advisory board member.

In addition, the researchers found that the protein protects against the damage caused by heart attacks induced in mice by tying off their coronary arteries. Treated mice have less heart-muscle scarring and their hearts beat more strongly than those of controls. "All this happens with a single cardiac dose at the time of [arterial] ligation," Srivastava says.

The idea that thymosin β_4 can aid heart function got a further boost in January when Paul Riley of the UCL Institute of Child Health in London and colleagues reported the results of experiments in which they used RNA interference to block thymosin β_4 production in the hearts of developing mouse embryos. In the absence of the thymosin, the researchers found disruptions in all aspects of the development of the coronary blood vessels and a consequent disruption of the development of the heart itself. The finding suggests that thymosin β_4 might promote blood-vessel regrowth following a heart attack.

Still, there are concerns about administering thymosin β_4 to human patients. Several investigators have evidence suggesting that it promotes the growth of cancerous tumors, possibly by enhancing new blood-vessel formation. Sosne says, however, that he never saw angiogenesis in the eyes of mice treated with thymosin β_4 for 30 days. And Kleinman says she and her colleagues "saw no increase in spontaneous tumors and also none in the number of chemically induced tumors" in a transgenic strain of mice that overproduces the protein. Even so, patients who have ever received a cancer diagnosis will be barred from the clinical trials.

More than a quarter-century after that first medical experiment with thymosins at UCSF, the clinical prospects for at least two thymosin proteins are finally looking brighter.

–JEAN MARX

CREDITS (TOP TO BOTTOM): BOCK-MARQUETTE *ET AL.*, *NATURE* **432**, 466 (2004); DAWN GARROTT/GWU MEDICAL SCHOOL; ISTITUTO SUPERIORE DI SANITÀ

Frozen. Construction of an ambitious new university library in Bulawayo has been in limbo for years.

SCIENCE IN ZIMBABWE

Researchers Struggle to Adapt To Economic, Political Turmoil

With minimal government support, soaring prices, and a steady exodus of talent, Zimbabwe's scientists must be inventive to keep labs going

BULAWAYO, ZIMBABWE—Lecturers were on strike, computers were down, and labs were still dark when Peter Mundy parked his bike and unlocked his office at the National University of Science and Technology (NUST) here. Although the latest power outage threatened to defrost the owl, cobra, and other specimens in his lab freezer, the ornithologist was more concerned by the news that inflation had spiked to nearly 2000%—further eroding his salary and grants.

Those distractions would have frazzled most scientists around the world, but for Mundy they were all in a typical day's work. Like the African wildlife he studies, Mundy has adapted to survive in a harsh environment. "There's no internal research funding to speak of, and I have no budget for buying lab equipment," says Mundy. "But we're trying to carry on."

Down the hallway, ecotoxicologist Yogeshkumar Naik has taped a motto above his desk: "The impossible we do at once; miracles take a little longer." These days, beleaguered researchers in Zimbabwe are in need of miracles. Their ranks are thinned by mass emigration, their budgets decimated by hyperinflation, and their international collaborations hurt by sanctions imposed against President Robert Mugabe's regime, which has unleashed police violence against its growing political opposition.

The contrasts are striking: Zimbabwe now has one of the world's lowest life expectancies, yet a massive investment in education during the 1980s and '90s gave the country Africa's highest literacy rate. Talented students and graduates are attractive to outside universities.

With many doctors and medical lecturers leaving the country, the University of Zimbabwe (UZ) in Harare recently asked one of the nation's best-known scientists—biochemist Christopher J. Chetsanga, a former member of UNESCO's executive board and until recently chair of Zimbabwe's National Council on Higher Education—to come out of retirement to teach biochemistry to medical students. "This country is in a terrible financial situation, but scientists have to find ways to carry on," says Chetsanga, who is also president of the Zimbabwe Academy of Sciences. He told *Science* that many of those talented students tell him that "they plan to leave the country soon after they graduate."

Getting by. Lack of funds hasn't stopped ecotoxicology studies at the National University of Science and Technology.

Conditions are "extremely difficult," acknowledges biomathematician John Hargrove, who left Zimbabwe last year to head a South African Centre of Excellence that develops mathematical models to track the HIV/AIDS and tuberculosis epidemics in southern Africa. But Hargrove has maintained his Zimbabwe ties and research interests, helping arrange for a grant to NUST's applied math department to model epidemics in Zimbabwe. "We aim to become one of Africa's strongest groups in modeling infectious diseases," says Winston Garira, whose NUST group has authored several recent papers in international journals.

Garira is one of a cadre of dedicated researchers who have opted, despite all the hardships, to stay put in Zimbabwe. Others at NUST include his colleague Mundy, who is trying to attract funding for a wildlife research unit; Naik, whose lab, with Swedish support, is investigating biomarkers for pesticide pollution; biochemist John S. Read, who is building an alternative-energy research group; and the dean of NUST's applied science faculty, Eddie Mwenje, who is studying gene flow between wild-type and genetically modified sorghum.

In what may be another sign that science is still hanging on, Zimbabwe founded an Academy of Sciences 2 years ago that has grown to 58 members and garnered international support. Its president, Chetsanga, says the academy helped convince the government last year to take steps to monitor bird flu and will sponsor a forum in June on the potential impact of global climate change in Africa. The academy is also trying to persuade the government to reconsider restrictive rules that ban planting genetically modified crops.

Universal chancellor

The chancellor of all public Zimbabwean universities, by decree, is President Mugabe, whose photo hangs in administrative offices. When he first came to power in 1980, the University of Rhodesia (now UZ) was the lone public institution of higher learning; today, there are a dozen universities and three more planned. But that rapid growth, critics

CREDITS (TOP TO BOTTOM): R. KOENIG/*SCIENCE*

say, has come at the expense of academic and research quality.

Although UZ remains influential, one of the most ambitious new universities is Bulawayo's NUST, which opened a dozen years ago and now has about 5000 students. At first glance, the campus seems to be growing, with attractive buildings and an imposing row of unfinished structures bristling with construction cranes. But there are no workmen in the empty shells. Construction has been virtually frozen for years, prompting one scientist to describe the campus as "a parking lot for unused cranes."

"We still hope to finish these buildings," says the optimistic vice chancellor, veterinary scientist Lindela R. Ndlovu. His deputy, organic chemist Samson Sibanda, is confident that the university can thrive despite its budget crunch by reaching out to Zimbabwe's "science diaspora," especially in neighboring countries such as South Africa, to "create research partnerships." NUST's aim is to tap foreign sources to help equip the rows of laboratories that stand empty, devoid of instruments or even reagents. "We've got the labs, but we need the hardware," says Mundy. The strategy has worked in a few cases: Naik was able to equip his NUST lab with hard-currency grants from Sweden's International Foundation for Science.

Last fall, the university hired Moses J. Chimbari, a former Fulbright student in public health at Johns Hopkins University in Baltimore, Maryland, to help other researchers land foreign grants. Chimbari is systematizing the process and educating the university staff. One of the biggest problems, he says, is "the great disparity between the government's official exchange rate and the unofficial rate." A large share of many grants goes to government currency traders.

Some foreign donors and their Zimbabwean grantees have been able to get around the official requirements, which at one point exchanged dollars at 80 times less than market value, by purchasing lab equipment and reagents through foreign accounts and then shipping them into Zimbabwe. But even if donors beat the exchange problem, inflation takes a toll. Says Hargrove: "When you give grants to Zim scientists, it's extremely difficult to get that money to the researchers without it being diluted."

Inflation's impact is insidious. Over the last couple of years, the Education Ministry has been in a constant battle over the wages it sets. University lecturers have gone on strike several times because their meager salaries have not kept up with inflation, which the International Monetary Fund predicts could reach 5000% by year's end. "I'm barely able to pay the rent and feed my family," lamented lecturer Donald Mlambo, who says prices increase so rapidly that "we would need a weekly salary adjustment to keep up." Students, unable to pay modest tuition costs, are angry, too. Last year, rioters at Bindura University of Science Education in northern Zimbabwe burned down a computer science laboratory.

"Hyperinflation affects everything," says medical researcher David Katzenstein of Stanford University in Palo Alto, California, who has worked with colleagues in Zimbabwe over 2 decades. "The economics are crazy, but the researchers have admirable talent and dedication."

Help from abroad

Although Mugabe harshly criticizes Western "imperialists," the government does not turn away help from an array of foreign sources, including the U.S. National Institutes of Health (NIH) in Bethesda, Maryland, and the Centers for Disease Control and Prevention in Atlanta, Georgia. "In medical research, most of the resources are coming from North America and Europe," says Katzenstein, who is working on a project with Peter Mason of the Biomedical and Research Training Institute in Harare to provide laboratory, clinical, and epidemiological training to Zimbabwean researchers.

That initiative, directed at the HIV/AIDS and tuberculosis epidemics, is funded by NIH's Fogarty International Center. Another NIH grant helps fund a collaborative research program between UZ and the University of California, San Francisco, on ways to reduce the vulnerability of women to HIV and other sexually transmitted diseases. Yet another NIH-funded program, which involves the University of Buffalo's School of Pharmacy, helps Zimbabwe monitor drugs to treat HIV and tuberculosis infections. The main partner in Harare is UZ pharmacologist Chiedza Maponga, who helped plan the 2002 rollout of Zimbabwe's free antiretroviral therapy program; with support from foreign donors, it now reaches an estimated 10% of the infected population.

"We need more bridge-building programs like this," says Maponga. His UZ department has devised ways to monitor the quality of generic antiretroviral drugs and conduct clinical studies of drug interactions with African herbal medicines that are sometimes used to treat HIV/AIDS. He is also developing a monitoring system "to help show international donors that their money is being put to good use." In particular, it is important to reassure American and European biomedical assistance programs that sanctions aimed mainly against Mugabe and high-ranking members of his government are being observed.

Lab without walls. Wildlife expert Peter Mundy (*right*) discusses mopane tree leaves with students.

The exodus of Zimbabwean physicians is another factor limiting the country's participation in research. The number of doctors remaining may have dropped, some observers say, to less than half the official level of about 2000. Rampant emigration and AIDS deaths have had a substantial impact; some demographers and epidemiologists suspect that the nation's population may have fallen more than 20% below the official level of 13 million.

Yet there is no dearth of young people who want to study science, researchers say. Even if the equipment is missing and labs are sometimes dark, the students are bright. The real challenge will be to persuade the best of them not to depart for greener pastures as soon as they get an opportunity. Says biochemist Read, who returned to teach in Zimbabwe after years of study abroad: "Our greatest assets are the bright young Zimbabweans we are privileged to teach and do research with."

–ROBERT KOENIG

CREDIT: R. KOENIG/SCIENCE

For the birds. The Clark's nutcracker prefers pinecones with thinner scales (*inset, right*), but with squirrels around, the cone's scales are thicker (*inset, left*).

EVOLUTIONARY ECOLOGY

Variable Evolution

Researchers are discovering the intricacies of relationships in which one organism sometimes influences the evolution of another and sometimes doesn't

Coevolution is a tale of intimacy. Two species—a parasite and its host; a pollinator and its plant—evolve in lockstep, adapting ways to deal with willing, and sometimes unwilling, partners. But occasionally, evolution gets off track.

In north-central Nevada, for example, the Clark's nutcracker has a cozy relationship with certain pine trees: The birds carry off seeds and cache some of them for future use, helping new seedlings get started. For its part, the pine tree has made extracting seeds child's play by evolving short cones bursting with seeds that are covered by thin, easy-to-remove scales. But in the Rocky Mountains, a ménage à trois has developed, in which the pine trees are torn between defending their seeds against squirrels and helping out the nutcracker. As a result, the birds must make do with long, heavy cones with thick scales and relatively few seeds. Coevolution has practically stalled out.

When biologists first started thinking about coevolution some 40 years ago, they didn't appreciate this complexity. Over the years, they have marveled at bird bills exquisitely shaped for feeding efficiently on products of specific plants, and they've learned about arms races in which snakes, insects, and other predators develop ways to outwit the ever-better defenses of their prey. But there have been nagging inconsistencies in many of these observations: Some species pairs don't have the same adaptations everywhere.

Ecologists have found that, in organisms from birds to bacteria, coevolution is not a sure thing. "The interactions between pairs of species have different intensities in different ecological settings," says May Berenbaum, an entomologist at the University of Illinois, Urbana-Champaign. A decade ago, evolutionary ecologist John Thompson of the University of California, Santa Cruz, came up with a theory to explain these geographical variations in coevolution and coined the term "geographic mosaics." And in the past few years, because of its relevance to understanding evolution, biodiversity, and species invasion, there has been "a surge in interest" in the theory, says Richard Gomulkiewicz, an evolutionary biologist at Washington State University in Pullman.

Coevolution's mosaics

Thompson proposed that the survival advantage provided by coevolution was inconsistent because environmental conditions, and hence the forces of natural selection, differ from place to place. In retrospect, this idea seems self-evident, but at the time "people generalized [what they found] from one location and extrapolated to everywhere else for that species," says Craig Benkman, an evolutionary ecologist at the University of Wyoming in Laramie.

If researchers looked more broadly at different populations of interacting species, Thompson predicted, they should discover "hot spots"—with intense interactions between partner species and rapid coevolutionary change—and "cold spots"—areas where the two species have little influence on each other's evolutionary trajectories. Environmental factors, including the presence of other species, should affect hot-spot distribution by making coevolution more or less advantageous to the partners. The mobility of the partners should matter as well: Gene flow from one set of coevolving populations to another should speed or impede the evolution of specializations.

Thompson's fellow ecologists were skeptical at first. "Many of us were left wondering how to address such a complex set of processes and were frustrated with the lack of very specific, testable predictions," says Edmund Brodie III, an evolutionary biologist at the University of Virginia, Charlottesville. Recalls Thompson, "The criticism I got was 'Show me the data.'"

Today, however, the theory is much more palatable. In 2005, Thompson published a book, *The Geographic Mosaic of Coevolution*. He and other theoretical biologists have come up with more detailed models to predict how species might change over space and time, helping field researchers focus their studies. In 2006, the number of publications was expected to be double that of 6 years ago. "We're suddenly seeing the data for a whole variety of interactions," Thompson says.

Third-party interference

Even as Thompson was first formulating his geographic-mosaic theory, Benkman was coming to similar conclusions based on his long-term studies of crossbills and other birds that feed on pine seeds. In the 1990s, his work suggested that the presence of squirrels in certain pine forests of the Rocky Mountains influences cone shape and scale size. Now he and Adam Siepielski have extended that work with a careful look at the ecological and evolutionary crosstalk between squirrels, Clark's nutcrackers, and pine trees in western North America. They find the geographic mosaic and the cold and hot spots Thompson envisioned.

CREDITS (TOP TO BOTTOM): PHOTO COURTESY OF WILLIAM C. GLADISH; A. SIEPIELSKI

The squirrels and birds both eat seeds, but only the nutcrackers help the tree by dispersing some seeds: A single bird can carry off up to 98,000 seeds a season, sometimes as far as 22 kilometers. When squirrels harvest cones, few seeds ever germinate. In 2004 and 2005, Siepielski and Benkman looked at limber pine or whitebark pine forests with or without squirrels and assessed cone and seed characteristics as well as bird and squirrel consumption of seeds.

The results were similar irrespective of the pine species. Nutcrackers preferred cones with thinner scales and more seeds, characteristics of the squirrel-free stands. But forests with squirrels had wider, heavier cones with thicker scales and fewer seeds that were harder for the birds to retrieve, Siepielski and Benkman report in the May issue of *Ecological Monographs*. Thus, squirrel-infested forests represented cold spots. "The presence or absence of the squirrel drives the interaction between the pines and the nutcrackers," says Benkman.

Sometimes three-way interactions can lead to new species, Benkman and Julie Smith of Pacific Lutheran University in Tacoma, Washington, reported in the April issue of *American Naturalist*. The newcomer, the South Hills crossbill, lives in pockets of Idaho forest where squirrels are absent. There, unusually thick scales have resulted in bigger bills, which in turn eventually led to changes in birds' calls. With that change, the birds' attractiveness to crossbills from elsewhere diminished. "The selection is so different with and without squirrels, it's causing one population to speciate from the others," says Benkman.

Arms races

Berenbaum has also found that a third species can throw a wrench in the works of coevolution. Over the past 15 years, she and entomologist Arthur Zangerl, also from the University of Illinois, had found a tight correspondence between the types of toxins produced by wild parsnip and the detoxifying capabilities of parsnip webworms found in the United States. Both plant and caterpillar are native to Europe, with the parsnip arriving in North America about 400 years ago, followed by the webworm about 250 years later.

What's striking, notes Berenbaum, is how quickly the webworm and the parsnip established a tight correspondence once the two met up in North America. Zangerl has analyzed the toxin profiles of herbarium specimens of wild parsnips from collections that date from 1836 to the present. His 2005 analysis shows that within 20 years of the webworm's arrival, the toxin content increased. And, judging from the U.S.–based webworm's current ability to chow down on parsnip with impunity, the webworm has rapidly improved its ability to break down parsnip toxins. "That's something we don't see happening in the European samples," Zangerl notes. The reason is the presence of a third player in Europe: Webworms there often munch on hogweed, a less toxic plant that's not present in North America, Berenbaum and Zangerl reported in the December 2006 issue of *Ecology*.

At the University of Virginia, Brodie is examining another coevolutionary tale, that between toxic newts and their snake predators. He and his colleagues have found hot spots—where garter snakes are rapidly evolving resistance to ill effects from snacking on newts—and cold spots, where resistance to the newt poisons has not evolved. They are now looking to see whether other predatory snakes have the same hot and cold spots. "If so, it is pretty strong evidence that there are major geographic or biogeographic patterns that influence the mosaic and not simply some stochastic process," Brodie says.

Chemical warfare. Wild parsnip battles the parsnip webworm by evolving ever-more-potent toxins in its tissues.

Brodie hopes to investigate how gene flow affects these geographic mosaics. When resistant snakes move into an area populated by vulnerable individuals, for example, they should have the advantage and "warm up" a cold spot. Brodie knows that mutations in a gene for a sodium channel in muscle confer resistance to the newt poisons, and he and his colleagues are sequencing this gene with the hope of using single-base differences between individuals as a way to monitor gene flow throughout the mosaic.

To date, though, the most solid evidence that gene flow plays a major role in geographic mosaics comes from an experiment in which Thompson and his colleagues monitored how quickly bacteria evolved resistance to bacterial viruses (which in turn develop ways to evade this resistance). In 2004, he, Samantha Forde in his lab, and Brendan Bohannan of the University of Oregon, Eugene, first showed that the intensity of this arms race depended on how nutrient-rich the environment was, with resistant bacteria evolving faster in richer media. But when the researchers put bacteria from rich media in with bacteria with suboptimal nutrients, the evolution of resistance sped up in those communities, thereby changing the coevolutionary dynamics.

Working out how geographic mosaics arise, and why, has important ramifications. Agencies charged with protecting borders against invasive species are struggling to predict the worst offenders. "The geographic-mosaic theory can be a tool for improving predictions," says Berenbaum. And Benkman thinks the data to date on the effects of a third-party species suggest caution to wildlife biologists thinking about reintroducing species, particularly mammals, into areas where they have not lived for centuries. Finally, conservation policies need to consider how species might differ genetically across space, and how the coevolutionary paths they travel might vary. "If in conserving biodiversity we aim to represent the full array of the species, then we need to cover a broad sweep of these areas," says Jeremy Burdon, an evolutionary biologist at the Commonwealth Scientific and Industrial Research Organisation Division of Plant Industry in Canberra, Australia.

For these reasons and others, testing the geographic-mosaic theory has increasing appeal. "People are motivated to see if these different processes are present and if they are important," notes Gomulkiewicz. And Paul Rainey, an evolutionary geneticist at the University of Auckland, New Zealand, agrees: "There is a huge opportunity here for research." **–ELIZABETH PENNISI**

CREDITS (TOP TO BOTTOM): ARTHUR ZANGERL/UNIVERSITY OF ILLINOIS

America's most favored drug
692

Environmental biosensors
695

LETTERS | BOOKS | POLICY FORUM | EDUCATION FORUM | PERSPECTIVES

LETTERS

edited by Etta Kavanagh

An Intelligent Crow Beats a Lab

I READ WITH INTEREST THE PROFILE OF NICOLA CLAYTON AND HER WORK ON COGNITION IN birds ("Nicky and the jays," News Focus, V. Morell, 23 Feb., p. 1074). As an amusing aside to bird intelligence and food hiding, I contribute this photograph taken in 1955. My father owned a seafood market on the central Oregon coast and was very fond of crows as pets, which he valued highly for their intelligence. The attached picture represents a regular ritual of food hiding and searching between our labrador retriever and pet crow.

After the crow ate his fill, he would hide surplus food in the market's backyard, which afforded many niches under wood chips and other detritus. Our dog, Jocko, was always interested in an extral morsel and would scour the yard using his nose as his prime detector. The crow followed alongside him and when Jocko came too close to the concealed prize, Jimmy the crow would hop ahead of him, knock the wood chips aside, grab his food, and move it to another location. The crow relied on his memory of his stashed food to beat the dog to the prize nearly every time.

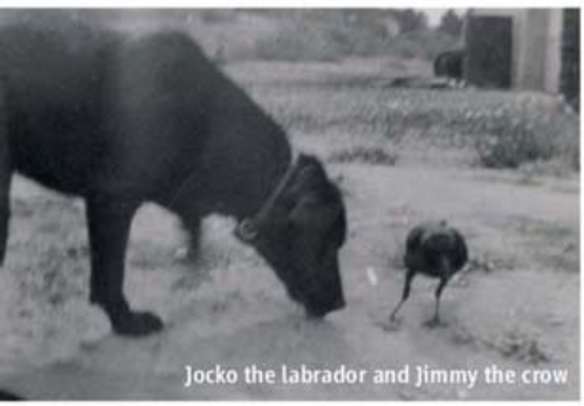

Jocko the labrador and Jimmy the crow

ARTHUR STRAUB

Reno, NV, USA.

Prototype Resilient, Self-Modeling Robots

THE MAIN CONTRIBUTION DESCRIBED IN THE Report "Resilient machines through continuous self-modeling" (J. Bongard *et al.*, 17 Nov. 2006, p. 1118, and the accompanying Perspective, "What do robots dream of?", C. Adami, p. 1093) is a robot that can autonomously recover from certain types of unexpected damage, through an adaptive self-model derived from actuation-sensation relationships, used to generate forward locomotion.

Neither the Report nor the Perspective mention that the first resilient, self-modeling machines of this type were built by Alexander Gloye-Förster *et al.*, who won the 2004 RoboCup in the very fast, small-size league (where human adversaries with a joystick have no chance). Gloye-Förster *et al.* equipped the RoboCup robots with self-models based on artificial neural networks, to model current properties of their four-wheel omni-directional drives. They showed that when a robot gets damaged and is no longer able to execute a precise driving pattern, it can heal itself by quickly adapting its model of the relation between motor commands and sensory inputs, and using the modified model to plan and optimize future driving trajectories (*1*, *2*).

JÜRGEN SCHMIDHUBER

Director, IDSIA, Galleria 2, 6928 Manno, Switzerland, and Institut für Informatik, Robotics and Embedded Systems, Technische Universität München, Boltzmannstrasse 3k, D-85748 Garching bei München, Germany.

References

1. A. Gloye, F. Wiesel, O. Tenchio, M. Simon, *IT Information Technol.* **47** (no. 5), 250 (2005).
2. See also www.idsia.ch/~juergen/resilientmachines.html.

Response

INDEED, MANY EXISTING APPROACHES SUCH as robust control (*1*, *2*) and reinforcement learning (*3*) allow artificial systems to sustain functionality despite variation and uncertainty in their internal structure, by adjusting controllers and estimating model parameters from data. Our self-modeling approach differs from these approaches in two key aspects, concerning both the way the data are collected and the properties of the resulting model.

First, our approach actively determines which data to collect in order to improve the model. This is in contrast to Gloye *et al.* (*4*), whose learning algorithm requires driving the robot through all possible combinations of driving situations "to cover all the regions of the input space" of the predefined neural network (*5*). Such an exhaustive approach does not scale to complex situations with many sensors, actuators, and complex environments, while the active learning method we use scales more favorably (*6*).

Second, our self-models are explicit body schemas useful in scenarios other than those they were trained in. This is in contrast to Gloye *et al.* (*4*), whose model implicitly maps inputs to outputs but has little predictive ability outside its training scenario [e.g., bumping into an obstacle would require retraining (*5*)]. Our robot could use the same explicit internal body schema to determine how to balance on an inclined plane or tackle an obstacle. The ability of a self-model to be useful beyond its training scope is critical to scaling the cognitive ability of machines and may underlay humans' remarkable ability to perform reasonably well in new and unforeseen situations.

HOD LIPSON,[1] VICTOR ZYKOV,[1] JOSH BONGARD[2]

[1]Department of Mechanical and Aerospace Engineering, Cornell University, Ithaca, NY 14853, USA. [2]Department of Computer Science, University of Vermont, Burlington, VT 05405, USA.

References

1. K. Zhou, J. C. Doyle, K. Glover, *Robust and Optimal Control* (Prentice-Hall, Upper Saddle River, NJ, 1996).
2. M. Gevers, *A. Rev. Control* **20**, 95 (1996).
3. L. P. Kaelbling, *Learning in Embedded Systems* (MIT Press, Cambridge, MA, 1993).
4. A. Gloye, F. Wiesel, O. Tenchio, M. Simon, *IT–Information Technol.* **47** (no. 5), 250 (2005).
5. S. Behnke, A. Egorova, A. Gloye, R. Rojas, M. Simon, *Predicting Away Robot Control Latency*, RoboCup '03 Symposium (2003), pp. 12–19.
6. J. Bongard, H. Lipson, *J. Machine Learn. Res.* **6**, 1651 (2005).

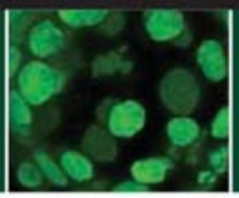

Watching embryos move 697

Mercury's molten interior 702

Can a Nuclear Weapon Really Be "Safer"?

IN HIS ARTICLE ON THE COMPETITION SPONsored by the U.S. Department of Energy to design a Reliable Replacement Warhead (RRW) ("Livermore Lab dips into the past to win weapons design contest," News of the Week, 9 Mar., p. 1348), Eli Kintisch includes the following sentence: "Although the focus is reliability, RRW is also intended to create safer, more secure, and greener weapons." I can understand more secure, even though I would argue that the best security would be universal elimination, an achievable target if the will is there. But, although I sympathize with the author's need to cover the new armaments program in real-world terms, there is something distinctly Orwellian about the use without comment of the words "safer" and "greener" to describe atomic bombs. At the very least, a phrase like "relatively speaking" would be in order, to remind us of what we are really talking about. Or is it 1984 already?

MICHAEL NEUSCHATZ

Riverdale, MD, USA.

Using Radiocarbon Dating in Jerusalem

THE ARTICLE "JUDGING JERUSALEM" (A. Lawler, News Focus, 2 Feb., p. 588) presents the diverse points of view of many archaeologists on the chronological and political implications of the findings from the City of David excavation. Most of these archaeologists agree that the relative chronology based on ceramic typology cannot determine the age of this site in relation to other sites. There is almost a consensus that radiocarbon dating is the only way to solve this problem. I would have expected the article to provide an evaluation of whether radiocarbon dating can solve this problem by consulting with experts in the field, rather than publishing a quote by an archaeologist comparing radiocarbon dating to a prostitute.

The problem translates into whether two events that occurred within a century can be differentiated. Bearing in mind the analytical uncertainty (±30 years) and that the calibration can sometimes significantly increase the probable range of the date, such precise dating is a major scientific challenge.

With Ilan Sharon (Hebrew University), Ayelet Gilboa (Haifa University), and Tim Jull (Arizona University), I addressed this issue by dating the transition from Iron Age I to Iron Age II. We compared samples prepared in three laboratories (Weizmann Institute of Science, University of Arizona, and the University of Groningen). No bias was detected, disproving

Julius Axelrod Prize

Supported by Eli Lilly and Company Foundation

The Society for Neuroscience is pleased to announce the inaugural year of the Julius Axelrod Prize. The prize was established to honor a scientist with distinguished achievements in the broad field of neuropharmacology or a related area and exemplary efforts in mentoring young scientists.

Deadline for receipt of nomination packages: Friday, June 15, 2007

For details please visit www.sfn.org/axelrod.

SOCIETY FOR NEUROSCIENCE

GrantsNet.

The first comprehensive science grants database.

GrantsNet is expanding its listings of some 900 funding programs from private foundations and not-for-profit organizations to include 400 to 500 new entries from the grants.gov site. **This provides the first comprehensive database of funding opportunities** to research scientists and administrators, career counselors, financial aid specialists, and undergraduate and graduate students. For listings, go to

www.grantsnet.org

ScienceCareers.org

We know science AAAS

eppendorf advantage

www.eppendorf.com/advantage
Get Eppendorf quality today!

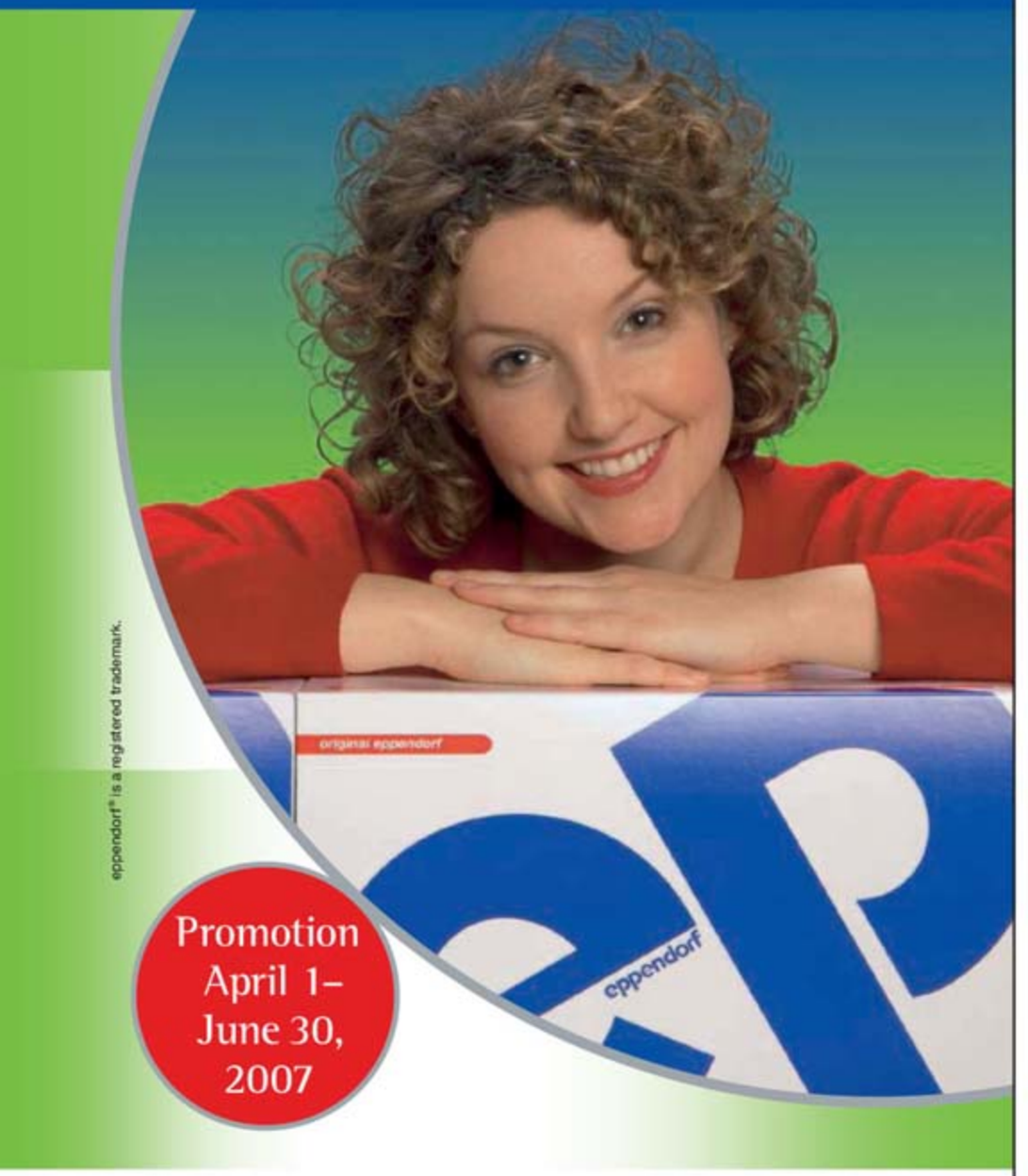

eppendorf® is a registered trademark.

Gentle & Easy!

With **Eppendorf Advantage** offers it is now easier than ever to add Eppendorf premium quality centrifuges to your lab.

Gentle & Easy: Centrifuge 5702/5702 R Bonus Packs
The Eppendorf 5702 family of centrifuges offers an outstanding combination of gentle treatment of sensitive clinical samples and ease-of-use.

Take advantage now!
From April 1–June 30, 2007, Centrifuge 5702 and Centrifuge 5702 R are available as attractive Bonus Packs at special prices that are too good to miss*.

Our exciting offers are just a few clicks away!
For more details visit www.eppendorf.com/advantage

*Offers may vary by country.

misconceptions that radiocarbon labs have specific agendas besides doing scientific research (*1*, *2*). We paid careful attention to the archaeological contexts of all samples, characterized their states of preservation, and analyzed more than 150 samples. The radiocarbon dates mentioned in the article by Eilat Mazar were performed by me on samples that were chosen after careful discussion with her. Radiocarbon analysis is not a routine technical operation.

Our Iron Age study proves that two events can be differentiated within a century. Much depends upon the reliability of the archaeological context from which the sample is taken and upon a deep understanding of the science involved with radiocarbon dating.

ELISABETTA BOARETTO

Radiocarbon Dating and Cosmogenic Isotopes Laboratory, Kimmel Center for Archaeological Science, Weizmann Institute of Science, Rehovot 76100, Israel, and Department of Land of Israel Studies and Archaeology, Bar Ilan University, Ramat Gan, Israel.

References

1. E. Boaretto, A. J. T. Jull, A. Gilboa, I. Sharon, *Radiocarbon* **47**, 39 (2005).
2. I. Sharon, A. Gilboa, A. J. T. Jull, E. Boaretto, *Radiocarbon*, in press.

Oops, That's Not Really a Diamond

THE ILLUSTRATION FOR THE INTERESTING Editors' Choice item "Diamond diversity" (23 Mar., p. 1638) appears, even to this biologist, not to be of diamonds at all. Rather than being rough and tetrahedral in form as diamond crystals typically present, these crystals are hexagonal, very clean surfaced, and optically clear, just as certain quartz crystals can be.

Furthermore, they appear to be doubly terminated, suggesting that they formed free-floating in a fluid-filled cavity rather than attached to a mineral matrix. They appear to be Herkimer diamonds, named for the town in upstate New York where they are found in cavities, or vugs, in the surrounding stoney matrix. They are very attractive, and it is entertaining to spend a Saturday picking these

Letters to the Editor

Letters (~300 words) discuss material published in *Science* in the previous 3 months or issues of general interest. They can be submitted through the Web (www.submit2science.org) or by regular mail (1200 New York Ave., NW, Washington, DC 20005, USA). Letters are not acknowledged upon receipt, nor are authors generally consulted before publication. Whether published in full or in part, letters are subject to editing for clarity and space.

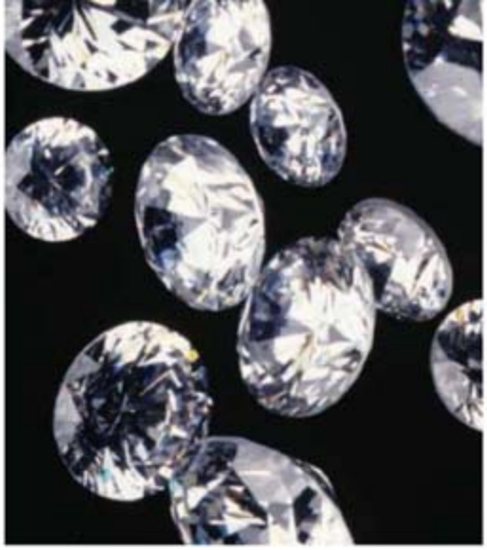

CREDIT: PAUL KATZ/CORBIS

"diamonds" from cavities in the rock, but they are not true diamonds, which are of course not crystallized silica but crystalline carbon.

ANDREW P. WHIPPLE

Department of Biology, Taylor University, Upland, IN 46989, USA.

Editor's Note: The letter writer is correct. The image that was chosen by *Science* staff to run with this item was not a diamond. The image shown here is diamonds.

Coal's Future: Clearing the Air

AS REPORTED BY ELI KINTISCH ("REPORT backs more projects to sequester CO_2 from coal," News of the Week, 16 Mar., p. 1481), the recent Massachusetts Institute of Technology (MIT) study (*1*) on the future of coal stresses the need for reducing the carbon intensity of coal use. More than two coal-fired power plants are projected to be built each week over the next 25 years, adding 1800 GW of electricity production (*2*) and at least doubling current coal-based CO_2 emissions unless CO_2 mitigation technologies are rapidly deployed. Although these technologies are still in the R&D phase, the report's authors rightly caution that we "not fall into the trap of picking a technology winner." Paradoxically, the report then goes on to discuss in great detail the capture and geologic storage of molecular CO_2 (CCS), to the exclusion of other options.

Current mitigation alternatives include the postcombustion chemical or biological uptake of CO_2 from waste streams or from air [e.g., (*3*–*5*)], often converting CO_2 into stable, benign chemical forms that need not be stored deep within the Earth. In certain settings, such approaches could avoid potential obstacles to widespread CCS use (*1*), including (i) the energy cost of capturing, concentrating, and compressing CO_2; (ii) risks associated with transporting and storing CO_2 under high pressure; and (iii) the inability to cost-effectively mitigate existing conventional coal-fired plants. Alternative technologies that can address this last point are critical since, according to the report, CCS only appears practical for new coal combustion technologies that will take decades to penetrate the power industry, time that we can ill afford.

As in the case of CCS, much work is needed to determine the safety, economics, capacity, and timeliness of these alternative CO_2 mitigation approaches. Yet this will never happen if industry and government decision-makers and R&D funders continue to treat conventional CCS as "the only game in town." At this early stage, it is imperative that our CO_2 mitigation strategy be broad in scope, acknowledging that multiple technologies are likely to be needed and that they may bear little resemblance to those currently favored. Given the magnitude and urgency of the CO_2/energy problem, it is unwise to plan the fate of both coal and our environment based on an unnecessarily narrow vision of the future.

GREG H. RAU[1] AND KEN CALDEIRA[2]

[1]Institute of Marine Sciences, University of California, Santa Cruz, CA 95064, USA. [2]Department of Global Ecology, Carnegie Institution, Stanford, CA 94305, USA.

References

1. MIT, *The Future of Coal: Options for a Carbon-Constrained World* (Massachusetts Institute of Technology, Cambridge, MA, 2007).
2. D. Hawkins, G. Peridas, *No Time Like the Present* (National Resources Defense Council, New York, 2007) (see www.nrdc.org/globalWarming/coal/mit.pdf).
3. IPCC, *Climate Change 2001: Mitigation* (Intergovernmental Panel on Climate Change, Cambridge Univ. Press, Cambridge, 2001).
4. IPCC, *Carbon Capture and Storage* (Intergovernmental Panel on Climate Change, Cambridge Univ. Press, Cambridge, 2005).
5. USCCTP, *U.S. Climate Change Technology Program Strategic Plan* (U.S. Climate Change Technology Program, Washington, DC, 2006) (see www.climatetechnology.gov/stratplan/final/index.htm).

CORRECTIONS AND CLARIFICATIONS

ScienceScope: "Bignami back in orbit" by F. De Prestis (23 Mar., p. 1649). Giovanni Bignami has been nominated as president, not director, of Italy's space agency, ASI. He is no longer chair of the Space Science Advisory Committee of the European Space Agency, as was reported. Bignami says he left his position as scientific director of ASI in 2002 when his contract expired, and that his departure was not connected to uncertainty at that time over government support for an Italian radar instrument on a NASA mission to Mars, as the ScienceScope item implied.

Perspectives: "Water from first principles" by A. J. Stone (2 Mar., p. 1228). The dotted lines indicating the hydrogen bonds between the water molecules were inadvertently removed from the top configuration.

Reports: "Water catalysis of a radical-molecule gas-phase reaction" by E. Vöhringer-Martinez *et al.* (26 Jan., p. 497). The third author is identified incorrectly; the correct name is H. Hernandez-Soto.

eppendorf advantage

5702/5702 R Bonus Packs

Centrifuge
+swing-bucket rotor
+4 round buckets
in one package!

Promotion April 1– June 30, 2007

*Offers may vary by country. ep-points are not available in all countries. For details see www.ep-points.com

Your additional bonus
Each Centrifuge 5702/5702 R Bonus Pack comes standard with:
- an extra 100 ep-points* registration bonus
- the chance to win one of 50 gift certificates (e.g., Amazon, American Express, or equivalent) to the amount of approx. 50 Euro each
- one unique Eppendorf pipette pen

More product details and contact information at
www.eppendorf.com/advantage

eppendorf
In touch with life

PUBLIC HEALTH

The Golden Weed, America's Most Deadly Drug

Robert N. Proctor

Tobacco is the world's largest single cause of preventable death. Five million people die every year from smoking, a number that will grow to circa ten million over the next two decades. A hundred million died from smoking in the 20th century, and ten times that will die in the present century if current trends continue.

The tobacco industry is notorious for its decades-long campaign to manufacture ignorance, to distract from hazards, to filibuster its way past inconvenient facts and the crushing weight of medical indictments. Theirs may well be the longest-running campaign of deception ever organized by an industry, and it was not until the 1990s that manufacturers admitted any real harms caused by smoking. Part of this about-face was dictated by a change in legal strategy, which by this time had recentered around the argument that "everyone has always known" that smoking is bad for you—so people have only themselves to blame for whatever diseases they contract from the habit.

Until recent years, much of the historiography of tobacco has been dominated by industry apologists. The industry has been training historians for years, using them either as consultants for litigation or as expert witnesses to deliver industry-friendly testimony in court. As of 2005, at least 35 historians had testified in court for the industry, versus only three for its opponents. Dozens of others have worked more secretively as consultants. That asymmetry helps explain why the industry has most often managed to come up victorious in court: Following decades of efforts to manipulate the science, they've turned to efforts to manipulate the history (*1*). And their power is not to be underestimated.

With Allan Brandt's *Cigarette Century*, however, a new era is dawning in tobacco historiography. A medical historian at Harvard University, Brandt has been working on the history of the cigarette for more than two decades. The book has been long in coming [I cited it as forthcoming in my 1995 *Cancer Wars* (*2*)], but the wait has been worth it. *The Cigarette Century* presents the most comprehensive account to date of how we came into this odd situation, where the burning of little sticks of leaves (with myriad flavorings and chemical modifiers) is the most deadly addiction on the planet.

The Cigarette Century
The Rise, Fall, and Deadly Persistence of the Product That Defined America

by Allan M. Brandt

Basic Books, New York, 2007. 640 pp. $36, C$43.50. ISBN 9780465070473.

Brandt's is principally a history of changing attitudes toward smoking in the United States, along with the science that led to the indictment of smoking and the myriad obstacles to its effective regulation. Buck Duke's consolidation of the early industry is covered, along with the rise of Camel in 1913 as the world's first "standard brand." Opposition to the cigarette collapsed following the First World War, when soldiers got cigarettes with their rations and the bans on the sale of cigarettes (enacted in more than a dozen states) began to lapse. Brandt does a fine job of tracing the epidemiology and animal experiments that led British and American scientists to recognize cigarettes as a cause of lung cancer and other maladies, although research traditions in other parts of the world—notably Germany—are slighted.

The book also does a fine job exposing the industry's use of medical authority to sell cigarettes—via R. J. Reynolds's "More Doctors Smoke Camels" campaign, for example, but also through advertisements urging smokers to "make your own test," which Brandt astutely identifies as part of an effort to subvert the growing evidence of hazards. The industry has always been adept at neutralizing threats: The "health scare" of the early 1950s, for example, was effectively countered by a campaign to foment doubt and reassurance. And in the 1980s, following demonstrations of a lung cancer hazard from secondhand smoke, the industry blitzed the airwaves with a campaign identifying smoking as essentially a form of free speech.

Brandt devotes a great deal of attention to the recent history of litigation, with a major theme again being the industry's nimbleness at escaping threats. He is rightly critical of the 1998 Master Settlement Agreement between the companies and 47 states, which basically amounted to a tax on cigarettes (circa 45 cents per pack). The agreement led to a kind of government-industry co-dependency, insofar as Master Settlement Agreement payments depend on the cigarette companies remaining solvent—which helps explain why so many states have submitted briefs on behalf of the companies opposing high punitive damages.

There are some weaknesses in the book. Some prominent early critics are conspicuously absent, including the great journalist George Seldes, a kind of Naderite avant la lettre, who in the 1940s publicized Raymond Pearl's work on the diminished longevity of smokers and Angel Roffo's pioneering work on experimental tobacco carcinogenesis. (Roffo, an Argentine physician, showed that cancers could be induced by painting tobacco "tars" on the skins of laboratory rabbits.) Seldes also denounced the inclusion of tobacco as a part of the Marshall Plan: Europeans had other priorities. But Senator Willis Robertson from Virginia (father of the televangelist Pat, interestingly) thought otherwise and got tobacco included as part of the U.S. effort to rebuild Europe.

Brandt does a great job, though, of showing how rights language was effectively used

Undermining an icon. This 1990s anti-smoking ad subverts the imagery of the classic Marlboro cigarette marketing campaign.

CREDIT: VIVIANE MOOS/CORBIS

The reviewer is at the Department of History, Building 200, Stanford University, Stanford, CA 94305–2024, USA. E-mail: rproctor@stanford.edu

to block restrictions on (for example) smoking on airplanes, which for decades caused grief (and death) to both passengers and flight attendants. Smoking sections were a compromise of the 1970s, which critics compared to "having a peeing section in a swimming pool." Powerful senators from tobacco-growing states opposed a total in-flight ban, and it was not until 1990 that smoking was eliminated from all domestic flights. The Environmental Protection Agency declared environmental tobacco smoke a class A human lung carcinogen in 1992, by which time grassroots campaigns were under way to protect both machines and people from this pollutant.

One reason we know a lot about the tobacco industry stems from the millions of pages of internal documents released in the course of litigation. Documents now available online (*4*) contain a vast and largely untapped wealth of information about the industry, including letters to and from consumers and relations with foreign tobacco entities. In 2006, some 45 million pages became full-text searchable. So anyone with an Internet connection can now call up all documents containing expressions like "please destroy," "mere statistics," "cold hard facts," "cigarettes don't cause," or "doubt is our product." Searches of this sort allow one to probe the rhetorical microstructure of a major corporation cluster, which has never before been possible. With simple Boolean operators and specification of document type (press release, consumer letter, etc.), the possibilities are virtually endless.

Brandt's book is oddly pessimistic on its final page, concluding that the cigarette industry "is here to stay." If recent events are any guide, however, it could well be that the reforms now sweeping Italy, France, Ireland, and even Germany could presage a broader rollback of the industry. The biggest threats to its continued success could come from unanticipated directions—if, for example, the industry's malfeasance could be shown to be a crime against humanity, or if people were to start looking more creatively at the causes of, say, global warming. Tobacco growing is among the world's leading causes of deforestation, and cigarettes are a leading cause of industrial and forest fires. Cigarette butts are also one of the world's largest sources of litter, and in the United States alone tobacco growers apply 23 million pounds of pesticides every year. The contribution from eliminating smoking would be equivalent to raising fuel economy standards by several miles per gallon.

And we're not talking about a cottage industry. Over 500 million kilometers of cigarettes are smoked every year, enough to make a continuous chain from Earth to the Sun and back, with enough left over for a couple of round-trips to Mars. Are the virtues of the golden weed really worth these unsurpassed health and environmental costs?

References and Notes

1. R. Proctor, *Tob. Control* **15** (suppl. 4), 117 (2006).
2. R. Proctor, *Cancer Wars: How Politics Shapes What We Know and Don't Know About Cancer* (Basic, New York, 1995).
3. R. Proctor, *The Nazi War on Cancer* (Princeton Univ. Press, Princeton, NJ, 1999).
4. For example, documents obtained by the National Association of Attorneys General in the litigation that led to the 1988 Master Settlement Agreement comprise the bulk of the collection available at http://ltdlftd.library.ucsf.edu/queryform.jsp.

10.1126/science.1140259

ENVIRONMENT

Because Computers Don't Compost

Robin Nagle

Scholars of material culture "read" objects in an attempt to learn about variables like social organization, technological advances and adaptations, family structure, religious practice, and even simple habits of everyday life. Archaeology, the granddaddy of material culture studies, grew out of gentlemanly attempts to enliven the past by scrutinizing and speculating about its human-made or human-marked leftovers. Anthropology more generally has studied material culture for a century and a half. Franz Boas, a prominent figure in anthropology's formative years, first made a name for himself when he broke with common museum practice by insisting that artifacts collected from small-scale societies be considered within their cultural contexts.

Today, across disciplines as far-ranging as American studies, folklore, sociology, cultural geography, and the history of consciousness (to name only a few), students of material culture ask questions of objects—even seeking narratives that objects might reveal—to better understand expressions of humanness as old as civilization and as young as yesterday's trash.

High Tech Trash
Digital Devices, Hidden Toxics, and Human Health

by Elizabeth Grossman

Island Press, Washington, DC, 2006. 351 pp. $25.95. ISBN 9781559635547.

The latter constitutes a particularly rich approach. William Rathje, a Harvard-trained archaeologist first based in Arizona and now at Stanford, has built a career around careful investigations of contemporary household garbage. He has also excavated some of the United States's most infamous landfills. Heavily compressed strata in some older landfills never decompose, making them vast inadvertent repositories of material traces of culture across the tumultuous 20th century. "The artifacts that will fully represent our lives are safely stored within mega-time-capsules, which we call landfills," he writes. "It is these anonymous, random remains that will tell our story to the future…" (*1*).

A landfill is literally stuffed with goods gone bad, things mundane and rejected, that suggest an infinite number of narratives. A recent but already ubiquitous example of such landfilled material culture, ripe with story, is the defunct electronic device. Cyber-tools become cyber-trash at a worldwide rate of 20 million to 50 million metric tons a year, says Elizabeth Grossman in her thoughtful and disturbing book, *High Tech Trash: Digital Devices, Hidden Toxics, and Human Health.* She notes that they contribute as much as 70% of the heavy metals and 40% of the lead in landfills today. But the end point, as Grossman ably demonstrates, is only one of many convoluted narratives. The stories that animate electronics have many plots, subtexts, and contradictions.

Grossman (an environmental writer based in Portland, Oregon) attempts a Herculean task when she sets out to tell these many tales through life-cycle analyses of digital devices, from extraction of their raw components through their design and manufacture to their final resting places. Wayne Rifer, an environmental consultant she quotes, neatly sums up the challenge, "What you measure, you manage." He is referring to U.S. Environmental Protection Agency policies instituted in 2005 to track electronics as its own category of refuse, but the phrase is shorthand for themes at the heart of this book. Global links among research, development, manufacture, distribution, consumption, and discard are almost impenetrably complex, making them extremely difficult to measure or manage. A persistent and chilling consequence weaving throughout the book is an environmental impact so profound and pernicious that the word "footprint" is too limp. The impact can more accurately be called a trampling.

Consider silicon. Grossman proves herself a graceful writer in explaining the many and

The reviewer is at the Draper Program, New York University, 14 University Place, New York, NY 10003, USA. E-mail: robin.nagle@nyu.edu

confusing processes that turn silicon into a chip. Much of the work relies on toxins and immense quantities of water, putting workers at risk and polluting heavily. The longer-term legacy of silicon and affiliated elements is where the human drama becomes especially poignant. For years, the town of Mountain View in California was proud to host companies like Fairchild Semiconductor, GTE, Intel, and Mitsubishi. On the other side of the country, in Endicott, New York, townsfolk were equally proud of the local IBM plant. Those same villages now host some of the nation's largest Superfund sites as they grapple with vast plumes of trichloroethylene (TCE) in their groundwater, aquifers, and private wells. Environmentalists and state regulators believe that TCE, thought to be a neurotoxin, found its way into local water supplies through persistently sloppy and even illegal disposal practices used by businesses engaged in allegedly "clean" electronics manufacturing.

In tracing the alphabet soup of metals commonly found in electronics (aluminum, cadmium, gold, iron, lead, mercury, nickel, silver, tin, and zinc are just some), Grossman delves deepest into copper. About two-thirds of the world supply is obtained from open-pit mines. A quarter of the annual global production is destined for digital devices; some computers can include up to 1.8 kilograms. Although copper is 100% recyclable, it is rarely retrieved. The challenge lies in the copper being scattered across millions of individual machines, built into components not easily disassembled.

Recycling computers and other high-tech trash, although technically feasible, is not yet practiced on a large scale. (According to Grossman, 90% of discarded electronics end up in landfills or incinerators.) Most e-junk sent to recyclers finds its way to the developing world. One of the book's most unsettling sections describes families in China and in India dismantling computers by hand in the open air, burning circuit boards in makeshift hearths, and sluicing computer innards in pans of acid to retrieve trace bits of metals. The fires foul the air, raising childhood asthma rates. The acid baths have made local water unpotable, so supplies arrive by truck (*2*).

The European Union leads worldwide efforts to regulate e-recycling and to prevent such abuses. Its Waste Electrical and Electronic Equipment directive requires manufacturers of all electronics to take back and recycle their spent goods, a policy known as extended producer responsibility. Consumers may return used digital gizmos to local collection centers or directly to manufacturers, without charge. In addition, makers must provide recyclers with materials lists, a novel requirement in the world of high tech, and nations that would import e-waste for recycling must have labor and environmental safeguards equal to those of the exporting country. In other words, if the nation that wants to recycle electronics allows conditions that would not be legal in Paris or Prague, export from Paris or Prague (or from anywhere else in the EU) is prohibited.

Similar national legislation in the United States does not exist. Grossman points to a thick collection of competing interests that will probably guarantee a continued stalemate at the federal level, one of many discouraging details that makes *High Tech Trash* a sobering read. The author strays occasionally toward the grim tradition of environmental journalism that catalogs crises so far gone as to preclude any real solutions, but she avoids a descent into pure gloom with accounts of individuals and organizations working hard for cures to a host of electronic ills.

Among those ills are literal physical ailments. A class of brominated flame retardants called polybrominated diphenyl ethers (PBDEs), used in the hard plastic casing of many electronics, have achieved thorough global distribution, an especially insidious fact because they accumulate in organisms. PBDEs are becoming the polychlorinated biphenyls (PCBs) of the 21st century—but are not to be confused with tetrabromobisphenol A (TBBPA), a different kind of flame retardant used in circuit board plastics and considered highly toxic to organisms living in water. Had Grossman included a glossary, it would have provided a quick reference and thus an easy way to recall specific details about the many substances she discusses. The book would also have benefited from lists of organizations, laws, and directives, because those, too, are shorthanded with a clutter of acronyms.

But that's a small quibble. *High Tech Trash* adds an important voice to a body of literature that dissects material culture to reveal "the politics of knowledge and of ignorance; the politics of expertise and of sumptuary control; the politics of connoisseurship and of deliberately mobilized demand" (*3*), forces that, in the life stories of electronics, can obscure real risks hidden within the tangles of a complex story.

Remember when the computer age was touted as a nostrum for the accumulated sins of the Industrial Revolution? In thorough detail, Grossman reveals how dangerously delusional this notion has become. The once liberating story of electronic devices has found a sequel as Grossman details concomitant narratives of waste, environmental degradation, and political weakness. The chips may be tiny, but their impact is vast and alarming.

Dealing with digital garbage in China. Large quantities of obsolete electronics are shipped to developing countries where labor is cheap and environmental protection lax.

CREDIT: BOB SACHA/CORBIS

Visit our Books *et al.* home page
www.sciencemag.org/books

References and Notes

1. W. Rathje, *Sci. Am. Discov. Archaeol.* **1**, 86 (November-December, 1999).
2. Photographer Edward Burtynsky includes arresting and magisterial portraits of communities wrecked by electronics recycling in his book *China: The Next Industrial Revolution* (Steidl, Göttingen, 2005).
3. A. Appadurai, in *The Social Life of Things: Commodities in Cultural Perspective*, A. Appardurai, Ed. (Cambridge Univ. Press, Cambridge, 1986), pp. 3–63.

10.1126/science.1133919

MEDICINE

Environmental Biology and Human Disease

Better environmental biosensors are needed to study gene-environment interactions associated with disease.

David Schwartz* and Francis Collins

The etiology of most chronic human diseases (such as asthma, atherosclerosis, and cancer) is complex, involving a mix of genetic and environmental factors interacting with each other over hours, days, months, or years. Until recently, however, the disciplines of environmental sciences and genetics have proceeded independently; investigators in the former discipline have focused primarily on adverse conditions and diseases that are etiologically driven by environmental factors (such as benzene-induced leukemia), and those in the latter field have been finding genetic factors for highly heritable conditions (such as cystic fibrosis). Progress is now being made in identifying common genetic variations that contribute to complex diseases such as age-related macular degeneration (*1*, *2*), type 2 diabetes (*3*, *4*), and prostate cancer (*5*). However, the best opportunity to reduce risk in genetically susceptible people for the foreseeable future will not be to re-engineer their genes, but to modify their environment. The successful dietary treatment of phenylketonuria is a clear example.

We need to understand how genetic factors and environmental exposures interact in individuals to alter normal biological function and to affect the risk of disease development. This basic information is critical to understanding why and under what circumstances certain individuals develop disease and others remain healthy. Defining environmental contributions is also critical in identifying how and under what circumstances DNA sequence variations affect disease pathogenesis. For example, polymorphisms in CD14 and Toll-like receptor 4 are relevant in endotoxin-induced asthma but not in other more common types of asthma (*6*, *7*).

Progress in identifying genetic variations that contribute to common disease has been rapid in the last few years. Building on the foundation provided by the Human Genome Project, the International HapMap Consortium provided a public map (*8*) of human genetic variation. Dramatic advances in genotyping technology have led to a drop in cost of more than two orders of magnitude in just 5 years.

The same rapid rate of progress has not been achieved for precise, quantitative assays to measure environmental factors that contribute to adverse health outcomes. Certainly, assessment of environmental contributions is much more difficult than for genetic ones. The genome of an individual represents a bounded set of information, remains basically stable over time, and is very well suited to multiple analytical approaches. The potential universe of medically significant environmental exposures is much less well defined, and disease may appear several years after the exposure has ended. However, another explanation is apparent by contrasting the extensive investments in new genetic and genomic technologies over the past two decades with the much more modest expenditures in exposure sciences.

Traditional methods of assessing human exposure to chemical, dietary, physical, and psychosocial factors involve measuring the potentially toxic agent or exposure in environmental samples (air, water, or food) or biological specimens of blood and urine or, more commonly, characterizing the exposure event itself with regard to frequency, duration, and severity through questionnaires and other methods of recall. For example, the Centers for Disease Control and Prevention (*9*) have developed an extensive array of precise assays for toxins (natural source) and toxicants (synthetic source) that can be measured in various human specimens. However, these assays are not intended to provide information on the extent of the environmental exposure, the individual biological response, or the temporal relation between exposure and biological response. Existing methods of exposure assessment fail to capture the individual and dynamic extent of the exposure and its impact on fundamental biological processes.

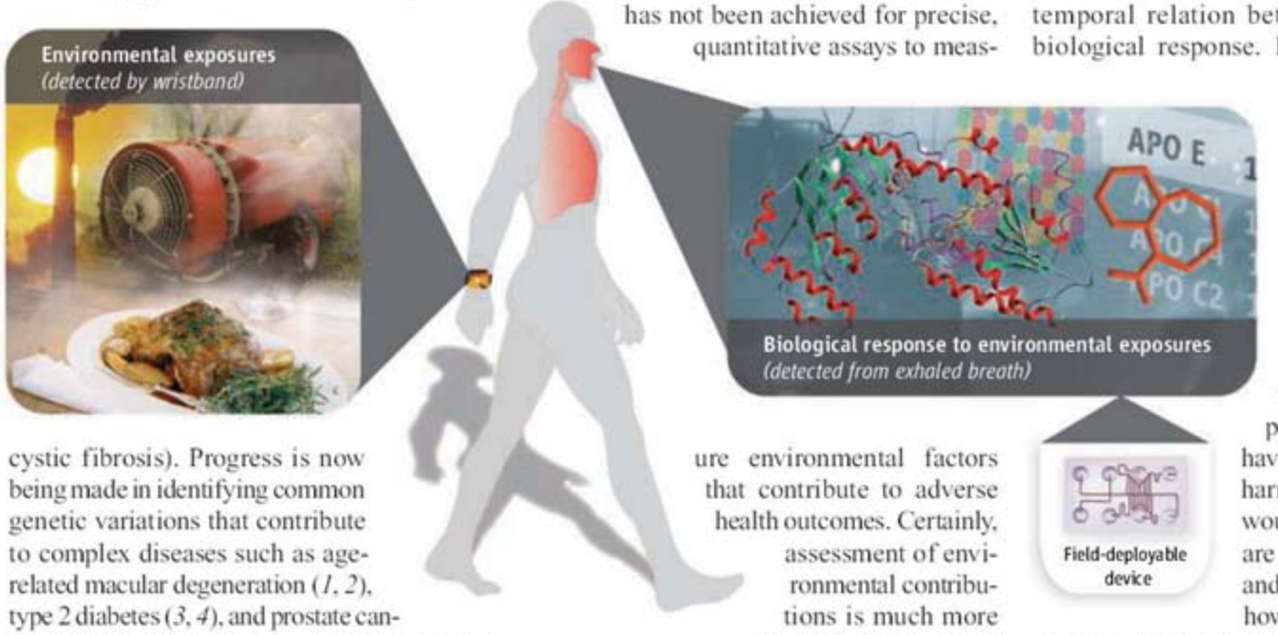

CREDIT: ADAPTED BY N. KEVITIYAGALA/SCIENCE; (PHOTOS) GETTY IMAGES; (PROTEIN STRUCTURE) NIST

Imagine that you could visit your family physician and be informed, by way of a personal sensor, that you have been exposed to a harmful substance that would explain why you are sick and inform you and your physician about how you should be treated. Imagine that you could wear a specialized wristband or a "smart shirt" that could alert you to the fact that your environment contains levels of air pollution that may increase your risk of having an asthma attack. Imagine that you had a hand-held device that could be used to determine whether the food you are eating contains harmful levels of trans fats, given your genetic predisposition to heart disease.

Recent advances in environmental and biological sensors suggest that the technologies are at hand, or can be readily engineered, to provide precise measures of chemical and biological hazards at the point of contact or to characterize the "biological fingerprint" left by a class of environmental stressors. Sensor technologies hold exceptional promise for providing critical information for continuous (real-time) data

collection and simultaneous measurement of multiple agents (multiplexing) within a single device. New sensing modalities have emerged from nanotechnology and nanoengineering, medical diagnostics, and biodefense arenas that could be adapted and developed for the exposure sciences. Artificial receptors such as molecularly imprinted polymers (MIPs) have potential as stable surrogates for biological recognition agents such as antibodies, enzymes, tissues, or cells (*10*).

In addition to being self-contained, these sensors should be capable of quantitative, continuous data capture in the field, without the need for sample processing and analysis at a laboratory. These devices must be easy-to-use; portable; minimally inconvenient (wristband, watch, phone, or lightweight purse); rugged; and inexpensive to deploy. This will require sophisticated computer systems and analytic approaches that can handle the immense volume and complexity of data generated for each individual and, also, would allow for integration of data on environmental exposures with genetic factors for the individual and the population.

Multiple molecular changes can result from environmental stressors, but not all of these changes are linked to increased disease risk. Thus, biosensors will need to record internal, molecular events that signify increased risk of disease from exposures to different forms of environmental stress, such as patterns of gene or protein expression (*11*), as well as to measure response indicators such as DNA or protein adducts (*12*) that persist even after the exposure has ended.

The importance of this opportunity has been recently highlighted at the National Institutes of Health by the launching of the Genes, Environment, and Health Initiative (GEI) (*13*), with strong support from U.S. Health and Human Services Secretary Michael Leavitt and NIH Director Elias Zerhouni. This $40 million-a-year interdisciplinary initiative, managed by a coordinating committee that we cochair, includes an Exposure Biology Program. The near-term goal of the program is to develop new noninvasive tools and biomarkers for assessing individual exposures to environmental stressors that interact with genetic variation to result in human disease. However, to fully appreciate the predictive importance of these measures of exposure, this technology needs to be deployed in large-scale case-control and population-based genetic studies of health and disease, some of which will include genome-wide association analysis through support from the Genetics Program of GEI and the National Children's Study (*14*).

Establishing partnerships in the scientific, technical, engineering, and business communities will be critical to our success. We need to define collectively appropriate milestones and deliverables for what can be achieved with this new technology, focusing on the types of environmental exposures and response indicators to be measured, the type of applications, and the level of temporal and spatial resolution. For example, there is a vast range of potential applications for small-scale sensing devices, such as cell-based microsystems or lab-on-a-chip technology, from the detection of individual molecules within single cells, to the measurement of global changes in genes, proteins, and metabolites in peripheral biofluids (*15*, *16*). We need to define the most critical questions in exposure biology up front so that scientists and the public understand the scope of technology that is required. In turn, engineers and manufacturers must identify the technological limitations and needs in this field.

Short-term strategies should target specific, attainable goals and deliverable devices that provide integrated panels of biomarkers for priority classes of environmental stressors, such as pesticides and solvents, as well as cholesterol-rich or heavy metal–contaminated foods. Immediately available technologies include point-of-contact environmental sensors and biosensors based on molecular assays, such as global protein or metabolite profiling and molecular imaging. Short-term strategies could be adapted for future applications that provide a much broader range of analytes and that include measurement of previously unknown stressors. More long-term investments should target high-risk, potentially high-benefit technologies, such as lab-on-a-chip or microfluidic devices, molecular probes, and imaging systems that incorporate multiplexed sensing capabilities for concurrent detection and quantification of environmental stressors with geospatial referencing and remote, real-time data capture.

A major hurdle is that the expertise needed to advance the science spans so many highly specialized fields and that interdisciplinary training and research opportunities are just beginning to evolve. In that regard, the National Institute for Environmental Health Sciences and the National Human Genome Research Institute have initiated a training program in environmental genomics (*17*) to bring these disciplines closer together and to train a new generation of scientists who are equally at home in both fields.

Initial field deployment will need to focus on small-scale studies and leverage, to the extent possible, existing population studies of environmental and genetic risk factors. This will allow time and opportunity to develop protocols that standardize methods of sample collection, processing, and storage; labeling molecules such as peptides with isotope tags; developing internal reference standards; and conducting data analysis. These steps are essential to achieve sufficient reproducibility and reliability of results that would make large-scale studies worthwhile. Concurrently, there would also be tremendous value to developing a biosample and data repository to promote sharing of scientific resources and discoveries made in exposure biology across multiple research programs. Of course, this would require a bioinformatics infrastructure to analyze the volumes of environmental and biomarker data generated and to integrate these data with the corresponding genomic information available for each individual and/or population. Ultimately, it is hoped that GEI will provide a way to identify subsets of individuals with high disease risks due to particular combinations of genetic variants and environmental exposures or stressors, as well as to lead to targeted therapies and intervention techniques for disease prevention and more effective health maintenance.

References and Notes

1. R. J. Klein *et al.*, *Science* **308**, 385 (2005).
2. Z. Yang *et al.*, *Science* **314**, 992 (2006).
3. S. F. Grant *et al.*, *Nat. Genet.* **38**, 320 (2006).
4. R. Sladek *et al.*, Nature **445**, 881 (2007).
5. L. T. Amundadottir *et al.*, *Nat. Genet.* **38**, 652 (2006).
6. F. D. Martinez, *Immunol. Allergy Clin. North Am.* **25**, 709 (2005).
7. N. C. Arbour *et al.*, *Nat. Genet.* **25**, 187 (2000).
8. International HapMap Consortium, *Nature* **437**, 1299 (2005).
9. National Center for Environmental Health, www.cdc.gov/nceh/.
10. V. B. Kandimalla, H. Ju, *Anal. Bioanal. Chem.* **380**, 587 (2004).
11. A. Spira *et al.*, *Proc. Natl. Acad. Sci. U.S.A.* **101**, 10143 (2004).
12. J. D. Groopman *et al.*, *Cancer Res.* **52**, 45 (1992).
13. Genes, Environment, and Health Initiative, http://genesandenvironment.nih.gov/.
14. National Children's Study, http://nationalchildrensstudy.gov.
15. J. El-Ali, P. K. Sorger, K. F. Jensen, *Nature* **442**, 403 (2006).
16. H. Craighead, *Nature* **442**, 387 (2006).
17. Training program in environmental genomics, http://staging.gei.nih.gov/traininggrants.asp.
18. Many of the ideas discussed in this manuscript evolved from the NIH Exposure Biology Workshop sponsored by National Institute of Environmental Health Sciences and National Human Genome Research Institute held in Greensboro, North Carolina, in May 2006 (www.gei.nih.gov/exposurebiology/meetings/exposurebiology06/). We thank the workshop participants for their commitment to this evolving field and B. Weis for her thoughtful advice and critical contributions to this manuscript.

10.1126/science.1141331

CREDITS (TOP TO BOTTOM):

DEVELOPMENTAL BIOLOGY

Dance of the Embryo

Imaging of early mouse embryonic development in vitro and in vivo raises new questions about how the embryo's initial axis is determined.

Richard R. Behringer

A picture may be worth a thousand words, but in biology it has become increasingly clear that static images are not sufficient to elucidate the complex behaviors of cells in their natural environment. This is especially true in the field of embryology, where snapshots of the progression from fertilized egg to a developing organism—with distinct tissues and a defined body axis—provide limited information about what happened before the picture was taken and offer little clue as to what might happen next. Technical difficulties have hindered progress in understanding the earliest stages of mammalian embryonic development—before implantation in the uterus. On page 719 in this issue, Kurotaki et al. (*1*) report using live fluorescent imaging to directly view a preimplantation-stage mouse embryo as it develops from a fertilized egg into a blastocyst, a spherical structure of about 50 to 60 cells. The cells (blastomeres) of these embryos move much more than previously thought, which has obscured our understanding of how the blastocyst is formed. The movies of Kurotaki *et al.* provide the clearest views of early mammalian embryo axis formation.

So-called preimplantation embryonic development includes fertilization of the oocyte followed by its cleavage to produce blastomeres. The first steps of cellular differentiation occur within an acellular glycoprotein-rich membrane called the zona pellucida (see the figure). Kurotaki *et al.* find that blastomeres move extensively, causing the embryo to wiggle and "dance" within the zona pellucida.

The author is in the Department of Molecular Genetics, University of Texas M. D. Anderson Cancer Center, Houston, TX 77030, USA. E-mail: rrb@mdanderson.org

The mammalian blastocyst consists of a single layer of cells called the trophoblast that surrounds a fluid-filled cavity. An inner cell mass of pluritpotent cells is located at one side of the blastocyst called the embryonic (E) pole. Opposite of this is the abembryonic (Ab) pole, creating the embryonic-abembryonic (E-Ab) axis (*2*). The trophoblast gives rise to placental tissues, whereas the inner cell mass gives rise to the embryo proper and some placental tissues. Although the functional importance of the E-Ab axis has yet to be determined, it is the first morphological axis that can be distinguished in the developing mouse embryo, and researchers have concentrated on the molecular and cellular mechanisms that lead to its formation (*3*). It has been thought that the E-Ab axis may presage the anterior-posterior body axis.

The ideal way to follow the fates of cells within a developing embryo is to watch the embryo, unperturbed, in its natural environment. Intrusive methods, such as injecting molecules into blastomeres to mark them, or removing or adding blastomeres, can alter normal development. In recent years, fluorescent proteins have been created to visualize specific organelles (for example, the nucleus) within live cells (*4*, *5*). Kurotaki *et al.* generated a transgenic mouse line in which the gene for a nuclear-localized green fluorescent protein was introduced into a ubiquitously expressed genetic locus. The fluorescent protein is thus expressed in all cells, and precisely pinpoints the position of each blastomere and its cellular progeny by "painting" chromosomes as the cells divide. The authors could continuously image the embryos from the two-cell stage to the blastocyst stage in vitro by fluorescence microscopy. Consistent with previous reports (*6*), Kurotaki *et al.* found that the blastomeres move extensively at each stage of cell cleavage, causing the embryos to move within the zona pellucida. By following the cellular progeny of each of the two initial blastomeres (of the two-cell stage embryo), the authors determined their final positions within the blastocyst. Each of the initial two blastomeres gives rise to cells in both the embryonic and abembryonic regions.

Of course, one could argue that in vitro conditions might alter normal embryonic development. Therefore, the authors developed another transgenic mouse line that ubiquitously expresses a green fluorescent protein but emits red fluorescence after exposure to weak ultraviolet light (*7*). As such, one blastomere of a two-cell-stage embryo could be labeled red, while the other remained labeled with green fluorescence. These dual-labeled embryos were then transferred into the oviducts of female mice for in vivo development to the blastocyst stage, and the distribution of green and red cells was determined. These in vivo results were essentially identical to the in vitro results.

The findings of Kurotaki *et al.* are generally consistent with other reports that each blastomere of the two-cell embryo will give rise to cells in both the embryonic and abembryonic regions, and with the relation of the positions of the blastomeres in the two-cell embryo (called the two-cell boundary or axis) to the E-Ab axis. The study also resolves some discrepancies between these previous studies by showing that when these "dancing" embryos within the zona pellucida are immobilized with alginate, there is a correlation between the two-cell boundary and that of the E-Ab axis. A controversial recent study (*8*) suggests that one blas-

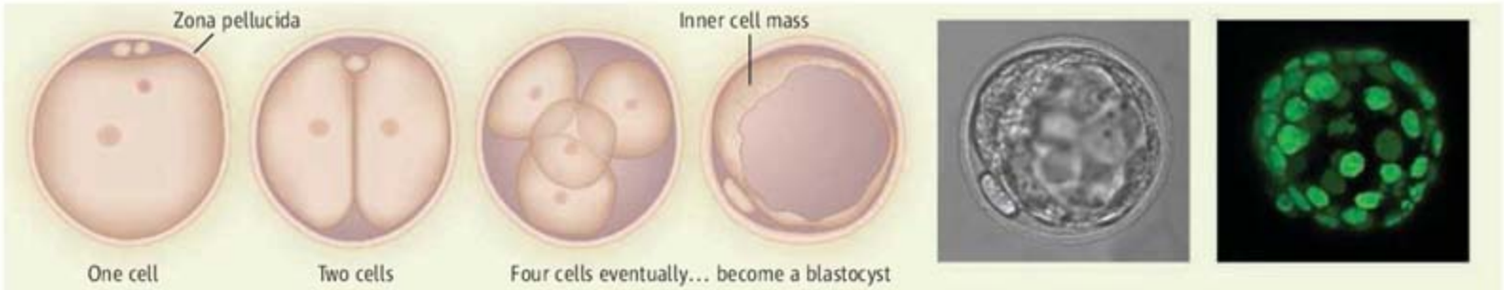

Watching every move. (Left) A schematic of four stages of early mouse embryonic development. The blastocyst-stage embryo of a transgenic mouse in which all the nuclei are labeled with a nuclear-localized fluorescent protein; bright-field (**middle**) and fluorescence (**right**) images.

PHOTO CREDITS: ANNA-KATERINA HADJANTONAKIS/SLOAN-KETTERING INSTITUTE

tomere of a two-cell embryo gives rise to the entire trophoblast and the other to the entire inner cell mass, and that these fates correlate with the localization of Cdx2 protein, a transcription factor. The elegant results of Kurotaki *et al*. clearly demonstrate that the establishment of the E-Ab axis does not depend on cell lineage; that is, each blastomere at the two- and four-cell stage gives rise to cells in the embryonic and abembryonic regions. These results are also consistent with the notion that E-Ab axis formation does not depend on localized molecules within the zygote (*3*, *6*).

Although much attention has centered on the formation of the E-Ab axis, there is still no evidence that this axis has any functional relevance for the development of subsequent axes in the mature organism. Kurotaki *et al*. also show that the zona pellucida is not spherical but rather ellipsoidal and that the E-Ab axis of the blastocyst aligns with the short axis of the zona likely because of the physical constraints exerted by this glycoprotein layer (*6*). The shape of the zona pellucida and alignment of the E-Ab axis may facilitate the movements of the zona pellucida–enclosed blastocyst from the oviduct into the uterus or movement through the uterus to implantation.

Is this E-Ab axis conserved in other mammals, including humans? Marsupial blastocysts do not have an inner cell mass, and egg-laying mammals do not generate a blastocyst (*9*). Snapshots of these other types of mammals still only offer a limited view of the true picture. Their embryonic dances remain a secret.

References

1. Y. Kurotaki, K. Hatta, K. Nakao, Y.-i. Nabeshima, T. Fujimori, *Science* **316**, 719 (2007).
2. P. P. Tam, R. R. Behringer, *Mech. Dev.* **68**, 3 (1997).
3. J. Rossant, P. P. Tam, *Dev. Cell* **7**, 155 (2004).
4. A. K. Hadjantonakis, V. E. Papaioannou, *BMC Biotechnol.* **4**, 33 (2004).
5. J. M. Rhee *et al*., *Genesis* **44**, 202 (2006).
6. N. Motosugi *et al*., *Genes Dev.* **19**, 1081 (2005).
7. K. Hatta, H. Tsujii, T. Omura, *Nat. Protocols* **1**, 960 (2006).
8. K. Deb, M. Sivaguru, H. Y. Yong, R. M. Roberts, *Science* **311**, 992 (2006).
9. R. R. Behringer, G. S. Eakin, M. B. Renfree, *Reprod. Fertil. Dev.* **18**, 99 (2006).

10.1126/science.1142967

MATERIALS SCIENCE

How Nanowires Grow

A controversy about the way in which semiconductor nanowires grow has been resolved.

Volker Schmidt and Ulrich Gösele

Many controversies boil down to which of two distinctly different explanations, models, or options is the correct one. On page 729 of this issue, Kodambaka *et al*. (*1*) address a long-standing controversy—whether, below a certain temperature, the growth of semiconductor nanowires involves a liquid droplet or a solid particle of the catalytic material. Unexpectedly, their elegant experiments show that both answers are correct: Under the same experimental conditions, growth may occur via a liquid droplet and via a solid particle. The results may help to devise methods for controlling the growth of nanowires.

Semiconductor nanowires have emerged alongside carbon nanotubes as a potential building block for future nanometer-scale electronic devices. Yet, in contrast to carbon nanotubes, which may be either semiconducting or metallic, the properties of semiconductor nanowires are always determined by the properties of the semiconductor material they are made of. Furthermore, a variety of semiconductor materials—such as silicon, germanium, gallium arsenide, and gallium nitride—with different electronic and optical properties may be fabricated in the form of nanowires. All these features make semiconductor nanowires especially attractive for future electronic and photonic nanodevices.

The authors are at the Max Planck Institute of Microstructure Physics, Weinberg 2, 06120 Halle, Germany. E-mail: vschmidt@mpi-halle.eu; goesele@mpi-halle.eu

Most semiconductor nanowires are fabricated by the vapor-liquid-solid (VLS) process originally suggested and investigated more than 40 years ago by Wagner and Ellis (*2*). In this process, the semiconductor material (usually supplied as a gas) is absorbed by liquid nanodroplets of an appropriate catalytic material such as gold. These nanodroplets, located at the nanowire tips, serve as seeds for nanowire growth and also determine the nanowire diameters. The semiconductor material condenses at the interface between the droplet and the nanowire, thereby extending the length of the nanowire. Morales and Lieber were the first to use the VLS process in 1998 in the context of nanoelectronics (*3*), triggering a worldwide avalanche of research activities into nanowire synthesis (*4*).

In VLS growth, the liquid droplet consists not only of the catalytic material but also of a certain amount of the semiconductor material in question. This is because the mixed material has a much lower melting temperature than each of the two constituents, for example, gold and germanium. The lowest possible melting temperature for a specific composition is called the eutectic temperature, T_E. For the gold-germanium system, this temperature is 361°C and occurs at a Ge:Au ratio of 7:18.

Above the eutectic temperature, semiconductor nanowires grow via the VLS mechanism. However, nanowire growth has also been reported to occur at temperatures below the eutectic temperature (*5*–*9*). Any growth observed in these cases should involve a solid catalytic particle. However, errors in the temperature measurement could not be excluded; furthermore, the eutectic temperature may shift as a result of nanometer-scale size effects. It there-

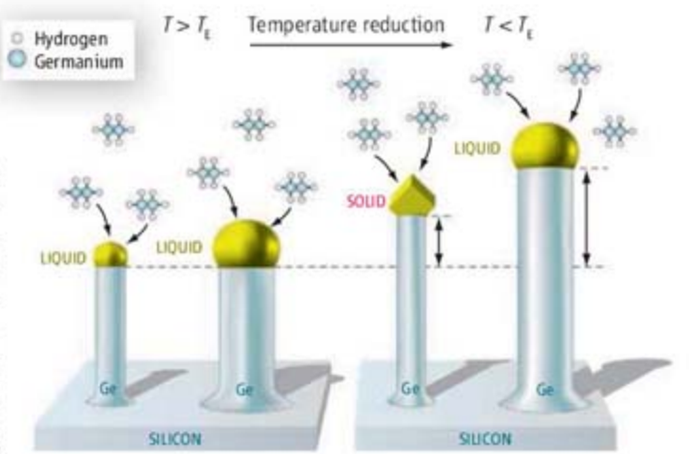

Germanium nanowires. The mechanism by which Ge nanowires grow may depend not only on the temperature but also on the diameter of the nanowire, as shown by Kodambaka *et al*. Above T_E **(left)**, the nanowires have a liquid gold cap and grow via VLS growth. Below T_E **(right)**, the cap of relatively thick nanowires is liquid, whereas the cap of relatively thin nanowires becomes a crystalline solid. The latter nanowires grow via a different mechanism that is slower than VLS growth.

CREDIT: ADAPTED BY P. HUEY/SCIENCE

fore remains hotly debated whether the catalyst in this case is a liquid droplet or a solid particle.

The problem with most investigations on this subject was that detailed structural analyses, for example, with electron diffraction methods, could only be performed after the growth had terminated, leading to additional uncertainties. In contrast, Kodambaka *et al.* (*1*) investigated the growth of gold-catalyzed germanium nanowires in situ in a transmission electron microscope that allows for the supply of germanium vapor in the form of digermane (Ge_2H_6) gas.

For the gold-germanium system, several reports have suggested nanowire growth below the eutectic temperature (*5*, *6*). A key indicator was the shape of the gold at the tip of the nanowire. A liquid gold droplet has a smooth, almost half-spherical shape, whereas solid gold shows planes, edges, and corners that may easily be identified.

As expected, above the eutectic temperature, nanowire growth involves a liquid droplet on top of the germanium nanowires (see the figure, left panel). However, when the authors reduced the temperature to below the eutectic temperature while keeping the supply of germanium constant, they observed two distinctly different phenomena (see the figure, right panel). Some gold nanodroplets remained liquid even though the temperature was, in one case, more than 100°C below the T_E of 361°C. The authors observed this VLS-type growth mostly for nanowires with relatively large diameters.

In contrast, for nanowires with relatively small diameters, the gold droplet became solid as the temperature fell below T_E. The nanowires continued to grow, but did so much more slowly than in the case of VLS growth (see the figure, right panel). Further cooling experiments showed that the transformation of the gold caps from liquid to solid at temperature below T_E could be delayed for tens of minutes. Kodambaka *et al.* show that this delay depends on various parameters, such as the vapor pressure, the temperature, and the diameter of the nanowires.

The experiments of Kodambaka *et al.* clearly demonstrate that—even well below the eutectic temperature—the gold catalyst droplet can remain liquid, corresponding to VLS growth, and that solid gold particles can also catalyze nanowire growth. Which situation is actually present in an experiment depends on specific parameters, including the thermal history of the samples. This opens new opportunities to control of the growth of germanium and other semiconducting nanowires, which will bring nanowires one step closer to real applications.

References

1. S. Kodambaka *et al.*, *Science* **316**, 729 (2007).
2. R. S. Wagner, W. C. Ellis, *Appl. Phys. Lett.* **4**, 89 (1964).
3. A. M. Morales, C. M. Lieber, *Science* **279**, 208 (1998).
4. C. M. Lieber, Z. L. Wang, *MRS Bull.* **32**, 99 (2007).
5. G. A. Bootsma, H. J. Gassen, *J. Crystal Growth* **10**, 223 (1971).
6. H. Adhikari *et al.*, *Nano Lett.* **6**, 318 (2006).
7. A. I. Persson *et al.*, *Nat. Mater.* **3**, 677 (2004).
8. K. A. Dick *et al.*, *Nano Lett.* **5**, 761 (2005).
9. Y. Wang *et al.*, *Nat. Nanotech.* **1**, 186 (2006).

10.1126/science.1142951

CHEMISTRY

The New Face of Catalysis

Platinum nanocrystals with unusual shapes show unusually high catalytic activity, suggesting possible ways to enhance catalysis in other materials.

Daniel L. Feldheim

A secure energy future depends heavily on whether chemists and materials scientists can discover more efficient, stable, and economical catalysts for the production and use of alternative fuels. Indeed, a recent report by the Department of Energy describes this as a grand challenge, specifically citing the need to understand the relationship between catalyst structure and chemistry, and to exploit advances in the synthesis of nanoscale materials (*1*). As reported on page 732 of this issue, Tian *et al.* have made a breakthrough in the synthesis of nanoscale catalysts (*2*). They describe the synthesis of platinum nanoparticles of an unusual shape. Remarkably, the crystals each possess 24 faces (see the figure), which confer an enhanced ability to oxidize organic fuels, such as formic acid and ethanol, compared with the analogous spherical polycrystalline particles.

Researchers have known that a material's size and shape strongly affect its properties since the 1850s, when Michael Faraday postulated that the color of ruby glass was due to finely divided gold particles. To test his hypothesis, Faraday developed a method for preparing aqueous gold colloids (*3*). Suspended in solution, these spherical colloids exhibited the same brilliant red colors observed in ruby glass. Today, the controlled synthesis of gold and silver rods, cubes, hollow shells, and triangular prisms allows their colors to be tuned across the visible spectrum and into the near-infrared range (*4*).

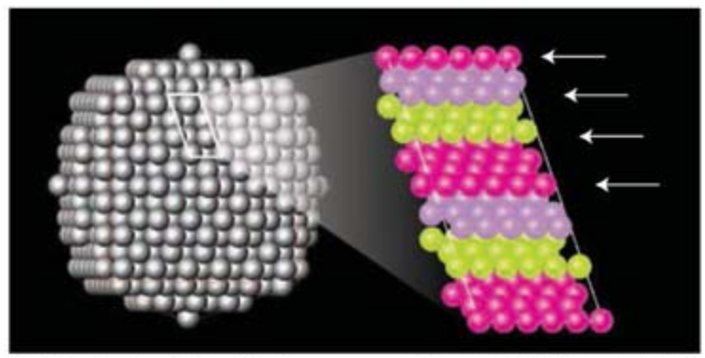

CREDIT: JAMES D. MARTIN

Multifaceted particles. Platinum nanoparticles with 24 high-index [730] faces (**left**) have an abundance of low-coordination, high-reactivity atomic edges sites (**right**). [Adapted from (*2*)]

The catalytic properties of metal nanoparticles are every bit as dramatic as their optical properties. Long considered an inert metal, gold nanoparticles supported on TiO_2 are highly active catalysts for the oxidation of CO (*4*). Moreover, gold reactivity appears to peak at nanoparticle diameter of 3 nm. The catalytic activities of platinum nanoparticles with tetrahedral, cubic, and spherical shapes also vary significantly (*5*). These reactivity differences can be attributed in part to the potential binding sites presented by atoms situated at the corners and edges of a nanoparticle. Indeed, the data show that the rate of a catalyzed reaction increases exponentially with the percentage of these atomic sites (*5*). A major challenge for catalysis researchers lies in understanding how to control nanoparticle shape to maximize the number of coordinatively unsaturated (open) surface sites.

For this reason, the results of Tian *et al.* are

The author is in the Department of Chemistry and Biochemistry, University of Colorado, Boulder, CO 80309, USA. E-mail: Daniel.Feldheim@Colorado.edu

most compelling. Most nanoparticle synthesis methods result in nanoparticles bounded by low-index, low-energy faces such as the {111} or {100} atomic planes (*6*). This makes intuitive sense, as any high-energy face should grow itself out of existence, leaving particles bound by more stable faces. Unfortunately, particles with mostly low-energy surfaces contain a low percentage of atomic edge and corner sites. The synthetic method of Tian *et al.* produces particles capped by {730} faces, a surface structure that contains a relatively high density of atomic step edges (see the right panel of the figure). The authors calculated that 43% of the total number of surface atoms reside along steps, which can be compared to 6%, 13%, and 35% for 5-nm-diameter platinum cubes, spheres, and tetrahedral particles, respectively (*5*).

Along with the increase in edge atoms, Tian *et al.* report an increase in the efficiency of ethanol and formate oxidation. The enhancement factor, defined as the ratio of fuel oxidation rates by Pt tetrahexadra (nanocrystals with 24 faces) versus spheres, was 400% for formate and 200% for ethanol. The platinum tetrahexahedra were also unexpectedly thermally stable, resisting morphological changes even at temperatures of 800°C. This is an important consideration in fuel cell applications where temperatures of hundreds of degrees Celsius are often employed to maximize efficiency and reduce problems with CO.

Perhaps as surprising as the resulting shape and catalytic activity of the platinum tetrahexahedra is the method Tian *et al.* used to fabricate the particles. A majority of synthetic methods aimed at manipulating the size and shape of nanoparticles have used molecules, surfactants, or polymers to mediate particle growth. When present in solution during particle nucleation and growth, these mediators can bind preferentially to certain faces of the growing particle. This can slow or speed growth along those faces relative to others, affecting the shape of the resulting nanoparticle.

Like Michael Faraday more than 150 years ago, however, Tian *et al.* used an electrochemical method to generate their nanoparticles, electrodepositing them onto a graphite electrode. Although the electrodeposition of spherical palladium nanoparticles and nanowires at constant potential has been demonstrated previously, those structures had a rough and granular morphology and grew along step edges on the graphite substrate (*7*).

Tian *et al.* first deposited platinum spheres on the electrode using a constant potential but then added a potential pulse sequence that alternated between reducing and oxidizing potentials at a rate of 10 Hz. The alternating potential caused electrochemical reactions on the nanoparticle surface that may affect its growth in much the same way that molecular mediators manipulate the growth of nanoparticles from solution. During the positive potential steps, a monolayer of PtO and PtOH is thought to form on the high-index {730} faces, which increases their stability. In contrast, oxygen atoms may diffuse into the lattice beneath the {111} faces, creating an unstable, disordered surface structure. As the electrode potential is gradually made negative, the oxide/hydroxide surface is removed, and fresh platinum is deposited in place of the atoms at the {111} face, preserving the {730} faces.

With this electrochemical approach to nanoparticle shape control, metal deposition times and adsorption reaction rates can be controlled precisely through applied potential and potential step frequency. It will be interesting to learn more about the role of these parameters in directing nanoparticle shape. It will also be exciting to explore the electrochemical synthesis of mixed metal and metal oxide nanoparticles, because the presence of other atoms at edge sites in the lattice could enhance catalytic reactivity further, while lessening the amount of expensive precious metal used.

References and Notes

1. Basic Energy Sciences Advisory Committee, "Opportunities for Catalysis in the 21st Century" (2002). Available at www.science.doe.gov/bes/reports/files/OC_rpt.pdf.
2. N. Tian, Z.-Y. Zhou, S.-G. Sun, Y. Ding, Z. L. Wang, *Science* **316**, 732 (2007).
3. M. Faraday, *Philos. Trans.* **147**, 145 (1857).
4. C. Burda *et al.*, *Chem. Rev.* **105**, 1025 (2005).
5. R. Narayanan *et al.*, *Nano Lett.* **4**, 1343 (2004).
6. The numbers in brackets constitute a Miller index. They are used to define atomic packing at the surface of a material. A low-index (small numbers) surface will generally have a lower energy than a high-index surface because the atoms are packed more tightly and will thus have fewer open coordination sites.
7. F. Favier, *Science* **293**, 2227 (2001).

10.1126/science.1143093

PLANT SCIENCE

Signaling to the Nucleus with a Loaded GUN

Da-Peng Zhang

Plant chloroplasts respond to environmental and developmental stress through a signaling pathway that controls gene expression in the nucleus.

Chloroplasts, the cellular organelle in plants where photosynthesis takes place, are responsible for capturing the solar energy that fuels the activities of many organisms on Earth. The ancestors of these plastids were cyanobacteria that were engulfed by a eukaryotic cell. Through a process of symbiogenesis, most symbiont genes were transferred to the host genome, such that more than 95% of chloroplast proteins are encoded by nuclear genes (*1*). This dispersal of genetic material requires plant cells to coordinate gene expression in both organelles. Much of this involves anterograde communication, from the nucleus to the chloroplast. In return, chloroplasts send retrograde signals to the nucleus to control the expression of nuclear genes that encode chloroplast proteins. This bidirectional signaling is necessary for plants to maintain their photoautotrophic lifestyle and adapt to challenging environments. On page 715 of this issue (*2*), Koussevitzky *et al.* begin to define a retrograde signaling pathway that multiple chloroplast signals use to communicate with the nucleus.

Three independent chloroplast retrograde signals have been identified in algae and higher plants (*3*). The best-defined signal is the accumulation of Mg–protoporphyrin IX (Mg-ProtoIX), a tetrapyrole that is generated during chlorophyll biosynthesis. Alterations in plastid gene expression and in the photosynthetic electron transport chain also trigger retrograde signals, generally in response to aberrant chloroplast development and to stressful environmental conditions. However, little has been known about how these events in the chloroplast impinge upon the nucleus. Koussevitzky *et al.* now report that in the model plant *Arabidopsis thaliana*, the chloroplast-localized pentatricopeptide-repeat protein GUN1 (genomes uncoupled 1) is a node where different chloroplast retrograde signals converge. They also identify the nuclear AP2 (APETALA 2)–type transcription factor ABI4

The author is in the State Key Laboratory of Plant Physiology and Biochemistry, College of Biological Sciences, China Agricultural University, 100094 Beijing, China. E-mail: zhangdp@souhu.net

[abscisic acid–insensitive 4] in this chloroplast-to-nucleus signaling pathway. This result not only identifies GUN1 as a central signaling component, but also establishes that one signaling pathway is common to three retrograde signals.

What is the identity of GUN1? Despite the isolation of the *gun1* mutant 14 years ago (*4*), it has only now been cloned by Koussevitzky *et al*. The *Arabidopsis GUN* loci include the genes *GUN1*, *2*, *3*, *4*, and *5* (*4*, *5*). The proteins GUN2, 3, 4, and 5 constitute the machinery that generates Mg-ProtoIX (*6*, *7*). Previous genetic studies suggested GUN1 involvement in both Mg-ProtoIX and plastid gene expression retrograde signaling (*3*, *4*). Koussevitzky *et al*. identify GUN1 as a member of pentatricopeptide-repeat superfamily, one of the largest and most enigmatic protein families in land plants. There are about 450 members in *Arabidopsis*. Pentatricopeptide-repeat proteins likely control gene expression by binding to RNA transcripts in mitochondria (another organelle that harbors a separate genome) and chloroplasts (*8*). Only a few family members, however, have been ascribed biological functions. Koussevitzky *et al*. show that GUN1 is a chloroplast-localized protein that binds to DNA, suggesting that it may regulate retrograde signaling by controlling plastid gene expression. Moreover, GUN1 regulates a set of nuclear target genes in common with GUN5, and acts downstream of the Mg-ProtoIX signal generators GUN2, 3, 4, and 5 (*2*).

What are the targets outside the chloroplast to which GUN1 relays the retrograde signals? Koussevitzky *et al*. show that the nuclear transcription factor ABI4 is activated downstream of GUN1. In response to GUN1 activation, ABI4 binds to a specific regulatory element in DNA, thereby repressing the expression of target genes. Furthermore, the GUN1-ABI4 pathway not only conveys the Mg-ProtoIX signal, but also the retrograde signals derived from alterations in plastid gene expression and in the photosynthetic electron transport chain. It is not clear whether the three chloroplast signals lead to the production of a common signal that is then perceived by GUN1, or whether GUN1 generates a common signal in response to the three signals. In either case, GUN1 appears to serve as a key relaying component, sending the pertinent message to the nucleus.

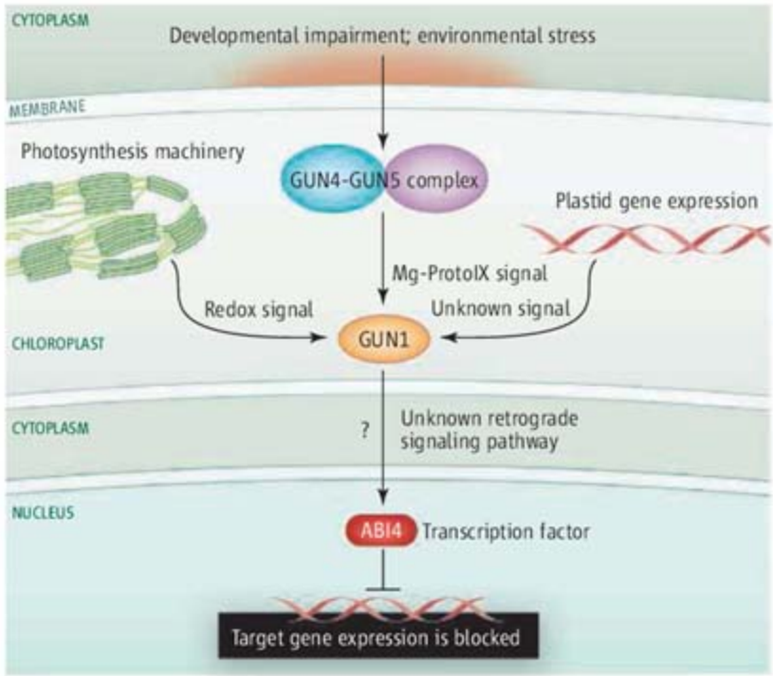

Backtalk. Three chloroplast signals—Mg-ProtoIX and signals derived from the chloroplast genome and the photosynthetic machinery—generate a common signal. GUN1 may either generate this common signal or perceive it. GUN1 then communicates with the nucleus (by an unknown pathway) to control gene expression by the transcription factor ABI4.

This is particularly interesting because the identity of plastid gene expression signal remains elusive. As well, the redox state of the plastoquinone pool or reactive oxygen species generated in chloroplasts elicits a nuclear response, but it has been unclear how redox signals are delivered to the nucleus. It now appears that these signals converge onto the GUN1-ABI4 pathway (see the figure).

ABI4 also regulates nuclear gene expression in response to the plant hormone abscisic acid (*9*), which plays an important role in chloroplast development and function. GUN5 also happens to be a receptor for abscisic acid (*10*). In addition, abscisic acid precursor biosynthesis occurs in chloroplasts, and the organelle harbors an intracellular pool of the hormone. This raises the question of whether the hormone signal and retrograde signals cross-talk to control nuclear gene expression. Regulatory elements that respond to abscisic acid are found in promoter region of many nuclear genes that encode chloroplast proteins. Moreover, abscisic acid represses the expression of nuclear genes that encode chloroplast proteins, including those involved in photosynthesis and tetrapyrrole biosynthesis (*11*). Many of these nuclear genes are also targets of the GUN1-ABI4 retrograde signaling pathway. However, Koussevitzky *et al*. show that GUN1-ABI4–mediated retrograde signaling is independent of hormone signaling. Shen *et al*. (*10*) also show that abscisic acid signaling through GUN5 is distinct from plastid retrograde signaling through GUN5. Both studies suggest that hormone signaling shares some components with chloroplast-to-nucleus signaling, but the two pathways do not appear to interact. But given the important role of abscisic acid in regulating the expression of nuclear genes that encode chloroplast proteins, it is worth further investigating whether the two signaling pathways intersect at some currently unidentified nodes or in some as yet unknown manner.

What might be the advantage of a single pathway that integrates numerous signals? Because of their fixed location, plants must endure various stressful conditions, and as such, generate multiple signals to ensure survival. The diversity of signals is necessary to maximize the chances of successfully altering gene expression. Integration of the multiple signals is essential for coordinating gene expression to achieve appropriate physiological responses. Such integration of multiple signals is seen in phytohormone signaling (*12*) and flowering regulation (*13*). It is not yet clear whether GUN1 functions alone, or whether additional regulators are at work or at least poised to function when the GUN1-mediated step is lesioned. It seems necessary, for example, to explore possible redundant functions of GUN1 homologs within the pentatricopeptide-repeat family in regulating the retrograde signaling, and to screen other downstream transcription factors. The story is only beginning to unfold.

References

1. G. I. McFadden, *Plant Physiol.* **125**, 50 (2001).
2. S. Koussevitzky *et al*., *Science* **316**, 715 (2007); published online 29 March 2007 (10.1126/science.1140516).
3. A. Nott, H. S. Jung, S. Koussevitzky, J. Chory, *Annu. Rev. Plant Biol.* **57**, 739 (2006).
4. R. E. Susek, F. M. Ausubel, J. Chory, *Cell* **74**, 787 (1993).
5. G. Vinti *et al*., *Plant J.* **24**, 883 (2000).
6. N. Mochizuki, J. A. Brusslan, R. Larkin, N. Nagatani, J. Chory, *Proc. Natl. Acad. Sci. U.S.A.* **98**, 2053 (2001).
7. R. M. Larkin, J. M. Alonso, J. R. Ecker, J. Chory, *Science* **299**, 902 (2003).
8. C. Lurin *et al*., *Plant Cell* **16**, 2089 (2004).
9. R. R. Finkelstein, S. S. L. Gampala, C. D. Rock, *Plant Cell* (suppl.), S15 (2002).
10. Y. Y. Shen *et al*., *Nature* **443**, 823 (2006).
11. S. Penfield, Y. Li, A. D. Gilday, S. Graham, I. A. Graham, *Plant Cell* **18**, 1887 (2006).
12. P. Achard *et al*. *Science*, **311**, 91 (2006).
13. S. D. Michaels, E. Himelblau, S. Y. Sang, F. M. Schomburg, R. M. Amasino, *Plant Physiol.* **137**, 149 (2004).

10.1126/science.1142703

CREDIT: P. HUEY/SCIENCE

PLANETARY SCIENCE

Hot News on Mercury's Core

Radar measurements show that the outer core of Mercury is molten, providing insight into the planet's history and the origin of its magnetic field.

Sean C. Solomon

Some 30 years ago the planetary science community was surprised when the Mariner 10 spacecraft flew by the planet Mercury and detected an internal magnetic field (*1*). Earth's internal field is produced by a magnetic dynamo sustained by convective motions in the planet's molten, iron-rich outer core. Although Mercury's high bulk density indicates that its dominantly iron central core is the largest by fractional mass among the planets (*2*), the detection of its magnetic field was surprising because Venus has no field and Mars and the Moon show evidence only for ancient global fields. With a mass about 5% that of Earth, Mercury had been expected to have cooled internally to the point where either the core had solidified or core convection no longer occurs. A necessary condition for Mercury's magnetic field to arise from an active Earth-like dynamo is that at least the outer shell of its core be molten. On page 710 of this issue, Margot *et al.* report new observations of variations in Mercury's spin rate made with Earth-based radar, providing strong evidence that this condition is met (*3*).

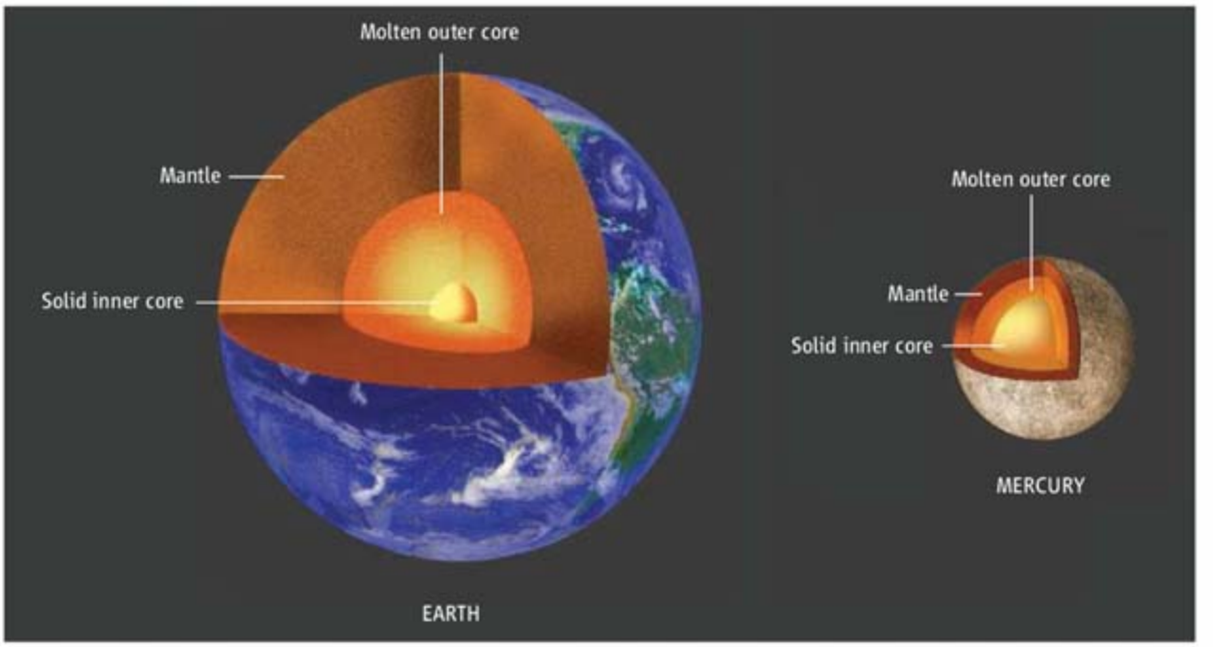

Core issues. The solid inner core and fluid outer core of Earth are shown to approximate scale. Mercury's outer core is now known to be fluid (*3*), but its radius and the nature and radius of any solid inner core remain to be determined.

The radar measurements constitute a triumph of two theoretical ideas developed decades ago. Shortly after the Mariner 10 discovery, Peale (*4*) outlined a procedure to determine whether the planet has a fluid outer core. His method was based on the observation that Mercury is in an orbital state in which the planet completes three rotations about its spin axis for every two revolutions around the Sun. The procedure requires the measurement of the small oscillation in the planet's spin rate (libration)—a few hundred meters in amplitude—forced by solar torques as Mercury follows its 88-day eccentric orbit. Additional parameters that must be known include the tilt of the spin axis and the components of the planet's gravity field describing the degree to which the field is flattened at the poles and out of round along the equator. The last two quantities have been estimated, albeit with low precision, from Mariner 10 tracking observations made during the probe's three encounters with Mercury during 1974–75, but the libration amplitude and a sufficiently accurate pole position were not known before now.

The second theoretical development, by Green (*5*) and Holin (*6*), stems from the recognition that irregularities, or speckles, in the radar signal returned from a planetary target rotate in space as the planet spins. Under suitable geometric constraints, analysis of radar signals recorded at two stations on Earth can detect this rotation as the speckle pattern sweeps coherently across Earth's surface. By combining many such paired measurements at different times and observing geometries, the position of the target planet's spin axis and periodic variations in the spin rate may be ascertained.

Margot and his team (*3*) applied these two theories with spectacular results. From radar signals bounced off Mercury and recorded at pairs of radio antennas in California, West Virginia, and Puerto Rico during more than 20 observation periods from 2002 through 2006, the group determined the position of Mercury's spin axis with a precision two orders of magnitude superior to the previous best estimate. Equally important, they detected Mercury's forced libration and determined its amplitude for the first time. The amplitude is sufficiently large that Mercury's solid mantle and crust must be decoupled from the planet's core on an 88-day time scale. This result indicates that Mercury has a molten outer core at 95% confidence, a level limited at present by uncertainty in the knowledge of Mercury's gravity field.

The presence of a molten outer core is consistent with dynamo models for generating Mercury's magnetic field but does not prove the existence of such a dynamo or distinguish among competing models. One of the problems with an Earth-like dynamo is that the dipole strength of Mercury's field is some three orders of magnitude less than that of Earth. Explanations for the weak field involving a dynamo otherwise broadly similar to Earth's include a thin-shell dynamo (*7*) and a dynamo that operates only deep in a fluid outer core beneath an electrically conductive but stable layer of liquid metal (*8*).

The author is in the Department of Terrestrial Magnetism, Carnegie Institution of Washington, Washington, DC 20015, USA. E-mail: scs@dtm.ciw.edu

CREDIT: NASA AND THE JOHNS HOPKINS UNIVERSITY APPLIED PHYSICS LABORATORY

Possible alternatives include a dynamo sustained by electrical currents driven by temperature variations along an uneven core-mantle boundary (*9*) or an entirely fossil magnetic field in an outer shell whose thickness varies with insolation as functions of latitude and longitude (*10*). Distinguishing among models requires measurement of the geometry of Mercury's field, particularly the nondipole components.

The evidence for a liquid outer core on Mercury and the specific value of the forced libration amplitude (*3*), inversely proportional to the moment of inertia of Mercury's mantle and crust (*4*), provide important new constraints on models for Mercury's thermal history and bulk composition. From these observations we know that a light element alloyed with iron is necessary to prevent the outer core from freezing completely during Mercury's lifetime. A core sulfur content of several percent, for instance, would maintain a fluid outer core to the present and yet permit the solidification of an inner core that would release energy or chemical buoyancy to stir a convective core dynamo (*11*). Mercury's bulk composition had previously been constrained only by its mean density. The new determination of the moment of inertia of the planet's solid outer shell (*3*) should narrow somewhat the constraints on the average density of that shell and on core radius, but these constraints will improve substantially when the gravitational field of the planet is better determined.

No spacecraft has visited Mercury since the Mariner 10 flybys, but that status is about to change. NASA's MESSENGER spacecraft (*12*) will fly by Mercury three times, the first next January, before achieving orbit about the planet in 2011. About 2 years later, the European Space Agency and the Japan Aerospace Exploration Agency will launch the BepiColombo mission to insert two spacecraft into coplanar Mercury orbits in 2019 (*13*). The latest discovery from Earth-based radar has whetted the appetites of the planetary science community for these two missions.

References

1. N. F. Ness, K. W. Behannon, R. P. Lepping, Y. C. Whang, *J. Geophys. Res.* **80**, 2708 (1975).
2. H. Harder, G. Schubert, *Icarus* **151**, 118 (2001).
3. J. L. Margot, S. J. Peale, R. F. Jurgens, M. A. Slade, I. V. Holin, *Science* **316**, 710 (2007).
4. S. J. Peale, *Nature* **262**, 643 (1976).
5. P. E. Green Jr., in *Radar Astronomy*, J. V. Evans, T. Hagfors, Eds. (McGraw-Hill, New York, 1968), pp. 1–78.
6. I. V. Holin, *Radiophys. Quant. Elec.* **31**, 515 (1988).
7. S. Stanley, J. Bloxham, W. E. Hutchison, M. T. Zuber, *Earth Planet. Sci. Lett.* **234**, 27 (2005).
8. U. R. Christensen, *Nature* **444**, 1056 (2006).
9. D. J. Stevenson, *Earth Planet. Sci. Lett.* **82**, 114 (1987).
10. O. Aharonson, M. T. Zuber, S. C. Solomon, *Earth Planet. Sci. Lett.* **218**, 261 (2004).
11. S. A. Hauck II, A. J. Dombard, R. J. Phillips, S. C. Solomon, *Earth Planet. Sci. Lett.* **222**, 713 (2004).
12. S. C. Solomon *et al.*, *Planet. Space Sci.* **49**, 1445 (2001).
13. R. Schulz, J. Benkhoff, *Adv. Space Res.* **38**, 572 (2006).

10.1126/science.1142328

BIOCHEMISTRY

Photosynthesis from the Protein's Perspective

Slow motions of proteins modulate electron-transfer rates during the early stages of photosynthesis.

Spiros S. Skourtis and David N. Beratan

Effective photosynthesis requires the efficient transfer of electrons across biomembranes (*1*). Yet, many aspects of how protein structure and dynamics control electron transfer—especially in the early stages of photosynthesis—remain only partly understood. On page 747 of this issue, Wang *et al.* (*2*) investigate the rate of the initial photosynthetic electron-transfer reaction in wild-type and mutant photosynthetic reaction centers of *Rhodobacter sphaeroides*. By combining their data with modeling of protein conformational changes in the photosynthetic reaction center, the authors show that protein motions modulate the electron-transfer rate.

The electron donor in the initial electron-transfer reaction of bacterial photosynthesis is a special pair of chlorophylls. When the latter are photoexcited, an electron transfers through a bridging chlorophyll to a pheophytin acceptor within 2 ps (1 ps = 10^{-12} s) (see the figure). Experimental studies of this process have focused on understanding the speed and high efficiency of the reaction (an electron is transferred for each photon absorbed) (*1*). Conventional electron-transfer theory does not fully describe this kind of electron-transfer reaction, because the theory assumes that electron transfer is slow compared to the relaxation of the medium (protein and chromophore), and the medium is therefore assumed to be equilibrated before the electron-transfer step. The protein motion in the initial photosynthetic reaction, however, cannot keep up with the pace of charge separation.

The study of Wang *et al.* indicates that a model for electron transfer controlled by slow atomic motion, the Sumi-Marcus model (*3*), produces a satisfactory description of the initial photosynthetic electron-transfer kinetics (*2*). The Sumi-Marcus model assumes that electron transfer is affected both by fast atomic motions $\mathbf{q}$ of the medium that are equilibrated before the electron-transfer step, and by motions $\mathbf{X}$ that are slow on the electron-transfer time scale. $\mathbf{X}$ modulate the speed of electron transfer. This model is similar in spirit to descriptions of ligand binding to heme proteins, which are also understood in the context of the slow interchange among protein substates (*4*).

Wang *et al.* use the absorption spectra of the protein's 39 tryptophan residues to track the medium's response to photoexcitation and initial photosynthetic electron transfer. The spectra are essentially identical in the wild type and in the 14 mutants, with electron-transfer times varying from 2 to tens of ps. Therefore, the protein motion that is tracked by the spectra is not affected by the rate of electron flow. Further, the time evolution of the absorption spectra is multiexponential, with time constants (3, 10, and 190 ps) that are similar to or longer than the time scales of electron transfer.

The authors find that the Sumi-Marcus model describes the observed electron-transfer kinetics if the diffusion constant for the slow coordinate $\mathbf{X}$ in the model is derived from the time evolution of the tryptophan absorption. The fit predicts changes in reaction free energy (ΔG) values that

S. S. Skourtis is in the Department of Physics, University of Cyprus, Nicosia 1678, Cyprus. D. N. Beratan is at the French Family Science Center, Departments of Chemistry and Biochemistry, Duke University, Durham, NC 27708, USA. E-mail: skourtis@ucy.ac.cy and david.beratan@duke.edu

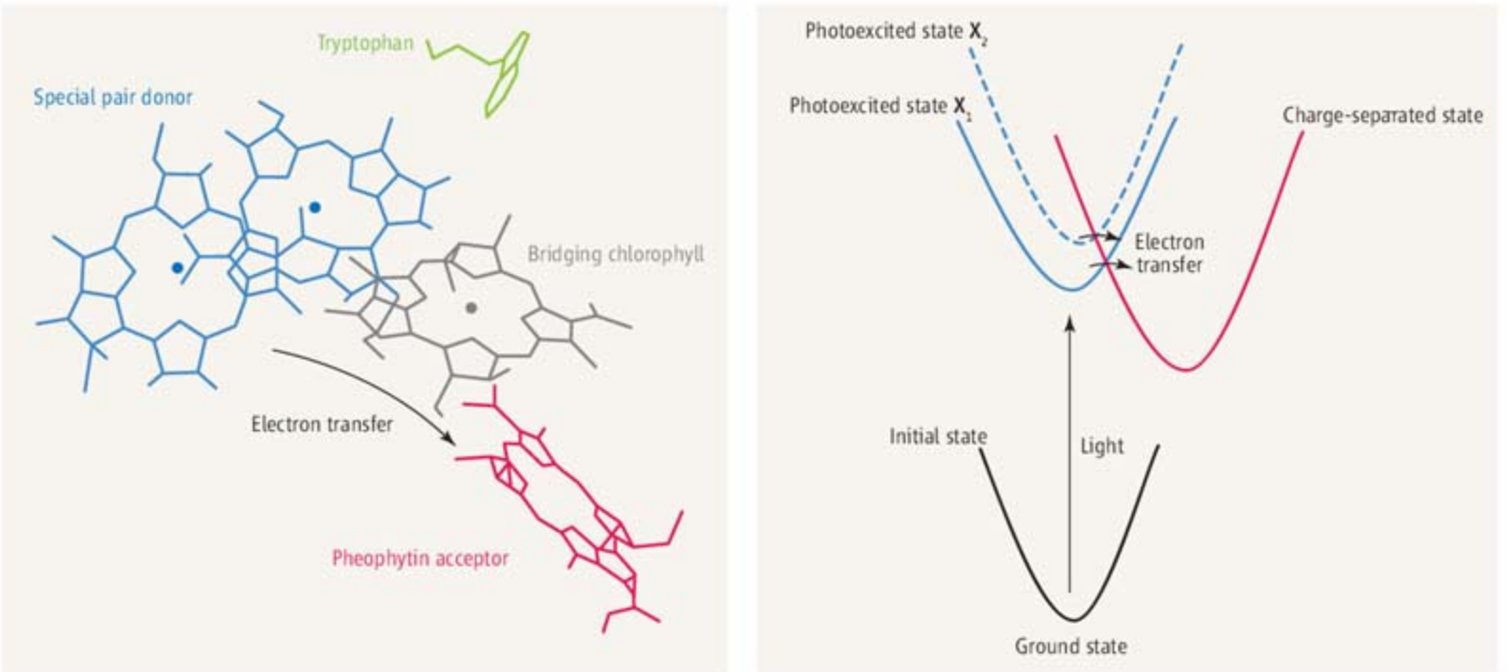

The initial photosynthetic electron-transfer reaction. (**Left**) In the photosynthetic reaction center, an electron is transferred from a special pair of chlorophylls via a bridging chlorophyll to the pheophytin acceptor. A nearby tryptophan—1 of 39 in the protein—is also shown. Wang *et al.* use the time evolution of the protein's tryptophan absorbance to track the protein's response (in the Sumi-Marcus model, motion along the **X** coordinate) following photoexcitation of the special pair. (**Right**) Application of the Sumi-Marcus model by Wang *et al.* (*2*) to the electron-transfer step shown in the left panel. The parabolas describe the energy of the electron-transfer system as a function of the motions **q** for the initial state of the system before photoexcitation (black), the photoexcited state before electron transfer (blue), and the final charge-separated state (red).The slow motion **X** shifts the photoexcited energy surface, thus modulating the speed of the electron-transfer step (horizontal arrows). The colors for the photoexcited and charge-separated energy surfaces correspond to the colors for the electron donor and acceptor moieties in the left panel.

are consistent with independent thermodynamic data for the mutants, a surprising result given the wide range of electron-transfer rates observed.

It is remarkable that changes in the tryptophan absorption spectra can track reorganizations in the electron-transfer medium that modulate the electron-transfer rate. These reorganizations are not the response of the protein to the arrival of the electron at the pheophytin. Rather, they are probably the protein's response to electron density changes in the donor special pair and the bridging chlorophyll upon photoexcitation. Indeed, the slowness of the protein dynamics on the electron-transfer time scale helps to explain the multiexponential nature of the initial photosynthetic electron-transfer kinetics.

Is the nature of the protein relaxation important for photosynthetic reaction center function? Wang *et al.* suggest that the slow protein dynamics discussed above may help to overcome reaction barriers produced by membrane potentials or by environmental factors that perturb the photosynthetic reaction center and potentially slow down the electron-transfer rate. Thus, protein motion could overcome reaction barriers produced by cellular factors that might otherwise perturb the electron-transfer kinetics.

The prediction by Wang *et al.* that slow protein motion modulates electron transfer and generates multiexponential kinetics in the photosynthetic reaction centers should encourage further single-protein studies of biological electron transfer similar to those reported in (*5*). The emerging physical picture for the photosynthetic reaction center suggests that the temperature dependence for electron transfer should be complex, because temperature variation will change the diffusion among protein substates as well as the access to the activated complex for any given substate. The relation between tryptophan absorption changes and protein reorganizations that affect electron transfer suggests the use of tryptophan transient absorption spectra as a further probe of protein reorganizations linked to protein function.

The experimental data reported by Wang *et al.* also encourage renewed theoretical attention to the early events in photosynthesis. Models that include quantized nuclear dynamics seem particularly important, because high-frequency quantum modes influence fast electron transfer, producing nonexponential kinetics and unusual temperature dependence (*6*).

The influence of biomolecular dynamics on electron-transfer rates is not limited to the regime of ultrafast electron-transfer reactions. Recent studies of nonadiabatic electron transfer over long distances show that protein motion also modulates the donor-acceptor electronic coupling interactions (*7*–*9*). Furthermore, the internal motions of electron-transfer macromolecules may also change the reaction mechanism from single-step electron tunneling to multistep hopping, a transition that is of great interest and importance—and of some mystery—in the fields of bioenergetics and of DNA damage and repair (*10*).

References

1. M. C. Wakeham, M. R. Jones, *Biochem. Soc. Trans.* **133**, 851 (2005).
2. H. Wang *et al.*, *Science* **316**, 747 (2006).
3. H. Sumi, R. A. Marcus, *J. Chem. Phys.* **84**, 4894 (1986).
4. H. Frauenfelder, S. G. Sligar, P. G. Wolynes, *Science* **254**, 1598 (1991).
5. H. Yang *et al.*, *Science* **302**, 262 (2003).
6. J. Jortner, M. Bixon, Eds., *Advances in Chemical Physics*, vols. 106–107, *Electron Transfer—From Isolated Molecules to Biomolecules* (Wiley, New York, 1999).
7. T. R. Prytkova, I. V. Kurnikov, D. N. Beratan, *Science* **315**, 622 (2007).
8. S. S. Skourtis, I. A. Balabin, D. N. Beratan, *Proc. Natl. Acad. Sci. U.S.A.* **102**, 3552 (2005).
9. K. E. Wheeler *et al.*, *J. Am. Chem. Soc.* **129**, 3906 (2007).
10. G. B. Schuster, Ed., *Long- Range Charge Transfer in DNA I*, vols. 236–237 of *Topics in Current Chemistry* (Springer, New York, 2004).

10.1126/science.1142330

Ultracold Neutral Plasmas

Thomas C. Killian*

Ultracold neutral plasmas occupy an exotic regime of plasma physics in which electrons form a swarming, neutralizing background for ions that sluggishly move in a correlated manner. Strong interactions between the charged particles give rise to surprising dynamics such as oscillations of the average kinetic energy during equilibration and extremely fast recombination. Such phenomena offer stimulating and challenging problems for computational scientists, and the physics can be applied to other environments, such as the interior of gas giant planets and plasmas created by short-pulse laser irradiation of solid, liquid, and cluster targets.

Most of the visible matter in the universe exists as ionized gas, or plasma, such as in stars and interstellar gas clouds. Closer to home, plasmas are found in lightning bolts, the aurora borealis, and the ionosphere surrounding our planet. They also have applications such as in lighting, surface processing, and the quest for fusion energy. Plasmas tend to be very hot because collision energies on the order of an electron volt are required to break neutral atoms and molecules into free electrons and ions (Fig. 1). New physics is often discovered by pushing the boundaries of what is found in nature. This raises questions about whether fundamental principles limit plasmas to high temperatures, or if it is possible to create neutral plasmas orders of magnitude colder than this. Small thermal energy violates basic assumptions underlying the concepts we use to understand plasmas, such as kinetic equations and Debye screening of Coulomb interactions by electrons. So if one could create such an ultracold system, how would it behave?

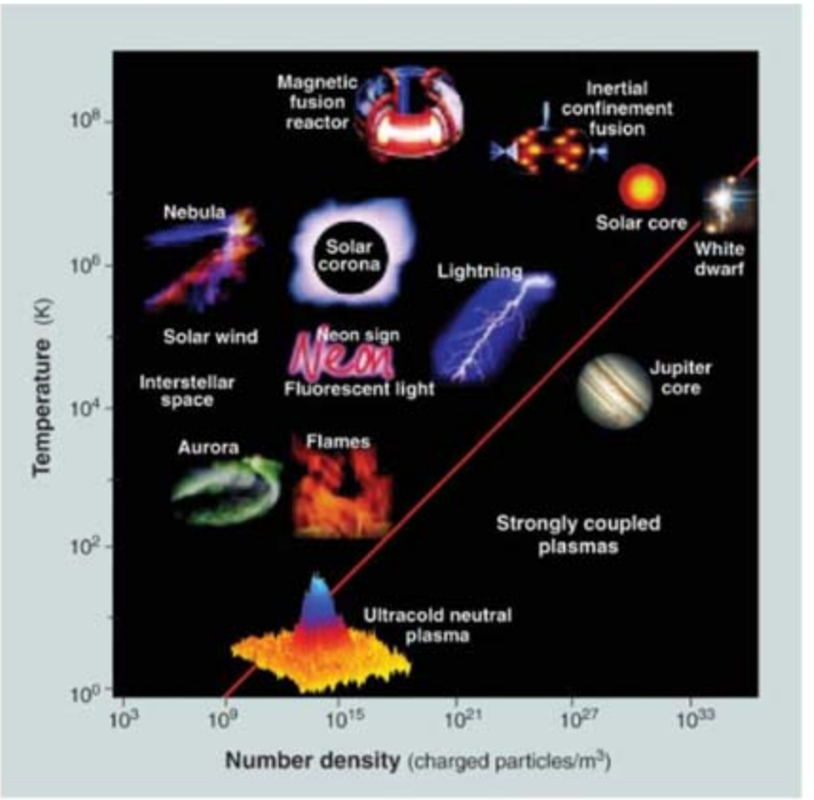

Fig. 1. Sample of neutral plasmas in the laboratory and nature. Most plasmas are hot, such as the surface of the Sun. A candle flame, with a temperature of about 1000 K, is considered a cold plasma. Ultracold neutral plasmas occupy a previously unexplored region of phase space and can be strongly coupled ($\Gamma > 1$). The graphic shown for ultracold neutral plasmas is an absorption image of ions in the plasma. One electron volt corresponds to about 12,000 K, and room temperature is 300 K. [Adapted with permission from the Contemporary Physics Education Project. Copyright 1996.]

Physicists have discovered ways to enter and explore the exotic regime of ultracold neutral plasmas, and they have learned that it straddles the normal boundaries between plasmas, neutral gases, and condensed matter. These studies have stretched our understanding of strongly interacting many-body systems, especially regarding their approach to thermal equilibrium. Surprisingly, these ideas can be applied to very energetic plasmas, such as in the interior of white dwarf stars or matter caught in the focus of ultra-intense laser beams. Work on ultracold neutral plasmas has also taken advantage of powerful diagnostics and excellent control of initial conditions, which have enabled the observation of fundamentally new phenomena and created close interaction between experiment and theory.

Department of Physics and Astronomy, Rice University, 6100 Main Street, Houston, TX 77005, USA.
*E-mail: killian@rice.edu

Creation of an Ultracold Neutral Plasma

To reach the ultracold regime, experimenters start by laser-cooling neutral atoms. This technique, which was the topic of the Nobel Prize in Physics in 1997, takes advantage of the momentum carried by laser photons to slow and trap atoms and cool them to temperatures as low as one-millionth of a degree above absolute zero. It is routine to create spherical clouds of about 1 mm in diameter containing ~1 billion ultracold atoms, with peak densities approaching 10^{12} atoms/cm^3. Such samples can be held in vacuum for many seconds, and they are the initial stage in experiments with Bose-Einstein condensates, high-technology applications like atomic clocks, and schemes to build quantum computers. [For an overview, see (*1*).] Many different elements can be used in these experiments, but for technical reasons, alkali, alkaline-earth, and noble gas atoms are the systems of choice, and each experiment typically works with a single element.

To create a plasma from ultracold atoms, a 10-ns pulse from a narrow-bandwidth laser irradiates the cloud and ionizes a large fraction of the atoms (*2*). (This occurs in the relatively low-intensity regime where only single-photon processes occur and only a single electron is liberated from each atom.) Because they are so light, each electron carries away any excess energy available from the ionizing photon, and by slightly tuning the laser wavelength in the region just above the ionization threshold, one can set the electron temperature in the range from a few to a few thousand kelvin. The ions receive only a small momentum kick during the process, and the ion kinetic energies are initially on the order of 10 mK. The size of the plasma and the number of ions and electrons created are easily controlled by varying the initial laser cooling parameters or the intensity of the photoionizing laser.

Strong Coulomb Coupling

An important quantity for ultracold plasmas is the Coulomb coupling parameter

$$\Gamma = E_{\text{interaction}}/E_{\text{thermal}} = \frac{e^2}{4\pi\varepsilon_0 a}/k_B T$$

which quantifies the relative importance of each particle's electrical interaction energy and thermal energy. Here $a = [3/(4\pi n)]^{1/3}$ is a typical interparticle spacing and n is the plasma density. T is the temperature, which can be different for ions and electrons, so each species can have a

different Γ. $e = 1.60 \times 10^{-19}$ C is the magnitude of each particle's electrical charge, and $\varepsilon_0 = 8.85 \times 10^{-12}$ F/m and $k_B = 1.38 \times 10^{-23}$ J/K are the electrical permittivity of space and Boltzmann's constant, respectively.

In conventional plasmas, thermal energies dominate and $\Gamma << 1$. This means that individual particles "feel" each other very weakly and move in an uncorrelated gaseous manner. However, in some extreme environments, such as the core of Jupiter, the crust of a neutron star (*3*), and shock waves produced by laser implosion (*4*), the density (and thus $E_{interaction}$) is so high that Γ becomes larger than 1, and spatial correlations develop as particles avoid their neighbors in order to minimize the potential energy. Such systems are called strongly coupled or nonideal (*5*). Plasmas with $1 < \Gamma < 170$ show liquidlike short-range spatial correlations, and if Γ increases above ~170, a first-order phase transition occurs to a state with long-range order characteristic of a solid (*6*). This has been shown in beautiful laboratory experiments on Wigner crystals in nonneutral plasmas of positive ions (*7*) that have been laser-cooled deep into the strongly coupled regime and in dusty plasmas of highly charged microscopic spheres in a discharge (*8*). Γ can characterize many features of plasmas differing in temperature by more than 10 orders of magnitude.

From the initial kinetic energies and densities of ions and electrons in ultracold neutral plasmas, one would expect that electrons would be a strongly coupled liquid and ions would condense into a frozen crystal. This neglects the fact that ultracold plasmas are formed in a completely disordered state far from equilibrium. As they equilibrate and spatial correlations develop, potential energy is converted into kinetic, and the plasma components heat. Both electrons and ions suffer this disorder-induced heating (*9*–*12*), and electrons can also heat rapidly due to recombination with ions, which forms neutral atoms (*13*–*16*). This yields electrons with $\Gamma_e \sim 0.2$ and ions with $\Gamma_i \sim 3$. The study of the establishment of equilibrium in or near the strongly coupled regime has been one of the most notable contributions from the field of ultracold neutral plasmas. This topic explores fascinating fundamental physics and is also important for laser-produced high–energy density plasmas (*17*).

Optical Probes of Strongly Coupled Ions

During the past few years, experiments have exploited near-resonant laser absorption (*11*) and fluorescence (*12*) to study the physics of strong coupling of ions in ultracold neutral plasmas. For example, Doppler broadening of the absorption spectrum serves as a measure of the ion kinetic energy, and when this tool was used to study ion equilibration during the first few hundred nanoseconds of plasma evolution (*11*), it provided the first experimental observation of disorder-induced heating (Fig. 2).

This heating has a relatively simple physical explanation. Ions have very little kinetic energy initially because of the controlled nature of the plasma-creation process. However, there is a tremendous amount of potential energy as a result of electrical interactions between ions in the random spatial distribution that was inherited from the original laser-cooled atoms. In a time equal to the inverse of the ion plasma oscillation frequency, $1/\omega_{pi} = (e^2 n/\varepsilon_0 m_i)^{-1/2} \sim 200$ ns, ions with mass m_i roll down a global potential-energy surface as spatial correlations develop and potential energy changes into kinetic. This establishment of correlations after rapidly changing the potential-energy landscape is the opposite of rapid melting recently described in (*18*, *19*).

The amount of energy released per particle during disorder-induced heating is $\sim e^2/4\pi\varepsilon_0 a$, and it can be calculated more accurately (*10*) by assuming complete initial disorder and modeling the Coulomb interaction between ions in the presence of screening electrons as a Yukawa potential. Disorder-induced heating would be unobservable if the plasma were not strongly coupled because the potential energy would be negligible compared to the kinetic energy in random thermal motion. Another way to say this is that spatial correlations would never develop.

Disorder-induced heating necessarily leaves $E_{thermal}$ comparable to $E_{interaction}$ after equilibration, which yields Γ_i only slightly larger than 1 for the ions. Several theorists have suggested ways of alleviating disorder-induced heating and producing much more strongly coupled plasmas, such as by photoionizing ultracold atoms with preset spatial correlations in optical lattices (*20*) or quantum degenerate Fermi gases (*10*).

Even with the moderate coupling parameter presently achievable, strong coupling leads to unusual effects that belie our intuition developed from study of weakly coupled plasmas or atomic gases. Figure 2 shows that the ion kinetic energy overshoots and oscillates before reaching equilibrium (*11*). This is odd behavior. Normally, the kinetic energy changes monotonically during equilibration of thermodynamic systems, such as during the cooling of a cup of hot coffee left standing for too long.

Oscillations reflect correlated motions that periodically increase and decrease the nearest-neighbor spacings between ions. This manifests nonequilibrium in a quantity known in the kinetic theory of gases as the two-particle distribution function, f_2, which describes spatial correlations between any two particles' positions and velocities. The standard descriptions of plasmas based on Vlasov, Boltzmann, or Fokker-Plank equations neglect f_2 or approximate it in a simple manner that neglects correlations. They focus on the approach of the one-particle distribution function (f_1) to something like a Maxwell-Boltzmann distribution. This recipe normally suffices because f_2 usually equilibrates much faster than f_1. Such a hierarchy of equilibration time scales is known as the Bogoliubov hypothesis, and it is an underlying assumption in traditional descriptions of weakly coupled plasmas. However, these time scales both become comparable to $1/\omega_{pi}$ in strongly coupled plasmas, which leads to oscillations in the kinetic energy during approach to equilibrium (*21*, *22*). Ultracold neutral plasmas provide the first experimental observation of this phenomenon, but similar behavior was predicted in the mid-70s (*23*) on the basis of molecular dynamics calculations. It has generated recent theoretical interest (*17*, *21*, *24*) because of the importance of relaxation dynamics after short-pulse excitation of semiconductors, gases, solids, clusters, and nuclear matter.

There is also a simple physical picture of the oscillations. Ions in the liquidlike plasma have approximately uniform spacing from their nearest neighbors. So each ion moves in a potential-energy well created by a cage of neighbors, and all the ions' potential-energy wells are roughly

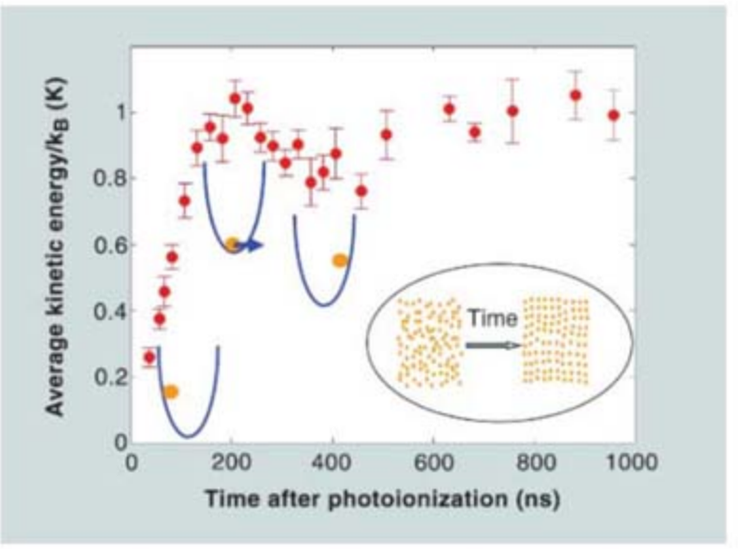

Fig. 2. Ion kinetic energy in an ultracold neutral plasma shortly after the plasma is created. Disorder-induced heating increases the kinetic energy in the first ~200 ns as ions equilibrate. The inset shows how heating arises from the release of Coulomb electrical potential energy as spatial correlations develop. For a strongly coupled plasma, the kinetic energy will overshoot and oscillate before equilibrating. This process can be understood as the periodic motion of ions (yellow) in the potential wells (blue) formed by their nearest neighbors.

similar. Ions roll down these wells during the disorder-induced heating phase, and one would expect each ion to roll back up the other side and then exhibit oscillations around the potential minimum. The observed oscillations damp rapidly, but the exact nature of the damping is still an open question.

Why have ultracold neutral plasmas provided the first experimental evidence for disorder-induced heating and kinetic-energy oscillations despite long interest in the phenomena and their probable occurrence in other plasmas? Ultralow temperature allows experiments to access strongly coupled physics at very low densities compared to high–energy density experiments, which typically work at close to solid densities. At low densities, the important time scales of the problem, such as the time between collisions and $1/\omega_{pi}$, are orders of magnitude longer, which makes it easier to study phenomena. In addition, ultracold neutral plasmas are "clean" systems in which the initial density profile, energy, and ionization state are accurately known and controllable, and optical probes have proven powerful for obtaining precise measurements of plasma properties.

Electron Dynamics

The electrons are not strongly coupled, but they do display a rich assortment of phenomena that characterize the ultracold regime. One might expect electrons to rapidly leave the plasma region because they are so light and thus have extremely high velocities (~10^4 m/s). But the plasma stays very close to neutral because of the low electron kinetic energy and the electrical attraction between positive and negative charges. On a 100-μs time scale, the plasma expands into the surrounding vacuum at the speed of an ion sound wave in a process that is analogous to ambipolar diffusion (*14*, *15*, *25*).

One of the most distinctive features of the electron dynamics during this time is the extremely rapid three-body recombination (TBR) (*26*) that can occur if the electron temperature, T_e, is on the order of 10 K or lower. In TBR, two electrons and an ion collide to form a highly excited Rydberg atom and an energetic electron. The TBR rate varies as $1/T_e^{9/2}$, and it can be the fastest process in the plasma. It will heat the remaining free electrons, which eventually slows the recombination, but not before as much as 30% of the ionized particles recombine into loosely bound atoms. In a closely related experiment (*27*), laser-cooled atoms are optically excited directly to weakly bound Rydberg levels, and they spontaneously ionize due to various collisional processes (*28*) to form an ultracold plasma. But then as the plasma expands, recombination returns much of the plasma to the neutral state. This behavior has demonstrated that the distinction between a cloud of highly excited neutral atoms and an ionized gas is blurred in the ultracold regime. These ideas relate to searches in gaseous systems (*29*) for an analog of the Mott insulator-to-conductor transition that is familiar from condensed-matter physics. In addition, recombination dynamics may be similar in experiments that create cold antihydrogen (*30*, *31*) in trapped ultracold plasmas of positrons and antiprotons.

Research has also focused on collective motions of electrons in ultracold neutral plasmas. For example, a recent experiment applied oscillating radiofrequency electric fields to the plasma and excited Tonks-Dattner resonances (*32*). These are standing electron sound waves that were first observed in experiments designed to simulate meteor tails (*33*). Sound waves arise because of thermal motion that modifies the mode structure and dispersion relation of the familiar electron plasma oscillation. The electron plasma oscillation is a local oscillation of the electron density at $\omega_{pe} = \sqrt{e^2 n/\varepsilon_0 m_e}$ that does not propagate like a sound wave. Careful measurement of the resonant frequencies of Tonks-Dattner modes may provide a sensitive probe of the electron temperature, which will prove valuable because of the many processes—such as TBR—that can change the electron temperature on a rapid time scale.

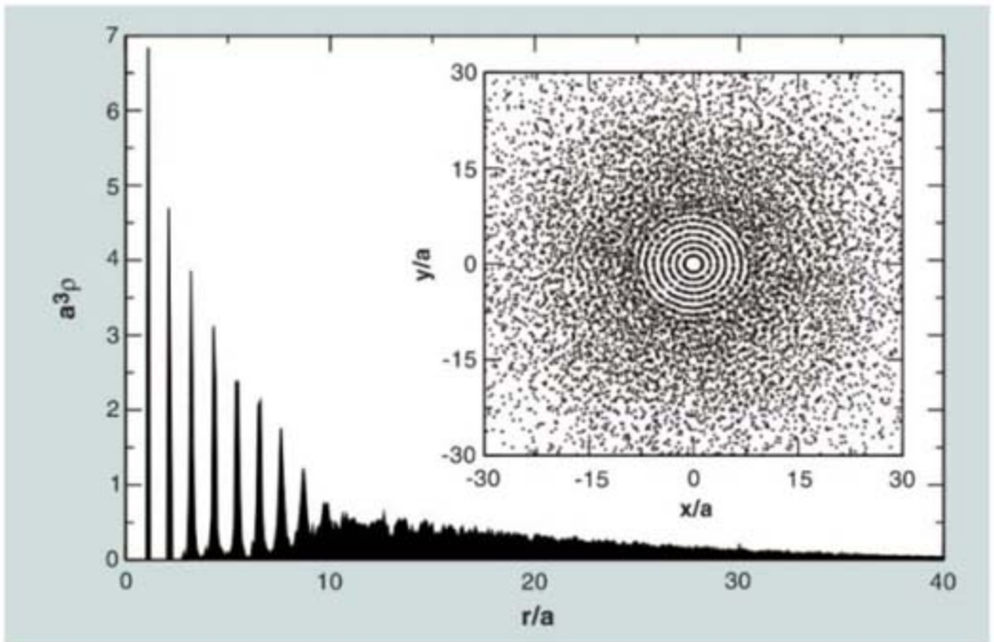

Fig. 3. Numerical simulations of laser-cooled ultracold neutral plasmas showing ion density (ρ) versus radius (*r*) normalized in units of the interparticle spacing (*a*). (**Inset**) A two-dimensional slice through the plasma showing concentric shells of ions. Ions within one shell show hexagonal ordering. [Reprinted with permission from (*35*). Copyright 2004, American Physical Society.]

Theory and Numerical Simulations

Ultracold neutral plasmas have generated much interest within the theoretical plasma and computational physics communities because of the appeal of the fundamental phenomena and because ultracold neutral plasmas pose particular challenges to theoretical analysis. To describe the spatial correlations inherent in strongly coupled plasmas, theorists must resort to molecular dynamics calculations in which each particle's trajectory is calculated according to the interaction with all other particles in the system. This is outside the realm of kinetic or hydrodynamic methods, and the treatment becomes intractably time-intensive when modeling the entire evolution from plasma formation to expansion. Small electron mass necessitates the use of small numerical integration time steps, whereas the sluggish ions extend the overall evolution time of the system to tens of microseconds. Work on this problem has broader significance because the underlying physics and basic codes can be used for warm dense matter and energetic laser-produced plasmas (*13*, *17*). Assessing the validity of the numerical results for such systems presents a great challenge [e.g., (*4*)], and the experiments are often difficult to diagnose. But ultracold neutral plasmas, with well-defined and controllable initial conditions and excellent diagnostics, do not suffer from this problem.

Computational codes originally developed to describe dynamics in astrophysical systems such as globular clusters have successfully described early electron dynamics and the first microsecond of ion equilibration (*9*, *34*) but have not been extended to describe the plasma expansion. Direct numerical simulation provides valuable information on dynamics at the single-particle level, such as the time scale for TBR (*14*) and the distribution of bound states resulting from this process (*13*). As computational speed continues to increase, there is hope that simulation of the entire plasma evolution may become possible.

A hybrid approach in which ions are treated exactly but the electrons are described with ki-

Recent Climate Observations Compared to Projections

Stefan Rahmstorf,[1] Anny Cazenave,[2] John A. Church,[3] James E. Hansen,[4] Ralph F. Keeling,[5] David E. Parker,[6] Richard C. J. Somerville[5]

Observations of the climate system are crucial to establish actual climatic trends, whereas climate models are used to project how quantities like global mean air temperature and sea level may be expected to respond to anthropogenic perturbations of the Earth's radiation budget. We compiled the most recent observed climate trends for carbon dioxide concentration, global mean air temperature, and global sea level, and we compare these trends to previous model projections as summarized in the 2001 assessment report of the Intergovernmental Panel on Climate Change (IPCC) (*1*). The IPCC scenarios and projections start in the year 1990, which is also the base year of the Kyoto protocol, in which almost all industrialized nations accepted a binding commitment to reduce their greenhouse gas emissions. Although published in 2001, these model projections are essentially independent from the observed climate data since 1990: Climate models are physics-based models developed over many years that are not "tuned" to reproduce the most recent temperatures, and global sea-level data were not yet available at the time. The data now available raise concerns that the climate system, in particular sea level, may be responding more quickly than climate models indicate.

Carbon dioxide concentration follows the projections almost exactly (Fig. 1), bearing in mind that the measurements shown from Mauna Loa (Hawaii) have a slight positive offset due to the slightly higher CO_2 concentration in the Northern Hemisphere compared with the global mean. The level of agreement is partly coincidental, a result of compensating errors in industrial emissions [based on the IS92a scenario (*1*)] and carbon sinks in the projections.

The global mean surface temperature increase (land and ocean combined) in both the NASA GISS data set and the Hadley Centre/Climatic Research Unit data set is 0.33°C for the 16 years since 1990, which is in the upper part of the range projected by the IPCC. Given the relatively short 16-year time period considered, it will be difficult to establish the reasons for this relatively rapid warming, although there are only a few likely possibilities. The first candidate reason is intrinsic variability within the climate system. A second candidate is climate forcings other than CO_2: Although the concentration of other greenhouse gases has risen more slowly than assumed in the IPCC scenarios, an aerosol cooling smaller than expected is a possible cause of the extra warming. A third candidate is an underestimation of the climate sensitivity to CO_2 (i.e., model error). The dashed scenarios shown are for a medium climate sensitivity of 3°C for a doubling of CO_2 concentration, whereas the gray band surrounding the scenarios shows the effect of uncertainty in climate sensitivity spanning a range from 1.7° to 4.2°C.

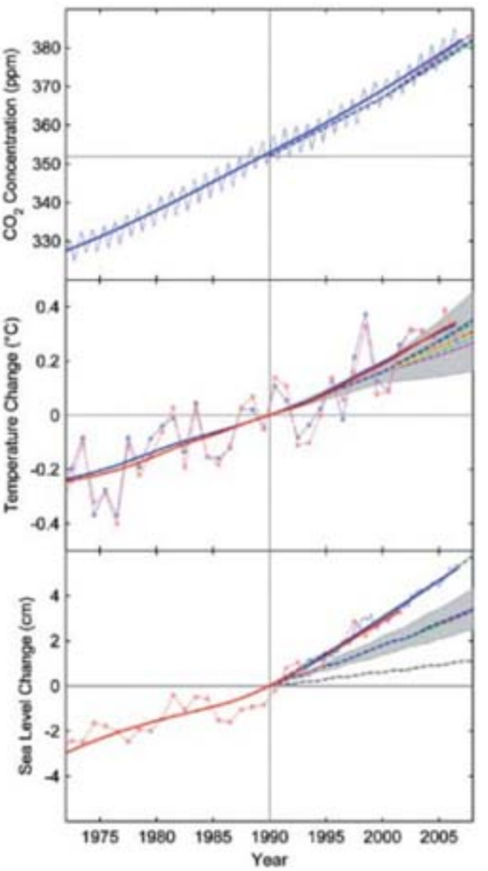

Fig. 1. Changes in key global climate parameters since 1973, compared with the scenarios of the IPCC (shown as dashed lines and gray ranges). (**Top**) Monthly carbon dioxide concentration and its trend line at Mauna Loa, Hawaii (blue), up to January 2007, from Scripps in collaboration with NOAA. ppm, parts per million. (**Middle**) Annual global-mean land and ocean combined surface temperature from GISS (red) and the Hadley Centre/Climatic Research Unit (blue) up to 2006, with their trends. (**Bottom**) Sea-level data based primarily on tide gauges (annual, red) and from satellite altimeter (3-month data spacing, blue, up to mid-2006) and their trends. All trends are nonlinear trend lines and are computed with an embedding period of 11 years and a minimum roughness criterion at the end (*6*), except for the satellite altimeter where a linear trend was used because of the shortness of the series. For temperature and sea level, data are shown as deviations from the trend line value in 1990, the base year of the IPCC scenarios.

Since 1990 the observed sea level has been rising faster than the rise projected by models, as shown both by a reconstruction using primarily tide gauge data (*2*) and, since 1993, by satellite altimeter data (*3*) (both series are corrected for glacial isostatic adjustment). The satellite data show a linear trend of 3.3 ± 0.4 mm/year (1993–2006) and the tide gauge reconstruction trend is slightly less, whereas the IPCC projected a best-estimate rise of less than 2 mm/year. Sea level closely follows the upper gray dashed line, the upper limit referred to by IPCC as "including land-ice uncertainty." The rate of rise for the past 20 years of the reconstructed sea level is 25% faster than the rate of rise in any 20-year period in the preceding 115 years. Again, we caution that the time interval of overlap is short, so that internal decadal climate variability could cause much of the discrepancy; it would be premature to conclude that sea level will continue to follow this "upper limit" line in future. The largest contributions to the rapid rise come from ocean thermal expansion (*4*) and the melting from nonpolar glaciers as a result of the warming mentioned above. Although the ice sheet contribution has been small, observations are indicating that it is rapidly increasing, with contributions both from Greenland and Antarctica [e.g., (*5*)].

Overall, these observational data underscore the concerns about global climate change. Previous projections, as summarized by IPCC, have not exaggerated but may in some respects even have underestimated the change, in particular for sea level.

References and Notes

1. IPCC, *Climate Change 2001: The Scientific Basis* (Cambridge Univ. Press, Cambridge, 2001).
2. J. A. Church, N. J. White, *Geophys. Res. Lett.* **33**, L01602 10.1029/2005GL024826 (2006).
3. A. Cazenave, R. S. Nerem, *Rev. Geophys.* **42**, 20 (2004).
4. J. K. Willis, D. Roemmich, B. Cornuelle, *J. Geophys. Res.* **109**, C12036 10.1029/2003JC002260 (2004).
5. A. Cazenave, *Science* **314**, 1250 (2006); published online 18 October 2006 (10.1126/science.1133325).
6. J. C. Moore, A. Grinsted, S. Jevrejeva, *Eos* **86**, 226 (2005).

27 October 2006; accepted 25 January 2007
Published online 1 February 2007;
10.1126/science.1136843
Include this information when citing this paper.

[1]Potsdam Institute for Climate Impact Research, 14482 Potsdam, Germany. [2]Laboratoire d'Etudes en Géophysique et Océanographie Spatiales, 31400 Toulouse, France. [3]Marine and Atmospheric Research and Antarctic Climate and Ecosystems Cooperative Research Centre, Commonwealth Scientific and Industrial Research Organisation, Hobart Tasmania, 7001, Australia. [4]NASA Goddard Institute for Space Studies (GISS), New York, NY 10025, USA. [5]Scripps Institution of Oceanography, University of California, San Diego, La Jolla, CA 92093, USA. [6]Hadley Centre, Met Office, Exeter EX1 3PB, UK.

Large Longitude Libration of Mercury Reveals a Molten Core

J. L. Margot,[1]* S. J. Peale,[2] R. F. Jurgens,[3] M. A. Slade,[3] I. V. Holin[4]

Observations of radar speckle patterns tied to the rotation of Mercury establish that the planet occupies a Cassini state with obliquity of 2.11 ± 0.1 arc minutes. The measurements show that the planet exhibits librations in longitude that are forced at the 88-day orbital period, as predicted by theory. The large amplitude of the oscillations, 35.8 ± 2 arc seconds, together with the Mariner 10 determination of the gravitational harmonic coefficient C_{22}, indicates that the mantle of Mercury is decoupled from a core that is at least partially molten.

Because Mercury is an end-member planet, the characterization of its interior properties is crucial to further our understanding of the formation and evolution of habitable worlds. A question that has challenged planetary scientists for more than three decades is the state of Mercury's core (*1*). Determining the nature and extent of the core would enable progress in four fundamental areas. First, models of the internal structure of the planet have so far been constrained only by its mean density of 5.43 g cm^{-3} (*2*), with early (*3*) and recent (*4*) calculations yielding a wide range of possible internal configurations. Although it is generally accepted that the planet differentiated early into an iron core and a silicate mantle (*5*), improved descriptions of the mass distribution within the planet require the measurement of core properties or moments of inertia. Second, thermal evolution models (*6*) predict a core that is fully or partially liquid, or completely solid. The outcome is particularly sensitive to the abundance of a light alloying element in the core, presumably sulfur, that lowers the melting temperature and allows the maintenance of a liquid outer core over billions of years (*7*). In order to focus the thermal evolution calculations, the extent and state of the core must be determined. Third, a long-standing puzzle relates to the origin of the magnetic field that was measured by Mariner 10 at a strength of roughly 1% that of Earth (*8*). A dynamo mechanism involving motion in an electrically conducting molten core is the preferred explanation (*9*, *10*), but alternative theories that do not require a currently liquid core, such as remanent magnetism in the crust, cannot be ruled out (*11*, *12*). Finally, the presence of a liquid core may bear on the unusual spin-orbit configuration of Mercury. It has been suggested that increased energy dissipation at a core/mantle interface would lead to almost certain capture in specific spin-orbit resonances (*13*, *14*), although this capture can also occur naturally as a result of the chaotic evolution of the orbital eccentricity, without the need for additional core/mantle friction (*15*).

One of us (Peale) devised an observational procedure to characterize the size and state of the core of Mercury, and showed that it is possible to detect a molten core by measuring subtle deviations from the mean resonant spin rate of the planet (*1*). The early expectation was that the experiment would require landers on the surface of the planet. Here we describe how we have used Earth-based radar instruments to make high-precision measurements of the instantaneous spin rate, and we present observational evidence indicating that Mercury has a molten core. We also provide observational confirmation that Mercury occupies a Cassini state (*16*) and a measurement of the obliquity of the planet, both of which are required for further characterization of the core with Peale's formalism (*1*).

Since the discovery that the spin period of Mercury differs from its orbital period (*17*), it has been hypothesized that the planet rotates on its spin axis three times for every two revolutions around the Sun (*18*) and occupies a Cassini state, in which its spin vector is nearly perpendicular to the orbital plane and precesses at the same rate as the orbital plane (*14*). As Mercury follows its orbit with eccentricity $e \sim 0.206$, it experiences periodically reversing torques due to the gravitational influence of the Sun on the asymmetric figure of the planet. The torques affect the spin angular momentum and cause small deviations of the spin rate from its resonant value of 3/2 times the mean orbital frequency. The resulting oscillations in longitude are called forced librations, where the forcing and the rotational response occur with a period $P \sim 88$ days, dictated by the orbital motion. The physical librations are characterized by an angle ϕ (*14*) representing the deviations of the orientation of the planet from the exact resonant value

$$\phi = \frac{3}{2}\frac{(B-A)}{C} f(e)\sin(nt) \qquad (1)$$

where $A < B < C$ are the principal moments of inertia, $f(e)$ is a power series in the eccentricity, and $n = 2\pi/P$ is the orbital (forcing) frequency. The gravitational torques and resulting angular deviations are proportional to the difference in equatorial moments of inertia ($B - A$), a measure of the asymmetry in the mass distribution. The polar moment of inertia C appears in the denominator because it represents a measure of the resistance to changes in rotational motion. If the core of Mercury is solid and the entire planet participates in the librations, C is the relevant moment of inertia. However, if the mantle is decoupled from a fluid core that does not follow the librations, the appropriate moment of inertia in the denominator of Eq. 1 is that of the mantle alone C_m or, more precisely, mantle plus crust. Because $C_m/C \leq 0.5$ in all plausible interior models (*3*, *4*), the amplitude of the librations in the presence of a liquid core is twice as large as it would be with a solid core. Therefore, a measurement of the libration amplitude provides a straightforward mechanism for determining the state of the core remotely. The quantity ($B - A$) is known from Mariner 10 measurements of the second-degree and -order gravitational coefficient C_{22} (*2*)

$$C_{22} = \frac{(B-A)}{4MR^2} = (1 \pm 0.5) \times 10^{-5} \qquad (2)$$

where M and R are the mass and radius of the planet, respectively. The moment of inertia C/MR^2 has not been measured, but interior models constrain it to the range from 0.325 to 0.380 (*4*), where the smallest value corresponds to the most centrally condensed configuration (*19*). Using these data in Eq. 1 shows that the amplitude of the forced librations in the case of a solid core should be within 50% of 19 to 22 arc sec. The amplitude that we measured is outside this range, suggesting a liquid core.

Method. Radar echoes from solid planets exhibit spatial irregularities in the wavefront caused by the constructive and destructive interference of waves scattered by the irregular surface. Because of the rotation of the planet, the corrugations in the wavefront, also called speckles, will sweep over the receiving station and give rise to fluctuations of the electromagnetic signal with time. It is fruitful to evaluate the degree of correlation between signals received at one station located in spacetime at $(\mathbf{x}, t)$ with respect to those received at another station at $(\mathbf{x} + \delta\mathbf{x}, t + \delta t)$. The properties of this spacetime correlation function were first analyzed by Green (*20*, *21*), who showed that for some orientation of the baseline $\delta\mathbf{x}$, there exists a time delay δt at which the correlation maximizes. When the trajectory of the wavefront corruga-

[1]Department of Astronomy, Cornell University, 304 Space Sciences Building, Ithaca, NY 14853, USA. [2]Department of Physics, University of California, Santa Barbara, CA 93106, USA. [3]Jet Propulsion Laboratory, 4800 Oak Grove Drive, Pasadena, CA 91109, USA. [4]Space Research Institute, Moscow, Russian Federation.

*To whom correspondence should be addressed. E-mail: jlm@astro.cornell.edu

tions is parallel to the antenna baseline, the value of the time delay that maximizes the correlation is related in a simple fashion to the magnitude and orientation of the spin vector of the planet. Green (*21*) gives an expression valid to first order

$$|\delta \mathbf{x}| = 2r\Omega\cos(\alpha)\delta t_{max} \quad (3)$$

where r is the range to the planet, Ω is the sidereal spin rate, and α is the tilt of the spin vector from perpendicularity with the line of sight.

That echoes received at two receivers can display a high degree of correlation under appropriate viewing geometry has been well known for some time in the radar astronomy community (*22*). But the power of the technique to measure planetary spin states was not fully appreciated until one of us (Holin) brought it to the attention of the rest of us in 2001. George (*23*) developed an expression for the cross-correlation function of the electric field scattered from a rough rotating sphere to two observation points. His formalism shows that speckles remain coherent over a rotation angle given approximately by $(\lambda/a)^{1/2}$, where λ is the wavelength and a is the radius of the sphere. For Earth-based observations of Mercury ($r \sim 100$ million km), it can be shown that the pattern of speckles remains frozen over a linear distance many times the radius of Earth (*24*, *25*). In practice, one illuminates the planet with monochromatic radiation and records the speckle pattern as it sweeps over two receiving stations. Because the wavefront corrugations are tied to the rotation of the planet, and because decorrelation of the speckle pattern can be neglected (*26*), the time lag obtained by cross-correlating the two echo time series yields a direct measurement of the instantaneous spin rate, as shown by Green's formula. The result holds for arbitrary topography (*27*).

A substantial requirement is that both receiving stations must record similar speckle patterns to produce a large correlation, and this can occur only when the trajectory of the speckles is aligned with the antenna baseline. The characteristic scale of the speckles is given by the classic diffraction formula $r\lambda/d$, where d is the size of the scattering patch on the surface, on the order of the planetary radius. This scale is small compared to the separation between antennas (~ 1 km versus ~ 3000 km in our experiment), so that a small (0.02°) misalignment of the speckle trajectory with respect to the baseline orientation results in appreciable decorrelation. For an east-west baseline that oscillates daily by ±23° with respect to the ecliptic, the high correlation condition is maintained each day for only ~20 s. This realization led one of us (Holin) to present results (*24*, *25*) showing that measurements of the epochs at which the correlation maximizes would provide tight constraints on the spin vector orientation. In practice, one makes use of the antenna spacetime locations that are known with great accuracy to derive the spin vector geometry. Because the time of day at which large correlations are observed is not particularly sensitive to α in Eq. 3, the experiment must be performed at multiple line-of-sight geometries to fully determine the direction of the spin axis in inertial space.

Observations. For most of our observations (Table 1) we used the NASA/Jet Propulsion Laboratory (JPL) 70-m antenna (DSS-14) at Goldstone, California (35.24°N, –116.89°E) and transmitted a circularly polarized monochromatic signal at a frequency of 8560 MHz (λ = 3.5 cm) and power of ~420 kW. Transmission typically occurred for the duration of the round-trip light time to the planet, and reception followed for an equivalent amount of time. Transmit times were carefully selected so that the daily maximum in the correlation would fall during a receive window. Radar echoes were recorded at Goldstone and at the Robert C. Byrd Green Bank Telescope (GBT) in West Virginia (38.24°N, –79.84°E) with fast sampling systems (*28*). Representative values of the signal-to-noise ratio (SNR) in the same (SC) and opposite (OC) circular polarizations as that transmitted were ~3 and ~20, respectively, in a 200-Hz bandwidth. Some of our observations made use of the Arecibo telescope in Puerto Rico (18.23°N, –66.75°E) as the transmitter (λ = 12.6 cm) and DSS-14 or a smaller 34-m antenna (DSS-13) as the receiver.

Complex cross-correlations (*29*) of the echo time series obtained at the receiving stations yield strong correlations near the predicted epochs. The time evolution of the rise and fall in the correlation is well approximated by a Gaussian curve (Fig. 1). For large SNRs, centroid locations can be determined with a precision that is a small fraction of the widths of the correlation functions (*30*). Epochs of correlation maximum and time lags can be determined to a precision of ~ 0.5 s and ~ 0.1 ms from initial widths of ~ 5 s and ~ 2.5 ms, respectively. Although the OC echo is dominated by a specular component representative of a smaller fraction of the planetary disk than that which produces the diffuse SC echo, measurements in the two receive polarizations exhibit a high degree of consistency.

Results. We used the epochs of correlation maximum (Table 1) in a least-squares fit to derive the position of the axis of rotation of Mercury in the J2000 equatorial frame (Fig. 2). Our calculations include the motions of the planets as given by the *JPL Planetary Ephemeris DE414* (*31*), an Earth orientation model incorporating up-to-date timing and polar motion data, time delays accounting for light-travel times, and general relativistic corrections to the time delays.

Table 1. Log of observations. Each data set identifier (ID) shows the date of observation in the format yymmdd followed by the frequency of observation (x = 8560 MHz and s = 2380 MHz), the observing stations involved (0 = DSS-14, 3 = DSS-13, G = GBT, and A = Arecibo), and the receive polarization (OC = opposite sense circular polarization to that transmitted; SC = same sense, not shown). The MJD gives the epoch of speckle correlation maximum, the centroid of a Gaussian of standard deviation w. The time lag (τ) indicates the time interval for speckles to travel from one station to the other at the corresponding epoch. The fractional uncertainty in the time lag and spin rate (σ) is empirically determined from successive measurements, except in the first four data sets, where it corresponds to a residual timing uncertainty of 0.2 ms. The last column indicates the instantaneous spin rate in units of 3/2 of the mean orbital frequency.

ID	MJD	w (s)	τ (s)	σ	Spin rate
020513x00Goc	52407.889680	4.41	–12.36958	1.61×10^{-5}	0.999985
020522x00Goc	52416.871258	6.27	–12.69218	1.58×10^{-5}	0.999893
020602x00Goc	52427.845539	5.98	–11.84078	1.69×10^{-5}	0.999861
020612x00Goc	52437.816052	6.35	–11.21227	1.78×10^{-5}	0.999945
030113x00Goc	52652.760205	10.32	–10.93565	1.37×10^{-5}	1.000097
030123x00Goc	52662.725791	8.40	–11.29540	5.28×10^{-6}	1.000073
030531x00Goc	52790.846925	7.76	–8.30671	8.21×10^{-6}	0.999932
030601x00Goc	52791.844164	7.37	–8.36904	1.02×10^{-5}	0.999949
030918sA3Aoc	52900.630649	26.79	–14.67124	5.03×10^{-5}	1.000093
030919sA3Aoc	52901.628954	28.95	–14.70674	5.50×10^{-5}	1.000065
030920sA3Aoc	52902.627306	26.94	–14.71705	5.18×10^{-5}	1.000067
040331x00Goc	53095.968346	5.92	–7.41574	1.20×10^{-5}	1.000098
041212x00Goc	53351.866334	7.86	–7.74059	1.55×10^{-5}	1.000070
041218x00Goc	53357.848521	7.75	–7.38323	1.05×10^{-5}	1.000067
041219x00Goc	53358.845401	8.13	–7.39330	9.67×10^{-6}	1.000075
050313x00Goc	53443.004320	7.04	–4.78491	3.19×10^{-5}	1.000035
050314x00Goc	53444.001094	6.87	–4.98779	9.83×10^{-6}	1.000056
050316x00Goc	53445.994761	6.72	–5.31606	1.45×10^{-5}	1.000047
050318x00Goc	53447.988621	6.24	–5.53562	1.52×10^{-5}	1.000056
060629x00Goc	53915.735467	8.03	–11.27627	8.35×10^{-6}	0.999866
060712x00Goc	53928.676641	7.94	–10.71493	6.43×10^{-6}	0.999882

The best spacecraft determination of the orientation of the rotation axis gives an obliquity of ~2° (with a 50% error ellipse of ±2.6° by ±6.5°) (*32*). The constraints obtained from previous Earth-based radar measurements are about 10 times better (*33*). Our measurements refine the knowledge of the pole orientation by two orders of magnitude. The measured obliquity is 2.11 ± 0.1 arc min, which is precisely within the range of theoretical expectations (*34*). Our adopted 1σ uncertainty exceeds the formal uncertainties of the fit to guard against undetected systematic effects.

Mercury is expected to be in a Cassini state in which its orbit pole, spin orientation, and perpendicular to the Laplacian plane remain coplanar (*14*). Numerical simulations (*35*, *36*) support this theoretical prediction. Our spin solution shows that, within observational errors, Mercury occupies Cassini state 1: The confidence regions for the spin orientation fall precisely on the locus of pole positions that satisfy the Cassini condition (Fig. 2). The latter condition relies on a numerical determination of the Laplacian plane (*35*) that is entirely independent of the radar data. If we use this Laplacian plane and assume that Mercury is in a Cassini state, the best-fit constrained pole solution is at J2000 right ascension 281.0097° and declination 61.4143°.

A detailed characterization of the core of Mercury in the manner described by Peale (*1*) requires not only the occupancy of the Cassini state but also a precise knowledge of the obliquity, amplitude of the librations, and second-degree gravitational harmonic coefficients. We provide observational confirmation that the first condition is satisfied and values for the first two quantities. Although current uncertainties on gravitational harmonic coefficients (*2*) prevent us from constraining the size of the core, it is possible to determine the state of the core by measuring the amplitude of the 88-day forced librations.

We determined the amplitude of the librations of Mercury by measuring the instantaneous spin rate of the planet at various epochs. Our fractional uncertainties, on the order of 1 part in 10^5, are such that the libration signature is readily apparent. In order to translate our time-lag measurements into values of the rotational velocity of Mercury at each observing epoch (Table 1), we fit for the spin rate value that best satisfies the coherence condition; namely, that the orientation of the planet as seen by the first transmitter-receiver pair at time t is similar to the orientation of the planet as seen by the second transmitter-receiver pair at time $t + \delta t_{max}$. This is accomplished by computing the trajectories of light rays between transmitter, bounce point, and receiver, taking light-travel times into account. A Lorentz transformation is used to obtain the orientation of the incoming and outgoing light rays in the moving frame in which Mercury is at rest. Those orientations are converted to planetocentric coordinates with the use of the appropriate rotation matrices. For each observation epoch, the spin rate is adjusted to minimize the difference between the longitudes corresponding to the first transmitter-receiver pair and the longitudes corresponding to the second transmitter-receiver pair, ensuring the coherence condition. Our measured angular velocities reliably trace the phase of the expected libration signature derived from the torque equation, indicating that the 88-day forced librations have been detected unambiguously (Fig. 3).

Results are very similar in the two circular polarizations. One-parameter fits to the spin rate variations, adjusting in a least-squares sense for the overall amplitude only, yield $(B - A)/C_m = (2.01 \pm 0.09) \times 10^{-4}$ and $(B - A)/C_m = (2.08 \pm 0.07) \times 10^{-4}$ with reduced chi-square (χ^2_ν) values of 2.3 and 1.3 for the OC and SC data, respectively. A fit to the combined OC and SC data yields $(B - A)/C_m = (2.04 \pm 0.06) \times 10^{-4}$, with $\chi^2_\nu = 1.8$. The best-fit libration amplitude is not sensitive to the exact spin vector orientation. All Cassini poles with obliquities spanning the range 2.11 ± 0.1 arc min yield consistent results.

To test for the presence of a long-period libration component superposed on the 88-day libration signature, we performed additional fits to the libration equation. A fully dynamical solution admits three free parameters: the overall amplitude, initial libration angle γ_0, and initial angular velocity $(d\gamma/dt)_0$, where we chose the 17 April 2002 perihelion passage [modified Julian date (MJD) 52381.480] as the initial epoch. The best-fit values ($\chi^2_\nu = 0.9$) to the combined OC and SC data are $(B - A)/C_m = (2.03 \pm 0.04) \times 10^{-4}$, $\gamma_0 = (0.07 \pm 0.01)°$, $(d\gamma/dt)_0 = (2.10 \pm 0.06)$ arc sec day^{-1}, corresponding to a long-period libration amplitude of ~300 arc sec. Because the data span less than a complete cycle, values for the long-period component need confirmation. The period of the free libration is $P \times \{3[(B - A)/(C_m)]\ (7e/2 - 123e^3/16)\}^{-1/2}$, or ~12 years (*37*).

Our adopted value of the moment ratio is $(B - A)/C_m = (2.03 \pm 0.12) \times 10^{-4}$, where the 1σ uncertainty captures the 1σ range of the OC-only and SC-only models. This corresponds to an amplitude of the forced librations $\phi = (35.8 \pm 2)$ arc sec. This value should be compared to the expected amplitude for a solid planet: ϕ within 50% of 19 to 22 arc sec for $C/MR^2 = 0.325$ to 0.380 (*4*) and $C_{22} = (1.0 \pm 0.5) \times 10^{-5}$ (*2*).

The large libration amplitude that we observe can be explained by a mantle that is decoupled

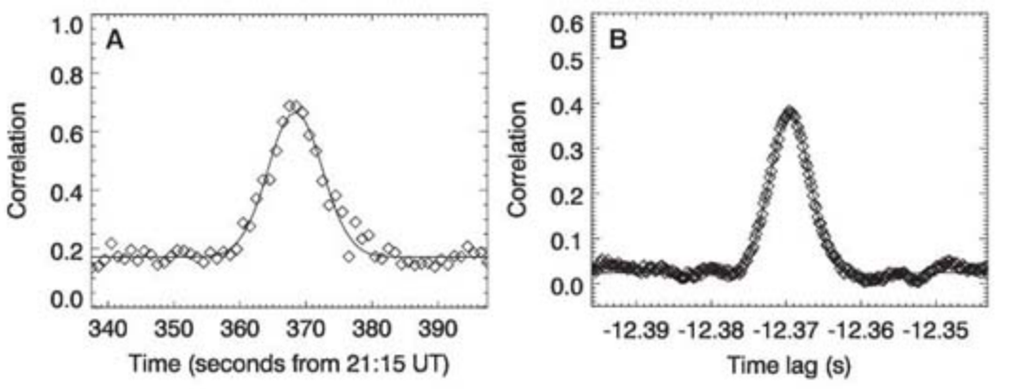

Fig. 1. Representative correlation functions obtained on the first observing run (13 May 2002) with integration times of 1 s (symbols) and corresponding Gaussian fits (solid lines). (**A**) Time evolution of the maximum in the cross-correlation function when using echo time series with 200-Hz sampling. The maximum in the function represents the epoch at which the speckle trajectory passes through both antenna spacetime locations. UT, universal time. (**B**) Cross-correlation of echo time series with 5000-Hz sampling at the time of the correlation maximum. Successive measurements of the Gaussian centroid were used to produce the time-lag estimates and fractional uncertainties listed in Table 1. Correlation is highest when the sampling rate matches about half the limb-to-limb bandwidth of the planet as in (A). Other sampling rates yield a lower SNR.

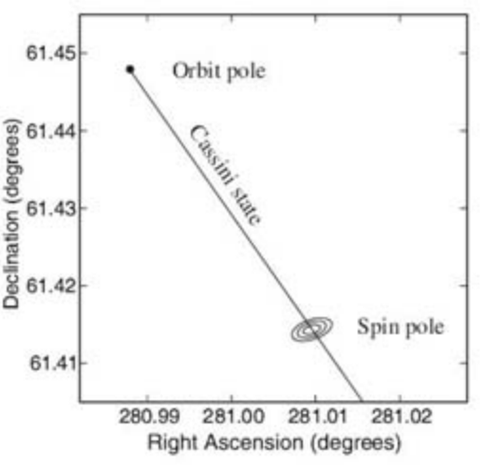

Fig. 2. Orientation of the spin axis of Mercury, based on the observed epochs of correlation maximum. The formal 68, 95, and 99% joint confidence regions for the spin orientation are shown as contours. The solution was not constrained to obey the Cassini state condition, which is represented by the straight solid line. The equatorial coordinate frame, pole orientations, and Cassini state locations all refer to the J2000 epoch.

from the core or by a serious underestimate of the C_{22} coefficient (*38*). To explain the nominal 35.8 arc sec libration amplitude with a solid core would require a C_{22} value at least 1.6 times larger than that obtained from Mariner 10 data. In the absence of any other constraint, one can estimate the probability of this occurring to be about 10%, assuming that errors are normally distributed. But because Mercury is in a Cassini state, an additional relationship exists between gravitational harmonic coefficients and obliquity (*14*). We can use this relationship with our obliquity determination to show that C_{22} values in excess of the nominal Mariner 10 range would require the quadrupole moment J_2 to also be outside the Mariner 10 range, a combination of circumstances with less than 10% probability.

In order to evaluate the impact of joint errors on the observables, we performed error propagation analysis and Monte Carlo simulations, where trial values for C_{22} and ϕ were drawn from normal distributions with mean and standard deviations corresponding to their measured values and error bars. We then computed the diagnostic ratio C_m/C (*39*) for extreme values of the moment of inertia allowed by interior models (*4*). The results (Fig. 4A) show that C_m/C is smaller than unity with 90% confidence, whereas a solid core requires $C_m/C = 1$. If one includes the additional constraint applicable in a Cassini state (Fig. 4B), the confidence level increases to 95%. The nominal $C_m/C \cong 0.5$ value implied by our measurements indicates that an outer shell participates alone in the librations, as opposed to the entire planet, and requires that the core of Mercury be at least partially molten.

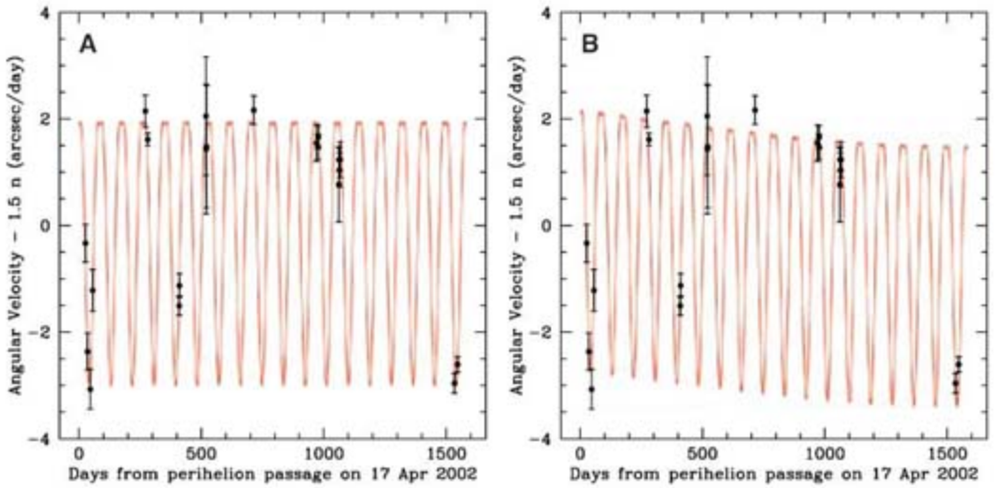

Fig. 3. Mercury spin rate deviations from the resonant rate of 3/2 times the mean orbital frequency. Observed data points and their error bars from Table 1 are shown at their respective epochs. The solid line is a numerical integration of the torque equation, the phase of which is dictated by the time of pericenter passage. (**A**) A one-parameter fit to the OC data (allowing for 88-day forced librations only). (**B**) A three-parameter fit to the OC data (allowing for an additional 12-year free libration component).

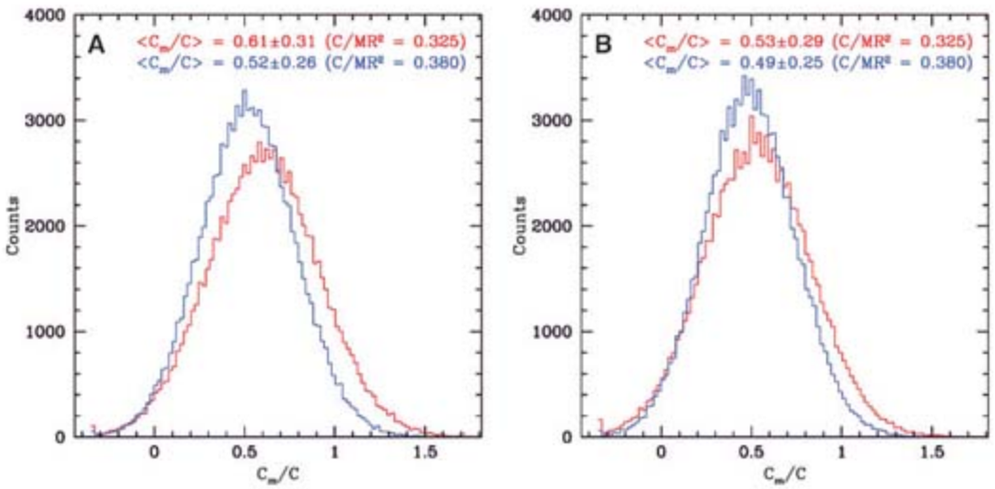

Fig. 4. Histograms of the diagnostic quantity C_m/C, where values less than unity indicate a liquid core, obtained by using 10^5 draws from normal distributions of ϕ and C_{22} values. Both extremes in the range of plausible interior models $C/MR^2 = 0.325$ (red) and $C/MR^2 = 0.380$ (blue) are considered. (**A**) shows the results without invoking the Cassini state, whereas (**B**) includes the additional constraint that exists between gravitational harmonic coefficients and obliquity in a Cassini state (*14*).

Implications. The presence of a magnetic field at Mercury (*8*) cannot be taken as observational evidence of a liquid core, because a currently active dynamo is not the only viable mechanism for producing the field (*11*, *12*). Our observations strengthen the dynamo hypothesis, in that a liquid core is a necessary condition for dynamo action. Although the sufficient conditions for a dynamo are not known, Stevenson (*10*) has shown that the existence of convection in a partially molten core, rather than the vigor of that convection, is the primary determinant. Thermal convection may arise if the heat flow exceeds the conductive heat flow that can be supported adiabatically. This will be facilitated by latent heat release if an inner core freezes. Inner core growth may also promote chemical convection as the freezing process excludes light alloying elements from the inner core, and as the material at the bottom of the outer core becomes compositionally buoyant because of an excess of those light elements. It is estimated that a fluid layer depth on the order of 100 km or more is required for sustaining convection by compositional buoyancy in Mercury (*10*). The effectiveness of dynamo processes in various geometries and whether such dynamos can reproduce the field observed by Mariner 10 are topics of active research. Simulations (*40*) indicate that some thin-shell dynamo configurations plausible for Mercury produce the observed field properties. Other geometries have been proposed, such as dynamos operating deeply underneath a stably stratified liquid outer core (*41*) or thick-shell dynamos (*42*). The MESSENGER spacecraft (*43*), en route to Mercury, is expected to map the magnetic field in detail and to determine the nature of its source (*44*).

The presence of a liquid core in Mercury has important implications for theories of planet formation and evolution. Thermal models predict a frozen core unless a sufficient amount of sulfur (at least 0.1% weight fraction) depresses the melting temperature of the core material (*6*). But chemical condensation models (*45*) indicate that sulfur cannot condense in the primordial solar nebula at the heliocentric distance of Mercury. Hence, the need for a sufficient amount of accreted sulfur to keep the core molten over the age of the solar system implies that Mercury was accreted from planetesimals that originated over a wide range of heliocentric distances. It may be possible to place further constraints on the amount of sulfur if it can be shown that the liquid core is convecting; that is, if it can be proven that a dynamo is responsible for the magnetic field. Although a minimum amount of sulfur is necessary to maintain a liquid core, too much sulfur inhibits inner core growth and core convection. If the sulfur abundance exceeds ~ 6 to 10% (*7*, *6*, *46*), the core would remain com-

pletely fluid over the age of the solar system, and a dynamo process would be unlikely.

Although the large amplitude of the forced librations indicates a liquid core, our observations cannot determine the size of the core, the extent of the inner core, or the polar moment of inertia of Mercury. These parameters are required to assemble a more complete picture of the internal structure of the planet and to probe the thermal evolution and magnetic field generation in much greater detail. Our error bars on C_m/C are currently dominated by uncertainties in the value of C_{22} (Fig. 4). But this gravitational harmonic can be constrained to the 1% level or better by tracking the orbit of a spacecraft. With such a measurement, expected from MESSENGER (*43*), our error bars on C_m/C would instantly drop to a level commensurate with uncertainties on the libration amplitude, roughly 6%. By assuming the densities of crust, mantle, and core material and using the integral relations for the ratio of moments of inertia, the C_m/C value could then be used to place a useful constraint on the size of the core. A superior estimate will require measurements of the polar moment of inertia of the planet (*1*, *14*, *34*, *39*), which can be derived by combining improved estimates of the gravitational harmonic coefficients with our values of the obliquity and libration amplitude.

Earth rotation studies demonstrate that the long-term monitoring of planetary rotations reveals excitations on a variety of time scales that can be used to constrain the underlying geophysical processes (*47*). The mechanisms affecting rotation also provide insights into interior structure, viscoelastic properties, and interactions at the core/mantle and atmosphere/surface boundaries. The capability to monitor the spins of terrestrial planets with Earth-based radar provides a new tool to probe the interiors of planets and opens new avenues in planetary physics.

References and Notes

1. S. J. Peale, *Nature* **262**, 765 (1976).
2. J. D. Anderson, G. Colombo, P. B. Esposito, E. L. Lau, G. B. Trager, *Icarus* **71**, 337 (1987).
3. R. W. Siegfried, S. C. Solomon, *Icarus* **23**, 192 (1974).
4. H. Harder, G. Schubert, *Icarus* **151**, 118 (2001).
5. C. Chapman, *Mercury*, F. Vilas, C. Chapman, M. Matthews, Eds. (Univ. of Arizona Press, Tucson, AZ, 1988), pp. 1–23.
6. G. Schubert, M. N. Ross, D. J. Stevenson, T. Spohn, *Mercury*, F. Vilas, C. Chapman, M. Matthews, Eds. (Univ. of Arizona Press, Tucson, AZ, 1988), pp. 429–460.
7. D. J. Stevenson, T. Spohn, G. Schubert, *Icarus* **54**, 466 (1983).
8. N. F. Ness, K. W. Behannon, R. P. Lepping, Y. C. Whang, K. H. Schatten, *Science* **185**, 151 (1974).
9. N. F. Ness, K. W. Behannon, R. P. Lepping, Y. C. Whang, *J. Geophys. Res.* **80**, 2708 (1975).
10. D. J. Stevenson, *Rep. Prog. Phys.* **46**, 555 (1983).
11. A. Stephenson, *Earth Planet. Sci. Lett.* **28**, 454 (1976).
12. O. Aharonson, M. T. Zuber, S. C. Solomon, *Earth Planet. Sci. Lett.* **218**, 261 (2004).
13. P. Goldreich, S. Peale, *Astron. J.* **72**, 662 (1967).
14. S. J. Peale, *Mercury*, F. Vilas, C. Chapman, M. Matthews, Eds. (Univ. of Arizona Press, Tucson, AZ, 1988), pp. 461–493.
15. A. C. M. Correia, J. Laskar, *Nature* **429**, 848 (2004).
16. A Cassini state is a stable dynamical configuration that is the result of tidal evolution. In this state, the spin axis remains coplanar with the orbit normal and the Laplacian plane normal as the former two precess around the latter from planetary perturbations of the orbit. The Laplacian plane is that plane about which Mercury's orbital plane precesses uniformly with a constant inclination.
17. G. H. Pettengill, R. B. Dyce, *Nature* **206**, 1240 (1965).
18. G. Colombo, *Nature* **208**, 575 (1965).
19. A uniform-density sphere has $C/MR^2 = 0.4$. Values for Earth and Mars are 0.331 and 0.366, respectively. The value for Venus has not been measured.
20. P. E. Green, *Radar Astronomy Measurement Techniques* (Technical Report 282, MIT Lincoln Laboratory, Lexington, MA, 1962).
21. P. E. Green, *Radar Astronomy* (McGraw-Hill, New York, 1968), chap. 1.
22. The property has been used to measure the topography of the Moon with receiving stations separated in space (*48*, *49*) or time (*50*) and led to the development of interferometric synthetic-aperture radar. On 31 January 1974, R. and S. Goldstein observed Venus with a Goldstone-Green Bank configuration and looked for a correlation between the two echo time series but did not detect it.
23. N. George, *J. Opt. Soc. Am.* **66**, 1182 (1976).
24. I. V. Kholin, *Radiophys. Quant. Elec.* **31**, 371 (1988) [translation from I. V. Holin, *Izv. Vyssh. Uchebn. Zaveden. Radiofiz.*, **31**, 515 (1988)].
25. I. V. Kholin, *Radiophys. Quant. Elec.* **35**, 284 (1992) [translation from I. V. Holin, *Izv. Vyssh. Uchebn. Zaveden. Radiofiz.*, **35**, 433 (1992)].
26. I. V. Kholin, *Solar System Res.* **38**, 449 (2004) [translation from I. V. Holin, *Astron. Vestnik* **38**, 513 (2004)].
27. An approximate expression for the field backscattered by a surface S can be written using the Fresnel-Kirchhoff diffraction formula (*50*): $E \propto \int_S \Gamma e^{-ik(r+s)} rsdS$, where E is the electric field, Γ is the complex reflection coefficient, $k = 2\pi/\lambda$, and r and s are the one-way distances for uplink and downlink. The cross-correlation of this echo with that received at a later time by a second receiving station is given by $\rho \propto \int_S \Gamma\Gamma^* e^{-ik(r+s-r'-s')} dS$, where geometric attenuation over the short observation time is assumed to be constant. Holin (*24*) demonstrated that if the surface is located in the Fresnel zone with respect to the source, the expression in parentheses can be reduced to a scalar product $\mathbf{r} \cdot \mathbf{x}$ where the first factor is the planetocentric surface location $\mathbf{r}$ and the second factor describes the motion but is independent of $\mathbf{r}$. If the condition $\mathbf{x} = 0$ is realized, contributions from individual scatterers add in phase and the correlation is large. This occurs when the translational and rotational components of the motion cancel in such a way that the speckle pattern observed at the first station is similar to that observed at the second station at a later time. Because the coherence condition is independent of $\mathbf{r}$, rotational parameters can be derived for arbitrarily shaped surfaces, as long as they exhibit diffuse scattering (*24*).
28. J. L. Margot, in *Proceedings of the 2002 URSI General Assembly*, paper 1949 (Maastricht, Netherlands, 2002).
29. We use $|E[x(t)y^*(t+\tau)]|$, where E is the expectation operator, and $x(t)$ and $y(t)$ are the complex voltage time series after demodulation to baseband.
30. J. S. Bendat, A. G. Piersol, *Random Data. Analysis and Measurement Procedures* (Wiley, New York, ed. 2, 1986).
31. E. M. Standish, *JPL Planetary Ephemeris DE414* (Technical Report IOM 343R-06-002, JPL, Pasadena, CA, 2006).
32. K. P. Klaasen, *Icarus* **28**, 469 (1976).
33. Initial radar images of the polar regions indicated that the component of the polar obliquity in the line-of-sight direction must be <1° (*52*). Improved images obtained 2 years later showed that the zero-obliquity case gave minimum smearing of the images (*53*). Further analysis showed a pole direction that yields a nominal obliquity of 0.5° (*53*).
34. S. J. Peale, R. J. Phillips, S. C. Solomon, D. E. Smith, M. T. Zuber, *Meteorit. Planet. Sci.* **37**, 1269 (2002).
35. M. Yseboodt, J. L. Margot, *Icarus* **181**, 327 (2006).
36. S. J. Peale, *Icarus* **181**, 338 (2006).
37. This is close to the orbital period of Jupiter, which may provide the required forcing. Another excitation mechanism is required if the long-period component is a true free libration that is not forced by Jupiter.
38. The C_{22} value was determined on the basis of the first and third Mariner 10 encounters, with different orbital inclinations (21.3° and 76.8°) and different close approach longitudes (99.9° at an altitude of 706 km and 52.2° at an altitude of 327 km). The Mariner 10 Radio Science team performed a careful analysis to arrive at realistic error bars. They concluded that "The resulting realistic errors, adjusted to include systematic effects, are about a factor of 10 larger than the formal errors on the gravity parameters."
39. The ratio $[(C_m)/(C)] = [(C_m)/(B-A)][(B-A)/(MR^2)][(MR^2)/(C)]$ was shown by Peale (*1*) to be a good diagnostic of the state of the core. In Peale's experiment, the three factors on the righthand side are determined from the amplitude of the longitude librations, the C_{22} gravitational harmonic, and a relation applicable if the planet is in a Cassini state, respectively. The latter relation involves the obliquity of the planet and second-degree gravitational harmonic coefficients.
40. S. Stanley, J. Bloxham, W. E. Hutchison, M. T. Zuber, *Earth Planet. Sci. Lett.* **234**, 27 (2005).
41. U. R. Christensen, *Nature* **444**, 1056 (2006).
42. M. H. Heimpel, J. M. Aurnou, F. M. Al-Shamali, N. Gomez Perez, *Earth Planet. Sci. Lett.* **236**, 542 (2005).
43. S. C. Solomon *et al.*, *Planet. Space Sci.* **49**, 1445 (2001).
44. Images from the spacecraft will also refine estimates of the amount of radial contraction sustained by Mercury. The existence of a partially liquid core may explain why compressional features on the surface appear to accommodate only 1 to 2 km of radial contraction, which is an order of magnitude less than predicted for complete core solidification (*55*).
45. J. S. Lewis, *Earth Planet. Sci. Lett.* **15**, 286 (1972).
46. S. A. Hauck, A. J. Dombard, R. J. Phillips, S. C. Solomon, *Earth Planet. Sci. Lett.* **222**, 713 (2004).
47. J. M. Wahr, *Annu. Rev. Earth Planet. Sci.* **16**, 231 (1988).
48. I. I. Shapiro, S. H. Zisk, A. E. E. Rogers, M. A. Slade, T. W. Thompson, *Science* **178**, 939 (1972).
49. J. L. Margot, D. B. Campbell, R. F. Jurgens, M. A. Slade, *Science* **284**, 1658 (1999).
50. N. J. S. Stacy, thesis, Cornell University, Ithaca, NY (1993).
51. M. Born, E. Wolf, *Principles of Optics* (Cambridge Univ. Press, 1997).
52. J. K. Harmon, M. A. Slade, *Science* **258**, 640 (1992).
53. J. K. Harmon *et al.*, *Nature* **369**, 213 (1994).
54. C. H. De Vries, J. K. Harmon, *Am. Astron. Soc. Meet.* **26**, 1376+ (1994).
55. S. C. Solomon, *Icarus* **28**, 509 (1976).

56. We thank J. Giorgini, A. Behrozi, J. Jao, R. Rose, J. Van Brimmer, D. Choate, D. Kelley, C. Franck, L. Juare, C. Bignell, F. Ghigo, M. Stennes, and R. Maddalena for assistance with the observations; J. Wisdom, D. Stevenson, D. Campbell, M. Standish, M. Yseboodt, J. Hilton, B. Bills, O. Aharonson, S. Stanley, J. Aurnou, S. Hauck, and S. Solomon for insightful discussions; P. Nicholson, S. Ostro, P. Taylor, and two reviewers for comments that improved the manuscript; and NASA's Navigation and Ancillary Information Facility for software and support. The National Radio Astronomy Observatory is a facility of NSF operated under cooperative agreement by Associated Universities, Inc. The Arecibo Observatory is part of the National Astronomy and Ionosphere Center, which is operated by Cornell University under a cooperative agreement with NSF. Part of this work was supported by JPL, operated by Caltech under contract with NASA. This material is based in part on work supported by NASA under the Science Mission Directorate Research and Analysis Programs. S.J.P. is supported in part by the NASA Planetary Geology and Geophysics program under grant NNG05GK58G. J.L.M. is supported in part by the NASA Planetary Astronomy program under grant NNG05GG18G.

29 January 2007; accepted 27 March 2007
10.1126/science.1140514

Signals from Chloroplasts Converge to Regulate Nuclear Gene Expression

Shai Koussevitzky,[1,2,3]* Ajit Nott,[1,2]* Todd C. Mockler,[2]† Fangxin Hong,[1,2]‡ Gilberto Sachetto-Martins,[2]§ Marci Surpin,[2]‖ Jason Lim,[1,2] Ron Mittler,[3,4] Joanne Chory[1,2,]¶

Plastid-to-nucleus retrograde signaling coordinates nuclear gene expression with chloroplast function and is essential for the photoautotrophic life-style of plants. Three retrograde signals have been described, but little is known of their signaling pathways. We show here that GUN1, a chloroplast-localized pentatricopeptide-repeat protein, and ABI4, an Apetala 2 (AP2)–type transcription factor, are common to all three pathways. ABI4 binds the promoter of a retrograde-regulated gene through a conserved motif found in close proximity to a light-regulatory element. We propose a model in which multiple indicators of aberrant plastid function in *Arabidopsis* are integrated upstream of GUN1 within plastids, which leads to ABI4-mediated repression of nuclear-encoded genes.

Chloroplasts contain about 3000 proteins, of which more than 95% are encoded by nuclear genes. As a result, enzymatic and photosynthetic complexes within chloroplasts contain subunits encoded by two spatially separated genomes (*1*). This necessitates a tight coordination of gene expression that involves two-way signaling between the chloroplasts and the nucleus. While plastid development is largely under nuclear control, developmentally arrested or damaged plastids can regulate nuclear gene expression via retrograde signaling pathways. Mitochondria also emit signals that regulate the expression of nuclear genes in response to its condition; this signaling is involved in important processes including senescence and tumor progression (*2*).

Three independent plastid-to-nucleus retrograde signaling pathways have been described (*3*–*5*). In the best-defined pathway, accumulation of Mg–protoporphyrin IX (Mg-protoPIX), a chlorophyll biosynthetic intermediate, leads to down-regulation of hundreds of genes in *Arabidopsis* and has been shown to be involved in gene regulation in *Chlamydomonas reinhardtii* (*6*). Gene products of four *Arabidopsis GENOMES UNCOUPLED* (*GUN*) loci, GUN2, 3, 4, and 5 (*6*), are involved in modulating Mg-protoPIX levels (*6*–*9*). A second pathway represses *Lhcb* expression in response to inhibition of plastid gene expression (PGE) and requires *GUN1* (*3*, *5*, *10*). The third signaling pathway mediates signals derived from the reduction/oxidation (redox) state of the photosynthetic electron transfer chain (PET) and affects both photosynthesis-related and stress-related genes (*3*, *5*). The redox state of the plastoquinone pool and other PET components, as well as reactive oxygen species (ROS), play a role in PET-derived signaling (*3*, *5*). In this work, we present evidence in support of a single retrograde signaling pathway that integrates information from multiple indicators of plastid functional state.

GUN1 encodes a chloroplast-localized pentatricopeptide-repeat protein. We identified seven new *gun1* alleles in two genetic screens (*11*) by using a transgenic *Arabidopsis* line carrying a luciferase reporter under the control of the *Lhcb* (encoding a light-harvesting chlorophyll a/b–binding protein) promoter, which is known to respond to retrograde signals (Col 6-3, Fig. 1A). We used either norflurazon (NF), an inhibitor of carotenoid biosynthesis that causes photo-oxidative damage and accumulation of Mg-protoPIX in the light, or lincomycin, an inhibitor of plastid protein synthesis. We mapped *GUN1* to a ~93-kilobase region on the bottom arm of chromosome 2. When we sequenced candidate genes, we found mutations in At2g31400 in all *gun1* alleles (Fig. 1B). Genomic fragments, encompassing the predicted open reading frame of At2g31400, fused at its C terminus to either green fluorescent protein (GFP) or six-hemagglutinin (6xHA) tags, were able to rescue the *gun1* phenotype (Fig. 1C).

GUN1 encodes a 918–amino acid polypeptide that is a member of the P subfamily of pentatricopeptide repeat (PPR)–containing proteins (*12*). PPR-protein coding genes are a vastly expanded family in land plants, with ~441 and >650 members in *Arabidopsis* and rice, respectively (*12*). Putative *GUN1* orthologs can be readily identified in rice (Os12g37550) and poplar (fig. S1). A majority of the PPR proteins are targeted to either mitochondria or plastids, where they have been proposed to function in processing, editing, stability, and translation of RNA molecules (*12*–*16*). In addition to the PPR motifs, GUN1 also has a small mutS–related (SMR) domain (*17*). The SMR domain is highly conserved across species and is found in small single-domain proteins, such as *Escherichia coli* Smr, as part of MutS2 (*17*), or in association with PPR motifs in higher plants. There are five other *Arabidopsis* proteins that have a domain structure similar to GUN1, i.e., several PPR motifs followed by a C-terminal SMR domain and one of those, pTAC2, is part of transcriptionally active complexes isolated from *Arabidopsis* and mustard (*18*). PPR motifs have been proposed to mediate interactions with nucleic acids (*12*), including DNA (*19*, *20*), and the SMR domain is found in proteins involved in DNA repair and recombination. We observed that a fragment of GUN1 containing both the PPR and SMR domains could bind DNA (fig. S2A). The SMR domain alone bound very strongly, whereas a fragment containing the PPR motifs alone showed weak binding. This suggests that GUN1 function may be distinct from the known PPR proteins, which are thought to be involved in RNA processing activities. GUN1 has a putative plastid-targeting signal sequence at its N terminus, and a construct lacking this sequence failed to rescue a *gun1* mutant plant. Full-length GUN1-GFP fusion constructs rescued the *gun1* phenotype, but we did not observe GFP fluorescence in several lines that we tested. Using *Agrobacterium*-mediated transient expression in *Nicotiana benthamiana* leaves (*21*), we found that GUN1– and pTAC2–yellow fluorescent protein (YFP) fusions localized to distinct foci within chloroplasts of mesophyll cells (Fig. 1D). When GUN1-YFP and pTAC2–cyan fluorescent protein (CFP) were coexpressed, we could clearly observe colocalization of the YFP and CFP signals (Fig. 1E), indicating that, like pTAC2, GUN1 is also associated with sites of active transcription on plastid DNA.

GUN1 is insensitive to accumulation of Mg-protoPIX. Among the known *gun* mutants only *gun1* has a *gun* phenotype when grown in the presence of either lincomycin or NF. However, NF treatment also results in photo-oxidative damage to plastid ribosomes, and it has been suggested that this could indirectly trigger the PGE pathway (*22*). Because the PGE pathway is active only during the first 3 days after germination (*10*), we treated older seedlings with NF to test whether GUN1 plays a role in the Mg-protoPIX pathway. Similar to *gun5* seedlings, 4-day-old light-grown *gun1* seedlings were unable to repress *Lhcb* expression when treated with NF (Fig. 2A). We then tested to see if *gun1* mutants were impaired in their response

[1]Howard Hughes Medical Institute, The Salk Institute for Biological Studies, 10010 North Torrey Pines Road, La Jolla, CA 92037, USA. [2]Plant Biology Laboratory, The Salk Institute for Biological Studies, 10010 North Torrey Pines Road, La Jolla, CA 92037, USA. [3]Department of Biochemistry and Molecular Biology, University of Nevada, Mail Stop 200, Reno, NV 89557, USA. [4]Department of Plant Sciences, The Hebrew University of Jerusalem, Jerusalem 91904, Israel.

*These authors contributed equally to this work.
†Present address: Department of Botany and Plant Pathology, Oregon State University, Corvallis, OR 97331, USA.
‡Present address: Department of Biostatistics, Division of Information Sciences, City of Hope National Medical Center and Beckman Research Institute, 1500 Duarte Road, Duarte, CA 91010, USA.
§Present address: Departamento de Genética, Universidade Federal do Rio de Janeiro, Rio de Janeiro, Caixa Postal 68011, 21941–970, Brazil.
‖Present address: Center for Plant Cell Biology, Department of Botany and Plant Sciences, University of California, Riverside, CA 92521, USA.
¶To whom correspondence should be addressed. E-mail: chory@salk.edu

to elevated Mg-protoPIX levels induced by dipiridyl (DP), which is known to restore the repression of *Lhcb* genes in *gun2* and *gun5* seedlings grown on NF (*6*). DP treatment did not restore *Lhcb* repression in *gun1* seedlings grown on NF or lincomycin (Fig. 2B). The results of the late NF treatment and the inability of DP to restore repression of *Lhcb* in *gun1* demonstrate that GUN1 plays a role in the Mg-protoPIX pathway. Unlike *gun2*, *3*, *4*, and *5*, *gun1* does not seem to be involved in chlorophyll biosynthesis, which indicates that it most likely acts downstream of Mg-protoPIX accumulation.

Common targets for *gun1* and *gun5*. To identify a comprehensive set of nuclear genes under the control of retrograde pathways, we analyzed the global gene expression response of wild-type, *gun1*, and *gun5* seedlings to NF, using the Affymetrix *Arabidopsis* ATH1 genome arrays. From these arrays, 7778 genes showed differential expression between either the condition (control versus NF) or the genotype (wild-type versus *gun1,gun5* and *gun1* versus *gun5*). A striking linear correlation was observed between the multiple of change (fold increase or decrease, logarithmic scale, hereafter, log fold change), in gene expression observed in NF-treated *gun1* or *gun5* compared with wild type (Fig. 2C). Clustering analysis of 1150 genes that were differentially expressed in *gun1* or *gun5* compared with wild type on NF showed a very similar pattern between *gun1* and *gun5* (Fig. 2D). Of these, 488 nuclear genes were repressed by NF in wild type [$P < 0.01$ RankProd (*23*)], and 370 of those had expression in either *gun1* or *gun5* on NF greater than twice what was seen in the wild type. Of these 370 genes, 329 (89%) were derepressed in both *gun1* and *gun5*, which strongly implicated GUN1 and GUN5 in the same pathway. The lack of an additive effect in a *gun1-9,gun5* double mutant grown on NF compared with individual mutants lends further support to this conclusion (fig. S2C).

Identification of ABI4 as a nuclear component of retrograde signaling. To identify regulatory elements enriched in the promoters of target genes of the retrograde signaling pathways, we analyzed 500–base pair (bp) regions of sequence upstream of the 329 genes derepressed in both *gun1* and *gun5*. An ACGT motif, the core of both the light-responsive G box (CACGTG) (*24*) and the abscisic acid (ABA) response element (ABRE) (*25*–*27*), appeared 944 times in the promoters of these genes compared with the expected 239 times (*11*); a *Z* score of 3.2 indicated that it is significantly overrepresented ($P < 0.01$).

To test whether components of the ABA signaling pathway play a role in retrograde signaling, we analyzed the retrograde response in ABA-deficient and ABA-insensitive mutants (*25*, *28*). Only one ABA-related mutant, *abi4*, showed *Lhcb* mRNA accumulation even when chloroplast function was impaired (Fig. 3A). Lincomycin treatment resulted in a reduction in *Lhcb* transcript levels to 1/10th those in the untreated seedlings, in either wild-type or *gun5* seedlings (Fig. 3B and fig. S3A) (*3*, *29*). In contrast, transcription in *gun1-1* or *abi4* (Fig. 3B) was reduced to one-third of controls, which indicated that, like GUN1, ABI4 plays a role in PGE-dependent signaling.

The identification of *abi4* as a retrograde signaling mutant suggested that ABA, a known stress hormone, might be a plastid-derived retrograde signal. This does not appear to be the case, because an ABA-deficient mutant (*aba1*) did not accumulate any *Lhcb* mRNA when grown on lincomycin (Fig. 3A). Furthermore, addition of 5 μM ABA, with or without NF, inhibited the accumulation of *Lhcb* transcripts in wild type and *gun1*, but had no effect on *abi4* seedlings (Fig. 3C, fig. S3B). *gun1* was also distinguished from *abi4* in germination assays (fig. S3C). Collectively, these results indicate that ABA is unlikely to be the actual retrograde signal. It is noteworthy that GUN5 has recently been shown to be an ABA receptor, but its Mg-chelatase activity appears to be distinct from its role in ABA signaling (*9*, *30*).

ABI4 acts downstream of GUN1 in retrograde signaling. Several lines of evidence indicate that GUN1 and ABI4 act in the same signaling pathway. First, *gun1* is epistatic to *abi4*; *Lhcb* mRNA levels in a *gun1-1,abi4* double mutant were similar to a *gun1-1* single mutant (fig. S3D). Second, we observed significant overlap in nuclear genes misregulated in *gun1-1* and *abi4*, 57% and 46% for genes that were either derepressed or repressed, respectively (fig. S4). Finally, overexpression of ABI4-GFP suppressed the *gun1-1* phenotype. We transformed *Lhcb::luciferase gun1-1* seedlings with an *ABI4-GFP* fusion driven by the cauliflower mosaic virus *CaMV 35S* promoter. Individual second-generation (T_2) seedlings were imaged for ABI4-GFP and luciferase expression. We detected no luciferase activity in lincomycin-treated T_2 seedlings that overexpressed the fusion protein (Fig. 3D).

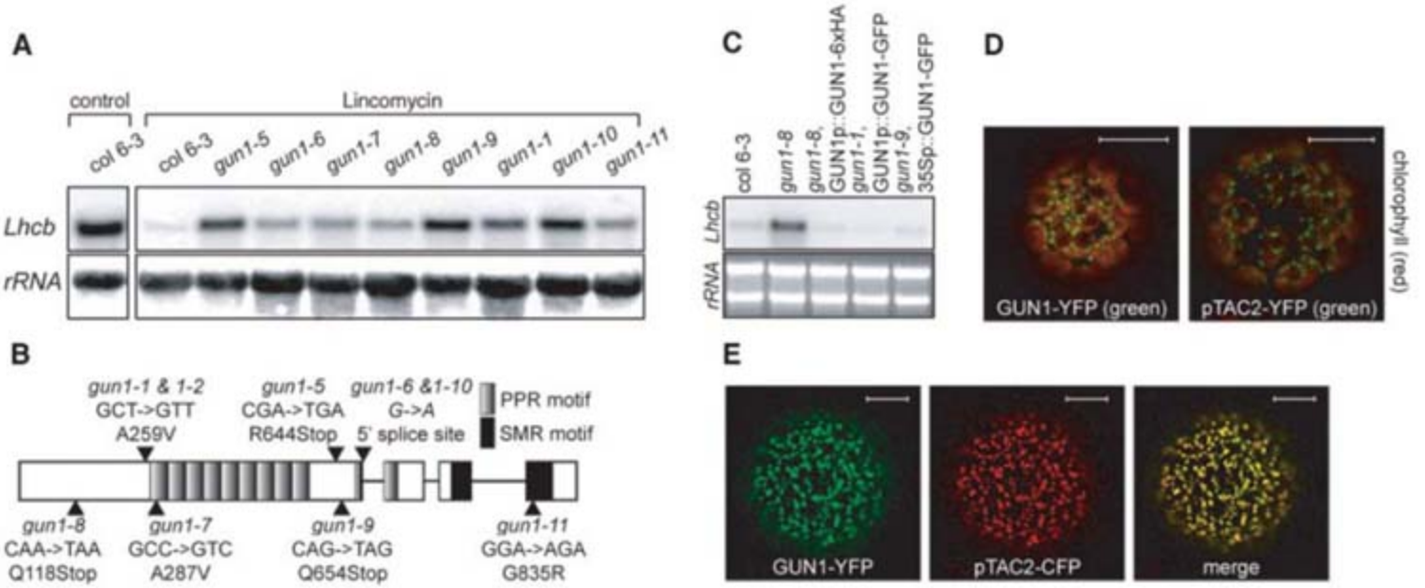

Fig. 1. GUN1 is a pentatricopeptide-repeat protein. (**A**) New alleles of *gun1* show enhanced derepression of *Lhcb*. Seedlings were treated with lincomycin for 6 days. *Lhcb* RNA was detected by Northern blotting. We used 25*S* ribosomal RNA *(rRNA)* as a loading control. (**B**) *GUN1* encodes a pentatricopeptide-repeat protein. Schematic representation of GUN1 shows the position and nature of the mutations in various alleles. Boxes and lines indicate exons and introns, respectively. (**C**) Genomic fragments of At2g31400 complement *gun1*. Total RNA was isolated from homozygous transgenic lines, and *Lhcb* RNA was detected by Northern blotting. Ethidium bromide–stained *rRNA* is shown as a loading control. (**D** and **E**) GUN1 and pTAC2 colocalize within chloroplasts. *N. benthamiana* leaves were infiltrated with *Agrobacterium* carrying the indicated constructs, and protoplasts were prepared 4 days postinfiltration. Fluorescence was imaged by confocal microscopy, and a representative image from a single protoplast is shown. Scale bar, 10 μM.

The GUN1-ABI4 pathway integrates multiple chloroplast-derived signals. We then tested whether ABI4 is also involved in the Mg-protoPIX pathway. Wild-type, *gun1*, *gun5*, and *abi4* were grown on NF for 4 days in the dark and then transferred to light. After 3 hours of illumination, all seedlings accumulated similar levels of *Lhcb* mRNA (fig. S3E), which confirmed that neither the Mg-protoPIX nor the PGE-dependent pathway had been triggered at this stage. With a prolonged light treatment, *gun1*, *gun5*, and *abi4* accumulated higher levels of *Lhcb* mRNA than wild type; this was also true when we measured luciferase activity in *Lhcb::luciferase* seedlings grown under these conditions (Fig. 4A). These results indicate that, like GUN1 and GUN5, ABI4, also plays a role in the Mg-protoPIX pathway.

We then tested if GUN1 and ABI4 are also involved in PET-derived signaling. *Lhcb* transcript levels were reduced in wild-type seedlings in response to intense light; this reduction was evident even after a 15-min exposure (Fig. 4B). *Lhcb* mRNA levels in both *gun1* and *abi4* were less affected by such exposure, although *Lhcb* levels declined in both mutants after 3 to 6 hours (Fig. 4B). We then studied the expression of *Zat12* and *Zat10*, two genes that encode zinc-finger DNA binding proteins, in response to intense light. *Zat12* is required for the expression of *APX1* under oxidative stress (*31*), and protein products of both these genes mediate the response of *Arabidopsis* to several abiotic stresses (*32*). Rapid, transient accumulation of both transcripts was observed within 15 min of exposure to intense light; a more sustainable accumulation was observed after 1 to 3 hours (Fig. 4C). The latter was delayed in both *gun1* and *abi4* seedlings, which suggests that not only repression, but also induction, of gene expression in response to a PET-derived signal, requires GUN1 and ABI4. The role of both GUN1 and ABI4 in all three retrograde signaling pathways is in agreement with a previously proposed "master switch," which controls the expression of a large number of nuclear genes in response to plastid-derived signals (*33*).

abi4 has also been identified as a sugar-insensitive mutant (*28*), and sugar signaling through ABI4 has been linked to chloroplast retrograde signaling (*34*). PET-induced gene expression is inhibited by sugar and this inhibition requires ABI4 (*34*). In *sucrose uncoupled 6* (an allele of *abi4*), exogenous sucrose does not inhibit the expression of nuclear-encoded photosynthetic genes (*35*). To understand the connection between sugar and retrograde signaling, we examined *Lhcb* expression in 4-day-old seedlings treated with exogenous glucose. *Lhcb* expression in wild type was significantly reduced in response to 7% glucose in the growth medium (Fig. 4D), but only slightly decreased in *abi4* and largely unchanged in *gun1* seedlings. Sorbitol did not affect *Lhcb* expression, which suggested that this is not a response to osmotic stress. Glucose also enhanced the greening of etiolated wild-type seedlings, whereas the greening of *gun1* and *abi4* seedlings was less affected (fig. S5). These results suggest that in addition to retrograde signaling, GUN1 and ABI4 are involved in glucose-mediated repression of photosynthetic gene expression and the transition from heterotrophic to photoautotrophic growth. Unlike *abi4*, germination of *gun1* was inhibited by 7% glucose, which suggested that it is not strictly a glucose-insensitive mutant. However, because it is required for the glucose-mediated *Lhcb* repression, it is possible that this represents a fourth, previously unidentified, plastid-derived signal.

ABI4 can bind the promoter of *Lhcb*. Our promoter analysis did not reveal any known binding sites for ABI4 (*27*, *36*), yet a yeast one-hybrid assay indicated that ABI4 could directly bind the promoter of *Lhcb* (Fig. 5A). In CUF1, which is a G-box element required for retrograde signaling (*6*), two cytosine residues precede the G box and that results in two overlapping elements, the CCAC and the ACGT core. The CCAC was overrepresented in the promoters of the 329 genes derepressed by *gun1* and *gun5*; it appeared 1048 times, although the expected frequency was only 302 (*Z* score of 11.34). About 70% of these promoters contained a CCAC/ACGT combination, and in the majority, these elements were either overlapping or closely spaced (1 to 3 bp), with about 70% having fewer than 20 bp between the two. A similar enrichment was found in the genes derepressed on lincomycin in *gun1* and *abi4* (fig. S4). When the CUF1 element was mutated to TTACGT (leaving the G-box core intact), ABI4 could not

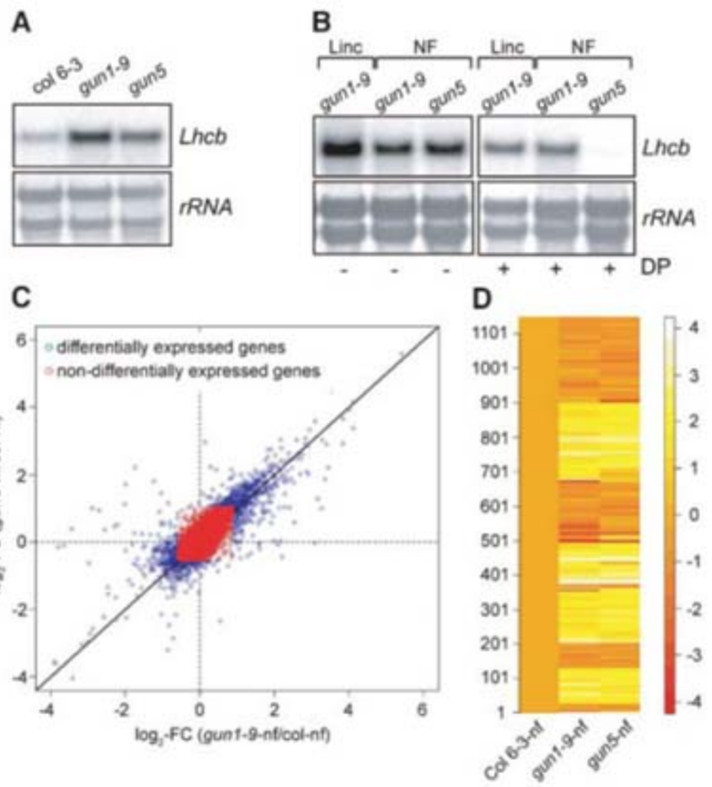

Fig. 2. GUN1 and GUN5 are components of the same signaling pathway. (**A**) *gun1* seedlings are impaired in retrograde regulation triggered by NF. Four-day-old green seedlings were treated with NF and harvested 9 days later. Methylene blue–stained membrane shows *rRNA* as a loading control. (**B**) *gun1* is insensitive to DP treatment. *gun1-9* and *gun5* seedlings were treated with lincomycin or NF for 5 days and harvested 24 hours after addition of 1 mM DP and 0.5 mM $MgCl_2$ (final concentration). Methylene blue–stained membrane shows rRNA as a loading control. (**C**) Microarray experiments indicate strong correlation between genes misregulated in *gun1-9* and *gun5*. Average log fold changes for 7778 nuclear genes are plotted. (**D**) *gun1* and *gun5* have a similar pattern of nuclear gene expression. Heat map depicts 1150 genes differentially expressed in *gun1-9* or *gun5* compared with wild type. Average values were calculated using Col 6-3-nf as reference.

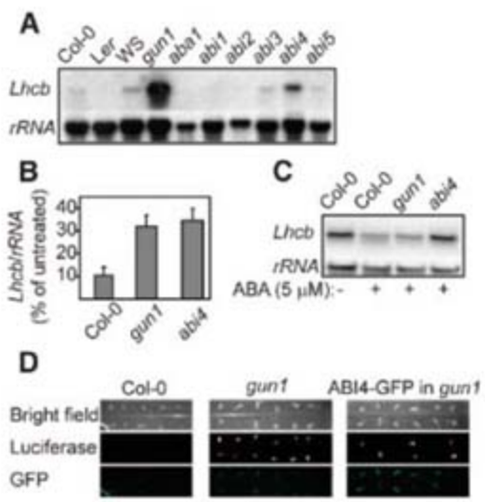

Fig. 3. *abi4* is a *gun* mutant. (**A**) *Lhcb1* mRNA accumulation in 6-day-old lincomycin-treated wild type (of three *Arabidopsis* ecotypes Col-0, Ler, and Ws), *gun1*, and ABA mutants. *gun1* and *abi4* are in the Col-0 background, *aba1*, *abi1*, *abi2*, and *abi3* are in Ler, and *abi5* is in Ws. (**B**) Quantitative analysis of three replicates showing the average ratio of *Lhcb/rRNA* between lincomycin-treated and untreated wild type, *gun1*, and *abi4*. (**C**) *Lhcb1* mRNA accumulation in 8-day-old ABA-treated wild type, *gun1*, and *abi4*. (**D**) Luciferase and GFP activity in lincomycin-treated seedlings of wild type, *gun1*, and *gun1* overexpressing an ABI4-GFP fusion protein.

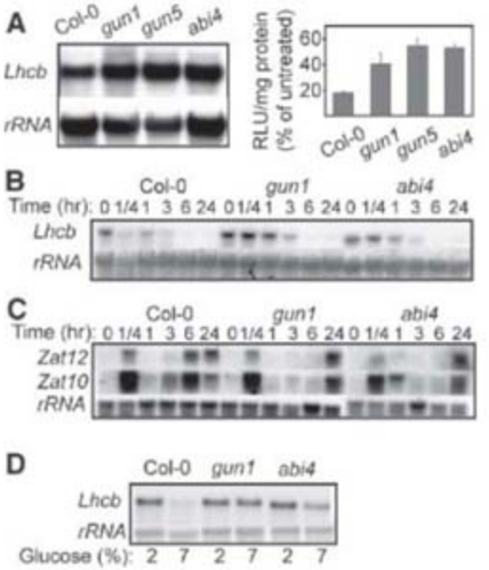

Fig. 4. GUN1 and ABI4 mediate several chloroplast-derived signals. (**A**) *Lhcb1* mRNA accumulation (left) and relative luciferase activity (right) in 7-day-old Norflurazon-treated wild type, *gun1*, *gun5*, and *abi4*. Plants were grown in the dark for 4 days and transferred to light for 3 more days. (**B**) *Lhcb1* mRNA levels in 4-week-old wild type, *gun1*, and *abi4* seedlings grown under low light and exposed to high light intensities for the indicated time. (**C**) *Zat12* and *Zat10* mRNA levels in seedlings described in (B). (**D**) *Lhcb1* mRNA accumulation in wild type, *gun1*, and *abi4* seedlings treated with 7% glucose.

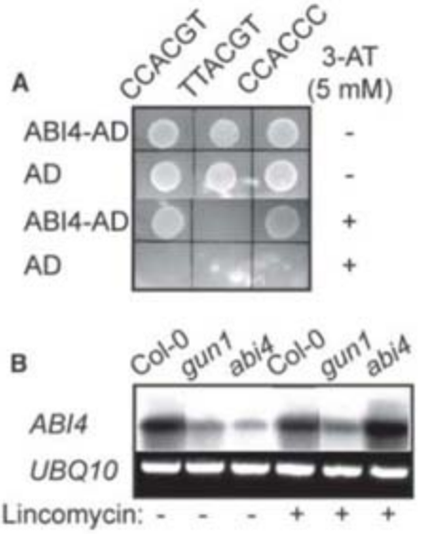

Fig. 5. ABI4 can bind the promoter of *Lhcb1*2*. (**A**) A yeast strain with the *HIS3* gene driven by a 200-bp *Lhcb1*2* promoter containing either wild type (CCACGT) or two mutated (TTACGT and CCACAA) motifs, was transformed with a plasmid encoding the GAL4 activation domain with (ABI4-AD) or without (AD) an ABI4 fusion. Transformants were grown on His-deficient media with or without 5 mM 3-amino-1,2,4-triazole. (**B**) *ABI4* expression is down-regulated in *gun1*. RNA was extracted from 5-day-old seedlings grown with or without lincomycin. First strand cDNA was used as template with *ABI4* or ubiquitin *UBQ10* specific primers. Polymerase chain reaction products were transferred to a membrane and probed with a radiolabeled *ABI4* probe.

facilitate growth on His-deficient media. In contrast, when the CUF1 element was mutated to CCACAA, which eliminated the G-box core, ABI4 enabled growth in the absence of His (Fig. 5A); this result suggested that ABI4 binds this CCAC motif. This motif is significantly smaller than previously described ABI4-binding sites, which suggests that it might be a core element required for ABI4 binding. It has been reported that light and retrograde signals are mediated by cis elements found in close proximity (*3*). It is conceivable that by binding to the CCAC motif, ABI4 inhibits G box–mediated, light-induced expression of photosynthetic genes when chloroplast development is arrested. Proteins that contain Apetala 2 (AP2) have been shown to act as transcriptional repressors in response to ABA, ethylene, and jasmonic acid (*37*). Not all of the promoters of retrograde-regulated genes contained the CCAC motif, and in some, it was too far from the G box to enable inhibition by competitive binding. Repression of those genes by retrograde signals might occur through different ABI4-binding sites.

ABI4 is highly expressed in seeds and is barely detectable in seedlings after germination (*38*); its expression is induced by glucose (*39*) and possibly other sugars (*40*). In wild-type seedlings, expression of *ABI4* did not change after lincomycin treatment; however, in both treated and untreated *gun1* seedlings *ABI4* mRNA levels were significantly lower than wild type (Fig. 5B). This suggests that, although *ABI4* expression is not directly induced by lincomycin, GUN1 is required for its expression. *ABI4* expression was up-regulated by lincomycin treatment of *abi4* seedlings (Fig. 5B), possibly in an attempt to compensate for the nonfunctional ABI4. Although originally identified as an ABA-insensitive mutant, *abi4* has since been identified in screens for sugar and salt resistance, as well as several others (*28*). Our data suggest that ABI4 may be the previously proposed master switch (*33*) required for the regulation of nuclear genes in response to developmental cues, as well as environmental signals, integrated within the chloroplast. Our findings also distinguish between chloroplast and mitochondria retrograde signaling, because neither organellar PPR-containing protein nor an AP2-type transcription factor are known to act in the mitochondria-derived signaling in plants (*41*), yeast, or mammalian cells (*2*).

In this study, we have presented genomic, genetic, and biochemical evidence that the three known retrograde signals, previously thought to be mediated by partially redundant signaling pathways, are integrated within the chloroplast upstream of GUN1 and that ABI4 acts downstream in the same pathway. We propose a model in which all three signals are integrated within plastids and GUN1 is required to either generate or transmit a second, common signal to the nucleus (fig. S6). In response to the GUN1-derived signal, ABI4 binds the promoter of *Lhcb*, which prevents the binding of G box–binding factors required for light-induced expression of nuclear photosynthetic genes (*24*). A potentially important benefit of multiple plastid-generated signals converging on one common pathway is that this convergence allows the monitoring of key parameters of a functional chloroplast while avoiding the potentially disastrous consequences of conflicting signals exerting control over nuclear gene expression. The chemical nature of this common signal now surfaces as the key question.

References and Notes

1. D. Leister, *Trends Genet.* **19**, 47 (2003).
2. R. A. Butow, N. G. Avadhani, *Mol. Cell* **14**, 1 (2004).
3. J. C. Gray, J. A. Sullivan, J. H. Wang, C. A. Jerome, D. MacLean, *Philos. Trans. R. Soc. London Ser. B* **358**, 135 (2003).
4. D. Leister, *Gene* **354**, 110 (2005).
5. A. Nott, H. S. Jung, S. Koussevitzky, J. Chory, *Annu. Rev. Plant Biol.* **57**, 739 (2006).
6. Å. Strand, T. Asami, J. M. Alonso, J. R. Ecker, J. Chory, *Nature* **421**, 79 (2003).
7. G. Vinti *et al.*, *Plant J.* **24**, 883 (2000).
8. R. M. Larkin, J. M. Alonso, J. R. Ecker, J. Chory, *Science* **299**, 902 (2003).
9. N. Mochizuki, J. A. Brusslan, R. Larkin, A. Nagatani, J. Chory, *Proc. Natl. Acad. Sci. U.S.A.* **98**, 2053 (2001).
10. R. Oelmüller, I. Levitan, R. Bergfeld, V. K. Rajasekhar, H. Mohr, *Planta* **168**, 482 (1986).
11. Materials and methods are available as supporting material on *Science* Online.
12. C. Lurin *et al.*, *Plant Cell* **16**, 2089 (2004).
13. E. Kotera, M. Tasaka, T. Shikanai, *Nature* **433**, 326 (2005).
14. C. Schmitz-Linneweber *et al.*, *Plant Cell* **18**, 2650 (2006).
15. S. Aubourg, N. Boudet, M. Kreis, A. Lecharny, *Plant Mol. Biol.* **42**, 603 (2000).
16. S. Mili, S. Pinol-Roma, *Mol. Cell. Biol.* **23**, 4972 (2003).
17. D. Moreira, H. Philippe, *Trends Biochem. Sci.* **24**, 298 (1999).
18. J. Pfalz, K. Liere, A. Kandlbinder, K. J. Dietz, R. Oelmuller, *Plant Cell* **18**, 176 (2006).
19. T. M. Ikeda, M. W. Gray, *Mol. Cell. Biol.* **19**, 8113 (1999).
20. N. Tsuchiya *et al.*, *Biochem. Biophys. Res. Commun.* **317**, 736 (2004).
21. O. Voinnet, S. Rivas, P. Mestre, D. Baulcombe, *Plant J.* **33**, 949 (2003).
22. J. C. Gray, *Trends Genet.* **19**, 526 (2003).
23. F. Hong *et al.*, *Bioinformatics* **22**, 2825 (2006).
24. W. B. Terzaghi, A. R. Cashmore, *Annu. Rev. Plant Physiol. Plant Mol. Biol.* **46**, 445 (1995).
25. C. D. Rock, *New Phytol.* **148**, 357 (2000).
26. T. Hattori, M. Totsuka, T. Hobo, Y. Kagaya, A. Yamamoto-Toyoda, *Plant Cell Physiol.* **43**, 136 (2002).
27. A. Himmelbach, Y. Yang, E. Grill, *Curr. Opin. Plant Biol.* **6**, 470 (2003).
28. R. R. Finkelstein, S. S. Gampala, C. D. Rock, *Plant Cell* **14** (suppl.), S15 (2002).
29. A. C. McCormac, M. J. Terry, *Plant J.* **40**, 672 (2004).
30. Y. Y. Shen *et al.*, *Nature* **443**, 823 (2006).
31. L. Rizhsky, S. Davletova, H. Liang, R. Mittler, *J. Biol. Chem.* **279**, 11736 (2004).
32. S. Davletova, K. Schlauch, J. Coutu, R. Mittler, *Plant Physiol.* **139**, 847 (2005).
33. E. Richly *et al.*, *EMBO Rep.* **4**, 491 (2003).
34. O. Oswald, T. Martin, P. J. Dominy, I. A. Graham, *Proc. Natl. Acad. Sci. U.S.A.* **98**, 2047 (2001).
35. P. P. Dijkwel, C. Huijser, P. J. Weisbeek, N. H. Chua, S. C. Smeekens, *Plant Cell* **9**, 583 (1997).
36. X. Niu, T. Helentjaris, N. J. Bate, *Plant Cell* **14**, 2565 (2002).
37. K. Kazan, *Trends Plant Sci.* **11**, 109 (2006).

38. E. M. Soderman, I. M. Brocard, T. J. Lynch, R. R. Finkelstein, *Plant Physiol.* **124**, 1752 (2000).
39. A. Arroyo, F. Bossi, R. R. Finkelstein, P. Leon, *Plant Physiol.* **133**, 231 (2003).
40. N. Avonce *et al.*, *Plant Physiol.* **136**, 3649 (2004).
41. D. Dojcinovic, J. Krosting, A. J. Harris, D. J. Wagner, D. M. Rhoads, *Plant Mol. Biol.* **58**, 159 (2005).
42. Seeds of ABA-related mutants were provided by the *Arabidopsis* Biological Resource Center (ABRC). We thank F. Parcy and S. Stehling (Max Planck institute, Tuebingen) for the pYI22670HIS vector, S. Kay (The Scripps Research Institute, La Jolla) for the *Lhcb*::luciferase lines, K. Todd for help with genetic screens, Y. Huang (Fred Hutchinson Cancer Research Center, Seattle) for assistance in statistical analysis of microarray experiments, J. Schroeder [University of California (UC), San Diego] and R. Finkelstein (UC Santa Barbara) for discussions about ABI4 and ABA signaling. J. Woodson, Y. Belkhadir, J. Umen, and S. Bagga provided lively discussion and helpful comments on the paper. This work was supported by a grant from the Department of Energy (DE-FG02-04ER15540) and the Howard Hughes Medical Institute (J.C.), NSF grants 0431327 and 0420033 (R.M.), EMBO long-term fellowship (ALTF 118-2000), and Howard Hughes Medical Institute fellowships to S.K. A.N. is supported by the Damon Runyon Cancer Research Foundation (DRG-1865-05). T.C.M. was an NIH postdoctoral fellow (F32 GM 69090) and was also supported by the Bechtel Foundation. G.S. was supported by a CAPES senior research fellowship. M.S. was an NIH postdoctoral fellow (F32 GM 18172).

Supporting Online Material

www.sciencemag.org/cgi/content/full/1140516/DC1
Materials and Methods
SOM Text
Figs. S1 to S6
References

29 January 2007; accepted 14 March 2007
Published online 29 March 2007;
10.1126/science.1140516
Include this information when citing this paper.

Blastocyst Axis Is Specified Independently of Early Cell Lineage But Aligns with the ZP Shape

Yoko Kurotaki,[1,2]* Kohei Hatta,[3]† Kazuki Nakao,[4] Yo-ichi Nabeshima,[1,2] Toshihiko Fujimori[1,2]‡

The mechanisms controlling the establishment of the embryonic-abembryonic (E-Ab) axis of the mammalian blastocyst are controversial. We used in vitro time-lapse imaging and in vivo lineage labeling to provide evidence that the E-Ab axis of the mouse blastocyst is generated independently of early cell lineage. Rather, both the boundary between two-cell blastomeres and the E-Ab axis of the blastocyst align relative to the ellipsoidal shape of the zona pellucida (ZP), an extraembryonic structure. Lack of correlation between cell lineage and the E-Ab axis can be explained by the rotation of the embryo within the ZP.

During vertebrate development, the fertilized egg gives rise to an embryo with an asymmetric body axis. In species such as the frog, information relating to the specification of the future body axis is asymmetrically localized as stored maternal factors in the fertilized egg (*1*). By contrast, in mammalian embryos, no proteins or other cellular components are known to be localized asymmetrically in the fertilized egg. Mammalian embryos possess a highly regulative character that is also a basis for recent regenerative medicine, and the pattern of cell division and allocation of cells within an embryo during the early stages vary between embryos. There are reports suggesting that intrinsic information relating the future embryonic axis is already present in early cleaving mouse embryos (*2*–*7*). However, several groups have presented data contradicting this hypothesis, suggesting instead that the bias relating to the embryonic axis is found relatively late in development (*8*–*13*). We have designed a series of experiments to directly address this controversial issue.

The blastocyst consist of two types of cells, those of the inner cell mass (ICM) and those of the trophectoderm (TE). After the fifth cell division, the mouse embryo starts to form a cavity (blastocoel or blastocyst cavity). The localization of the ICM on one side of this cavity marks the first appearance of an embryonic axis, known as the embryonic-abembryonic (E-Ab) axis. Thus, the differentiation of cells into ICM and TE is closely linked to the specification of the blastocyst E-Ab axis. There has been progress in understanding the molecular basis for the differentiation of ICM and TE (*14*, *15*). However, the onset of specification of these two cell types has still not been defined. One hypothesis is that the cells located inside the morula mainly contribute to the ICM whereas outside cells differentiate into TE cells (*16*–*19*). This "inside-outside" hypothesis has its basis in analyses of separated blastomeres, and continuous information from intact embryos is currently very limited. In this study, we focused on the preimplantation stage of mouse development to reveal factor(s) that function in specification of the blastocyst axis. Embryo shape [with and without the zona pellucida (ZP), the membrane surrounding the embryo proper] and the correlation between early cell lineages and cell fate were examined.

Analysis of cell behavior in developing preimplantation mouse embryos using a cell tracing system. One way to determine the correlation between cell lineage and axis formation in the mammalian embryo is to label and continuously observe all of the cells in live, undisrupted embryos during the entire period of interest. We generated a transgenic mouse line (R26H2BEGFP) that ubiquitously expresses EGFP (enhanced green fluorescent protein) fused to human histone H2B (*20*) under the control of the *Rosa26* locus (*21*). This allowed continuous labeling of chromosomes in the nuclei of all the cells with fluorescent signals. To record development from the two-cell to the blastocyst stage, we captured bright-field and fluorescence images every 10 min (Fig. 1, A to J). Fluorescence images with 5-μm steps were used to reconstruct images that can be viewed three-dimensionally with glasses colored in red and green (Fig. 1, G to J, and movie S1). The position of each nucleus was plotted on the images, and the *x*-*y* position recorded simultaneously (Fig. 1, K to O). A total of 124 embryos were recorded in 15 repetitions of the experiment. Of these embryos, 108 (87%) developed into blastocysts, and in most cases the initial formation of the blastocoel was seen after the fifth cell division. The number of nuclei identified and traced varied between embryos. We traced as many cells as possible and the average number of traced cells was 31.8 per embryo. The embryos attached weakly to the culture plate, and the position of the ZP relative to the bottom of the culture plate remained fixed, judging from its shape and pigmentation pattern. By contrast, the position of the embryo proper within the ZP was not fixed, but embryos rotated within the ZP, as reported previously (*8*). A typical result of tracing the nuclei of an embryo from the two-cell stage is shown in Figs. 1 and 2A. When the traced points were plotted against time, a cell lineage map could be drawn (Fig. 2B). Because of technical limitations, we could not apply molecular markers to distinguish the ICM and TE in embryos used for time-lapse recording. However, whether a cell was in the embryonic region of the blastocyst (ICM and polar TE) or in the abembryonic region (mural TE) was judged from bright-field images, and the

[1]Department of Pathology and Tumor Biology, Graduate School of Medicine, Kyoto University, Yoshida-Konoe-cho, Sakyo-ku, Kyoto 606-8501, Japan. [2]Core Research for Evolutional Science and Technology (CREST), Japan Science and Technology Agency (JST), 4-1-8, Honcho, Kawaguchi, Saitama 332-0012, Japan. [3]Vertebrate Body Plan Group, RIKEN Center for Developmental Biology (CDB), 2-2-3 Minatojima-minami-cho, Chuo-ku, Kobe, Hyogo 650-0047, Japan. [4]Laboratory for Animal Resources and Genetic Engineering (LARGE), RIKEN CDB, 2-2-3 Minatojima-minami-cho, Chuo-ku Kobe, Hyogo 650-0047, Japan.

*Present address: International University of Health and Welfare Graduate School, Kitakanemaru, Otawara, Tochigi 324-8501, Japan.
†Present address: Laboratory for Biological Information, Graduate School of Life Science, University of Hyogo, 3-2-1 Kouto, Kamigori-cho, Ako-gun, Hyogo 678-1297, Japan.
‡To whom corrrespondence should be addressed. E-mail: fujimori@lmls.med.kyoto-u.ac.jp

H2BEGFP-labeled nuclei was scored appropriately (blue or red, respectively, in Fig. 2, D and E) and traced back to the two- or four-cell stage. In 66 embryos analyzed from the two-cell stage, all of the descendants of two-cell blastomeres contributed to both embryonic and abembryonic regions. When the analysis was carried out from the four-cell stage, a wide range of ratios was observed for cells contributing to the embryonic or abembryonic regions (fig. S1). Out of 264 four-cell blastomeres analyzed, 222 (84%) contributed to both embryonic and abembryonic regions. No contribution to the embryonic region was observed for 20 (7.6%) four-cell blastomeres, whereas the descendants of 22 (8.3%) four-cell blastomeres were found only in the embryonic region (table S1). No correlation was found between the division order of the blastomeres and their future fates. We tried to classify the division patterns in the same way as applied previously (*3*, *22*). However, we were unable to determine the type of the pattern which portion of cytoplasm was divided during the cleavage, because the relative position of the blastomeres changed and the second polar body moved on the surface of blastomeres during cleavage. Thus, we could not reproduce previous results indicating differences in future fates between blastomeres of the four-cell stage after a specific type of cleavage. By contrast, our results suggest that the blastocyst axis is formed independently of the early cell lineage up to the four-cell stage. When cell lineage was examined in later stages, such as the 16-cell stage, cells located relatively close to each other had common fates in the blastocyst. This suggests that future cell fate does relate to the position of the cells in later stages. It was also noticed from the time lapse movies that the speed of embryonic rotation within, and relative to, the ZP is reduced in later morula stages compared with the speed of earlier stages. This observation might explain why a cell labeled in the late morula remains in a similar position at the blastocyst stage, as reported by Gardner and Davies (*23*).

Lineage tracing in blastocysts developed in vivo. The above experiments and those examining the correlation between the two-cell lineage and the E-ab axis of the blastocyst (*2*, *3*, *5*, *6*, *8*–*12*, *23*, *24*) were carried out with embryos developing in vitro. However, these conditions might not be optimal for embryonic development. We therefore carried out lineage tracing in vivo with a labeling method that is noninvasive and milder compared with conventional labeling methods using microinjection of lineage tracers (*25*). A transgenic mouse strain was established that ubiquitously expresses Kikume Green-Red (MBL, Nagoya, Japan), a fluorescent protein that emits green fluorescence that can be converted to red after exposure to weak ultraviolet (UV) light (*26*, *27*). For cell labeling, a part of a single two-cell blastomere was exposed to weak UV light (Fig. 3, A and B). The converted red proteins were observed throughout the whole blastomere (Fig. 3B). A total of 74 embryos labeled in this way at the two-cell stage were transferred immediately to the oviducts of pseudo-pregnant females. Of these embryos, 70 were recovered: 53 were at the blastocyst stage, and the remaining 17 embryos were at the morula stage. Two colors were distinguishable in 41 embryos. In 29 (71%) embryos examined by confocal microscopy, cells with red and green fluorescence formed two distinct clusters, as seen in Fig. 3, D to S. In the remaining 12 (29%) embryos, cells of different colors were intermingled, at least partially, and two or more clusters of cells with the same color were observed. In most of the embryos with only two clusters of red and green cells, the boundary between these clusters was not straight. It was therefore not easy to determine the angle between the boundary and the E-Ab axis of the blastocyst. For example, in the embryo shown in Fig. 3, the boundary seemed approximately parallel to the E-Ab axis at the focal plane shown in Fig. 3I around the embryonic region. However, this was not the case at the focal plane shown in Fig. 3L, and the boundary between the two colors was roughly perpendicular to the E-Ab axis. Because the distribution of labeled cells differed along the *z* positions in this embryo (compare Fig. 3, E to I, and Fig. 3, N to S), it was categorized as an example of an embryo in which the boundary was neither parallel nor perpendicular to the E-Ab axis. In two embryos (5%), the boundary of the two colors was close to perpendicular to E-Ab axis. On the other hand, in another four embryos (10%) the angle was close to parallel. In the rest of the embryos (23, 56%), the boundary varied along the *z* axis. These results suggest that there is no such tendency that the one of two-cell blastomeres contribute mainly to either embryonic or abembryonic region of the blastocyst. These in vivo experiments produced the same results as the in vitro time-lapse analysis, namely, that the axis of the blastocyst is formed independently of cell lineage from the two-cell stage.

Correlation between the shape of the ZP and the blastocyst axis. In most embryos, the first cleavage plane and the E-Ab axis of the blastocyst are close to perpendicular (*2*, *5*, *6*, *12*, *22*, *28*).

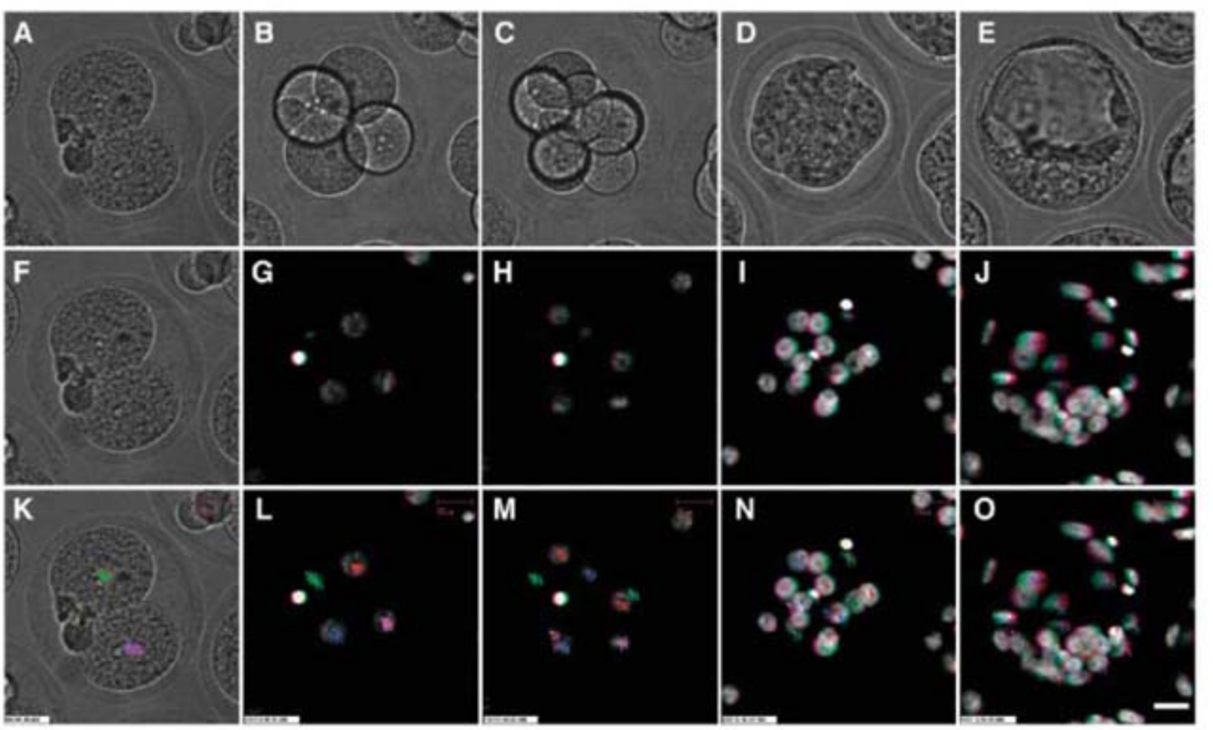

Fig. 1. Time-lapse recording and tracing of nuclei in developing preimplantation R26H2BEGFP homozygous embryos. Bright field images (**A** to **F**) and images of EGFP (**G** to **J**) were captured simultaneously. The position of each nucleus was plotted and numbered (**K** to **O**). In this embryo, 35 cells were identified in the blastocyst, and the behavior of all of them was analyzed from the two-cell stage. The four colors (red, green, blue, and purple) correspond to each of the four-cell blastomeres. The second polar body is yellow. This analysis was carried out in reverse order from the blastocyst stage. Thus, several points are overlapping in nuclei of early stages. Scale bar indicates 20 μm.

There are reports that suggest that the shape of the ZP is not a sphere but sometimes ellipsoidal in preimplantation stages (*6*, *8*, *23*, *24*, *28*–*30*). It has also been proposed that this ellipsoidal shape provides asymmetrical physical pressure to orient the blastocyst axis (*8*). We analyzed the three-dimensional shape of the ZP [Supporting Online Material (SOM) text] and noticed that it was ellipsoidal and that two-cell blastomeres settled along the longest diameter of the ZP (fig. S2). The shape of the ZP was maintained from the one-cell (fig. S3) to early blastocyst stage (movie S1) before the blastocoel expands. We found that the embryo proper rotates within the ZP. Consequently, the positions of the first cleavage plane and the boundary between the two-cell blastomeres at the end of the two-cell stage (defined as the two-cell boundary, 2CB) were not identical in most embryos, although they were relatively close (fig. S3F). Thus, it is possible that in previous studies the 2CB was used instead of the first cleavage plane to determine the position of the two-cell embryo relative to the blastocyst axis. Two independent methods were therefore used to test the correlation between the 2CB and the E-Ab axis. First, we measured the angle between the E-Ab axis and the 2CB from time-lapse images (Fig. 4, A to C). In 64% of embryos (47 out of 74), this angle was more than 70°. Second, a localized region of the ZP over the polar body was labeled with the lectin WGA-Alexa594 (Invitrogen, Carlsbad, CA) at the late two-cell stage (Fig. 4, D and E). Then, labeled embryos were either cultured in a conventional CO_2 incubator or allowed to develop in the oviducts of pseudopregnant females. In both cases, a similar distribution of angles between the labeled point and the E-Ab axis was observed (Fig. 4, H and I). In 52% (65 of 124) and 67% (25 of 36) of embryos developed in vitro and in vivo, respectively, the angle was more than 70°. These results suggest that the shorter diameter of the ZP and the E-Ab axis of the blastocyst become nearly perpendicular, not only under cultured conditions but also during normal development in vivo. The ellipsoidal shape of the ZP might affect both the position of the two-cell blastomeres and the orientation of the blastocyst axis, as discussed previously (*8*, *9*). Because a blastocyst can be formed without the ZP, it is not required for the formation of the blastocyst axis, but it might function as a kind of restriction for axis orientation during normal development. This conclusion was also supported by the results of experiments in which embryos were cultured in alginate gel after removal of the ZP (*6*). In this case, the two-cell stage embryo was used as a template to make a mold in the alginate gel. Under these conditions, the configuration of the alginate gel restricted embryonic shape instead of the ZP.

To test whether the ZP has an effect on the blastocyst axis, we examined the development of two-cell stage embryos after removal of the ZP with acid tyrode solution (Fig. 4, J to L). Embryos developed to the blastocyst stage without the ZP at a relatively high rate (43/50), and the shape of the blastocoel was closer to spherical in these embryos than in controls (Fig. 4K). This result suggests that physical pressure from the blastocoel overcomes the tension of the embryonic surface. The correlation between the 2CB and blastocyst E-Ab axis was lost when the ZP was removed (Fig. 4L). This finding suggests that the shape of the ZP is an important factor for the positioning of the blastocyst axis,

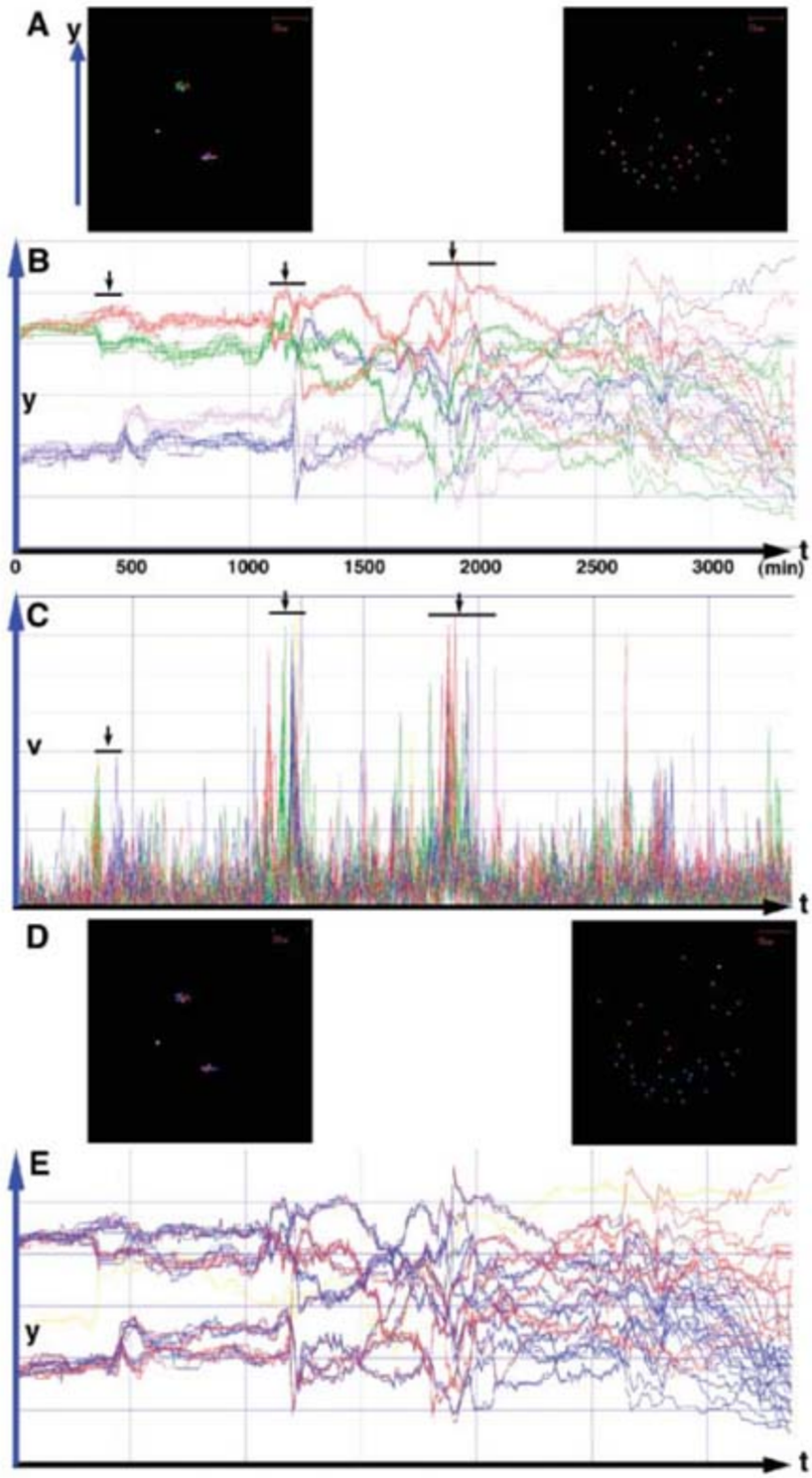

Fig. 2. Positions and velocity of movement of nuclei plotted against time from traced images. After the nuclei were traced (**A**), their positions on the *y* axis were plotted against time (*t*) (**B**). (**C**) The velocity (*v*) of each nucleus was plotted against time. Because the nuclei moved a long distance during cleavage, the peaks of the graphs correspond to the period of each cleavage (shown by bars and arrows). (**D** and **E**) The same plot points as (A) and (B) are shown in red and blue, corresponding to cells in the abembryonic (mural TE) and embryonic (the ICM and polar TE) regions at the blastocyst stage, respectively. In this embryo, both colors were seen in all of the four-cell blastomeres.

although not predictive of the E-Ab direction. These results also support the idea that the major factor determining the correlation between the 2CB plane and the E-Ab axis of the blastocyst lies not within the embryo proper but in the shape of the ZP.

If this hypothesis is correct, movement of the embryo within the ZP might be the major reason for the lack of correlation between cell lineage and the spatial orientation of the blastocyst axis. In other words, although there is a geographical relation between the position of the two two-cell blastomeres and the future blastocyst axis, a consistent correlation between cell lineage and axis specification is not observed. These two observations seem inconsistent and have resulted in a major point of controversy in the field. In previous reports, lineage dependency was concluded on the basis of analyzing the spatial relation between the position of the two-cell blastomeres and the axis of the blastocyst (*6*, *23*). We noticed that embryos rotated within the ZP (movie S1) and that the relative position of each cell changed during cleavage. This might explain the inconsistency mentioned above. When embryos were embedded within alginate gel, the movement of embryos within the ZP was also restricted (movie S2). Under these conditions, none of the 21 embryos examined rotated or changed their position relative to the ZP. The E-Ab axis formed nearly perpendicular to the short diameter of the ZP. Cells derived from a two-cell blastomere (colored in green and red in movie S2) localized mainly in the embryonic region, whereas cells derived from the other two-cell blastomere were found mainly in the abembryonic region of the blastocyst. This shows that a correlation between cell lineage and the axis of the blastocyst can be observed when the movement of the embryos within the ZP is restricted. In a previous study, we reported that descendants of a two-cell blastomere localized along the E-Ab axis in 73% of blastocysts (*12*). These embryos were also cultured in alginate gel, and thus the movement of the embryos within the ZP might have been restricted. This may explain why we observed lineage dependency in these experiments. This argument might also apply to other experiments carried out under the similar conditions restricting embryonic movements (*2*, *7*).

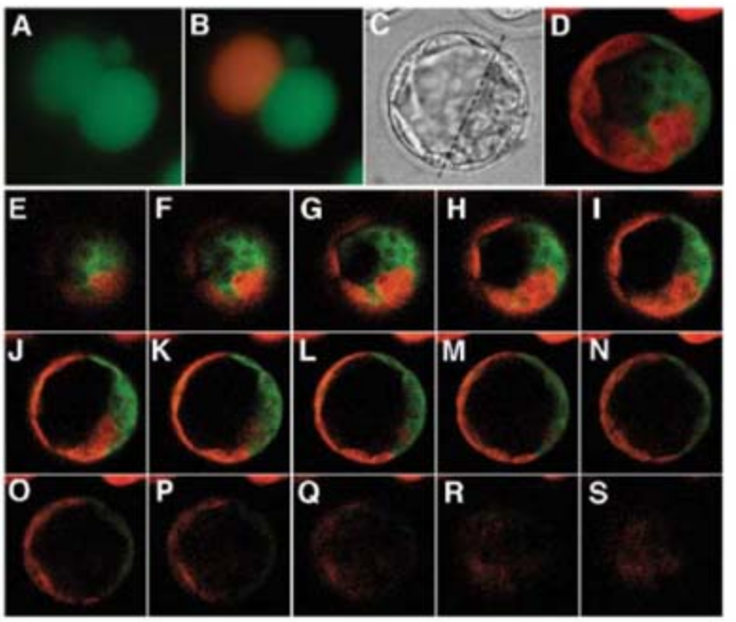

Fig. 3. Lineage tracing of embryos developed in vivo after labeling a blastomere by photoconversion at the two-cell stage. A two-cell blastomere of CAG-KikGR-1 mouse embryo (**A**) was labeled by photoconversion (**B**). Labeled embryos developed in vivo to the blastocyst stage (**C** to **S**) were collected. Embryonic regions are observed on the right of the dashed line (C). The distribution of labeled cells was observed by using laser scanning microscopy [(E) to (S)] at several focal planes.

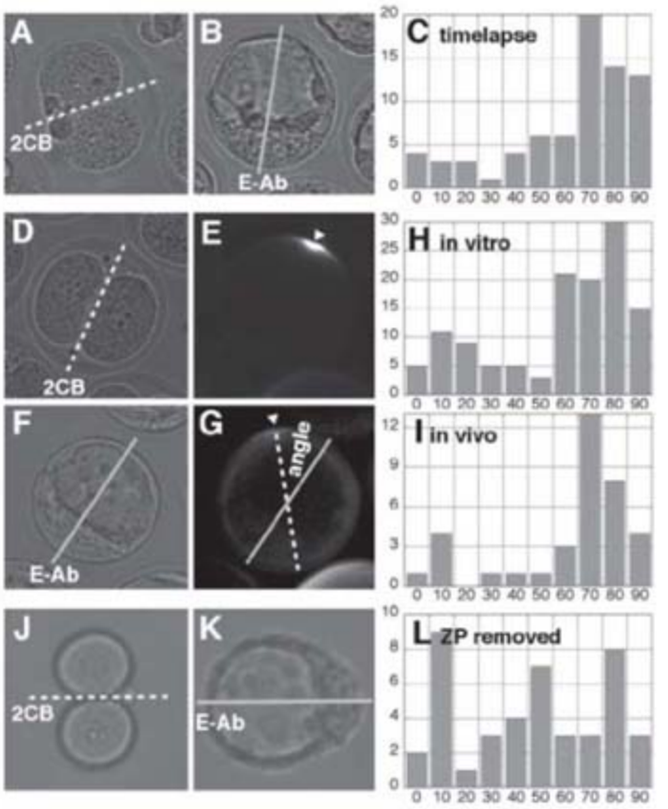

Fig. 4. E-Ab axis was close to perpendicular to the 2CB both in vitro and in vivo, and it is regulated by the ZP. By using time-lapse images (**A** and **B**), we measured the angle between the 2CB and the E-Ab axis of the blastocyst. The distribution of the angles is shown in (**C**). (**D** to **I**) A point on the ZP over the 2CB was labeled [(D) and (E)]. Embryos developed to the blastocyst stage were then analyzed [(F) and (G)]. The angle between the fluorescent label (G, arrowhead) and the E-Ab axis was measured in blastocysts developed in vitro (H) or in vivo (I). (**J** to **L**) Development of embryos without the ZP was recorded with the time-lapse system, and the angles between the 2CB and E-Ab axis were analyzed.

The molecular mechanisms controlling the formation and specification of the blastocyst axis have not been studied in this paper. In the future, the localization of functional molecules such as Cdx-2, Nanog, and Oct4 (*14*, *15*) must be examined in developing live embryos utilizing imaging techniques similar to those described here to reveal the mechanism of differentiation. In addition, examination of ZP shape in other mammalian embryos may provide information about whether our findings with the mouse embryo are applicable to other species.

Conclusion. We have shown that the specification of the mouse blastocyst E-Ab axis is not dependent on early cell lineage. By contrast, the position of the blastocyst axis coincides with the ellipsoidal shape of the ZP, which is maintained during preimplantation stages. Thus, the bias for axis positioning in early-stage mouse embryos is imposed by factors outside the embryo, namely the ZP and its shape, and not by intrinsic factors residing within the blastomeres.

References and Notes

1. D. S. Kessler, D. A. Melton, *Development* **121**, 2155 (1995).
2. K. Piotrowska, F. Wianny, R. A. Pedersen, M. Zernicka-Goetz, *Development* **128**, 3739 (2001).
3. K. Piotrowska-Nitsche, A. Perea-Gomez, S. Haraguchi, M. Zernicka-Goetz, *Development* **132**, 479 (2005).

4. K. Piotrowska, M. Zernicka-Goetz, *Development* **129**, 5803 (2002).
5. K. Piotrowska, M. Zernicka-Goetz, *Nature* **409**, 517 (2001).
6. R. L. Gardner, *Development* **128**, 839 (2001).
7. B. Plusa *et al.*, *Nature* **434**, 391 (2005).
8. N. Motosugi, T. Bauer, Z. Polanski, D. Solter, T. Hiiragi, *Genes Dev.* **19**, 1081 (2005).
9. V. B. Alarcon, Y. Marikawa, *Biol. Reprod.* **69**, 1208 (2003).
10. V. B. Alarcon, Y. Marikawa, *Mol. Reprod. Dev.* **72**, 354 (2005).
11. A. Chroscicka, S. Komorowski, M. Maleszewski, *Mol. Reprod. Dev.* **68**, 308 (2004).
12. T. Fujimori, Y. Kurotaki, J. Miyazaki, Y. Nabeshima, *Development* **130**, 5113 (2003).
13. M. Waksmundzka, A. Wisniewska, M. Maleszewski, *Biol. Reprod.* **75**, 582 (2006).
14. H. Niwa *et al.*, *Cell* **123**, 917 (2005).
15. D. Strumpf *et al.*, *Development* **132**, 2093 (2005).
16. T. P. Fleming, *Dev. Biol.* **119**, 520 (1987).
17. A. H. Handyside, *J. Embryol. Exp. Morphol.* **45**, 37 (1978).
18. M. H. Johnson, C. A. Ziomek, *Cell* **24**, 71 (1981).
19. A. K. Tarkowski, J. Wroblewska, *J. Embryol. Exp. Morphol.* **18**, 155 (1967).
20. T. Kanda, K. F. Sullivan, G. M. Wahl, *Curr. Biol.* **8**, 377 (1998).
21. P. Soriano, *Nat. Genet.* **21**, 70 (1999).
22. K. Piotrowska-Nitsche, M. Zernicka-Goetz, *Mech. Dev.* **122**, 487 (2005).
23. R. L. Gardner, T. J. Davies, *Hum. Reprod.* **21**, 492 (2006).
24. R. L. Gardner, *Development* **124**, 289 (1997).
25. Materials and methods are available on *Science* Online.
26. H. Tsutsui, S. Karasawa, H. Shimizu, N. Nukina, A. Miyawaki, *EMBO Rep.* **6**, 233 (2005).
27. K. Hatta, H. Tsuji, T. Omura, *Nat. Protoc.* **1**, 960 (2006).
28. R. L. Gardner, *Hum. Reprod.* **22**, 798 (2007).
29. R. L. Gardner, T. J. Davies, *Hum. Reprod.* **17**, 1839 (2002).
30. D. Gray *et al.*, *Curr. Biol.* **14**, 397 (2004).
31. Contact K.H. (khatt@sci.u-hyogo.ac.jp) for CAG-KikGR-1 mouse. The authors acknowledge the members of the animal facility for the care of the mice used in this study, S. Yoshida for critical reading of the manuscript, and S. Aizawa for encouragement. We thank the LARGE in CDB, RIKEN for providing the CAG-KikGR-1 transgenic mouse (CDB0201T) and P. Soriano for providing genomic DNA fragments of the Rosa26 locus. This work was initiated with support from PRESTO (Precursory Research for Embryonic Science and Technology), JST, and supported by grants-in-aid for scientific research from Ministry of Education, Culture, Sports, Science, and Technology of Japan.

Supporting Online Material

www.sciencemag.org/cgi/content/full/1138591/DC1
Materials and Methods
SOM Text
Figs. S1 to S3
Movies S1 and S2

8 December 2006; accepted 21 March 2007
Published online 19 April 2007;
10.1126/science.1138591
Include this information when citing this paper.

REPORTS

Quantum Coherent Tunable Coupling of Superconducting Qubits

A. O. Niskanen,[1,4] K. Harrabi,[1] F. Yoshihara,[2] Y. Nakamura,[1,2,3]* S. Lloyd,[5] J. S. Tsai[1,2,3]

To do large-scale quantum information processing, it is necessary to control the interactions between individual qubits while retaining quantum coherence. To this end, superconducting circuits allow for a high degree of flexibility. We report on the time-domain tunable coupling of optimally biased superconducting flux qubits. By modulating the nonlinear inductance of an additional coupling element, we parametrically induced a two-qubit transition that was otherwise forbidden. We observed an on/off coupling ratio of 19 and were able to demonstrate a simple quantum protocol.

Macroscopic quantum coherence of superconducting structures is an intriguing physical phenomenon. The reasons for studying it include not only the prospect of constructing a quantum computer but also the possibility of realizing quantum-mechanical coherence in artificially fabricated structures. The properties of superconducting qubits (*1*–*3*) are being vigorously studied, with the relevant coherence times of the quantum states now extending to the microsecond range (*4*–*7*), in particular because the qubits are being operated at optimal bias points (*4*). When two or more qubits are coupled, quantum mechanics predicts that the combination can be, roughly speaking, more than the sum of its constituents. This entirely nonclassical concept is called entanglement. The existing quantum algorithms rely heavily on the use of entangled states. With tunable couplings between individual qubits, the design of control pulses for even a large set of qubits is relatively straightforward because the system can be divided into small noninteracting blocks. With nontunable couplings, as in nuclear magnetic resonance quantum computing, a large fraction of the quantum operations performed has to be devoted to effective decoupling procedures (*8*). Recently, several experiments on coupled superconducting qubits have been carried out with both fixed (*9*–*15*) and tunable (*16*–*18*) coupling. Unfortunately, most coupling schemes for superconducting qubits are efficient only away from the optimal point, which results in a shorter coherence time. Thus, realizing tunable coupling at the coherence optimal bias point is crucial for future scalability.

We studied superconducting flux qubits (*19*), which are superconducting loops interrupted by Josephson junctions. When a magnetic flux Φ_j close to half-flux quantum $\Phi_0/2$ is applied through the loop of qubit j, the two lowest-energy states have the supercurrents $\pm I_{pj}$ rotating in opposite directions. The magnetic energy difference $\varepsilon_j = 2I_{pj}(\Phi_j - \Phi_0/2)$ between these states can be controlled via Φ_j. The tunnelling energy between the states is Δ_j. The qubit states have eigenenergies $\pm\omega_j/2$, where $\omega_j = \sqrt{\{\Delta_j^2 + \varepsilon_j^2\}}$, as shown schematically in Fig. 1A. Resonant control of qubits is possible by modulating ε_j at the frequency ω_j. At the flux optimal point $\Phi_j = \Phi_0/2$, the eigenstates are equal superpositions of the circulating current states, and therefore the expectation value of current vanishes. At this point, the quantum coherence is found to be far superior (*6*, *7*) to the case where $\Phi_j \neq \Phi_0/2$, because $d\omega_j/d\Phi_j = 0$ and thus the accumulated quantum phase proportional to the time integral of ω_j is insensitive to flux noise.

The natural coupling between qubits k and l is via mutual inductance $M_{kl} > 0$, resulting in the antiferromagnetic coupling $J_{kl} = M_{kl}I_{pk}I_{pl}$. A collection of n qubits can be described by the Hamiltonian

$$H = -\frac{1}{2}\sum_{j=1}^{n}(\Delta_j\sigma_z^j + \varepsilon_j\sigma_x^j) + \sum_{k=1}^{n}\sum_{l=k+1}^{n} J_{kl}\sigma_x^k\sigma_x^l \qquad (1)$$

where σ_x^j and σ_z^j are Pauli matrices operating on qubit j. Owing to vanishing persistent currents (or the off-diagonal coupling term), the coupling only has a weak second-order effect at the optimal point ($\varepsilon_k = \varepsilon_l = 0$) if $J_{kl} \ll |\Delta_k - \Delta_l|$. It is thus easy to decouple qubits at the optimal point. To realize universal two-qubit gates (that is, to turn the coupling on), it would be ideal to drive either the $|00\rangle \leftrightarrow |11\rangle$ or the $|10\rangle \leftrightarrow |01\rangle$ transition, where $|jk\rangle$ are the two-qubit eigenstates. This results in a gate equally as efficient as the controlled-NOT (CNOT). However, simply driving the fluxes Φ_1 and Φ_2 with microwaves in resonance with such transitions cannot realize the desired operation because the microwave essen-

[1]CREST, Japan Science and Technology Institute, Kawaguchi, Saitama 332-0012, Japan. [2]The Institute of Physical and Chemical Research (RIKEN), Wako, Saitama 351-0198, Japan. [3]NEC Fundamental and Environmental Research Laboratories, Tsukuba, Ibaraki 305-8501, Japan. [4]VTT Technical Research Centre of Finland, Sensors, Post Office Box 1000, 02044 VTT, Finland. [5]Massachusetts Institute of Technology, Cambridge, MA 02139, USA.

*To whom correspondence should be addressed. E-mail: yasunobu@ce.jp.nec.com

tially couples through single-qubit operators σ_x^j. In general, the corresponding transitions are forbidden for any value of J_{kl}, although the eigenstates are modified. Different ways to overcome this problem are being pursued (*20*–*23*).

Our approach (*22*) is to couple two qubits via a third adiabatic qubit ($n = 3$) with higher Δ_3, which results in an effective coupling between qubits 1 and 2 given by

$$J_{12}^{\text{eff}} \approx \left(M_{12} + \frac{M_{13}M_{23}}{L_Q}\right) I_{p1} I_{p2} = J_{12} - \frac{2J_{23}J_{13}\Delta_3^2}{\omega_3^3} \quad (2)$$

The coupling can be interpreted as a sum of direct inductive coupling J_{12} and indirect coupling via the nonlinear ground-state inductance $L_Q = -2(d^2\omega_3/d\Phi_3^2)^{-1}$ of qubit 3. Applying a microwave through the loop of qubit 3 at the frequency $(\Delta_2 \mp \Delta_1)/h$ modulates L_Q via ω_3 and results in a term proportional to $\sigma_x^1\sigma_x^2 \pm \sigma_y^1\sigma_y^2$ in the rotating frame for which the desired transitions are allowed. The induced coupling can be thus attributed to the parametric modulation of the coupling energy at a microwave frequency. In the linear approximation, the two-qubit oscillations have the frequency $\Omega_{12}/h = (dJ_{12}^{\text{eff}}/d\varepsilon_3)\delta\varepsilon_3/h$, where $\delta\varepsilon_3$ is the amplitude of the microwave driving applied to qubit 3. This has a maximum around $\varepsilon_3 = \pm\Delta_3/2$ and vanishes at $\varepsilon_3 = 0$ and at $|\varepsilon_3| >> \Delta_3$. We focus here on the sum-frequency transition $|00\rangle \leftrightarrow |11\rangle$. The functioning of the tunable parametric coupling is very convenient. When the microwave at the sum frequency is off, the coupling is also off. Vice versa, when the microwave is turned on, the coupling goes on. The reduced two-qubit rotating-frame Hamiltonian

$$H_{\text{rot}} = \sum_{j=1}^{2} \frac{\Omega_j}{2}(\cos\phi_j\sigma_x^j - \sin\phi_j\sigma_y^j) + \frac{\Omega_{12}}{4}(\sigma_x^1\sigma_x^2 - \sigma_y^1\sigma_y^2) \quad (3)$$

where Ω_j is the (resonant) microwave-induced single-qubit Rabi frequency of qubit j and ϕ_j is the microwave phase, offers full control and can in principle be set to zero by turning off all microwaves.

Figure 1 describes our experimental setup. By using the kinetic inductance of shared superconducting wires, we couple two qubits ($\Delta_1 < \Delta_2$) to a third qubit with a larger gap Δ_3. Direct coupling J_{12} is expected to be small. On the basis of a series of spectroscopic measurements (*24*), we know that we can rely on the accuracy of lithography and have very similar areas (within ~0.5% difference) of qubits 1 and 2. Therefore, we have $\Phi_1 \approx \Phi_2$ even with a single uniform flux bias, whereas Φ_3 is deliberately offset to have a finite Ω_{12}. We can write $\Phi_j = \Phi_3 + \Delta\Phi_j$, where $\Delta\Phi_j$ ($j = 1,2$) is a small offset. To manipulate the qubits, we apply microwaves of controllable duration via an on-chip microwave line. During the manipulation with the microwaves that are assumed to couple to all loops, we apply a small bias current (a few percent of critical current) through the readout superconducting quantum interference device (SQUID) to fine-tune the biases of both qubits 1 and 2 to be at the optimal point. Figure 2 illustrates the measured spectrum when the minima of the qubit transition frequencies are aligned. Qubits 1 and 2 have

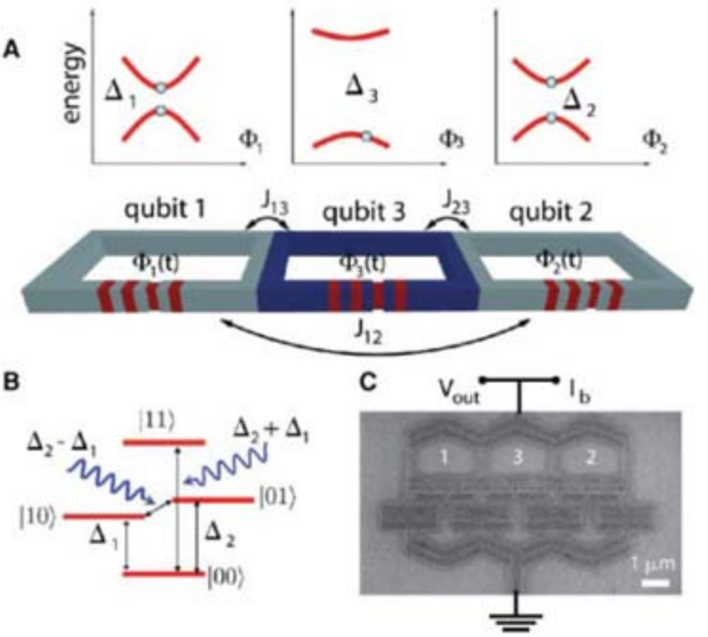

Fig. 1. Schematic of the experiment. (**A**) The system consists of three four-junction flux qubits. In each qubit, one junction is about 0.5 times smaller than others. Qubits 1 and 2 (with energies Δ_1 and Δ_2) are coupled via the kinetic inductance of the shared loop edge to the third. The middle qubit with large Δ_3 is biased slightly away from the half-flux quantum, whereas qubits 1 and 2 are optimally biased. The qubits are controlled via the fluxes $\Phi_j(t)$. (**B**) Level diagram of qubits 1 and 2. Two-qubit operations were carried out using microwaves at either the sum frequency $(\Delta_2 + \Delta_1)/h$ or the difference frequency $(\Delta_2 - \Delta_1)/h$. (**C**) Scanning electron micrograph of the sample fabricated by electron beam lithography and shadow evaporation of aluminum with 20-nm and 35-nm layer thicknesses. The junction oxidation was done with a mixture of Ar and O_2 (90%/10%) at 35 mTorr for 8 min. The qubits couple to a four-junction readout SQUID. When a pulse of the bias current I_b is applied to the SQUID, the probability of switching to the voltage state (monitored via V_{out}) depends on the state of the qubit system. The on-chip circuitry is similar to the single-qubit experiment reported in (*7*), along with a gold bias resistor and a shunt capacitor for the SQUID. The measurements were made at temperatures around 10 mK in a dilution refrigerator.

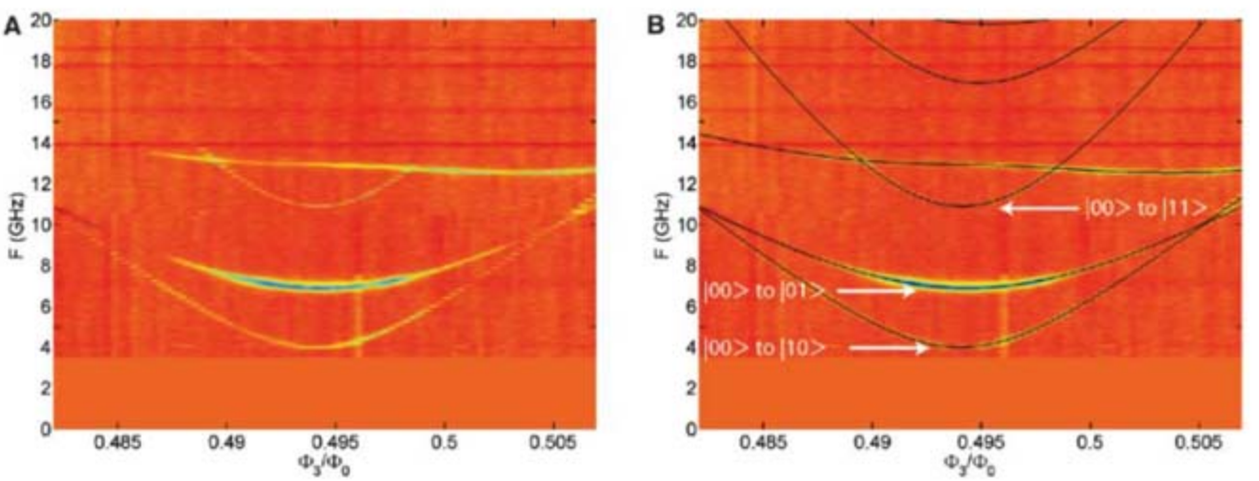

Fig. 2. Large-scale spectrum of the three-qubit system. (**A**) Measured spectrum as a function of flux and frequency (F) from 3.5 to 20 GHz. Blue means a low switching probability, whereas red means a high switching probability. The contrast is at best about 25%. (**B**) The black lines indicate the theoretical spectrum calculated from the three-qubit Hamiltonian. The parameters obtained from the least-squares fitting are $I_{p1}/h = 873 \pm 13$ GHz/Φ_0, $I_{p2}/h = 705 \pm 19$ GHz/Φ_0, $I_{p3}/h = 516 \pm 35$ GHz/Φ_0, $\Delta_1/h = 4.022 \pm 0.078$ GHz, $\Delta_2/h = 6.915 \pm 0.075$ GHz, $\Delta_3/h = 12.454 \pm 0.074$ GHz, $\Delta\Phi_1 = 5.58 \pm 0.11$ mΦ_0, $\Delta\Phi_2 = 5.31 \pm 0.22$ mΦ_0, $J_{12}/h = -0.003 \pm 0.066$ GHz, $J_{13}/h = 0.715 \pm 0.130$ GHz, and $J_{23}/h = 0.482 \pm 0.171$ GHz.

sufficiently different gaps as designed, and a sign of the desired sum-frequency transition is also visible.

To show that the coupling scheme is indeed tunable and coherent, we have to be able to set the rotating-frame Hamiltonian to zero as well as to drive the single-qubit transitions in time domain regardless of the input state (off). Also, we have to be able to drive, in a time domain, the two-qubit transition (on). Figure 3 shows measured examples of this at the combined optimal point of qubits 1 and 2. It is clear that a single-qubit transition frequency does not depend significantly on the state of the other. On the other hand, we can drive the sum-frequency transition as fast as $\Omega_{12}^{max}/h = 23.2$ MHz, which is obtained with the maximum power we can apply with the present microwave source and attenuation of our setup. The minimum time for a universal gate is given by half of the period; that is, 22 ns. A quantitative measure of the on/off ratio is obtained by comparing the maximal two-qubit oscillation frequency to the frequency at which unwanted coupling takes place. Using a Ramsey fringe measurement of the different transitions, we find that the Hamiltonian in the energy eigenbasis (and thus the logical rotating-wave Hamiltonian) has a spurious term $-(\kappa/2)\sigma_z^1\sigma_z^2$, with $\kappa/h = 1.23$ MHz, which is quite small compared to the single-qubit frequencies of about 4.000 GHz and 6.889 GHz. Because this term results in unwanted phase rotation at the frequency κ/h, we conclude that the demonstrated on/off ratio of our coupling scheme is $\Omega_{12}^{max}/\kappa \approx 19$. In addition to the high degree of tunability, the coherence properties are quite good, as characterized by the relaxation time T_1 and the Ramsey dephasing time T_2^{Ramsey}. Qubit 2 has about $T_1 = 1.0$ μs and $T_2^{Ramsey} = 0.8$ μs, whereas qubit 1 has $T_1 = 0.3$ μs and $T_2^{Ramsey} = 0.2$ μs. The lifetime of the state $|11\rangle$ is limited by qubit 1, and we get $T_2^{Ramsey} = 0.2$ μs for the sum-frequency transition. The reduced coherence time of qubit 1 is caused by a resonance close by. The fact that the resonant frequency of the two-qubit transition is reduced at large driving amplitudes can be understood from simulation as the effect of unwanted coupling of the microwave to qubits 1 and 2 (*6*, *25*), which is unavoidable in the present sample design.

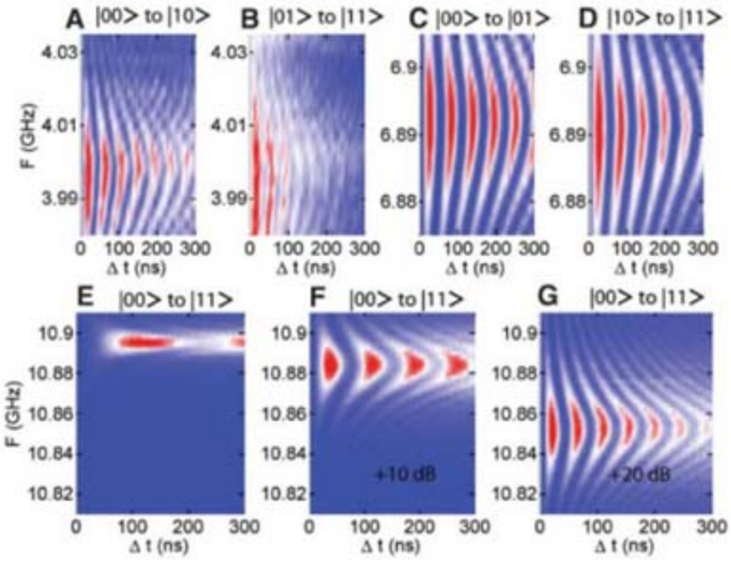

Fig. 3. Examples of single-qubit transitions and the two-qubit operation. (**A** to **D**) Single-qubit Rabi oscillations as a function of microwave frequency and time with different initial states. Δt, change in time. (A) and (B) illustrate the $|00\rangle \leftrightarrow |10\rangle$ and $|01\rangle \leftrightarrow |11\rangle$ transitions, respectively, both corresponding to qubit 1 but with different initial states of qubit 2. Similarly, (C) and (D) show the $|00\rangle \leftrightarrow |01\rangle$ and $|10\rangle \leftrightarrow |11\rangle$ transitions of qubit 2. We see that single-qubit resonant frequencies do not depend on the state of the other qubit by more than a couple of megahertz. (**E** to **G**) Examples of the coherent oscillations of the two-qubit $|00\rangle \leftrightarrow |11\rangle$ transitions with three different powers. The applied power increases from (E) in steps of 10 dB. The shift of the resonant frequency with higher power is qualitatively explained by simulation to be due to cross-coupling of the microwave to qubits 1 and 2. The visibility in the readout signal in the case of qubit 1 is about 12% and in the case of qubit 2 is about 30%. The sum-frequency transition has a visibility of about 40%. However, the readout is not designed to distinguish between the four possible outcomes. For qubit 1, the visibility and coherence time are reduced by the presence of an unidentified resonance around 4.05 GHz. This may be responsible for the change in Rabi frequency for qubit 1 for different initial states as well.

As further proof of the functioning of the scheme and the good coherence properties combined with a high on/off ratio, we have demonstrated a simple multipulse quantum protocol related to quantum coin tossing (*26*). One application of quantum coin tossing is to store classical information in a way that is immune to certain types of intervention and noise. For example, if one stores classical bits on eigenstates of σ_x, then these bits are immune to the action of a malicious quantum hacker who breaks into one's quantum computer and flips bits about the x axis: Because of the coding, the hacker may think he or she is flipping bits but is in fact only applying a global phase to each bit. Our protocol is complementary to this: We detect the presence of a classically benign hacker, who performs an operation whose sole effect is to multiply certain logical states by a phase. Such a phase is classically undetectable: The operation of the benign hacker on classical bits is to apply a global phase. Quantum-mechanically, however, one can detect this hacker by using superposition and entanglement. Figure 4 shows the performance of the protocol.

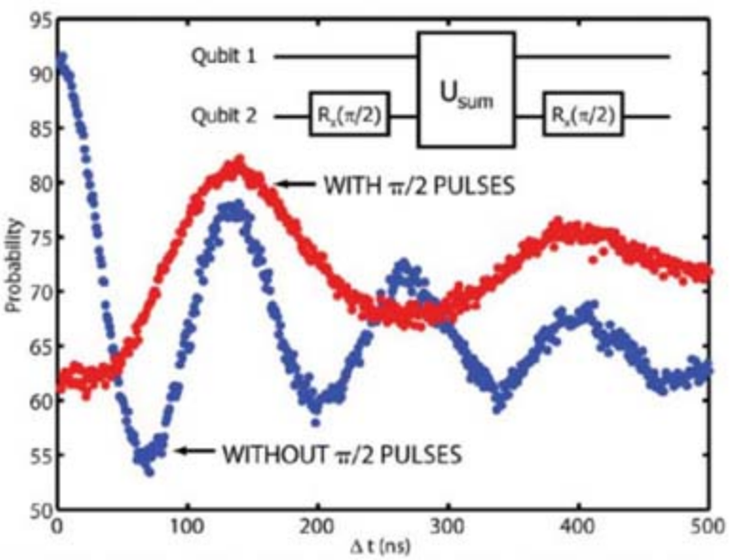

Fig. 4. Example of a simple quantum protocol. The inset at top illustrates the quantum circuit of the protocol for detecting the 4π periodicity of the sum-frequency gate U_{sum}. Here, $R_x(\pi/2)$ stands for the rotation of a qubit around the x axis. Applying the $\pi/2$ pulse on qubit 2 rather than qubit 1 is more practical with the present readout visibilities. The blue curve shows the regular two-qubit coherent oscillations. The red curve shows the result of the protocol with the extra $\pi/2$ pulses. Both measurements were carried out using the same microwave power for the sum frequency. The used microwave frequencies were 10.878 GHz for the sum-frequency transition and 6.889 GHz for qubit 2. The microwave sources were phase-locked together with the chopping pulse. The oscillation period is doubled in the case of the protocol, as expected.

Driving at the sum-frequency transition induces the unitary gate $U_{sum} = \exp[-i\theta/4(\sigma_x^1\sigma_x^2 - \sigma_y^1\sigma_y^2)]$, where θ is varied by the microwave duration. When $\theta = \pi$, the gate is equivalent to the double-CNOT (or the iSWAP) up to single-qubit rotations. Three applications of this gate suffice to generate any two-qubit gate when supplemented by single-qubit gates (*27*). At $\theta = 2\pi$, the gate is diagonal with the entries $(-1,1,1,-1)$, and if the input state is an eigenstate, the resulting oscillation thus has a 2π period. But the underlying period is actually 4π, which can be revealed

using superposition states. We do this by applying a $\pi/2$ rotation on qubit 2 before and after the application of U_{sum}. The experimental confirmation of this purely quantum-mechanical effect is shown in Fig. 4, where we see that the oscillation frequency is halved and phase-shifted when $\pi/2$ rotations are used. There is no analogy for this effect for a single qubit, because there the phase is just global and undetectable. The measurement result demonstrates the familiar quantum fact that you have to rotate by 4π, not 2π, to get back to where you started and is clear evidence of the entanglement inherent in the correlations between the qubits during their time evolution.

Our experiments demonstrate that the tunable coupling between flux qubits can be realized entirely using the application of microwaves at the coherence optimal point, which is very important for scalability. This indicates that parametric couplers are strong candidates as fundamental building blocks of gate-based quantum computers, but optimization of the scheme requires further study. We expect the coherence time of tunably coupled qubits to reach the same level as that of individual optimized qubits when, for example, independent readouts allowing for bias optimization (*6*, *7*) are combined with this coupling scheme in a future device.

References and Notes

1. Y. Nakamura, Yu. A. Pashkin, J. S. Tsai, *Nature* **398**, 786 (1999).
2. J. M. Martinis, S. Nam, J. Aumentado, C. Urbina, *Phys. Rev. Lett.* **89**, 117901 (2002).
3. I. Chiorescu, Y. Nakamura, C. J. P. M. Harmans, J. E. Mooij, *Science* **299**, 1869 (2003).
4. D. Vion *et al.*, *Science* **296**, 886 (2002).
5. A. Wallraff *et al.*, *Phys. Rev. Lett.* **95**, 060501 (2005).
6. P. Bertet *et al.*, *Phys. Rev. Lett.* **95**, 257002 (2005).
7. F. Yoshihara, K. Harrabi, A. O. Niskanen, Y. Nakamura, J. S. Tsai, *Phys. Rev. Lett.* **97**, 167001 (2006).
8. D. G. Cory *et al.*, *Fortschr. Phys.* **48**, 875 (2000).
9. Yu. A. Pashkin *et al.*, *Nature* **421**, 823 (2003).
10. T. Yamamoto, Yu. A. Pashkin, O. Astafiev, Y. Nakamura, J. S. Tsai, *Nature* **425**, 941 (2003).
11. A. J. Berkley *et al.*, *Science* **300**, 1548 (2003).
12. J. B. Majer, F. G. Paauw, A. C. J. ter Haar, C. J. P. M. Harmans, J. E. Mooij, *Phys. Rev. Lett.* **94**, 090501 (2005).
13. R. McDermott *et al.*, *Science* **307**, 1299 (2005).
14. M. Steffen *et al.*, *Science* **313**, 1423 (2006).
15. M. Grajcar *et al.*, *Phys. Rev. Lett.* **96**, 047006 (2006).
16. S. H. W. van der Ploeg *et al.*, *Phys. Rev. Lett.* **98**, 057004 (2007).
17. R. Harris *et al.*, preprint available at http://arxiv.org/abs/cond-mat/0608253.
18. T. Hime *et al.*, *Science* **314**, 1427 (2006).
19. J. E. Mooij *et al.*, *Science* **285**, 1036 (1999).
20. C. Rigetti, A. Blais, M. Devoret, *Phys. Rev. Lett.* **94**, 240502 (2005).
21. P. Bertet, C. J. P. M. Harmans, J. E. Mooij, *Phys. Rev. B* **73**, 064512 (2006).
22. A. O. Niskanen, Y. Nakamura, J. S. Tsai, *Phys. Rev. B* **73**, 094506 (2006).
23. M. Grajcar, Y. X. Liu, F. Nori, A. M. Zagoskin, *Phys. Rev. B* **74**, 172505 (2006).
24. A. O. Niskanen, K. Harrabi, F. Yoshihara, Y. Nakamura, J. S. Tsai, *Phys. Rev. B* **74**, 220503 (2006).
25. D. I. Schuster *et al.*, *Phys. Rev. Lett.* **94**, 123602 (2005).
26. D. A. Meyer, *Phys. Rev. Lett.* **82**, 1052 (1999).
27. J. Zhang, J. Vala, S. Sastry, K. B. Whaley, *Phys. Rev. A* **69**, 042309 (2004).

28. We thank A. Maassen van den Brink, A. Zagoskin, A. Smirnov, and S. Ashhab for discussions.

14 February 2007; accepted 22 March 2007
10.1126/science.1141324

Beating the Standard Quantum Limit with Four-Entangled Photons

Tomohisa Nagata,[1] Ryo Okamoto,[1,2] Jeremy L. O'Brien,[3,4] Keiji Sasaki,[1] Shigeki Takeuchi[1,2]*

Precision measurements are important across all fields of science. In particular, optical phase measurements can be used to measure distance, position, displacement, acceleration, and optical path length. Quantum entanglement enables higher precision than would otherwise be possible. We demonstrated an optical phase measurement with an entangled four-photon interference visibility greater than the threshold to beat the standard quantum limit—the limit attainable without entanglement. These results open the way for new high-precision measurement applications.

Quantum metrology involves using quantum mechanics to realize more precise measurements than can be achieved with classical methods (*1*). The canonical example uses entanglement of N particles to measure a phase with a precision $\Delta\phi = 1/N$—the Heisenberg limit. Such a measurement outperforms the $\Delta\phi = 1/\sqrt{N}$ precision limit possible with N unentangled particles—the standard quantum limit (SQL). Progress has been made with trapped ions (*2*–*4*) and atoms (*5*, *6*), while high-precision optical phase measurements have many important applications, including microscopy, gravity-wave detection, measurements of material properties, and medical and biological sensing. Although a reduced de Broglie wavelength (*7*) has been reported for three (*8*), four (*9*, *10*), and even six (*11*) photons, the SQL has been beaten only with two photons (*12*–*16*).

We demonstrated an entangled four-photon phase measurement with a visibility that exceeds the threshold to beat the SQL. We used an ultrastable displaced-Sagnac implementation of a scheme with a high intrinsic efficiency to achieve a four-photon interference visibility of 91%. We also demonstrated that measuring a reduced de Broglie wavelength does not mean beating the SQL, in another experiment that shows high-visibility multiphoton fringes, but cannot beat the SQL. The high-precision multiphoton quantum interference demonstrated here is key, not only to quantum metrology and quantum lithography (*14*, *17*, *18*), but also to other optical quantum technologies.

The Heisenberg limit and the SQL can be illustrated with reference to an interferometer (Fig. 1, inset) (*19*–*23*). We represent a single photon in mode a and no photons in mode b by the quantum state $|10\rangle_{ab}$. After the first beam splitter, this photon is in a quantum mechanical superposition of being in both paths of the interferometer: $(|10\rangle_{cd} + |01\rangle_{cd})/\sqrt{2}$. This superposition evolves to the state $(|10\rangle_{cd} + e^{i\phi}|01\rangle_{cd})/\sqrt{2}$ after the ϕ phase shift in mode d. After recombining at the second beam splitter, the probability of detecting the single photon in mode e is $P_e = (1 - \cos\phi)/2$, which can be used to estimate ϕ. If we repeat this experiment N times, then the uncertainty in this estimate is $\Delta\phi = 1/\sqrt{N}$—the SQL. If instead we were able to prepare the maximally entangled N-photon state $(|N0\rangle_{cd} + |0N\rangle_{cd})/\sqrt{2}$ inside the interferometer, this state would evolve to $(|N0\rangle_{cd} + e^{iN\phi}|0N\rangle_{cd})/\sqrt{2}$ after the ϕ phase shift. From this state we could estimate the phase with an uncertainty $\Delta\phi = 1/N$—the Heisenberg limit—an improvement of $1/\sqrt{N}$ over the SQL. Beating the SQL is known as phase supersensitivity (*8*, *11*).

The $N\phi$ dependence of the phase of the maximally entangled state $(|N0\rangle_{cd} + |0N\rangle_{cd})/\sqrt{2}$ is a manifestation of the N-photon de Broglie wavelength λ/N. This dependence can give rise to an interference oscillation N times faster than that of single photons—phase superresolution (*8*, *11*). Observation of this reduced de Broglie wavelength has sometimes been interpreted in the context of beating the SQL. However, it has been shown recently that high-visibility (*24*) λ/N resolution can be observed with a purely classical system (*11*). This demonstrates that phase superresolution by itself does not guarantee a quantum-mechanical advantage. Rather, phase supersensitivity, or beating the SQL, is the most important criterion.

[1]Research Institute for Electronic Science, Hokkaido University, Sapporo 060-0812, Japan. [2]Japan Science and Technology Agency, Honcho, Kawaguchi-shi, Saitama, 332-0012, Japan. [3]Department of Electrical and Electronic Engineering, University of Bristol, Merchant Venturers Building, Woodland Road, Bristol BS8 1UB, UK. [4]H. H. Wills Physics Laboratory, University of Bristol, Tyndall Avenue, Bristol BS8 1TL, UK.

*To whom correspondence should be addressed. E-mail: takeuchi@es.hokudai.ac.jp

If we put a single photon in each input of the interferometer in Fig. 1(inset), $|11\rangle_{ab}$, the state after the first beam splitter is $(|20\rangle_{cd} + |02\rangle_{cd})/\sqrt{2}$; quantum interference of the two-photon amplitudes cancels the $|11\rangle_{cd}$ term—the Hong-Ou-Mandel (HOM) effect (*25*). This state evolves to $(|20\rangle_{cd} + e^{i2\phi}|02\rangle_{cd})/\sqrt{2}$. The probability of detecting two photons in the modes *e* and *f*, after the second beam splitter, is then $P_{ef} = (1 - \cos 2\phi)/2$, which shows both phase superresolution and phase supersensitivity.

Unfortunately, this behavior does not generalize to larger photon number: If we input $|22\rangle_{ab}$, the state after the first beam splitter is:

$$\sqrt{3/4}\left(|40\rangle_{cd} + |04\rangle_{cd}\right)/\sqrt{2} + 1/\sqrt{4}|22\rangle_{cd} \quad (1)$$

where quantum interference cancels the $|31\rangle_{cd}$ and $|13\rangle_{cd}$ terms (*26*, *27*), but the unwanted $|22\rangle_{cd}$ term remains. However, after the second beam splitter, only the $|40\rangle_{cd}$ and $|04\rangle_{cd}$ terms give rise to $|31\rangle_{ef}$ and $|13\rangle_{ef}$ terms. This is the basis for our experimental scheme (*28*): The probability of detecting three photons in output *e* and 1 in *f* is $P_{3ef} = 3/8\ (1 - \cos 4\phi)/2$, which shows phase superresolution.

Using state (1) rather than $(|40\rangle_{cd} + |04\rangle_{cd})/\sqrt{2}$ means that our method, like those used previously, can only use a fraction of the initial photons in the $|22\rangle_{ab}$ state, given by the intrinsic efficiency η_i: $P = \eta_i(1 - \cos N\phi)/2$. To beat the SQL we therefore need to obtain a precision better than $\sqrt{\eta_i/N}$. Because the precision of *N*-photon interference with a visibility V (≤ 1) is $1/VN$, the SQL is beaten for experimentally achieved visibilities above the threshold $V_{th} = 1/\sqrt{\eta_i N}$ [compare to (*11*)]. In our case ($\eta_i = 3/8$, $N = 4$), $V_{th} = \sqrt{2/3} \approx 81.6\%$. Even though most of the photons pass through the interferometer without leading to a 3*ef* detection event, this scheme can still beat the SQL, because $V_{th} < 100\%$. Note that a scheme with $V_{th} > 100\%$ can never beat the SQL even with unity-efficiency photon sources and detectors.

The existence of V_{th} highlights the need for achieving high-visibility multiphoton interference fringes. Our scheme requires two quantum-interference and two classical-interference conditions for multiphoton states to be met simultaneously, in a highly time-stable configuration. Therefore, we have designed the intrinsically stable displaced-Sagnac experimental architecture shown schematically in Fig. 1.

To test the performance of our four-photon interferometer, we used pulsed spontaneous parametric down-conversion to produce the four-photon input state (see legend to Fig. 1). This source produced not only $|22\rangle$ (2.8×10^{-4} per pulse), but also $|11\rangle_{ab}$ (1.7×10^{-2} per pulse) states. However, $|11\rangle$ states do not contribute to the four-photon coincidence detection. The $|33\rangle$ component (4.7×10^{-6}) is two orders of magnitude smaller than $|22\rangle$.

The above discussion requires that the four-photon input state be $|22\rangle_{ab}$—four photons in two spatial and one temporal mode—and not $|1111\rangle_{a^\dagger a^{\prime\dagger} b^\dagger b^{\prime\dagger}}$—four photons in two spatial and two temporal modes—i.e., the two photons in each mode must be indistinguishable (*16*, *29*–*31*). We have developed a technique for differentiating these two four-photon states using a multiphoton quantum interference generalization of the HOM effect: If the state $|22\rangle_{ab}$ is input onto a 50:50 beam splitter, the probability of detecting two photons in each output is ¼; whereas for $|1111\rangle_{a^\dagger a^{\prime\dagger} b^\dagger b^{\prime\dagger}}$ the probability is ½. If there is no quantum interference, the probability is $3/8$ for both four-photon input states. As we scan the relative delay Δt between the arrival time of the photons, we move from a regime where $|\Delta t| >> 0$, and there is no quantum interference, through $\Delta t = 0$, where quantum interference occurs. From the observed data (Fig. 2), we find that the ratio of the coincidence rate at $\Delta t = 0$ to that at $|\Delta t| >> 0$ is $\approx 3/5$, consistent with the ratio of ¼ to $3/8$, indicating that our source generates almost purely $|22\rangle_{ab}$ (supporting online text).

Figure 3 shows the key experimental results of this paper. First, we confirmed the high-visibility classical operation of our interferometer by inputting single photons in mode *a* $|10\rangle_{ab}$ and

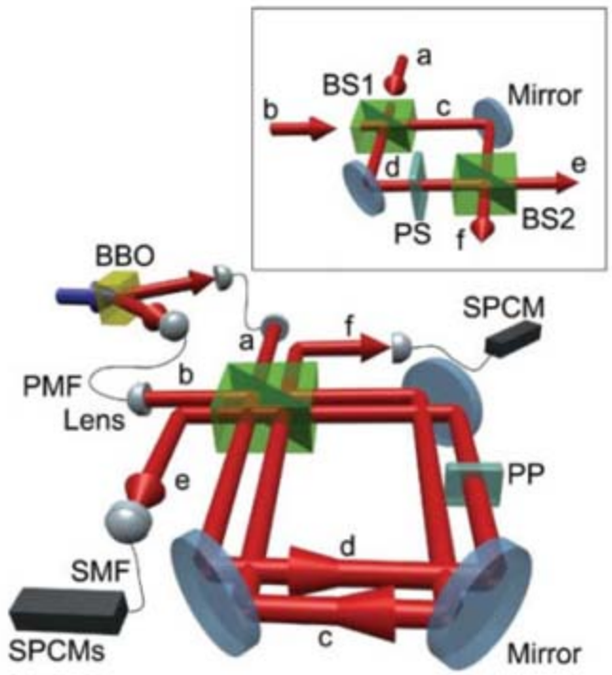

Fig. 1. An optical interferometer for beating the SQL. (**Inset**) A schematic of a Mach-Zehnder (MZ) interferometer consisting of two 50:50 beam splitters (BS1 and BS2). Photons are input in modes *a* and/or *b*, and detected in modes *e* and/or *f*, after a phase shift (PS) is applied to mode *d*. (Main panel) A schematic of the intrinsically stable displaced-Sagnac architecture used to ensure that the optical path lengths in modes *c* and *d* are subwavelength (nm) stable. A frequency-doubled 780-nm fs-pulsed laser (repetition interval 13 ns) pumps a type I phase-matched beta barium borate (BBO) crystal to generate the state $|22\rangle_{ab}$ via spontaneous parametric down-conversion. Interference filters (not shown) with a 4-nm bandwidth were used. The photons are guided via polarization-maintaining fibers (PMFs) to the interferometer, which has the same function as the MZ interferometer in the inset. A variable phase shift in mode *d* is realized by changing the angle of the phase plate (PP) in the interferometer. Photons are collected in single-mode fibers (SMFs) at the output modes and detected with a single-photon counting module (SPCM, detection efficiency 60% at 780 nm) in mode *f* and three cascaded SPCMs in mode *e*.

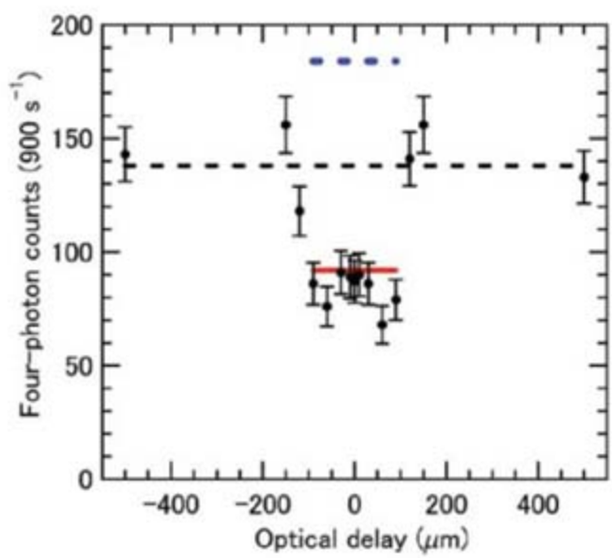

Fig. 2. Multiphoton interference at a 50:50 beam splitter demonstrating four-photon indistinguishability. The coincidence count rates of detecting two photons in each output of the beam splitter are recorded as a function of the optical path delay. The ratio of four-photon coincidence counts at delay time $\Delta t = 0$ to that at $|\Delta t| >> 0$ is important in order to distinguish the state $|22\rangle_{ab}$ from $|1111\rangle_{a^\dagger a^{\prime\dagger} b^\dagger b^{\prime\dagger}}$ (see text and supporting online text). The theoretically expected coincidence rate for $|22\rangle_{ab}$ at $\Delta t \cong 0$ (red line, lower) based on the average count rates at $|\Delta t| >> 0$ (black dashed line, middle) agrees well with experimental data (dots). This result indicates that our source almost purely generates $|22\rangle_{ab}$. The dashed blue line (upper) is the theoretically expected coincident rate for $|1111\rangle_{a^\dagger a^{\prime\dagger} b^\dagger b^{\prime\dagger}}$. Error bars in Figs. 2 to 4 show $\pm\sqrt{\text{counts}}$.

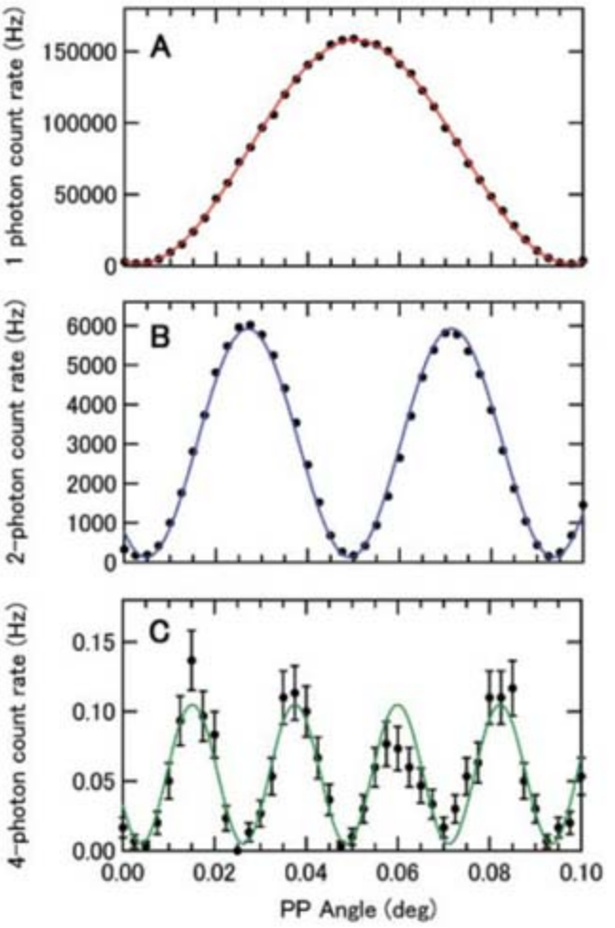

Fig. 3. Beating the SQL with four-entangled photons. (**A**) Single-photon count rate in mode e as a function of phase plate (PP) angle with single-photon input $|10\rangle_{ab}$. (**B**) Two-photon count rate in modes e and f for input state $|11\rangle_{ab}$. (**C**) Four-photon count rate of three photons in mode e and one photon in mode f for the input state $|22\rangle_{ab}$. Accumulation times for one data point were (A) 1s, (B) 300s, and (C) 300s.

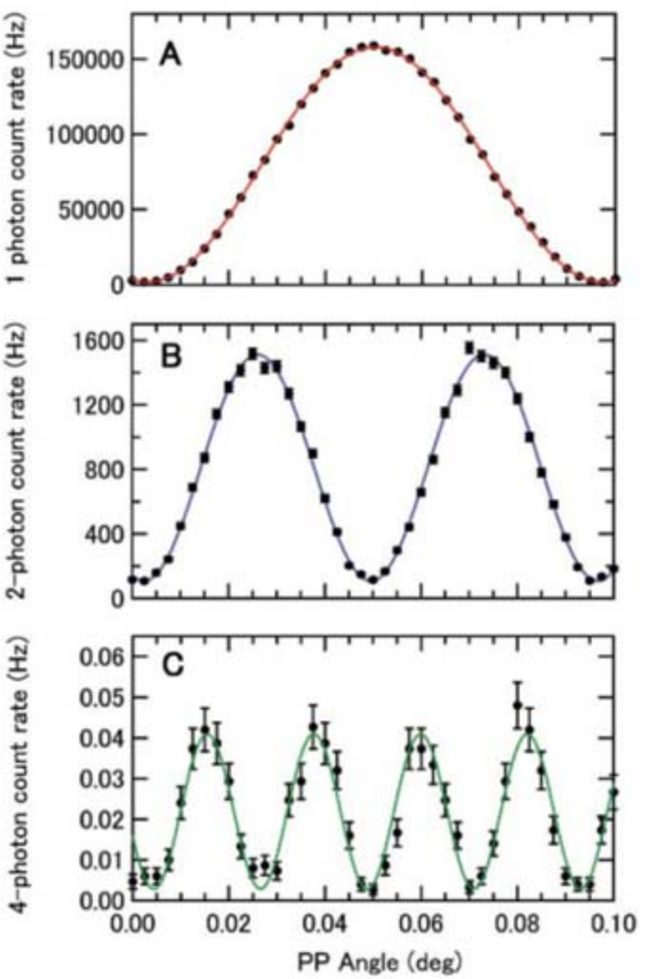

Fig. 4. Demonstration of reduced de Broglie wavelength without beating the SQL. We prepare distinguishable photon inputs by changing the arrival times of the photons at the input to the interferometer and/or changing the detection window. (**A**) A single-photon (classical) interference fringe provides a reference period. (**B**) Two photons are input into modes a and b at times t and t', where $\delta\tau = t' - t$ is larger than the coherence time of the photons: $|11\rangle_{a'b'}$. Two-photon count rates in mode e are shown with a gate timing window larger than $\delta\tau$. (**C**) Four-photon coincidence events showing phase superresolution with two independent $|11\rangle_{ab}$ inputs: $|1111\rangle_{a'a''b'b''}$. We collected the $|11\rangle_{ef}$ coincidence events that occurred within 200 ns (15 pulses) after a $|20\rangle_{ef}$ event was detected for an accumulation time of 300 s. The count rate per pulse was calculated by including the reduced detection efficiency of the setup. Accumulation times for one data point for (A) and (B) were 1 s.

detecting the rate of single photons measured in mode e; we observed an interference fringe with high visibility ($98 \pm 0.5\%$) as a function of the optical phase in mode d (Fig. 3A). Next, we input pairs of photons $|11\rangle_{ab}$ and measured the rate of two photons detected in modes e and f; again, we observed a high-visibility fringe ($96 \pm 1\%$), but with half the period of that observed for single photons (Fig. 3B). This visibility is greater than the threshold to beat the SQL ($V_{th} = 1/\sqrt{2}$). Finally, we input the state $|22\rangle_{ab}$ and observed the rate of detecting three photons in mode e and one photon in mode f, as described above; again, we observed a high-visibility fringe ($V = 91 \pm 6\%$), but with a period one-fourth that observed for single photons, demonstrating a four-photon de Broglie wavelength (Fig. 3C). More important, the fringe visibility is greater than the threshold $V_{th} = \sqrt{2/3} \approx 81.6\%$ to beat the SQL.

The distinction between a reduced de Broglie wavelength (phase superresolution) and beating the SQL (phase supersensitivity) has been described above. An important illustration of this distinction is provided by comparing Figs. 3 and 4; Fig. 4 shows a two-photon de Broglie wavelength $\lambda/2$ (B) and a four-photon de Broglie wavelength $\lambda/4$ (C), via high-visibility ($V = 87 \pm 1\%$ and $V = 87 \pm 5\%$, respectively) interference fringes, but cannot demonstrate phase measurement below the SQL. In this case, we have used exactly the same experimental setup as before, but have intentionally used distinguishable photon inputs (see the legend to Fig. 4). In Fig. 4C, we use the input state $|1111\rangle_{a'a''b'b''}$, described above. In this case, the probability of detecting three photons in mode e and one photon in mode f is given by $P_{3ef} = {}^1/_8\,(1 - \cos 4\phi)/2$, which still shows a 4ϕ dependence on phase. However, because the intrinsic efficiency is $\eta_i = {}^1/_8$, such a scheme can never show a phase sensitivity below the SQL: $V_{th} = \sqrt{2}$. For Fig. 4B, the input is $|11\rangle_{a'b'}$ and the probability of detecting two photons in mode e is $P_{2e} = {}^1/_4(1 - \cos 2\phi)/2$, which shows a 2ϕ phase dependence, but again such a scheme cannot beat the SQL because $V_{th} = \sqrt{2}$. Note that the reduced count rates in Fig. 4, B and C, relative to Fig. 3, B and C, correspond to the reduced η_i's.

Our results point toward the ultimate sensitivity for optical measurements. To test the performance of the four-photon interferometer, we used a relatively low-efficiency source and modest-efficiency detectors, which means that many more photons pass through the interferometer than lead to a four-photon detection event. For applications (such as biological sensing) in which photon flux is important, higher-efficiency sources might be realized with single-photon sources and a HOM interferometer as a heralded two-photon source, and high-efficiency number–resolving visible-light photon counters (*32*) would markedly improve detection efficiency. Future possible applications of ultrahigh-precision phase measurements range from cosmology to medicine.

References and Notes

1. V. Giovannetti, S. Lloyd, L. Maccone, *Science* **306**, 1330 (2004).
2. V. Meyer *et al.*, *Phys. Rev. Lett.* **86**, 5870 (2001).
3. D. Leibfried *et al.*, *Nature* **438**, 639 (2005).
4. C. F. Roos, M. Chwalla, K. Kim, M. Riebe, R. Blatt, *Nature* **443**, 316 (2006).
5. A. Widera *et al.*, *Phys. Rev. Lett.* **92**, 160406 (2004).
6. J. M. Geremia, J. K. Stockton, H. Mabuchi, *Science* **304**, 270 (2004).
7. J. Jacobson, G. Björk, I. Chuang, Y. Yamamoto, *Phys. Rev. Lett.* **74**, 4835 (1995).
8. M. W. Mitchell, J. S. Lundeen, A. M. Steinberg, *Nature* **429**, 161 (2004).
9. P. Walther *et al.*, *Nature* **429**, 158 (2004).
10. F. W. Sun, B. H. Liu, Y. F. Huang, Z. Y. Ou, G. C. Guo, quant-ph/0512212 (2005).
11. K. J. Resch *et al.*, quant-ph/0511214 (2005).
12. J. G. Rarity *et al.*, *Phys. Rev. Lett.* **65**, 1348 (1990).
13. A. Kuzmich, L. Mandel, *Quant. Semiclass. Opt.* **10**, 493 (1998).
14. E. J. S. Fonseca, C. H. Monken, S. Pádua, *Phys. Rev. Lett.* **82**, 2868 (1999).
15. K. Edamatsu, R. Shimizu, T. Itoh, *Phys. Rev. Lett.* **89**, 213601 (2002).
16. H. S. Eisenberg, J. F. Hodelin, G. Khoury, D. Bouwmeester, *Phys. Rev. Lett.* **94**, 090502 (2005).
17. A. N. Boto *et al.*, *Phys. Rev. Lett.* **85**, 2733 (2000).
18. M. D'Angelo, M. V. Chekhova, Y. Shih, *Phys. Rev. Lett.* **87**, 013602 (2001).
19. M. J. Holland, K. Burnett, *Phys. Rev. Lett.* **71**, 1355 (1993).
20. J. J. Bollinger, W. M. Itano, D. J. Wineland, D. J. Heinzen, *Phys. Rev. A.* **54**, R4649 (1996).
21. Z. Y. Ou, *Phys. Rev. A.* **55**, 2598 (1997).
22. J. P. Dowling, *Phys. Rev. A.* **57**, 4736 (1998).
23. R. A. Campos, C. C. Gerry, A. Benmoussa, *Phys. Rev. A.* **68**, 023810 (2003).
24. The visibility $V = (max - min)/(max + min)$, where *max* and *min* are the extreme values of the sinusoidal multiphoton interference fringe; $0 \leq V \leq 1$.
25. C. K. Hong, Z. Y. Ou, L. Mandel, *Phys. Rev. Lett.* **59**, 2044 (1987).
26. R. A. Campos, B. E. A. Saleh, M. C. Teich, *Phys. Rev. A.* **40**, 1371 (1989).
27. Z. Y. Ou, J.-K. Rhee, L. J. Wang, *Phys. Rev. Lett.* **83**, 959 (1999).
28. O. Steuernagel, *Phys. Rev. A.* **65**, 033820 (2002).
29. K. Tsujino, H. F. Hofmann, S. Takeuchi, K. Sasaki, *Phys. Rev. Lett.* **92**, 153602 (2004).
30. Z. Y. Ou, *Phys. Rev. A.* **72**, 053814 (2005).
31. G. Y. Xiang *et al.*, *Phys. Rev. Lett.* **97**, 023604 (2006).
32. S. Takeuchi, J. Kim, Y. Yamamoto, H. H. Hogue, *Appl. Phys. Lett.* **74**, 1063 (1999).

33. We thank H. F. Hofmann, K. J. Pregnell, G. J. Pryde, J. G. Rarity, K. J. Resch, and A. G. White for helpful discussions. This work was supported by the Japan Science and Technology Agency (JST), Ministry of Internal affairs and Communication (MIC), Japan Society for the Promotion of Science (JSPS), 21st Century Centers of Excellence program, Special Coordination Funds for Promoting Science and Technology, and the Daiwa Anglo-Japanese Foundation. J.L.O'B. was supported by an Australian Academy of Science–JSPS Fellowship.

Supporting Online Material

www.sciencemag.org/cgi/content/full/316/5825/726/DC1
SOM Text

27 November 2006; accepted 18 January 2007
10.1126/science.1138007

Germanium Nanowire Growth Below the Eutectic Temperature

S. Kodambaka,* J. Tersoff, M. C. Reuter, F. M. Ross†

Nanowires are conventionally assumed to grow via the vapor-liquid-solid process, in which material from the vapor is incorporated into the growing nanowire via a liquid catalyst, commonly a low–melting point eutectic alloy. However, nanowires have been observed to grow below the eutectic temperature, and the state of the catalyst remains controversial. Using in situ microscopy, we showed that, for the classic Ge/Au system, nanowire growth can occur below the eutectic temperature with either liquid or solid catalysts at the same temperature. We found, unexpectedly, that the catalyst state depends on the growth pressure and thermal history. We suggest that these phenomena may be due to kinetic enrichment of the eutectic alloy composition and expect these results to be relevant for other nanowire systems.

Self-assembled semiconducting nanowires are promising candidates for applications in nanoelectronics, optoelectronics, and sensors (*1*–*4*). Progress in designing more complex structures, such as branched or compositionally modulated wires, requires a clear understanding of nanowire growth mechanisms. Nanowires are conventionally assumed to grow via the vapor-liquid-solid (VLS) process (*5*), in which material from the vapor is incorporated via a liquid catalyst, commonly a low–melting point eutectic alloy. Yet, in many important semiconductor/catalyst systems [e.g., Si/Al (*6*), Si/Cu (*7*), Si/Ti (*8*), Ge/Au (*9*–*14*), GaAs/Au (*15*–*18*), and InAs/Au (*15*, *19*, *20*)], nanowire growth can occur below the bulk eutectic temperature T_e. The state of the catalyst remains controversial, but it is important because it is expected to influence growth kinetics, orientation, and morphology. Most importantly, because interface formation in heterostructure nanowires depends on diffusive processes through the catalyst, the catalyst state is also expected to determine interface sharpness. Post-growth analyses have yielded contradictory conclusions regarding the catalyst state; speculations include the existence of a liquid catalyst below T_e (*17*) stabilized by nanoscale size effects (*20*) and growth via a vapor-solid-solid (VSS) mechanism (*8*, *9*) with a solid catalyst. Using in situ microscopy, we show for the classic Ge/Au system that catalysts can be either liquid or solid below T_e, depending on thermal history. Moreover, nanowires grow in both cases (i.e., both VLS and VSS processes occur), although at different rates. Unexpectedly, the catalyst state depends on Ge_2H_6 pressure as well as temperature: The supersaturation of Ge in the alloy caused by the growth process appears to be essential in stabilizing the liquid below T_e.

Ge wire growth experiments were carried out in a multichamber ultrahigh vacuum system (base pressure, 2×10^{-10} Torr) based around a transmission electron microscope (TEM) with in situ physical and chemical vapor deposition facilities (*21*). Si(111) substrates were loaded into the TEM and cleaned by heating resistively to 1250°C. After cooling, a 2- to 3-nm-thick Au film was evaporated onto the polished surface. The sample was vacuum annealed at ~400°C for 5 min, allowing the Au film to agglomerate, and wire growth was initiated by cooling to the growth temperature and leaking in a gas mixture composed of 20% Ge_2H_6 and 80% He. The temperature versus heating current curve

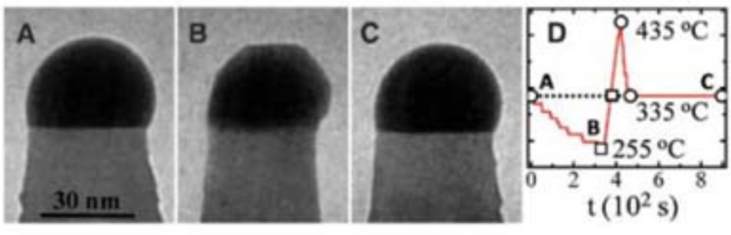

Fig. 1. (**A** to **C**) Bright-field TEM images showing the solid-to-liquid and liquid-to-solid transitions in a Au-Ge catalyst particle at the tip of a Ge wire during cooling and heating, acquired at times $t = 0$ s (A), 328 s (B), and 897 s (C), respectively. (**D**) The sample temperature versus time and catalyst state (open circle, liquid; open square, solid) are shown. The letters "A," "B," and "C" refer to the images in the respective panels in the figure. We initiated wire growth by first heating to above T_e (361°C) and then cooling to T_0 ~335°C while maintaining a constant digermane pressure of 1.6×10^{-6} Torr. After a period of growth, the sample temperature is reduced to 255°C, at which point the catalyst solidifies (B). On heating, the catalyst does not melt until 435°C, after which the temperature is returned to 335°C (C).

IBM T. J. Watson Research Center, Yorktown Heights, NY 10598, USA.

*Present address: Materials Science Department, University of California Los Angeles, Los Angeles, CA 90024, USA.
†To whom correspondence should be addressed. E-mail: fmross@us.ibm.com

was calibrated post-growth for each specimen, with the use of both pyrometry and a thermocouple mounted on the specimen's back surface. This procedure allows us to estimate the substrate temperature T_0 to within 50 K, and relative changes in temperature in a single experiment can be determined more accurately.

In the pressure range accessible in our in situ system (Ge_2H_6 pressures between 10^{-7} and 10^{-5} Torr), we typically observe sustained growth of ⟨111⟩-oriented Ge wires at temperatures in the 250° to 400°C range. Under these conditions, most wires grow perpendicular to the substrate and are imaged with the electron beam perpendicular to the wire axis (*21*). Bright-field and dark-field imaging show that the wires are epitaxial, single-crystal, and are bounded by smooth sidewalls. Furthermore, by the acquisition of video images at 30 frames per second, growth kinetics for individual wires can be measured.

Figure 1 shows a series of bright-field images of a single Ge nanowire during growth at constant Ge_2H_6 pressure as the temperature is varied. The image in Fig. 1A, at T_0 = 335°C, is typical of wire growth by the VLS process. The tip is composed of a Au-Ge eutectic droplet with a smoothly curved surface. Upon cooling to a lower temperature, in this case ~106 K below T_e = 361°C, we observe abrupt solidification of the droplet, as indicated both by the facetted surface (Fig. 1B) and by the dark-field contrast (fig. S1). We also see an abrupt increase (within a single video frame) in the length of the wire, indicating that Ge is coming out of solution as the droplet solidifies, as expected. On increasing the temperature again to the original value T_0, we find that the solid particle does not transform back into a liquid. Reestablishing the liquid phase requires a temperature well above T_0 (Fig. 1C). However, once the liquid has re-formed, upon cooling to T_0, we return to VLS growth with the same growth rate as initially observed. This hysteresis in the solid-liquid phase transformation is seen in all our Ge growth experiments and for wires with a range of diameters (20 to 140 nm).

Hysteresis with temperature is normal for first-order phase transitions and is likely to be exacerbated at the nanoscale (*22*, *23*). Thus, it is not surprising that hysteresis is so clearly visible in these experiments. However, close inspection of video images such as those in Fig. 1 shows that the wires continue to grow even after the catalyst particle has solidified.

This VSS growth process is illustrated in Fig. 2. Figure 2A shows a Ge wire at three successive times during VLS growth at 340°C and 4.8×10^{-6} Torr Ge_2H_6. In this experiment, we initiated wire growth ~78 min before acquiring the first image at time t = 0. After cooling the specimen to solidify the catalysts and then reheating to 340°C, all at constant Ge_2H_6 pressure, we observed wire growth to continue with solid catalysts (Fig. 2B). Measurements made on several wires show that VSS growth is 10 to 100 times slower than VLS growth at the same Ge_2H_6 pressure and temperature, presumably as a result of weaker surface reactivity and/or lower diffusivity through the solid. We can obtain prolonged wire growth by either VLS or VSS mechanisms at identical temperatures and Ge_2H_6 pressures, depending (via hysteresis) on the thermal history of the sample. We have actually seen VLS and VSS growth occurring simultaneously on neighboring wires in some instances. All the wires, irrespective of the growth mode, are crystalline, and the only obvious difference between the growth modes is that the VSS process yields more tapered wires owing to their relatively slower growth rates. This demonstration of dual growth modes may be relevant to the controversy regarding the role of VSS and VLS growth in other systems (*6*, *16*–*20*).

We also find that Ge_2H_6 pressure can be as important as temperature in controlling the growth mode. Indeed, a substantial Ge_2H_6 pressure appears to be essential for stabilizing the liquid state below T_e. Whenever the Ge_2H_6 pressure is reduced during VLS growth, we find that the catalyst droplets solidify. The fact that the droplets can solidify confirms that the temperature is definitely below T_e, independent of any uncertainties in temperature calibration.

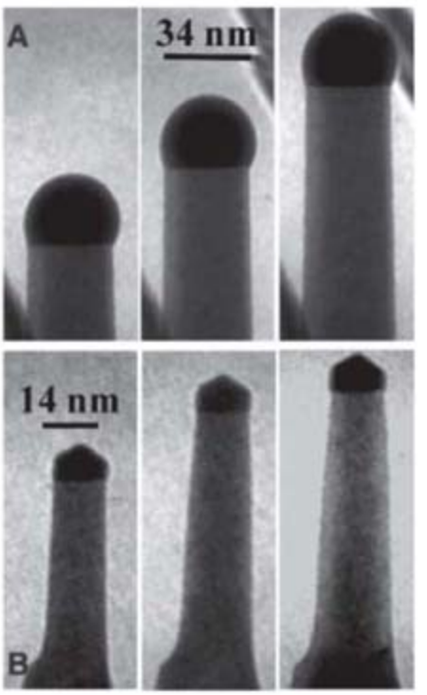

Fig. 2. (**A**) Series of images of a single Ge wire acquired at times t = 0, 309, and 618 s (from left to right, respectively) during growth by the VLS mechanism at 340°C and 4.6×10^{-6} Torr Ge_2H_6. The background features act as markers, showing a growth rate of 9.9×10^{-2} nm/s. (**B**) Another image series for a second wire growing at the same temperature and pressure but with a solid catalyst at t = 0, 1340, and 1824 s (from left to right, respectively). The growth rate for this VSS mode is 1.3×10^{-2} nm/s.

The role of Ge_2H_6 pressure (i.e., growth rate) in the nanowire growth mode is illustrated in Fig. 3A. The first image (Fig. 3A, left panel) shows two Ge wires after 3 hours and 24 min of stable VLS growth at 4.8×10^{-6} Torr. The Ge_2H_6 pressure was then reduced to 8.6×10^{-7} Torr while a constant temperature was maintained. Within 106 s, the droplet on the narrower wire abruptly solidifies (Fig. 3A, middle panel), while the droplet on the wider wire solidifies later (Fig. 3A, right panel). This behavior has been verified for larger samples of wires. Figure 3B shows the catalyst state versus wire diameter in one experiment at an intermediate time. The reduction in Ge_2H_6 pressure causes all the droplets to solidify, although there can be a time delay of several minutes, with the smaller droplets solidifying earlier. (The exact time delay between smaller and larger droplets depends on the growth history and in some cases were as long as 20 to 60 min.

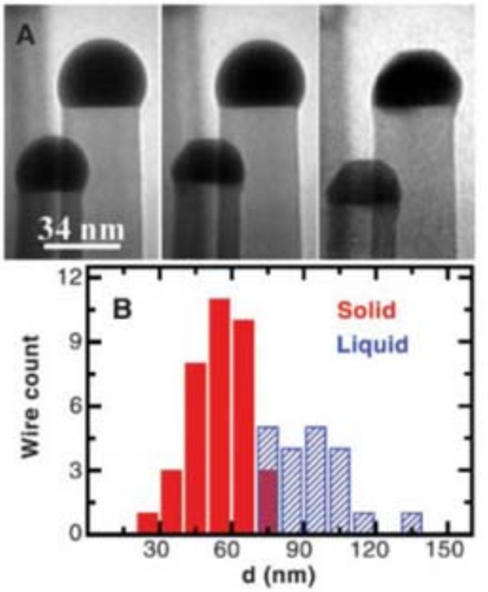

Fig. 3. (**A**) Representative bright-field TEM image series showing the solidification of Au-Ge catalysts on top of two Ge wires (29 and 34 nm in diameter) when the pressure is reduced during growth at constant temperature. We carried out wire growth at 350°C using 4.8×10^{-6} Torr Ge_2H_6 for 3 hours 24 min (left panel), after which we reduced the pressure to 8.6×10^{-7} Torr. After 106 s, the catalyst in the narrower wire solidified (middle panel) and, after a further 283 s, the catalyst on the wider wire solidified (right panel). (**B**) Histogram showing the diameter dependence of the catalyst state at a fixed time after reducing the pressure. Wire growth is carried out at 8×10^{-6} Torr and 355°C for 2 hours. At this time, the Ge_2H_6 pressure is reduced to 5×10^{-7} Torr; no change is observed after 15 min. The Ge_2H_6 supply is then switched off (leaving a background pressure of 6×10^{-10} Torr), and the state of the catalysts on 56 wires is recorded after 14 min. Wires with diameters (d) less than 70 nm have solid tips, whereas the tips of those with diameters larger than 80 nm are still liquid.

Au-catalyzed growth of Ge wires below T_e is generally assumed to occur by a VLS process (i.e., via a liquid catalyst) (*9*, *11*–*14*). The existence of a liquid alloy phase below T_e has been attributed to nanoscale size effects and, in particular, to a lowering of the droplet eutectic temperature to below T_e by the Gibbs-Thomson effect (*14*). This picture naturally leads to a dependence on size but does not directly involve growth pressure or growth rate.

Nevertheless, the fact that Ge_2H_6 pressure affects the droplet state does not in itself rule out a Gibbs-Thomson effect, because pressure could influence surface energies (for example, through changes in hydrogen coverage). In situ imaging allows us to examine the effect of Ge_2H_6 pressure on surface energies. Any change in surface energies will modify the force balance at the triple phase line and, hence, the steady-state droplet shape and wire diameter (*24*). We therefore measured the shapes of droplets during wire growth as a function of Ge_2H_6 pressure. Figure 4 is a typical plot of droplet heights and base diameters for an individual wire, as the pressure is varied repeatedly between higher and lower values. Although the changes are small, we find consistently that when the Ge_2H_6 pressure is decreased, the droplet height decreases while the droplet diameter increases. Clearly, the droplet shape is varying with Ge_2H_6 pressure, suggesting that there are observable changes in surface energy with pressure.

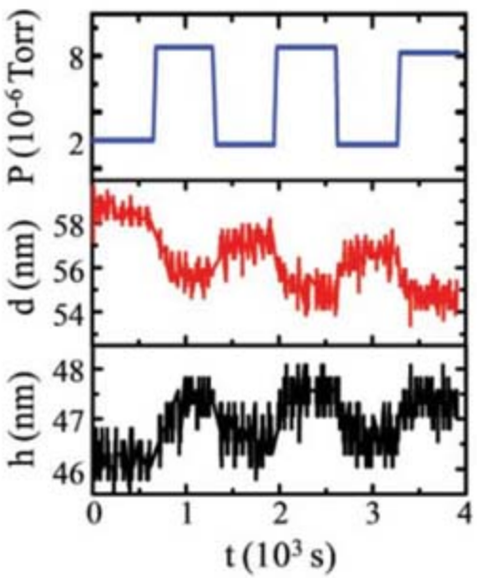

Fig. 4. The shape of a single droplet on a 59-nm-diameter Ge wire as a function of pressure, at a constant temperature of 355°C. Ge_2H_6 pressure P (blue curve), droplet base diameter or nanowire diameter d (red curve), and droplet height h (black curve) are plotted versus deposition time t as P is cycled repeatedly between 1.9×10^{-6} and 8.4×10^{-6} Torr. The measurements are taken from a video sequence of bright-field images, with h defined as the maximum normal distance from the drop boundary to the solid-liquid interface and with d defined as the width of the solid-liquid interface.

If the Gibbs-Thomson effect were stabilizing liquid-phase catalysts at temperatures below T_e, we would expect that droplets on narrower wires would be more resistant to solidification. In contrast, we observe that smaller droplets solidify sooner than larger ones, as in Fig. 3. This diameter dependence of solidification suggests that the principal cause of VLS growth below T_e is probably not the Gibbs-Thomson effect or any direct effect of small size.

Why then does the liquid phase persist below T_e? Some degree of undercooling is normal and may become more extreme at the nanoscale, but that does not explain the observed dependence on Ge_2H_6 pressure and diameter. We can rule out a dependence of the wire tip temperature on the wire diameter [via thermal conductivity (*25*)] or on the Ge_2H_6 pressure [via the heat of reaction (*9*)]: For wires with lengths <2 μm and for low pressures (10^{-7} to 10^{-5} Torr), both of which are typical in our experiments, we do not expect any appreciable variation in the tip temperature from these effects (*26*, *27*). Electron beam–induced temperature changes, if any, are small and are about the same for all wires being imaged simultaneously; hence, such changes should not affect the diameter dependence.

We suggest instead that the liquid phase may be effectively stabilized against solidification by Ge supersaturation, which arises from the growth process. Solidification requires some undercooling to overcome the nucleation barrier for a new phase. Here, crystalline Ge is already present. The key step for solidification is nucleation of a solid Au particle, and this step controls the degree of undercooling. Once Au nucleates, the liquid solidifies abruptly, with Ge coming out of solution and incorporating into the wire within a single video frame, as discussed earlier with reference to Fig. 1. Thus, the question to be addressed is why Au nucleation depends on Ge_2H_6 pressure.

By analogy with Si nanowire growth, we expect that the rate of dissociative adsorption of Ge_2H_6 at the droplet surface rises linearly with Ge_2H_6 pressure (*21*). Then, the supersaturation of Ge in the droplet must rise until the rate of incorporation from the liquid into the wire equals the rate of arrival of Ge from the vapor. However, the liquid-solid interface is a nanoscale (111) facet, so incorporation requires continuous nucleation of steps, which is difficult because of the small facet area (*28*) and the high step energy expected for (111). Therefore, even a modest growth rate in this system may require an anomalously large supersaturation.

Such a Ge supersaturation inhibits nucleation of solid Au. This can be seen by referring to the phase diagram (*29*) in Fig. 5, where the "V" shape of the liquidus arises as follows. At a temperature T, solid Au is unstable in the presence of a liquid that is more Ge-rich than a composition $c_{Au}(T)$. Similarly, solid Ge is unstable with a liquid that is more Au-rich than $c_{Ge}(T)$. Above their crossing point at T_e, these lines correspond to the liquidus, defining a region where neither solid is stable. As discussed above, for our growth conditions, solidification occurs by nucleation of solid Au; apparently, nucleation of solid Ge in the liquid is kinetically excluded. Therefore, solidification can only occur in the region where solid Au is stable, below the curve $c_{Au}(T)$ shown in green in Fig. 5. Under Ge-rich conditions, this curve goes below T_e (dashed portion of green line). (We also expect some undercooling with respect to this curve, but we do not speculate about its magnitude.)

This mechanism could also explain why narrower wires solidify first. When the Ge_2H_6 pressure is lowered, the supersaturation begins to decrease as excess Ge is incorporated into the wire, either at the growth facet or by diffusing to the sidewall (*30*). This Ge loss occurs at a rate that scales with cross-sectional area or circumference of the wire, whereas the amount of excess Ge scales with droplet volume, so the time scale for the loss of supersaturation increases with increasing wire diameter, explaining the observed trend.

The most speculative point is whether the Ge supersaturation can be quantitatively large enough to account for the observations. We estimate that a 1% increase in Ge concentration

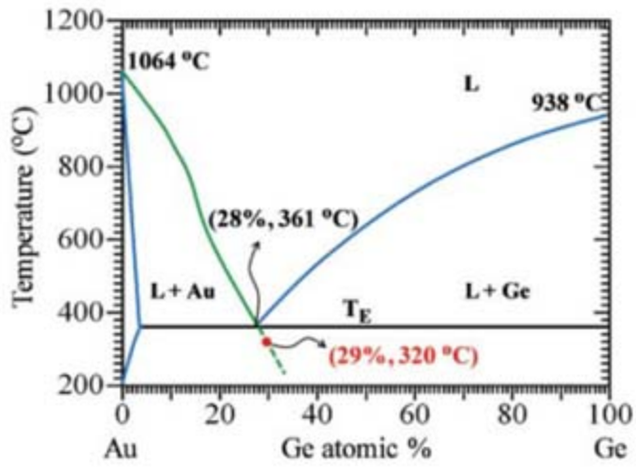

Fig. 5. Au-Ge binary alloy phase diagram [after (*29*)]. The solid green and blue curves are the Au and Ge liquidus lines, respectively. The dashed green curve is the extension of the Au liquidus line below T_e; Au nucleation cannot occur above this line. A 1% increase in Ge supersaturation in the liquid phase results in a ~40 K drop in the solid Au nucleation temperature, as shown by the red dot. "L" denotes liquid.

can lower the Au nucleation temperature by roughly 40 K, and a 4% increase in Ge might stabilize the liquid phase against Au nucleation at temperatures as low as 260°C. Such large kinetically driven supersaturations are not expected in typical macroscopic systems but become increasingly likely in strongly facetted systems as they shrink to the nanoscale (*28*, *31*). The degree of supersaturation would increase with growth rate, which could explain the successful growth of Ge nanowires at temperatures as low as 260°C in conventional chemical vapor deposition, where the growth rate is far higher than that in our experiments.

In conclusion, we have shown that during the growth of Ge wires using Au, the catalyst state may be either solid or liquid below T_e, with the state depending not just on temperature but also on Ge_2H_6 pressure and history. Nanowire growth continues regardless of the state the catalyst is in. In other words, both VLS and VSS processes can operate under the same conditions to grow Ge wires. A substantial Ge_2H_6 pressure is essential for growth via VLS below T_e. We propose a possible mechanism for the existence of a liquid catalyst at these temperatures, which is consistent with the observed dependence on Ge_2H_6 pressure and wire diameter. These results demonstrate that source gas pressure, though generally not considered a key factor, is actually crucial in determining the growth mode. The role of growth pressure and history may be relevant to controlling nanowire synthesis below T_e and to resolving the controversy surrounding the catalyst state in other materials systems.

References and Notes

1. K. Haraguchi, T. Katsuyama, K. Hiruma, K. Ogawa, *Appl. Phys. Lett.* **60**, 745 (1992).
2. J. Hu, T. W. Odom, C. M. Lieber, *Acc. Chem. Res.* **32**, 435 (1999).
3. L. Samuelson, *Mater. Today* **6**, 22 (2003).
4. H. J. Fan, P. Werner, M. Zacharias, *Small* **2**, 700 (2006).
5. R. S. Wagner, W. C. Ellis, *Appl. Phys. Lett.* **4**, 89 (1964).
6. Y. Wang, V. Schmidt, S. Senz, U. Gösele, *Nat. Nanotechnol.* **1**, 186 (2006).
7. Y. Yao, S. Fan, *Mater. Lett.* **61**, 177 (2007).
8. T. I. Kamins, R. S. Williams, D. P. Basile, T. Hesjedal, J. S. Harris, *J. Appl. Phys.* **89**, 1008 (2001).
9. G. A. Bootsma, H. J. Gassen, *J. Cryst. Growth* **10**, 223 (1971).
10. Y. Miyamoto, M. Hirata, *Jpn. J. Appl. Phys.* **14**, 1419 (1975).
11. D. Wang, H. Dai, *Angew. Chem. Int. Ed.* **41**, 4783 (2002).
12. T. I. Kamins, X. Li, R. S. Williams, *Nano Lett.* **4**, 503 (2004).
13. A. B. Greytak, L. J. Lauhon, M. S. Gudiksen, C. M. Lieber, *Appl. Phys. Lett.* **84**, 4176 (2004).
14. H. Adhikari, A. F. Marshall, C. E. D. Chidsey, P. C. McIntyre, *Nano Lett.* **6**, 318 (2006).
15. K. Hiruma *et al.*, *J. Appl. Phys.* **77**, 447 (1995).
16. A. I. Persson *et al.*, *Nat. Mater.* **3**, 677 (2004).
17. J. C. Harmand *et al.*, *Appl. Phys. Lett.* **87**, 203101 (2005).
18. M. Tchernycheva, J. C. Harmand, G. Patriarche, L. Travers, G. E. Cirlin, *Nanotechnology* **17**, 4025 (2006).
19. K. A. Dick *et al.*, *Nano Lett.* **5**, 761 (2005).
20. H. D. Park, A.-C. Gaillot, S. M. Prokes, R. C. Cammarata, *J. Cryst. Growth* **296**, 159 (2006).
21. S. Kodambaka, J. Tersoff, M. C. Reuter, F. M. Ross, *Phys. Rev. Lett.* **96**, 096105 (2006).
22. O. G. Shpyrko *et al.*, *Science* **313**, 77 (2006).
23. Q. Xu *et al.*, *Phys. Rev. Lett.* **97**, 155701 (2006).
24. F. M. Ross, J. Tersoff, M. C. Reuter, *Phys. Rev. Lett.* **95**, 146104 (2005).
25. F. Glas, J.-C. Harmand, *Phys. Rev. B* **73**, 155320 (2006).
26. Using 160 kJ/mol for the heat of reaction $Ge_2H_6 \rightarrow 2Ge + 3H_2$ (*32*) and a thermal conductivity of 5 W/mK for a 20-nm-wide wire, and assuming that all heat is conducted away, we estimate a maximum temperature difference ΔT of $\sim 10^{-5}$ K between the base and the tip of a 1-μm-long wire growing at 10^{-5} Torr of Ge_2H_6. In case of heat loss through radiation to the ambient, $\Delta T \sim 10^{-2}$ K.
27. N. Mingo, L. Yang, D. Li, A. Majumdar, *Nano Lett.* **3**, 1713 (2003).
28. S. D. Peteves, R. Abbaschian, *Metall. Trans. A* **22A**, 1259 (1991).
29. T. B. Massalski, J. L. Murray, L. H. Bennett, H. Baker, Eds. *Binary Alloy Phase Diagrams* (American Society for Metals, Metals Park, OH, 1986), vol. 1, pp. 263–264.
30. J. L. Taraci *et al.*, *Appl. Phys. Lett.* **84**, 5302 (2004).
31. M. J. Aziz, in *The Selected Works of John W. Cahn*, W. C. Carter, W. C. Johnson, Eds. (Minerals, Metals, and Materials Society, Warrendale, PA, 1998), pp. 207–209.
32. D. R. Lide, Ed., *CRC Handbook of Chemistry and Physics* (CRC Press, Boca Raton, FL, 2005).

33. We acknowledge R. M. Tromp, S. Guha, M. A. Aziz, and E. Tutuc for helpful discussions; A. Ellis for the development of in situ microscopy facilities; and L. Gignac and K. B. Reuter for energy-dispersive x-ray and electron energy-loss spectroscopy analyses of the wires. This work was partially supported by Defense Advanced Research Projects Agency (DARPA) under contract N66001-05-C-6030.

Supporting Online Material

www.sciencemag.org/cgi/content/full/316/5825/729/DC1
Fig. S1

20 December 2006; accepted 21 March 2007
10.1126/science.1139105

Synthesis of Tetrahexahedral Platinum Nanocrystals with High-Index Facets and High Electro-Oxidation Activity

Na Tian,[1] Zhi-You Zhou,[1] Shi-Gang Sun,[1]* Yong Ding,[2] Zhong Lin Wang[2]*

The shapes of noble metal nanocrystals (NCs) are usually defined by polyhedra that are enclosed by {111} and {100} facets, such as cubes, tetrahedra, and octahedra. Platinum NCs of unusual tetrahexahedral (THH) shape were prepared at high yield by an electrochemical treatment of Pt nanospheres supported on glassy carbon by a square-wave potential. The single-crystal THH NC is enclosed by 24 high-index facets such as {730}, {210}, and/or {520} surfaces that have a large density of atomic steps and dangling bonds. These high-energy surfaces are stable thermally (to 800°C) and chemically and exhibit much enhanced (up to 400%) catalytic activity for equivalent Pt surface areas for electro-oxidation of small organic fuels such as formic acid and ethanol.

Generally, catalytic performance of nanocrystals (NCs) can be finely tuned either by their composition, which mediates electronic structure (*1*, *2*), or by their shape, which determines surface atomic arrangement and coordination (*3*, *4*). Fundamental studies of single-crystal surfaces of bulk Pt have shown that high-index planes generally exhibit much higher catalytic activity than that of the most common stable planes, such as {111}, {100}, and even {110}, because the high-index planes have a high density of atomic steps, ledges, and kinks, which usually serve as active sites for breaking chemical bonds (*5*–*7*). For example, a bulk Pt(210) surface possesses extremely high catalytic reactivity for electroreduction of CO_2 (*8*) and electro-oxidation of formic acid (*9*). The bulk Pt(410) surface exhibits unusual activity for catalytic decomposition of NO, a major pollutant of automobile exhaust (*10*). Thus, the shape-controlled synthesis of metal NCs bounded by high-index facets is a potential route for enhancing their catalytic activities.

It is, however, rather challenging to synthesize shape-controlled NCs that are enclosed by high-index facets because of their high surface energy. Crystal growth rates in the direction perpendicular to a high-index plane are usually much faster than those along the normal direction of a low-index plane, so high-index planes are rapidly eliminated during particle formation (*11*). During the past decade, a variety of face-centered cubic (fcc) structured metal NCs with well-defined shapes have been synthesized, but nearly all of them are bounded by the low-index planes, such as tetrahedron, octahedron, decahedron, and icosahedron, enclosed by {111} facets (*12*–*14*), cube by {100} (*12*, *15*), cuboctahedron by {111} and {100} (*16*), and rhombic dodecahedron by {111} (*17*). Here we describe an electrochemical method for the synthesis of tetrahexahedral (THH) Pt NCs at high purity. The THH shape is bounded by 24 facets of high-index planes ~{730} and vicinal planes such as {210}

[1]State Key Laboratory of Physical Chemistry of Solid Surfaces, Department of Chemistry, College of Chemistry and Chemical Engineering, Xiamen University, Xiamen 361005, China. [2]School of Materials Science and Engineering, Georgia Institute of Technology, Atlanta, GA 30332–0245, USA.

*To whom correspondence should be addressed. E-mail: sgsun@xmu.edu.cn (S.G.S.); zhong.wang@mse.gatech.edu (Z.L.W.)

and {310}. The synthesized THH Pt NCs show enhanced catalytic activity in electro-oxidation of small organic fuels of formic acid and ethanol, demonstrating their potential for use in the traditional applications of Pt group metal nanoparticles, including catalysts (*18*), automotive catalytic converters (*19*), fuel cells (*20*), and sensors (*21*).

Several electrochemical methods have been reported for the synthesis of Pt NCs. Sun and coworkers used a fast potential cycling to grow nanostructured film on a Pt microelectrode surface (*22*), and Arvia *et al.* employed an electrochemical square-wave potential route to shape bulk Pt electrode (*23*), which could yield several high-index planes of bulk crystals in some cases (*24*). However, these methods have limited practical applications because of a low specific surface area and the high cost of the bulk Pt electrode. We have developed a route for shape-controlled synthesis of Pt NCs through a square-wave potential. Starting from Pt nanospheres electrodeposited on glassy carbon (GC) substrate instead of bulk Pt, we obtained THH Pt NCs at high yield. Electrochemical preparation was carried out in a standard three-electrode cell at room temperature (*25*). All electrode potentials are reported on the scale of a saturated calomel electrode (SCE). In a typical experiment, polycrystalline Pt nanospheres of size about 750 nm (fig. S1) were electrodeposited on a GC electrode in a solution of 2 mM K_2PtCl_6 + 0.5 M H_2SO_4. The Pt nanospheres were then subjected to a square-wave treatment, with upper potential 1.20 V and lower potential between –0.10 and –0.20 V, at 10 Hz in a solution of 0.1 M H_2SO_4 + 30 mM ascorbic acid for 10 to 60 min. As illustrated schematically by Fig. 1A, THH Pt NCs were grown exclusively on GC surface at the expense of Pt nanospheres.

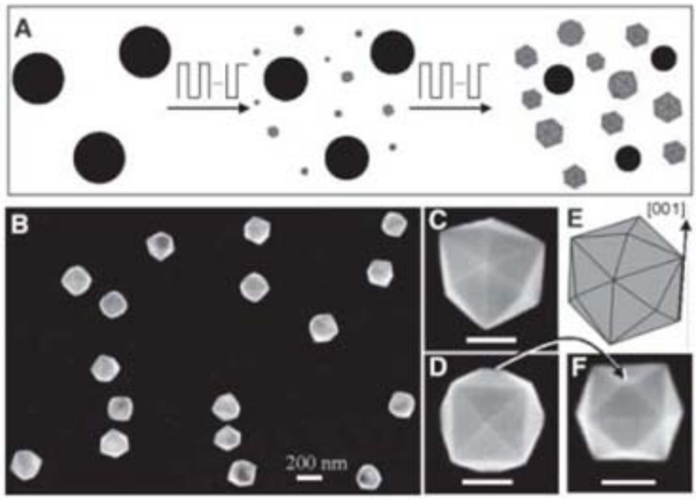

Fig. 1. (**A**) Scheme of electrochemical preparation of THH Pt NCs from nanospheres. The Pt nanosphere is an agglomeration of tiny Pt nanoparticles of irregular shapes (fig. S1). Under the influence of the square-wave potential, new Pt NCs of THH shape grow at the expense of the large nanospheres (the large nanosphere is "dissolved" into smaller ones, which eventually transform into THH shape). (**B**) Low-magnification SEM image of THH Pt NCs with growth time of 60 min. (**C** and **D**) High-magnification SEM images of Pt THH viewed down along different orientations, showing the shape of the THH. (**E**) Geometrical model of an ideal THH. (**F**) High-magnification SEM image of a THH Pt NC, showing the imperfect vertices as a result of unequal size of the neighboring facets. Scale bars in (C), (D), and (F), 100 nm.

The shape of the NCs was determined initially by scanning electron microscopy (SEM). An SEM image of THH Pt NCs produced with a growth time of 60 min is shown in Fig. 1B (an overview SEM image including THH Pt NCs and residual Pt nanospheres is shown in fig. S2). The yield of the THH Pt NCs in the final product is >90%, and most other shapes are an agglomeration of imperfect THH NCs (fig. S3). Their average size (Heywood diameter) was 217 nm, with a standard deviation of 23 nm. By controlling the experimental conditions, the smallest THH NCs received and identified by SEM are ~20 nm (fig. S3). The THH Pt NCs on GC surface are randomly oriented. High-magnification SEM images of THH Pt NCs oriented nearly along the three- and four-fold axes are presented in Fig. 1, C and D, respectively.

The THH shape is based on a cube with each face capped by a square-based pyramid (Fig. 1E). Three perfect square-based pyramids in Fig. 1C and nearly octagonal projection in Fig. 1D can be seen clearly, which confirms the THH shape of the Pt NC. In some cases, imperfection can be introduced at vertices (fig. S4), as presented by the SEM image in Fig. 1D, which is not caused by the {100} truncation of the THH but rather because crystal facets of different sizes are produced by substrate effects (Fig. 1F). Transmission electron microscopy (TEM) analysis of such structure clearly reveals the three-dimensional (3D) structure of the NC (fig. S5). In comparison with previous electrochemical faceting of bulk Pt electrodes (*24*), the use of Pt nanospheres deposited on GC substrate is vital to the production of nearly perfect THH Pt NCs, because GC is an inert substrate on which isolated Pt NCs grow in island (Volmer-Weber) mode but not columnar mode (*26*).

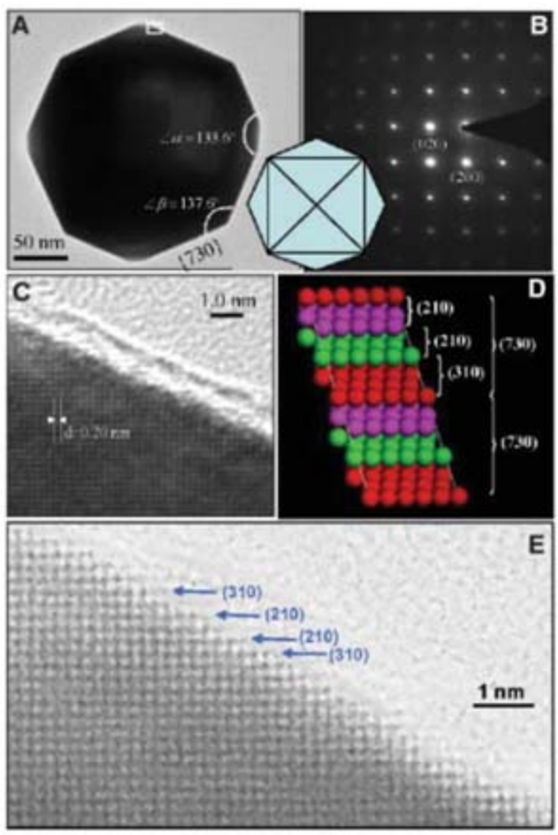

Fig. 2. (**A**) TEM image of THH Pt NC recorded along [001] direction. A careful measurement of the angles between surfaces indicates that the profiles of the exposed surfaces are {730} planes (α = 133.6°, β = 136.4°) (see fig. S6). The inset is a [001] projected model of the THH. (**B**) Corresponding SAED pattern with square symmetry, showing the single-crystal structure of the THH Pt NC. (**C**) High-resolution TEM image recorded from the boxed area marked in (A). An amorphous thin layer is shown at the surface, which may be introduced by contamination during specimen handling and/or TEM observation. (**D**) Atomic model of Pt(730) plane with a high density of stepped surface atoms. The (730) surface is made of (210) and (310) subfacets. The local surface of THH Pt NC can be (210) if the size of the crystal surface increases, although the overall profile of the facets is (730). (**E**) HRTEM image recorded from another THH Pt NC to reveal surface atomic steps in the areas made of (210) and (310) subfacets. The image reveals the surface atomic steps.

THH-shaped crystals in nature exist occasionally in fluorite and diamond but very rarely in metals. To the best of our knowledge, only copper crystals of truncated THH shape were found in copper minerals (*27*). The THH (O_h symmetry) belongs to Catalan solids or Archimedean duals; the THH shape is bounded by 24 high-index planes of {hk0} (h≠k≠0) (*28*). We determined the facets of the THH Pt NCs by selected-area electron diffraction (SAED) and high-resolution TEM (HRTEM).

The facets are best revealed by imaging the NC along [001], parallel to which 8 of the 24 facets are imaged edge-on (Fig. 2, A and B).

The fourfold symmetry of the SAED pattern confirms that the THH Pt NC is a single crystal. The HRTEM image in Fig. 2C recorded from a boxed area in Fig. 2A shows continuous lattice fringes with lattice spacing of 0.20 nm, which corresponds to the {200} planes of Pt. The Miller indices of exposed facets of the THH can be identified by a conjunction of the angles between the facets, the TEM image, and the ED pattern of the Pt NC (Fig. 2, A and B), whose border can be looked at as the projection of eight {hk0} facets parallel to the [001] zone axis. As shown in Fig. 2A, two surface angles of 133.6 ± 0.3° and 137.6 ± 0.3° are measured, which are in good agreement with theoretical values of angle $\alpha = 133.6°$ and angle $\beta = 136.4°$ between {730} facets (fig. S6). The results show that the dominant facets of the THH Pt NC are {730}. Although most of the THH Pt NCs are bounded by the {730} facets, some THH Pt NCs bounded by {210}, {310}, or {520} had also been observed [fig. S7 (*25*)].

The atomic arrangement of the Pt(730) surface (Fig. 2D) is periodically composed of two (210) subfacets followed by one (310) subfacet, that is, a multiple-height stepped structure (*6*). These steps have been directly captured in an HRTEM image recorded from another THH, as indicated by arrows in Fig. 2E. Thus, the single-crystal THH is enclosed by 24 high-index facets of ~{730}.

In addition to the HRTEM results, the surface structure of THH Pt NCs can also be characterized by cyclic voltammograms (fig. S8), in which the features of oxygen adsorption and desorption are similar to those on a bulk Pt(210) surface but are different from those on a polycrystalline Pt surface. In a common point, these high-index facets exhibit an open structure. In the case of a Pt(730) surface, its density of stepped atoms is as high as 5.1×10^{14} cm^{-2}, that is, 43% of the total number of atoms on the surface. It is thus reasonable to expect that the THH Pt NCs will display high catalytic activity.

The size of the THH Pt NCs can be controlled by varying the growth time. The SEM images of THH Pt NCs produced with growth times of 10, 30, 40, and 50 min are shown in Fig. 3, A to D, respectively. The corresponding average sizes are measured, respectively, to be 53, 100, 126, and 144 nm. The histograms of size distributions of these particles are shown in Fig. 3E, with a relative standard deviation (RSD) of 12%, 10%, 14%, and 14%, respectively. The particle size is also correlated with the density of THH Pt NCs on the substrate surface. The (210) and (310) planes, the major subfacets for composing of the (730) as shown in Fig. 2D, exhibited high stability under electrochemical conditions and solid-gas environments in both oxidative and reducing atmospheres (*9*, *29*–*31*). The THH Pt NCs are thermally stable; in situ TEM observation showed that the THH Pt NCs were thermally stable to temperatures of ~800°C with the preservation of the shape and facets (Fig. 3F). (Note the large size of the particles.)

Why are the {730} or the {210} type of facets that define the THH shape stable during growth? We have found that ascorbic acid is not the intrinsic reason to produce the THH shape, because THH Pt NCs can still be harvested in ascorbic acid–free solution, although the yield and quality degrade (fig. S9). In the original synthesis procedures (Fig. 1A), the initial stage of treating the nanospheres by square-wave potential, the following processes may occur (*25*). First, at 1.20 V, the surface Pt atoms on the nanospheres can be oxidized and partially dissolved to form Pt ions. Then, these Pt ions diffuse to the GC surface and are reduced to Pt atoms between –0.20 and –0.10 V. In the square-wave potential procedure, the two processes were repeated periodically at a frequency of 10 Hz, and new Pt NCs grow through nucleation and growth on GC surface with a continuous dissolving of the original Pt nanospheres, because the small nanoparticles grow more rapidly than the larger ones (*32*).

It has been reported that the surface structure of Pt single crystals could be changed by periodic adsorption and desorption of oxygen, depending on their Miller indices (*33*). At 1.20 V, Pt surface is oxidized and covered by oxygen species (O_{ad} and OH_{ad}) originated from the dissociation of H_2O in solution. As for the low-energy planes, surface atoms have larger coordination numbers (CNs), such as 9 for atoms on the (111) plane, so oxygen atoms are relatively difficult to adsorb at such surface sites; instead, some oxygen atoms might preferentially diffuse or invade into a Pt surface to form a Pt-O lattice through place-exchange between oxygen and Pt atoms. After reduction between –0.20 and –0.10 V, these displaced Pt atoms cannot always return to their original positions because the synthesis was carried out at room temperature, which then disorders surface structure (*33*). However, for high-index planes, the CNs of surface atoms are relatively low, only 6 for stepped atoms on the {730} plane. The oxygen atoms preferentially adsorb at such stepped atoms without replacing them, and ordered surfaces are preserved (*33*, *34*). The dynamic oxygen adsorption-desorption mediated by square-wave potential and the different degrees of place-exchange between oxygen and Pt atoms on Pt single-crystal surfaces show that only high-index planes with an open structure, such as the {730} and {210} facets, can survive in the treatment of square-wave potential (fig. S10).

The catalytic activity of THH Pt NCs is superior to that of the spherical Pt nanoparticles. The NCs have been applied to promote the electro-oxidation of formic acid and ethanol, which are promising alternative fuels for direct fuel cells. Figure 4A shows a comparison of transient current density of formic acid oxidation at 0.25 V on the THH Pt NCs [$\bar{d}$ = 81 nm (fig. S11)], the electrodeposited polycrystalline Pt nanospheres [$\bar{d}$ = 115 nm (fig. S12)], and the commercial 3.2-nm Pt/C catalyst from E-TEK, Inc. (Somerset, New Jersey, USA) (fig. S13) at room temperature. The oxidation current has been normalized to electroactive Pt surface area so that the current density (j) can be directly used

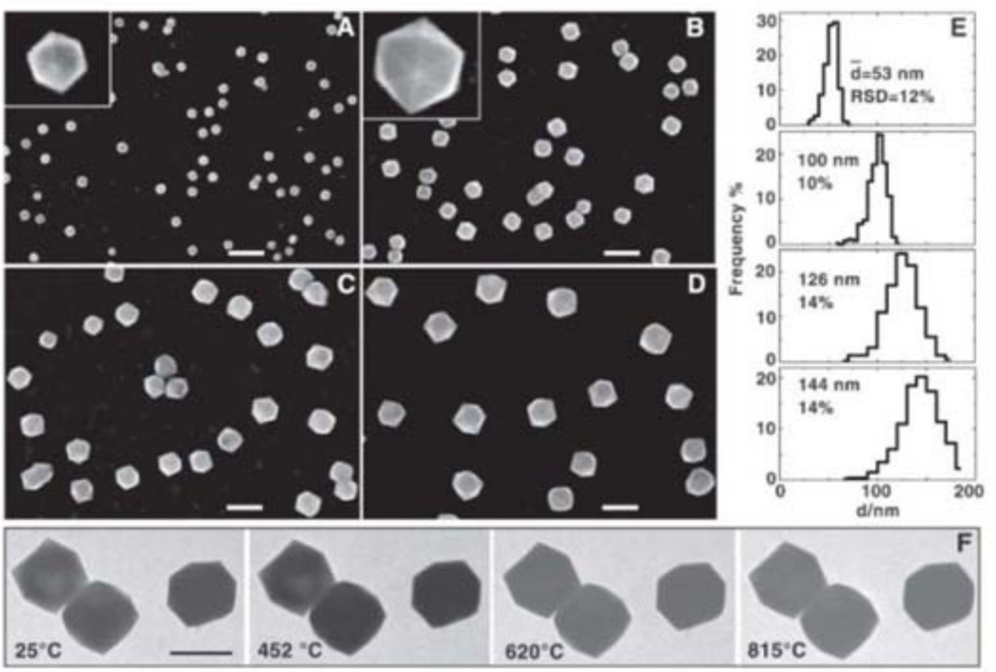

Fig. 3. Size control of THH Pt NCs and their thermal stability. SEM images of THH Pt NCs grown at (**A**) 10, (**B**) 30, (**C**) 40, and (**D**) 50 min. The insets in (A) and (B) are the high-magnification SEM images that confirm the shape of THH. Scale bars, 200 nm. (**E**) Size distributions of THH Pt NCs in (A), B), (C), and (D), respectively, after counting more than 500 particles for each sample. (**F**) In situ TEM observation on the thermal stability of THH Pt NCs. The images were recorded at various temperatures in TEM at a heating rate of 7°C/min. The NC preserves its shape to ~815°C and even higher with a slight truncation at the corners and apexes, as seen in the TEM image.

to compare the catalytic activity of different samples (*25*). The oxidation current density on THH Pt NCs is nearly double that on Pt nanospheres or Pt/C catalyst. The potential dependence of the steady-state current density recorded at 60 s is shown in Fig. 4B. The current density of formic acid oxidation on THH Pt NCs is higher than that on the Pt nanospheres or the Pt/C catalyst, and the enhancement factor *R*, which is defined as the ratio of the current density measured on THH Pt NCs versus that acquired on Pt nanospheres or Pt/C catalyst, varies from 160% to 400% for Pt nanospheres and from 200% to 310% for Pt/C catalyst, depending on electrode potential. The THH Pt NC showed no appreciable morphological change after the reaction, as indicated by an SEM image of a THH Pt NC inset in Fig. 4B, which still preserves the THH shape, showing its chemical stability.

For ethanol oxidation, the transient current density on THH Pt NCs at 0.30 V is enhanced to 230% of that on the nanospheres and 330% of that on the Pt/C catalyst (Fig. 4C). A comparison of the steady-state current densities obtained on THH Pt NCs, Pt nanospheres, and 3.2-nm commercial Pt/C catalyst is shown in Fig. 4D, in which the enhancement factor *R* varies between 200% and 430% for Pt nanospheres and between 250% and 460% for Pt/C catalyst in the potential region of 0.20 to 0.55 V. In addition, we have measured that, at a given oxidation current density of technical interest in fuel cell application, as indicated by dashed lines in Fig. 4, B and D, the corresponding potential on THH Pt NCs is much lower than that on Pt nanospheres or Pt/C catalyst. In the case of formic acid oxidation, the potential on THH Pt NCs is shifted negatively by ~60 mV as compared with Pt nanospheres at the same current density of 0.5 mA cm^{-2}, whereas for ethanol oxidation, the negative shift is ~80 mV at a current density of 0.2 mA cm^{-2}. The above results show that THH Pt NCs exhibit much enhanced catalytic activity per unit surface area for the oxidation of small organic molecules. This may be attributed to the high density of stepped atoms on the surfaces of THH Pt NCs. However, for catalytic activity per unit weight of Pt, our estimation indicates that, when the transformation is complete, the overall activity of these larger THH NCs is less than that of the 3-nm commercial Pt nanoparticles (~10% as active). Future research will be needed to improve the synthesis technique so that smaller-size THH NCs are made in high yield and still consume almost all of the starting Pt nanoparticles.

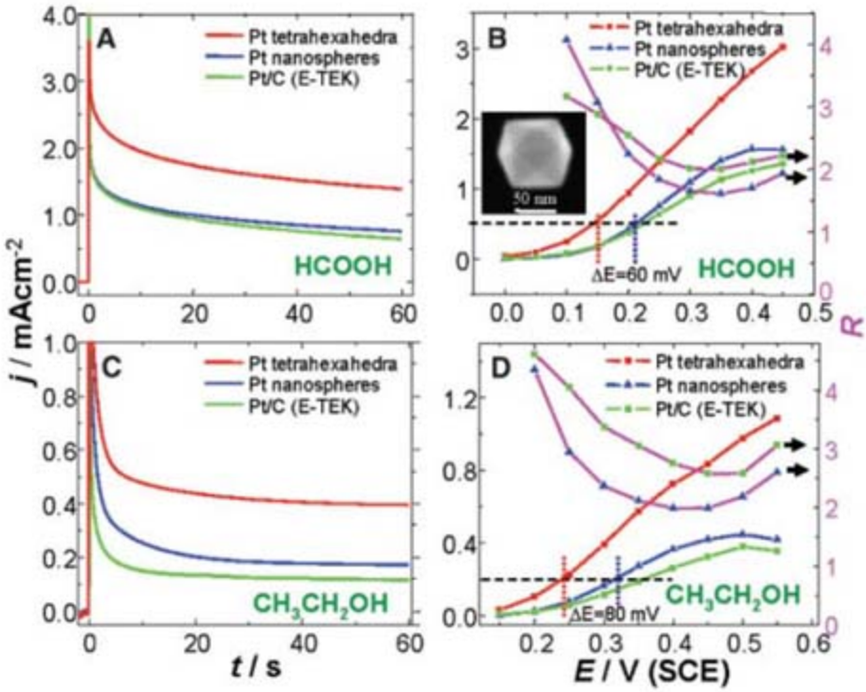

Fig. 4. Comparison of catalytic activity per unit Pt surface area among THH Pt NCs, polycrystalline Pt nanospheres, and 3.2-nm Pt/C catalyst. (**A**) Transient current density curves of formic acid oxidation at 0.25 V. (**B**) Potential-dependent steady-state current density (left, recorded at 60 s) of formic acid oxidation on THH Pt Ncs, Pt nanospheres, and commercial Pt/C catalyst, and the ratios *R* (right) between that of THH with the latter two, respectively. The inset in (B) is an SEM image of a THH Pt NC after reaction, indicating the preservation of shape. (**C**) Transient current density curves of ethanol oxidation at 0.30 V for the THH, Pt nanospheres, and Pt/C catalyst. (**D**) Potential-dependent steady-state current density (left) of ethanol oxidation on THH Pt NCs, Pt nanospheres, and commercial Pt/C catalyst, and the ratios *R* (right). The current density *j* was normalized in reference to the electrochemical active surface area for each sample, so that the current density *j* directly corresponds to the catalytic activity of unit Pt surface area of the sample. Thus, it can be directly compared for three types of particles. The results clearly demonstrate the largely enhanced catalytic activities of the THH Pt NCs per unit surface area.

References and Notes

1. J. Zhang, K. Sasaki, E. Sutter, R. R. Adzic, *Science* **315**, 220 (2007).
2. V. R. Stamenkovic *et al.*, *Science* **315**, 493 (2007).
3. R. Narayanan, M. A. El-Sayed, *Nano Lett.* **4**, 1343 (2004).
4. F. J. Vidal-Iglesias *et al.*, *Electrochem. Commun.* **6**, 1080 (2004).
5. G. A. Somorjai, D. W. Blakely, *Nature* **258**, 580 (1975).
6. G. A. Somorjai, *Chemistry in Two Dimensions: Surfaces* (Cornell University Press, Ithaca, NY, 1981).
7. S. G. Sun, A. C. Chen, T. S. Huang, J. B. Li, Z. W. Tian, *J. Electroanal. Chem.* **340**, 213 (1992).
8. N. Hoshi, S. Kawatani, M. Kudo, Y. Hori, *J. Electroanal. Chem.* **467**, 67 (1999).
9. S. G. Sun, J. Clavilier, *Chem. J. Chin. Univ.* **11**, 998 (1990).
10. W. F. Banholzer, R. I. Masel, *J. Catal.* **85**, 127 (1984).
11. H. E. Buckley, *Crystal Growth* (Wiley, New York, 1951).
12. T. S. Ahmadi, Z. L. Wang, T. G. Green, A. Henglein, M. A. El-Sayed, *Science* **272**, 1924 (1996).
13. F. Kim, S. Connor, H. Song, T. Kuykendall, P. D. Yang, *Angew. Chem. Int. Ed.* **43**, 3673 (2004).
14. Y. J. Xiong, J. M. McLellan, Y. D. Yin, Y. N. Xia, *Angew. Chem. Int. Ed.* **46**, 790 (2007).
15. Y. Sun, Y. Xia, *Science* **298**, 2176 (2002).
16. H. Song, F. Kim, S. Connor, G. A. Somorjai, P. D. Yang, *J. Phys. Chem. B* **109**, 188 (2005).
17. X. G. Liu, N. Q. Wu, B. H. Wunsch, R. J. Barsotti, F. Stellacci, *Small* **2**, 1046 (2006).
18. A. Wieckowski, E. Savinova, C. G. Vayenas (Eds.), *Catalysis and Electrocatalysis at Nanoparticle Surfaces* (Marcel Dekker, Inc., New York, 2003).
19. R. M. Heck, R. J. Farrauto, *Appl. Catal. Gen.* **221**, 443 (2001).
20. J. Larminie, A. Dicks, *Fuel Cell Systems Explained, 2nd Edition* (Wiley, Chichester, West Sussex, 2003).
21. F. Favier, E. C. Walter, M. P. Zach, T. Benter, R. M. Penner, *Science* **293**, 2227 (2001).
22. H. Gong, S. G. Sun, Y. J. Chen, S. P. Chen, *J. Phys. Chem. B* **108**, 11575 (2004).
23. A. Visintin, J. C. Canullo, W. E. Triaca, A. J. Arvia, *J. Electroanal. Chem.* **239**, 67 (1988).
24. W. A. Egli, A. Visintin, W. E. Triaca, A. J. Arvia, *Appl. Surf. Sci.* **68**, 583 (1993).
25. Materials and methods are available as supporting material on *Science* Online.
26. G. H. Gilmer, H. Huang, C. Roland, *Comput. Mater. Sci.* **12**, 354 (1998).
27. A. E. Seaman Mineral Museum of Michigan Technological University (available at www.museum.mtu.edu/Gallery/copper.html).
28. A. A. Proussevitch, D. L. Sahagian, *Comput. Geosci.* **27**, 441 (2001).
29. S. G. Sun, D. F. Yang, S. J. Wu, J. Ociepa, J. Lipkowski, *J. Electroanal. Chem.* **349**, 211 (1993).
30. D. W. Blakely, G. A. Somorjai, *Surf. Sci.* **65**, 419 (1977).
31. P. J. Knight, S. M. Driver, D. P. Woodruff, *Chem. Phys. Lett.* **259**, 503 (1996).
32. H. Reiss, *J. Chem. Phys.* **19**, 482 (1951).
33. N. Furuya, M. Shibata, *J. Electroanal. Chem.* **467**, 85 (1999).
34. A. V. Tripkovic, R. R. Adzic, *J. Electroanal. Chem.* **205**, 335 (1986).

35. This work was supported by grants from the Natural Science Foundation of China (20433060, 20503023, and 20673091) and Special Funds for Major State Basic Research Project of China (2002CB211804). Y.D. and Z.L.W. were supported by U.S. NSF grant DMR 9733160 and by the Georgia Institute of Technology. N.T. thanks the Ph.D. program of Xiamen University for support.

Supporting Online Material

www.sciencemag.org/cgi/content/full/316/5825/732/DC1
Materials and Methods
Figs. S1 to S13
References

29 January 2007; accepted 12 March 2007
10.1126/science.1140484

Roadless Space of the Conterminous United States

Raymond D. Watts,[1]* Roger W. Compton,[2] John H. McCammon,[2] Carl L. Rich,[2] Stewart M. Wright,[2] Tom Owens,[2] Douglas S. Ouren[1]

Roads encroaching into undeveloped areas generally degrade ecological and watershed conditions and simultaneously provide access to natural resources, land parcels for development, and recreation. A metric of roadless space is needed for monitoring the balance between these ecological costs and societal benefits. We introduce a metric, roadless volume (RV), which is derived from the calculated distance to the nearest road. RV is useful and integrable over scales ranging from local to national. The 2.1 million cubic kilometers of RV in the conterminous United States are distributed with extreme inhomogeneity among its counties.

The road network of the United States exceeds 6.3 million km in aggregate length (*1*) and fills the national landscape so fully that, except in Alaska, one can get no farther from a road than 35 km (*2*). This extensive road network provides societal benefits by bringing natural resources to consumers, linking workers to jobs, and connecting people to urban services. It is in the spaces between the roads that valuable natural resources are present and ecosystem services are rendered. Road encroachment affects ecological resources, primarily in negative ways (*1*, *3*–*8*), usually by fragmenting habitats and introducing chemical contaminants and exotic species to the ecosystem. Roads have been demonstrated to have dozens, if not hundreds, of effects on ecosystems and watersheds (*1*, *3*–*5*, *7*–*11*). Physical, chemical, and biological processes transmit influences from roads to their surroundings in a mélange of deterministic, stochastic, and chaotic processes that are made even more complex through their interactions with the variability of the landscape. The span of documented effects ranges from a few meters to many kilometers (*1*) and depends not only on the roads themselves but also on the volume and types of traffic that they carry. These complexities make it impractical to measure or estimate the area of influence without extensive local observation. Our work is aimed at bridging these details in order to answer two questions: (i) how much space is there between the roads, and (ii) how much is lost as new roads are added to the network, penetrating roadless space? These questions cannot be answered by measuring either the length or surface area of roads because these metrics do not respond to road placement. We sought a metric that would have a greater response to a road penetrating deeply into otherwise roadless space than to a road of similar length lying close to other roads.

We introduce a metric called roadless volume (RV). RV calculation begins with the computation of the horizontal distance to the nearest road (DTR), which is most accurately done with fast-marching methods (*12*) or adequately done with network methods (*13*); the network computation method is available in many geographic information systems. In practice, DTR is computed for points on a square grid (we used a 30-m grid); grid size does not bias results, but it affects accuracy. RV for an area is the integral of DTR over the area, which is estimated to be the total of the DTR cell values multiplied by cell area, with resulting units of cubic meters or cubic kilometers. Calculation accuracy depends on cell size, the quality of the road data set used for DTR computation, the sinuosity of roads, and (to a small degree) the method of calculation. RV is objective; there are no arbitrary factors.

RV can be described and visualized as follows: Substitute DTR for elevation to create a pseudotopographic surface (real topography plays no role in our definition of RV). RV of a footprint area is the volume of the pseudotopography above that footprint (Fig. 1). Roads of equal length produce different RV changes, depending on their alignments with respect to other roads (Fig. 2). RV responds simultaneously to footprint area, footprint shape, and the alignment of roads within the footprint. Compact footprints with no internal roads produce maximum RV. Meandering boundaries and internal roads diminish RV. The greatest reduction comes from roads that penetrate places that otherwise would be most remote from roads. Roads placed close to other roads only modestly reduce RV.

We calculated DTR for the entire United States on a 30-m grid aligned with the National Land Cover Dataset (NLCD), thus enhancing a national geospatial resource that is used for a wide variety of ecological and land-use analyses (*6*, *14*, *15*). RV for any footprint is $A\langle DTR\rangle$, where A is the area of the footprint and $\langle DTR\rangle$ is its mean DTR. With this definition, footprints need not be bounded by roads, enabling calculations of RV for counties (*16*). By summing county RV values, we estimated the RV of the conterminous United States to be 2.1×10^6 km^3. Maps inherently provide visual weighting by area, so we color-coded county results (Fig. 3) by $\langle DTR\rangle$ values rather than by RV, thus avoiding double emphasis of county size.

Roadless space is an asset that is unequally distributed by county and further unequally distributed among the population. Residents of two counties with equal RV have different per-capita shares of the roadless-space resource in inverse proportion to the county populations. Figure 4 shows per-capita RV by county, which can also be interpreted as the pressure of population against the counties' roadless spaces. Comparing Figs. 3 and 4, one sees that some counties with high DTR, and therefore high RV, have low per-capita RV. Prominent examples occur on the Pacific coast, along the Wasatch Front in Utah, along the Front Range in Colorado, and at the southern tips of Nevada and Florida; all these counties have metropolitan areas closely juxtaposed with mountains, deserts, or (in Florida) extensive wetlands. In contrast, low county populations create high per-capita RV in a band of counties stretching from the Dakotas to western Texas, in spite of relatively low DTR in most of these counties.

The county with the lowest per-capita RV is Kings County in New York (Brooklyn; roughly 4000 m^3 per capita, giving each person the equivalent of a 45° pyramid that is 30 m long on a side) (*17*), and the county with the highest per-

Fig. 1. RV is calculated by substituting DTR for elevation and then calculating the volume beneath the pseudotopographic surface. Two examples are shown, with perimeter roads in blue (there is a hidden road along the back of each volume). (**Left**) For a 1-km-square road pattern, the pyramid has a height of 0.5 km and a volume of 0.167 km^3. (**Right**) The elongated pyramid measures 0.333 by 3 km and therefore has the same footprint area as the square pyramid, but its volume is 47% of the square pyramid volume. RV simultaneously accounts for area and shape.

Fig. 2. (**Left**) A square road pattern produces a pyramid of roadless volume. (**Center**) Four added roads, each of length = 0.5 × (the length of one pyramid side) and intersecting at the center (the two roads parallel to the long side of the image are mostly hidden), reduce the pyramid volume by 50%. (**Right**) Four roads of the same length, starting at the corners and angled slightly toward the center (tan divergence angle = 0.1), diminish the pyramid volume by only 13.5%.

[1]U.S. Geological Survey (USGS), Fort Collins, CO 80526-8118, USA. [2]USGS, Denver, CO 80225-0046, USA.

*To whom correspondence should be addressed. E-mail: rwatts@usgs.gov

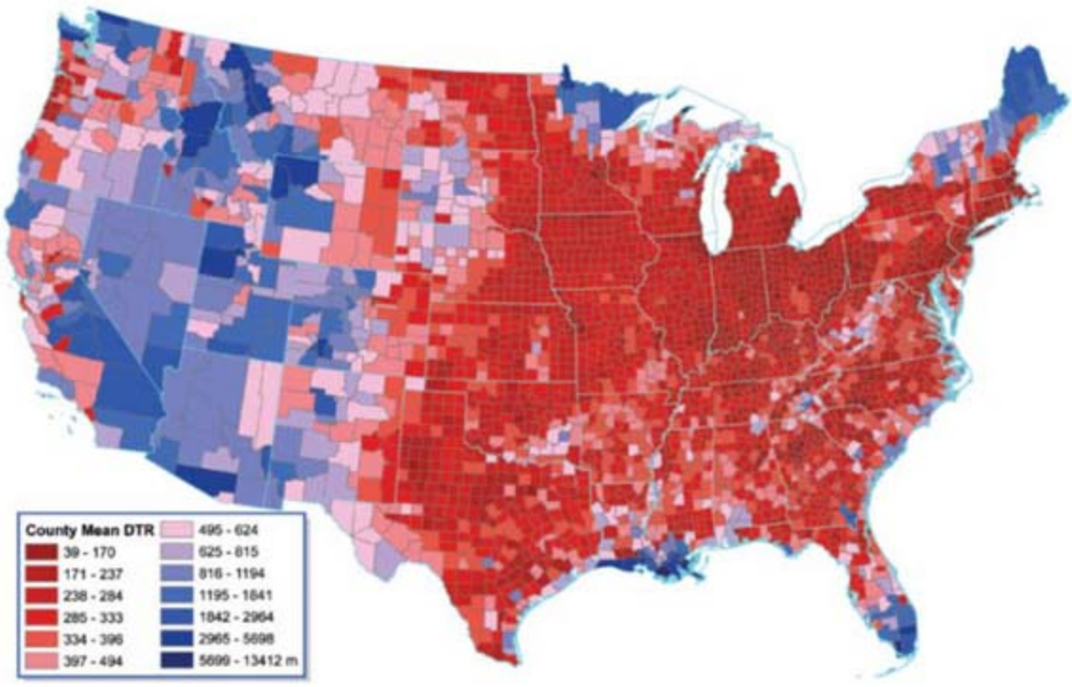

Fig. 3. Map of <DTR> by county in the conterminous United States. DTR legend classes are of approximately equal area, and color rendering closely follows area-adjusted county rank.

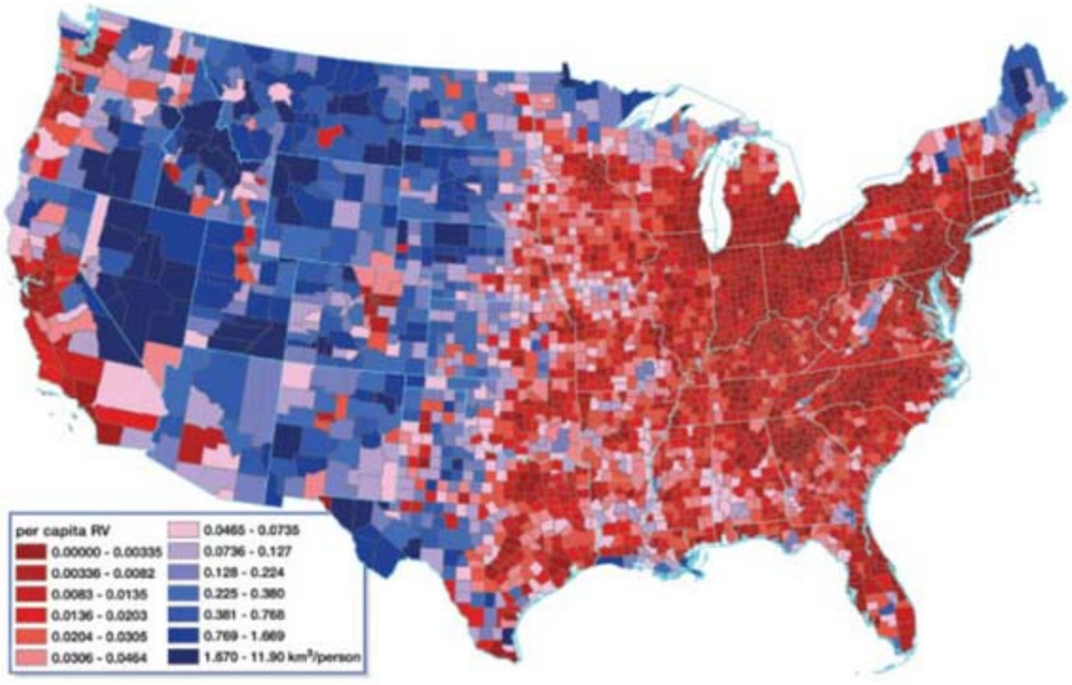

Fig. 4. Per-capita RV by county for the conterminous United States. Legend classes are of approximately equal area, and color rendering closely follows area-adjusted county rank.

capita RV is Hinsdale County in southern Colorado (11.9 km^3 per capita, giving each person a pyramid that is 4.1 km long on a side). The contrast in ecological conditions between these counties is extreme: One county is a dense urban area; the other is largely wilderness. The ratio of least to greatest roadless space per person in the conterminous United States, measured at the county scale, is approximately $1:3 \times 10^6$: a greater dynamic range than that of other common socioeconomic statistics at the county scale, such as population density ($1:7 \times 10^5$) (*18*) or mean income (1:7.8) (*19*). This large dynamic range implies that counties with low population densities also have few roads, large values of <DTR>, and large RV.

Socioeconomic processes add roads, diminishing DTR and RV. An assessment of changes in RV requires detailed and consistent maps on multiple dates, which are available in only a few places. One such place is the Front Range in Colorado, for which we made a movie of the change of RV from 1937 to 1997 (*20*). Here, nearly half of the initial RV was lost during the 60-year study period, as a result of urban expansion, growth of small towns, and housing dissemination—all occurring on agricultural land.

It is reasonable to postulate that distance from roads, on average, diminishes road influences, an application of a geographic law introduced by Tobler (*21*). Thus, although we cannot trace the details of road-induced effects, it may nevertheless be useful to know the extent to which we are diminishing the space where these effects are least likely and least intense. RV is a sensitive indicator that summarizes the status of this space.

References and Notes

1. R. T. T. Forman *et al.*, *Road Ecology: Science and Solutions* (Island Press, Washington, DC, 2003).
2. There are other places that are more remote from roads on islands and in Louisiana coastal swamps. The 35-km landlocked maximum distance occurs in Wyoming, near the southeast corner of Yellowstone National Park.
3. D. G. Havlick, *No Place Distant: Roads and Motorized Recreation on America's Public Lands* (Island Press, Washington, DC, 2002).
4. S. C. Trombulak, C. A. Frissell, *Conserv. Biol.* **14**, 18 (2000).

5. R. T. T. Forman, R. D. Deblinger, *Conserv. Biol.* **14**, 36 (2000).
6. K. H. Riitters, J. D. Wickham, *Front. Ecol. Environ.* **1**, 125 (2003).
7. R. T. T. Forman, L. E. Alexander, *Annu. Rev. Ecol. Syst.* **29**, 207 (1998).
8. J. L. Gelbard, J. Belnap, *Conserv. Biol.* **17**, 420 (2003).
9. R. L. DeVelice, J. R. Martin, *Ecol. Appl.* **11**, 1008 (2001).
10. I. F. Spellerberg, *Ecological Effects of Roads, Land Reconstruction and Management* (Science Publishers, Enfield, NH, 2002).
11. A. C. Yost, R. G. Wright, *Arctic* **54**, 41 (2001).
12. J. A. Sethian, *Level Set Methods and Fast Marching Methods: Evolving Interfaces in Computational Geometry, Fluid Mechanics, Computer Vision, and Materials Science* (Cambridge Univ. Press, Cambridge, ed. 2, 1999).
13. E. W. Dijkstra, *Numer. Math.* **1**, 269 (1959).
14. H. John Heinz III Center for Science, Economics, and the Environment, *The State of the Nation's Ecosystems: Measuring the Lands, Waters, and Living Resources of the United States* (Cambridge Univ. Press, Cambridge, 2002).
15. C. Homer, M. Coan, C. Huang, L. Yang, B. Wylie, *Photogramm. Eng. Remote Sens.* **70**, 829 (2004).
16. Materials and methods, including a table of county values of mean DTR and RV, are available as supporting material on *Science* Online.
17. Because calculations were done with a 30-m grid, the accuracy of the calculations is low where roads are dense. The approximate RV per-capita value for Kings County in New York is provided to illustrate the great contrast with the value for Hinsdale County in Colorado.
18. Bureau of the Census, in National Atlas of the United States, 2006 (www.nationalatlas.gov).
19. Bureau of Economic Analysis, in National Atlas of the United States, 2006 (www.nationalatlas.gov).
20. The movie of RV change for the Colorado Front Range is available as supporting material on *Science* Online.
21. W. R. Tobler, *Econ. Geogr.* **46**, 234 (1970).
22. We thank the Southern Rockies Ecosystem Project for introducing us to large-area DTR maps nearly a decade ago. Support for the development and analysis of national DTR data was provided by the USGS Geographic Analysis and Monitoring Program.

Supporting Online Material

www.sciencemag.org/cgi/content/full/316/5825/736/DC1
Materials and Methods
SOM Text
Tables S1 and S2
References
Movie S1

29 November 2006; accepted 22 March 2007
10.1126/science.1138141

Pyroclastic Activity at Home Plate in Gusev Crater, Mars

S. W. Squyres,[1] O. Aharonson,[2] B.C. Clark,[3] B. A. Cohen,[4] L. Crumpler,[5] P. A. de Souza,[6] W. H. Farrand,[7] R. Gellert,[8] J. Grant,[9] J. P. Grotzinger,[2] A. F. C. Haldemann,[10] J. R. Johnson,[11] G. Klingelhöfer,[12] K. W. Lewis,[2] R. Li,[13] T. McCoy,[14] A. S. McEwen,[15] H. Y. McSween,[16] D. W. Ming,[17] J. M. Moore,[18] R. V. Morris,[17] T. J. Parker,[10] J. W. Rice Jr.,[19] S. Ruff,[19] M. Schmidt,[14] C. Schröder,[12] L. A. Soderblom,[11] A. Yen[10]

Home Plate is a layered plateau in Gusev crater on Mars. It is composed of clastic rocks of moderately altered alkali basalt composition, enriched in some highly volatile elements. A coarse-grained lower unit lies under a finer-grained upper unit. Textural observations indicate that the lower strata were emplaced in an explosive event, and geochemical considerations favor an explosive volcanic origin over an impact origin. The lower unit likely represents accumulation of pyroclastic materials, whereas the upper unit may represent eolian reworking of the same pyroclastic materials.

Home Plate is a light-toned plateau ~90 m in diameter and 2 to 3 m high within the Inner Basin of the Columbia Hills, at Spirit's landing site in Gusev crater (*1*–*3*). Home Plate appears prominent from orbit, and was identified after landing as a high-priority target. It is the most extensive exposure of layered bedrock encountered by Spirit at Gusev to date.

Spirit arrived at the northern edge of Home Plate on sol 744 (*4*), following the path shown in Fig. 1. Images of the plateau show a thick stack of layered rocks, with a lower coarse-grained unit and an upper finer-grained unit (Fig. 2). The lower unit is characterized by prominent parallel layering with low apparent dips and a coarse granular texture (Fig. 2B). Individual granules are roughly equant, and typically 0.5 to 3 mm in size. It is difficult to determine in Microscopic Imager (MI) images whether the granules are original clasts, such as accretionary lapilli, or textures reflecting postdepositional cementation (fig. S1). Toward the top of the lower unit is a massive section roughly 10 cm thick where layering becomes indistinct (Fig. 3) and grains are difficult to identify in MI images (fig. S2).

A particularly notable feature in the lower unit is a ~4-cm clast with deformed layers beneath it, interpreted to be a bomb sag (Fig. 3). Bomb sags are found in volcaniclastic deposits on Earth, where outsized clasts ejected from an explosive vent are emplaced ballistically into deformable materials, causing downward deflection of layering.

In contrast to the lower unit, the upper unit is fine grained, well sorted, and finely laminated, and it exhibits cross-stratification. On the northern edge of Home Plate, the upper unit exposes a facies that is well bedded and characterized by ubiquitous fine lamination that is arranged in bed sets with planar to low-angle cross-stratification (Fig. 2C). Other features of this facies include gently dipping curved or irregular surfaces of erosion, small-scale cut-and-fill structures, convex-upward laminations, and occasional intercalation of thin beds of high-angle cross-bedding. In MI images, this facies exhibits a distinctly clastic texture, with grains 200 to 400 μm in diameter that are exceptionally well rounded and sorted (fig. S3).

A second facies in the upper unit that is particularly well developed at the eastern edge of Home Plate exhibits high-angle cross-bedding (Fig. 4). Here, the geometry is expressed as wedge sets up to several tens of centimeters thick of distinctly trough-shaped cross-strata. Internal stratification ranges from finely laminated to more thickly laminated. Cross-strata also preserve evidence of reactivation surfaces, cut at variable angles and generally backfilled by cross-strata concordant with the scour surface. Such geometries typically form during reconfiguration of the bed in response to scouring during flow bursting, migration of three-dimensional bedforms with frontal scour pits, and at times when the sediment concentration of a flow is decreased.

We used planar fits to bedding seen in Pancam images to estimate the structural attitudes of beds in the upper unit of Home Plate, at four locations that sample roughly a third of the plateau's perimeter (fig. S4). At all four locations, the beds dip inward toward the center of Home Plate. The 1σ range of derived dips is 5° to 20°, with occasional values up to 30°. Dips are consistent within each outcrop, suggesting that the measurements reflect a true structural trend and are not greatly influenced by low-angle cross-bedding.

Chemical compositions analyzed by the Alpha Particle X-ray Spectrometer (APXS) are

[1]Department of Astronomy, Space Sciences Building, Cornell University, Ithaca, NY 14853, USA. [2]Division of Geological and Planetary Sciences, California Institute of Technology, Pasadena, CA 91125, USA. [3]Lockheed Martin Corporation, Littleton, CO 80127, USA. [4]Institute of Meteoritics, University of New Mexico, Albuquerque, NM 87131, USA. [5]New Mexico Museum of Natural History and Science, Albuquerque, NM 87104, USA. [6]Vallourec Research Center, F-59260 Aulnoye-Aymeries, France. [7]Space Science Institute, Boulder, CO 80301, USA. [8]Department of Physics, University of Guelph, Guelph, ON, N1G 2W1, Canada. [9]Center for Earth and Planetary Studies, Smithsonian Institution, Washington, DC 20560, USA. [10]Jet Propulsion Laboratory, California Institute of Technology, Pasadena, CA 91109, USA. [11]United States Geological Survey, Flagstaff, AZ 86001, USA. [12]Institut für Anorganische und Analytische Chemie, Johannes Gutenberg-Universität, Mainz, Germany. [13]Department of Civil and Environmental Engineering and Geodetic Science, Ohio State University, Columbus, OH 43210, USA. [14]Department of Mineral Sciences, National Museum of Natural History, Smithsonian Institution, Washington, DC 20560, USA. [15]Lunar and Planetary Laboratory, University of Arizona, Tucson, AZ 85721, USA. [16]Department of Earth and Planetary Sciences, University of Tennessee, Knoxville, TN 37996, USA. [17]Astromaterials Research and Exploration Science, NASA Johnson Space Center, Houston, TX 77058, USA. [18]NASA Ames Research Center, Moffett Field, CA 94035, USA. [19]Department of Geological Sciences, Arizona State University, Tempe, AZ 85287, USA.

given in Table 1. The outcrops Posey and Cool Papa Bell (5) from the upper unit were brushed with the Rock Abrasion Tool (RAT) before analysis. Barnhill, from the lower unit, could not be brushed; Pancam color images were used to select relatively dust-free regions. Fuzzy Smith, a small (~10-cm) loose rock on the plateau, also could not be brushed. The lack of strong SO_3 and Cl enrichments for unbrushed surfaces relative to brushed ones suggests that surface dust contamination was modest.

Most Home Plate outcrop rocks are fairly uniform in elemental composition, except for Barnhill Fastball, which has lower Al_2O_3 and Na_2O and higher MgO. They are most similar to Masada, a scoriaceous float rock in the Inner Basin, and Irvine (6), a basaltic rock at the summit of Husband Hill. Home Plate outcrop rocks have a basaltic composition with high alkali contents similar to some other basalts in Gusev crater (6). However, they have markedly higher abundances of some volatile minor and trace elements (Cl, Br, Zn, and Ge).

Multispectral imaging of Home Plate outcrop rocks shows that clean surfaces have low albedo and exhibit ~930-nm band absorptions consistent with the presence of low-calcium pyroxene or possibly ferric oxyhydroxides (fig. S5). Such absorptions are similar to those observed in Clovis Class rocks on the west spur of Husband Hill (7).

Miniature Thermal Emission Spectrometer (Mini-TES) infrared spectra of dark-toned outcrops at Home Plate (fig. S6) indicate a strong component (~45%) that resembles basaltic glass, similar to the spectra of Clovis Class rocks (8). In addition, deconvolution using a spectral library yields a best fit with ~30% pigeonite (a clinopyroxene), ~5% olivine, and ~10% plagioclase. A small amount of sulfate (~10%) is also suggested. The surfaces that give Home Plate its light tone when viewed from orbit display the same spectrum of surface dust observed on other dust-covered rocks in Gusev crater (9).

Mössbauer Spectrometer (MB) mineralogy for Home Plate outcrop rocks is given in table S1. Barnhill, Posey, and Cool Papa Bell are similar to one another. Of the total Fe present (Table 1), 16 to 18% resides in olivine, 22 to 24% in pyroxene, 27 to 29% in nanophase oxide, and 26 to 32% in magnetite. These are among the most magnetite-rich rocks at Gusev crater (10). The ratio of Fe^{3+} to total iron (Fe^{3+}/Fe_{Total}) is ~0.52.

Chemical analyses were recast into mineralogy by calculating norms (Table 1) with the use of MB determinations of Fe^{3+}/Fe_{Total}. The differences between the calculated mineralogy and the actual mineralogy determined by Mini-TES and MB indicate that Home Plate outcrop rocks did not form through equilibrium crystallization from anhydrous silicate liquids, as a norm calculation assumes.

Both MB and Mini-TES detected olivine and pyroxene, although abundances cannot be compared directly because of uncertainties in the Fe content of both phases. Mini-TES deconvolution yields ~45% basaltic glass and no magnetite, whereas MB yields abundant Fe from magnetite (26 to 32%) and nanophase oxide (npOx) (27 to 29%). This apparent difference

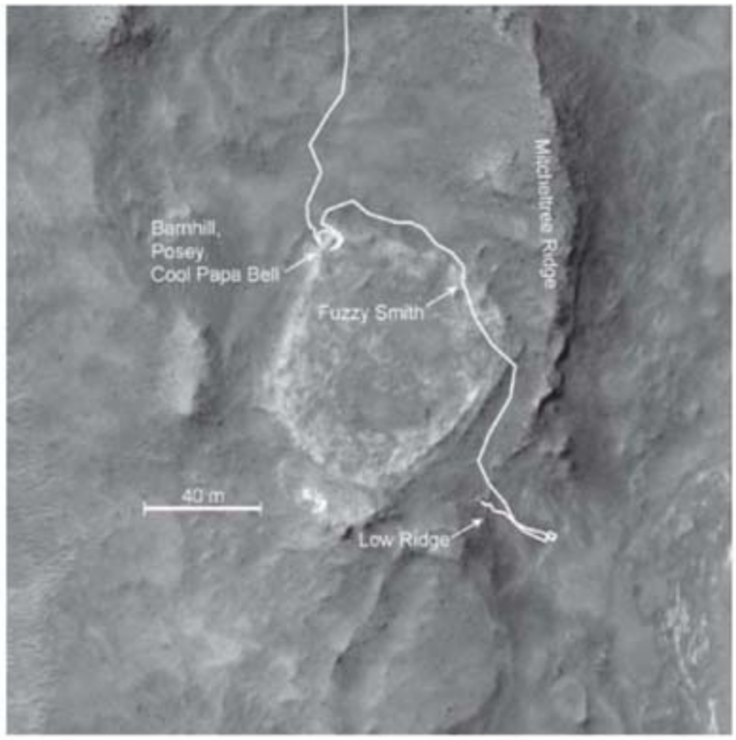

Fig. 1. Home Plate as viewed from orbit. North is at the top. The path followed by the rover is shown, and the locations of rocks discussed in the text are shown. [High-Resolution Image Science Experiment image PSP_001513_1655, acquired on 22 November 2006.] Image scale is 27.1 cm/pixel, map-projected to 25 cm/pixel. The scene is illuminated from the west with an incidence angle of 60°.

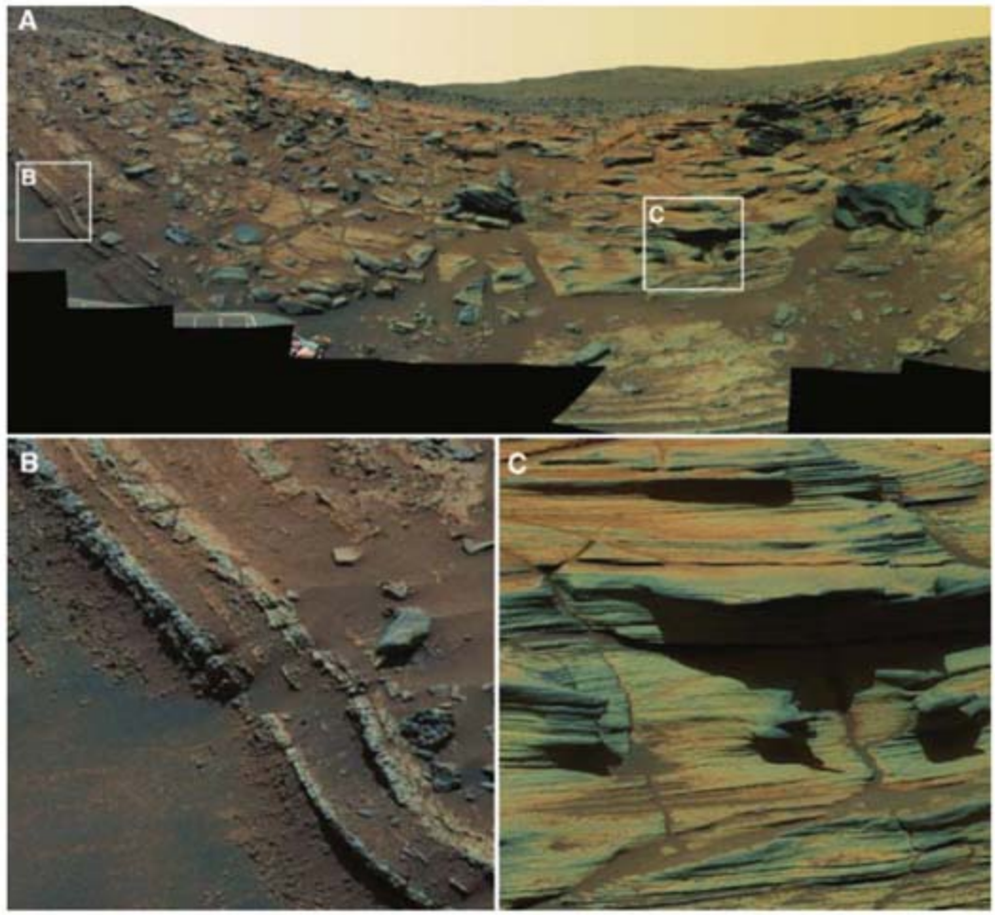

Fig. 2. The northern edge of Home Plate (**A**), showing the coarse-grained lower unit (**B**) and the fine-grained upper unit (**C**). False color image obtained using Pancam's L2, L5, and L7 filters (753, 535, and 440 nm, respectively) on sols 748 to 751. Approximate scale across both (B) and (C) is ~45 cm. The apparent curvature of the horizon in (A) results from the high rover tilt when the image was acquired.

suggests that the npOx for these rocks may be spectrally similar to the Mini-TES glass component. Nondetection of magnetite by Mini-TES is expected; the instrument's detection limit for magnetite is high because some magnetite spectral features are longward of its bandpass and others are obscured by the atmospheric CO_2 band at 15 μm.

Loose rocks atop Home Plate include the small, irregularly shaped rock Fuzzy Smith (fig. S7). Its chemical composition is unlike any other rock investigated by either rover, with high Zn; the highest Si, K, and Ge measured at Gusev crater; and very low Ca and Fe (Table 1). No Mini-TES data were acquired for Fuzzy Smith. Mössbauer data revealed unique Fe mineralogy, with most of the Fe (64%) in a phase we refer to as Fe?D1 that has not been detected in any other martian rock (table S1). The Mössbauer parameters of Fe?D1 [isomer shift (±2 SD) δ = 0.28 ± 0.02 mm/s and quadrupole splitting ΔE_Q = 0.67 ± 0.02 mm/s] are consistent with an Fe sulfide such as pyrite and/or marcasite ($Fe^{2+}S_2$ polymorphs) or with tetrahedrally coordinated Fe^{3+} in some phase (*11*). If the APXS and MB analyzed exactly the same material, then molar S/Fe does not favor the sulfide interpretation. Some phyllosilicates have tet-Fe^{3+} doublets with similar parameters, but the contribution of the subspectrum to the total MB spectrum (unlike what is observed in Fuzzy Smith) is <50%. Without additional chemical and mineralogical information (e.g., detection of sulfide or phyllosilicate by Mini-TES), we are not able to assign a mineralogical composition or an oxidation state to the Fe?D1 doublet.

Acid-sulfate leaching of basalt by volcanic vapors can produce amorphous, SiO_2-rich residues (*12*), and such a process may have been involved in the formation of Fuzzy Smith. While Fuzzy Smith is highly quartz-normative, the calculated mineralogy is unlikely to be representative of a leached rock.

Several characteristics of Home Plate implicate an explosive process in its origin. These include the bomb sag, rounded granules in the lower unit that might be accretionary lapilli, and an infrared spectral signature suggesting basaltic glass. A coarse-grained lower unit that grades upward into finer materials is also consistent with an explosive origin. Both a volcanic explosion and an impact are candidate formative events.

Compositional evidence favors a volcanic origin. Home Plate outcrops are similar in chemistry and mineralogy to vesicular alkali-rich basalts that are abundant in the Inner Basin. This relationship suggests a common magmatic source and a volcanic origin for Home Plate, although clearly the style of emplacement is different.

An unusual aspect of Home Plate rocks is fractionation of Cl (and in some cases Br) from S. Chlorine does not show correlations with incompatible elements such as K that could point to igneous fractionation as its source, nor with Al that might point to weathering or aqueous alteration. Instead, the Cl enrichment might be explained as interaction of magma with a brine. Alternatively, the enrichment in Cl but not in S could reflect degassing in an oxidized basaltic magma, causing S to partition preferentially into the vapor phase (*13*) and decreasing the S/Cl and S/Br ratios. In either case, a volcanic origin would be implied. However, we cannot rule out the possibility that the Cl enrichment is present in a surface coating that is resistant to RAT brushing, rather than in the bulk rock.

Home Plate is also strongly enriched in the volatile elements Ge and Zn. Although Ge tends to be high in meteoritic material, the lack of a corresponding Ni enrichment suggests that the Ge in Home Plate is not primarily of meteoritic origin. Instead, the enrichment in these volatile elements may reflect condensation of volcanic vapor. Germanium is also well known for enrichment in sulfides and zinc mineralizations, especially under hydrothermal conditions (*14*). Again, a volcanic origin for Home Plate is implied by either interpretation.

Taken together, our observations suggest that Home Plate is composed of debris deposited from a hydrovolcanic explosion that occurred when alkali-rich basaltic magma came into con-

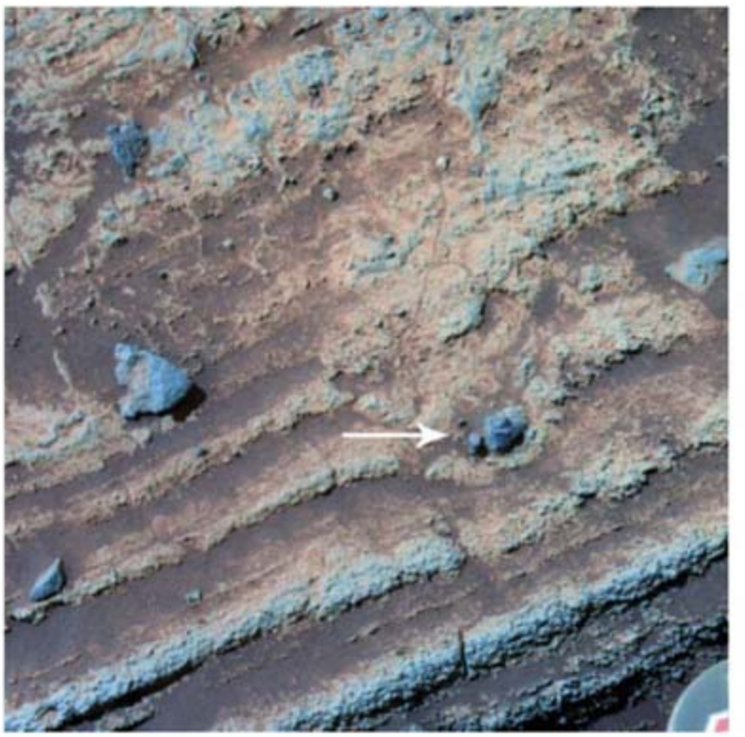

Fig. 3. The lower coarse-grained unit, showing granular textures toward the bottom of the image and massive textures with rectilinear fracturing toward the top. Also shown is a feature that we interpret to be a bomb sag (arrow). The bomb is about 4 cm across. False color image obtained using Pancam's L2, L5, and L7 filters on sol 751.

Fig. 4. High-angle cross-bedded sandstone at the northeast edge of Home Plate. Scale across the image is ~1.5 to 2 m. [Pancam image 2P195076279, acquired on sol 774.]

tact with subsurface fluid, perhaps brine. Both the bomb sag and the compositional similarity of Home Plate to basalts found nearby suggest that the deposits lie close to the source vent. Bomb sags on Earth typically indicate that the deformed materials were wet at the time of emplacement, but we cannot rule out the possibility of sag formation resulting from compaction and gas-supported flow of dry materials.

Some aspects of the cross-stratification in the upper unit are consistent with deposition from a volcanic surge (*15*, *16*). However, because they develop from highly turbulent flows, surge deposits close to the source vent are often coarsely stratified, and on average poorly sorted with a component of coarser grains including outsized bombs and blocks (*17*). These attributes are not observed in the upper unit. Furthermore, the cross-strata of surge deposits commonly exhibit deposition along the stoss side as well as the lee side of the bedforms; in contrast, the cross-strata preserved at Home Plate are dominated by stoss-side truncation (only one observed set shows stoss-side accretion), suggesting little deposition from fallout.

The upper unit at Home Plate shows persistently fine lamination, and very well sorted and rounded grains. These observations point toward a process like eolian transport that increased the textural maturity of the sediments, suggesting that the upper unit may have formed by eolian reworking of pyroclastic debris derived from the same source as the lower unit. The planar to low-angle stratification could have formed by the migration of impact ripples over a sand sheet surface, whereas the large-scale cross-stratification could have been produced by migration of dunes. This interpretation is consistent with the abrupt contact between lower unit facies with upper unit facies and with the lack of any evidence for depositional continuity.

Home Plate is a quasi-circular plateau with beds that dip toward its center. One plausible explanation for this geometry is that either a volcanic structure (e.g., a maar or tuff ring) or an impact crater provided bowl-shaped relief that was filled with pyroclastic materials. Because settling from suspension tends to produce layers that conform to and drape underlying topography, emplaced layers may have conformed to the depression's shape. Postdepositional compaction that induced subsidence in the deepest portions could have further rotated beds toward the center. Subsequent erosion may have stripped away both the original confining structure and pyroclastic materials that lay outside it, leaving behind a raised platform of layered materials that dip inward. Indeed, the Columbia Hills exhibit a paucity of small impact craters relative to the stratigraphically younger lava plains nearby, indicating that substantial amounts (perhaps meters) of erosion have occurred (*18*). Although there is strong evidence that the rocks of Home Plate lie close to their source vent, we have not found evidence that Home Plate itself is the location of the vent. Indeed, a probable source vent has not yet been found along Spirit's traverse. If, as we suspect, Home Plate is a remnant of a formerly more extensive explosive volcanic deposit, then investigation of other nearby layered materials may reveal a genetic relationship to Home Plate.

Home Plate was identified before Spirit's landing as a high-priority target, and its apparently layered character led to suggestions of lacustrine, eolian, or pyroclastic origin (*19*). Deposits of similar appearance are common on Mars. Our conclusions suggest that pyroclastic deposits may be common elsewhere, particularly in settings where magmas have come into contact with ground ice or water.

Table 1. APXS analyses and calculated normative mineralogy for Home Plate rocks. Analyses are in weight %, except for Ni, Zn, Br, and Ge, which are in parts per million. Sample homogeneity is assumed. Uncertainties represent 1σ errors in x-ray peak area. Posey and both spots on Cool Papa Bell (Stars and Crawfords) were brushed using the RAT; the others were not brushed. Fe was partitioned between FeO and Fe_2O_3 with the use of Mössbauer-determined Fe^{3+}/Fe_{Total} ratios (table S1). For rocks where no Mössbauer data were obtained, all Fe is reported as FeO and norms were calculated with the use of the average value for Home Plate outcrop rocks of $Fe^{3+}/Fe_{Total} = 0.52$. Norms were calculated without S, because S is assumed to be present as sulfate rather than sulfide.

Rock	Barnhill		Posey	Cool Papa Bell		Fuzzy Smith
	Ace	Fastball		Stars	Crawfords	
Oxide						
SiO_2	45.2 ± 0.27	45.3 ± 0.29	45.4 ± 0.38	46.0 ± 0.29	46.6 ± 0.39	68.4 ± 0.62
TiO_2	0.74 ± 0.06	0.67 ± 0.06	1.01 ± 0.06	0.93 ± 0.06	1.11 ± 0.07	1.71 ± 0.08
Al_2O_3	8.91 ± 0.08	7.85 ± 0.08	9.31 ± 0.10	9.30 ± 0.09	9.98 ± 0.12	6.31 ± 0.08
Fe_2O_3	10.4 ± 0.04		8.73 ± 0.05	9.77 ± 0.04		4.84 ± 0.04
Cr_2O_3	0.45 ± 0.03	0.49 ± 0.03	0.32 ± 0.03	0.39 ± 0.03	0.34 ± 0.03	0.06 ± 0.03
FeO	8.32 ± 0.03	17.8 ± 0.07	7.55 ± 0.04	8.11 ± 0.03	15.4 ± 0.09	2.45 ± 0.02
MnO	0.39 ± 0.01	0.47 ± 0.01	0.32 ± 0.01	0.31 ± 0.01	0.29 ± 0.01	0.15 ± 0.01
MgO	9.19 ± 0.09	12.0 ± 0.11	9.48 ± 0.10	9.59 ± 0.09	10.3 ± 0.12	4.16 ± 0.08
CaO	6.07 ± 0.04	5.80 ± 0.04	6.65 ± 0.04	6.50 ± 0.04	6.74 ± 0.05	1.93 ± 0.02
Na_2O	3.10 ± 0.17	2.35 ± 0.17	3.50 ± 0.19	3.25 ± 0.18	3.36 ± 0.21	2.92 ± 0.21
K_2O	0.32 ± 0.05	0.23 ± 0.05	0.42 ± 0.06	0.21 ± 0.05	0.32 ± 0.06	2.76 ± 0.07
P_2O_5	0.87 ± 0.07	0.79 ± 0.07	1.37 ± 0.07	1.12 ± 0.07	1.27 ± 0.08	0.68 ± 0.07
SO_3	5.67 ± 0.06	4.63 ± 0.06	4.81 ± 0.06	3.75 ± 0.05	2.91 ± 0.05	3.39 ± 0.05
Cl	1.31 ± 0.02	1.57 ± 0.02	1.94 ± 0.02	1.74 ± 0.02	1.35 ± 0.02	0.63 ± 0.01
Ni	317 ± 35	352 ± 39	379 ± 35	318 ± 37	297 ± 40	272 ± 33
Zn	400 ± 11	415 ± 14	407 ± 11	422 ± 13	314 ± 14	679 ± 14
Br	475 ± 17	370 ± 18	181 ± 15	203 ± 16	91 ± 15	21 ± 13
Ge	70 ± 15	70 ± 15	30 ± 10	30 ± 10	30 ± 10	190 ± 20
Mineral						
Quartz	2.3	2.6		1.9	0.5	35.3
Feldspars	37.6	31.5	40.6	38.9	41.5	33.4
Orthoclase	1.9	1.4	2.5	1.2	1.9	16.3
Albite	26.2	19.9	29.6	27.5	28.4	17.1
Anorthite	9.5	10.2	8.5	10.2	11.2	
Actinolite						6.7
Diopside	11.9	10.7	12.4	11.7	11.0	4.0
Hypersthene	23.0	31.3	22.6	23.8	25.2	8.5
Olivine			0.3			
Forsterite			0.3			
Fayalite						
Magnetite	15.1	14.9	12.7	14.2	12.7	3.3
Chromite	0.7	0.7	0.5	0.6	0.5	0.1
Ilmenite	1.4	1.3	1.9	1.8	3.3	3.3
Apatite	2.1	1.9	3.2	2.7	3.0	1.6
Hematite						0.2

References and Notes

1. S. W. Squyres *et al.*, *Science* **305**, 794 (2004).
2. H. Y. McSween *et al.*, *Science* **305**, 842 (2004).
3. R. E. Arvidson *et al.*, *J. Geophys. Res.* **111**, E02S01, 10.1029/2005JE002499 (2006).
4. A martian solar day has a mean period of 24 hours 39 min 35.244 s and is referred to as a sol to distinguish it from a ~3% shorter solar day on Earth.
5. All of the rocks at Home Plate are named after players from the Negro League of baseball that existed prior to the racial integration of Major League Baseball. The names are informal and not approved by the International Astronomical Union.
6. H. Y. McSween *et al.*, *J. Geophys. Res.* **111**, E09S91, 10.1029/2006JE002698 (2006).
7. W. H. Farrand, J. F. Bell III, J. R. Johnson, S. W. Squyres, J. Soderblom, D. W. Ming, *J. Geophys. Res.* **111**, E02S15, 10.1029/2005JE002495 (2006).

8. S. W. Squyres *et al.*, *J. Geophys. Res.* **111**, E02S11, 10.1029/2005JE002562 (2006).
9. S. W. Ruff *et al.*, *J. Geophys. Res.* **111**, E12S18, 10.1029/2006JE002747 (2006).
10. R. V. Morris *et al.*, *J. Geophys. Res.* **111**, E02S13, 10.1029/2005JE002584 (2006).
11. R. G. Burns, in *Remote Geochemical Analysis: Elemental and Mineralogical Composition*, C. M. Pieters, P. A. J. Englert, Eds., (Cambridge Univ. Press, Cambridge, 1993), pp. 539–556.
12. R. V. Morris *et al.*, Abstract #2014, presented at the 31st Lunar and Planetary Science Conference, Houston, TX, 13 to 17 March 2000 (available on CD-ROM).
13. B. Scaillet, B. Clemente, B. W. Evans, M. Pichavant, *J. Geophys. Res.* **103**, (B10), 23937 10.1029/98JB02301 (1998).
14. L. R. Bernstein, *Geochim. Cosmochim. Acta* **49**, 2409 (1985).
15. R. V. Fisher, A. C. Waters, *Am. J. Sci.* **268**, 157 (1970).
16. K. H. Wohletz, M. F. Sheridan, *Geol. Soc. Am. Spec. Pap.* **180**, 177 (1979).
17. D. M. Rubin, *Cross-Bedding, Bedforms, and Paleocurrents* (Society of Economic Paleontologists and Mineralogists, Tulsa, OK, 1987).
18. J. A. Grant, S. A. Wilson, S. W. Ruff, M. P. Golombek, D. L. Koestler, *Geophys. Res. Lett.* **33**, L16202, 10.1029/2006GL026964 (2006).
19. N. A. Cabrol *et al.*, *J. Geophys. Res.* **108**, (E12), 8076 10.1029/2002JE002026 (2003).

20. This research was carried out for the Jet Propulsion Laboratory, California Institute of Technology, under a contract with the NASA.

Supporting Online Material

www.sciencemag.org/cgi/content/full/316/5825/738/DC1
Figs. S1 to S7
Table S1

19 December 2006; accepted 26 March 2007
10.1126/science.1139045

Local Replenishment of Coral Reef Fish Populations in a Marine Reserve

Glenn R. Almany,[1]* Michael L. Berumen,[1,2] Simon R. Thorrold,[3] Serge Planes,[4] Geoffrey P. Jones[1]

The scale of larval dispersal of marine organisms is important for the design of networks of marine protected areas. We examined the fate of coral reef fish larvae produced at a small island reserve, using a mass-marking method based on maternal transmission of stable isotopes to offspring. Approximately 60% of settled juveniles were spawned at the island, for species with both short (<2 weeks) and long (>1 month) pelagic larval durations. If natal homing of larvae is a common life-history strategy, the appropriate spatial scales for the management and conservation of coral reefs are likely to be much smaller than previously assumed.

Many of the desired outcomes of marine protected areas (MPAs) in fisheries management and biodiversity conservation rely on untested assumptions about the degree to which fish populations are connected by larval dispersal (*1*–*3*). Connectivity is a critical parameter in models for optimizing the size and spacing of MPAs (*4*–*6*), but the scarcity of direct information on larval dispersal limits the models' utility (*7*). Because larvae typically spend times ranging from days to months in the pelagic environment before seeking suitable habitat to begin adult life, direct measurements of connectivity are challenging (*7*–*9*). Thus, although larvae have the potential to travel far from their birthplace, realized dispersal distances are seldom known.

We studied populations of two species of coral reef fishes with different reproductive strategies, occupying a 0.3-km^2 coral reef surrounding a small island that was recently designated an MPA (Kimbe Island in Kimbe Bay, Papua New Guinea). Orange clownfish (*Amphiprion percula*; Pomacentridae) spawn demersal eggs that hatch after several days of parental care, and larvae then spend ~11 days in the pelagic environment. In contrast, vagabond butterflyfish (*Chaetodon vagabundus*; Chaetodontidae) release gametes directly into the water column (that is, there is no parental care), and larvae spend an average of 38 days in the pelagic environment (Fig. 1). The reproductive characteristics of the vagabond butterflyfish are found in most marine fish species and in nearly all species targeted by fisheries throughout the world's oceans.

In December 2004, we tagged larvae using a method whereby mothers transmit stable barium (Ba) isotopes to their offspring before hatching and dispersal (*10*). A total of 176 clownfish females and 123 butterflyfish from the reef surrounding Kimbe Island (Fig. 2) were captured and injected with a $BaCl_2$ solution that was highly enriched in ^{137}Ba and depleted in ^{135}Ba as compared to natural Ba isotope values. In February 2005, we returned to Kimbe Island and collected 15 clownfish and 77 butterflyfish that had recently settled into benthic reef habitats after completing their pelagic larval phase. The analysis of daily growth increments of sagittal otoliths (ear bones) confirmed that each of the recent settlers was born after the injection of the adults with $BaCl_2$. We then quantified Ba isotope ratios in the otolith cores of settlers, using laser ablation inductively coupled plasma mass spectrometry (ICP-MS). Ba isotope ratios in the otoliths of all individuals fell on the theoretical mixing curve between the enriched isotope spike and natural Ba, with values that were similar to those from otoliths of larvae from three reef fish species injected with enriched ^{137}Ba

[1]Australian Research Council Centre of Excellence for Coral Reef Studies and School of Marine and Tropical Biology, James Cook University, Townsville QLD 4811, Australia. [2]Department of Biological Sciences, University of Arkansas, Fayetteville, AR 72701, USA. [3]Department of Biology, Woods Hole Oceanographic Institution, Woods Hole, MA 02543, USA. [4]Joint Research Unit 5244, Ecole Pratique des Hautes Etudes–CNRS, Centre de Biologie et d'Ecologie Tropicale et Mediterraneenne, Universite de Perpignan, F-66860 Perpignan Cedex, France.

*To whom correspondence should be addressed. E-mail: glenn.almany@jcu.edu.au

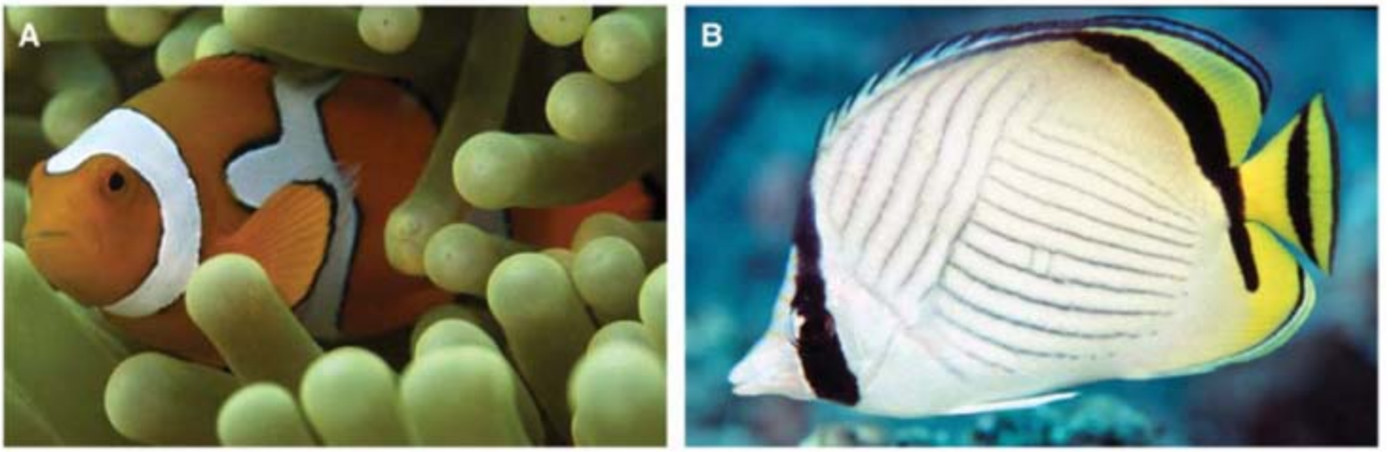

Fig. 1. Study species. An adult (**A**) *A. percula* (photo by S. R. Thorrold) and (**B**) *C. vagabundus* (photo by R. Patzner).

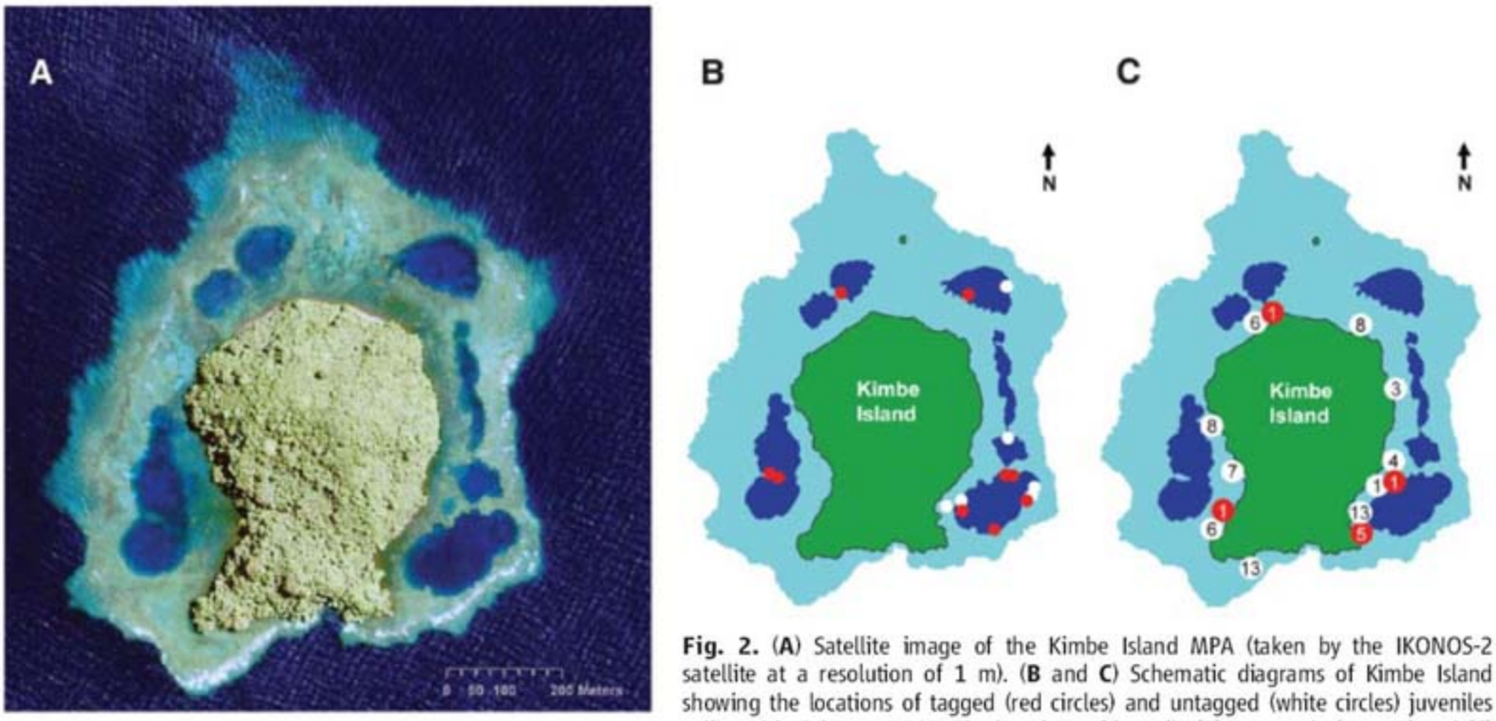

Fig. 2. (**A**) Satellite image of the Kimbe Island MPA (taken by the IKONOS-2 satellite at a resolution of 1 m). (**B** and **C**) Schematic diagrams of Kimbe Island showing the locations of tagged (red circles) and untagged (white circles) juveniles collected in February 2005. The locations of juvenile (B) *A. percula* (n = 15) and (C) *C. vagabundus* (n = 77) are shown. In (C), the number in each circle corresponds to the number of juveniles collected from that location.

under controlled laboratory conditions (Fig. 3). Definitive identification of tagged fish was based on otolith $^{138}Ba/^{137}Ba$ ratios because they converged on the natural ratios much more slowly than did $^{138}Ba/^{135}Ba$ values (Fig. 3). A fish was considered tagged if the $^{138}Ba/^{137}Ba$ ratio of its otolith core was more than 3σ lower than the mean value from measurements of control otoliths (n = 86) assayed throughout the ICP-MS runs.

Otoliths of nine clownfish and eight butterflyfish were identified as tagged based on $^{138}Ba/^{137}Ba$ ratios, providing incontrovertible evidence that these fish had returned to their natal reef (Fig. 3). Assuming that we tagged all clownfish larvae produced from Kimbe Island, 60% of juveniles made the return journey—a conservative estimate if we failed to locate any breeding pairs. For butterflyfish, we estimated the proportion of the total adult population captured and injected with Ba as 17.3% [95% confidence interval (CI): 14.4 to 20.0%) via a population survey conducted after 123 adults had been injected with Ba and externally tagged. Scaling the proportion of tagged juveniles (8 of 77) to the proportion of adults injected with Ba indicated that a remarkable 60.1% (95% CI: 52.0 to 72.2%) of juvenile butterflyfish returned to their natal reef. Tagged juveniles were found in a variety of locations scattered around Kimbe Island, although the larvae of both species that returned settled in the greatest numbers at the southeastern corner of the island (Fig. 2).

Our direct estimate of ~60% self-recruitment for these two species demonstrates that larvae are capable of returning to a very small target reef (only 0.3 km^2), even after an extended larval duration. Although there is much recent indirect evidence for the limited dispersal of marine larvae (*11*), our results, in combination with two previous mark/recapture studies of larval dispersal (*12*, *13*), suggest that self-recruitment in marine fish populations may be common and take place on a smaller scale than previously realized. For example, a recent Caribbean-wide biophysical model of population connectivity in reef fishes highlighted larval capabilities as a key factor determining levels of self-recruitment (*14*). When active larval behavior was introduced in the model within a few days after hatching, self-recruitment of virtual larvae averaged ~21% to reef areas delineated by 450 km^2. In our study, the proportion of self-recruitment was three times greater to a reef more than three orders of magnitude smaller.

The observation that parental habitat is demonstrably of sufficient quality for survival and reproduction provides a compelling argument for the presence of some degree of self-recruitment

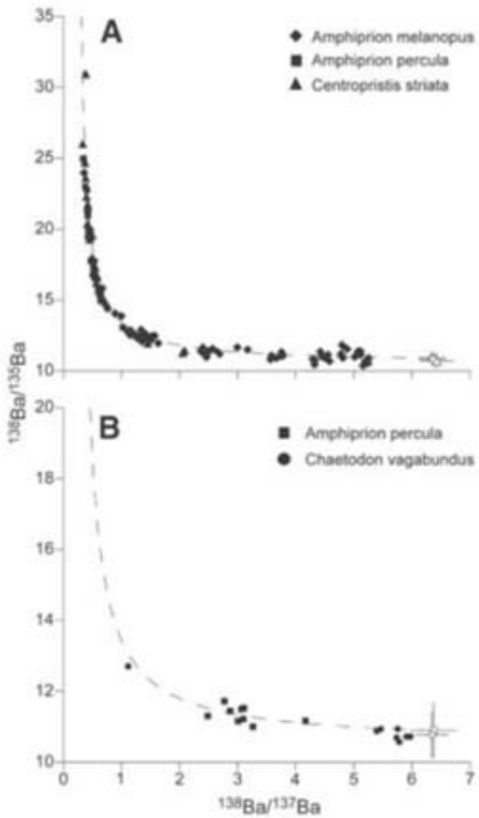

Fig. 3. (**A**) Ba isotope ratios in otolith cores from juveniles of three reef fish species: *A. melanopus* (diamonds), *A. percula* (squares), and *Centropristis striata* (triangles), spawned from females injected with $^{137}BaCl_2$ up to 3 months after the injections and reared in the lab through settlement (*10*); and mean values (±3σ) from controls for each species (open symbols), along with the theoretical mixing curve (dashed line) between the enriched Ba isotope spike and natural Ba ratios. (**B**) Ba isotope ratios in otolith cores of tagged *A. percula* (squares) and *C. vagabundus* (circles) juveniles and mean (±3σ) values from the otoliths of all unmarked juveniles (open symbols), along with the theoretical mixing curve (dashed line) between the enriched Ba isotope spike and natural Ba ratios.

in fish populations. Selection may therefore favor the retention of many larvae, especially if the probability of encountering better adult habitat by dispersing is low (*15*) or advantages accrue through local adaptation (*16*). A number of mechanisms may be used by larvae to avoid being swept away from natal reefs. Field evidence suggests that reef fish larvae migrate vertically in the water column to exploit currents at different depths and thereby avoid dispersal away from spawning locations (*17*). Larvae are also capable of sustained directional swimming soon after hatching (*18*), and possess a range of well-developed sensory systems to locate and orient to reefs, including sight, smell, and sound (*18*–*21*).

Despite the high levels of self-recruitment we detected, ~40% of juveniles of both species came from outside the MPA. The reef nearest to Kimbe Island is 10 km away, and reefs in this region are typically separated by 5 to 20 km. Ecologically important larval exchange must occur between populations at these scales. Thus, the Kimbe Island MPA is likely to be self-sustaining as well as providing recruitment subsidies to populations beyond its boundaries. Although levels of retention and connectivity may differ where reefs are closer and populations are less isolated, the Kimbe Island example sets a new boundary condition for the scale at which self-recruitment can occur.

Ideally, the size and spacing of marine reserves should be predicated on an understanding of larval dispersal distances (*3*–*6*, *22*). The optimal design should be one in which individual MPAs are large enough so that populations within reserves can sustain themselves, yet small enough and spaced so that a proportion of larvae produced inside the MPA is exported to unprotected areas (*3*, *5*, *12*). Our study suggests that the spatial scale at which coral reef MPAs can achieve these dual goals may be relatively small. However, if natal homing and larval retention are common, some MPAs may fail to deliver substantial recruitment subsidies to locations beyond their boundaries. We therefore support recent suggestions (*23*, *24*) that MPA networks should be combined with conventional management strategies to both protect threatened species and ensure the sustainability of fisheries on coral reefs.

References and Notes

1. E. Sala *et al.*, *Science* **298**, 1991 (2002).
2. F. R. Gell, C. M. Roberts, *Trends Ecol. Evol.* **18**, 448 (2003).
3. B. S. Halpern, R. R. Warner, *Proc. R. Soc. London Ser. B* **270**, 1871 (2003).
4. L. W. Botsford, A. Hastings, S. D. Gaines, *Ecol. Lett.* **4**, 144 (2001).
5. A. L. Shanks, B. A. Grantham, M. H. Carr, *Ecol. Appl.* **13**, S159 (2003).
6. S. R. Palumbi, *Ecol. Appl.* **13**, S146 (2003).
7. P. F. Sale *et al.*, *Trends Ecol. Evol.* **20**, 74 (2005).
8. R. R. Warner, R. K. Cowen, *Bull. Mar. Sci.* **70**, 245 (2002).
9. S. R. Thorrold *et al.*, *Bull. Mar. Sci.* **70**, 291 (2002).
10. S. R. Thorrold, G. P. Jones, S. Planes, J. A. Hare, *Can. J. Fish. Aquat. Sci.* **63**, 1193 (2006).
11. S. E. Swearer *et al.*, *Bull. Mar. Sci.* **70**, 251 (2002).
12. G. P. Jones, S. Planes, S. R. Thorrold, *Curr. Biol.* **15**, 1314 (2005).
13. G. P. Jones, M. J. Milicich, M. J. Emslie, C. Lunow, *Nature* **402**, 802 (1999).
14. R. K. Cowen, C. B. Paris, A. Srinivasan, *Science* **311**, 522 (2006).
15. R. R. Strathmann *et al.*, *Bull. Mar. Sci.* **70**, 377 (2002).
16. D. O. Conover, L. M. Clarke, S. B. Munch, G. N. Wagner, *J. Fish Biol.* **69**, 21 (2006).
17. C. B. Paris, R. K. Cowen, *Limnol. Oceanogr.* **49**, 1964 (2004).
18. J. M. Leis, *Adv. Mar. Biol.* **51**, 57 (2006).
19. G. Gerlach, J. Atema, M. J. Kingsford, K. P. Black, V. Miller-Sims, *Proc. Natl. Acad. Sci. U.S.A.* **104**, 858 (2007).
20. D. Lecchini, J. Shima, B. Banaigs, R. Galzin, *Oecologia* **143**, 326 (2005).
21. S. D. Simpson, M. Meekan, J. Montgomery, R. McCauley, A. Jeffs, *Science* **308**, 221 (2005).
22. L. W. Botsford, F. Micheli, A. Hastings, *Ecol. Appl.* **13**, S25 (2003).
23. R. Hilborn, F. Micheli, G. A. De Leo, *Can. J. Fish. Aquat. Sci.* **63**, 642 (2006).
24. L. W. Botsford, *Bull. Mar. Sci.* **76**, 245 (2005).

25. We thank S. Sheppard of The Nature Conservancy for satellite imagery analyses; E. Laman-Trip for aging juvenile butterflyfish; J. Almany, D. DeVere, N. Gardiner, V. Messmer, M. Srinivasan, C. Syms, and H. Walsh for field and lab assistance; and the Global Environmental Fund, Connectivity Working Group, for providing a forum for discussing different approaches to evaluating marine connectivity. This project was financially supported by an Australian Research Council (ARC) Discovery Grant (DP0208120), the ARC Centre of Excellence for Coral Reef Studies, a Coral Reef Initiative for the South Pacific grant, and NSF through an International Research Fellowship to G.R.A. and grants OCE-0215905 and OCE-0424688.

Supporting Online Material

www.sciencemag.org/cgi/content/full/316/5825/742/DC1
Materials and Methods
References

30 January 2007; accepted 2 April 2007
10.1126/science.1140597

Developmentally Regulated piRNA Clusters Implicate MILI in Transposon Control

Alexei A. Aravin, Ravi Sachidanandam, Angelique Girard, Katalin Fejes-Toth, Gregory J. Hannon*

Nearly half of the mammalian genome is composed of repeated sequences. In *Drosophila*, Piwi proteins exert control over transposons. However, mammalian Piwi proteins, MIWI and MILI, partner with Piwi-interacting RNAs (piRNAs) that are depleted of repeat sequences, which raises questions about a role for mammalian Piwi's in transposon control. A search for murine small RNAs that might program Piwi proteins for transposon suppression revealed developmentally regulated piRNA loci, some of which resemble transposon master control loci of *Drosophila*. We also find evidence of an adaptive amplification loop in which MILI catalyzes the formation of piRNA 5′ ends. *Mili* mutants derepress LINE-1 (L1) and intracisternal A particle and lose DNA methylation of L1 elements, demonstrating an evolutionarily conserved role for PIWI proteins in transposon suppression.

Known piRNAs are not expressed until spermatocytes first enter mid-prophase (pachytene stage) at ~14 days after birth (P14) (*1*–*4*). However, *Mili* expression begins in primordial germ cells at embryonic day 12.5 (*5*, *6*), and transposons, such as L1, can be expressed in both premeiotic and meiotic germ cells (*7*, *8*). We therefore probed a connection between *Mili* and transposon control by examining MILI-bound small RNAs in early-stage spermatocytes. Notably, MILI-associated RNAs could be detected at all developmental time points tested (Fig. 1 and fig. S1). Northern blotting revealed that pre-pachytene piRNAs join MILI before pachytene piRNAs become expressed at P14 (Fig. 1B). The appearance of pre-pachytene piRNAs was MILI-dependent, suggesting a requirement for this protein in either their biogenesis or stability (Fig. 1C). These results raised the possibility that MILI might be programmed by distinct piRNA populations at different stages of germ cell development.

To characterize pre-pachytene piRNAs, we isolated MILI complexes from P10 testes and deeply sequenced their constituent small RNAs. Like pachytene populations, pre-pachytene piRNAs were quite diverse, with 84% being cloned only once. The majority of both pre-pachytene (66.8%) and pachytene (82.9%) piRNAs map to single genomic locations. However, a substantial fraction (20.1%) of pre-pachytene piRNAs had more than 10 genomic matches, as compared to 1.6% for pachytene piRNAs.

Annotation of pre-pachytene piRNAs revealed three major classes (Fig. 2A). The largest (35%) corresponded to repeats, with most matching short interspersed elements (SINEs) (49%), long interspersed elements (LINEs) (15.8%), and long terminal repeat (LTR) retrotransposons (33.8%). Although pachytene piRNAs also match repeats (17%), the majority (>80%) map

Watson School of Biological Sciences, Cold Spring Harbor Laboratory, Howard Hughes Medical Institute (HHMI), 1 Bungtown Road, Cold Spring Harbor, NY 11724, USA.

*To whom correspondence should be addressed. E-mail: hannon@cshl.edu

uniquely in the genome, with only 1.8% mapping more than 1000 times (fig. S2). In contrast, 22% of repeat-derived pre-pachytene piRNAs map more than 1000 times and correspond closely to consensus sequences for SINE B1, LINE L1, and IAP retrotransposons (fig. S2). A second abundant class of pre-pachytene piRNAs (29%) matched genic sequences, including both exons (22%) and introns (7%). A third class matched sequences without any annotation (28%). All three major classes shared signature piRNA characteristics, including a preference for a uridine (U) at their 5′ end (>80%) (Fig. 2A).

Pachytene piRNAs derive from relatively few extended genomic regions, with hundreds to thousands of different species encoded from a single genomic strand (*1*, *3*, *4*). Cluster analysis of pre-pachytene piRNAs yielded 909 loci, covering ~0.2% of the mouse genome (5.3 megabases; table S1). Pachytene and pre-pachytene clusters show little overlap (Fig. 2, B and C, and table S1). Overall, pachytene clusters were larger, and each produced a greater fraction of the piRNA population than early clusters, which average 5.8 kb in size (Fig. 2B). Only 56.5% of uniquely mapped pre-pachytene piRNAs can be attributed to clusters, as compared to 95.5% in pachytene piRNA populations. Considered together, these results demonstrate that pre-pachytene and pachytene piRNAs are derived from different genomic locations, with pre-pachytene piRNAs being produced from a broader set of loci.

We were unable to intuit the functional importance of those pre-pachytene clusters that correspond solely to unannotated regions of the genome. The 28% of pre-pachytene piRNAs that correspond to protein coding genes were concentrated in 3′ untranslated regions (3′UTRs) (fig. S3) and showed a strong bias for certain loci, with 8% of the total coming from only 10 genes. However, these were invariably derived from the sense strand, implying that these piRNAs would

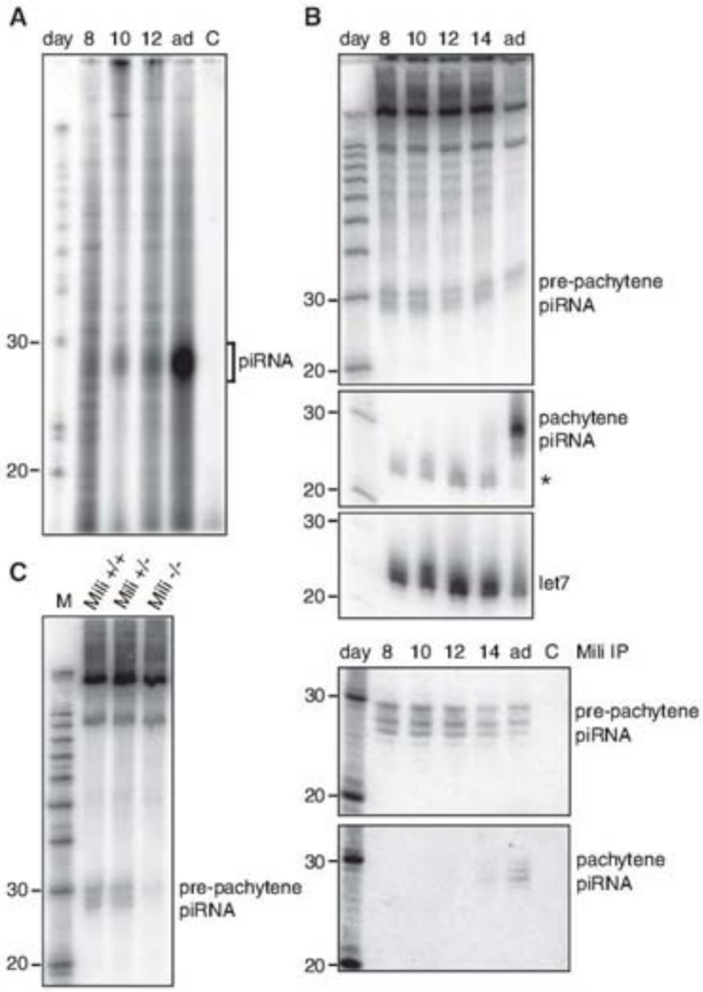

Fig. 1. MILI associates with distinct small RNA populations during spermatogenesis. (**A**) MILI-associated RNAs were analyzed from testes of 8-, 10-, and 12-day-old and adult (ad) mice. C, control immunoprecipitation. (**B**) Testes RNA (three top panels) or RNA from MILI immunoprecipitates (IP) (two bottom panels) from mice of indicated ages was analyzed by Northern blotting for a pre-pachytene piRNA, a pachytene piRNA, or let-7. The asterisk indicates the residual let-7 signal. (**C**) Northern hybridization of RNA isolated from P10 testes of WT mice and *Mili*-heterozygous and *Mili*-homozygous mutants, as indicated. The probe is as in (B). M, RNA size markers.

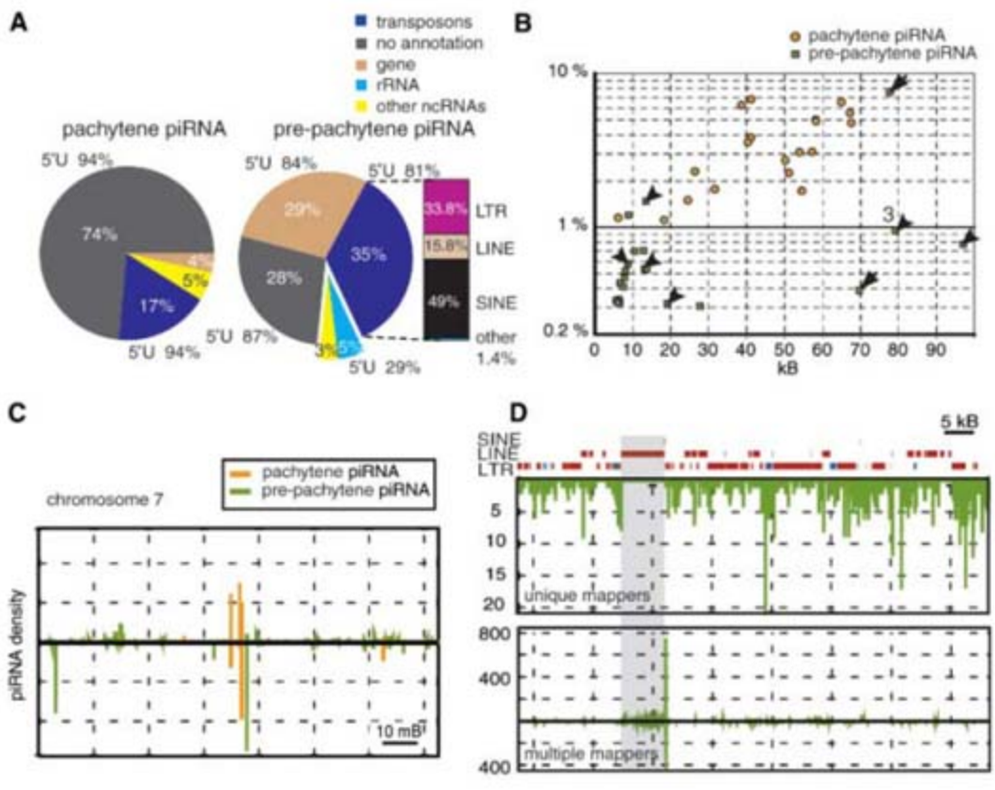

Fig. 2. Characteristics of pachytene and pre-pachytene piRNAs. (**A**) Genomic annotation of piRNA populations and the fraction of sequences with a 5′ U are indicated. rRNA, ribosomal RNA; ncRNA, noncoding RNA. (**B**) The top 20 pachytene and pre-pachytene piRNA clusters are displayed according to the fraction of uniquely mapped piRNAs produced (*y* axis) and cluster sizes (*x* axis). The cluster on chromosome 17, expressed at both stages, is marked with an arrow. Pre-pachytene clusters, enriched in repeat-derived piRNAs, are marked with arrowheads. (**C**) The density of uniquely mapped piRNAs on chromosome 7 is plotted for the plus and minus genomic strands (above and below the axis, respectively). (**D**) Transposable element fragments and piRNA density are plotted for a repeat-rich pre-pachytene piRNA cluster ["3" in (B)]. Elements, separated by type, are indicated as red boxes on the plus strand and as blue boxes on the minus strand. Gray shadowing indicates LINE and adjacent SINE fragments that closely match their consensus.

be unable to direct posttranscriptional gene silencing. Using semiquantitative reverse transcription polymerase chain reaction (RT-PCR), we were unable to detect differences in the expression of genes corresponding to piRNA clusters by comparing wild-type (WT) to *Mili*-mutant animals. We do not yet understand what distinguishes genes that contribute piRNAs but do note that at least some have repetitive elements resident in their 3′UTRs (fig. S3).

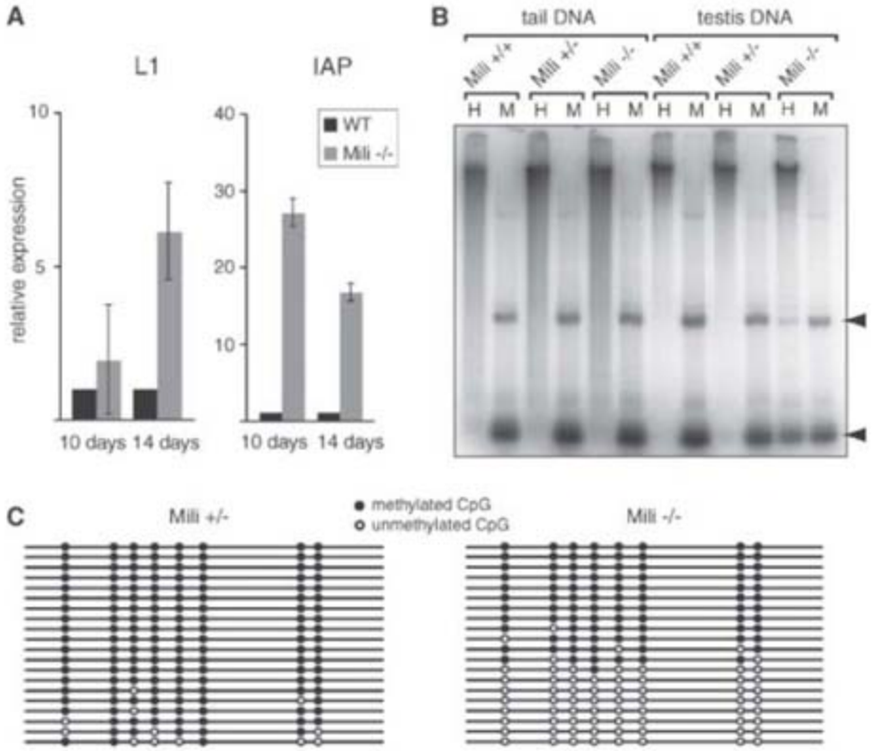

Fig. 3. *Mili* regulates L1 and IAP elements. (**A**) Quantitative RT-PCR for IAP and L1 expression in testes from WT or *Mili*-null mice, as indicated. Expression was assessed at P10 and P14. Error bars indicate SD. (**B**) DNA was isolated from the tails or testes of $Mili^{+/+}$, $Mili^{+/-}$, or $Mili^{-/-}$ animals; digested with either a methylation-insensitive [Msp I (M)] or a methylation-sensitive [Hpa II (H)] restriction enzyme; and used in a Southern blot with a probe from the LINE-1 5′UTR. Arrowheads indicate bands arising from loss of methylation in the Mili-null animals. (**C**) Bisulfite sequencing of the first 150 bases of a specific L1 element was done in $Mili^{+/-}$ or $Mili^{-/-}$ animals.

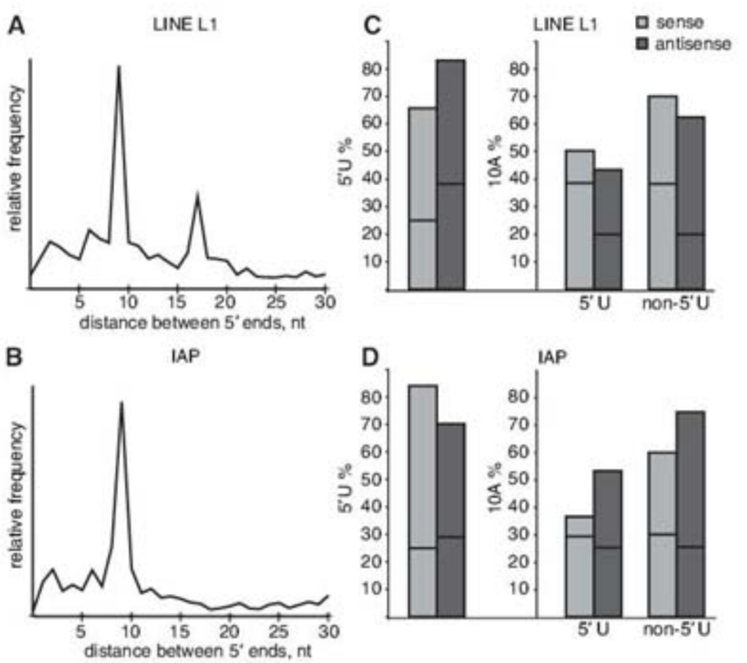

Fig. 4. A Piwi-mediated piRNA amplification loop in mammals. L1 (**A**) and IAP (**B**) piRNAs were aligned to their consensus sequences allowing up to three mismatches, and distances separating 5′ ends of complementary piRNA were plotted. nt, nucleotide. Nucleotide biases were calculated for L1 (**C**) and IAP (**D**) piRNAs analyzed in (A) and (B). The fraction of A at position 10 was plotted both for piRNA classes that contain and lack a 5′ U. For each bar, the percentage of U or A residues that would be expected by random sampling is indicated by a solid line across the bar.

Clusters that are rich in transposon sequences were among the most prominent, as judged by either their size or the number of piRNAs that they generate. Two of these were the largest prepachytene clusters (97 and 79 kb, respectively). Although uniquely mapping piRNAs were derived largely from one genomic strand, the mixed orientations of transposable elements within clusters led to the production of both sense and antisense piRNAs. As is observed in *Drosophila*, repeat-rich mouse piRNA clusters typically contained multiple element types, many of which comprise damaged or fragmented copies (*9*). In many repeat-rich clusters, the orientation of most elements was similar. For example, similarly oriented elements in the two longest clusters (Fig. 2D and table S1) resulted in the production of mainly antisense piRNAs, similar to the *flamenco* piRNA locus in *Drosophila* (*9*, *10*).

We examined the possibility that prepachytene piRNAs might program MILI to repress transposon activity. *Mili* mutation showed substantial effects on L1 and IAP expression, with each increasing its levels by a factor of at least 5 to 10 (Fig. 3A). These studies were carried out at P10 and P14, before an overt *Mili* phenotype becomes apparent.

Although posttranscriptional mechanisms likely contribute to silencing, CpG methylation is critical for transposon repression in mammals (*11*–*16*). Both analysis with methylation-sensitive restriction enzymes and bisulfite DNA sequencing revealed substantial demethylation of L1 elements in *Mili*-mutant testes (Fig. 3, B and C). In the latter case, the ~50% of L1 sequences that remain methylated in the mutant are likely derived from the somatic compartment. Considered together, our data suggest that pre-pachytene piRNAs might help to guide methylation of L1 elements, although we cannot distinguish between roles in de novo versus maintenance methylation.

In *Drosophila*, Piwi-mediated cleavage promotes the formation of secondary piRNAs (*9*, *17*). This allows active transposons and piRNA clusters to participate in a feed-forward loop that both degrades transposon mRNAs and amplifies silencing (*9*). The presence of both sense and antisense piRNAs from mammalian transposable elements creates the potential for engagement of a similar amplification cycle. This cycle creates two tell-tale features. First, because Piwi proteins cleave targets opposite nucleotides 10 and 11 of the guide, piRNAs generated within the loop overlap their partners by precisely 10 nucleotides (*9*, *17*). As predicted, we observed enrichment for piRNAs corresponding to L1 and IAP retrotransposons, in which the 5′ ends of sense and antisense partners are separated by precisely 10 nucleotides (Fig. 4, A and B). Second, because most piRNAs begin with a U, piRNAs produced by Piwi-mediated cleavage are enriched for adenine (A) at position 10 (*9*, *17*). This bias was prevalent in L1- and IAP-derived piRNAs [the fraction of A at position 10 (10A) in

Fig. 4, C and D]. For piRNAs to be cleavage-competent and active in the amplification cycle, they must retain a high degree of complementarity to their targets (fig. S4). Consistent with this hypothesis, piRNAs that map uniquely in the genome have a lower bias for 10A (e.g., 38.7% for non-5′U piRNAs matching LTR-containing retrotransposons) than do piRNAs with many (e.g., >1000) genomic matches (61.5%).

Our results suggest a conserved pathway through which a developmentally regulated cascade of piRNA clusters programs Piwi proteins to repress transposons in mammals. One key difference between transposon control in *Drosophila* and mammals is the role of cytosine methylation in maintaining stable repression. In plants, it is well established that small RNAs can guide methylation of complementary sequences (*18*, *19*). The observations that *Miwi2* (*20*) and *Mili* mutations strongly affect methylation of L1 elements and that MILI binds L1-targeted small RNAs suggest that mammals may also harbor an RNA-dependent DNA methylation pathway.

References and Notes

1. N. C. Lau *et al.*, *Science* **313**, 363 (2006).
2. S. T. Grivna, E. Beyret, Z. Wang, H. Lin, *Genes Dev.* **20**, 1709 (2006).
3. A. Aravin *et al.*, *Nature* **442**, 203 (2006).
4. A. Girard, R. Sachidanandam, G. J. Hannon, M. A. Carmell, *Nature* **442**, 199 (2006).
5. S. Kuramochi-Miyagawa *et al.*, *Mech. Dev.* **108**, 121 (2001).
6. S. Kuramochi-Miyagawa *et al.*, *Development* **131**, 839 (2004).
7. H. H. Kazazian Jr., *Science* **303**, 1626 (2004).
8. D. Branciforte, S. L. Martin, *Mol. Cell. Biol.* **14**, 2584 (1994).
9. J. Brennecke *et al.*, *Cell* **128**, 1089 (2007).
10. A. Bucheton, *Trends Genet.* **11**, 349 (1995).
11. G. Liang *et al.*, *Mol. Cell Biol.* **22**, 480 (2002).
12. F. Gaudet *et al.*, *Mol. Cell Biol.* **24**, 1640 (2004).
13. Z. Lippman, B. May, C. Yordan, T. Singer, R. Martienssen, *PLoS Biol.* **1**, E67 (2003).
14. D. Bourc'his, T. H. Bestor, *Nature* **431**, 96 (2004).
15. J. A. Yoder, C. P. Walsh, T. H. Bestor, *Trends Genet.* **13**, 335 (1997).
16. T. H. Bestor, D. Bourc'his, *Cold Spring Harbor Symp. Quant. Biol.* **69**, 381 (2004).
17. L. S. Gunawardane *et al.*, *Science* **315**, 1587 (2007).
18. W. Aufsatz, M. F. Mette, J. van der Winden, A. J. Matzke, M. Matzke, *Proc. Natl. Acad. Sci. U.S.A.* **99** (suppl. 4), 16499 (2002).
19. O. Mathieu, J. Bender, *J. Cell Sci.* **117**, 4881 (2004).
20. M. A. Carmell *et al.*, *Dev. Cell* **12**, 503 (2007).
21. piRNA sequences are available in the Gene Expression Omnibus (GEO) database (accession # GSE7414). We thank H. Lin (Yale University) for the *Mili* knockout mouse. A.A.A. is supported by a Cold Spring Harbor Laboratory Association fellowship. A.G. is a Florence Gould Fellow of the Watson School of Biological Sciences. G.J.H. is an HHMI investigator. This work was supported by grants from NIH and from Katherine W. Davis (G.J.H.).

Supporting Online Material

www.sciencemag.org/cgi/content/full/1142612/DC1
Materials and Methods
Figs. S1 to S4
Table S1
References

16 March 2007; accepted 30 March 2007
Published online 19 April 2007;
10.1126/science.1142612
Include this information when citing this paper.

Protein Dynamics Control the Kinetics of Initial Electron Transfer in Photosynthesis

Haiyu Wang,[1,2] Su Lin,[1,2] James P. Allen,[2] JoAnn C. Williams,[2] Sean Blankert,[1,2] Christa Laser,[1,2] Neal W. Woodbury[1,2]*

The initial electron transfer dynamics during photosynthesis have been studied in *Rhodobacter sphaeroides* reaction centers from wild type and 14 mutants in which the driving force and the kinetics of charge separation vary over a broad range. Surprisingly, the protein relaxation kinetics, as measured by tryptophan absorbance changes, are invariant in these mutants. By applying a reaction-diffusion model, we can fit the complex electron transfer kinetics of each mutant quantitatively, varying only the driving force. These results indicate that initial photosynthetic charge separation is limited by protein dynamics rather than by a static electron transfer barrier.

Solar energy conversion in photosynthesis involves electron transfer between an excited donor molecule and a neighboring acceptor molecule that are embedded in the reaction center, an intrinsic membrane protein-pigment complex. In the photosynthetic reaction centers of *Rhodobacter sphaeroides*, an excited electron donor, P* (P is a pair of bacteriochlorophylls) transfers an electron in picoseconds to a neighboring bacteriochlorophyll, B_A, and subsequently to a bacteriopheophytin, H_A (Fig. 1). The state $P^+H_A^-$ exists for about 200 ps before the electron is transferred to a quinone Q_A (*1*–*3*). One aspect of reaction center function that is challenging to understand quantitatively is the dependence of the initial charge separation kinetics on driving force (the free energy difference between P* and the initial charge-separated state). Many mutants with altered standard free energies for the initial charge separation have been studied, and in general the dependence of the electron transfer rate on driving force is not consistent with the weak temperature dependence of this reaction (*4*–*6*). Additionally, the kinetics of the charge separation are complex, requiring multiple decay components for an accurate description in both wild-type and mutant reaction centers (*4*–*8*). Many different kinetic models have been developed to explain these features on the basis of vibrational nonequilibrium (*9*–*11*), static inhomogeneity (*4*, *7*, *12*), and multiple interacting states (*8*, *13*). However, none of these quantitatively predicts the complex reaction center kinetics as a function of driving force.

The protein environment of the reaction center represents an inhomogeneous solvent, which relaxes upon excitation and charge separation over many different time scales (*11*, *14*–*16*). Thus, a complete model of electron transfer must take into account protein motion, a concept suggested previously by Chandler and co-workers on the basis of molecular dynamics simulations (*15*). Molecular dynamics simulations modeling the electron transfer reaction, as pioneered by Warshel and Parson (*11*, *14*), suggest that the energy fluctuations between states due to protein movement are correlated with initial electron transfer kinetics.

The structure-based theoretical treatments described above give detailed mechanistic information but are challenging to apply directly to the analysis of experimental data. Fortunately, simplified models have been developed to describe electron transfer between small molecules in viscous solvents, resulting in the reduction of the solvent motion to one or two generalized dimensions (*17*–*19*). One way to represent such a reaction is to divide the solvent response (the solvent reorganization) into two dimensions: the instantaneous response of the solvent (much faster than electron transfer) and the slower, longer-range solvent reorganization that occurs on the time scale of electron transfer and longer. For this situation, the kinetic time course can be described by the reaction-diffusion equation (*19*)

$$\frac{\partial \rho(x,t)}{\partial t} = [\hat{L} - K(x)]\rho(x,t) \qquad (1)$$

Here, $\rho(x,t)$ is the distribution of the initial electron donor state (P*) along a reaction coordinate, x, as a function of time, t. The reaction coordinate x is associated with the motion of the solvent (protein) on the time scale of the electron transfer. $K(x)$ is the rate constant for electron transfer at the reaction coordinate position x (*20*):

$$K(x) = \frac{J^2}{h}\sqrt{\frac{\pi}{\lambda_f k_B T}}\exp\left[-\frac{(\Delta G^0 + \lambda - 2x\sqrt{\lambda_p})^2}{4\lambda_f k_B T}\right] \qquad (2)$$

where J is the electronic coupling matrix element; ΔG^0 is the standard free energy difference between the reactants and the products; λ is the total

[1]Biodesign Institute, Arizona State University, 1001 South McAllister Avenue, Tempe, AZ 85287–5201, USA. [2]Department of Chemistry and Biochemistry, Arizona State University, Tempe, AZ 85287–1604, USA.

*To whom correspondence should be addressed. E-mail: Nwoodbury@asu.edu

reorganization energy and represents the sum of λ_f (nuclear relaxation that is fast on the time scale of charge separation) and λ_p (protein relaxation along the reaction coordinate x that is comparable to or slower than charge separation); and k_B and T are the Boltzmann constant and temperature, respectively. In Eq. 1, $\hat{L}$ is an operator that describes the time-dependent movement and diffusion of the protein along the reaction coordinate x. $\hat{L}$ is proportional to a diffusion rate that, for complex solvents such as proteins, is a function of time and is derived from the time course of the dielectric solvent relaxation, $C_p(t)$ (see below and eq. S2). Lastly, the observable time-dependent population of the electron donor, $P^*(t)$, is given by

$$P^*(t) = \int \rho(x,t)dx \qquad (3)$$

The difficulty in applying this formalism to the analysis of electron transfer dynamics in the reaction center is that the time course of protein relaxation, $C_p(t)$, is unknown and hence the operator $\hat{L}$ cannot be determined. One approach for the empirical determination of $C_p(t)$ is to monitor the tryptophan absorbance as a function of time. Tryptophan has a large difference dipole between the excited and ground states, making its absorbance spectrum and oscillator strength sensitive to the dielectric nature of its surroundings (*21*–*23*).

The reaction center contains 39 tryptophan residues in the L and M subunits, with L156W and M185W (*24*) being closest to the cofactors involved in initial electron transfer (Fig. 1). Initiation of the electron transfer reaction by excitation in the near-infrared region results in a transient change in the absorbance at 280 nm, which is near the peak of the tryptophan absorbance band. Figure 2A shows the transient signal at 280 nm in wild-type reaction centers. This transient signal can be fit by two short time constants (3 ps and 10 ps) and one long constant (190 ps). The quinones were removed from the reaction centers for these measurements because they also absorb in the 280-nm region, resulting in an additional transient on the 200-ps time scale because of electron transfer from H_A to Q_A (the 280-nm signal from reaction centers with and without quinones are compared in fig. S1). There are two lines of evidence that the 280-nm signal that remains upon quinone removal arises from absorbance changes in tryptophan. First, when M185W and L156W were both mutated to nontryptophan residues, the 10-ps and 190-ps components of the transient were

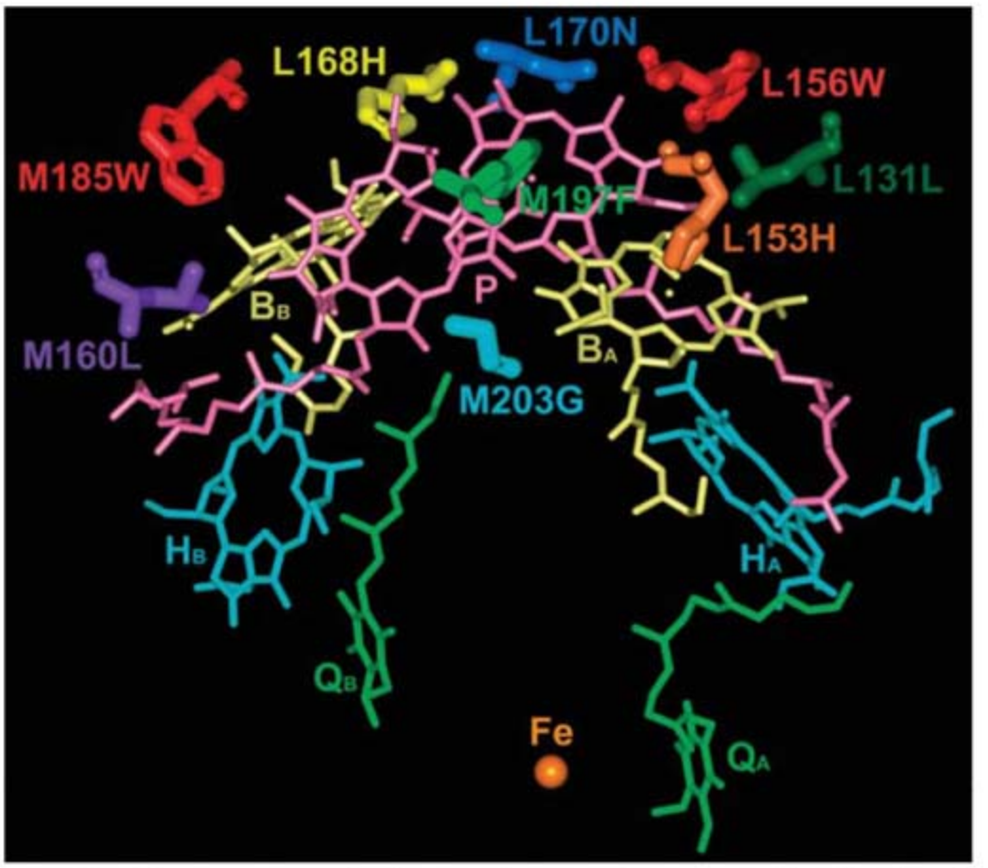

Fig. 1. The cofactor arrangement of wild-type reaction centers from *R. sphaeroides*. P is a bacteriochlorophyll dimer. B_A and B_B are bacteriochlorophyll monomers. H_A and H_B are bacteriopheophytins. Q_A and Q_B are ubiquinones. The A and B subscripts denote the two potential electron transfer branches (A is the active side in wild type). The amino acid residues that were altered to vary the driving force for electron transfer are shown in shades of blue, green, yellow, purple, and orange. There were a total of 14 different electron transfer mutants used in this study, including single, double, and triple mutants of the residues shown. These are L131LH (*24*), L168HF, M160LH, and M197FH [all mutants that alter hydrogen bonding to P (*26*)]; M203GL [making B_A harder to reduce (*25*)]; L153HF, L153HV, L153HS, and L153HD [all alter the histidine that coordinates the Mg in B_A, making it harder to reduce (*28*)]; L170ND and L168HE [both introduce charges in the vicinity of P (*27*)]; as well as the double mutants L131LH+M160LH and L131LH+M197FH (*26*) and the triple mutant L131LH+M160LH+M197FH (*29*). In addition, two tryptophan residues (shown in red) near the cofactors involved in initial electron transfer have been mutated both singly and together, resulting in the mutants L156WF, M185WY, and L156WF+M185WY.

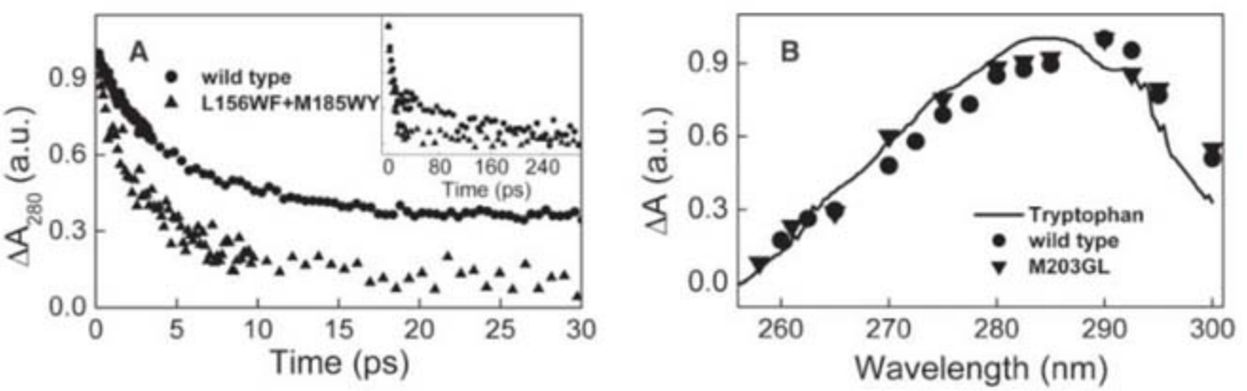

Fig. 2. (**A**) Comparison of the time-dependent changes in the tryptophan absorbance band at 280 nm in quinone-removed reaction centers from wild type (average of 10 traces) and the L156WF+M185WY mutant (average of two traces). (Inset) The same kinetics on a longer time scale. (**B**) The difference in the absorbance spectrum measured at 1 ps and 30 ps for quinone-removed wild-type (circles) and M203GL (triangles) reaction centers. All points represent an average of three measurements, and the error in the mean is about ±0.05 on the scale given. The solid line is the absorbance spectrum of an individual tryptophan (Trp^{94}) in the enzyme barnase [taken from figure 2 in (*21*)]. a.u., arbitrary units.

greatly decreased relative to the 3-ps component (Fig. 2A). The individual mutations result in smaller perturbations of the 280-nm signal. The kinetics of electron transfer do not change in either the single or the double tryptophan mutants. In contrast, mutants with modifications at the seven nontryptophan residues shown in Fig. 1 changed the electron transfer rate constant by as much as an order of magnitude but did not detectably alter the 280-nm transient. Second, the amplitude spectrum of the 280-nm transient (Fig. 2B) is essentially identical to the ground state spectrum of a single tryptophan residue in the enzyme barnase (*21*). This is true both for wild-type reaction centers and for the mutant M203GL (Fig. 1) (*24*, *25*) that undergoes electron transfer an order of magnitude more slowly than wild type (Fig. 2B). Thus, the 280-nm transient absorbance signal is sensitive to local tryptophan mutations and has the spectral characteristics of tryptophan, implying that it reflects changes in the protein environment probed by local tryptophan residues. This signal was used to provide an experimental measure of the protein dynamics during initial electron transfer [i.e., to determine $C_p(t)$].

The protein dynamics probed in this way were compared with the kinetics of initial electron transfer determined by following the decay of the 930-nm stimulated emission signal from P* (Fig. 3). In addition to wild type, measurements were performed on 14 reaction center mutants, all of which are thought to primarily affect the driving force for the initial electron transfer rather than reaction center structure or dynamics (Fig. 1 legend). The overall electron transfer kinetics in these mutants vary by more than an order of magnitude, from about 2 ps to tens of picoseconds (Fig. 3A and fig. S2A) (*25*–*29*). One might expect that protein relaxation would simply follow the time course of electron transfer in each mutant. In other words, the formation of the charge-separated state would be rate limiting, and protein relaxation would track this reaction. In contrast, the transient signal at 280 nm for all of these mutants is the same within experimental error (Fig. 3B and fig. S2B) (*30*). The invariance of the tryptophan signal across mutants with widely varying electron transfer dynamics leads to a notable conclusion: The local protein movement initiated by formation of the initial excited state of the reaction center is independent of the kinetics of charge separation on the picosecond time scale.

Because the protein relaxation on the picosecond time scale is independent of electron transfer kinetics, this movement must be initiated by events occurring at very early times upon light absorption. In this view, it is possible that the kinetics of the electron transfer reaction are strongly influenced by protein dynamics, rather than the protein simply responding to charge separation. This would be true if the inherent rate of charge separation is fast once the protein, responding to an initial excitation event, has achieved an appropriate nuclear configuration. In that case, protein dynamics control the overall electron transfer kinetics, and the dielectric relaxation term in the reaction-diffusion model has a large effect. To test this concept, we used the multiexponential fit of the 280-nm transient from quinone-removed reaction centers as the dielectric relaxation function, $C_p(t)$, to determine $\hat{L}$ in Eq. 1 [see (*20*) for the detailed relationship between $\hat{L}$ and $C_p(t)$]. The measured P* decay kinetics was then fit to this expression (fitting parameters given in Fig. 3 legend). The key finding in this work is that, for all 14 mutants, it was only necessary to adjust ΔG^0 during the fitting to obtain excellent fits of the complex kinetic traces (the fits to five mutants are shown in Fig. 3A, and the rest are given in fig. S2A); all other parameters in the fit were held constant (*31*). The values of the driving force for initial electron transfer for each of the 14 mutants relative to that of wild type ($\Delta\Delta G^0_{fit}$) are given in the Fig. 3 legend and in table S1 (*32*).

Two lines of evidence suggest that the relative free energy changes resulting from these fits are reasonable. First, for each of the double and triple mutants tested, the overall $\Delta\Delta G^0_{fit}$ is in fact very close to the sum of the individual

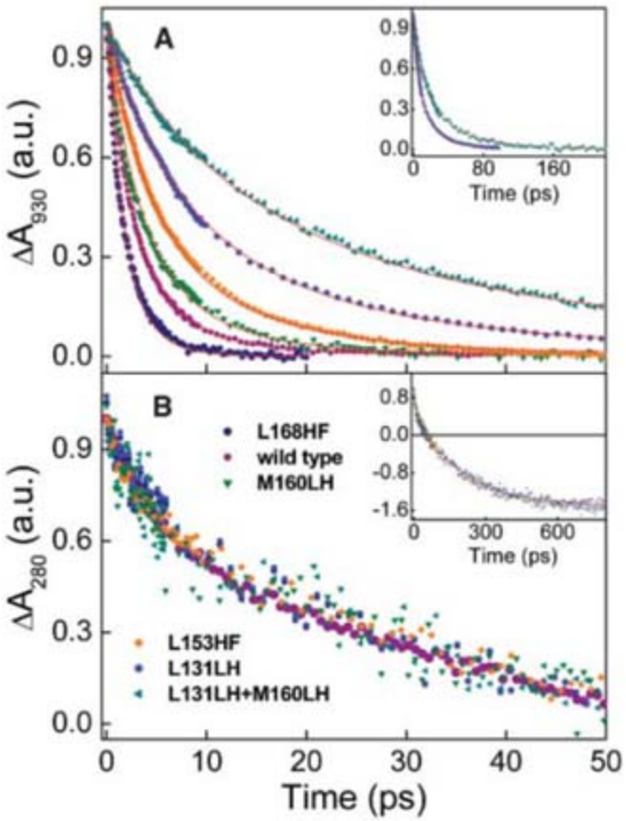

Fig. 3. (**A**) Charge separation kinetics of reaction centers from wild type and 14 mutants determined from transient absorbance changes at 930 nm (stimulated emission from P*) by using 860-nm excitation. Five of those mutants (L168HF, M160LH, L153HF, L131LH, and L131LH+M160LH) are shown here, and the rest are given in fig. S2A. The solid lines are fitting results with use of the reaction-diffusion model. The fitting parameters used for wild-type reaction centers are $(\Delta G^0 + \lambda) = 150$ meV, $J = 39$ cm^{-1}, $\lambda_f = 280$ meV, and $\lambda_p = 70$ meV. The mutants were fit by varying only the free energy difference. The resulting free energy differences relative to wild type ($\Delta\Delta G^0_{fit}$) were L168HF (–75 meV), L168HE (–48 meV), L170ND (–7 meV), wild type (0 meV by definition), M160LH (27 meV), L153HV (28 meV), L153HS (37 meV), M197FH (40 meV), L153HF (57 meV), L131LH (99 meV), M203GL (105 meV), L131LH+M160LH (136 meV), L131LH+M197FH (140 meV), L153HD (148 meV), and L131LH+M160LH+M197FH (180 meV), with fitting errors of about ±3 meV. (Inset) Kinetics of L131LH and L131LH+M160LH over a 220-ps time scale. (**B**) Transient absorbance change in the tryptophan absorbance band at 280 nm for the same reaction center samples as in (A) using 800-nm excitation. (Inset) The same transients on an 800-ps time scale. The 280-nm transients shown are from quinone-containing reaction centers, because most of the mutants were not stable to quinone removal. However, over the first 25 ps, the quinone has little effect on the signal (fig. S1), and the tryptophan transients from quinone-removed reaction centers in the mutants where this was possible were all the same (*30*). In both (A) and (B), the measurements were performed at least 10 times for wild type and two to three times for all mutants shown.

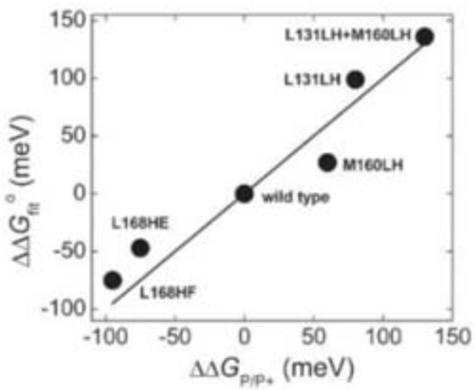

Fig. 4. The *y* axis describes the relative free energy change $\Delta\Delta G^0_{fit}$ associated with the initial electron transfer reaction as determined via fitting with a reaction-diffusion model for five of the mutants studied. This value could only be varied by ±3 meV before a significant decrease in fitting quality was observed. The *x* axis describes the change in the $\Delta\Delta G^0_{P/P+}$ calculated from the P/P$^+$ midpoint potential for each mutation (*26*, *27*). These mutations were selected because they are thought to predominantly affect the midpoint potential of the initial electron donor (P) and not the acceptor, making it possible to directly calculate the change in driving force for the reaction from the change in the P/P$^+$ midpoint potential (it is not possible to directly measure the midpoint potential of the initial electron acceptor in the reaction center).

$\Delta\Delta G^0_{fit}$. In addition to this, for five of the mutants studied, it was possible to perform an independent check of the $\Delta\Delta G^0_{fit}$ value obtained by comparing the $\Delta\Delta G^0_{fit}$ with the relative free energy difference determined from electrochemical measurements of the reaction center ($\Delta\Delta G^0_{P/P+}$, Fig. 4 and table S1). In these mutants, only the P/P^+ midpoint potential (and not the midpoint potentials of B_A/B_A^- or H_A/H_A^-) are thought to change. Therefore, the relative driving force for each of these mutants should be directly related to the measured P/P^+ midpoint potential via the Nernst equation (*26*, *27*). $\Delta\Delta G^0_{fit}$ and $\Delta\Delta G^0_{P/P+}$ agree to within about 30 meV in all five mutants (Fig. 4), demonstrating that the relative free energies determined from the reaction-diffusion formalism are in line with independently measured values.

These results provide strong experimental evidence for the concept that the complex nonexponential charge separation kinetics in reaction centers largely reflect the time course of protein dynamics rather than the inherent electron transfer rate between two static states. This evidence supports the concept that protein movement plays a key role in the kinetics of the primary electron transfer reaction, as previously modeled in structurally based simulations of electron transfer in reaction centers (*14*, *15*). Apparently, the observed kinetics are determined by protein conformational changes initiated by the light absorption event rather than a static barrier crossing between two potential surfaces. The dependence of electron transfer dynamics on protein movement lends a robustness to the electron transfer process that is likely very advantageous; changes in the local environment that alter the free energy of the charge-separated states (such as membrane potentials, for example) will only have minor effects on the speed and efficiency of the electron transfer reactions, because the protein effectively relaxes through a regime in which the activation energy is nearly zero, almost irrespective of the initial energetics. Given the similarity of the core features of the photosynthetic complexes from bacteria and plants, it is very likely that this same framework holds true for the initial electron transfer reaction of photosynthesis in general and possibly for other protein-mediated electron transfer reactions on similar time scales.

References and Notes

1. N. W. Woodbury, J. P. Allen, in *Anoxygenic Photosynthetic Bacteria*, R. E. Blankenship, M. T. Madigan, C. E. Bauer, Eds. (Kluwer, Dordrecht, Netherlands, 1995), vol. 2, pp. 527–557.
2. C. Kirmaier, D. Holten, in *The Photosynthetic Reaction Center*, J. Deisenhofer, J. R. Norris, Eds. (Academic Press, San Diego, CA, 1993), pp. 49–70.
3. W. Zinth, W. Kaiser, in *The Photosynthetic Reaction Center*, J. Deisenhofer, J. R. Norris, Eds. (Academic Press, San Diego, CA, 1993), pp. 71–88.
4. Y. Jia *et al.*, *J. Phys. Chem.* **97**, 13180 (1993).
5. P. Huppman *et al.*, *Biophys. J.* **82**, 3186 (2002).
6. A. L. M. Haffa *et al.*, *J. Phys. Chem. B* **106**, 7376 (2002).
7. M. Du *et al.*, *Proc. Natl. Acad. Sci. U.S.A.* **89**, 8517 (1992).
8. P. Hamm *et al.*, *Biochim. Biophys. Acta* **1142**, 99 (1993).
9. M. H. Cho, R. J. Silbey, *J. Chem. Phys.* **103**, 595 (1995).
10. K. Ando, H. Sumi, *J. Phys. Chem. B* **102**, 10991 (1998).
11. W. W. Parson, A. Warshel, *J. Phys. Chem. B* **108**, 10474 (2004).
12. C. Kirmaier, D. Holten, *Proc. Natl. Acad. Sci. U.S.A.* **87**, 3552 (1990).
13. P. D. Laible, S. R. Greenfield, M. R. Wasielewski, D. K. Hanson, R. M. Pearlstein, *Biochemistry* **36**, 8677 (1997).
14. A. Warshel, Z. T. Chu, W. W. Parson, *Science* **246**, 112 (1989).
15. J. N. Gehlen, M. Marchi, D. Chandler, *Science* **263**, 499 (1994).
16. B. H. McMahon, J. D. Muller, C. A. Wraight, G. U. Nienhaus, *Biophys. J.* **74**, 2567 (1998).
17. K. Tomingaga, G. C. Walker, T. J. Kang, P. F. Barbara, T. Fonseca, *J. Phys. Chem.* **95**, 10485 (1991).
18. B. Bagchi, G. R. Fleming, D. W. Oxtoby, *J. Chem. Phys.* **78**, 7375 (1983).
19. H. Sumi, R. A. Marcus, *J. Chem. Phys.* **84**, 4272 (1986); a more complete description of this function as used in the modeling described is given in (*20*).
20. Materials and methods are available on *Science* Online.
21. K. Willaert *et al.*, *Biochemistry* **31**, 711 (1992).
22. S. W. Lin, T. P. Sakmar, *Biochemistry* **35**, 11149 (1996).
23. S. Schenkl, F. van Mourik, G. van der Zwan, S. Haacke, M. Chergui, *Science* **309**, 917 (2005).
24. The notation we use for identifying amino acid residues includes the protein subunit letter, the number for the amino acid in the peptide sequence, and the single-letter amino acid abbreviation. Therefore, M185W indicates the Trp at position 185 in subunit M. Single-letter abbreviations for the amino acid residues are as follows: A, Ala; C, Cys; D, Asp; E, Glu; F, Phe; G, Gly; H, His; I, Ile; K, Lys; L, Leu; M, Met; N, Asn; P, Pro; Q, Gln; R, Arg; S, Ser; T, Thr; V, Val; W, Trp; and Y, Tyr. For mutants, we include the original and mutant amino acid. Therefore, L131LH indicates a Leu-to-His mutation at position 131 in subunit L.
25. J. A. Potter *et al.*, *J. Biol. Chem.* **280**, 27155 (2005).
26. X. Lin *et al.*, *Proc. Natl. Acad. Sci. U.S.A.* **91**, 10265 (1994).
27. J. C. Williams, A. L. M. Haffa, J. L. McCulley, N. W. Woodbury, J. P. Allen, *Biochemistry* **40**, 15403 (2001).
28. E. Katilius, J. L. Babendure, S. Lin, N. W. Woodbury, *Photosynth. Res.* **81**, 165 (2004).
29. N. W. Woodbury *et al.*, *Chem. Phys.* **197**, 405 (1995).
30. Figure 3B shows the 280-nm signal from reaction centers that contain quinones. This is because not all of the mutants were stable to quinone removal. As shown in fig. S1, the decay is the same for the first roughly 25 ps, and therefore the fact that the decay kinetics on this time scale are identical for all the electron transfer mutants suggests that indeed the time course of protein relaxation is the same for each mutant. This comparison has also been made between wild type and four of the mutants where it was possible to remove quinones without reaction center degradation [M203GL (*24*), L168HE, L153HS, and L170ND]. All of these kinetic traces are also identical to within the noise of the measurement.
31. Besides the electron transfer, another decay path with a time constant of 160 ps is included in the fit, representing the inherent lifetime of P* in the absence of electron transfer. It only affects significantly the kinetics of the double mutants, triple mutant, and L153HD.
32. In Eq. 2, the distinction between ΔG^0 and λ is not very strong. Thus, we report in the text simply the value for the sum. A more complex analysis is required to assign absolute values of these parameters. The value that worked best for ΔG^0 in these fits was −200 meV for wild type, but it is possible to obtain reasonable fits with other values by adjusting λ, although this changes the $\Delta\Delta G^0_{fit}$ values obtained for the mutants. The ratio of λ_p and λ_I does not vary appreciably with ΔG^0. In addition, although the reaction-diffusion theory is stated in terms of reorganization occurring on the time scale of electron transfer, it would presumably also be possible to model the system in terms of relaxation of the driving force on the time scale of electron transfer. It should be noted that the exact shape of $C_p(t)$ is not very critical, as explained in the Supporting Online Material (SOM) text.

33. This work was supported by NSF grants MCB0131776, MCB0642260, and MCB0640002. The laser equipment used in this work was purchased with funds from NSF grant BIR9512970. The authors would like to thank E. Katilius for help with the preparation of the L153 mutants and W. Parson, G. Fleming, L. Dutton, N. Hush, S. Boxer, and D. Matyushov for helpful discussions.

Supporting Online Material

www.sciencemag.org/cgi/content/full/316/5825/747/DC1
Materials and Methods
SOM Text
Figs. S1 and S2
Table S1
References

17 January 2007; accepted 16 March 2007
10.1126/science.1140030

Reducing Endogenous Tau Ameliorates Amyloid β–Induced Deficits in an Alzheimer's Disease Mouse Model

Erik D. Roberson,[1,2]* Kimberly Scearce-Levie,[1,2] Jorge J. Palop,[1,2] Fengrong Yan,[1] Irene H. Cheng,[1,2] Tiffany Wu,[1] Hilary Gerstein,[1] Gui-Qiu Yu,[1] Lennart Mucke[1,2]*

Many potential treatments for Alzheimer's disease target amyloid-β peptides (Aβ), which are widely presumed to cause the disease. The microtubule-associated protein tau is also involved in the disease, but it is unclear whether treatments aimed at tau could block Aβ-induced cognitive impairments. Here, we found that reducing endogenous tau levels prevented behavioral deficits in transgenic mice expressing human amyloid precursor protein, without altering their high Aβ levels. Tau reduction also protected both transgenic and nontransgenic mice against excitotoxicity. Thus, tau reduction can block Aβ- and excitotoxin-induced neuronal dysfunction and may represent an effective strategy for treating Alzheimer's disease and related conditions.

Deposits of amyloid-β peptide (Aβ) and tau are the pathological hallmarks of Alzheimer's disease (AD). Treatments aimed at Aβ production, clearance, or aggregation are all in clinical trials. However, interest in tau as a target has been muted, partly because tau pathology seems to occur downstream of Aβ (*1*–*4*), making it uncertain whether tau-directed therapeutics would prevent Aβ-induced impairments. Also, tau is posttranslationally modified in

AD (*5*–*8*), and debate continues about which modifications should be targeted. Reducing overall tau levels might be an alternative approach (*9*). As tau haplotypes driving slightly higher tau expression increase AD risk (*10*), reducing tau levels might be protective. Therefore, we determined the effect of reducing endogenous tau expression on cognitive deficits in transgenic mice expressing human amyloid precursor protein (hAPP) with familial AD mutations that increase Aβ production.

We crossed hAPP mice (*11*) with *Tau*$^{-/-}$ mice (*12*) and examined hAPP mice with two (hAPP/*Tau*$^{+/+}$), one (hAPP/*Tau*$^{+/-}$), or no (hAPP/*Tau*$^{-/-}$) endogenous tau alleles, compared with *Tau*$^{+/+}$, *Tau*$^{+/-}$, and *Tau*$^{-/-}$ mice without hAPP (*13*). Tau reduction did not affect hippocampal hAPP expression, and conversely, hAPP did not affect hippocampal tau levels (fig. S1). The six genotypes showed no differences in weight, general health, basic reflexes, sensory responses, or gross motor function.

To test learning and memory, we used the Morris water maze. In the cued version, mice learn to find the target platform using a conspicuous marker placed directly above it. At 4 to 7 months of age, *Tau*$^{+/+}$, *Tau*$^{+/-}$, and *Tau*$^{-/-}$ mice learned quickly, but as expected (*14*, *15*), hAPP/*Tau*$^{+/+}$ mice took longer to master this task (Fig. 1A; $P < 0.001$). In contrast, hAPP/*Tau*$^{+/-}$ and hAPP/*Tau*$^{-/-}$ mice performed at control levels.

The more difficult hidden-platform version of the water maze demands spatial learning. Mice without hAPP learned this task over 3 days of training regardless of tau genotype, whereas hAPP/*Tau*$^{+/+}$ mice showed no evidence of learning until days 4 and 5 ($P < 0.001$; Fig. 1B). Notably, hAPP/*Tau*$^{+/-}$ mice were less impaired than hAPP/*Tau*$^{+/+}$ mice ($P < 0.02$), and hAPP/*Tau*$^{-/-}$ mice did not differ from controls without hAPP (Fig. 1B). Probe trials, in which the platform was removed and mice were given 1 min to explore the pool, confirmed the beneficial effect of tau reduction (Fig. 1, C to E). In an initial probe trial 24 hours after 3 days of training, hAPP/*Tau*$^{+/+}$ mice had no apparent spatial memory of the platform location, crossing the target platform location no more than they crossed equivalent areas in nontarget quadrants (Fig. 1D). However, hAPP/*Tau*$^{-/-}$ mice, similar to mice without hAPP, did cross the target platform location more often ($P < 0.01$; Fig. 1D). After two additional days of training, hAPP/*Tau*$^{+/-}$ mice also had more target than nontarget crossings ($P < 0.01$), whereas hAPP/*Tau*$^{+/+}$ mice still showed no spatial learning and memory (Fig. 1E). Thus, the tau reduction gene dose-dependently ameliorates Aβ-dependent water maze learning and memory deficits.

Increased exploratory locomotor activity is seen after entorhinal cortex lesions and may reflect deficits in spatial information processing (*16*); hAPP mice show similar hyperactivity (*15*). hAPP/*Tau*$^{+/+}$ mice were hyperactive in the Y maze ($P < 0.001$; Fig. 2A), a new cage ($P < 0.05$; Fig. 2B), and the elevated plus maze ($P < 0.001$; Fig. 2C). In contrast, these abnormalities were not seen in hAPP/*Tau*$^{+/-}$ and hAPP/*Tau*$^{-/-}$ mice (Fig. 2, A to C). To determine whether the benefits afforded by tau reduction were sustained, we examined older mice. Hyperactivity persisted in hAPP/*Tau*$^{+/+}$ mice and remained absent in hAPP/*Tau*$^{-/-}$ mice at 12 to 16 months ($P < 0.05$; Fig. 2D).

Premature death of unclear etiology was also observed in hAPP mice ($P < 0.005$; Fig. 2E) (*17*, *18*). Again, both hAPP/*Tau*$^{-/-}$ and hAPP/*Tau*$^{+/-}$ mice were protected from this early mortality. Thus, tau reduction prevented major Aβ-dependent adverse effects in hAPP mice. We examined several plausible mechanisms by which tau reduction might exert protective effects and we eventually discovered an unexpected role for tau.

We first ruled out the possibility that tau reduction altered Aβ levels or aggregation. Tau reduction did not alter hAPP expression (fig. S1), soluble $Aβ_{1-x}$ or $Aβ_{1-42}$ levels, or the $Aβ_{1-42}/Aβ_{1-x}$ ratio (fig. S2). In addition, hAPP/*Tau*$^{+/+}$, hAPP/*Tau*$^{+/-}$, and hAPP/*Tau*$^{-/-}$ mice had similar plaque load at

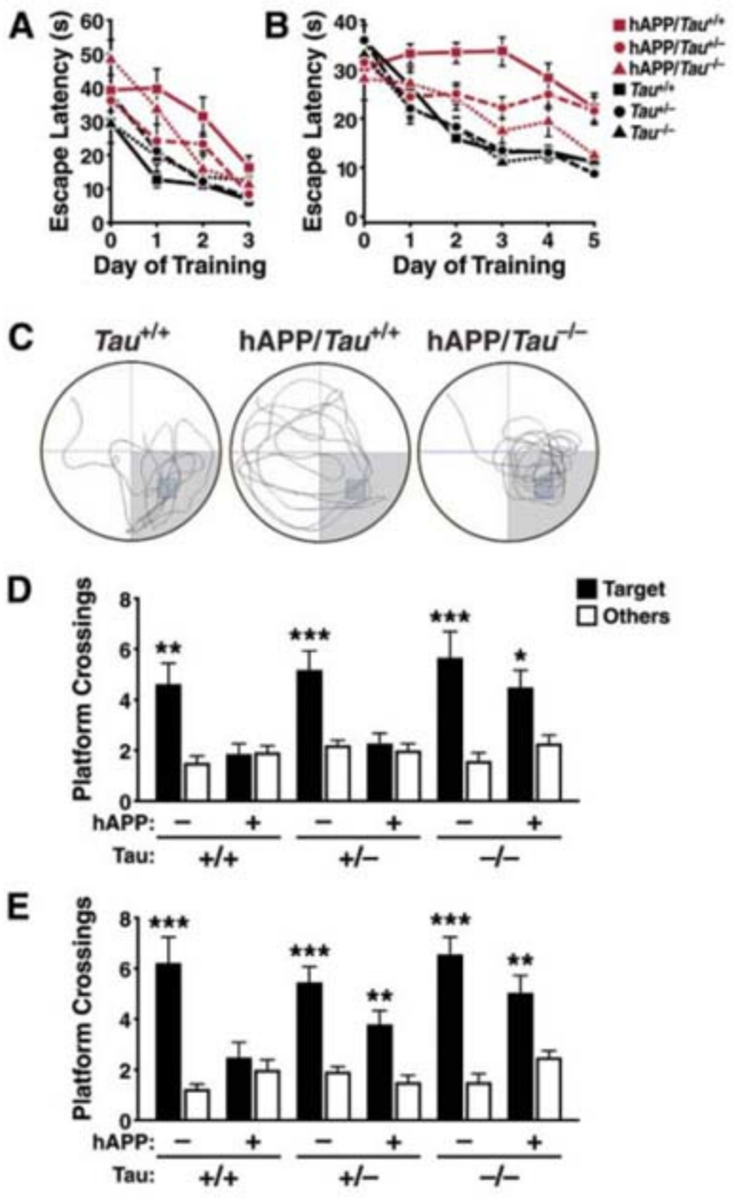

Fig. 1. Tau reduction prevented water maze deficits in hAPP mice (n = 7 to 11 mice per genotype, age 4 to 7 months). (**A**) Cued platform learning curves. Day 0 indicates performance on the first trial, and subsequent points represent average of all daily trials. Performance differed by genotype (repeated measures analysis of variance (RMANOVA): $P < 0.001$; hAPP by tau interaction, $P = 0.058$). In post-hoc comparisons, only hAPP/*Tau*$^{+/+}$ differed from groups without hAPP ($P < 0.001$). (**B**) Hidden platform learning curves differed by genotype (RMANOVA: $P < 0.001$; hAPP by Tau interaction, $P < 0.02$). In post-hoc comparisons, hAPP/*Tau*$^{+/+}$ differed from all groups without hAPP ($P < 0.001$); hAPP/*Tau*$^{+/-}$ differed from hAPP/*Tau*$^{+/+}$ ($P < 0.02$) and groups without hAPP ($P < 0.01$); hAPP/*Tau*$^{-/-}$ differed from hAPP/*Tau*$^{+/+}$ ($P < 0.001$) but not from any group without hAPP. (**C** and **D**) Probe trial 24 hours after completion of 3 days of hidden-platform training. (C) Representative path tracings. (D) Number of target platform crossings versus crossings of the equivalent area in the three other quadrants differed by genotype (target crossing by genotype interaction, $P < 0.001$). In post-hoc comparisons, all genotypes except hAPP/*Tau*$^{+/+}$ and hAPP/*Tau*$^{+/-}$ exhibited a preference for the target location over equivalent areas in the other three quadrants (*$P < 0.05$; **$P < 0.01$; ***$P < 0.001$). (**E**) Probe trial 72 hours after completion of 5 days of hidden-platform training. Target platform preference differed by genotype (target crossing by genotype interaction, $P < 0.001$; target crossing by hAPP by tau interaction, $P < 0.05$). In post-hoc comparisons, all genotypes except hAPP/*Tau*$^{+/+}$ exhibited a preference for the target location (**$P < 0.01$; ***$P < 0.001$). Error bars show SEM.

[1]Gladstone Institute of Neurological Disease, San Francisco, CA 94158, USA. [2]Department of Neurology, University of California, San Francisco, CA 94158, USA.

*To whom correspondence should be addressed. E-mail: eroberson@gladstone.ucsf.edu (E.D.R); lmucke@gladstone.ucsf.edu (L.M.)

4 to 7 months (fig. S3) and 14 to 18 months (Fig. 3, A and B). We also found no effect of tau reduction on levels of Aβ*56, a specific Aβ assembly linked to memory deficits (*19*) (fig. S4). Thus, the beneficial effects of reducing tau were observed without detectable changes in Aβ burden, suggesting that tau reduction uncouples Aβ from downstream pathogenic mechanisms.

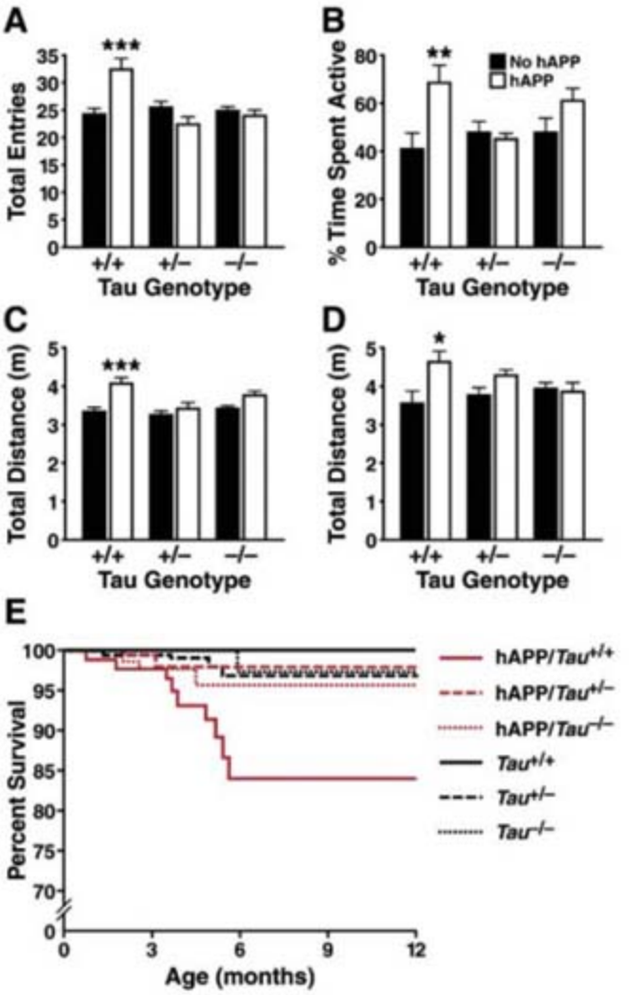

Fig. 2. Tau reduction prevented behavioral abnormalities and premature mortality in hAPP mice. (**A**) Total arm entries during a 6-min exploration of the Y maze (n = 49 to 58 mice per genotype; age 4 to 7 months; ANOVA: genotype effect, $P < 0.0001$; hAPP by tau interaction, $P < 0.0001$; $^{***}P < 0.001$ versus groups without hAPP). (**B**) Percentage of time spent active during a 5-min exploration of a new cage (n = 7 to 14 mice per genotype; age 4 to 7 months; ANOVA: genotype effect, $P < 0.01$; hAPP by tau interaction, $P < 0.05$; $^{*}P < 0.05$ versus groups without hAPP). (**C**) Total distance traveled in both open and closed arms during a 10-min exploration of the elevated plus maze (n = 49 to 59 mice per genotype; age 4 to 7 months; ANOVA: genotype effect, $P < 0.0001$; hAPP by tau interaction, $P < 0.05$; $^{***}P < 0.001$ versus groups without hAPP). (**D**) Total distance traveled during exploration of elevated plus maze (n = 6 to 13 mice per genotype; age 12 to 16 months; ANOVA: hAPP effect, $P < 0.01$; hAPP by tau interaction, $P = 0.079$; $^{*}P < 0.05$ versus groups without hAPP). Error bars in (A) to (D) show SEM. (**E**) Kaplan-Meier survival curves showing effect of tau reduction on premature mortality in hAPP mice. All genotyped mice in the colony (n = 887) were included in the analysis. By log-rank comparison, only hAPP/*Tau*$^{+/+}$ mice differed from all other groups ($P < 0.005$).

Next, we looked for abnormal forms of tau that might act as downstream effectors of Aβ in hAPP/*Tau*$^{+/+}$ mice. Major AD-related phosphorylation sites in human tau are conserved in murine tau, including those phosphorylated by proline-directed kinases, such as glycon synthase kinase (GSK)–3β and cdk5, or by microtubule affinity–regulating kinase (MARK). Changes in murine tau phosphorylation at these sites are easily detected, for example after brief hypothermia (*20*) (fig. S4). However, in hippocampal homogenates of 4- to 7-month-old hAPP/*Tau*$^{+/+}$ mice, we did not find changes in tau phosphorylation at proline-directed kinase sites, including Thr^{181}, Ser^{202}, Thr^{231}, and Ser$^{396/404}$, or at the primary site for MARK, Ser^{262} (fig. S5). Generation of neurotoxic tau fragments has also been implicated as a mechanism of Aβ toxicity (*21*). Tau-deficient primary neurons are resistant to Aβ-induced degeneration (*3*, *22*), apparently because Aβ toxicity in vitro involves production of a 17-kD tau fragment (*21*). We confirmed the presence of a 17-kD tau fragment in lysates of Aβ-treated primary neurons, but found no abnormal tau proteolysis in hippocampal homogenates from hAPP mice (fig. S6), suggesting that the neuroprotective effects of tau reduction in the two systems are mechanistically different. The relative lack of modified tau also distinguishes our model from transgenic lines overexpressing tau with mutations that cause frontotemporal dementia, but not AD, in humans (*2*, *4*, *23*). In our study, reduction of endogenous, wild-type tau protected hAPP mice against Aβ-dependent cognitive impairments, and this did not involve the elimination of a large pool of tau with typical AD-associated modifications. Our experiments do not rule out the possibility that another type

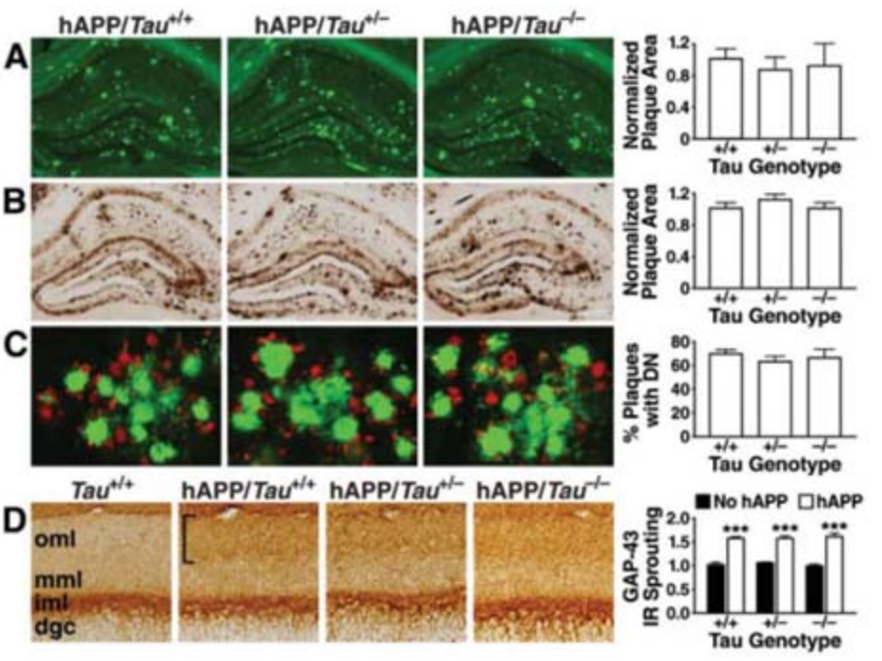

Fig. 3. Tau reduction did not change Aβ plaque deposition, neuritic dystrophy, or aberrant sprouting. (**A**) Thioflavin-S staining of hippocampal amyloid plaques in hAPP mice. Percentage of hippocampal area covered by plaques was normalized to the mean value in hAPP/*Tau*$^{+/+}$ mice (n = 6 to 11 mice per genotype; age 14 to 18 months). (**B**) Immunostaining of hippocampal Aβ deposits in hAPP mice. Percentage of hippocampal area covered by plaques was normalized to the mean value in hAPP/*Tau*$^{+/+}$ mice (n = 6 to 11 mice per genotype; age 14 to 18 months). (**C**) Double-labeling of hippocampus for dystrophic neurites (antibody 8E5, red) and amyloid plaques (thioflavin-S, green) in hAPP mice aged 14 to 18 months, with quantification of dystrophic neurites expressed as percentage of thioflavin-S–positive plaques with surrounding neuritic dystrophy (n = 9 to 11 mice per genotype). (**D**) GAP43 immunostaining of aberrant axonal sprouting in the molecular layer of the dentate gyrus (oml, outer molecular layer; mml, middle molecular layer; iml, inner molecular layer; dgc, dentate granule cells). Bracket highlights GAP43-positive sprouting in the outer molecular layer of hAPP mice. Sprouting was quantified by densitometry and normalized to the mean value in *Tau*$^{+/+}$ mice (n = 7 to 14 mice per genotype; age 4 to 7 months; $^{***}P < 0.001$ versus groups without hAPP). Error bars show SEM.

of tau modification, or a small pool of modified tau in a restricted subcellular compartment or cellular population, could play a role downstream of Aβ.

To begin addressing this possibility, we stained brain sections from *Tau*$^{+/+}$ and hAPP/*Tau*$^{+/+}$ mice with phospho-tau antibodies. We saw little difference overall between *Tau*$^{+/+}$ and hAPP/*Tau*$^{+/+}$ mice in phospho-tau immunoreactivity, but we did observe scattered phospho-tau–positive punctae in dystrophic neurites surrounding amyloid plaques (fig. S7). We thus wondered whether the benefits of tau reduction in hAPP mice could relate to prevention of neuritic dystrophy, which may contribute to AD-related cognitive decline (*24*). Despite the differences in their behavior, hAPP/*Tau*$^{+/+}$, hAPP/*Tau*$^{+/-}$, and hAPP/*Tau*$^{-/-}$ mice had similar amounts of neuritic dystrophy (Fig. 3C). Thus, tau is not required for the formation of plaque-associated dystrophic neurites. Given that tau reduction prevented behavioral deficits but not neuritic dystrophy, these may represent parallel, rather than causally linked, disease manifestations, or tau reduction may act downstream of neuritic dystrophy.

Tau has a well-characterized role in axonal outgrowth (*12*), so we tested whether tau reduction prevented the aberrant sprouting of hippocampal axons observed in AD (*25*) and hAPP mice (*18*). Similar degrees of sprouting were observed, regardless of tau genotype (Fig. 3D). Thus, although tau reduction affected important outcome measures related to Aβ-induced neuronal dysfunction, not all effects of Aβ were blocked.

Excitotoxicity is implicated in the pathogenesis of AD (*26*, *27*). Consistent with the increased incidence of seizures in AD patients (*28*), TgCRND8 hAPP mice are more susceptible to the γ-aminobutyric acid type A ($GABA_A$) receptor antagonist pentylenetetrazole (PTZ) (*29*). Using a similar paradigm, we found that hAPP/*Tau*$^{+/+}$ mice were also abnormally sensitive to PTZ, with 20% suffering fatal status epilepticus at a dose that was not lethal to mice without hAPP ($P < 0.05$). Tau reduction prevented this effect, as no hAPP/*Tau*$^{+/-}$ or hAPP/*Tau*$^{-/-}$ mice died. Seizures in hAPP/*Tau*$^{+/-}$ and hAPP/*Tau*$^{-/-}$ mice were less severe and occurred at longer latencies than in hAPP/*Tau*$^{+/+}$ mice ($P < 0.01$; Fig. 4, A and B).

Tau reduction also increased resistance to PTZ in hAPP-nontransgenic mice, lowering seizure severity and delaying seizure onset ($P < 0.01$; Fig. 4, A and C). To confirm that tau reduction could reduce aberrant neuronal overexcitation, we challenged mice with excitotoxic doses of the glutamate receptor agonist kainate. As expected, intraperitoneal injection of kainate dose-dependently induced seizures in *Tau*$^{+/+}$ mice (Fig. 4D). In contrast, *Tau*$^{+/-}$ and *Tau*$^{-/-}$ mice were resistant to kainate across a range of doses ($P < 0.05$; Fig. 4D). Thus, tau modulates sensitivity to excitotoxins and may be involved in regulating neuronal activity. The excitoprotective effect of tau reduction in mice without hAPP is more likely related to a physiological function of tau than to the removal of a pathological form of the protein. Sensitization of neurons to Aβ by physiological forms of tau could explain why tau reduction is effective in hAPP/*Tau*$^{+/+}$ mice despite their lack of obvious tau modifications.

Our findings raise the possibility that tau reduction could protect against AD and other neurological conditions associated with excitotoxicity. Of course, the therapeutic implications of our findings must be interpreted with caution. First, there are differences between the mouse model and AD, including the absence of substantial neuronal loss or neurofibrillary pathology in hAPP mice. The contribution of these abnormalities to AD-related cognitive impairment, relative to the role of reversible Aβ-induced neuronal dysfunction that is modeled in hAPP mice, remains to be determined (*30*). Second, microdeletions of chromosome 17q21 encompassing the tau gene are associated with learning disabilities in humans (*31*), although abnormalities in these individuals may relate to insufficiency of other genes in the region, such as the corticotropin-releasing hormone receptor gene, which is implicated in neuropsychiatric disease (*32*). We found no adverse effects of tau reduction on health or cognition in mice, and the evidence that even partial tau reduction robustly protected mice from Aβ and excitotoxic agents highlights its potential benefits.

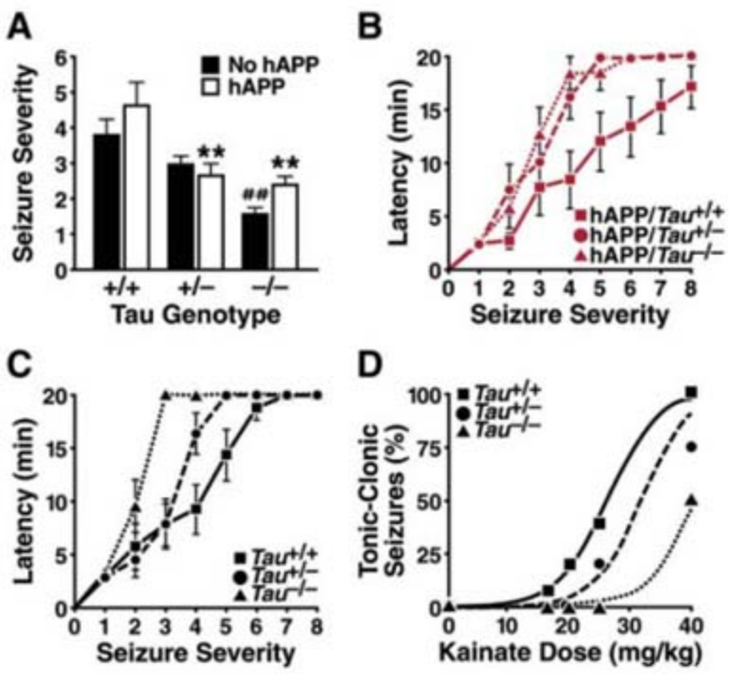

Fig. 4. Tau reduction increased resistance to excitotoxin-induced seizures. (**A**) Tau reduction lowered seizure severity after a single intraperitoneal injection of PTZ (40 mg/kg; $n = 10$ to 11 mice per genotype; age 4 to 7 months; ANOVA: tau effect, $P < 0.0001$). Seizures were less severe in hAPP/*Tau*$^{+/-}$ and hAPP/*Tau*$^{-/-}$ mice than in hAPP/*Tau*$^{+/+}$ mice ($^{**}P < 0.01$ versus hAPP/*Tau*$^{+/+}$). Seizures were also less severe in *Tau*$^{-/-}$ mice than in *Tau*$^{+/+}$ mice ($^{\#\#}P < 0.01$ versus *Tau*$^{+/+}$). (**B** and **C**) Latency to reach each stage of seizure severity after PTZ administration. (B) PTZ-induced seizures occurred more rapidly in hAPP/*Tau*$^{+/+}$ mice than hAPP/*Tau*$^{+/-}$ and hAPP/*Tau*$^{-/-}$ mice (RMANOVA: $P < 0.01$). (C) Tau reduction also slowed the onset of PTZ-induced seizures in mice without hAPP (RMANOVA: $P < 0.001$). Error bars in (A) to (C) show SEM. (**D**) After a single intraperitoneal injection of kainate at the doses indicated, occurrence of generalized tonic-clonic seizures was scored. Tau reduction lowered susceptibility to kainate, shifting dose-response curves to the right ($n = 19$ to 24 mice per genotype; age 2 to 5 months; logistic regression: $P < 0.05$).

References and Notes

1. R. Tanzi, L. Bertram, *Cell* **120**, 545 (2005).
2. J. Lewis *et al.*, *Science* **293**, 1487 (2001).
3. M. Rapoport, H. N. Dawson, L. I. Binder, M. P. Vitek, A. Ferreira, *Proc. Natl. Acad. Sci. U.S.A.* **99**, 6364 (2002).
4. S. Oddo, L. Billings, J. P. Kesslak, D. H. Cribbs, F. M. LaFerla, *Neuron* **43**, 321 (2004).
5. C. X. Gong, F. Liu, I. Grundke-Iqbal, K. Iqbal, *J. Neural Transm.* **112**, 813 (2005).
6. K. Iqbal *et al.*, *Biochim. Biophys. Acta* **1739**, 198 (2005).
7. W. H. Stoothoff, G. V. Johnson, *Biochim. Biophys. Acta* **1739**, 280 (2005).
8. I. Khlistunova *et al.*, *J. Biol. Chem.* **281**, 1205 (2006).
9. C. A. Dickey *et al.*, *FASEB J.* **20**, 753 (2006).
10. A. J. Myers *et al.*, *Hum. Mol. Genet.* **14**, 2399 (2005).
11. L. Mucke *et al.*, *J. Neurosci.* **20**, 4050 (2000).
12. H. N. Dawson *et al.*, *J. Cell Sci.* **114**, 1179 (2001).
13. Materials and methods are available as supporting material on *Science* Online.
14. J. J. Palop *et al.*, *Proc. Natl. Acad. Sci. U.S.A.* **100**, 9572 (2003).
15. D. T. Kobayashi, K. S. Chen, *Genes Brain Behav.* **4**, 173 (2005).
16. O. Steward, J. Loesche, W. C. Horton, *Brain Res. Bull.* **2**, 41 (1977).
17. K. K. Hsiao *et al.*, *Neuron* **15**, 1203 (1995).
18. J. Chin *et al.*, *J. Neurosci.* **24**, 4692 (2004).
19. S. Lesné *et al.*, *Nature* **440**, 352 (2006).
20. E. Planel *et al.*, *J. Neurosci.* **24**, 2401 (2004).
21. S. Y. Park, A. Ferreira, *J. Neurosci.* **25**, 5365 (2005).
22. T. Liu *et al.*, *J. Neurochem.* **88**, 554 (2004).
23. K. SantaCruz *et al.*, *Science* **309**, 476 (2005).
24. R. B. Knowles *et al.*, *Proc. Natl. Acad. Sci. U.S.A.* **96**, 5274 (1999).
25. J. W. Geddes *et al.*, *Science* **230**, 1179 (1985).
26. M. P. Mattson, *Nature* **430**, 631 (2004).
27. J. W. Olney, D. F. Wozniak, N. B. Farber, *Arch. Neurol.* **54**, 1234 (1997).
28. J. C. Amatniek *et al.*, *Epilepsia* **47**, 867 (2006).
29. R. A. Del Vecchio, L. H. Gold, S. J. Novick, G. Wong, L. A. Hyde, *Neurosci. Lett.* **367**, 164 (2004).
30. J. J. Palop, J. Chin, L. Mucke, *Nature* **443**, 768 (2006).
31. J. R. Lupski, *Nat. Genet.* **38**, 974 (2006).

32. F. Holsboer, *Curr. Opin. Investig. Drugs* **4**, 46 (2003).

33. We thank M. Vitek and H. Dawson for tau knockout mice; P. Seubert and P. Davies for antibodies; H. Solanoy, X. Wang, and Y. Zhou for technical assistance; C. McCullough for advice on statistics; D. McPherson and L. Manuntag for administrative support; and G. Howard and S. Ordway for editorial review. L.M. received consulting fees from Merck and honoraria from Amgen, Elan, and Pfizer. E.D.R. received consulting fees from Rinat Neuroscience. Supported by NIH grants AG011385 and AG022074 (L.M.), MH070588 (K.S.L), and NS054811 (E.D.R); the Giannini Foundation (E.D.R.); the S.D. Bechtel Jr. Young Investigator Award (E.D.R.); and the NIH National Center for Research Resources grant RR18928-01.

Supporting Online Material
www.sciencemag.org/cgi/content/full/316/5825/750/DC1
Materials and Methods
Figs. S1 to S7
References

26 February 2007; accepted 27 March 2007
10.1126/science.1141736

Regulation of NF-κB Activation in T Cells via Association of the Adapter Proteins ADAP and CARMA1

Ricardo B. Medeiros,[1]* Brandon J. Burbach,[1]* Kristen L. Mueller,[1] Rupa Srivastava,[1] James J. Moon,[2] Sarah Highfill,[1] Erik J. Peterson,[3] Yoji Shimizu[1]†

The adapter protein ADAP regulates T lymphocyte adhesion and activation. We present evidence for a previously unrecognized function for ADAP in regulating T cell receptor (TCR)–mediated activation of the transcription factor NF-κB. Stimulation of ADAP-deficient mouse T cells with antibodies to CD3 and CD28 resulted in impaired nuclear translocation of NF-κB, a reduced DNA binding, and delayed degradation and decreased phosphorylation of IκB (inhibitor of NF-κB). TCR-stimulated assembly of the CARMA1–BCL-10–MALT1 complex was substantially impaired in the absence of ADAP. We further identified a region of ADAP that is required for association with the CARMA1 adapter and NF-κB activation but is not required for ADAP-dependent regulation of adhesion. These findings provide new insights into ADAP function and the mechanism by which CARMA1 regulates NF-κB activation in T cells.

Adapter proteins nucleate multimolecular complexes that are essential for effective transmission of intracellular signals during an adaptive immune response (*1*). In T lymphocytes, the adhesion- and degranulation-promoting adapter protein (ADAP) regulates T cell receptor (TCR)–dependent changes in the function of integrin adhesion receptors (*2*, *3*). ADAP-deficient ($ADAP^{-/-}$) T cells also exhibit impaired proliferation and cytokine production after stimulation of the TCR and the CD28 co-stimulatory receptor (*2*, *3*). Stimulation of these receptors leads to activation of the NF-κB family of transcription factors, which are critical for T cell activation and survival (*4*). A multiprotein complex consisting of the membrane-associated adapter protein CARMA1 (*5*, *6*), the caspase-like protein MALT1 (*7*, *8*), and the adapter protein BCL-10 (*9*) is critical for TCR-dependent activation of the IκB kinase complex and subsequent NF-κB nuclear translocation (*10*).

Like ADAP-deficient T cells, protein kinase Cθ (PKCθ)–deficient T cells exhibit defective TCR-mediated proliferation, even though proximal TCR signaling events, such as extracellular signal–regulated kinase (ERK) activation, are normal (*11*). Therefore, we examined PKCθ-dependent signaling in $ADAP^{-/-}$ T cells (*12*). Membrane localization of PKCθ was similar in $ADAP^{+/-}$ and $ADAP^{-/-}$ T cells upon stimulation with antibodies to CD3 and CD28 (Fig. 1, A and B). Stimulated $ADAP^{+/-}$ and $ADAP^{-/-}$ T cells also showed similar levels of PKCθ phosphorylation (Fig. 1C). Thus, ADAP is not required for TCR signaling events leading to and including PKCθ activation. Because PKCθ regulates NF-κB activation downstream of the TCR (*11*, *13*), we next examined NF-κB signaling in $ADAP^{-/-}$ T cells. Image scanning flow cytometry (*14*, *15*) (fig. S1) revealed a striking defect in p65 nuclear translocation after stimulation of $ADAP^{-/-}$ lymph node T cells (Fig. 2, A and B) or CD4 T cells (fig. S2) by CD3 and CD28 (CD3/CD28). In contrast, no impairment in NF-κB activation was detected after stimulation with tumor necrosis factor–α (TNF-α), which activates NF-κB independently of the TCR. These results were confirmed with electrophoretic mobility shift assays (Fig. 2C). $ADAP^{-/-}$ T cells also displayed defective NF-κB translocation after treatment with phorbol 12-myristate 13-acetate (PMA), which activates PKC (Fig. 2, A and B).

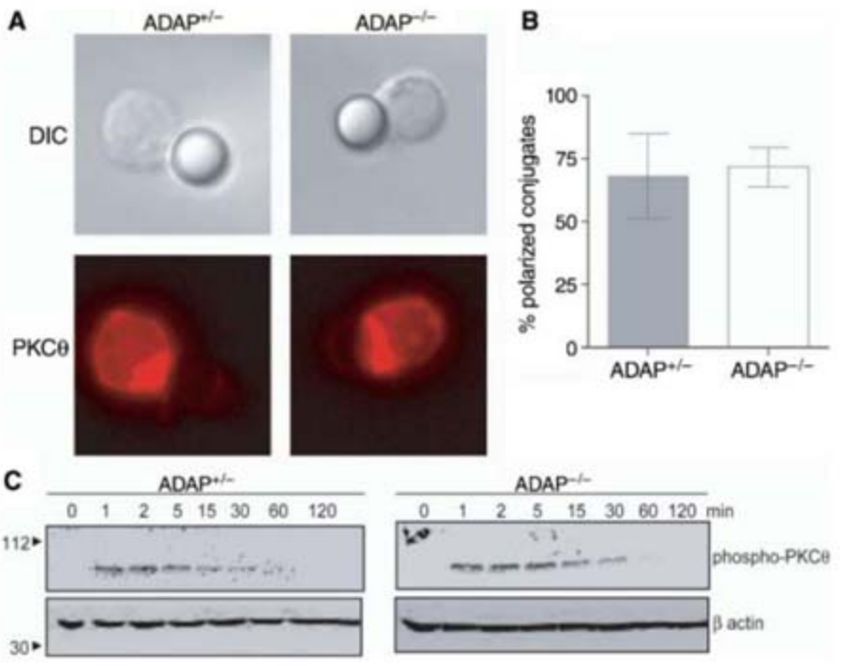

Fig. 1. TCR-dependent membrane localization and activation of PKCθ in ADAP $^{-/-}$ T cells. (**A**) Localization of PKCθ (bottom) in $ADAP^{+/-}$ and $ADAP^{-/-}$ T cells to the contact site with beads coated with antibodies to CD3 and CD28. Differential interference contrast (DIC) images are shown in top panels. (**B**) Quantification of PKCθ localization. T cell–bead conjugates (minimum 90 per group) were scored for PKCθ polarization from two independent experiments. Graph shows the average percent of T cell–bead conjugates with polarized PKCθ (±SD). (**C**) Phosphorylation of PKCθ after CD3/CD28 stimulation of $ADAP^{+/-}$ and $ADAP^{-/-}$ T cells for the indicated time points was assessed by Western blotting of whole-cell lysates with antibody to phosphorylated PKCθ (Thr^{538}) (top panels). Blots were also probed with antibody to β-actin (bottom panels).

[1]Department of Laboratory Medicine and Pathology, Center for Immunology, Cancer Center, University of Minnesota Medical School, Minneapolis, MN 55455, USA. [2]Department of Microbiology, Center for Immunology, University of Minnesota Medical School, Minneapolis, MN 55455, USA. [3]Department of Medicine, Center for Immunology, Cancer Center, University of Minnesota Medical School, Minneapolis, MN 55455, USA.

*These authors contributed equally to this work.
†To whom correspondence should be addressed. E-mail: shimi002@umn.edu

CD3/CD28 stimulation of ADAP$^{-/-}$ T cells also resulted in reduced induction of intercellular adhesion molecule–1 (ICAM-1), which is encoded by a NF-κB–regulated gene (*16*) (Fig. 2D).

We also examined signaling events proximal to nuclear translocation of the p65 NF-κB subunit in ADAP$^{-/-}$ T cells. In resting T cells, NF-κB subunits are sequestered in the cytoplasm via interactions with IκBα (*4*). Relative to ADAP$^{+/-}$ T cells, CD3/CD28 stimulation of ADAP$^{-/-}$ T cells led to a delay in IκBα degradation and decreased IκB phosphorylation (Fig. 2E and fig. S3). Consistent with previous results (*2*, *3*), the kinetics of ERK phosphorylation after CD3/CD28 stimulation were not affected by loss of ADAP (Fig. 2E). Activation of the IκB kinase (IKK) complex, which phosphorylates IκBα, was also impaired after CD3/CD28 stimulation of ADAP$^{-/-}$ T cells (fig. S4). Thus, ADAP acts as a positive regulator of TCR-dependent NF-κB activation, downstream of PKCθ yet upstream of IKK activation, IκBα degradation, and NF-κB subunit translocation.

We next examined the role of ADAP in inducible membrane localization of BCL-10, MALT1, and CARMA1 (*17*, *18*). In unstimulated ADAP$^{+/-}$ or ADAP$^{-/-}$ T cells, only low levels of BCL-10 and MALT1 were detected in membrane fractions (Fig. 3A). CD3/CD28 or PMA stimulation of ADAP$^{+/-}$ T cells, but not ADAP$^{-/-}$ T cells, resulted in enhanced membrane localization of both BCL-10 and MALT1 (Fig. 3A). ADAP also localized to the membrane in stimulated ADAP$^{+/-}$ T cells (Fig. 3A). The levels of CARMA1 in membrane fractions were comparable between ADAP$^{+/-}$ and ADAP$^{-/-}$ T cells both before and after stimulation (Fig. 3A), consistent with previous results (*17*). Thus, ADAP is critical for the activation-dependent membrane localization of BCL-10 and MALT1.

To define potential interactions between ADAP and the CARMA1–BCL-10–MALT1 signaling complex, we performed coimmunoprecipitation experiments. ADAP could be immunoprecipitated only from membrane fractions isolated from activated T cells (Fig. 3B). Coimmunoprecipitation of CARMA1, BCL-10, and MALT1 with ADAP was observed from stimulated membrane fractions of either lymph node T cells (Fig. 3B) or purified CD4 T cells (fig. S5). Similarly, MALT1, BCL-10, and ADAP coimmunoprecipitated with CARMA1 only after T cell stimulation (Fig. 3B). However, in activated ADAP$^{-/-}$ T cells, MALT-1 and BCL-10 did not coimmunoprecipitate with CARMA1 (Fig. 3B), and CARMA1 and MALT-1 did not coimmunoprecipitate with BCL-10 (Fig. 3C and fig. S6). To confirm that ADAP is required for inducible complex assembly, we used resting T cells expressing the hCAR adenovirus receptor to permit adenoviral-mediated expression of ADAP (*19*). ADAP reexpression in ADAP$^{-/-}$ T cells restored coimmunoprecipitation of CARMA1 and MALT1 with BCL-10 after CD3/CD28 or PMA stimulation (Fig. 3C). Thus, ADAP is a component of the CARMA1–BCL-10–MALT1 complex and is required for normal complex formation.

We next examined interactions between ADAP and purified BCL-10, MALT1, and CARMA1. A glutathione *S*-transferase (GST)–ADAP fusion protein interacted in vitro with purified CARMA1, but not with purified BCL-10 or MALT1 (Fig. 3D). A truncated form of CARMA1 (CARMA1/651-1147) containing just the C-terminal PDZ, SH3, and GUK-like domains typical of membrane-associated guanylate kinase (MAGUK)–family proteins (*20*) (Fig. 3E) also interacted with GST-ADAP in vitro (Fig. 3D). Thus, the interaction of ADAP with CARMA1 is not dependent on the caspase-recruiting domain that mediates the interaction of CARMA1 with BCL-10. Colocalization of ADAP with CARMA1 was also observed at the contact site between wild-type T cells and beads coated with antibodies to CD3 and CD28 (fig. S7).

Truncation and deletion mutants of ADAP were used to define sites within ADAP critical for its interaction with CARMA1 (Fig. 4A). Wild-type and mutant forms of hemagglutinin (HA) epitope–tagged ADAP were immunoprecipitated from transiently transfected Jurkat T cells after PMA stimulation, and these immunoprecipitates were analyzed for the presence of coimmunoprecipitating BCL-10, MALT1, and CARMA1 proteins (Fig. 4B). Wild-type ADAP and an

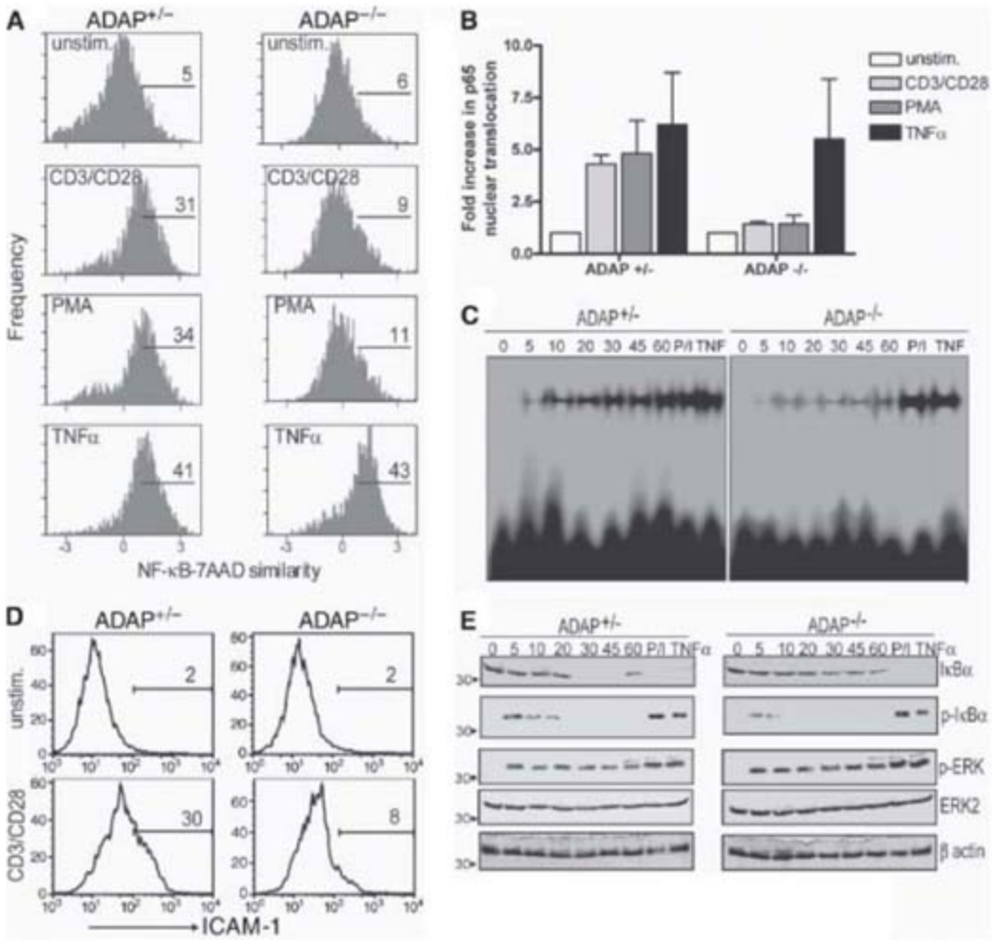

Fig. 2. Activation of the NF-κB pathway is impaired in ADAP$^{-/-}$ T cells. (**A**) ADAP$^{+/-}$ and ADAP$^{-/-}$ T cells were unstimulated (unstim.) or stimulated for 10 min with antibodies to CD3 and CD28, PMA, or TNF-α, stained with 7-AAD and fluorescein isothiocyanate–conjugated antibody to p65, and analyzed on a multispectral imaging flow cytometer (*15*). Histograms show the NF-κB–7-AAD similarity index, which reflects colocalization of the 7-AAD and p65 signals in the population of T cells analyzed. Marker values indicate the percentage of T cells in each sample with translocated p65. (**B**) Nuclear localization of p65 in unstimulated T cells was set to 1; results show the average increase (±SD) in p65 nuclear translocation in stimulated T cells relative to unstimulated T cells for four independent experiments. (**C**) Electrophoretic mobility shift assay (EMSA) of NF-κB in ADAP$^{-/-}$ T cells. ADAP$^{+/-}$ or ADAP$^{-/-}$ lymph node T cells were stimulated with antibodies to CD3 and CD28 for the indicated time periods (in minutes), or for 10 min with PMA and ionomycin (P/I) or with TNF-α. Nuclear extracts were prepared and EMSA was performed with a biotin-labeled NF-κB probe. (**D**) ADAP$^{+/-}$ and ADAP$^{-/-}$ lymph node T cells were stimulated in vitro with antibodies to CD3 and CD28 for 24 hours. Cells were harvested and ICAM-1 expression on CD4 T cells was determined by flow cytometry. (**E**) IκBα degradation and phosphorylation. ADAP$^{+/-}$ and ADAP$^{-/-}$ T cells were either unstimulated or stimulated as in (C) before lysis. Lysates were analyzed by Western blotting with antibodies specific for IκBα, phosphorylated IκBα, phosphorylated ERK, ERK2, or β-actin.

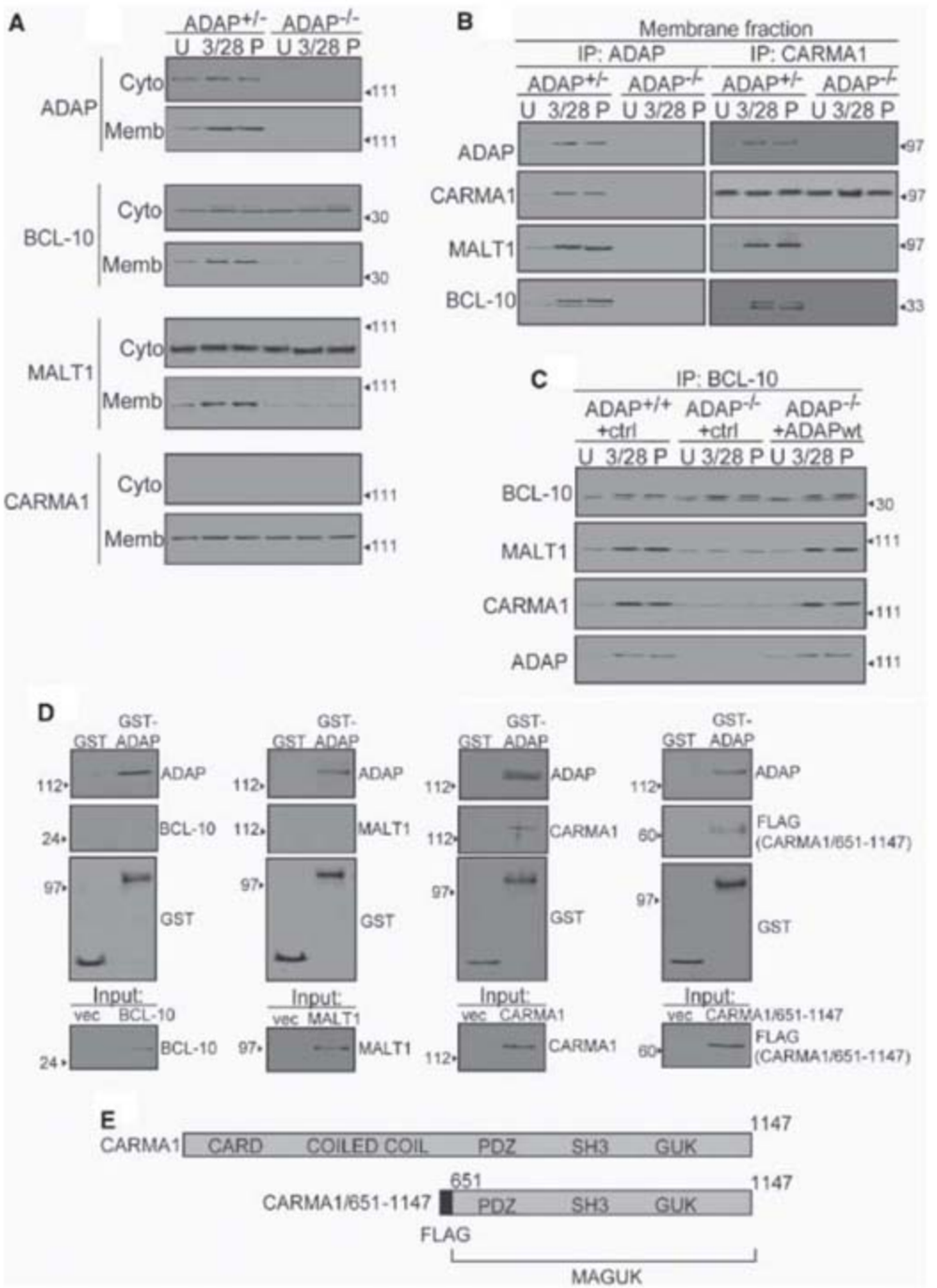

Fig. 3. ADAP is critical for the assembly of the CARMA1–BCL-10–MALT1 complex and associates directly with the C-terminal end of CARMA1. (**A**) ADAP$^{+/-}$ and ADAP$^{-/-}$ T cells were either unstimulated (U) or stimulated with antibodies to CD3 and CD28 (3/28) or with PMA (P). Cytosolic (Cyto) and membrane (Memb) fractions were prepared from each cell sample and analyzed by Western blotting with the indicated antibodies. (**B**) Membrane fractions were prepared from unstimulated and stimulated ADAP$^{+/-}$ and ADAP$^{-/-}$ T cells as in (A). ADAP or CARMA1 was immunoprecipitated and the immunoprecipitates analyzed as in (A). (**C**) T cells isolated from ADAP$^{+/-}$ and ADAP$^{-/-}$ transgenic mice expressing the hCAR adenovirus receptor were transduced with control adenovirus encoding Thy1.1 (ctrl) or adenovirus expressing wild-type mouse ADAP and Thy1.1 (ADAPwt). T cells were then left unstimulated or were stimulated with antibodies to CD3 and CD28 or with PMA before lysis and immunoprecipitation with a monoclonal antibody (mAb) to BCL-10. Immunoprecipitates were analyzed by Western blotting as in (A). (**D**) Interaction of ADAP with CARMA1 in vitro. GST only or GST-ADAP fusion proteins were incubated with in vitro transcribed/translated BCL-10, MALT1, CARMA1, or truncated FLAG epitope–tagged CARMA1/651-1147. GST pull-downs were analyzed by Western blotting for the presence of the indicated proteins. An equivalent amount of the purified proteins used in the pull-down assays, along with a sample from in vitro transcription and translation reactions using a control vector (vec), were analyzed in separate gels (input). (**E**) Diagram of CARMA1 and CARMA1/651-1147 constructs used in (D).

ADAP mutant lacking the N-terminal 327 amino acids (ADAPΔ1-327), but not an ADAP mutant containing only the N-terminal 426 amino acids (ADAP-426), coimmunoprecipitated the CARMA1–BCL-10–MALT1 complex (Fig. 4B). The CARMA1 binding site in ADAP was mapped to a region of ADAP between amino acids 426 and 541 (Fig. 4A), because a deletion mutant of ADAP lacking this region (ADAPΔ426-541) was completely unable to coimmunoprecipitate the CARMA1–BCL-10–MALT1 complex (Fig. 4B). This region of ADAP contains the N-terminal helical SH3 (hSH3) domain (*21*–*23*) between amino acids 482 and 541, and an adjacent region rich in Glu and Lys residues (E/K-rich region) between amino acids 426 and 481. ADAP deletion mutants lacking either the N-terminal hSH3 domain (ADAPΔ482-541) or the E/K-rich region (ADAPΔ426-481) (Fig. 4A) showed weak coimmunoprecipitation of the CARMA1–BCL-10–MALT1 complex relative to wild-type ADAP (Fig. 4B). A GST-ADAP fusion protein expressing both the hSH3 domain and the E/K-rich region of ADAP was able to associate with the truncated CARMA1/651-1147 protein in vitro (fig. S8), which suggests that this region of ADAP is sufficient for CARMA1 association.

Expression of wild-type ADAP in resting ADAP$^{-/-}$ T cells restored the ability of PMA (Fig. 4C) or CD3/CD28 stimulation (Fig. 4D) to induce nuclear translocation of p65. ADAP expression in transduced T cells was verified by intracellular flow cytometry (fig. S9). Expression of the ADAPΔ1-327 mutant, but not the ADAP-426 mutant, in ADAP$^{-/-}$ T cells was also able to fully restore CD3/CD28-mediated NF-κB translocation (Fig. 4D). In contrast, the ADAPΔ426-541 deletion mutant did not restore CD3/CD28-mediated NF-κB translocation after expression in ADAP$^{-/-}$ T cells (Fig. 4E). Expression of either the ADAPΔ426-481 or ADAPΔ482-541 deletion mutants partially restored NF-κB p65 nuclear translocation (Fig. 4E).

ADAP also regulates TCR-mediated integrin activation (*2*, *3*) and thus ADAP$^{-/-}$ T cells exhibit impaired integrin-dependent conjugate formation with antigen-pulsed antigen-presenting cells (*24*) (Fig. 4F). Expression of either wild-type ADAP or the ADAPΔ426-541 mutant in ADAP$^{-/-}$ T cells restored TCR-induced conjugate formation to levels observed in control T cells (Fig. 4F). Thus, the region of ADAP between amino acids 426 and 541 is critical for NF-κB activation but is not required for the regulation of integrin-dependent conjugate formation.

We have identified a novel function for ADAP in the regulation of NF-κB activation in T cells. We propose that the association between the C-terminal end of CARMA1 and the region of ADAP between amino acids 426 and 541 is critical for assembly of the CARMA1–BCL-10–MALT1 complex at the membrane. ADAP may provide mechanisms for membrane localization and stabilization of the CARMA1–BCL-10–MALT1 complex, as the C-terminal ADAP hSH3 domain can associate

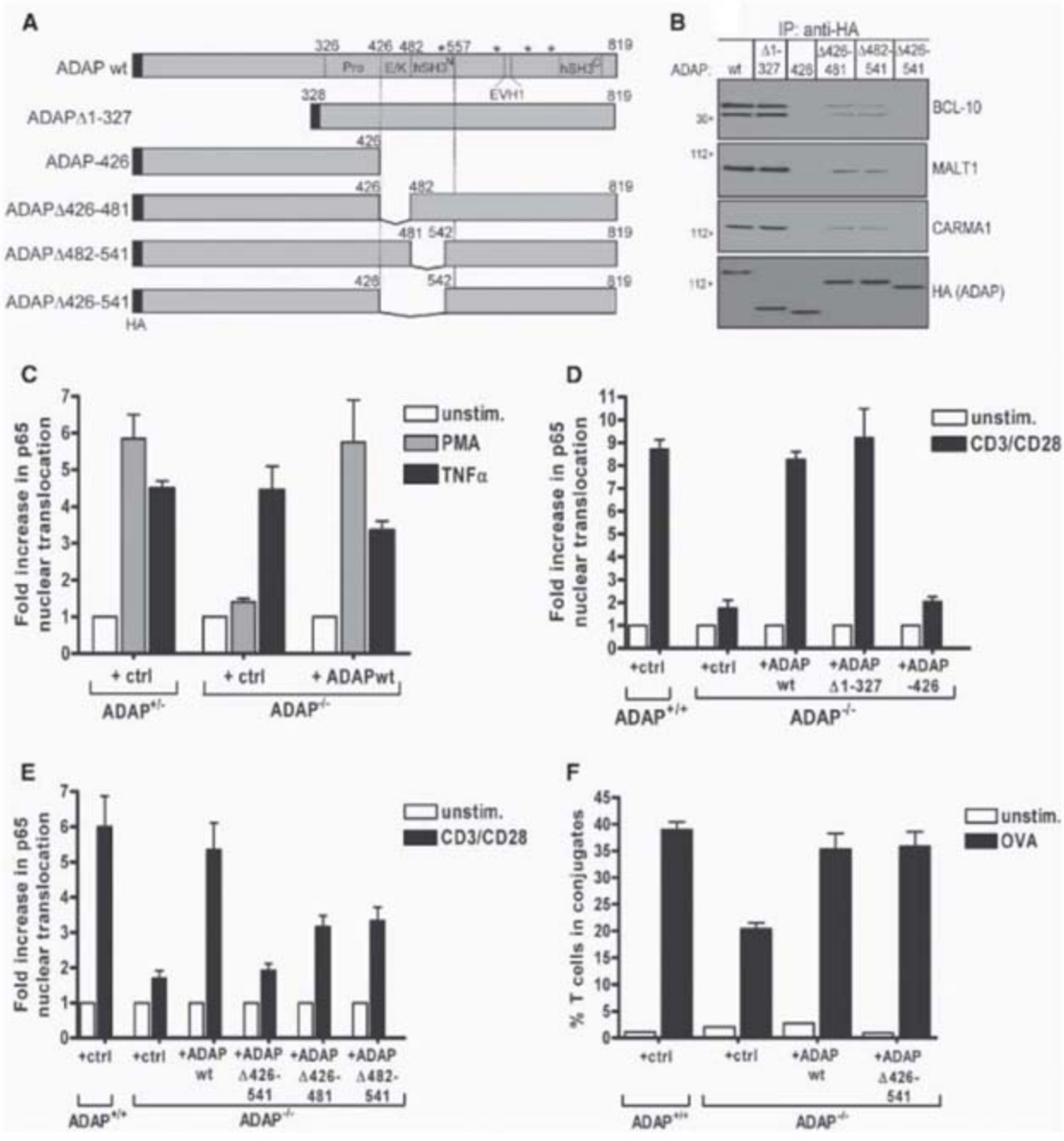

Fig. 4. The region of ADAP containing the N-terminal helical SH3 domain and an E/K-rich region is critical for ADAP-CARMA1 association and TCR-dependent activation of NF-κB, but is dispensable for ADAP-dependent regulation of antigen-dependent conjugate formation. (**A**) Diagram of the HA-tagged ADAP truncation and deletion mutants used in this study. Numbers indicate amino acid position in mouse ADAP. Asterisks indicate Tyr residues (amino acids 547/549, 584, 615, and 687) implicated in ADAP binding to the SLP-76 adapter protein. (**B**) Jurkat T cells were transiently transfected with the indicated HA-ADAP constructs and then stimulated with PMA before immunoprecipitation with BCL-10 mAb, followed by Western blotting with antibodies specific for the indicated proteins. (**C**) T cells isolated from ADAP$^{+/-}$ and ADAP$^{-/-}$ hCAR transgenic mice were transduced with control adenovirus encoding Thy1.1 (ctrl) or adenovirus encoding wild-type ADAP and Thy1.1 (ADAPwt). Cells were either unstimulated or stimulated with PMA or TNF-α before analysis of NF-κB p65 nuclear translocation as in Fig. 2. (**D** and **E**) T cells isolated from ADAP$^{+/+}$ and ADAP$^{-/-}$ hCAR transgenic mice were transduced as in (C) with either a control adenovirus or adenovirus encoding the indicated ADAP constructs. Cells were either unstimulated or stimulated with antibodies to CD3 and CD28 before analysis of NF-κB p65 nuclear translocation. Graphs show the average increase (±SD) in p65 nuclear translocation in stimulated relative to unstimulated T cells for three [(C) and (E)] or two (D) independent experiments. (**F**) T cells isolated from ADAP$^{+/+}$ and ADAP$^{-/-}$ DO11.10/hCAR transgenic mice were transduced as in (E) with control adenovirus or the indicated ADAP constructs. T cells were then analyzed by flow cytometry for their ability to form conjugates with unpulsed (unstim.) or ovalbumin-pulsed (OVA) splenocytes.

with membrane phospholipids (*22*). The interaction of ADAP with the MAGUK region of CARMA1 may also alter intramolecular interactions within CARMA1 (*25*, *26*), thereby promoting recruitment of BCL-10 and MALT1. The region of ADAP critical for association with CARMA1 is not required for ADAP-dependent regulation of integrins (*2*, *3*), which involves the association of ADAP with the SKAP-55 and SLP-76 adapters (*27*–*29*). Two biochemically distinct pools of ADAP can be identified in CD3/CD28-stimulated T cells: one that interacts with the CARMA1–BCL-10–MALT1 complex, and one that interacts with SLP-76 (fig. S10). In contrast, CARMA1 is required for NF-κB activation (*2*, *3*, *30*, *31*) but is not required for conjugate formation (*31*). Thus, ADAP serves distinct roles downstream of the TCR that promote functions critical to T cell immune responses.

References and Notes

1. L. E. Samelson, *Annu. Rev. Immunol.* **20**, 371 (2002).
2. E. J. Peterson *et al.*, *Science* **293**, 2263 (2001).
3. E. K. Griffiths *et al.*, *Science* **293**, 2260 (2001).
4. J. Schulze-Luehrmann, S. Ghosh, *Immunity* **25**, 701 (2006).
5. J. Bertin *et al.*, *J. Biol. Chem.* **276**, 11877 (2001).
6. L. M. McAllister-Lucas *et al.*, *J. Biol. Chem.* **276**, 30589 (2001).
7. A. G. Uren *et al.*, *Mol. Cell* **6**, 961 (2000).
8. P. C. Lucas *et al.*, *J. Biol. Chem.* **276**, 19012 (2001).
9. J. Ruland *et al.*, *Cell* **104**, 33 (2001).
10. D. J. Rawlings, K. Sommer, M. E. Moreno-Garcia, *Nat. Rev. Immunol.* **6**, 799 (2006).
11. Z. Sun *et al.*, *Nature* **404**, 402 (2000).
12. See supporting material on *Science* Online.
13. C. Pfeifhofer *et al.*, *J. Exp. Med.* **197**, 1525 (2003).
14. T. C. George *et al.*, *Cytometry* **59**, 237 (2004).
15. T. C. George *et al.*, *J. Immunol. Methods* **311**, 117 (2006).
16. C. C. Chen, A. M. Manning, *Agents Actions Suppl.* **47**, 135 (1995).
17. O. Gaide *et al.*, *Nat. Immunol.* **3**, 836 (2002).
18. D. Wang *et al.*, *Mol. Cell. Biol.* **24**, 164 (2004).
19. V. Hurez, R. Dzialo-Hatton, J. Oliver, R. J. Matthews, C. T. Weaver, *BMC Immunol.* **3**, 4 (2002).
20. S. D. Dimitratos, D. F. Woods, D. G. Stathakis, P. J. Bryant, *Bioessays* **21**, 912 (1999).
21. K. Heuer *et al.*, *J. Mol. Biol.* **361**, 94 (2006).
22. K. Heuer, A. Arbuzova, H. Strauss, M. Kofler, C. Freund, *J. Mol. Biol.* **348**, 1025 (2005).
23. K. Heuer, M. Kofler, G. Langdon, K. Thiemke, C. Freund, *Structure* **12**, 603 (2004).
24. J. N. Wu *et al.*, *J. Immunol.* **176**, 6681 (2006).
25. A. W. McGee *et al.*, *Mol. Cell* **8**, 1291 (2001).
26. G. A. Tavares, E. H. Panepucci, A. T. Brunger, *Mol. Cell* **8**, 1313 (2001).
27. S. Kliche *et al.*, *Mol. Cell. Biol.* **26**, 7130 (2006).

28. H. Wang *et al.*, *J. Exp. Med.* **200**, 1063 (2004).
29. H. Wang *et al.*, *Nat. Immunol.* **4**, 366 (2003).
30. T. Egawa *et al.*, *Curr. Biol.* **13**, 1252 (2003).
31. H. Hara *et al.*, *J. Exp. Med.* **200**, 1167 (2004).
32. We thank T. George, M. Schwartz, G. Veltri, K. Pavlovich, H.-D. Nguyen, L. Nacusi, K.-S. Tudor, and J. Hanson Ostrander for technical support; C. Weaver for hCAR transgenic mice; and M. Jenkins, J. DeGregori, G. Koretzky, S. Jameson, and P. Holman for reagents and advice. Supported by NIH grants R01AI038474 (Y.S.) and R01AI056016 (E.J.P.), the Arthritis Foundation (E.J.P.), NIH grant T32DE007288 (B.J.B.), American Heart Association grant 0415400Z (K.L.M.), and NIH grant F32AI063793 (J.J.M.). Y.S. is supported in part by the Harry Kay Chair in Biomedical Research at the University of Minnesota.

Supporting Online Material
www.sciencemag.org/cgi/content/full/316/5825/754/DC1
Materials and Methods
Figs. S1 to S10
References

22 November 2006; accepted 26 March 2007
10.1126/science.1137895

Specialized Inhibitory Synaptic Actions Between Nearby Neocortical Pyramidal Neurons

Ming Ren, Yumiko Yoshimura, Naoki Takada, Shoko Horibe, Yukio Komatsu*

We found that, in the mouse visual cortex, action potentials generated in a single layer-2/3 pyramidal (excitatory) neuron can reliably evoke large, constant-latency inhibitory postsynaptic currents in other nearby pyramidal cells. This effect is mediated by axo-axonic ionotropic glutamate receptor–mediated excitation of the nerve terminals of inhibitory interneurons, which connect to the target pyramidal cells. Therefore, individual cortical excitatory neurons can generate inhibition independently from the somatic firing of inhibitory interneurons.

In the mammalian brain, neurons integrate synaptic inputs onto their somatodendritic domains, which control the generation of action potentials propagating through the axonal arbor to axon terminals, at which signals are transmitted to postsynaptic neurons. Action potential–dependent transmitter release from axon terminals is modulated by ionotropic glutamate and γ-aminobutyric acid (GABA) receptors that are present, either synaptically or extrasynaptically, on the axon terminals (*1*, *2*).

We used dual whole-cell recording under microscopic observation to study synaptic connections from pyramidal and nonpyramidal neurons to nearby (<75 μm) pyramidal neurons in layer 2/3 of the mouse visual cortex (*3*). Single action potentials in a pyramidal neuron could produce inhibitory postsynaptic current (IPSC)–like outward currents in another pyramidal neuron held at the reversal potential (0 mV) of excitatory postsynaptic currents (EPSCs) (Fig. 1A). These currents were evoked by individual action potentials with relatively constant latencies that were comparable to those seen in monosynaptic connections (Fig. 1A). The responses were abolished by bath application of the GABA type A ($GABA_A$) receptor antagonist bicuculline methiodide (BMI) (20 μM) and after reversal could then be abolished again by application of the non–*N*-methyl-D-aspartate (NMDA) glutamate receptor antagonist 2,3-dioxo-6-nitro-1,2,3,4-tetrahydrobenzo[f]quinoxaline-7-sulphonamide (NBQX) (10 μM, $n = 6$ neuron pairs), indicating that they were polysynaptic IPSCs (Fig. 1B).

Department of Neuroscience, Research Institute of Environmental Medicine, Nagoya University, Nagoya 464-8601, Japan.
*To whom correspondence should be addressed. E-mail: komatsu@riem.nagoya-u.ac.jp

To further characterize these interpyramidal IPSCs (ip IPSCs), we compared them with two kinds of monosynaptic currents: unitary EPSCs (uEPSCs) recorded from pyramidal neuron pairs at the reversal potential (–70 mV) of IPSCs (Fig. 1C) and unitary IPSCs (uIPSCs) from nonpyramidal neurons to pyramidal neurons (Fig. 1D). In pyramidal neuron pairs, the probability of detecting an ip IPSC [28%; 31 out of 110 (31/110)] was slightly higher than that for the detection of an EPSC (22%; 24/110). NBQX blocked ip IPSCs in all of the tested pairs ($n = 27$). Reciprocal interpyramidal inhibitory connections were never observed. Six pairs had both inhibitory and excitatory connections. The direction was the same for three pairs and opposite for three pairs. In these pyramidal neuron pairs, patch pipettes containing a Cs^+-based internal solution were used for recording from both pre- and postsynaptic neurons. Similar ip IPSCs were also recorded with a K^+-based internal solution (fig. S1). Recordings from pairs involving an inhibitory neuron and a pyramidal neuron had a detection probability for uIPSCs of 32% (19/60), which was slightly higher than that for ip IPSCs.

The amplitudes of ip IPSCs were significantly larger ($P < 0.01$) than those of uIPSCs (Fig. 1E), and their time course was similar to that of uIPSCs (Fig. 1, A and D, and fig. S2). Although the average latency of ip IPSCs was significantly ($P < 0.02$) longer than that of either uIPSCs or uEPSCs, it was distributed in a wide range that included latency values for the two monosynaptic connections (Fig. 1F). If ip IPSCs resulted from conventional polysynaptic activation involving action-potential generation at the somata of inhibitory neurons, the expected variation in latency for each pair should be far larger than that in monosynaptic connections. However, the coefficient of variation of their latency was indistinguishable ($P > 0.2$) from those for either uEPSCs or uIPSCs (Fig. 1G), suggesting that they were unlikely to be mediated by the generation of somatic action potentials in inhibitory interneurons. Consistent with this supposition, the failure rate of ip IPSCs was not significantly different ($P > 0.1$) from that of uIPSCs or uEPSCs (fig. S3). This interpretation is also supported by the observation that unitary excitatory inputs alone induce only small postsynaptic responses that are subthreshold for action-potential generation in inhibitory interneurons (*4*–*7*). Thus, we hypothesized that ip IPSCs are generated by direct excitation of the presynaptic terminals of inhibitory neurons, which in turn connect to the target pyramidal neuron (Fig. 2A). This mechanism implies that the axo-axonic synaptic transmission must be strong enough to release GABA immediately from the inhibitory terminals. If this synaptic transmission is very strong, extraordinarily quick depolarization would occur at the terminals because of their small volume and lack of strong filtering effects on input signals seen in dendrites. This may, at least in part, explain the short latency of ip IPSCs, together with the absence of conduction time in interneurons. We tested this hypothesis, as described below.

If such excitatory axo-axonic synapses are present, the frequency of miniature IPSCs (mIPSCs) recorded from pyramidal cells in the presence of 1 μM tetrodotoxin (TTX), a sodium channel blocker, may be affected by glutamatergic agents. Bath application of glutamate (10 μM) significantly ($P < 0.02$) increased the frequency of mIPSCs without any significant ($P > 0.6$) changes in their amplitude (Fig. 2, B, D, and E). Similar facilitative effects were produced by the selective activation of AMPA receptors with AMPA (1 μM) and kainate receptors with (*RS*)-2-amino-3-(3-hydroxy-5-*tert*-butylisoxazol-4-yl) propanoic acid (ATPA) (1 μM) (*8*) or a low dose (200 nM) of domoic acid (*9*), suggesting that both AMPA and kainate receptors contribute to the facilitation of mIPSC frequency (Fig. 2, D and E). We confirmed this supposition with a pharmacological blockade of these receptors (fig. S4). The effect of these receptors may be mediated by the depolarization of nerve terminals, because the facilitation of mIPSC frequency was not found in the presence of Co^{2+}, which blocks voltage-gated Ca^{2+} channels, and because the metabotropic action of kainate receptors was not involved in this process (fig. S5).

The application of NBQX significantly ($P < 0.02$) reduced the frequency of mIPSCs without any significant ($P > 0.9$) changes in their ampli-

tude in control solution (Fig. 2, C, D, and E), indicating that the basal level of extracellular glutamate facilitates mIPSC frequency. The activation of AMPA and kainate receptors on inhibitory presynaptic terminals increases or decreases evoked-IPSCs in various connections (*10*–*18*). It is likely that inhibitory synaptic transmission is not affected by the basal level of extracellular glutamate in our experimental condition because NBQX application produced no change in uIPSCs (fig. S6).

Excitatory synaptic transmission seems to be mediated mostly by AMPA receptors in neocortical inhibitory interneurons (*6*). We confirmed that AMPA (but not kainate) receptors mediated excitatory synaptic transmission from pyramidal to nonpyramidal neurons (fig. S7). Thus, an investigation of glutamate receptors involved in ip IPSCs may provide important information on the validity of our hypothesis. We conducted additional dual whole-cell recordings from pyramidal neurons. In all of the tested pairs with latencies shorter than 3 ms ($n = 6$ pairs), ip IPSCs were not affected by the AMPA receptor antagonist SYM 2206 (30 μM) (*19*, *20*), but they were reduced substantially by the subsequent application of SYM 2081 (1 μM, $n = 6$), a kainate receptor ligand that causes potent receptor desensitization (*19*, *21*) (Fig. 3A and fig. S8A). In two cases of these pair recordings, the responses were completely abolished by further application of UBP 301 (50 μM), a kainate receptor antagonist (*22*).

In the pairs with latencies longer than 5 ms ($n = 10$ pairs), most ip IPSCs were completely abolished by SYM 2081 ($n = 5$) (Fig. 3B) or UBP 301 ($n = 3$) (fig. S8B). In the remaining two pairs, ip IPSCs were partially blocked by SYM 2081 (about half of the control amplitude), and the remaining responses were completely abolished by the subsequent application of SYM 2206. In addition, long-latency ip IPSCs were completely abolished by the application of SYM 2206 alone ($n = 6$) (Fig. 3C and fig. S8C). These results strongly suggest that ip IPSCs with short latencies are mediated mostly by kainate receptors, whereas those with long latencies are mediated by both AMPA and kainate receptors to a comparable degree. The consistent contribution of kainate receptors to ip IPSCs strongly supports the intervention of axo-axonic synapses in these responses. Although SYM 2081 incompletely blocked short-latency ip IPSCs, it completely blocked most long-latency ip IPSCs (Fig. 3, A and B, and fig. S8), suggesting that the latency depends, at least in part, on the number of kainate receptors implicated.

To further test for the possibility that ip IPSCs are mediated by the excitation of inhibitory terminals in close proximity to the postsynaptic pyramid, we used a paradigm that allowed local glutamatergic blockade, far from the likely location of the dendrites of inhibitory neurons that might mediate the IPSCs (Fig. 3D). Monosynaptic-like IPSCs were evoked in layer-2/3 pyramidal neurons by stimulation with bipolar metal electrodes placed in layer 4. They were decreased by bath application of NBQX (10 μM) without substantial changes in their time courses, as shown in the superimposed traces of control and reduced IPSCs, scaled to the same amplitude (Fig. 3E). Thus, these IPSCs probably comprise a mixture of ip IPSCs (arising from antidromic activation of layer-2/3 pyramidal neurons) and uIPSCs (due to direct input from inhibitory interneurons). Brief pressure application of NBQX (10 μM) from another patch pipette placed near (<5 μm) the soma of the recorded neuron produced similar reductions in IPSCs, whereas the same NBQX application far from the soma (50 to 70 μm) failed to produce such reductions (Fig. 3, E to H), suggesting that most non-NMDA receptors mediating ip IPSCs are located in close proximity to the cell body of the target pyramidal neuron. This observation further implicates inhibitory basket cells as likely mediators of at least some ip IPSCs (*23*, *24*).

The hypothesis that excitatory axo-axonic synapses mediate ip IPSCs would be strengthened if iontophoretic application of glutamate to inhibitory nerve terminals onto pyramidal cells induces IPSCs in the presence of TTX, which localizes glutamate-induced depolarization to the applied area (Fig. 3I). The application of glutamate, at high intensities of ejection currents, to the soma of pyramidal cells produced slow inward currents at –70 mV, presumably mediated by AMPA and kainate receptors on the soma of recorded pyramidal cells, but it produced large outward currents at 0 mV (Fig. 3J and fig. S9). The outward currents had a much faster time course than did the inward currents ($P < 0.03$) (Fig. 3J and fig. S9). In addition, glutamate application at low intensities of ejection currents evoked asynchronous outward currents exhibiting a fast time course. These currents were comparable to mIPSCs, but their amplitudes were much larger than those of mIPSCs (fig. S10). Thus, glutamate-evoked synchronous outward currents are considered to be compound IPSCs, resulting from the simultaneous release of GABA from multiple inhibitory nerve terminals quickly depolarized by glutamate. This suggests that glutamatergic transmission at the GABAergic terminal is very effective. Similar outward currents were also induced by AMPA ($n = 5$ cells), kainate (an agonist for both AMPA and kainate receptors, $n = 5$), and ATPA application ($n = 5$), suggesting that they are mediated by both AMPA and kainate receptors (Fig. 3J and fig. S9). AMPA ($n = 5$), kainate ($n = 5$), or ATPA-induced outward currents ($n = 5$) were abolished by bath application of BMI without any reduction in inward currents, and inward and outward currents were both abolished by

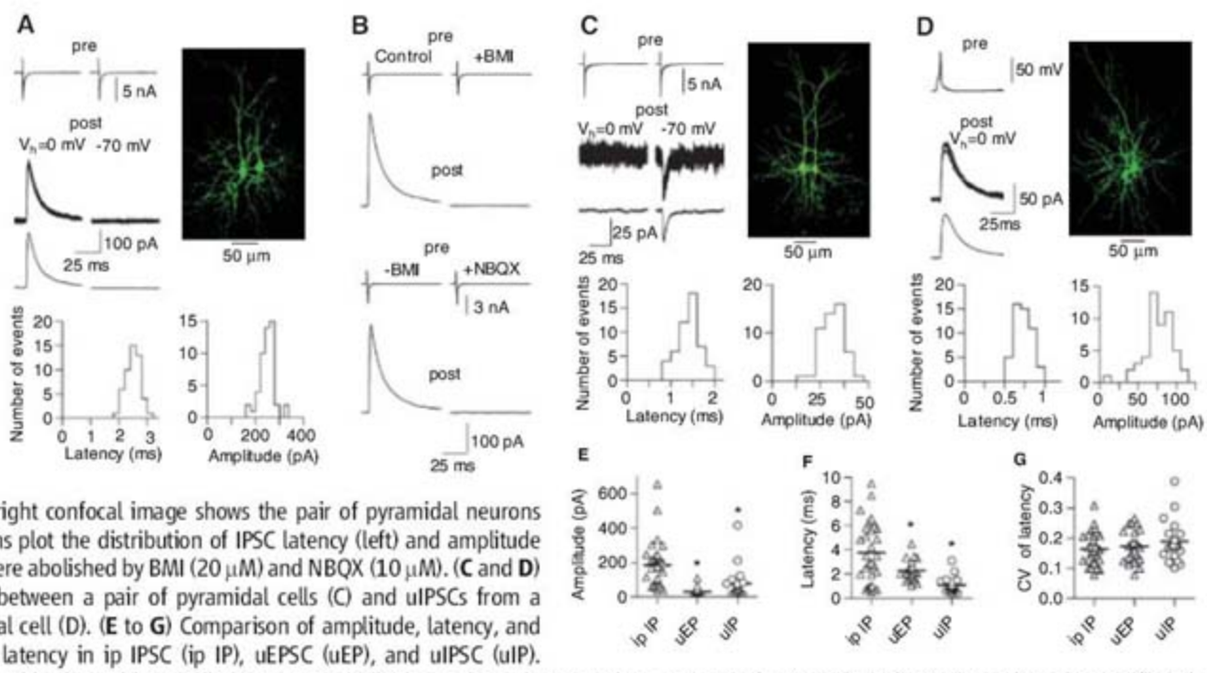

Fig. 1. Comparison of ip IPSCs with unitary EPSCs and IPSCs. (**A**) Action potentials elicited in a pyramidal cell produced IPSCs, but not EPSCs, with a constant latency in another nearby pyramidal cell. The traces show superimposed ($n = 5$) spikes elicited by depolarizing voltage pulses in the source cell (top) and superimposed (middle, $n = 5$) and average (bottom, $n = 50$) postsynaptic currents recorded from the target cell at the holding potential (V_h) of 0 mV (left) and −70 mV (right). The right confocal image shows the pair of pyramidal neurons stained with biocytin. Histograms plot the distribution of IPSC latency (left) and amplitude (right) in the pair. (**B**) ip IPSCs were abolished by BMI (20 μM) and NBQX (10 μM). (**C** and **D**) Similar to (A), but for uEPSCs between a pair of pyramidal cells (C) and uIPSCs from a nonpyramidal cell to a pyramidal cell (D). (**E** to **G**) Comparison of amplitude, latency, and coefficient of variation (CV) of latency in ip IPSC (ip IP), uEPSC (uEP), and uIPSC (uIP). Symbols (triangles and circles) and horizontal bars indicate values in individual pairs and mean values, respectively. Asterisks indicate that values are significantly different from those for ip IPSCs ($P < 0.05$).

NBQX (fig. S11). These observations strongly support our hypothesis about ip IPSCs.

Finally, we attempted to demonstrate morphologically, using mechanically dissociated neurons from slices, that GABAergic terminals on the soma of layer-2/3 pyramidal neurons have non-NMDA receptors and that they are apposed by glutamatergic synaptic terminals. Dissociated cells had a pyramidal-like shape, and mIPSCs could be measured (n = 4) (Fig. 4A), indicating that some inhibitory synaptic terminals remained attached to the soma and dendrites. Iontophoretic application of kainate to the soma of these neurons induced outward and inward currents, similar to those observed in slices (n = 3) (Fig. 4B). Thus, we used this preparation for immunocytochemical staining.

Staining for synaptophysin, a presynaptic terminal marker, showed bouton-like structures (presumably presynaptic terminals) surrounding the soma of neurons (Fig. 4C). Double staining for synaptophysin and the GABA synthetic enzymes glutamic acid decarboxylase 65 and 67 (GAD65/67) showed that >50% of synaptophysin-positive terminals expressed GAD65/67, confirming the presence of GABAergic terminals on the dissociated neuron (Fig. 4, C and F). GAD65/67 was absent inside of the dissociated neurons, consistent with the morphological supposition that they were pyramidal neurons. We used an antibody against glutamate receptor 5 (GluR5) as a marker of non-NMDA receptors because the application of ATPA, activating GluR5-containing kainate receptors selectively (*8*), produced compound IPSCs (Fig. 3J). Double staining for GAD65/67 and GluR5 demonstrated that ~40% of GABAergic terminals expressed GluR5 receptors (Fig. 4, D and F). Double staining for GAD65 and VGluT1, a vesicular glutamate transporter located at pyramidal neuron nerve terminals (*25*, *26*), demonstrated that more than half of the GAD-positive terminals adjoined VGluT1-positive terminals (Fig. 4, E and F), consistent with an

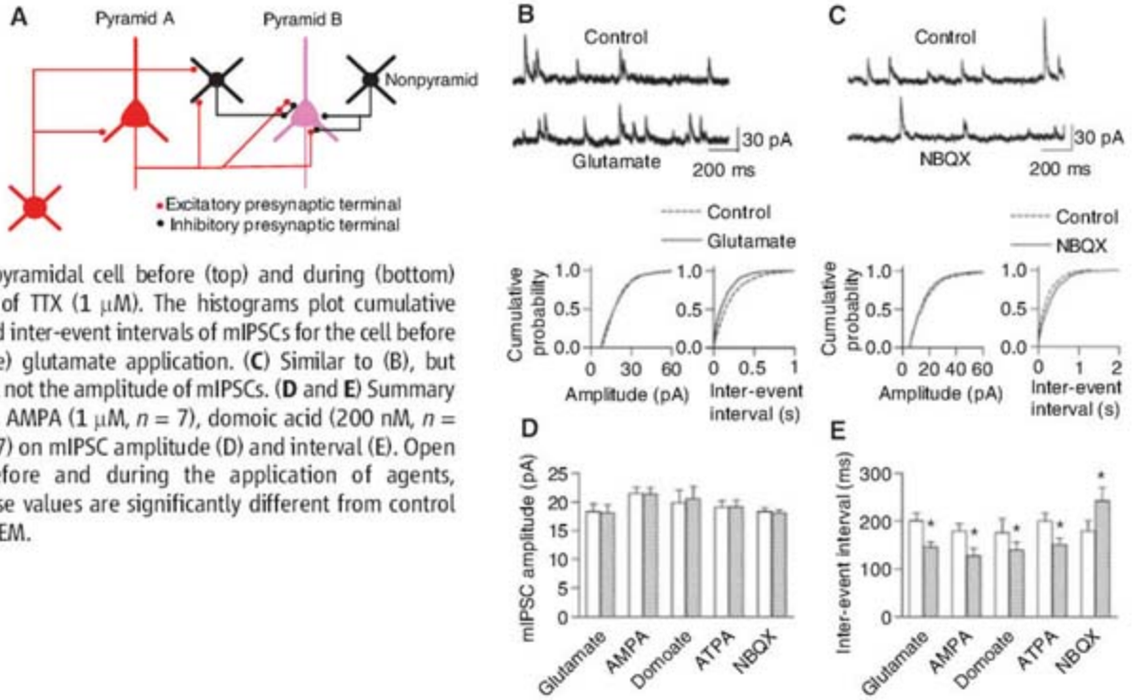

Fig. 2. Hypothesized interpyramidal inhibitory connection and presence of AMPA and kainate receptors on presynaptic inhibitory terminals. (**A**) Schematic illustration of interpyramidal inhibitory connection from pyramid A to pyramid B. (**B**) Glutamate (10 μM) decreased the interval but not the amplitude of mIPSCs. The traces show mIPSCs recorded from a pyramidal cell before (top) and during (bottom) glutamate application in the presence of TTX (1 μM). The histograms plot cumulative probability distributions of amplitude and inter-event intervals of mIPSCs for the cell before (interrupted line) and during (solid line) glutamate application. (**C**) Similar to (B), but NBQX (10 μM) increased the interval but not the amplitude of mIPSCs. (**D** and **E**) Summary of the effects of glutamate (n = 7 cells), AMPA (1 μM, n = 7), domoic acid (200 nM, n = 6), ATPA (1 μM, n = 7), and NBQX (n = 7) on mIPSC amplitude (D) and interval (E). Open and striped bars indicate values before and during the application of agents, respectively. Asterisks indicate that these values are significantly different from control values ($P < 0.05$). Error bars indicate SEM.

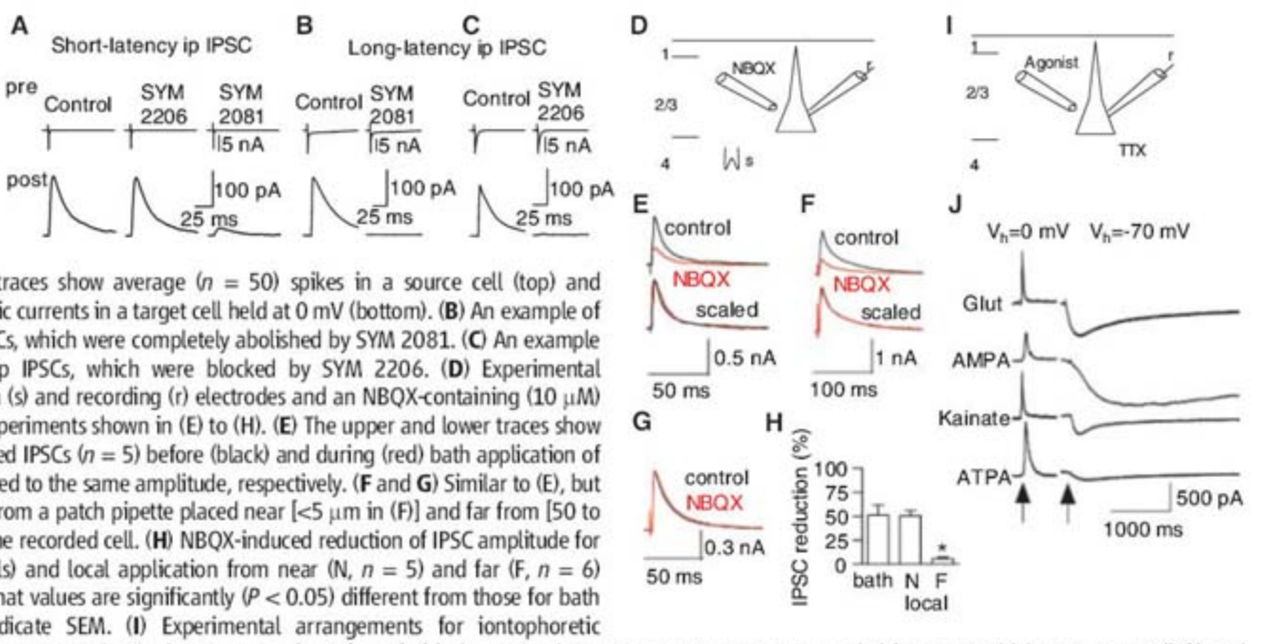

Fig. 3. Non-NMDA receptors on inhibitory terminals mediate ip IPSCs. (**A**) Short-latency (2.2 ms) ip IPSCs were not affected by SYM 2206 (30 μM), but they were greatly reduced by the subsequent application of SYM2081 (1 μM). The traces show average (n = 50) spikes in a source cell (top) and average (n = 50) postsynaptic currents in a target cell held at 0 mV (bottom). (**B**) An example of long-latency (5.2 ms) ip IPSCs, which were completely abolished by SYM 2081. (**C**) An example of long-latency (5.6 ms) ip IPSCs, which were blocked by SYM 2206. (**D**) Experimental arrangements of stimulation (s) and recording (r) electrodes and an NBQX-containing (10 μM) patch pipette used in the experiments shown in (E) to (H). (**E**) The upper and lower traces show superimposed average evoked IPSCs (n = 5) before (black) and during (red) bath application of 10 μM NBQX and those scaled to the same amplitude, respectively. (**F** and **G**) Similar to (E), but for local NBQX application from a patch pipette placed near [<5 μm in (F)] and far from [50 to 70 μm in (G)] the soma of the recorded cell. (**H**) NBQX-induced reduction of IPSC amplitude for bath application (n = 6 cells) and local application from near (N, n = 5) and far (F, n = 6) pipettes. Asterisk indicates that values are significantly ($P < 0.05$) different from those for bath application. Error bars indicate SEM. (**I**) Experimental arrangements for iontophoretic application of glutamate receptor agonists in the presence of TTX (1 μM). (**J**) The traces show raw current responses recorded from pyramidal neurons at 0 (left) and −70 mV (right) in response to glutamate (Glut), AMPA, kainate, and ATPA application. Arrows indicate the onset of iotophoretic application. Time and current calibrations are common to all traces.

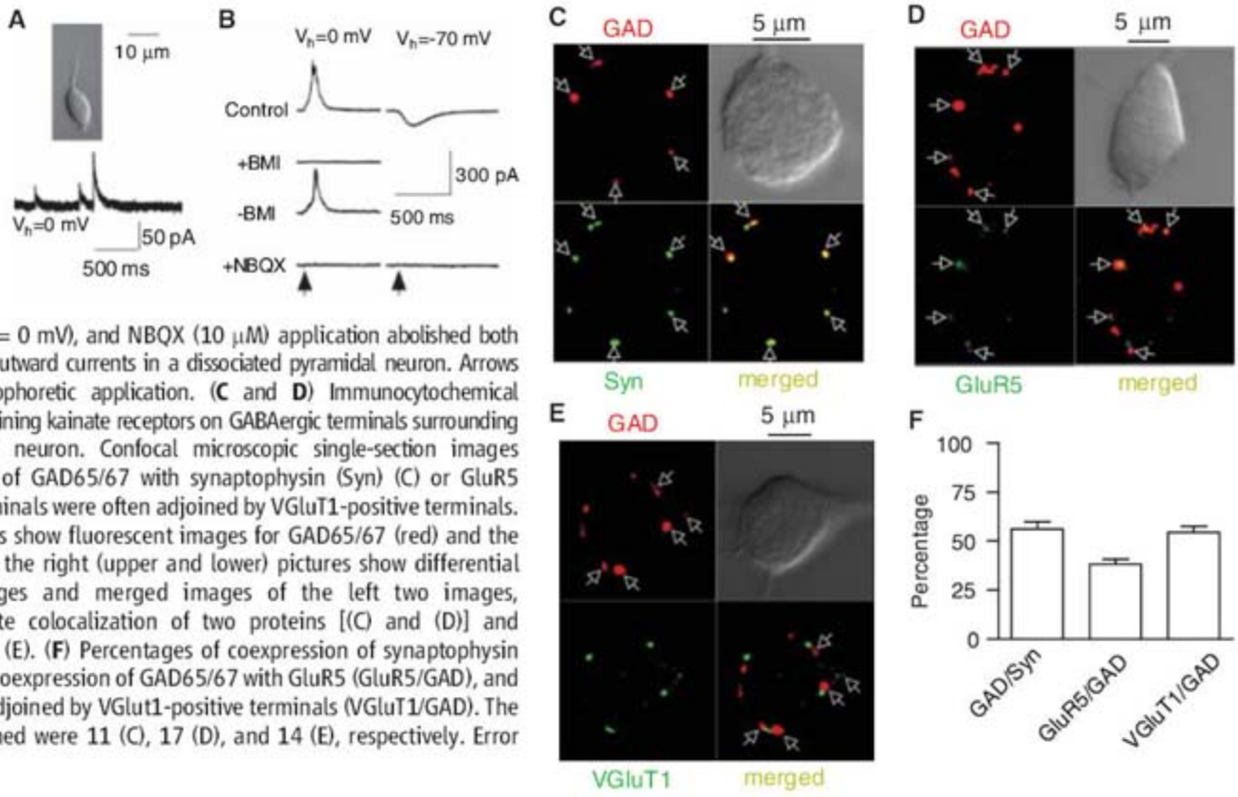

Fig. 4. Glutamatergic synapses exist on GABAergic terminals presynaptic to pyramidal cells. (**A**) mIPSCs (V_h = 0 mV) recorded from a mechanically dissociated layer-2/3 pyramidal neuron (upper picture, differential interference image). (**B**) Bath application of BMI (20 μM) abolished kainate-evoked outward currents (V_h = 0 mV), and NBQX (10 μM) application abolished both inward (V_h = −70 mV) and outward currents in a dissociated pyramidal neuron. Arrows indicate the onset of iontophoretic application. (**C** and **D**) Immunocytochemical demonstration of GluR5-containing kainate receptors on GABAergic terminals surrounding the soma of a dissociated neuron. Confocal microscopic single-section images demonstrate colocalization of GAD65/67 with synaptophysin (Syn) (C) or GluR5 (D). (**E**) GAD65-positive terminals were often adjoined by VGluT1-positive terminals. In (C) to (E), the left pictures show fluorescent images for GAD65/67 (red) and the other proteins (green), and the right (upper and lower) pictures show differential interference contrast images and merged images of the left two images, respectively. Arrows indicate colocalization of two proteins [(C) and (D)] and GAD65 apposed by VGluT1 (E). (**F**) Percentages of coexpression of synaptophysin with GAD65/67 (GAD/Syn), coexpression of GAD65/67 with GluR5 (GluR5/GAD), and GAD65-positive terminals adjoined by VGlut1-positive terminals (VGluT1/GAD). The numbers of neurons examined were 11 (C), 17 (D), and 14 (E), respectively. Error bars indicate SEM.

immunocytochemical study in the rat somatosensory cortex (*27*). These morphological data suggest that glutamate released from the axon terminals of a pyramidal neuron quickly activates non-NMDA receptors on inhibitory nerve terminals that connect to the soma of other pyramidal neurons. In addition, axons of pyramidal neurons stained with biocytin in slice preparations were often found on the soma of presumed pyramidal neurons. Those axons had multiple synaptic terminal-like boutons, apposed by GAD-positive terminals surrounding neurons lacking GAD inside their soma (fig. S12). This anatomical feature of connections may, at least partly, explain the large amplitude of ip IPSCs. However, it is uncertain whether the axo-axonic transmission is mediated by synapses with a structure commonly demonstrated by electron microscopy (*28*).

We demonstrated that layer-2/3 pyramidal neurons, sending output signals to other cortical areas, exert strong inhibitory effects on nearby pyramidal cells via the direct activation of nerve terminals of inhibitory interneurons, bypassing their somatodendrite domain (Fig. 2A). Our analysis suggests that the activation of inhibitory terminals is mediated by axo-axonic signaling, although we cannot rule out partial involvement of dendro-axonic signaling (*29*). This inhibition may play a crucial role in the regulation of the cortical output signal. According to traditional views, pyramidal neurons receive inhibitory inputs via action potentials initiated in inhibitory interneurons after integration of synaptic inputs to their somatodendritic domain. Thus, synaptic transmission from inhibitory nerve terminals to layer-2/3 pyramidal cells is driven by two distinct signaling pathways: (i) via an integration of feedforward and feedback signals in inhibitory interneurons (*30*) and (ii) more directly via output signals of nearby pyramidal cells. The presence of interpyramidal inhibition suggests that the functional influence of inhibitory neurons can be far greater than might be predicted by their relatively small numbers (~20% of cortical neurons) (*23*, *31*).

References and Notes

1. A. B. MacDermott, L. W. Role, S. A. Siegelbaum, *Annu. Rev. Neurosci.* **22**, 443 (1999).
2. H. S. Engelman, A. B. MacDermott, *Nat. Rev. Neurosci.* **5**, 135 (2004).
3. Materials and methods are available as supporting material on *Science* Online.
4. A. M. Thomson, J. Deuchars, *Cereb. Cortex* **7**, 510 (1997).
5. E. H. Buhl *et al.*, *J. Phyisiol.* **500**, 689 (1997).
6. A. Rozov, J. Jerecic, B. Sakmann, N. Burnashev, *J. Neurosci.* **21**, 8062 (2001).
7. C. Holmgren, T. Harkany, B. Svennenfors, Y. Zilberter, *J. Physiol.* **551**, 139 (2003).
8. V. R. J. Clarke *et al.*, *Nature* **389**, 599 (1997).
9. I. Bureau, S. Bischoff, S. F. Heinemann, C. Mulle, *J. Neurosci.* **19**, 653 (1999).
10. S. Satake, F. Saitow, J. Yamada, S. Konishi, *Nat. Neurosci.* **3**, 551 (2000).
11. M.-Y. Min, Z. Melyan, D. M. Kullmann, *Proc. Natl. Acad. Sci. U.S.A.* **96**, 9932 (1999).
12. C. Mulle *et al.*, *Neuron* **28**, 475 (2000).
13. A. Rodriguez-Moreno, J. C. Lopez-Garcia, J. Lerma, *Proc. Natl. Acad. Sci. U.S.A.* **97**, 1293 (2000).
14. A. B. Ali, J. Rossier, J. F. Staiger, E. Audinat, *J. Neurosci.* **21**, 2992 (2001).
15. G. A. Kerchner, G.-D. Wang, C.-S. Qiu, J. E. Heuttner, M. Zhuo, *Neuron* **32**, 477 (2001).
16. R. Cossart *et al.*, *Neuron* **29**, 497 (2001).
17. L. Jiang, J. Xu, M. Nedergaard, J. Kang, *Neuron* **30**, 503 (2001).
18. M. F. M. Braga, V. Aroniadou-Anderjaska, J. Xie, H. Li, *J. Neurosci.* **23**, 442 (2003).
19. P. Li *et al.*, *Nature* **397**, 161 (1999).
20. J. C. Pelletier, D. P. Hesson, K. A. Jones, A.-M. Costa, *J. Med. Chem.* **39**, 343 (1996).
21. T. J. Wilding, J. E. Huettner, *J. Neurosci.* **17**, 2713 (1997).
22. J. C. A. More, H. M. Troop, N. P. Dolman, D. E. Jane, *Br. J. Pharmacol.* **138**, 1093 (2003).
23. P. Somogyi, G. Tamas, R. Lujan, E. H. Buhl, *Brain Res. Rev.* **26**, 113 (1998).
24. Y. Kawaguchi, S. Kondo, *J. Neurocytol.* **31**, 277 (2002).
25. R. T. Fremeau *et al.*, *Neuron* **31**, 247 (2001).
26. F. Fujiyama, T. Furuta, T. Kaneko, *J. Comp. Neurol.* **435**, 379 (2001).
27. L. Alonso-Nanclares *et al.*, *Neuroscience* **123**, 547 (2004).
28. P. De Camilli, V. Haucke, K. Takei, E. Mugnaini, in *Synapses*, W. M. Cowan, T. C. Sudhof, C. F. Stevens, K. Davies, Eds. (Johns Hopkins Univ. Press, Baltimore, 2000), chap. 2.
29. Y. Zilberter, *J. Physiol.* **528**, 489 (2000).
30. J. L. Dantzker, E. M. Callaway, *Nat. Neurosci.* **3**, 701 (2000).
31. R. J. Douglas, K. A. C. Martin, *Annu. Rev. Neurosci.* **27**, 419 (2004).

32. We thank E. M. Callaway for critical reading of this manuscript, T. Kaneko and F. Fujiyama for providing an antibody to VGluT1, and J. Nabekura for technical advice. This study was supported by grants from the Japanese Ministry of Education, Culture, Science, Sports and Technology to Y.Y. (17500208 and 18021018) and Y.K. (17300101 and 18021017) and a grant from Core Research for Evolutional Science and Technology of the Japan Science and Technology Agency to Y.Y.

Supporting Online Material

www.sciencemag.org/cgi/content/full/316/5825/758/DC1
Materials and Methods
Figs. S1 to S12
Table S1
References

22 September 2006; accepted 29 March 2007
10.1126/science.1135468

Microbalances

The Excellence XP microbalances are designed for micro-dosing into large tare containers. They offer innovative features coupled with an inner draft shield to provide user protection, measurement performance, data security, and seamless traceability. The innovative grid-style weighing pan and the inner draft shield minimize the effects of air turbulence in the weighing chamber, which shortens stabilization times. Spilled samples sift through the grid and are caught in the underlying tray without affecting the weighing result, reducing cross-contamination and speeding up cleaning times. The micro MinWeigh Door allows dosing through a small window directly into the tare container without opening the draft shield. The automatic outer draft shield doors open horizontally and the inner draft shield opens vertically. Both can be configured individually to allow easier access to the weighing pan. A full line of accessories includes the micro ErgoClips to allow secure fastening of small and odd-shaped tare containers to the weigh pan. Programmable infrared sensors allow for hands-free operation.

Mettler Toledo For information 614-438-4936 www.mt.com

Rat Druggable Genome

The Rat Druggable Genome siRNA Set V1.0 enables potent and specific knockdown of about 6,000 rat genes that correspond to human genes of potential therapeutic value. The small-interfering (si) RNAs are designed through HP OnGuard siRNA Design, which incorporates an innovative neural network, proprietary homology analysis, and advanced design features based on the most up-to-date knowledge of the mechanism of RNA interference. Subsets targeting 426 G-protein-coupled receptor genes, 738 kinase genes, and 198 phosphatase genes are also available.

Qiagen For information +49 2103 29 12400 www.qiagen.com

Blot-Stripping Buffer

The Restore Plus Western Blot Stripping Buffer quickly and efficiently removes high-affinity antibodies from protein immunoblots without damaging the transferred proteins, thus allowing multiple re-probes for the target protein. The buffer is stored at room temperature and used without dilution. It is effective with nitrocellulose and poly(vinylidine fluoride) membranes, a variety of blocking buffers, horseradish peroxidase and alkaline phosphatase antibody conjugates, and various chemiluminescent substrates.

Thermo Fischer Scientific
For information 815-968-0747 www.thermofisher.com

Comet Assay Control Cells

In a typical single-cell gel electrophoresis, or comet assay, electrophoresis methods and differences in cell preparations create a significant source of variation in comet tail parameters. To overcome this problem, Trevigen offers a set of stable control cell populations containing incremental levels of DNA damage for use when performing the CometAssay. These control cells, when electrophoresed in the CometAssay, consistently produce comets with predetermined percents of DNA in the tails. These cryopreserved control cells are designed to act as controls to standardize alkaline electrophoresis methods between individual users and laboratories.

Trevigen For information 800-873-8443. www.trevigen.com

Microbial and Nucleic Acid Removal

MicroSol 3+ is for disinfection of surfaces, pipettes, and other small laboratory instruments, with proven efficacy against bacteria, fungi, yeasts, DNA, and more. It was recently reformulated to include a synergistic blend of twin-chain quaternary ammonium compounds and amphoteric biocides. MicroSol 3+ offers an enhanced broad spectrum efficacy and improved environmental safety. It is effective against key human pathogenic microorganisms and interacts with DNA and RNA molecules to have a deleterious effect on their secondary structure, deactivating them within blood, plasma, and other samples.

Anachem For information +44 (0) 1582 745006 www.anachem.co.uk

Laser-Induced Breakdown Spectroscopy

The LIBS2500, a laser-induced breakdown spectroscopy (LIBS) system permits instant qualitative measurements of elements in solids, solutions, and gases for use in materials analysis, biomedical and forensic analysis, environmental monitoring, and more. Designed to be smaller and lighter than its predecessor, the slimmed-down system features an improved sensitivity of 10 to 50 ppm, a series of 2048-element, linear charge-coupled device detectors, and a seven-fiber optical sampling probe with a collimating lens and a sampling lens. In contrast to the small spectral range of other LIBS systems, the LIBS2500 incorporates up to seven high-resolution spectrometers for spectral coverage as broad as 200 to 980 nm. The system operates with any 32-bit, USB-compatible Windows personal computer over a USB 1.1 or 2.0 interface. Integral application software fires the laser and identifies the element being analyzed, performing element identification, reference correlation by full pixel, reference correlation by spectral line, time-dependent analysis, and line tracking over multiple samples.

Ocean Optics For information 727-733-2447 www.OceanOptics.com

Hot/Cold Plate Analgesia Instrument

The Combination Hot/Cold Plate Analgesia Instrument can be used either as a conventional hot plate or cold plate for demonstrating that animals' receptors respond differently between "hot" and "cold" pain. This single device can test reactions in mice and rats to temperatures between 4° C and 66° C. The hot/cold plate carries out a rapid, precise screening of analgesic drugs and their effect on hot and cold receptors in the brain. The animal is placed on the surface as a foot pedal is pressed to start a clock. The observer presses the foot pedal again when the animal makes a stereotyped paw lick in response to the temperature change.

Stoelting For information 630-860-9700 www.stoeltingco.com/physio

Newly offered instrumentation, apparatus, and laboratory materials of interest to researchers in all disciplines in academic, industrial, and government organizations are featured in this space. Emphasis is given to purpose, chief characteristics, and availability of products and materials. Endorsement by *Science* or AAAS of any products or materials mentioned is not implied. Additional information may be obtained from the manufacturer or supplier.

ScienceCareers.org

Classified Advertising

From life on Mars
to life sciences

For full advertising details, go to
www.sciencecareers.org and click on
For Advertisers, or call one of our representatives.

United States & Canada

E-mail: advertise@sciencecareers.org
Fax: 202-289-6742

IAN KING Sales Manager/Industry
Phone: 202-326-6528

NICHOLAS HINTIBIDZE West
Phone: 202-326-6533

DARYL ANDERSON Midwest/Canada
Phone: 202-326-6543

ALLISON MILLAR Northeast
Phone: 202-326-6572

TINA BURKS Southeast
Phone: 202-326-6577

Europe & International

E-mail: ads@science-int.co.uk
Fax: +44 (0) 1223 326532

TRACY HOLMES Sales Manager
Phone: +44 (0) 1223 326525

CHRISTINA HARRISON
Phone: +44 (0) 1223 326510

LOUISE MOORE
Phone: +44 (0) 1223 326528

ALEX PALMER
Phone: +44 (0) 1223 326527

Japan

JASON HANNAFORD
Phone: +81 (0) 52-757-5360
E-mail: jhannaford@sciencemag.jp
Fax: +81 (0) 52-757-5361

To subscribe to *Science*:
In U.S./Canada call 202-326-6417 or 1-800-731-4939
In the rest of the world call +44 (0) 1223-326-515

Science makes every effort to screen its ads for offensive and/or discriminatory language in accordance with U.S. and non-U.S. law. Since we are an international journal, you may see ads from non-U.S. countries that request applications from specific demographic groups. Since U.S. law does not apply to other countries we try to accommodate recruiting practices of other countries. However, we encourage our readers to alert us to any ads that they feel are discriminatory or offensive.

ScienceCareers.org
We know science AAAS

POSITIONS OPEN

UNIVERSITY of CALIFORNIA, IRVINE
Department of Medicine (Infectious Diseases) and Department of Microbiology and Molecular Genetics

The Division of Infectious Diseases and the Department of Microbiology and Molecular Genetics are seeking candidates with an M.D. or M.D./Ph.D. degree(s) and a research interest in *Mycobacterium tuberculosis*. This is a tenure-track position at the **ASSISTANT PROFESSOR** level, with up to 75 percent time allotted to research. Board certification or eligibility in infectious diseases is required. Candidates must be able to perform independent research and either have current federal funding or be poised to obtain such funding. Laboratory space will be available on the University of California (UC) Irvine campus, as are multiple collaborative opportunities with clinicians and scientists in a wide variety of disciplines. The successful candidate should have a research interest related to Latino communities and will support the needs and objectives of UC Irvine's Program in Medical Education for the Latino Community **(PRIME-LC), website: http://www.ucihs.uci.edu/som/meded/primelc/.** Responsibilities to PRIME-LC will include teaching, mentoring students, and service on administrative committees. PRIME-LC is a unique program designed to provide specialized training for future physicians committed to careers in public service, health care delivery, research, and policy in underserved Latino communities. Applicants should send curriculum vitae and names and addresses of three references to: **Donald Forthal, M.D., Chief, Division of Infectious Diseases, Department of Medicine, University of California, Irvine, 3044 Hewitt Hall, Irvine, CA 92697-4028.** *The University of California, Irvine, is an Equal Opportunity Employer, committed to excellence through diversity and strongly encourages applications from all qualified applicants, including women and minorities. UCI is responsive to the needs of dual-career couples, is dedicated to work-life balance through an array of family-friendly policies, and is the recipient of an NSF Advance Award for gender equity.*

The Department of Biology, University of Missouri, St. Louis, invites applications for two full-time instructional positions: (1) **VISITING ASSISTANT PROFESSOR** (ecology, conservation), a nine-month, nonrenewable appointment to teach a graduate course in conservation biology, population biology, and other courses based on qualifications; a Ph.D. is required. (2) **LECTURER or ASSISTANT/ASSOCIATE TEACHING PROFESSOR** (general/introductory biology), a renewable appointment to teach introductory biology lecture and laboratory, plus other courses based on qualifications; biochemistry laboratory or microbiology laboratory teaching experience desirable; Master's degree and prior teaching experience required; Ph.D. applicants are encouraged. Review of applications will begin May 23, 2007, and appointments will begin August 15, 2007. Submit an application letter describing teaching interests and experience, curriculum vitae, and three letters of reference to: **Maryann Hempen, e-mail: hempenm@umsl.edu.** For additional information contact **James H. Hunt, e-mail: jimhunt@umsl.edu.**

The University of Missouri, St. Louis, is an Affirmative Action, Equal Opportunity Employer committed to excellence through diversity.

The USDA, Animal and Plant Health Inspection Service, Foreign Animal Disease Diagnostic Laboratory on Plum Island, New York, is seeking a full-time **SUPERVISORY VETERINARY MEDICAL OFFICER** (GS-15; annual salary of $115,929 to $145,400 plus benefits). Incumbent will serve as the **DIRECTOR** of the facility. *The incumbent must be a U.S. citizen and able to obtain a secret security clearance while employed for the position.* A copy of announcement number 24VS-2007-0175 (open to the public) or 6VS-2007-0223 can be obtained at **website: http://jobsearch.usajobs.opm.gov,** or call **telephone: 515-663-7266** for aplication procedures. This position will be open April 30 through May 29, 2007. *The Federal Government is an Equal Employment Opportunity Employer.*

POSITIONS OPEN

The University of Utah
Moran Eye Center

The University of Utah's Department of Ophthalmology seeks new **TENURE-TRACK FACULTY** at all academic levels with research interests in visual system function and/or disease. All research will be based in the new Moran Eye Center.

The University of Utah offers a rich academic environment with strong professional training programs in medicine, neuroscience, molecular biology, bioengineering, and computer sciences. Successful candidates will be expected to be active in professional education and demonstrate strong extramural funding potential.

Applicants should send their curriculum vitae, a statement of research interests, and names and contact information for three references to **e-mail: julee.lamothe@hsc.utah.edu.** Applications will be accepted until a suitable candidate is identified.

The University of Utah is an Equal Opportunity Affirmative Action Employer, and encourages applications from women and minorities and provides reasonable accommodations to the known disabilities of applicants and employees.

ASSOCIATE/FULL PROFESSOR
(Histology/Cell Biology/Tenure or Tenure Track)
Comparative Biomedical Sciences

Department of Comparative Biomedical Sciences, with numerous funded investigators in cell and molecular biology (including cancer biology), seeks a faculty person in histology/cell biology. Requirements: Ph.D. or equivalent degree in biological/biomedical sciences or related field; postdoctoral experience; research background in cell/molecular biology; ability to teach histology and coordinate a team-taught course in cell biology and histology in the professional curriculum; have (or will have) extramural funding. Responsibilities: establishes and maintains an extramurally funded research program; teaches in the professional curriculum; contributes to the graduate program. Salary and rank will be commensurate with qualifications. An offer of employment is contingent upon a satisfactory pre-employment background check. Application deadline is May 18, 2007, or until candidate is selected. Submit letter of application and resume (including e-mail address) to: **Dr. George M. Strain, Professor, Department of Comparative Biomedical Sciences, School of Veterinary Medicine, Louisiana State University, Reference 000490, Baton Rouge, LA 70803, telephone: 225-578-9758, e-mail: strain@lsu.edu.**

Louisiana State University is an Equal Opportunity/Equal Access Employer.

ASSISTANT (SCIENCE) CORPORATE DIRECTOR for RESEARCH PROGRAM (CDRP)

Shriners Hospitals for Children (SHC), **website: http://www.shrinershq.org/,** invites applications for the position of Assistant (Science) Corporate Director for Research Program (CDRP) at their headquarters in Tampa, Florida. We have an extensive program in basic translational and clinical research in congenital orthopedic diseases, spinal cord injury and burns in children at its 22 hospitals and eight research centers, with an annual budget of $37 million.

The successful applicant will assist the CDRP in the management of the research program, including review of research grant applications, grants administration, biomedical research related regulatory issues, program planning and evaluation, budgetary planning, research facilities development, and other research administration related activities.

Requirements: Must have a Ph.D. in a biomedical scientific area, preferably in one of the SHC's mission areas, with a background in research funding and research administration.

Submit curriculum vitae with five references by June 15, 2007, to **e-mail: ebayron@shrinenet.org** or by **fax: 813-281-7102.** *Equal Opportunity Employer/Drug-Free Workplace Program.*

ScienceCareers.org

National University *of* Singapore

NATIONAL RESEARCH FOUNDATION RESEARCH FELLOWSHIP SCHEME

The National Research Foundation (NRF), established in 2006 under the Prime Minister's Office in Singapore is charged to increase national R&D efforts, to fund basic and applied research as well as to enhance our research ability with human capital development. The NRF Research Fellowship is a major programme introduced to attract the best and brightest young scientists to carry out independent research in Singapore.

Established in 1905, the National University of Singapore (NUS) has evolved into a quality teaching and research-intensive institution, which is acknowledged as one of the premier research universities in the Asia-Pacific. The University is currently ranked in the top 20 universities by the Times Higher Education Supplement.

NUS is actively seeking outstanding young PhD graduates and post-doctoral fellows for the prestigious NRF Research Fellowship.

Eligibility

1. The Fellowship is open to all areas in science and technology with no quota on specific disciplines.
2. Young talented post-doctoral fellows at or below the age of 35 should apply.
3. There is no restriction in nationality

Terms & Remuneration

1. Gross annual salary is pegged to that of an Assistant Professor and ranges from S$72,000 to S$144,000 (approx. US$47,300 to US$94,700).
2. Successful applicants will receive research funding of up to US$1.5 million dollars over three years.
3. Outstanding Fellows may be offered tenured track or permanent positions at the appropriate academic departments in NUS.

Singapore is a vibrant garden city with year round tropical climate and rich multicultural heritage. Many top international scientists have made Singapore their home taking advantage of the excellent facilities and strong support for R&D.

Closing Date: 17 July 2007

Shortlisted applicants will be invited to Singapore to present their proposals and undergo an interview session conducted by the NRF Scientific Advisory Board.

For further information please contact:

Director, Office of Research
National University of Singapore
Singapore

Website: http://www.nus.edu.sg/ore
Email: orefellow@nus.edu.sg

NUS National University of Singapore

Northeastern UNIVERSITY

Higher Learning. Richer Experience.

Northeastern University (**http://www.biology.neu.edu/index.html**). The successful candidate will lead and expand an evolving department that plays a key role in the research and educational missions of the University.

We are seeking nationally recognized leaders who have an on-going record of competitive research funding. The **Biology Department** has 28 faculty and is currently searching to fill two additional **tenure track positions**. The Department's undergraduate programs enroll 450 biology majors and 270 undergraduates in two interdepartmental programs, biochemistry and behavioral neuroscience. Graduate programs serve 50 PhD students. There are also professional MS programs in Bioinformatics, Biotechnology, and Marine Biology.

Research interests in the department are diverse and span the spectrum from organismal to molecular studies. The successful candidate will complement these areas or will bring his/her own theme and cluster of key hires. We are especially interested in an individual who will foster and expand collaborative and interdisciplinary research. Existing interdisciplinary initiatives include Biotechnology, Neurobiology, Sensing and Imaging, and Nanotechnology, with participants from Chemistry and Chemical Biology, Physics, Engineering and the College of Health Sciences. As part of the University's continuing growth as a research institution, Northeastern is in the process of hiring 30 outstanding faculty to pursue interdisciplinary research and teaching.

A competitive start-up package will be provided. Please send a letter of application, curriculum vitae, the names and contact information for five references, and a brief description of research interests. The earliest anticipated start date is fall of 07, and the search will continue until the position is filled. Applications should be submitted electronically to **biojobs@neu.edu**.

Northeastern University is an Equal Opportunity/Affirmative Action Employer. Candidates from groups underrepresented in science are especially encouraged to apply.

FACULTY POSITIONS
Cancer Biology and Epigenomics Program (CBEP)
Children's Memorial Research Center (CMRC)
Children's Memorial Hospital
and Northwestern University
Chicago, IL

Applications are solicited for two Assistant Professor level positions in the CBEP at CMRC, with start dates in the Spring/Summer and Fall/Winter of 2007. We seek Ph.D. and M.D./Ph.D. candidates with outstanding graduate and post-doctoral training, a potential to attract external funding, and a commitment to develop an interactive research program. New laboratory space and state of the art equipment are in place. Start up packages will be generous and successful applicants will be eligible for tenure-track faculty positions in the Department of Pediatrics, Feinberg School of Medicine, Northwestern University. Candidates with research interests in these topics will be considered: cancer development and metastasis, tumor heterogeneity and drug resistance, genomic instability, tumor-microenvironment signaling, high-throughput identification of germline and somatic mutations, and integrated analyses of cancer-"omics". For further details see **http://www.childrensmrc.org/cancer_genetics/**.

Please send *curriculum vitae*, a statement of research interests, contact information of three referees, and .pdf files of most relevant publications to: **Ms. Lara Hess [lhess@childrensmemorial.org], Senior Administrative Assistant, Cancer Biology and Epigenomics Program, CMRC, 2430 N Halsted Street, Chicago, IL 60614. USA**. Review of applications will continue until positions are filled.

Northwestern University is an Affirmative Action/Equal Opportunity Employer. Hiring is contingent upon eligibility to work in the United States. Women and minority candidates are strongly encouraged to apply.

CHIEF, BIOSTATISTICS BRANCH

The Division of Cancer Epidemiology and Genetics (DCEG) of the National Cancer Institute is recruiting a Chief for its Biostatistics Branch(BB). DCEG scientists carry out a comprehensive program of research on the genetic and environmental causes of cancer, with a strong emphasis on molecular epidemiology. BB scientists play an integral role in the design, analysis and interpretation of DCEG studies, conduct independent statistical and computational research on methods for such studies, including methods for genetic epidemiology, conduct selected epidemiologic studies, improve methods for gathering and analyzing epidemiologic, clinical and laboratory data, and train pre- and post-doctoral fellows and others in biostatistics and descriptive epidemiology.

The Branch Chief directs an intramural and contract-supported research program, provides leadership and facilitates research activities of Branch scientists, and plans and directs a program of independent statistical and computational research. In addition to overseeing the administrative management of the Branch, responsibilities include supervising staff members, mentoring tenure-track investigators and post-doctoral fellows, and ensuring the scientific quality of the Branch research portfolio. BB currently has a staff of 21 scientists, including 10 tenured or tenure-track independent investigators, and additional recruitments are anticipated. Resources available to BB include contracts for computer programming and for epidemiologic field studies and access to extensive molecular epidemiology data, such as whole genome scans.

The successful candidate must hold a doctoral degree in biostatistics, statistics or a related field. He or she must demonstrate knowledge of epidemiologic and statistical methods and ability to: (1) conduct high-quality original research using mathematical and biostatistical approaches; and (2) publish such work in peer-reviewed scientific or medical journals and present it at scientific meetings. The candidate must also demonstrate administrative experience, including supervision and scientific management. The Chief, Biostatistics Branch, will be appointed with tenure at a salary commensurate with qualifications and experience. Full Federal benefits including leave, health and life insurance, long-term care insurance, retirement, and savings plan (401k equivalent) will be provided. Qualified candidates may be considered for the NIH Senior Biomedical Research Service.

Interested individuals should send a cover letter, curriculum vitae and bibliography, a brief summary of research interests and accomplishments, scientific administrative experience, copies of up to five publications or preprints, and the names and addresses of three references to: **Sandy Rothschild, Division of Cancer Epidemiology and Genetics, National Cancer Institute,6120 Executive Blvd., Room 8063, Bethesda, MD 20892, E-mail: rothschs@mail.nih.gov**.

The search will continue indefinitely until a qualified applicant is found. However, no candidate will be considered before **June 30, 2007**.

This position is subject to a background investigation.

CHIEF, OFFICE OF EDUCATION

The Division of Cancer Epidemiology and Genetics (DCEG) of the National Cancer Institute (NCI) in Rockville, Maryland, is recruiting a Chief to lead its Office of Education (OE). The DCEG OE oversees the recruitment of high-caliber post-doctoral and pre-doctoral fellows; provides oversight of fellows' training and career progression; and develops and promotes graduate program partnerships with public health and medical schools in the U.S. and abroad. Currently, there are approximately 65 post-doctoral and pre-doctoral fellows in DCEG. The OE also coordinates the DCEG summer research program that offers fellowships to high school, college, and graduate students interested in exploring careers in cancer epidemiology and genetics. The Chief represents DCEG at NCI and National Institutes of Health (NIH) meetings relevant to the coordination of training, recruitment, and educational activities. The possibility of research resources and appointment is subject to negotiation.

The successful candidate must hold a medical or doctorate degree in epidemiology, biostatistics, or a related field or demonstrate the equivalent level of epidemiologic training. He or she must possess strong communication skills, both oral and written, and provide evidence of successful mentoring, along with other relevant administrative experience. Salary will be commensurate with qualifications and experience. Full Federal benefits including leave, health and life insurance, long-term care insurance, retirement, and savings plan (401k equivalent) will be provided.

Interested individuals should send a statement of interest, curriculum vitae and bibliography, and the names and addresses of three references to: **Ms. Sandy Rothschild, Division of Cancer Epidemiology and Genetics, National Cancer Institute, 6120 Executive Blvd., Room 8063, Bethesda, MD 20892, E-mail: rothschs@mail.nih.gov, http://dceg.cancer.gov**. The search will continue indefinitely until a qualified applicant is found. This position is subject to a background investigation.

Office of the Director
Office of Intramural Research

The National Institutes of Health (NIH) in Bethesda, Maryland, the world's largest biomedical research community, is seeking applications from exceptional candidates for the position of Deputy Director in the Office of Intramural Research (OIR), Office of the Director, NIH. The NIH Intramural Research Program (IRP) has national and international recognition as it conducts laboratory, clinical, and population-based research in the interest of improving public health. The OIR coordinates functions specifically for oversight of all clinical and laboratory research in the IRP, as well as career development; the NIH animal care and use program; and human subjects research. The IRP has research partners in the public and private sectors who share common goals and work in partnership by means of specific tools, e.g., Cooperative Research and Development Agreements, which are managed by an OIR office--the NIH Office of Technology Transfer.

The incumbent has the professional management responsibility to assist the Deputy Director for Intramural Research in the planning, development, organization, coordination, and implementation of the administrative and organizational policies affecting the entire NIH. The incumbent represents the Office of the Director at the NIH Medical Executive Committee and supports the clinical research interface between the IRP, the Clinical Center and the Institutes and Centers. This position supports the work of the ongoing Advisory Board for Clinical Research that is composed of intramural and outside experts in clinical research who advise on directions for the entire intramural clinical research program. The incumbent plays an active role in research training for medical students as well.

Candidates are required to have a doctoral level degree and extensive experience in managing a biomedical research institution. Salary will be commensurate with experience. Please send applications (statement of interest, CV, bibliography and names of three references) to **Nadine Fonrose, 2 Center Drive, Room 2W09, Bethesda, MD 20892**. Applications due by **June 4, 2007**. This position is subject to a background investigation.

ScienceCareers.org

The Cyprus Institute (CyI)

Recruits Associate Directors for (A) Environmental, (B) Energy and (C) Policy Research for its Energy, Environment and Water Research Center (EEWRC)

The EEWRC is intended as an important research resource for the Eastern Mediterranean, Middle East, and North Africa, and as a gateway between the EU and the region for addressing energy, environment and water issues on the basis of science, technology and analysis. The EEWRC is a research Center under the auspices of the Cyprus Institute (CyI) which has been established in Cyprus as a novel non-profit research and educational institution. The CyI and its Research Centers strive to achieve the highest standards of excellence with an emphasis on international partnerships with world-class universities and research organizations. The EEWRC is being established in close collaboration with the Massachusetts Institute of Technology (MIT).

Position Description:
The EEWRC Associate Directors for: (A) Environmental, (B) Energy and (C) Policy Research will direct the corresponding divisions of the Center and will be responsible for the conduct of (A) Scientific research and technology development addressing environmental issues of regional and global relevance. (B) Scientific research and technology development including the generation, storage and transport of energy; the development of research thrust in the area of solar energy is considered as a high priority thrust for the Center. (C) Integrative research addressing economic and policy research in the fields of environment, energy and water development, utilization and management of significance to Europe and to the region.

The Associate Directors will report to the Director of the EEWRC. The incumbents will work in Cyprus, and will be offered a 5-year appointment, renewable upon mutual agreement, with an attractive salary and benefits package, commensurate to his/her high degree of responsibility and qualification.

Responsibilities:
The Associate Directors and Division Heads will be responsible for:
(1) Shaping the respective Divisions' research agendas of the Center in collaboration with the Director of the EEWRC. (2) Developing and implementing strategies appropriate to the Center's missions and objectives. (3) Assisting the Director of the EEWRC in recruiting staff for his/her Division within the Center. (4) Realizing and implementing the design of the research facilities appropriate to the research of the Center. (5) Developing a world-class research program, in the candidate's field of interest. (6) Contributing to the educational mission of the EEWRC and of the Cyprus Institute. (7) Raising financial and other resources for the needs of respective Divisions. (8) Initiating and sustaining high-level contacts with leading institutions throughout the world which conduct research in areas related to the respective fields.

Profile:
The incumbents should be outstanding scholars of international standing, with a minimum of 10 years' experience in conducting research. Previous responsibility for building research groups and/or managing complex projects from development to implementation would be a strong advantage. The incumbents must have excellent interpersonal skills, with strong capacities for managing human resources, and for generating and maintaining contacts in the academic, business and governmental circles, as well as obtaining support from them for the Center. Proficiency in spoken and written English is indispensable.

Applicants should clearly state for which of the three positions (A: Environment, B: Energy, C: Policy) they apply and submit: (i) a CV including a list of publications and a compilation of research grants obtained, (ii) a Vision Statement about their plans in developing the respective Division of the EEWRC, and (iii) a list of five potential referees.

Please reply before ***10 June 2007*** *to Dr. Michalis Yiangou – Cyprus Research and Educational Foundation, Alpha House, 50 Archbishop Makarios III Ave, Nicosia 1065 Cyprus, PO Box: 22745 CY 1523 Nicosia, Cyprus*
Email: ***sec.cref@cytanet.com.cy*** *Tel+357 22 761101 Telefax: +357 22 447800* ***www.cyprusinstitute.ac.cy***

Full time Tenure Track or Tenured Faculty Member

Department of Otolaryngology – Head and Neck Surgery University of California, Irvine, School of Medicine

The Department of Otolaryngology – Head and Neck Surgery at the University of California, Irvine, School of Medicine seeks a full time tenure track or tenured professor.

The successful candidate will possess a Ph.D. or MD/Ph.D. with the Ph.D. in a field related to Auditory Neuroscience. In addition he/she will have a track record of outstanding achievement in auditory research, an exceptional record of peer reviewed publications, and a history of NIH grant funding. It is preferable that the successful candidate has research interests that merge **with current departmental research**, particularly in auditory prostheses and electrophysiology.

It is expected that the candidate would be a qualified lecturer/ teacher and participate in departmental service.

Academic rank and salary will be commensurate with qualifications and experience.

Candidates are invited to submit their curriculum vitae and names of five references to:

NeuroScience Search Committee
Attn: Ms. Cathy Ta
Fan-Gang Zeng, PhD. - Committee Chair
Department of Otolaryngology – Head and Neck Surgery
101 The City Drive, South
Bldg 56, Suite 500
Orange, CA 92868-5386
Fax: (714) 456-5747

The University of California, Irvine has an active career partner program and an NSF ADVANCE Program for Gender Equity and is an Equal Opportunity Employer committed to excellence through diversity.

All Souls College Oxford

Senior Research Fellowships

All Souls College intends to elect three Senior Research Fellows with effect from 1st October 2008 (or an agreed later date): in Philosophy, in History, and in Theoretical Life Sciences (all subjects broadly conceived). The Fellowships are open to women and men.

The College regards a Senior Research Fellowship as being of comparable academic standing to an Oxford University Professorship, and applicants are expected to have a correspondingly distinguished record of achievement in research.

Further particulars, including details of emoluments and terms of appointment, application form, and copies of a memorandum for referees may be obtained from the Warden's Secretary, **All Souls College, Oxford OX1 4AL; mary.yoe@all-souls.ox.ac.uk**. See also the College's website: **www.all-souls.ox.ac.uk**. Applications, on the application form, should reach the Warden not later than **Monday, 10th September 2007.**

Environmental Energy Technologies Division Director

Lawrence Berkeley National Laboratory (LBNL) is located in the San Francisco Bay Area on a 200-acre site in the hills above the University of California's Berkeley campus and is managed by the University. A leader in science and engineering research for more than 75 years, Berkeley Lab is the oldest of the U.S. Department of Energy's National Laboratories.

Lawrence Berkeley National Laboratory (LBNL) is seeking an internationally renowned scientific leader to direct the Environmental Energy Technologies Division (EETD). EETD performs research on energy technologies, energy efficiency, indoor environmental quality, atmospheric science, and climate change. The Division has substantial effort in energy analysis, including both demand and end-use efficiency. EETD research is also coupled with Laboratory-wide initiatives on new and secure energy sources for the U.S. For more information about EETD's scientific programs, visit their website at **http://eetd.lbl.gov**.

The EETD Director plays a critical role in providing scientific leadership for the Division. The Director will develop new programs that address the national needs in the energy and environmental areas, and act as chief spokesperson for the Division in interactions with the U.S. Department of Energy (DOE) and other government agencies. The candidate should possess a distinguished record of scientific accomplishment in a discipline relevant to the Division's research, and have demonstrated experience with scientific management and development. Proven experience in building and leading collaborations among multidisciplinary teams is required. The Director is expected to build collaborative programs with UC Berkeley and other research institutions. In addition, the Director has final responsibility for all areas of management within the Division, including operations, environmental health and safety, administration, budget, and human resources.

The EETD is a multidisciplinary organization with approximately 425 scientists, engineers, technical, and administrative personnel, including participating faculty and students from the nearby UC Berkeley campus. The Division has an annual budget of approximately $50M. EETD's research is primarily funded by the DOE Office of Energy Efficiency and Renewable Energy, with significant support from other DOE offices, other federal agencies, and the State of California.

For a complete job description, or to apply online, visit: **http://jobs.lbl.gov**, select "Search Jobs", and enter **20349** in the keyword search field. Enter "Science Magazine" as your source.

LBNL is an Affirmative Action/Equal Opportunity Employer committed to the development of a diverse workforce.

For more information about LBNL and its programs, visit **www.lbl.gov**.

NIMS

National Institute for Materials Science, a Japanese national institute specializing in research on materials science, employs 550 people, including 400 researchers.

RESEARCHER POSITIONS

1. Recruiting field

a. Fuel Cell Materials; Hetero-interface, Electrode, Solid Electrolyte, Separator
b. Functional Materials and Physics, Ferroic Materials, Novel piezoelectrics
c. Molecular biology, Cell biology, Nanobiology
d. Solid-state electrochemistry, ionic conduction at heterojunctions, ion-conductive solids

2. Any field of Materials Science

We are seeking researchers in metals, ceramics, organics, biomaterials, semiconductors, compound materials, and so on.

For more details, **http://www.nims.go.jp/eng/employment/index.html**

Giving the Gift of Breath

Lovelace Respiratory Research Institute is the only institute fully devoted to respiratory research & works under an endowment w/substantial intramural support for emerging programs. We also work in alliance with the University of New Mexico Health Science Center.

Associate Scientist & Postdoctoral Opportunities

Associate Scientist in Physiology (S1207): Ph.D. & laboratory experience in respiratory & cardiovascular physiology. Aerosol delivery in toxicological/biological laboratory, immunology or virology experience highly desirable. ABSL-3 experience ideal.

Associate Scientist (N4307) or Postdoctoral Fellow (N4107), w/Dr. K.C. Kim: Ph.D. & a strong background in molecular/ cell biology, preferably in lung physiology & cell signaling &/or lung pharmacology. Will focus on the elucidation of the molecular mechanism of the anti-inflammatory role of Muc1 mucin using both in vivo & in vitro systems.

Postdoctoral Fellow (E5402), w/Dr. K. Harrod, to study immunology of emerging and biothreat pathogens. Established background in molecular and cellular immunology.

Postdoctoral Fellow or Associate Research Scientist (E4407), w/Dr. J.C. Seagrave, with experience in proteomics, including 2D gels, protein identification, biomarker discovery, protein/peptide mass spectrometry required. SELDI experience desired but not required. Documented record of publication in the field.

Postdoctoral Fellow or Associate Research Scientist (E1001), w/Dr. Y. Tesfaigzi, to study the role of inflammatory mediators in regulating signaling of apoptosis & autophagy in airway epithelial cells of mice & humans. Experience in analysis of cell signaling, transcriptional regulation, &/or genomic & proteomic techniques is desirable.

Postdoctoral participants are encouraged to write grants & become members of our scientific staff.

Senior Research Associate & Associate Research Scientist positions are available in the above & other areas as well.

Send CV, research goals & 3 references w/ contact information, referencing position # to
HR Office, 2425 Ridgecrest Drive SE
Albuquerque, NM 87108
Fax: 505-348-4976; E-mail: hrmail@lrri.org.
Visit: www.lrri.org. EOE/MF

Lovelace

www.LRRI.org

Cincinnati Children's Research Foundation (CCRF)

Division of Experimental Hematology (Director: Dr. David Williams, MD)

Cincinnati Children's Hospital Medical Center

The Division of Experimental Hematology is pursuing excellence in research with Programs in Hematopoietic Stem Cells, Cancer, Cell Signaling, Leukemia and Molecular and Gene Therapy. The Division is seeking to recruit

Molecular and Gene Therapy Faculty

We seek to fill several faculty positions with candidates interested in basic or translational research focusing on the molecular treatment of inherited or acquired genetic diseases and cancer to expand/complement our expertise in gamma-retroviral, AAV and lentiviral vectors. We seek faculty with substantial experience (1) in the area of innovative stable vector systems/targeted genetic correction, and (2) clinical gene therapy trials. Academic rank will depend on faculty credentials and experience. Close collaboration is available with the existing faculty and other divisional programs (**www.cincinnatichildrens.org/research/div/exp-hematology/**) and the Division of Hematology/Oncology. The Program supports a range of projects from basic research to translational development to facilitate implementation of phase I/II trials in Molecular and Gene Therapy.

To apply, please forward your CV and a brief statement of your research interests to: **David A. Williams, MD**, Director, Division of Experimental Hematology and **Punam Malik, MD**, Program Leader, Molecular and Gene Therapy Program; via E-mail to **Ms. Joyce Lewis, Business Manager, Division of Experimental Hematology: joyce.lewis@chmcc.org**; **CCRF, Cincinnati Children's Hospital Medical Center, 3333 Burnet Ave ML 7013, Cincinnati OH 45229-3039**.

Cincinnati Children's Hospital Medical Center is an Affirmative Action/Equal Opportunity Institution. Women and minorities are encouraged to apply.

DIRECTOR

Metabolic Diseases Research Program

The **Singapore Institute for Clinical Sciences (SICS)** is a new institute within the Agency for Science, Technology and Research (A*STAR). Our mission is to develop disease-oriented clinical and translational research programs in focused disease areas. SICS is based at the Biopolis, Singapore's world-class biomedical sciences complex, and adjacent to other A*STAR research institutes. SICS also has a research building that is in close proximity to the National University of Singapore and the National University Hospital.

The **Metabolic Diseases Research Program** is a new initiative, intended as a multi-disciplinary program involving disease-oriented laboratory and clinical research in diabetes and obesity. This program will span the molecular basis of disease through the development of new therapies and diagnostics, and will include investigational medicine studies in humans. We seek an internationally renowned specialist in the field of metabolic diseases as the **Program's Director** - to define the specific research focus, recruit and support an internationally competitive team of principal investigators as well as to develop the program as a bridge for collaborations between basic scientists and clinical investigators. Excellent funding has been allocated by A*STAR to enable the recruitment of up to 5 principal investigators and a total of up to 70 staff members, plus equipment purchases and laboratory running costs.

The Director and the research teams will work closely with a number of other programs in Singapore that provide important and useful synergies, including:

- Singapore Consortium of Cohort Studies
- Singapore Bioimaging Consortium
- Singapore Tissue Network
- National University of Singapore
- NUS - Duke Graduate Medical School
- Clinical research facilities (inpatient and outpatient)
- NUS - Lilly Centre for Clinical Pharmacology
- A*STAR funded graduate students and postdoctoral scholars (both M.D. and PhD) selected for training in Program laboratories

We invite senior internationally-recognised investigators in the area of metabolic diseases to apply for the Directorship. Preference will be given to physician scientists and clinician investigators with a track record of publication in international refereed journals as well as a demonstrated ability to lead a major research program and to collaborate with other groups. Candidates will be offered joint appointment at the National University of Singapore. Remuneration will be commensurate with the experience and qualifications of the successful candidate.

Singapore Institute for Clinical Sciences
A*STAR

Interested applicants, please enclose your curriculum vitae and indicate your area of interest to:

Professor Judith Swain (Judith_swain@sics.a-star.edu.sg)
or Dr Kevin Young (Kevin.young@thersagroup.com)

All applications will be treated in strict confidence.

ScienceCareers.org

ScienceCareers.org

FACULTY OF MEDICINE
HEALTH SCIENCE CENTRE
DEPARTMENT OF PHARMACOLOGY AND TOXICOLOGY

The Department of Pharmacology and Toxicology, Faculty of Medicine, University of Kuwait invites applications for the following academic position:

Assistant/Associate/Full Professor in:

1. **Clinical Toxicologist:** Applicants should have experience in Clinical Pharmacology and Toxicology.
2. **Clinical Pharmacologist:** Applicants should have experience in Clinical Pharmacology.

CONDITIONS OF APPOINTMENT: Total monthly salaries will be within the following scale according to qualifications and experience (1 KD = 1.9 St. Pound, US $3.4 approximately).

	Professors Min-Max	Associate Min-Max	Assistant Min-Max
Clinical	KD. 3930 – 4172	KD. 3275 – 3517	KD. 2810 – 3050
Non-Clinical	KD. 2950 – 3192	KD. 2265 – 2507	KD. 2950 - 3192

OTHER BENEFITS: Conference attendance. Gratuity. Housing/furniture allowance. Free medical treatment in Kuwait. Free annual round-trip air tickets from country of citizenship or permanent residence for self and family up to three dependent children. Baggage and freight allowance. Education fees for a maximum of three children in Kuwait from elementary through high school. Tax-free salary. Currency is transferable without restriction. 60 days paid annual leave.

METHOD OF APPLICATION: Curriculum vitae which should include the names of 3 referees; personal particulars; copy of the relevant pages of passport, qualifications with dates, career history, teaching experience, research accomplishments and where appropriate clinical experience should be sent no later than 60 days from the date of this advertisement to:

THE DEAN
(RECRUITMENT OFFICE)
FACULTY OF MEDICINE
KUWAIT UNIVERSITY
P.O. BOX 24923
13110 SAFAT, KUWAIT
FAX: (+965) 5318454

Do what you love.

Love what you do.

www.sciencecareers.org

ScienceCareers.org
We know science AAAS

UNIVERSITY MEDICAL CENTER
THE UNIVERSITY OF TOLEDO

Tenure-track Faculty Positions in Immunology

The Department of Medical Microbiology and Immunology at the University of Toledo College of Medicine, formerly known as Medical University of Ohio (**www.meduohio.edu**), is seeking to hire several tenure-track faculty members at the level of Assistant/Associate Professor. Immunology has recently been identified as a specific target area of institutional programmatic growth. Candidates must hold a Ph.D., M.D., or equivalent degrees and have at least three years of relevant postdoctoral experience (Assistant Professor) or faculty appointment (Associate Professor). Independent funding is highly desirable.

A successful candidate will be expected to develop/maintain an externally funded, basic and/or translational research program in the fields, including (but not limited to) transplant immunology, autoimmunity, host immune responses to pathogens, and vaccine development and to participate actively in the departmental teaching mission.

Applications should include: (a) CV, (b) a brief summary of research interests, past accomplishments, and future plans, and (c) names and addresses of three references. All materials should be sent to:

Akira Takashima, M.D., Ph.D., Professor and Chairman
Department of Medical Microbiology and Immunology
University of Toledo, Health Science Campus
3000 Arlington Ave.
Toledo, OH, 43614-2598

Applications will be reviewed immediately upon receipt.

The University of Toledo is committed to diversity and equal opportunity. Applications from women and minority candidates are strongly encouraged.

DUKE NUS
GRADUATE MEDICAL SCHOOL SINGAPORE

Director, Program in Emerging Infectious Diseases

The Duke-NUS Graduate Medical School Singapore (GMS) is unique in bringing post-baccalaureate, research-intensive medical education to Asia, and represents a truly global partnership between two leading universities: National University of Singapore and Duke University. The GMS shares a modern campus with Singapore's largest hospital and several national research centers. The GMS is creating a world-class, academically based Program in Emerging Infectious Diseases that will both enhance health care in Singapore and serve as a national and international resource of excellence in emerging infectious diseases. The mission of the Program faculty will be to conduct high-level basic and applied research, and to train graduate students, post-doctoral fellows, and physician scientists in the disciplines relevant to emerging infectious diseases.

We are seeking an individual with exceptional scientific credentials and leadership skills to head the Program. The position of founding Director will include full salary, a very generous start-up and five years of annual research funding. The Director will be provided with the space and resources necessary to recruit 6-8 outstanding faculty members at all academic ranks. The packages for these faculty recruits would include full salary, generous start-up, and five years of annual research funding of up to S$500K/p.a., assuring a stable base of support that can be supplemented by competitive grant awards, which are expanding rapidly in Singapore. The director and the faculty members he/she recruits will join the pioneering Duke and Singapore investigators already affiliated with the GMS (see **www.gms.edu.sg**).

Interested candidates should send a CV and the names of three references to: **Mariano A. Garcia-Blanco, M.D., Ph.D., Chair, Search Committee on Emerging Infections, Duke-NUS Graduate Medical School, Singapore by email to: director.id@gms.edu.sg**

The GMS is a collaboration of the Duke University School of Medicine and the National University of Singapore.

ASSISTANT/ASSOCIATE/ FULL PROFESSORS CHEMISTRY, STRUCTURAL BIOLOGY & DRUG DISCOVERY/PROTEOMICS

The College of Medicine and the H. Lee Moffitt Cancer Center & Research Institute, a comprehensive NCI designated center, at the University of South Florida is seeking applications from Assistant, Associate and Full Professor level individuals to participate in the Department of Interdisciplinary Oncology and the Drug Discovery Program. The Drug Discovery Program (http://www.moffitt.usf.edu/research/molecular/drugdisc.htm) is expanding Synthetic Organic Chemistry, Structural Biology and Proteomics components to synergistically grow with its outstanding Cancer Biology/Signal Transduction/Gene Regulation components. Structure-based drug design and focused combinatorial chemistry library approaches will be strongly supported by the current and developing research infrastructure. The Moffitt Cancer Center has several core lab facilities and services available such as: NMR, structural biology, molecular modeling, high throughput screening, proteomics and microarray shared facilities.

Chemistry, position #11911: Synthetic organic chemists looking for strong biological collaborators with outstanding core facilities or industrial synthetic organic chemists looking for a wide open research agenda are encouraged to apply. Successful candidates must possess a Ph.D. in synthetic organic chemistry or related areas with preferred experience in molecular recognition and/or bioorganic/synthetic/medicinal chemistry.

Structural biology, position #14600: Applicants must possess a Ph.D. in Structural Biology or related area and have a demonstrated track record in X-ray crystallography and the elucidation of structure-function relationships. Areas of research focus could include protein structure-function relationships, protein/drug interactions and protein/protein interactions. Experience in the areas of growth factor signal transduction, proteins involved in oncogenesis or tumor suppression, and cell cycle regulation is preferred. Applicants should have a strong desire to interact with scientists engaged in drug discovery and design including synthetic organic chemists and computational chemists.

Proteomics, position #13301: Candidates must possess a Ph.D. degree and a demonstrated expertise in Drug Discovery or Proteomics in the cancer area with a minimum of five years experience. We are looking for individuals with proven experience in cancer drug discovery; experience in utilizing or developing proteomics techniques will be a plus. The individual will be expected to develop independent, fundable research projects and collaborate with other investigators at Moffitt.

Candidates for the rank of Assistant Professor must have at least two years postdoctoral experience. Candidates for the rank of Associate Professor must have a proven track record of independent federal funding and research and at least five years experience at the Assistant Professor level. Candidates for Full Professor must have a proven track record of independent research and a national/international reputation in their field and at least five years experience at the Associate Professor level. The Moffitt Cancer Center and Research Institute, a National Cancer Institute-designated comprehensive cancer center, and USF offer an outstanding salary, benefits and relocation package. Academic rank and salary will be commensurate with experience and qualifications. These tenure track positions will be assigned to the Department of Interdisciplinary Oncology within the College of Medicine.

Please send curriculum vitae, statement of research interests, and the names and addresses of three or more references to Professor Said Sebti, Drug Discovery Program, H. Lee Moffitt Cancer Center, 12902 Magnolia Drive, SRB-3, Tampa, Florida 33612. Electronic CVs preferred to said.sebti@moffitt.org. The selection committee will begin reviewing applications May 1, 2007 and will continue until a suitable candidate is hired. Important: Please state on your cover letter which of the 3 positions you are applying for by indicating the actual position number.

H. LEE MOFFITT Cancer Center & Research Institute

The End Of Cancer Begins Here.

A National Cancer Institute Comprehensive Cancer Center At the University of South Florida

USF HEALTH

USF Health is committed to increasing its diversity and will give individual consideration to qualified applicants for this position with experience in ethnically diverse settings, who possess varied language skills, or who have a record of research that supports/benefits diverse communities or teaching a diverse student population. The University of South Florida is an EO/EA/AA Employer. For disability accommodations, contact Kathy Jordan at (813) 745-1451 a minimum of five working days in advance. According to FL law, applications and meetings regarding them are open to the public.

www.moffitt.org

CSIRO

Post Doctoral Fellowships 2007

CSIRO is Australia's national science organisation with over 6,500 staff located across the country. It is one of the largest and most diverse research organisations in the world, with its research delivering solutions for agribusiness, the environment, information and communication technologies, health, advanced materials and manufacturing, minerals and energy, services, transport and infrastructure.

The CSIRO Postdoctoral Fellowship Scheme provides the opportunity for postgraduates to undertake postdoctoral research projects within CSIRO for a period of three years. 19 postdoctoral positions are now being offered across a broad range of disciplines, as follows:

- Deep radio imaging techniques;
- Modeling of nanoscale heat transfer;
- Advanced biomaterials synthesis by plasma processing;
- Ecosystem modeler for savanna and climate;
- Atmospheric instrumentation scientist in geosequestration studies;
- Molecular approaches to marine nutrient cycles;
- Multiscale modeling of bulk nanomaterials;
- Designing smart nuclear instruments – mathematical/ computational physicist;
- Physical oceanographer Southern Ocean processes;
- Wireless ad hoc and sensor networks;
- Drosophilia chemoreception;
- Host-pathogen coevolutionary biology;
- Protein cross-linking technologies tailored for biomedical applications;
- Structural studies on the organisation of the basement membrane;
- Epigenetic mechanisms in an animal model: the aphid;
- Gut microbiome interrelationships and human health;
- Functional genomic approaches for plant resistance to sap-sucking insect pests;
- Early detection of Alzheimer's disease and development of a blood diagnostic test;
- Biofibre informatics.

Full details of the positions being offered can be found on the CSIRO Careers website.

For further information, selection documentation and details on how to apply, visit **www.csiro.au/careers**
Alternatively contact CSIRO on 1300 301 509

hrmC052104

www.csiro.au

ScienceCareers.org

ScienceCareers.org

From life on Mars to life sciences

For careers in science, turn to *Science*

If you want your career to skyrocket, visit ScienceCareers.org. We know science. We are committed to helping you find the right job, and to delivering the useful advice you need. Our knowledge is firmly founded on the expertise of *Science*, the premier scientific journal, and the long experience of AAAS in advancing science around the world. ScienceCareers.org is the natural selection.

www.sciencecareers.org

Features include:

- Thousands of job postings
- Career tools from Next Wave
- Grant information
- Resume/CV Database
- Career Forum

ScienceCareers.org
We know science AAAS

What's your next career move?

- Job Postings
- Job Alerts
- Resume/CV Database
- Career Advice from Next Wave
- Career Forum

Get help from the experts.

ScienceCareers.org
We know science AAAS

www.sciencecareers.org

Department of Health and Human Services
National Institutes of Health
National Institute on Aging

Health Scientist Administrators
Aging Physiology Branch And Biological Resources Branch

The Biology of Aging Program (BAP) in the National Institute on Aging (NIA), a major research component of the National Institutes of Health (NIH) and the Department of Health and Human Services (DHHS), is recruiting for two positions:

- **Health Scientist Administrator, Aging Physiology Branch** - preferred expertise in the areas of musculoskeletal biology including basic bone, muscle and/or cartilage biology and/or extensive research background in cell biology, molecular biology and physiology. The incumbent will work with a team of Health Scientist Administrators covering the areas of cardiovascular, immunology, physiology and endocrinology of aging, including research on stem cell biology and aging that is administered by the Aging Physiology Branch. Incumbent will provide scientific and administrative leadership in assisting in the direction and management of a program of research in the area of Musculoskeletal Biology. The selected candidate will assist in the program development and administration of research grants, training grants, fellowships and cooperative agreements and contracts dealing with the areas of expertise listed above.
- **Health Scientist Administrator, Biological Resources Branch** - preferred expertise in the use of animal models, and in the areas of cell and molecular biology, physiology or biochemistry. Incumbent will provide scientific and administrative leadership in assisting in the direction and management of a program of research in the area of Animal Models of Aging. The selected candidate will assist in the program development and administration of research grants, training grants, fellowships, cooperative agreements, and contracts dealing with the areas of expertise listed above.

Both positions involve close interaction with scientific investigators, scientific administration of grants and contracts, program planning and development, reporting on scientific progress, and identifying opportunities for future research.

Salary is commensurate with qualifications and research experience (research experience in basic aspects of the biology of aging is highly desirable). For qualifications required, evaluation criteria, and application instructions search for the vacancy announcements at: **http://jobsearch.usajobs.opm.gov/a9nih.asp** - Announcement Numbers: **NIA-07-181800-DE-CR** and **NIA-07-181801-MP-CR** (**Health Scientist Administrator, Aging Physiology Branch**) and **NIA-07-178013-DE-CR** and **NIA-07-178014-MP-CR** (**Health Scientist Administrator, Biological Resources Branch**). If additional information is needed, call Cheryl Caponiti at (301) 594-2147. Applications must be received no later than July 13, 2007.

DHHS and NIH are Equal Opportunity Employers.

Tulane University
Health Sciences Center

Faculty Position in Immunology

The Department of Microbiology and Immunology at Tulane University School of Medicine invites applications for a tenure track faculty position in immunology at the rank of **Associate Professor** or **Professor**. We are primarily interested in investigators whose research complements existing strengths in host-pathogen interaction and vaccine development, although outstanding investigators working in other areas of immunology are encouraged to apply. The successful candidate will join a multidisciplinary department focusing on molecular, cellular, and genetic aspects of infectious diseases and cancer. He/she is expected to possess and maintain a dynamic, extramurally funded research program and to contribute to the teaching of medical and graduate students.

Tulane University is a world class educational and research institute. In the post-Katrina era, Tulane University School of Medicine is undergoing a period of unprecedented expansion and renewal; and will be hiring new faculty at all ranks. The Department of Microbiology and Immunology offers generous recruitment packages, renovated laboratory space, and an interactive environment. For further information about the Department and Tulane University School of Medicine, visit our web site at: **http://www.som.tulane.edu/departments/microbiology**.

Essential qualifications for the position include a Ph.D. or M.D. degree and a demonstrated record of accomplishment in extramural funding, publication, and teaching. Applicants should submit a curriculum vitae, statement of research interests and goals, and the names, addresses, e-mail addresses, and telephone numbers of three qualified references to: **Faculty Search Committee, Tulane University Health Sciences Center SL38, Department of Microbiology and Immunology, 1430 Tulane Avenue, New Orleans, LA 70112**. Completed applications may be sent by e-mail to **aepick@tulane.edu**. Initial review of applications will begin **July 1, 2007** and will remain open until the position is filled.

Tulane University is an Equal Opportunity, Affirmative Action Employer and encourages applications from minorities, women, and other qualified persons.

The University of Iowa

Chair Department of Biology

The College of Liberal Arts and Sciences seeks a Chair for the Department of Biology at the rank of Professor. The candidate should be an internationally recognized scientist with an outstanding research program. We welcome applicants from any area of the biological sciences, while particularly encouraging candidates who would enhance one or more of our existing strengths in cell and developmental biology, evolution, genetics, and neurobiology.

The Department has embarked on an aggressive program of growth that includes ongoing faculty recruitment, the recent modernization of the biology complex, and the addition of a new building. It is active in interdisciplinary programs, with strong ties to the other colleges involved in biomedical research. The Biology faculty is well funded by both federal and private sources. The successful candidate will bring vision, energy, and a demonstrated commitment to diversity to shape the future of the Department through hiring and mentoring of new faculty, with an aim to further improve the Department's strong national reputation for research and teaching. More about the department may be viewed at **www.biology.uiowa.edu**.

The Applicant should submit a curriculum vitae, a statement of research interests and administrative philosophy, and the names and addresses of at least three references to: **Dean Joseph Kearney, College of Liberal Arts and Sciences, 240 Schaeffer Hall, The University of Iowa, Iowa City, IA 52242-1409**. Applications accepted by mail or electronically to **biology-chairsearch@uiowa.edu**.

The University of Iowa is an Affirmative Action/Equal Opportunity Employer. Minority candidates and women are encouraged to apply.

ScienceCareers.org

From physics to nutrition

For careers in science, turn to *Science*

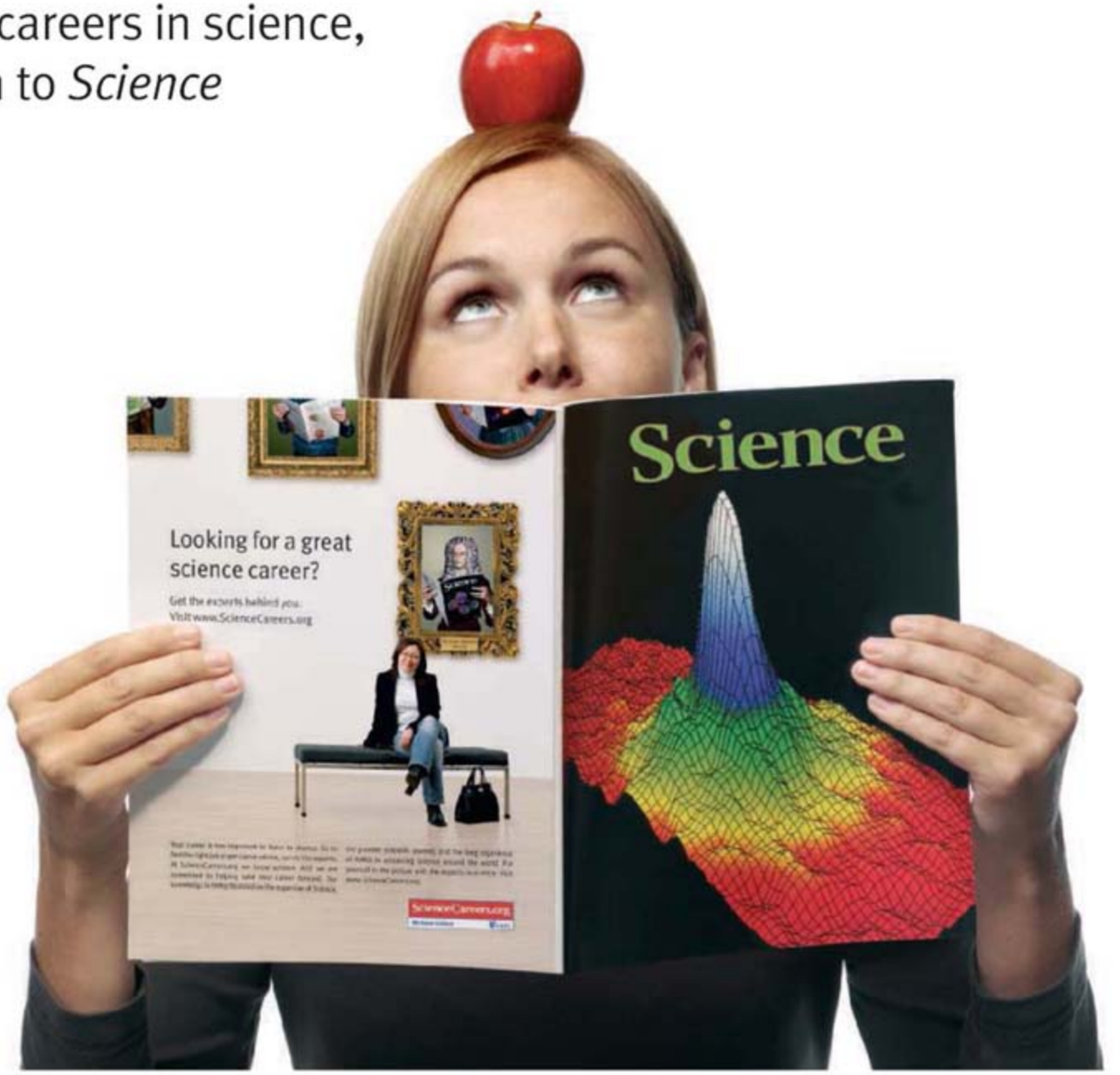

If you want your career to bear fruit, don't leave it to chance. At ScienceCareers.org we know science. We are committed to helping you find the right job, and to delivering the useful advice you need. Our knowledge is firmly founded on the expertise of *Science*, the premier scientific journal, and the long experience of AAAS in advancing science around the world. ScienceCareers.org is the natural selection. www.sciencecareers.org

Features include:

- Thousands of job postings
- Career tools from Next Wave
- Grant information
- Resume/CV Database
- Career Forum

ScienceCareers.org
We know science AAAS

FOCUS ON CAREERS

Searching for Information on Career Trends?

Don't miss *Science's* Career Features for the latest in career reports and practical advice.

UPCOMING FEATURES:

May 11: Focus on Diversity

June 8: Regional Focus: NC/Research Triangle

June 22: International Careers Report: UK and Ireland

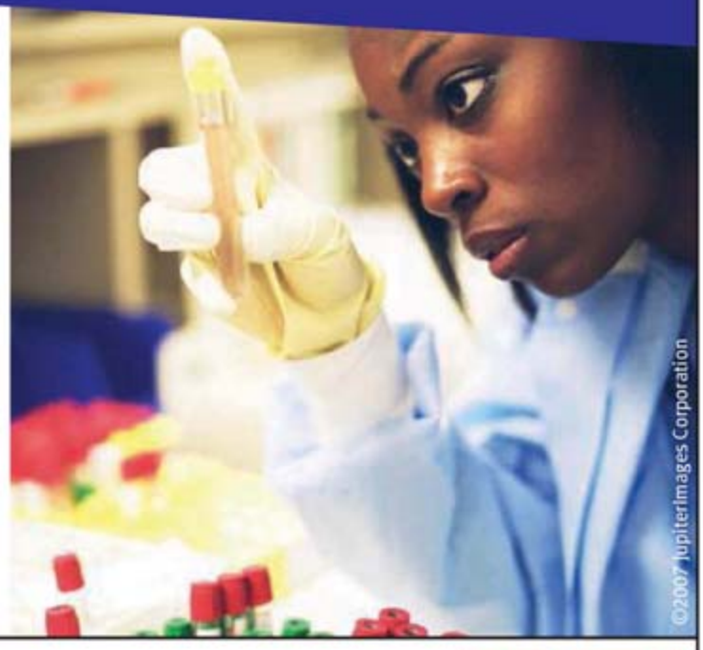

Also available online at www.sciencecareers.org/businessfeatures

ScienceCareers.org
We know science AAAS

Get the experts behind you.
www.ScienceCareers.org

- Search Jobs
- Next Wave *now* part of ScienceCareers.org
- Job Alerts
- Resume/CV Database
- Career Forum
- Career Advice
- Meetings and Announcements
- Graduate Programs

All these features are FREE to job seekers.

ScienceCareers.org
We know science AAAS

Principal Investigator Positions
The Institute of Brain Science, Fudan University

The Institute of Brain Science, Fudan University, Shanghai, China, is a newly established research institution, supported by the National "985" Program of the Ministry of Education, People's Republic of China. The Institute is currently recruiting principal investigators (PIs) in the field of neuroscience, with an emphasis on the areas of cognitive neuroscience and developmental neurobiology.

I. Senior PI

- Candidates should have a Ph.D. and/or M.D. degree and possess a long-standing research experience in brain science. Independent research capacity is absolutely needed. Those who have the experience of leading a laboratory or research unit will be given a favorable consideration.
- Candidates should have a systematic and impressive research record, with important papers published in peer-reviewed international journals of high reputation as a corresponding author.
- Candidates must work in the Institute for more than 9 months per year, when appointed.

II. Junior PI

- Candidates should have a Ph.D. and/or M.D. degree and possess at least 2-year experience of post-doctoral training.
- Candidates should have a good research record in brain science, with substantial papers published in peer-reviewed international journals as a corresponding author or the first author.
- Candidates must work in the Institute for more than 9 months per year, when appointed.

Interested individuals please contact the Institute of Brain Science (E-mail: ibs@fudan.edu.cn. TEL: +86-21-54237641, Fax: +86-21-54237643) for the application form, or send a package including curriculum vitae, a list of publications, reprints of 3-5 representative papers, a one page summary of the research accomplishments, and a one to two page research proposal, and arrange to have three letters of reference sent to: Ms. Rong Chen, Institute of Brain Science, Mail Box 236, Fudan University, 138 Yixueyuan Road, Shanghai 200032, China.

The closing date for applications is June 20, 2007. Applications received after this date or those which do not conform to the above criteria will not be accepted.

POSITIONS OPEN

University of Michigan Geriatrics Center

BIOGERONTOLOGY
University of Michigan

The University of Michigan Geriatrics Center is seeking one or more junior or senior faculty members to carry out independent research focused on the biology of aging and its impact on late life pathophysiology. Research that emphasizes mammalian models, or use of proteomic and genomic approaches, would be of particular interest. Successful candidates will be housed in newly constructed Geriatrics Center space, and will receive a primary tenure-track or tenured appointment in a basic science or clinical Department as appropriate. Minimum qualifications are a Ph.D., M.D., or equivalent degree, several years of highly productive postdoctoral research, and a clear interest in problems relevant to biogerontology. Substantial startup funding will be available for each selected candidate.

Applicants should submit curriculum vitae, a brief (one to two-page) description of research interests, a synopsis of current and previous research support, and contact information for three to five referees, to: **Rich Miller, 3001 BSRB, P.O. Box 2200, 109 Zina Pitcher Place, Ann Arbor, MI 48109-2200.**

The University of Michigan is an Equal Opportunity Employer committed to maintaining diversity in its hiring programs.

PHARMACOLOGY ASSISTANT PROFESSOR
Tenure Track, Begin July 1, 2007

The Philadelphia College of Pharmacy, the founding unit of the University of the Sciences in Philadelphia, invites applications for a new position in the Deparment of Pharmaceutical Sciences. Ph.D. degree in an area relevant to pharmaceutical sciences, strong research interests that complement existing areas within the Department, and demonstrated record or potential of obtaining extramural funding required. Successful candidate will teach pharmacology at undergraduate, professional (Pharm.D.), and graduate levels.

The Department consists of 13 tenure-track and two nontenure-track faculty, three postdoctoral fellows, five staff members, and approximately 165 undergraduates in the B.S. Programs in Pharmacology/Toxicology and Pharmaceutical Sciences, as well as about 55 graduate students. The Department has a state-of-the-art, Association for Assessment and Accreditation of Laboratory Animal Care-accredited, fully staffed vivarium, tissue culture facilities, and a wide array of analytical instruments including high performance liquid chromatography, liquid chromatography/mass spectrometry, flow cytometer, absorbance and fluorescent plate readers, image analyzers and scanning electron microscopes. Our manufacturing/industrial pharmacy laboratory is used for teaching and academic/contract research. Our new McNeil Science and Tech Center provides increased space for research and/or teaching in line with the University's strategic imperative to increase research activities. We also have fluorescence spectrophotometers, infrared spectrometers, nuclear magnetic resonance, and confocal microscopes.

For more information consult our **website: http://www.usip.edu.** Submit curriculum vitae, letter of application that addresses research interests and teaching experience, and contact information for (a minimum of) three references as soon as possible to: **Ruy Tchao, Ph.D., Chair, Faculty Search Committee, 600 S. 43rd Street, Philadelphia, PA 19104, e-mail: r.tchao@usip.edu, telephone: 215-596-8978.** Application review will begin immediately and will be accepted until position is filled. *Affirmative Action/Equal Opportunity Employer.*

POSITIONS OPEN

HAYWARD ENDOWED CHAIR in GENETICS, GENETIC EPIDEMIOLOGY, and COMPARATIVE MEDICINE

The Department of Comparative Pathobiology in the School of Veterinary Medicine at Purdue University invites applications for the Hayward Endowed Chair in Genetics, Genetic Epidemiology, and Comparative Medicine from individuals with an established record of scholarship in comparative genomics and genomic approaches to disease prevention. Individuals with expertise in the areas of comparative oncology and environment-gene interactions in the etiology of cancer are especially invited to apply. The School is committed to building a program in comparative genomics and has dedicated three additional faculty positions. The successful candidate for the Hayward Endowed Chair will have the opportunity to participate in the search and recruitment of these positions with the goal of building a focused research and training program. For information on the Department please visit **website: http://www.vet.purdue.edu/cpb/.**

Purdue University is undergoing a rapid expansion of life sciences and biomedical research. The University has an NCI-designated cancer center **(website: http://www.cancer.purdue.edu/)** and new laboratory facilities for interdisciplinary research in Discovery Park **(website: http://www.purdue.edu/dp),** including the Bindley Bioscience Center and the Birck Nanotechnology Center. Additional opportunities for collaboration and translational research are available through the expanding cooperation with the Indiana University School of Medicine in Indianapolis.

Candidates should have a Ph.D., M.D. and/or D.V.M. or equivalent degrees and a successful record of scholarship and extramural research funding. They should have a commitment to the educational and outreach missions of the University. The successful candidate is expected to have the qualifications for appointment at the Full Professor level. This is a ten-month academic year appointment.

Applicants should submit via e-mail complete curriculum vitae, statement of research and teaching interests, and the names and addresses of three references in PDF format to: **Dr. Harm HogenEsch, Department of Comparative Pathobiology, Purdue University. E-mail: whiteb@purdue.edu.** Review of applications will begin June 1, 2007, and continue until the position is filled. Women and individuals in underrepresented groups are encouraged to apply. *Purdue University is an Equal Opportunity/Equal Access/Affirmative Action Employer.*

POSTDOCTORAL POSITION in TRANSLATIONAL IMMUNOLOGY
Yale University School of Medicine

Postdoctoral position to study the molecular, cellular, and immunobiology of the innate immune response is available at the Yale School of Medicine. Candidates should have a Ph.D. degree and experience in molecular biology, microbial pathogenesis, or immunology. The research will be under the supervision of **Richard Bucala, M.D., Ph.D.** in the Department of Internal Medicine. Please submit your curriculum vitae along with a copy of a prior publication and the names of three references to **e-mail: richard.bucala@yale.edu.** *Yale is an Affirmative Action/Equal Opportunity Employer.*

POSTDOCTORAL POSITION available immediately in the Transplant Immunology Laboratory, Northwestern University, Chicago, to study tolerance in transplant models. The position requires a Ph.D. or equivalent with background in immunology, molecular and cell biology. Animal experience, particularly microsurgery skills preferred but not required. Send curriculum vitae to: **Xunrong Luo, M.D., Ph.D., Northwestern University,** via **e-mail: xunrongluo@northwestern.edu.**

POSITIONS OPEN

EDGEWOOD Chemical Biological Center

Since 1917 - a Tradition of Solutions

SENIOR RESEARCH SCIENTIST FOR CHEMISTRY
U.S. Army Research, Development and Engineering Command
U.S. Army Edgewood Chemical Biological Center
Aberdeen Proving Ground, Maryland

The U.S. Army Edgewood Chemical Biological Center seeks a Senior Scientist to conduct research in chemical defense. Primary areas of interest are reaction mechanisms, reaction kinetics, advanced analytical chemistry, and molecular recognition technologies. The successful candidate will conduct targeted laboratory studies to fill critical information gaps, including characterization of agent physical and chemical properties; development of toxicological data; and development of agent fate data. The application of this research includes detection and decontamination of chemical agents. Incumbent will select areas of investigation in fundamental mechanistic chemistry, reaction dynamics, or related aspects of experimental physical chemistry. The position requires a Ph.D in chemistry, preferably physical chemistry, or equivalent experience and must possess expertise in analytical methodology with substantial background in relevant research. Candidates must be able to work independently as a Senior Scientist. In-depth research and some nanotechnology experience and demonstrated creativity and productivity through patents, inventions, and/or significant publications are essential. *Applicants for this position must obtain and maintain a secret security clearance. U.S. citizenship required.* Salary commensurate with experience (ST $129,024 to $152,000). For detailed vacancy announcement, including specific qualification and application requirements, refer to announcement DAST-07-05 at **website: http://www.usajobs.gov.** Deadline for application is 15 June 2007.

The U.S. Army is an Equal Opportunity Employer.

LECTURER in the BIOLOGICAL SCIENCES
The University of Chicago Biological Sciences Collegiate Division

Biological Sciences. The University of Chicago invites applications for a nontenure-track, four-quarter position as **LECTURER-CORE BIOLOGY LABORATORY DIRECTOR** starting fall 2007. The responsibilities will include teaching one section per quarter of introductory biology for nonmajors, planning, coordinating, and teaching all sections of the state-of-the-art introductory biology laboratories, and coordinating the biology laboratories with the co-requisite Biological Sciences Writing Program courses. Further, the position will include opportunities to design and develop curricula for both the lecture and the laboratory portions of our introductory biology program for nonmajors. We are seeking broadly trained Ph.D. applicants with teaching and research experience and competency in cell and molecular, genetics, microbiology, physiology, and ecology and evolution at the introductory level. In addition, he/she may also develop and teach an introductory course for nonmajors in one of these areas. Send curriculum vitae, three letters of reference, and a statement of teaching interest by June 18, 2007, to: **Kila Roberts, The University of Chicago, 924 E. 57th Street, Room 328, Chicago, IL, 60637.** *The University of Chicago is an Equal Opportunity/Affirmative Action Employer.*

Poster Deadline June 15/07
20 Poster Awards available

Inflammatory Diseases of Barrier Organs

July 12-14 2007 in Kiel/ Germany

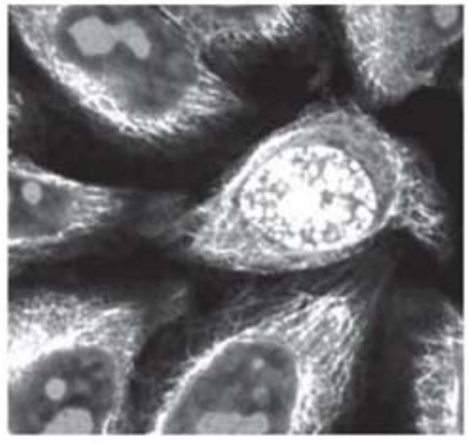

The understanding of the function of an intact barrier and the pathophysiology of its impairment in diseases affecting barrier organs is of increasing clinical importance. In the National Genome Research Network (NGFN), key molecular pathways in chronic inflammatory disorders such as Crohn´s disease, asthma, psoriasis and sarcoidosis have been discovered. Focus of the research consortium is the genetic and functional genomic exploration of innate and adaptive immunity and the interplay with environmental factors.

The international **NGFN-Symposium Inflammatory Barrier Diseases Meeting 2007** will represent many of the leading research groups in this field. A comprehensive programme is offered that will discuss primary genetic etiology, epithelial defence mechanisms, the molecular pathophysiology of impaired barrier integrity and its translation into clinical research programs. A satellite meeting dealing with the genetics and functional genomics of human aging will complete the programme.

Especially young researchers are invited to join the symposium. An interactive poster session but also the social events will ensure discussions between a renowned international faculty and young colleagues. The presenters of the 20 best posters will be awarded a travel stipend for the symposium.

We are looking forward to welcoming you and your colleagues in Kiel!

Find more information, programme and registration forms at:

www.ikmb.uni-kiel.de/bm2007

NGFN Nationales Genomforschungsnetz

Federal Ministry of Education and Research

University Hospital Schleswig Holstein
Institute for Clinical Molecular Biology
Schittenhelmstrasse 12
24105 Kiel Germany

POSITIONS OPEN

MOLECULAR INTERACTIONS
University of Victoria, Victoria
British Columbia, Canada

The Department of Biochemistry and Microbiology invites applications for a tenure-track **ASSISTANT PROFESSOR.** We are particularly interested in a **BIOCHEMIST** who has a research focus of molecular interactions in immunology or bacterial pathogenesis. The appointment is to complement existing strengths in macromolecular structure, cellular signaling, regulation of gene expression, proteomics, and infectious disease. Applications from excellent scientists working in other areas of biochemistry will be considered. The University of Victoria offers outstanding research infrastructure, particularly in proteomics, DNA sequencing, and X-ray crystallography. There are ample opportunities to collaborate with researchers in the Faculty of Science, the Island Medical Program, and the British Columbia Cancer Research Centre. The appointee will be expected to develop a rigorous, independent research program, funded by external support, and participate in teaching the undergraduate curriculum. The start date is 1 July 2008.

Qualifications include a Ph.D., postdoctoral experience, demonstrated research excellence, and teaching potential. Letters of application should clearly outline research and teaching interests, be accompanied by curriculum vitae, and provide the names and contact information of at least three referees. Applications should be submitted by July 15, 2007.

All qualified candidates are encouraged to apply; *however, in accordance with Canadian Immigration requirements, Canadians and permanent residents will be given priority.*

Dr. Robert D. Burke, Chair
Department of Biochemistry and Microbiology
University of Victoria
P.O. Box 3055 STN CSC
Victoria BC V8W 3P6
Canada
E-mail: biocmicr@uvic.ca
Website: http://web.uvic.ca/biochem

The University of Victoria is an Equity Employer and encourages applications from women, persons with disabilities, visible minorities, Aboriginal Peoples, people of any sexual orientation or gender, and others who may contribute to the further diversification of the University.

UNIVERSITY of NEW MEXICO
Department of Chemistry and Chemical Biology
Position Announcement

The Department of Chemistry and Chemical Biology at the University of New Mexico (UNM) invites applications and nominations for an open-rank faculty position in chemical biology. This is a probationary appointment leading to a tenure decision or may be tenured depending on the title and qualifications. The University is located in beautiful Albuquerque, New Mexico, in close proximity to the Sandia National Laboratories and Los Alamos National Laboratory. Opportunities for collaborations with the National Laboratories and with other research centers on campus are abundant and strongly encouraged. Both beginning and established investigators are welcome, but must have a Ph.D. by appointment date with strong training in one or more areas of bioorganic/biochemistry. Postdoctoral experience, the potential for excellence in teaching and for developing an outstanding, externally funded, and nationally competitive program at the University and national levels are preferred. For complete information you may access Faculty Postings, or request a copy of the announcement from the **Search Chair.** For best consideration, applications should be received by May 30, 2007. The position will remain open until filled. **Website: http://chemistry.unm.edu.** *UNM is an Equal Employment Opportunity/Affirmative Action Employer/Educator and a renowned minority serving institution. The Department strongly encourages women and minorities to apply.*

POSITIONS OPEN

COLLEGE of PHARMACY
THE UNIVERSITY OF TEXAS AT AUSTIN

DEAN, COLLEGE of PHARMACY
The University of Texas

The University of Texas at Austin invites nominations and applications for the position of Dean, College of Pharmacy.

The University of Texas at Austin is the oldest and largest of the University of Texas System's 15 component institutions. It has a main campus of more than 350 acres and 115 buildings, approximately 50,000 students, about 2,800 faculty members, and a staff of more than 14,500. The College of Pharmacy has 44 tenure/tenure-track faculty, 45 nontenure-track faculty, and 518 Pharm.D. students enrolled.

As Chief Executive Officer of the College, the Dean is expected to provide vision and leadership for the college. We are looking for a dynamic, congenial leader with outstanding abilities in communication, research, and scholarship; administration; fundraising; teaching; and service to the community. Evidence of having secured financial support for research and/or educational purposes and knowledge of, or experience in, raising funds from alumni and in the public and private sectors must be shown. The Dean reports to the Executive Vice President and Provost of the University.

The candidate must qualify for appointment to the rank of Professor with tenure in an academic unit of the college and have an earned Ph.D. in Pharmacy or a related pharmacy field and/or a Pharm.D. with appropriate residency or fellowship training. An undergraduate pharmacy degree (B.S. or entry-level Pharm.D.) is preferred. The Dean must demonstrate a strong national and international record of academic accomplishment.

We welcome interested parties to submit application materials by June 15, 2007. Review of applications will begin immediately upon receipt and will continue until the finalists are named. Letters of application from interested candidates should be submitted electronically (only), along with curriculum vitae and the names of five references, to the following e-mail address, **e-mail: phrmdean@uts.cc.utexas.edu.**

Robert O. (Bill) Williams III, Ph.D.
Johnson & Johnson Centennial Professor of Pharmacy
Consultative Committee for the Selection of the Dean of Pharmacy
College of Pharmacy
The University of Texas at Austin
Austin, TX 78712

E-mail address for inquiries: **e-mail: phrmdean@uts.cc.utexas.edu.**

The University of Texas is an Equal Opportunity and Affirmative Action Employer.

POSTDOCTORAL SCIENTIST POSITIONS

We looking to fill fully supported Postdoctoral positions at Seattle Biomedical Research Institute (SBRI). These positions are in the Laboratory of **Dr. Patrick Duffy (website: http://www.sbri.org/research/duffy.asp)** and **Dr. Leo Stamataos (website: http://www.sbri.org/research/stamatatos.asp).** The research will be conducted at SBRI (see **website: http://www.sbri.org),** an independent, nonprofit research institute that is affiliated with the University of Washington. SBRI's research facility is in the fast-developing South Lake Union biotechnology hub that is home to many research organizations on the forefront of life science research. In addition to an exciting work environment, we also offer a competitive salary and benefits package. Apply online directly to the SBRI job postings webpage at **website: http://www.sbri.org.** *SBRI values a diverse workforce and is an Equal Opportunity Employer.*

POSITIONS OPEN

DIRECTOR. Applications and/or nominations are sought for the Director of the new Washington, Wyoming, Alaska, Montana, Idaho (WWAMI) Medical Education Program at Washington State University-Spokane. This position is also appointed as Assistant Dean at the University of Washington School of Medicine. Please see our full ad in the April 27, 2007, issue of *Science* or visit us online at **website: http://www.hrs.wsu.edu.**

Find your future here.
↓
ScienceCareers.org
We know science AAAS

Get your questions answered.
Careers Forum
ScienceCareers.org
We know science AAAS

MARKETPLACE

Widely Recognized Original & Guaranteed
KlenTaq1
8¢/u Truncated Taq DNA Polymerase Withstand 99°C
US Pat #5,436,149
Call: **Ab Peptides**
Fax: 314•968•8988
e-mail: abpeps@msn.com
1•800•383•3362
www.abpeps.com

Oligo Synthesis Reagents
Specialty CPG Supports
Linkers, Spacers, & Modifiers
Bulk Reagent Pricing Available
BIOSEARCH TECHNOLOGIES
+1.800.GENOME.1
www.btisynthesis.com

For news and research with impact, turn to *Science*

There's only one source for news and research with the greatest impact – *Science*. With over 700,000 weekly print readers, and millions more online, *Science* ranks as one of the most highly read multidisciplinary journals in the world. And for impact, *Science* can't be beat. According to the recently released Thomson ISI Journal Citation Report 2005, *Science* ranked as the No. 1 most-cited multidisciplinary journal with a citation factor of 31. Founded in 1880 by inventor Thomas Edison, and published by the nonprofit AAAS, *Science*'s reputation as the leading source for news, research, and leading edge presentation of content continues to grow. Looking for news and research that will impact the world tomorrow? Then look in *Science*.

www.sciencemag.org

To join AAAS and receive your own personal copy of *Science* every week go to www.aaas.org/join

Science
AAAS

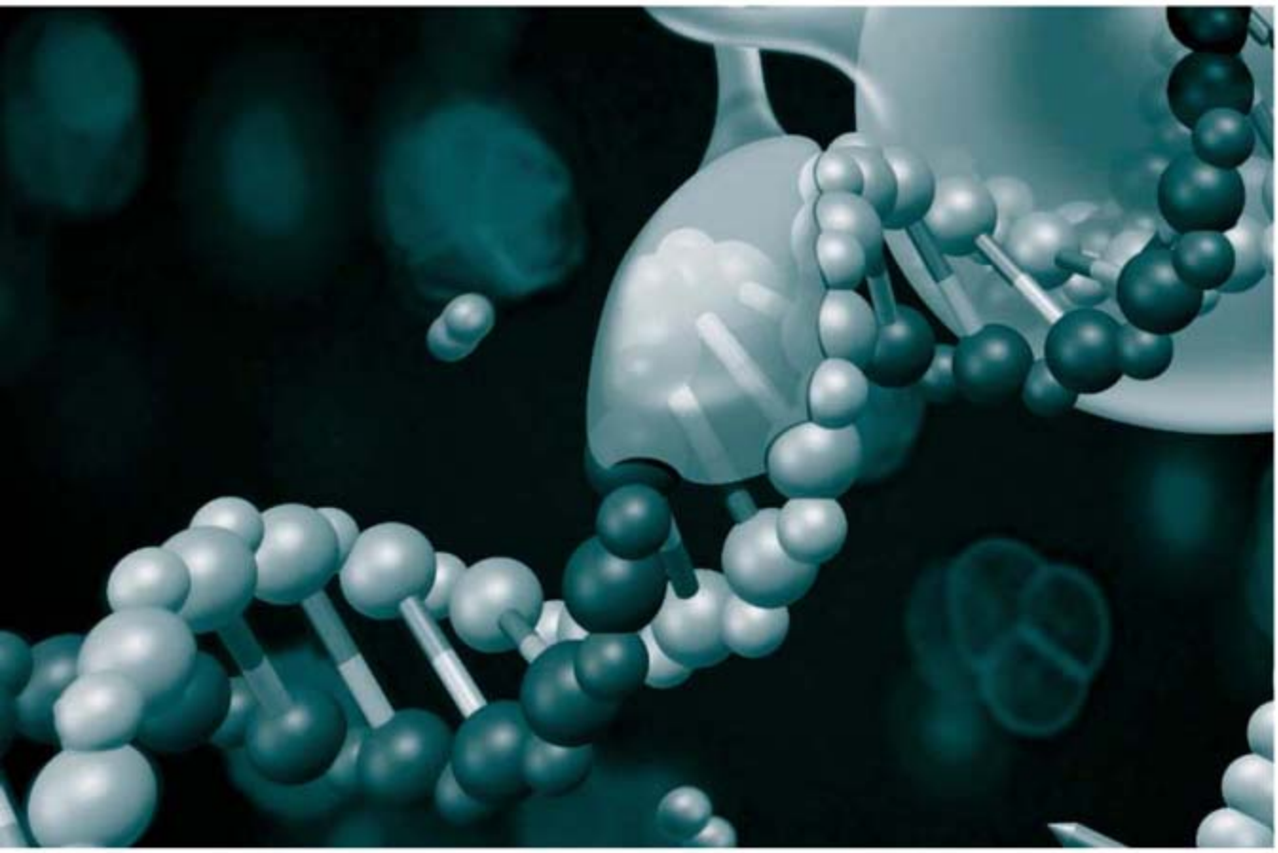

Redefining Fast PCR

Bio-Rad's unique iProof™ high-fidelity DNA polymerase delivers unsurpassed speed and fidelity, with higher yields and fewer reaction failures, for all your PCR needs.

Features and Benefits

- Extreme speed — Increased processivity dramatically reduces extension steps (to 15–30 sec/kb) and overall run times (to 25–35 min)
- Unmatched fidelity — Novel proofreading enzyme is the most accurate thermostable polymerase (52-fold more accurate than *Taq*)
- Minimal enzyme usage — Enhanced processivity enables the use of less enzyme (0.25–1 U/reaction)

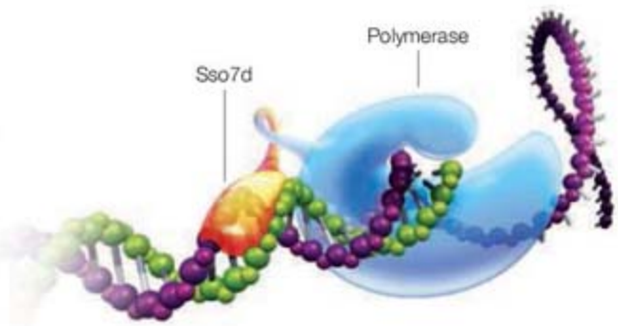

Fusing the double-stranded DNA binding protein Sso7d to iProof polymerase gives it a powerful sliding grip on the replicated DNA.

For more information, visit us on the Web at
www.bio-rad.com/ad/iProof/

Practice of the polymerase chain reaction (PCR) may require a license.

Visit us on the Web at **discover.bio-rad.com**
Call toll free at 1-800-4BIORAD (1-800-424-6723);
outside the US, contact your local sales office.

BIO-RAD